

# Machine-makers matter

*Nature* is pleased to name Lyn Evans, the project manager of the Large Hadron Collider, as its 2008 newsmaker of the year.

In its purest form, science stands above the individual. Evidence does not depend on who discovers it, and scientists must willingly give up ideas that evidence does not support.

The world's most powerful particle accelerator — the Large Hadron Collider (LHC) — is a monument to this ethos. Based at CERN, the particle-physics laboratory near Geneva, Switzerland, the collider has faced some tough times — not least of which is an accident that has left the collider out of commission until at least July 2009. Once the damage is repaired, however, thousands of physicists will watch as the massive machine begins to probe some of the most fundamental laws of nature. And they will eagerly test their theories against the collider's output.

Yet the LHC, like science itself, is not just a platonic ideal. It lives because of the very real individuals who believe in its purpose. And one individual stands out in this regard: Lyn Evans. Evans has spent the past decade and a half as the LHC's project manager, a role that has at times required him to be a scientist, diplomat, politician and foreman. His unique blend of political acumen and technical skill has been instrumental in seeing the project through to its completion, and for this reason *Nature* has singled Evans out as its newsmaker of the year (see page 862).

Evans has taken a personal approach to building this imposing collider. His meetings are often small and casual, and he has been known to settle project schedules over a beer. This informal approach has not always worked to the LHC's advantage: a cost increase in 2001 was in part due to poor bookkeeping, and Evans's one-on-one approach sometimes left managers out of the loop.

On balance, however, Evans's mild-mannered but intellectually critical management style and his unfailing optimism have helped

see the project through the difficult times to its completion.

Evans should also be recognized for the place he occupies in the social structure of science. In devoting so much of his career to the LHC, he joins a long tradition of scientists who have committed their lives to producing the telescopes, microscopes, accelerators and laboratory methods that others will use to make discoveries. Sometimes the individuals who make these commitments are celebrated; witness this year's Nobel Prize in Chemistry for the development of green fluorescent protein. But more often, they labour in comparative obscurity. Singling out Evans serves as a reminder of the vital importance of these pioneers. Evans is unlikely to be an author on the papers that will someday announce the LHC's breakthroughs, but without him, these discoveries would never have come to pass.

Perhaps because of the diverse roles he has played in his career, Evans seems to appreciate the importance of all the individuals involved in the project. He will happily spend his time chatting with the hundreds of physicists, engineers and shop-floor technicians who have laboured on the LHC's construction. And he will just as happily talk with any of the thousands of politicians, executives and citizens who have supported its completion. Twenty-five nations backed the project, and by some estimates, as many as a billion people watched when the machine circulated its first protons this September.

The LHC is an example of truly global scientific imagination, and Lyn Evans exemplifies the spirit that brings such imagination to fruition. Science may be greater than any one individual, but it is people such as Lyn Evans who allow its progress to continue. ■

**"Lyn Evans exemplifies the spirit that brings truly global scientific imagination to fruition."**

## Facilitating the future

Europe needs a better way to plan, prioritize and fund the next generation of research infrastructure.

A newly released 'roadmap' for Europe's future research infrastructure is, first, a reminder that the continent already has quite a lot of it. The list ranges from the Large Hadron Collider at CERN, the particle-physics laboratory near Geneva, Switzerland, to the five campuses of the European Molecular Biology Laboratory, to the Isaac Newton Group of Telescopes in the Canary Islands near Spain. Such facilities open up research opportunities for scientists across the continent — and are particularly important for tapping the talents of scientists in smaller countries, who generally have less access to the kind of national facilities built by richer nations such as the United Kingdom, France or Germany.

Unfortunately, the roadmap is also a reminder that Europe still does not have any systematic way to plan, prioritize or fund these infrastructure projects. Each joint facility to date has been an ad hoc effort, with scientists often working for years to forge a coalition of nations willing to pay for it.

The resulting delays can be costly or even fatal. Biologists warn that life-science infrastructures, such as archives or access to distributed specialist resources, have not kept pace with the progress of the field (see *Nature* **447**, 377–378; 2007). And Earth scientists are beginning to worry about the slow progress in finding partners for *Aurora Borealis*, a planned €635-million (US\$870-million) research icebreaker ship, the technical design of which was finalized earlier this month.

The governments of the European Union are aware of the problem. In 2002, they set up the European Strategy Forum on Research Infrastructures (ESFRI), a group of senior science administrators who advise national governments and the European Commission on

infrastructure needs. In 2006, the ESFRI released its first roadmap: a list of 35 already-proposed infrastructure projects that the forum deemed to be of pan-European interest. The projects on that list ranged from the large — a €1-billion, 5-megawatt neutron spectroscopy facility known as the European Spallation Source — to the small: a €12-million digital infrastructure for the arts and humanities.

Then on 9 December, at its meeting in Versailles, France, the ESFRI released an updated roadmap that lists 44 projects, including all but one of the original 35. The construction cost for all 44 initiatives over the next 12 years would be about €18 billion. But the EU's Seventh Framework research programme allocates just €1.7 billion to such costs; the shortfall will need to come from elsewhere.

The creation of the ESFRI is an important first step, but it is not nearly enough: the forum neither funds the projects nor sets explicit priorities among them. Some research communities have started to set their own priorities — a notable recent example being the astronomers (see *Nature* 456, 427; 2008) — and other communities should certainly follow their lead. But no one is setting Europe's infrastructure priorities across science as a whole.

Such priority-setting is only going to become more urgent as budgets tighten during the economic downturn. So the EU's next

step should be to set up an independent European authority that has the power to evaluate infrastructure projects on the basis of their scientific promise, to prioritize them and, ultimately, to fund them. The European Research Council (ERC), which funds basic research on the sole basis of scientific excellence, could serve as a model.

Indeed, such a 'European Research Infrastructure Council' might even serve to stimulate additional funding — just as the ERC process has encouraged member states to fund top-notch projects that have been rejected by the ERC on the basis of its limited budget.

Granted, the creation of such a body would require a transfer of national responsibility and substantial research money — things that are hard to make palatable to national governments. And the new organization would have to deal with the headaches that follow from Europe's wildly varying finance, licensing, tax and social-security systems. Nonetheless, it could pool money, competence and negotiating power, and vastly improve the painstakingly slow process of supplying scientists in Europe with the tools they need to produce the kind of collaborative research they are expected to deliver.

Scientists prove every day that true collaboration can be every bit as successful in Europe as it is elsewhere. It is the responsibility of EU policy-makers to make sure that this doesn't change. ■

## Eyes west

Could the United States topple Europe as the driver of international climate-change regulations?

**T**he recently concluded United Nations conference on climate change, in Poznań, Poland (see page 846), marked the last phase of eight years of foot-dragging by US negotiators. For one last time, the designated US representatives at international climate talks came from the administration of President George W. Bush, who rejected the Kyoto Protocol almost immediately after taking office and whose team has stalled any meaningful progress since.

But by this time next year, when the world's negotiators convene in Copenhagen to try to hammer out a deal to succeed the Kyoto accord, the lame ducks will be gone. In their place will be representatives of a new US president, Barack Obama, who has promised to make control of greenhouse-gas emissions a central focus of his administration.

How much progress Obama can make in his first 11 months remains to be seen, and it is far from clear that the world will be able to fashion a workable consensus in Copenhagen. But a consensus now seems much more likely than it was.

As if to dramatize how difficult the task will be, European Union (EU) representatives crashed and burned last week as they attempted to lay out the next phase of Europe's otherwise groundbreaking emissions trading scheme (see page 847). Caving to political pressure from Italy and Poland, among others, French president and outgoing EU chief Nicolas Sarkozy crafted a compromise that satisfies many — in the fossil-fuel industry, that is. Rather than holding heavy industries accountable for their emissions, the new deal gives the heaviest polluters significant leeway. The very industries that account for some of the highest levels of emissions, such as steel and cement, can now apply

for exemptions that could grant them free emissions permits even after 2020. Everyone else will have to start paying in 2013.

EU leaders praised the deal, but the concessions it contains are likely to harm the trading system irrevocably, allowing industry to further delay the radical changes needed to clean up its business.

Climate leadership may pass instead to the United States, which will need to set tough emissions limits — and stick to them — if it wants to do better than Europe. If Obama is as serious as he dares to be about establishing a cap-and-trade regime, his administration will need to carefully consider the lessons of the European experience. For starters, a US system should avoid giving away emission permits so freely, and consider setting a minimum price for them.

A promising development on this front is Obama's appointment of Steven Chu, a Nobel prizewinning physicist and energy-technology advocate, as secretary of energy (see page 849). The energy department spent US\$1.4 billion on research and development for renewable, fossil and nuclear energies in 2008 — less than a quarter of what it was 30 years before, when adjusted for inflation. Chu, who made renewable energy the *raison d'être* of California's Lawrence Berkeley National Laboratory, which he has led since 2004, should reverse that trend. Chu not only 'gets' climate change, he gets its urgency. Private investment is making incremental advances in the short-term cost-effectiveness of renewable energy. But technology-driven, order-of-magnitude leaps are essential in the medium term: time for the long term has run out.

It was in 1997 — the year the Kyoto Protocol was adopted — that Chu won his Nobel prize for cooling atoms to a near standstill with laser light. He did the work at the now-moribund Bell Labs in New Jersey — a place Chu fondly remembers for favouring boldness. "Some failure was expected," Chu said at a recent seminar, "but there was an emphasis on recognizing failure quickly, and moving on to other opportunities." That is a credo worth adopting — both in the creation of carbon-free energies, and in the creation of carbon-emission markets. ■

# RESEARCH HIGHLIGHTS 2008

As an end of the year round-up we asked *Nature's* editors to nominate their favourite papers published elsewhere this year. For a pick of favourites from *Nature* itself, see page xii.

## A healthier haul

*Science* **321**, 1678–1681 (2008)

With the biomass of the world's top marine predators at about a tenth of what it was in the 1950s, fisheries need management that will stop them collapsing. In September, Christopher Costello of the University of California, Santa Barbara, and his colleagues used data from 1950 to 2003 and 11,135 fisheries to conclude that individual tradable quotas (ITQs) could help.

ITQs avoid the misaligned incentives of the 'tragedy of the commons' whereby people plunder resources as quickly as possible. The quotas divide a limited total catch exclusively among fishermen who work a fishery, and allow them to sell the rights to their share. Because the value of these shares increases with the overall productivity of the fishery, each fisherman has an incentive to manage it well. Costello's team found that the proportion of ITQ-managed fisheries that had collapsed by 2003 was half that of the non-ITQ fisheries.



D. WHITESIDE/REUTERS

## BIOPHYSICS

### Mob rule

*Proc. Natl Acad. Sci. USA* **105**, 11754–11759 (2008)

The crowding inherent within cells may affect not only protein movement and folding, but also shape, according to Pernilla Wittung-Stafshede at Rice University in Houston, Texas, and her colleagues.

They focused on the VlsE protein, a proposed virulence factor in *Borrelia burgdorferi*, the bacterium that causes Lyme disease. VlsE is usually rugby-ball shaped, but the team found that it adopts different equilibrium shapes *in vitro* in the presence of varying levels of a polymeric 'crowding agent' that mimics cytoplasmic macromolecules. When the native protein is loosened up by a denaturing agent or by heat, two new structures — a 'bean' shape and a roughly spherical conformation — intervene between the rugby ball and the denatured protein as soon as the crowding agent is added.

If crowding can be 'tuned', it might be

possible to expose different sites in proteins and alter their behaviour.

## NEUROSCIENCE

### Glia on fire

*Nature Neurosci.* **11**, 450–456 (2008)

Glial cells in the brain are generally considered to be electrically inert, simply providing a support system for excitable neurons. But at least one class of glial cell can fire action potentials, scientists showed this year.

Ragnhildur Káradóttir, now at the University of Cambridge, UK, and her colleagues reported that about half of NG2-expressing glia in the rat brain receive input from synapses. The cells also show currents when stimulated by the neurotransmitter glutamate.

The excitable NG2 glia were much more vulnerable to oxygen starvation, which promotes glutamate release, than were non-excitable glia. Such oxygen starvation occurs in stroke, cerebral palsy and spinal-cord injury.

less sophisticated food. In March, researchers from the Australian National University in Canberra discovered how the jelly might confer royal status.

When Ryszard Maleszka and his colleagues silenced the expression of a DNA methyltransferase enzyme called Dnm13 in larvae, 72% of them developed into queens, as though they had been fed royal jelly. This enzyme has an important role in packaging DNA across the genome and thus influences gene expression.

## NANOTECHNOLOGY

### Super speakers

*Nano. Lett.* **8**, 4539–4545 (2008)

Imagine a loudspeaker that is bendy, transparent and stretches to twice its length without breaking or changing the intensity of the sound it amplifies. This is what Kaili Jiang and Shoushan Fan of Tsinghua University in Beijing, China, and their colleagues have made. By attaching one of their prototype films to the screen of an iPod they have used it to play sound from the device.

The invention exploits the thermoacoustic effect, which was first realized in the nineteenth century with the platinum thermophone. The effect describes what happens when a material is heated and cooled, thus expanding and contracting the air around it, which creates sound waves. The film on the researchers' iPod generates sound 260 times more efficiently than this historical gadget because the sheets of parallel carbon nanotubes that it is made of warm up and transfer heat to air faster.

## ZOOLOGY

### Queen Bee

*Science* **319**, 1827–1830 (2008)

Fertile queen honeybees (*Apis mellifera*; pictured left, queen shown centre) and sterile workers develop from genetically identical larvae, but the former are fed royal jelly, whereas the latter gobble





## GENETICS

## Many but rare

*Science* **320**, 539–543 (2008)

In April, Jon McClellan at the University of Washington in Seattle and his colleagues confirmed that schizophrenia is largely genetic in origin, and found many individually rare mutations that make a person more likely to develop it. Scientists had thought that the combined effects of common variants were responsible.

The team analysed the DNA of 150 individuals with schizophrenia and 83 with childhood-onset schizophrenia, searching their subjects' genomes for rare deletions and duplications that disrupt genes. These were much more common in the genomes of people with schizophrenia than in those of healthy controls. Most schizophrenia patients had mutations that others did not have but that tended to be in the same genes. The genes altered by these mutations were disproportionately involved in neurodevelopmental pathways.

## ASTROPHYSICS

## Cosmic tiara

*Astrophys. J.* **680**, 295–311 (2008)

A halo of stars surrounds the Milky Way, but researchers disagree how it got there. One theory proposes that it formed from the same cloud of gas as the Galaxy itself; the other says the halo is the remains of several 'dwarf galaxies' that were originally separate from but close to the Milky Way proper. A survey of about three million halo stars weighs heavily in favour of the latter hypothesis.

Eric Bell of the Max Planck Institute for Astronomy in Heidelberg, Germany, and his colleagues compared data from the Sloan Digital Sky Survey with several models. The halo's structure, they say, suggests that it is what remains of several smaller galaxies that were subsumed into the Milky Way after it formed.

## EVOLUTION

## Genetic bric-a-brac

*Science* **320**, 1210–1213 (2008)

Many single-celled organisms collect genes from other organisms — a process known as horizontal gene transfer — but multicellular organisms tend not to. Tiny invertebrates called bdelloid rotifers were found to buck this trend, taking on genetic material from a range of other species, including bacteria, fungi and plants.

Multicellular creatures rarely do this because their germ line is sequestered in the gonads, explain Eugene Gladyshev,

Matthew Meselson and Irina Arkhipova at Harvard University. Bdelloid rotifers are different. They often experience desiccation, potentially opening up their cell membranes to chunks of outsider DNA. This unusual way of injecting diversity into their genomes may help to explain why these rotifers have gone 40 million years without having sex.

## BIOCHEMISTRY

## Catalytic creator

*Science* **319**, 1387–1391 (2008)

In March, David Baker at the University of Washington in Seattle and his colleagues reported the rational design of enzymes for reactions that have no known catalysts.

The team took advantage of the down time of many other people's computers to perform the calculations necessary to build models of how synthetic enzymes would interact with substrates. They then made 72 different enzymes (including that pictured above), 32 of which catalyse a 'retro-aldol' reaction, which involves the breaking of a carbon–carbon bond in a certain non-biological molecule. They verified the structures of two of their enzymes with X-ray crystallography.

Many other labs have since worked with Baker's enzymes and confirmed their activity.

## ORGANIC CHEMISTRY

## Tag-team catalysts

*Science* **322**, 77–80 (2008)

David Nicewicz and David MacMillan at Princeton University in New Jersey created a double-headed catalytic system to give an

aldehyde molecule an alkyl group in a specific position, and with a specific geometry.

Their technique depends on a pincer movement. A ruthenium-based 'photoredox' catalyst that shifts electrons one at a time when hit with fluorescent light is one prong; an organocatalyst developed to move single electrons is the other.

The light-activated ruthenium catalyst creates an alkyl halide radical; the aldehyde is dealt with by the organocatalyst; and the reactants are brought together with precision so as to give most of the product the desired handedness. The reaction is easy to perform and broadly applicable, say the authors, and will make life easier for those developing new drugs.

## NEUROSCIENCE

## MRI beebop

*PLoS ONE* **3**, e1679 (2008)

The inside of an MRI scanner may not have the ambience of a jazz club, but Charles Limb and

Allen Braun of the National Institutes of Health in Bethesda,

Maryland, think it brings out the process of improvisation in unprecedented detail.

They watched six professional jazz pianists first playing a scale on a specially created keyboard, and then improvising using only the notes from that scale. In a second experiment, the musicians followed a given melody exactly and then made up new trills and transitions around it. A pre-recorded quartet occasionally provided accompaniment.

When the musicians improvised, their brains showed greater activity in the medial prefrontal cortical area — a region associated with self-expression. Lateral prefrontal areas, which are linked to self-monitoring, became less active. These changes (pictured as warm and cool colours, respectively, left) may occur in all types of spontaneous creativity, Limb and Braun say.

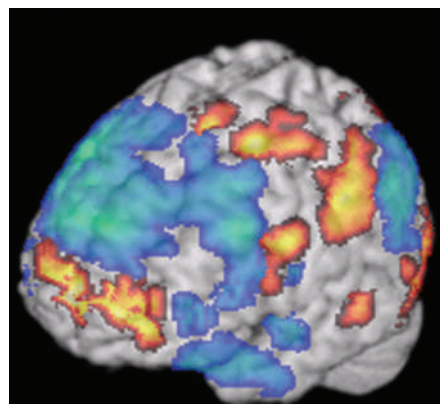
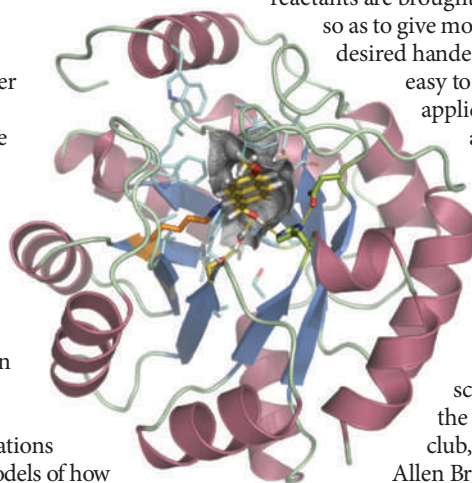
## HUMAN BIOLOGY

## Bird's eye view

*Biol. Psychiatry* **65**, 17–21 (2009)

People with autism have incredibly keen eyesight, seeing almost as acutely as birds of prey.

The surprise finding from Emma Ashwin and her colleagues at the University of Cambridge, UK, showed that the unusually keen senses that have been associated with







the condition since the 1940s stem not from how intensely autistic people feel their senses, but from how sharp their senses actually are.

Ashwin and her team tested 15 men with autism-spectrum disorders using the Freiburg Visual Acuity and Contrast Test, and found them to have, on average, 20:7 vision. This means they can see the same detail on an object 20 metres away that a person with average vision can see at 7 metres. Birds of prey have roughly 20:6 vision. What gives people with autism hawk-like vision isn't known.

## PHYSICS

### Black holes on the strand

*Science* **319**, 1367-1370 (2008)

Researchers are unlikely to travel to a black hole any time soon, but they have managed to recreate a bit of one in the lab.

Ulf Leonhardt of the University of St Andrew's, UK, and his colleagues made an artificial event horizon — the point beyond which nothing can escape — inside a fibre-optic cable. The cable was designed such that its optical properties would be altered by an ultrashort pulse of light. A beam of light on the same strand experienced the equivalent of an event horizon as it travelled near the first flash.

The authors hope that the system can be used to recreate Hawking radiation, a glow believed to surround real black holes as a result of quantum effects.

## CELL BIOLOGY

### Bent out of shape

*Cell* **132**, 807-817 (2008)

A fundamental question about how cell membranes can get dents in them was answered by Vinzenz Unger of Yale

University School of Medicine and his colleagues.

They found that proteins containing a region called an F-BAR domain form scaffolds in the peripheral cytoplasm and bring about invaginations in the cell membrane. Unger's team recreated the interactions between membranes and F-BAR proteins in a test tube, and then observed the results using electron microscopy.

F-BAR proteins, which have an elongated crescent shape, are exceptionally rigid and interact with membranes through their charged surfaces, according to the study. The proteins assemble into helical lattices and form clusters on membranes; the lattices can then bend the membranes to adopt the F-BAR protein's curved shape.

## EVOLUTION

### Yeast rewired

*PLoS Biol.* **6**, e38 (2008)

Evolution has massively rewired molecular circuits controlling gene expression in yeast, Hao Li and Alexander Johnson of the University of California, San Francisco, and their colleagues showed.

They studied how *Saccharomyces cerevisiae*, *Candida albicans* and *Kluyveromyces lactis* use the regulatory protein Mcm1, which directs the transcription of 4–12% of these three species' genes with the help of various partner

proteins. The three yeasts differ radically in the genes that are under the influence of the different Mcm1-partner pairs.

Of hundreds of Mcm1-controlled genes studied, fewer than one-fifth respond to Mcm1 in all three yeasts. The protein has picked up and lost partners as the species diverged, and in *C. albicans* has gained a new DNA-binding site that may help it thrive in human hosts.

## GEOLOGY

### Magma mix-up

*Geology* **36**, 51-54 (2008)

Basalts from the Snake River Plain (pictured left) in Yellowstone National Park in the northern United States look like they originate from deep in Earth's mantle. But they have the characteristic isotopic signature of rocks from shallower reaches — from the continental lithosphere. This curiosity has been explained by Barry Hanan of San Diego State University, California, and his colleagues.

Using mass spectrometry on samples of volcanic rock, the authors showed that deep-mantle magma can inherit the lithosphere's isotopic signature when it rises and picks up contamination.

The findings warn geologists about assuming too much from isotopic signatures.

## MOLECULAR BIOLOGY

### Shaping up

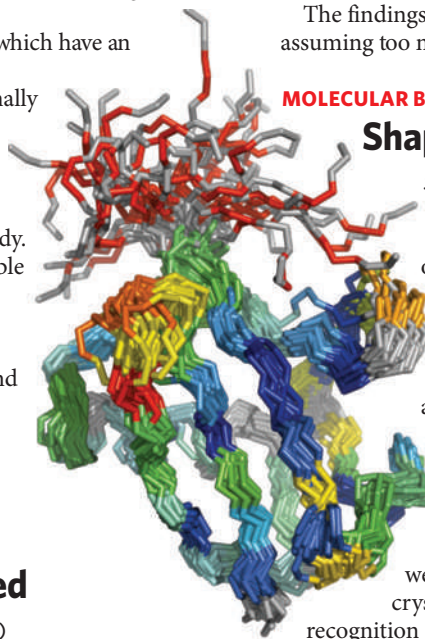
*Science* **320**, 1471-1475 (2008)

How does ubiquitin, a regulatory protein that labels other proteins for destruction, bind to so many different structures? By shuffling between arrangements until it finds the best option, according to Bert de Groot of the Max Planck Institute for Biophysical Chemistry in Göttingen, Germany, and his team.

Forty six of the arrangements were already known from X-ray crystallography of ubiquitin

recognition complexes. The researchers followed ubiquitin's structure (pictured) over pico- to microseconds in various solutions and from many angles, showing that all these conformations are likely to be adopted in living cells.

This work adds to evidence that many conformations of the same protein often exist in dynamic equilibrium before a binding partner comes along, a model that is at odds with the 'induced fit' hypothesis.



## A breath of fresh air

*Lancet* 372, 2023–2030 (2008)

In June, doctors successfully replaced a damaged portion of a 30-year-old woman's windpipe with a section grown from her own cells. Claudia Castillo (right) had a 3-centimetre-long collapsed section in her left bronchus from a tuberculosis infection.

Paolo Macchiarini at the University of Barcelona in Spain and his colleagues extracted a stretch of windpipe from a deceased donor. They washed this 25 times over a six-week period to remove all of the donor's cells, leaving only the windpipe's extracellular structure, which they seeded with Claudia's stem cells and cells from the bronchial surface.

The bioengineered trachea was then transplanted, providing Castillo with immediate respiratory relief. It continues to work well.



P. MACCHIARINI: HOSPITAL CLINIC OF BARCELONA/AP

## IMMUNOLOGY

### Successful delivery

*Cell* 134, 577–586 (2008)

Researchers for the first time reversed symptoms of HIV infection in a living animal using the technique of RNA interference. They constructed an antibody that targets T cells — in which HIV lurks — and linked it to a peptide carrying small RNA molecules, called siRNAs. The peptide helps these siRNAs enter T cells, where they silence certain host and virus genes crucial to the virus's replication.

Premlata Shankar, now at the Texas Tech University Health Sciences Center in El Paso, Sang-Kyung Lee of Hanyang University in Seoul, South Korea, and their colleagues injected the construct into mice genetically engineered to be easy to infect with HIV. The construct protected the mice from infection. It also restored the suppressed immune systems of mice that bore HIV-infected immune cells.

## PHOTONICS

### Telescopic TV

*Nature Photon.* 2, 492–495 (2008)

Telescopes often have a ring-shaped primary mirror to concentrate light onto a secondary mirror, which, in turn, reflects it through the hole in the primary. The same principle informs a new design for backlit screens.

In the 'telescopic pixels' described by Anna Pyayt of the University of Washington in Seattle and her team, the shape of the primary mirrors is under electronic control.

When their shape is near-parabolic, they bounce light onto the secondaries,

illuminating the holes in the primaries. When they are flat, no light hits the secondaries and the holes remain dark.

The prototype pixels transmit more than three times as much light as comparable liquid crystal displays. At present, the contrast they achieve is low, but models suggest that this can be improved. The technology may be suited to large, energy-efficient flat panels.

## NEUROBIOLOGY

### The motor-neuron driver

*Cell* 134, 304–316 (2008)

The diversity and direction of the nerve cells responsible for muscle movements are controlled by a protein called FoxP1, according to research published this year.

Such neurons are known as motor neurons. In the spine, motor neurons that control muscles in different regions of the body segregate into columns. Jeremy Dasen and Thomas Jessell of Columbia University in New York and their colleagues found that the amount of FoxP1 present alters the proportions of the different column types that neurons form. Increasing the expression of FoxP1 in embryonic mouse and chick motor neurons, for example, led to more neurons in the columns that innervate muscles in limbs.

Meanwhile, removing the FoxP1 gene not only affected column diversity but also altered the connections among motor neurons in limbs, and the patterns of axons that project into individual muscles.

## GEOSCIENCE

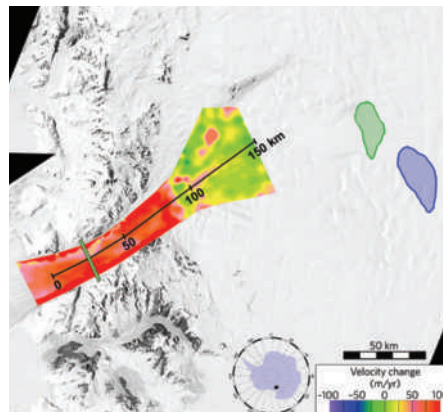
### The speed of ice

*Nature Geosci.* 1, 827–831 (2008)

Until recently, lakes beneath glaciers were regarded as static things. But Leigh Stearns of the University of Maine in Orono and her colleagues discovered that the gain and loss of water in such lakes contributes to the movement of the ice they underlie.

The team correlated a 10% increase in the flow speed of the Byrd Glacier in Antarctica between December 2005 and February 2007 (pictured left) with satellite measurements showing a huge discharge of water from two subglacial lakes 200 kilometres upstream.

The lakes released about 1.7 cubic kilometres of water over roughly the same period, submerging spots at which the glacier was sticking and hence lubricating it.





# THE YEAR IN NATURE

*Nature's* manuscript editors made a selection of 'favourites' from the papers we published in 2008.

## Where to look for monopoles

**Magnetic monopoles in spin ice**

C Castelnovo, R Moessner & S L Sondhi

*Nature* **451**, 42–45 (3 January 2008)

All magnets have north and south poles. Except that in the thirties, Dirac invoked monopoles to explain charge quantization; now they crop up elsewhere in particle physics — in theory. Physicists searched in vain for monopoles in cosmic rays and particle accelerators. Then this theoretical study suggested a better place to look: in exotic magnetic 'spin ice' materials. The search, though, continues...

## Nanostructures via DNA

**Programming biomolecular self-assembly pathways**

P Yin, H M T Choi, C R Calvert & N A Pierce

*Nature* **451**, 318–322 (17 January 2008)

**DNA-guided crystallization of colloidal nanoparticles**

D Nykypanchuk, M M Maye, D van der Lelie & O Gang

*Nature* **451**, 549–552 (31 January 2008).

**DNA-programmable nanoparticle crystallization**

S Y Park *et al.*

*Nature* **451**, 553–556 (31 January 2008)

Three nanotechnology papers with DNA the common thread. First a proof-of-principle experiment that recruits DNA hairpins to program biomolecular synthesis. The eventual goal is the automated design of biomolecules with specific functions. The other two put a 10-year-old theory into practice by showing that DNA attached to gold nanoparticles can be selected to self-assemble as nanocrystalline structures of the type that may serve as the optical and electronic materials of the future.

## The missing antimatter

**Difference in direct charge-parity violation between charged and neutral *B* meson decays**

The Belle Collaboration

*Nature* **452**, 332–335 (20 March 2008)

Intriguing results from the 'B factory' electron-positron collider at the KEK high-energy physics facility: the measurement of anomalous asymmetry in the decay rates of the exotic particles known as *B* mesons. Physicists say that the new value, taken with similar results from an experiment run on the SLAC linear accelerator, may help explain the near disappearance of antimatter from the Universe.

## Artificial enzymes

**Kemp elimination catalysts by computational enzyme design**

D Röthlisberger *et al.*

*Nature* **453**, 190–195 (8 May 2008)

This example of computational protein design is a major step towards the goal of designing artificial enzymes to catalyse reactions beyond the repertoire of natural biocatalysts. Potential



enzymes comprising about 200 amino acids were synthesized and the best, at removing a proton from carbon, underwent 'directed evolution' to make them even better. The design strategy, which mobilizes the power of many thousands of home computers via the Rosetta@home project, is generally applicable.

## Atmospheres from the past

**High-resolution carbon dioxide concentration record 650,000–800,000 years before present**

D Lüthi *et al.*

*Nature* **453**, 379–382 (15 May 2008)

**Orbital and millennial-scale features of atmospheric CH<sub>4</sub> over the past 800,000 years**

*Nature* **453**, 383–386 (15 May 2008)

L Loulergue *et al.*

Direct evidence of ancient environments is rare and therefore extremely valuable, and that's what the air bubbles trapped in polar ice cores provide. The evidence is hard-won: quite apart from obtaining and handling the core, extracting the gases intact is technically demanding. With these two publications adding new data from the EPICA Dome C core, the record of past atmospheres is extended to 800,000 years ago. Included is the lowest CO<sub>2</sub> concentration so far measured in an ice core.

## The day the temperature fell

**A large discontinuity in the mid-twentieth century in observed global-mean surface temperature**

D W J Thompson, J J Kennedy, J M Wallace & P D Jones

*Nature* **453**, 646–649 (29 May 2008)

How come nobody noticed? The record of global sea-surface temperatures during the past century has underpinned much of our thinking on the effect of human activity on climate. Surely there were no surprises left in the data. But this paper identified a 'glitch' — a fall of

about 0.3 °C coinciding with a change in the equipment used to measure the temperatures in 1945. The discontinuity is 40% as large as the century-long warming trend, so correcting for it may change the overall record substantially.

## Your tissues in colour

**Micro-engineered local field control for high-sensitivity multispectral MRI**

G Zabow, S Dodd, J Moreland & A Koretsky

*Nature* **453**, 1058–1063 (19 June 2008)

MRI scans are one of the big success stories of medical diagnostics. This clever piece of microengineering could refine the technique by adding 'colour'. It uses tiny injectable metallic microstructures to respond to a range of radiofrequency signals that can be displayed as different colours. There's more work to be done — finding a less toxic metal than the nickel used initially for a start — but information-rich colour MRI scans are now a distinct possibility.

## Enter the 'adipomyocyte'

**PRDM16 controls a brown fat/skeletal muscle switch**

P Seale *et al.*

*Nature* **454**, 961–967 (21 August 2008)

This was a surprise. Brown fat cells, the ones that burn calories to generate body heat, were found to share a common origin with skeletal muscle cells. White fat cells, the energy stores, have a quite separate origin. The zinc-finger protein PRDM16 is a powerful regulator of the cell fate switch between muscle and brown fat, so may have therapeutic potential in obesity.

## An upheaval in ocean biology

**Major viral impact on the functioning of benthic deep-sea ecosystems**

R Danovaro *et al.*

*Nature* **454**, 1084–1087 (28 August 2008)

The way that biologists and climatologists view the impact of viruses on the carbon cycle was transformed this year, and this was one of several papers that began the transformation. Ocean sediments contain large numbers of prokaryotes involved in organic carbon degradation, but the impact of viruses on these deep-sea ecosystems was unknown. The discovery that most deep-sea bacteria are infected by bacteriophage that kill their hosts, releasing sequestered carbon into the waters above and at the same time stimulating bacterial growth, means that this 'viral shunt' may be a key driver in the global carbon cycle.

## Found horizon

**Event-horizon-scale structure in the supermassive black hole candidate at the Galactic Centre**

S S Doeleman *et al.*

*Nature* **455**, 78–80 (4 September 2008)

You can't 'see' a black hole but this piece of

observational astronomy gets close by picking out structure in the radio emission just outside the event horizon of Sgr A\*, the supermassive black hole candidate at the centre of the Milky Way.

## An artificial tree

The transpiration of water at negative pressures in a synthetic tree

T D Wheeler & A D Stroock

*Nature* 455, 208–212 (11 September 2008)

The 'synthetic tree' that validates the cohesion-tension theory of transpiration has trunk and root systems in the shape of centimetre-scale disks of a hydrogel that contains tiny, homogeneous pores. Water evaporates from the 'leaves' to generate a transpirational pull a hundredfold greater than the pull in a synthetic wick. This 'tree' is a good starting point for new technologies for the management of water — even devices able to mimic the ability of plants to extract purified water from the soil.

## Cell biology revisited

Frequency-modulated nuclear localization bursts coordinate gene regulation

L Cai, C K Dalal & M B Elowitz

*Nature* 455, 485–490 (25 September 2008)

Here's an example of how systems biology can completely change the way we think about a familiar cellular process. Traditional biochemistry pictured cells as responding to environmental changes by sending regulatory proteins to the nucleus in an all-or-none fashion to activate target genes. This Article, combining cutting-edge single-cell imaging, cellular noise biophysics and computational modelling, reveals that translocation from cytoplasm to cell nucleus in the yeast cell occurs in bursts. The frequency — but not amplitude — of these bursts varies in response to extracellular signals, maintaining the relative rates of expression among target genes despite their varying absolute levels.

## Watching speciation

Speciation through sensory drive in cichlid fish

O Seehausen *et al.*

*Nature* 455, 620–626 (2 October 2008)

This elegant demonstration of speciation in action filled in important mechanistic gaps in our knowledge about the barriers that prevent mating between species. The cichlids of the African lakes are the most rapidly speciating species known. Here it was a change in the visual system, which affects females' preference for mating with different coloured males, that was the driver for a parting of the ways.

## Turn on the insulin

In vivo reprogramming of adult pancreatic exocrine



cells to  $\beta$ -cells

Q Zho, J Brown, A Kanarek, J Rajagopal & D A Melton

*Nature* 455, 627–632 (2 October 2008)

Various strategies exist to 'dedifferentiate' mature cells to a state where they resemble an embryonic cell with the potential to regenerate to perform a new function. Here though, there is no 'in-between' stage: mature exocrine pancreatic cells in live diabetic mice were reprogrammed to produce insulin by exposure to a cocktail of three transcription factors.

## Crossing the membrane

Structure of a complex of the ATPase SecA and the protein-translocation channel

J Zimmer, Y Nam & T A Rapoport

*Nature* 455, 936–943 (16 October 2008)

The determination of the crystal structure of a complex between a single bacterial protein



conducting channel and the SecA motor that powers the protein across the cell membrane was an impressive technical feat. And — with two other papers in this issue tackling the mechanisms involved — it revealed some of the details about how proteins make their way through the cell membrane.

## The personal touch

Accurate whole human genome sequencing using reversible terminator chemistry

D R Bentley *et al.*

*Nature* 456, 53–59 (6 November 2008)

The diploid genome sequence of an Asian individual  
J Wang *et al.*

*Nature* 456, 60–65 (6 November 2008)

Feats of DNA sequencing that once took many years and millions of dollars can now be achieved in just months and for several thousand dollars. The 6 November issue included these landmark papers — genome sequences of Yoruba African and Han Chinese individuals — to be added to the three personal genomes already published (those of Craig Venter, Jim Watson and the NIH reference sequence). Also in this issue is the genome sequence of a patient with leukaemia and a series of features on what the new era of personal genomics has in store for us.

## Cancer stem cells in the news

Efficient tumour formation by single human melanoma cells

E Quintana *et al.*

*Nature* 456, 593–598 (4 December 2009)

This demonstration that most cells in mouse melanomas are capable of continuous proliferation has caused a flurry of interest in the cancer stem cell hypothesis. The hypothesis assumes that only a few cells in a solid tumour are tumorigenic — and that targeting those cells may be the best form of therapy. The new results question this approach for some melanomas, but the cancer stem cell hypothesis remains in the frame for other cancers, such as leukaemia.

## Neuromotor prosthetics

Direct control of paralysed muscles by cortical neurons  
C T Moritz, S I Perlmutter & E E Fetz

*Nature* 456, 639–642 (4 December 2008)

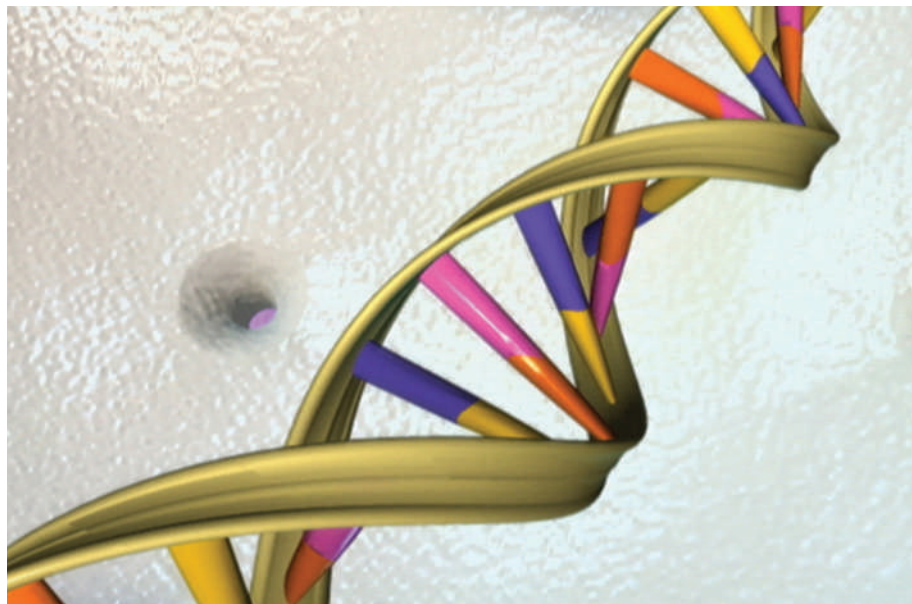
Advances in brain-machine interfaces came thick and fast this year. This work followed on from research in which monkeys were trained to move robotic arms by signalling through electrodes implanted into the brain by showing that a single neuron not previously associated with controlling movement can be co-opted to restore movement to a paralysed arm. Such techniques are beginning to look like a plausible strategy that could be used in humans.



# NEWS 2008: THE YEAR IN WHICH ...

Words: Ashley Yeager

NATL HUMAN GENOMES RES. INST.



## Personal genomics goes mainstream

In January, an international consortium announced the launch of the 1,000 Genomes Project, which aims to provide a catalogue of human genetic variation. In October, the Personal Genome Project, which hopes to sequence and publish the genomes of as many people as possible, released initial data for ten participants. Meanwhile, as researchers wondered what they could glean

from the results coming from personal-genomics companies, the prices of such services dropped. The firm 23andMe, based in Mountain View, California, for instance, now offers personalized genetic information for \$399. And finally, two more human genomes — one of an anonymous African, the other an Asian — were decoded, bringing the world's total of published human genomes to four.

## The US election offers science a rejig

The election of Barack Obama as the next US president suggests that science in the United States will change in many ways. Researchers are watching to see whether Obama fulfils campaign promises to lift federal restrictions on human embryonic stem-cell research and to institute a cap-and-trade system to regulate greenhouse gases. Other promises, such as a \$15-billion-a-year investment in clean-energy technologies and research, lie more at the whims of Congress, which allocates funding. And scientists who have complained about the lack of science input into decisions made by some federal agencies under George W. Bush are waiting to see how research will be treated in an Obama administration.

## The first synthetic genome is made

By stitching together more than 500,000 base pairs of DNA, scientists created the first synthetic genome from scratch. The team at the J. Craig Venter Institute in Rockville, Maryland, had already managed to transplant DNA from one bacterial species into another, transforming the second into the species of the first. The genome synthesis is the next step towards booting-up the world's first artificial organism — a breakthrough that could come as early as 2009.

## The LHC starts up, then stops

Near Geneva, Switzerland, physicists switched on the world's largest particle accelerator, the Large Hadron Collider (LHC). Nine days later the US\$5-billion machine broke down (see page 862). An electrical failure caused almost 6 tonnes of ultracold liquid helium to leak into the LHC tunnels; nearly 40 of the magnets used to guide its proton beam need to be rebuilt before it can start operating again — not expected before summer 2009.

## Phoenix lands on Mars

NASA made it to the Martian arctic. The Phoenix Mars Lander touched down in late May and began digging around with its robotic arm. But problems with sticky soil stifled early efforts to sniff the Martian soil for traces of water and organic materials. Scientists finally got a taste of ice in August and later detected a compound called perchlorate. In late October, communications with Phoenix became patchy, and they ceased for good on 2 November.

## Biodiversity gets catalogued online

An ambitious project to publish an expert-created web page for each of Earth's 1.8 million named species produced its first 30,000 chapters in February. With support from many of the world's leading natural-history institutions, the 'Encyclopedia of Life' aims to provide video, sound, images, graphics and text covering the planet's entire biodiversity, including the pygmy hippopotamus *Hexaprotodon liberiensis* (right). Since 2007, the project has added more than US\$6 million in donations and grants to its funding pool of \$2.5 million from the Sloan Foundation and \$50 million promised by the MacArthur Foundation — putting it on track to have 90–95% of all known species catalogued by 2017.



SOLENT NEWS/REX FEATURES



**2008 IN REVIEW**

For more about this year's top stories, see:

[www.nature.com/2008](http://www.nature.com/2008)

**The US anthrax case is declared closed**

Bruce Ivins, a biodefence researcher at a US Army research complex in Maryland, committed suicide in July as the Federal Bureau of Investigation was preparing to indict him in relation to the 2001 anthrax attacks. FBI agents said that Ivins had access to the bacterial spores sent to several members of Congress and the media; Ivins's lawyer maintains his innocence. The agency's scientific evidence has not yet been released in full; the US National Academy of Sciences has convened an independent panel to review the information.

**Asia's space race heats up**

The Indian Space Research Organisation added the nation's flag to the lunar surface when its first lunar orbiter, Chandrayaan-1, dropped a probe into Shackleton crater on 14 November. India joins China and Japan in having spacecraft currently orbiting the Moon. In an even more spectacular feat in September, China became the third nation — after the United States and Russia — to have its astronauts perform a spacewalk.



NASA/GSFC

**All eyes turn to Arctic sea ice**

Mid-September brought the annual low for the layer of sea ice that covers the Arctic Ocean. This year's 4.52 million square kilometres was still 9.4% more ice cover

compared with 2007, which holds the record for the least amount of sea ice recorded in the satellite era. Fewer warm days in 2008 and changes in wind patterns may account for the difference between the years.



H. STRAND/CORBIS

**Polar bear makes endangered list**

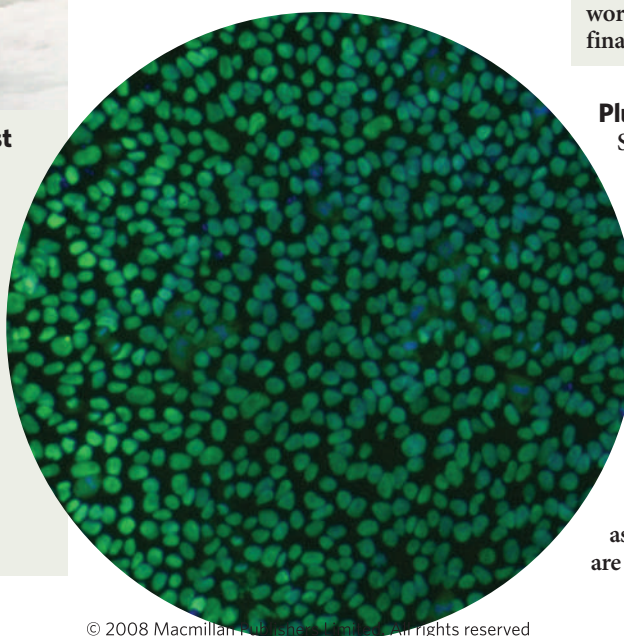
In May, the US government moved to protect polar bears under the Endangered Species Act (ESA) — the first time it had based a species listing on the threat of climate change. But the listing triggered internal spats at the Department of the Interior, and by year's end the administration of George W. Bush had changed the rules for ESA listings so that the agency is no longer required to consult independent scientists before making a decision as to whether to list a species.

**Beijing Olympics highlights air pollution**

Tackling Beijing's poor air quality became an obsession for the Chinese government in preparation for what it hoped would be a 'green' Olympics. In large part, the effort paid off: Beijing's Air Pollution Index was markedly lower — below 100 on its 500-point scale — throughout August. Compared with the summer of 2007, concentrations of larger particulates dropped by about 50% and smaller particulate levels by 25%.

**The financial crisis affects research**

The effect of the financial crisis, and the global economic downturn that helped to precipitate it, is still playing out in the research realm. Charities such as the Wellcome Trust in London and Cold Spring Harbor Laboratory in New York reported the first drop in their endowments for years. Harvard University, among other institutions, is no longer hiring new staff for non-critical positions. Biotech firms and industry research and development arms are working to get a footing in the changed financial landscape (see page 852).



NATURE BIOTECHNOLOGY

**Pluripotent stem cells are created**

Shinya Yamanaka's 2007 discovery of induced pluripotent stem (iPS) cells (left) sparked a new flurry of stem-cell research across the globe. This year, US-based scientists showed that they could make iPS cells from the skin of octogenarians with a chronic neurodegenerative disease. Another US team showed that it could make the cells using an adenovirus, which stays out of a cell's own DNA, rather than a normal virus that does not. The technique should prevent serious side effects such as cancer from occurring when the cells are used in clinical treatment.



visa applications for foreign researchers and give international science and engineering students an automatic one-year visa extension to seek work or advanced study.

## Suspended urologist set to return to Austrian university

The urologist at the centre of Austria's biggest-ever research scandal can return to work at the Medical University of Innsbruck, a disciplinary committee has ruled.

Hannes Strasser was suspended from clinical, teaching and research duties in September 2008 following accusations of malpractice in a clinical trial using stem cells to treat urinary incontinence (see *Nature* 454, 922; 2008).

The national disciplinary committee responsible for university staff has now concluded that the suspension was not legally justified, as more than three years had passed since the alleged misdemeanour occurred.

Strasser, who is facing criminal charges relating to harming patients or putting them at risk of harm, is on paid leave until the end of January. He will not be allowed to treat patients until the criminal case is resolved — which is likely to take at least a year. An investigation by the Austrian National Academy of Sciences is also ongoing.

## Coal conversion plant fires up in China

China's first coal-liquefaction plant is up and running. Located in Inner Mongolia, the facility is run by the state-owned Shenhua Group.

According to a statement issued by Shenhua last week, the plant has been turning coal into liquid fuel and chemical products since December. The technique, which is also widely used in South Africa, has been criticized for its high emissions of carbon dioxide.

Last year, the Chinese government issued a moratorium on new coal-liquefaction facilities, but allowed Shenhua to complete its Mongolia plant and continue work on a second. The company says it is developing ways to capture and store the CO<sub>2</sub> emitted during the process.

## Italian universities lose freedom to appoint staff

Italian universities will have little say in choosing their own professors thanks to a law approved by parliament last week.

According to the new rules, a five-person selection committee will oversee each

appointment. But a university recruiting a professor can appoint only one member to the board. The other four members will be picked at random from a list of twelve voted for by the relevant community of scientists across Italy.

The existing *concorsi* system is similar, but it allowed universities to have more control over selection — a privilege that was sometimes abused to make appointments based on local politics rather than on merit. Many academics had lobbied for a reform that would allow universities to make their own free choice, but lose funds if their chosen professors underperformed.

### Corrections

The News round-up item 'Biodiversity gets catalogued online' (*Nature* 456, 844–845; 2008) gave incorrect funding numbers for the Encyclopedia of Life. The total budget for the project's first five years is US\$50 million; \$2.5 million came from the Sloan Foundation and \$10 million from the MacArthur Foundation in 2007.

The News story 'Good grades, but who gets the cash?' (*Nature* 457, 13; 2009) incorrectly calculated the number of staff submitted by the University of Oxford who were rated world-leading and internationally excellent in the biological-sciences category of the 2008 Research Assessment Exercise. The correct number is 75, putting the university in second place behind the University of Cambridge.



Climate activists packed the Poland meeting.

# Climate talks defer major challenges

Minor progress in Poland on adaptation and deforestation sets the stage for Copenhagen in 2009.

## POZNAN, POLAND

International climate negotiators left Poland last week with a roadmap for completing work on a global-warming treaty in 2009 — a small yet critical step in the face of the global economic meltdown.

With the US delegation in a state of post-election limbo and Europe locked in a battle over its new climate initiative (see page 847), developing nations captured the limelight in Poznań by ramping up their own commitments and calling for industrialized nations to do the same. The talks — the 14th UN Conference of the Parties (COP), held on 1–12 December — also saw the launch of a fund to help countries cope with a warmer world. And negotiators made some progress on ways to include deforestation in the successor to the Kyoto Protocol, which expires in 2012.

But delegates largely spent the two weeks positioning themselves for the formal negotiations process leading up to Copenhagen, where the talks are scheduled to conclude in December 2009. They adopted what is being called the 'Poznań package', which lays out a necessarily aggressive — and perhaps optimistic — agenda, but remains silent on the most vexing questions, including how to divvy up responsibility for reducing greenhouse gases.

"The best thing you can say about this COP is that we didn't lose ground," says Kevin Knobloch, president of the Union of Concerned Scientists in Cambridge, Massachusetts. "But

that is saying something, especially in this period of financial crisis." And Knobloch thinks that new proposals from emerging economies could open the door to a deal in 2009. "I don't think it will be easy, but we will have squandered an opportunity of historic proportions if we don't get this done," he says.

In Poznań, Mexico announced that it will commit to reducing emissions to 50% below 2002 levels by mid-century. South Africa said it would halt the growth in its emissions by 2020–25 and begin reducing them by 2030. China is aggressively pursuing alternative energy, and Brazil showed up with a climate plan that would, among other things, curb Amazon deforestation by 70% within nine years. (The plan back-pedals on an earlier pledge to halt deforestation by 2015, although Brazil says that by then it will be planting as many trees as it cuts down.)

"Everybody is waiting for everybody else to make a move," Brazil's environment minister, Carlos Minc, told reporters in Poznań. Rather than wait for the UN process to play out, Brazil unilaterally launched an international fund earlier this year to protect the Amazon rainforest, and called for US\$21 billion to help pay for its plan. Norway has pledged \$1 billion towards it, and Minc says he is now in talks with Germany and the United Kingdom. "We are showing that developing countries can do their part," Minc said.

**"Everybody is waiting for everybody else to make a move."**

Brazil is to a certain extent isolated, however, in its opposition to a market-based approach. Environmentalists accused the country of trying to block progress in Poznań by raising what they called disingenuous questions about the current methodologies for tracking and assessing deforestation emissions. Papua New Guinea and other members of the Coalition for Rainforest Nations are leading the charge for a market-based approach, which would allow developed nations to offset their emissions by paying for forest conservation in the developing world. Such an approach would in

theory provide more reliable access to private capital, thereby eliminating the need to seek money from wealthy nations. In the end, Brazil withdrew its opposition, and delegates on

a technical committee produced a decision reiterating that existing science, technology and methodologies are sufficient.

But delegates left the basic questions about how to structure the deforestation deal for next year. Frances Seymour, who heads the Center for International Forestry Research in Bogor Barat, Indonesia, says the architecture will have to be flexible: a market-based approach might breed corruption in countries with poor governance and weak institutions, but could do well where the problem is one of resources. "This is the biggest thing that has happened in forest conservation in 15 years," she says. "But

J. SKARZYŃSKI/AFP/GETTY IMAGES



it also has the potential to crash and burn if we get it wrong."

On the subject of facilitating adaptation to climate change, negotiators finally settled their differences over the launch of a fund to help poor countries cope with global warming. Developing countries prevailed in their efforts to get direct access to the money through a board established under the UN convention, a move that bypasses institutions such as the World Bank. The agreement on the fund is "one small piece of good news", says Keya Chatterjee, deputy director of the climate-change programme of the conservation group WWF in Washington DC. "Now we just need to get money into it."

The conference ended without a decision on how to increase revenues for the fund, currently valued at about \$200 million — far from the tens to hundreds of billions of dollars annually that many think will be needed to help countries adapt their agricultural systems, cope with freshwater shortages and address rising sea levels. The sole revenue source at present is a 2% levy on projects that industrialized nations fund in emerging economies to offset their own emissions.

Moving forward, perhaps the biggest question is how high to aim in Copenhagen. Last week, UN climate chief Yvo de Boer lashed out at those suggesting that delegates might have to settle for some kind of agreement on principles rather than a complete and ratifiable treaty. But many experts say it will be extraordinarily difficult for US President-elect Barack Obama to get a greenhouse-capping bill through Congress and negotiate a complex international treaty, all in 11 months. And without the United States, there is no deal.

"We shouldn't expect too much from Copenhagen," says Ottmar Edenhofer, who oversees work on mitigation for the Intergovernmental Panel on Climate Change. Edenhofer would like to see an overarching agreement on a global emissions trajectory that stabilizes emissions by 2015 and halves them by mid-century. The United States could then move forward with its cap-and-trade system, and link it to the European scheme, while various bilateral and multi-lateral negotiations continue.

"I'm a moderate optimist," Edenhofer says. "There is no need for us to do everything in one treaty. We can go step by step."

Jeff Tollefson

For our blog report from Poznań, see <http://tinyurl.com/6edhzi>.

See Editorial, page 838.

## Europe agrees emissions deal

European heads of state struck a deal on 12 December on how to go about reducing Europe's greenhouse-gas emissions to 20% below 1990 levels by 2020.

But the plans got a lukewarm response from environmentalists and climate scientists because of the far-reaching concessions given to industry in the deal brokered by France's Nicolas Sarkozy, the outgoing European Union (EU) president.

The compromise overturns contentious plans to force the power sector to buy all of its emissions permits in the EU's mandatory emissions-trading system from 2013. Instead, power plants and other emissions-intensive industries will only need to buy up to 30% of their allowances from 2013; currently they get all of them for free.

The deal means that "Europe has passed its credibility test", says José Manuel Barroso, president of the European Commission. "It means business."

By 2020, the power sector will need to pay for all of its allowances. But sectors that can prove they are facing serious competitive disadvantages — as is claimed by the steel, cement and aluminium industries — can apply for exemptions to grant them up to 100% free emission permits, even after 2020.

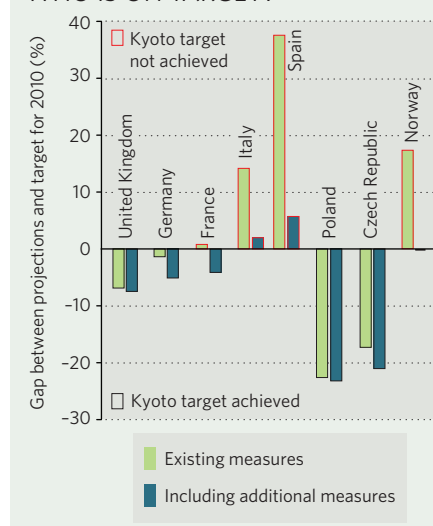
To qualify, firms must show that the burden from emissions trading would add at least 5% to their overall production costs, and that more than 10% of their imports and exports are exposed to international competition, which might shift such businesses to countries with less intensive regulations. Heavy industries that cannot prove these risks will have to buy 20% of allowances by 2013, and 70% by 2020.

"EU climate leadership is in meltdown," says Satu Hassi, a Finnish Green League politician and vice-chair of the European parliament's environment committee. "The only good news is that the agreement on renewables will not be reopened." That agreement includes a target of producing 20% of the EU's energy needs from renewable sources by 2020.

The European parliament was expected to vote on the deal on 17 December. By spring 2010, the commission must provide parliament with a detailed analysis of the outcome of the United Nations climate-change conference, to be held in Copenhagen in December next year. The council will then decide whether to increase the 2020 reduction goal to 30% relative to 1990.

Sarkozy's deal was hammered out to

EUROPE'S EMISSIONS:  
WHO IS ON TARGET?



SOURCE: EUROPEAN ENVIRONMENT AGENCY

satisfy lobbying from industry and several eastern European countries. Some industries had threatened to flee the EU, and some governments, including those of Poland and Italy, threatened to veto the legislation.

Italian prime minister Silvio Berlusconi was eventually content with the softened quotas. Poland's agreement was sweetened by promises of a multibillion-euro 'solidarity fund' for member states with lagging economies. The fund, to be financed with revenues from 12% of the emission permits sold at auctions, is to help Poland and eight other countries in eastern Europe to switch to cleaner energy production.

Furthermore, at least half of the overall auction revenues — estimated at €50 billion (US\$68 billion) annually by 2020 — are to be invested in technologies such as carbon capture and storage throughout the EU.

Even so, the softened quotas will still allow the power sector to make windfall profits from factoring in the 'costs' of free allowances in the consumer price of energy. This practice, although economically legitimate, has been a main reason for widespread criticism of the emissions-trading scheme in its current form.

"Emissions trading can work only if emission allowances are auctioned, ideally without exception," says Claudia Kemfert, a climate and energy expert at the German Institute for Economic Research in Berlin, and a climate policy adviser to Barroso.

Quirin Schiermeier

See Editorial, page 838.

**STORMY SKIES**

Water and perhaps weather spied on a distant planet.

[www.nature.com/news](http://www.nature.com/news)

T. PYLE/NASA/JPL-CALTECH

# Nobel physicist to run energy agency

Obama appointments likely to focus on renewable energy and implementing cap and trade.



By choosing Nobel-prizewinning physicist Steven Chu to head the Department of Energy (DoE), US President-elect Barack Obama has sent a clear message: solving climate issues in a world dependent on fossil fuels will depend on science coming up with new energy technologies.

Three other key positions in Obama's climate and energy team have also been settled, and they point to an administration that will be serious about climate change and the regulation of emissions. Carol Browner, who was director of the Environmental Protection Agency (EPA) during the 1990s, will become a new Cabinet-level climate and energy coordinator. Taking over the EPA will be Lisa Jackson, the former head of New Jersey's Department of Environmental Protection. And Nancy Sutley, a deputy mayor of Los Angeles who has worked on California climate and water issues, is to be named head of the White House Council on Environmental Quality.

But it is the selection of Chu, director of the Lawrence Berkeley National Laboratory (LBNL) in California, that has excited academics across the country. They interpret it as a message that not only will energy research be an administration priority, but that science itself will have a voice at the table. "It's really pulling science out of the shadows in the United States," says Philip Bucksbaum, a physicist at Stanford University in California and a friend of Chu's since graduate school in the 1970s. "It's just exciting to know that there's a physicist — a really smart one and not at all quiet

and retiring — sitting at the Cabinet table."

Chu will move from the LBNL, a US\$600-million, 4,000-employee lab, to the \$24-billion DoE, sometimes called the 'Department of Everything' because it oversees 17 national labs with missions varying from renewable energy research to particle physics, and from the design of nuclear weapons to the disposal of nuclear waste. It is rare for a DoE secretary to rise from within, and just as rare for the secretary — typically a politician or businessperson — to have a science background at all. (The current secretary, Samuel Bodman, does have a doctorate in chemical engineering from the Massachusetts Institute of Technology in Cambridge.)

## Big step up

But there are some concerns about Chu's ability to manage such an unwieldy agency: he had never managed anything more unruly than an academic department of scientists before taking over the LBNL in 2005. Chu did his PhD in atomic physics at the University of California, Berkeley; in the late 1970s, he moved to Bell Labs in New Jersey, where he used lasers to cool atoms nearly to a standstill, creating the 'optical molasses' that led to his 1997 Nobel prize. He moved on to Stanford University, where his interests slowly shifted towards energy.

Bucksbaum says that if Chu could make the leap from Stanford department chair to the top of the LBNL, then he can survive atop the DoE. "My prediction is that he'll learn how to live in their world," he says. "He's a quick study." Chu is likely to need some help navigating the political

world, as well as with the nuclear-weapons complex and non-proliferation issues, says physicist Michael Lubell, head of public affairs for the American Physical Society in Washington DC.

Chu has refocused the LBNL on its new mission: renewable energy. He has been creative in seeking new streams of funding, establishing a trio of related programmes under the umbrella of the Helios initiative. One programme seeks chemical improvements to harvesting solar power; a second, a \$134-million, five-year programme called the Joint BioEnergy Institute, is working to improve biofuels. A third, the Energy Biosciences Institute, is pursuing similar goals with a different pot of money: \$500 million over 10 years, in a partnership with other universities and the oil company BP. This has raised concerns about undue industry influence at the LBNL's neighbouring institute partner, the University of California, Berkeley (see *Nature* 445, 688–689; 2008).

But Graham Fleming, who was Chu's deputy at the LBNL before returning to the University of California, Berkeley, to work as a chemist, says it shows Chu's pragmatism. Chu's Nobel-prize autobiography speaks glowingly of his time at Bell Labs, then a Mecca for industry-supported, but unconstrained, pure research. "He doesn't feel that there is anything unclean or inappropriate about having connections with industry," says Fleming.

Nor does Chu seem bound ideologically to any one energy approach. Chu has said that nuclear power and carbon sequestration will play important parts, even as he has advocated

LBNL



► energy efficiency as the quickest way to make major gains. Still, he has called coal his “worst nightmare” of a fuel.

Chu has also shown enthusiasm for biotechnology, which can be used to engineer better biofuel plants or microbes with advanced abilities to convert cellulose into fuel. His optimism for biotechnology stands in contrast to the record of Browner, who as the head of the EPA in the 1990s instituted strict rules that regulated biotech research and development (R&D) in the same way as agricultural chemicals. Roger Beachy, president of the Donald Danforth Plant Science Center in St Louis, Missouri, says he hopes the agency will soften its stance towards plant-science R&D. “They’ve taken a very risk-averse approach,” he says. “I’m not sure that that’s going to be good for the environment or the economy.”

Frank O’Donnell, president of Clean Air Watch, a non-profit organization in Washington DC, says that Browner will bring a political tenacity that helped her to update national clean-air standards for ozone and fine particulates. “She was faced with massive opposition, even within the administration itself, and she managed to prevail,” he says.

Browner’s precise duties and powers have not yet been specified, but she is likely to play referee to inter-agency squabbles, says O’Donnell. “We’ve seen the DoE fight against the EPA,” he says. “I think the new climate and energy adviser is going to tell these agencies, ‘Knock it off, we’re all on one team.’”

Having someone at Cabinet level to represent the EPA director — which is not a Cabinet slot — would also be helpful as Browner and Jackson work to implement what is likely to be another Obama priority: a cap-and-trade system to curb carbon emissions. Jackson, a chemical engineer by training, helped to push New Jersey into adopting the 2007 Global Warming Response Act, which calls for ambitious greenhouse-gas cuts.

O’Donnell says Jackson and Browner are sure to work quickly to take advantage of a 2007 Supreme Court ruling that will allow them to treat carbon dioxide as a pollutant under the Clean Air Act. Browner, as a seasoned politician, could also provide some cover for Chu, a rookie in Washington DC. “Someone’s going to come up with the right idea, and someone’s going to figure out how to get it done,” says Fleming. ■

Eric Hand

See Editorial, page 838.

## Imaging advances provide immune-cell breakthroughs

A technology that helps scientists spy on the inner workings of mice is empowering immunologists, researchers said in San Francisco, California, this week at the 13–17 December American Society for Cell Biology annual meeting.

Multiphoton microscopy uses pulsed lasers to track single cells deep inside animal tissues, revealing how they interact with the cells around them. The technique uses lower-energy lasers than other light-microscopy methods, and so it is less toxic to cells — and less prone to the light scattering that can blur images.

‘Intravital imaging’ experiments that use multiphoton microscopy inside living animals were confined to a handful of labs until a couple of years ago. Now, says Jeffrey Segall of the Albert Einstein College of Medicine of Yeshiva University in New York, the technique “has reached a critical mass” — thanks to the renewed interest in cell environments, and the availability of cheaper, more reliable, multiphoton microscopes.

At a 15 December workshop at the meeting, Jackson Egen of the National Institute of Allergy and Infectious Disease in Bethesda, Maryland, showed how his group, led by Ronald Germain, has used multiphoton intravital microscopy to discover how a particular gene mutation causes a human immunodeficiency disease. The team found that the mutation disrupts the interactions between T cells and B cells that are critical to the immune response<sup>1</sup>.

And Segall described how scientists at the Einstein biophotonics centre take intravital imaging deeper inside tissues. They construct a tiny glass window that is surgically grafted inside a mouse. They then inject the mice with fluorescently labelled cells, which change colour when hit by a laser light, and can be tracked through the mouse’s body via the window. This allows researchers to follow the cells’ movements for days.

On 15 December, in a symposium at the meeting, Bojana Gligorijevic, a research associate at the Albert Einstein College of

Medicine, described how Einstein scientists used this technique to trace cancerous cells in a model of breast cancer<sup>2</sup>. They gained a real-time view of the events that lead to metastasis, in which cancer cells move away from primary tumours. They have found, for example, that tumour cells are more likely to metastasize if close to a major blood vessel. This underscores the need to study tissues in their natural context. “These tumour cells are all equal when we inject them,” says Gligorijevic. “The only reason their behaviour is different in tumour, is because

they are in different microenvironments.”

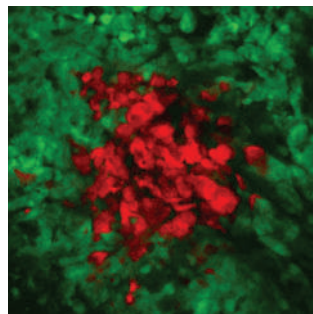
Early multiphoton intravital microscopy studies focused on simply observing the behaviour of cells, but the field is now shifting towards examining how cells respond to external and internal disruptions, such as infections or molecular modifications.

For example, Egen

has used the technique to watch how certain immune cells help sandflies transmit through their bites the parasite that causes leishmaniasis<sup>3</sup>. And Ulrich von Andrian of Harvard Medical School in Boston, Massachusetts, has used multiphoton intravital microscopy to answer long-standing immunological questions, such as which specific cells recognize viruses that infect the lymph nodes and present them to cells that will fight the infection<sup>4</sup>.

“The prevailing view was a very static one of two cells interacting without much else going on,” says von Andrian. “Now that we can actually watch these movies, we realize it is nothing like that — there’s this orchestrated dance going on at all times that needs to be taken into account if you want to understand the immune response.” ■

Erika Check Hayden



Breast cancer cells (red) caught in the act of migrating.

1. Qi, H., Cannons, J. L., Klauschen, F., Schwartzberg, P. L. & Germain, R. N. *Nature* **455**, 764–769 (2008).
2. Kedrin, D. et al. *Nature Meth.* **5**, 1019–1021 (2008).
3. Peters, N. C. et al. *Science* **321**, 970–974 (2008).
4. Junt, T. et al. *Nature* **450**, 110–114 (2007).

Movies from these labs can be seen at <http://tinyurl.com/55lg3d> and <http://tinyurl.com/5j4fxk>.

**EARTHQUAKE ALERT**

Ancient corals reveal cycles of seismic activity around Sumatra.

[www.nature.com/news](http://www.nature.com/news)

SCIENCE

# Salary for CIRM head despite deficit

The board of California's state stem-cell agency has voted to pay its chairman a salary, even as the state plunges deeper into financial crisis.

Robert Klein, architect of the ballot initiative that led to the creation of the California Institute for Regenerative Medicine (CIRM), is a real-estate developer who has chaired CIRM's board without pay since the agency was conceived in 2004. On 10 December, the board decided to give Klein \$150,000 a year for his work, defining his role as a half-time position.

The vote took place on the same day that governor Arnold Schwarzenegger described the state's growing budget shortfall — almost \$15 billion for the current fiscal year — as a potential “financial Armageddon”. On 4 December, Schwarzenegger had sent a letter to CIRM's board expressing “deep concern” about

the plan to award salaries to its chairman and vice-chairman. “I urge you to ensure that compensation for these positions is offered only if and to the extent absolutely necessary to implement its mission,” Schwarzenegger wrote.

But Klein said last year that he needed the salary owing to the bad economic climate, leading CIRM to conduct a survey and set the salary range for Klein's position with an upper



CIRM chairman Robert Klein.

limit of about \$500,000 a year. Some, such as John Simpson of the taxpayer's group Consumer Watchdog in Santa Monica, had objected to that figure, pointing out that the director of the National Institutes of Health makes about \$200,000 a year.

Simpson called the salary agreed by the board last week “at the high end of reasonable,” and said that Klein will have new responsibilities: “Now that Klein

is taking a salary he must truly act like a state employee, something he's not always done in the past.” For instance, while chairman, Klein vilified state senator Deborah Ortiz (Democrat) and served as head of an advocacy organization, Americans for Cures, that attacked another lawmaker, Sheila Kuehl (Democrat). He has since resigned as president of that organization.

Klein's salary also raises issues about the board's vice-chair position. That open slot was previously held by Ed Penhoet, a businessman who took no compensation. Two competing candidates for the job have been nominated. One, Art Torres, leader of the state's Democratic party, requires a salary; the other, Duane Roth, is already on the CIRM board and would not need a salary. The position could be worth up to \$332,000 a year.

Klein's term is set to expire in 2010; he has said he won't be seeking to extend it, but in the past also said he would serve just three years. ■

**Erika Check Hayden**



## US bioindustry calls for government bailout

The Biotechnology Industry Organization (BIO), a trade body based in Washington DC, is asking members of the US Congress to consider giving financial aid to small technology companies struggling in the present financial crisis.

Small biotech firms, many of which are not profitable, have been hard hit by the downturn. BIO says that nearly a third of the 370 publicly traded US biotech companies have less than six months of cash left.

Now BIO is proposing a temporary US tax reform that would allow the firms to cash in early on a tax break normally allotted to them when they become profitable. The proposal would also apply to other investor-backed small companies, such as those developing alternative-energy technologies.

## Vatican formalizes rules on human stem-cell research

The Roman Catholic Church has reaffirmed its opposition to human embryonic stem-cell research in a document that updates its 20-year-old position on biomedical research and reproductive medicine.



The Vatican has clarified its position on stem cells.

The instruction *Dignitas Personae* formalizes many previous positions, including a ban on stem cells derived from human cloning and aborted fetuses. Work using adult stem cells, umbilical-cord cells or stem cells from fetuses that died naturally is morally acceptable.

"The Vatican is entitled to its theological position," says Insoo Hyun, chair of the Ethics and Public Policy Committee at the International Society for Stem Cell Research. But, he adds, "many other world

religions have a permissive view on human embryonic stem-cell research".

For a longer version of this story, see <http://tinyurl.com/6codqu>

## Michigan State wins battle to host isotope accelerator

The US Department of Energy has approved a \$550-million facility that will generate rare isotopes for the study of fundamental nuclear physics, astrophysics and medical diagnostics.

Michigan State University in East Lansing beat the Argonne National Laboratory in Illinois to host the Facility for Rare Isotope Beams (FRIB). FRIB's centrepiece will be a linear accelerator that will smash ions into fixed targets to generate exotic isotopes. Construction is planned from 2013 until 2017.

FRIB is a scaled-down version of the Rare Isotope Accelerator (RIA), a doubly expensive design advanced by nuclear physicists since 1999. If RIA was to have been the "absolute Cadillac", then FRIB is more of a "souped-up Chevrolet", says Konrad Gelbke, who directs the National Superconducting Cyclotron Laboratory at Michigan State University. Still, he adds, "I would say the community is delighted".

## US nanotechnology plan lacks risk research

An independent review has slammed the United States' strategy for research into nanotechnology's potential health and environmental risks.

Generated by the National Research

Council, which provides independent scientific advice for the US government, the 10 December report criticizes the federal plan for not having specific goals, central accountability or sufficient input from interested parties. It also says that unrelated research, such as projects on the delivery of medicines using nano-sized tools, is passed off as research on health risks. That work is

“really tangential”, says report chair David Eaton, a professor of environmental health at the University of Washington in Seattle.

Changes to the government's plan that would have addressed some of these concerns were nearly legislated by Congress this year, but the effort quietly expired in the Senate.

## Rift-valley countries set for geothermal power

The successful completion of a pilot project in Kenya has opened the way for exploitation of some 4,000 megawatts (MW) of geothermal energy that are thought to be available in the East African Rift Valley (pictured).

The project, funded by the Global Environment Facility (GEF), used advanced drilling and seismic techniques to dig 18 cost-effective steam wells, each generating around 4–5 MW of electricity. The results of the pilot project were announced at last week's UN Climate Change Conference in Poznań, Poland.

The African Rift Geothermal Development Facility (ARGeo), an intergovernmental project that will kick off in 2009, will underwrite private drilling operations in Kenya and several neighbouring nations. ARGeo is backed by US\$18 million from the GEF, the UN Environment Programme and the World Bank. Kenya has set a goal of generating 1,200 MW of geothermal electricity by 2015.



GALLO IMAGES/GETTY IMAGES

## Lectures gain electronic life in Egyptian library

Scientists from around the world are donating their lectures to the Bibliotheca Alexandrina in Alexandria, Egypt. These ‘golden PowerPoint’ presentations will be available from January for any academic to download and use.

The resource is aimed primarily at teachers and scholars in developing countries — as long as they have Internet access. The goal is to gather 100,000 lectures on medicine, engineering, environmental sciences and agriculture within the first year.

The Bibliotheca Alexandrina was opened six years ago, nearly two millennia after the original library, which housed all the knowledge of the Ancient Greeks and Persians, was destroyed. The new project aims to evoke its mission in the digital age.

► [www.bibalex.org/supercourse](http://www.bibalex.org/supercourse)



## 2008 GALLERY

## IMAGES OF THE YEAR

This gallery showcases some of the year's most eye-catching science, from a close encounter with squid suckers that look like a carnivorous cartoon choir to mathematical forms given shape in purple yarn.

It also recalls some of the biggest science news stories: the staggering devastation wrought by Hurricane Ike; a Nobel prize for putting a glowing protein to work; and the ongoing robotic exploration of Mars.

Researched and written by Emma Marris.

J. HART, S. TAWFICK, M. DE VOLDER & W. WALKER/UNIV. MICHIGAN

**NANOBAMAS**

These half-millimetre-wide portraits of the next president of the United States are each composed of 150 million carbon nanotubes — the same figure as the number of people who voted in the US election. No prizes for guessing who John Hart, a mechanical engineer at the University of Michigan in Ann Arbor, supported.

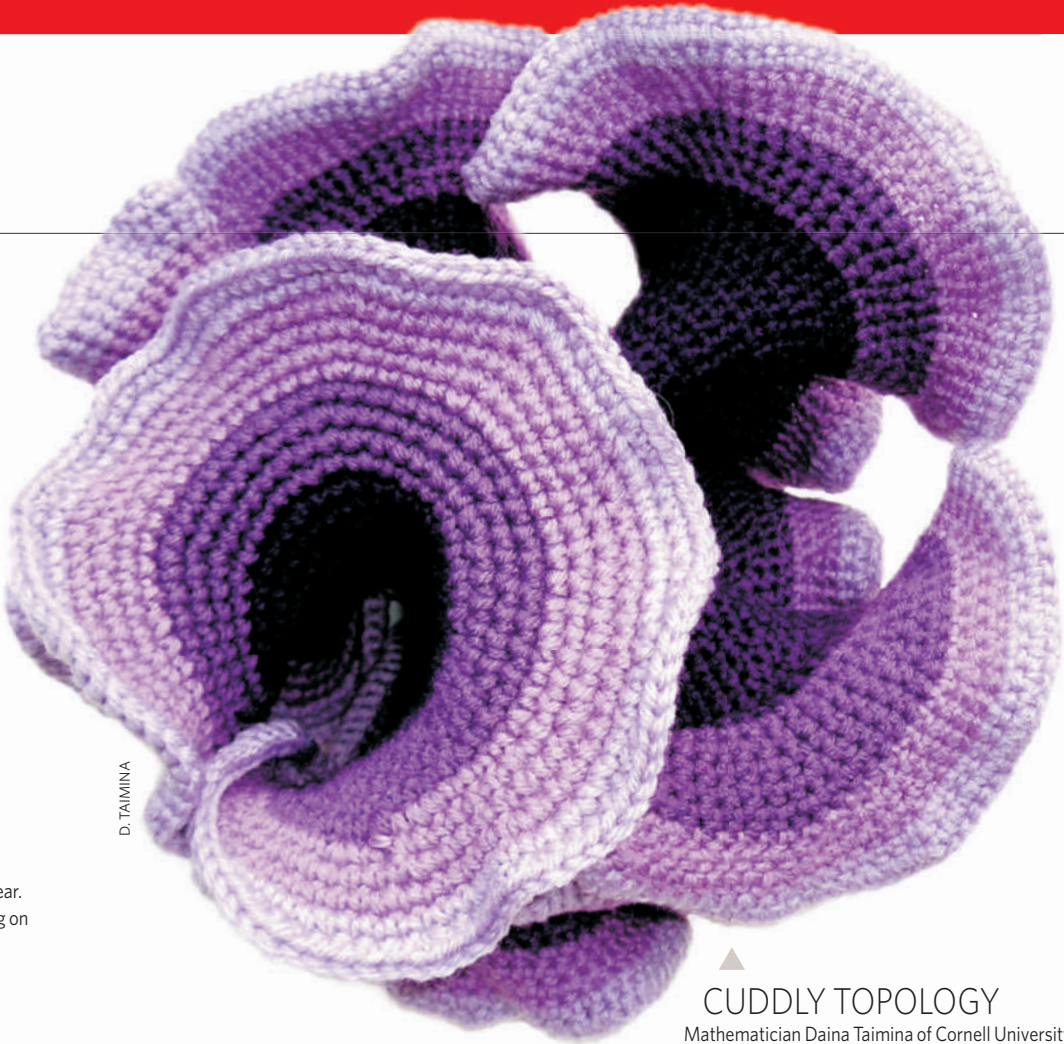


F. ROVERO



HELLO, SENGI

In the northern Udzungwa Mountains of Tanzania, researchers discovered a new species of sengi, or elephant shrew. The grey-faced sengi (*Rhynchocyon udzungwensis*), the largest yet known, was introduced to the world in January in the pages of the *Journal of Zoology*.



D. TAIMINA

CUDDLY TOPOLOGY

Mathematician Daina Taimina of Cornell University in Ithaca, New York, displayed this crocheted hyperbolic plane as part of the 'Beyond Measure' exhibition at Kettle's Yard gallery in Cambridge, UK.

S. N. POOL/GETTY IMAGES

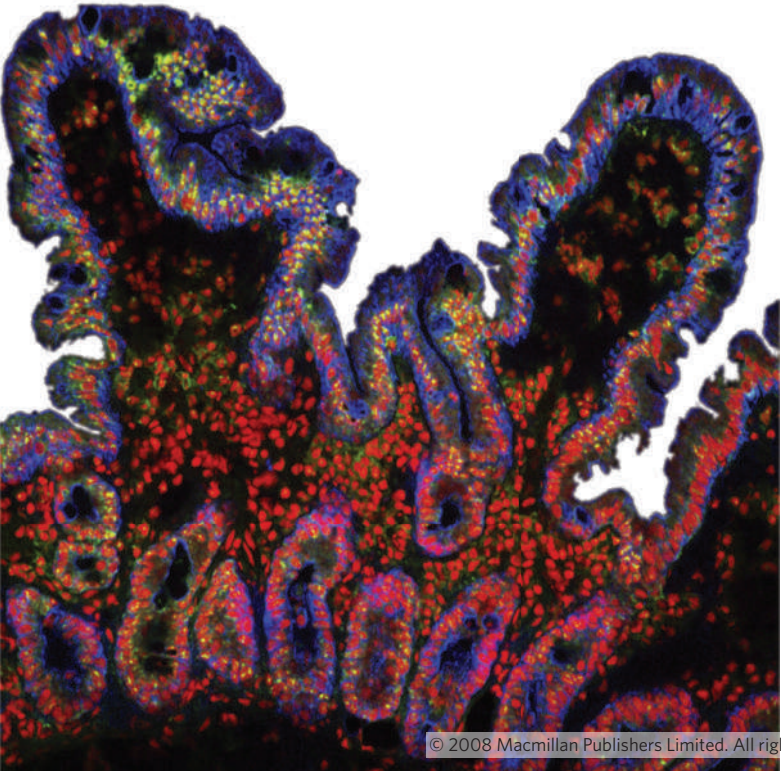


THE IRE OF IKE

Hurricane Ike killed more than 100 people and did billions of dollars' worth of damage this year. Gilchrist, Texas, took a battering on 13 September.

FLUORESCENT VILLI

Stunning images of biological structures such as these intestinal villi — fingerlike projections that increase the surface area of the gut available to absorb food — are made possible by glowing fluorescent proteins used to tag specific proteins in cells. The technology won the Nobel Prize in Chemistry this year.



S. SCHULLER/WELLCOME IMAGES

NASA/JPL-CALTECH



OPPORTUNITY ESCAPES

After investigating Victoria crater on Mars for almost a year, the rover Opportunity retraced its tracks out onto level ground in late August.



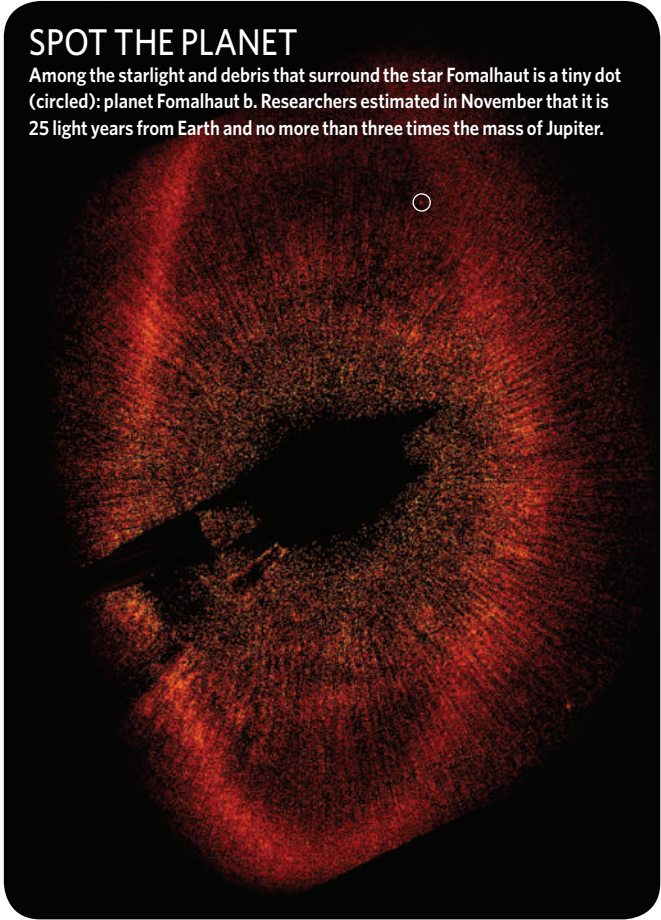
NANOTINSEL

This coloured scanning electron microscope image shows zinc oxide nanowires grown on carbon fibres, each about 10 micrometres wide. The image, created by graduate student Sharvari Dalal, was part of the annual photo competition organized by the engineering department of the University of Cambridge, UK.

S. DALAL

SPOT THE PLANET

Among the starlight and debris that surround the star Fomalhaut is a tiny dot (circled): planet Fomalhaut b. Researchers estimated in November that it is 25 light years from Earth and no more than three times the mass of Jupiter.



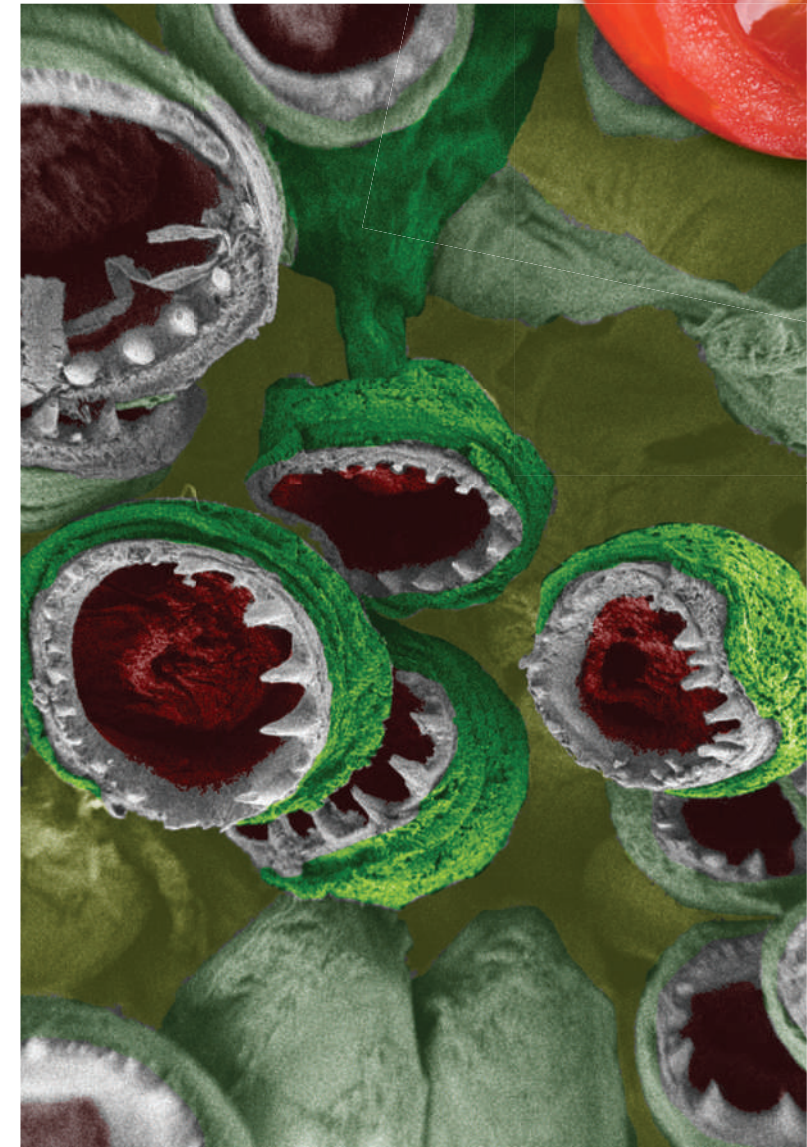
NASA/ESA/P. KALAS, J. GRAHAM, E. CHANG, E. KITE (UNIV. CALIFORNIA, BERKELEY)/M. CLAMPIN (NASA GODDARD SPACE FLIGHT CENTER)/M. FITZGERALD (LAWRENCE LIVERMORE NAT'L LAB.)/K. STAPELDELT, J. KRIST (NASA JPL)



SQUID SUCKERS

When deciding how to colour the various parts of a squid's suckers in this electron micrograph, Jessica Schiffman of Drexel University in Philadelphia, Pennsylvania, thought of the film *Little Shop of Horrors*. The resulting image won an honourable mention in the International Science and Engineering Visualization Challenge.

J.D. SCHIFFMAN & C.L. SCHAUER (DREXEL UNIV.)



NASA/JPL-CALTECH/UNIV. WISCONSIN

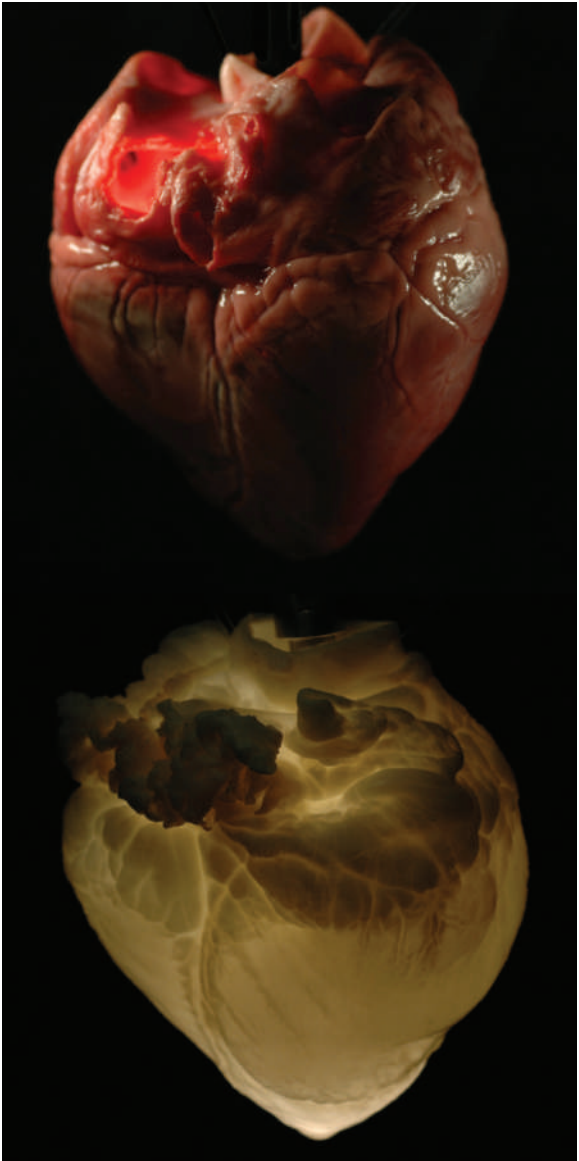


JOHN INNES CENTRE

GHOST HEART

The rat heart at the top is recognizably red and fleshy. The bottom heart has been stripped of all its cells with detergent, and is now nothing more than collagen and other bits of the extracellular matrix. These structures could one day be used as scaffolds for engineered hearts, according to bioengineers at the University of Minnesota in Minneapolis.

H. OTT/T. MATTHIEN



TOMORROW'S TOMATO

A dash of snapdragon genes turns a run-of-the-salad tomato into a deep purple, anthocyanin-packed life-extender — at least for mice susceptible to cancer, says tomato-gene juggler Cathie Martin of the John Innes Centre in Norwich, UK.

NASA/JSC

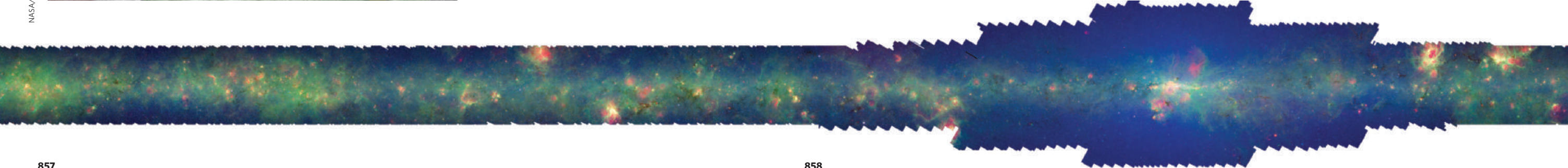
ORION OR ICARUS?

It "dropped faster than intended", explained NASA. This mock-up of the Orion crew exploration vehicle, lying nose down in the dust outside Yuma, Arizona, was undergoing a parachute test in July as part of NASA's Constellation programme to send human explorers back to the Moon.



MEET THE MILKY WAY

This is a section from a very long image of our Galaxy, as seen at infrared frequencies by the Spitzer Space Telescope. The full image, 60 metres long at full resolution, was made up of 800,000 frames and debuted at the American Astronomical Society meeting in St Louis, Missouri, in June.

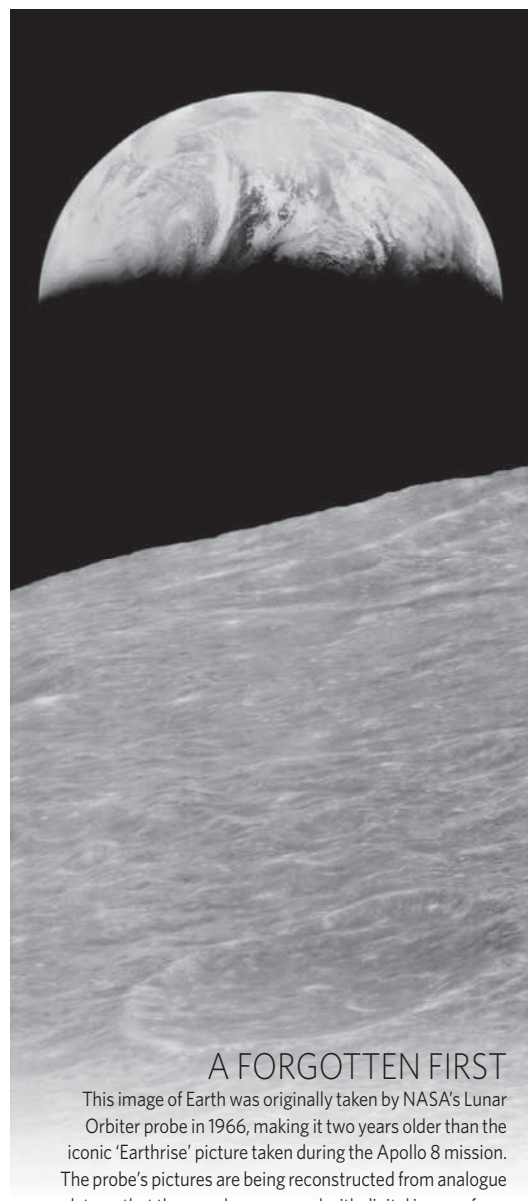






## ◀ COUGH!

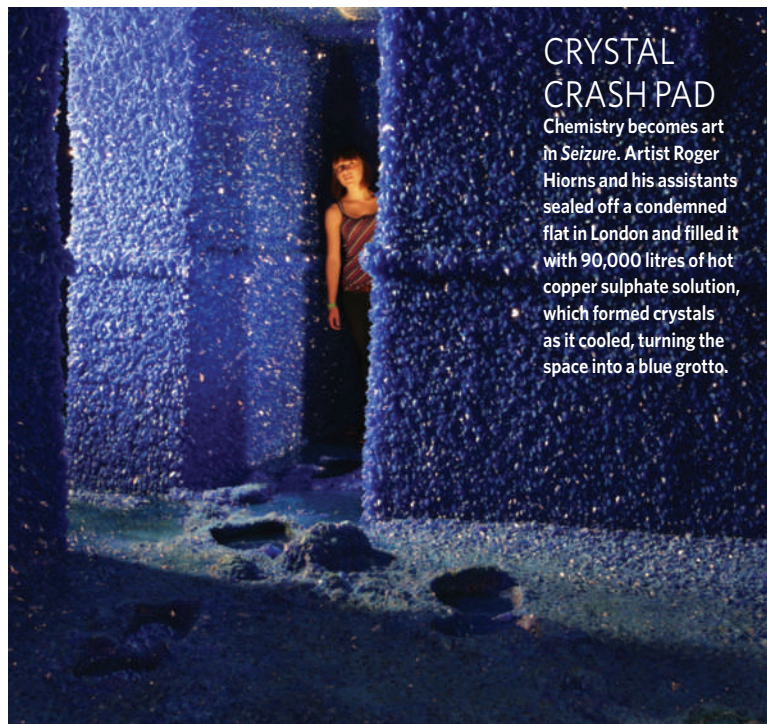
Researchers at the gas-dynamics laboratory of Pennsylvania State University in University Park visualized a cough by tracking changes in air density, and provided compelling evidence that it really is polite to cover your mouth as you hack away.



## A FORGOTTEN FIRST

This image of Earth was originally taken by NASA's Lunar Orbiter probe in 1966, making it two years older than the iconic 'Earthrise' picture taken during the Apollo 8 mission. The probe's pictures are being reconstructed from analogue data so that they can be compared with digital images from the 2009 Lunar Reconnaissance Orbiter mapping mission.

N. COBBING



## CRYSTAL CRASH PAD

Chemistry becomes art in *Seizure*. Artist Roger Hiorns and his assistants sealed off a condemned flat in London and filled it with 90,000 litres of hot copper sulphate solution, which formed crystals as it cooled, turning the space into a blue grotto.

© 2008 MASSACHUSETTS MEDICAL SOCIETY. ALL RIGHTS RESERVED

NASA/LOIRP



# PRIZEWINNERS OF THE YEAR

Medals, cash and fame rained down on the heads of prominent scientists in 2008. **Ashley Yeager** rounds up some of them.

## ROBERT LANGER: BRINGING HOME THE MEDALS

Chemical and biomedical engineer Robert Langer, of the Massachusetts Institute of Technology in Cambridge, racked up more major science prizes than any other researcher this year — the Millennium Technology Prize and the Max Planck Research Award, along with a share of the Prince of Asturias Award for Technical and Scientific Research. Total haul: about US\$2 million.

### What will you do with the money you've won?

One of the awards, the Max Planck, can be used for unrestricted research. I plan to do materials and nanotechnology research, in part with people from Germany.

As for the rest, my wife and I haven't figured out yet what we will use it for. We will probably use it for our children's education. Another top priority involves science education. We might use some of the money to help improve science education at

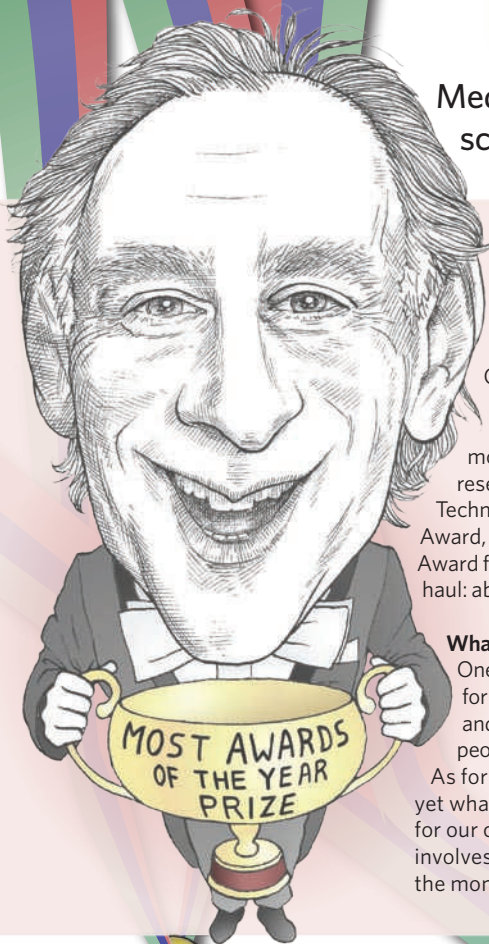
the high-school or college level.

### What is your recipe for success?

To the extent that I've been successful in research, it may be because I've often tried to do high-risk projects. When I was done with my PhD in chemical engineering in 1974, my colleagues were all going into petroleum engineering and chemical engineering. I decided to work in a surgery lab, the lab of Judah Folkman at the Children's Hospital Boston and at Harvard Medical School. It's like Robert Frost's *The Road Not Taken*. I didn't take the road most chemical engineers took.

### Ever thought about going back to petrochemicals?

Never. I struggled hard to learn the biology I needed. I never thought about other areas of chemical engineering. All I thought about was that I wanted to make a difference in people's lives, whether it was through education or health.



ILLUSTRATIONS: J. H. VAN DIJENDONCK





## BEATRIZ BARBUY: RISING STAR

Brazilian astrophysicist Beatriz Barbuy won one of the two Trieste Science Prizes given out this year by TWAS, the academy of sciences for the developing world. Barbuy, of the University of São Paulo, was honoured for her work on the evolution of the chemical composition of stars and the formation of the Milky Way.

### How important is it to have a prize that recognizes researchers from developing countries?

It is indeed very important. There is a group of people like me who devote a lot of effort to doing good work, and we have been fighting for better infrastructure. This recognition will help going ahead with having

better conditions for doing astronomy in Brazil.

### How did you react when you learned you had won?

I knew that I was submitted as a candidate, but I was surprised with being chosen. This is my first prize.

### How do you think astronomy can grow in Brazil?

We really need better observing conditions. The way to go with the expensive instruments nowadays clearly is through consortia involving other countries.



## SUMIO IIJIMA: BIG PRIZES FOR SMALL WORK

Sumio Iijima, a physicist at Japan's Meijo University who is widely credited as the discoverer of carbon nanotubes, has racked up numerous awards. In 2008, among other prizes, he won the the inaugural Kavli Prize in Nanoscience and shared the Prince of Asturias Award for Technical and Scientific Research.

### What does winning the inaugural Kavli Prize mean to you?

I feel a kind of responsibility; I have to behave well as a recipient since people may pay me special attention.

### How does it feel to win two major prizes?

I am extremely happy and glad to

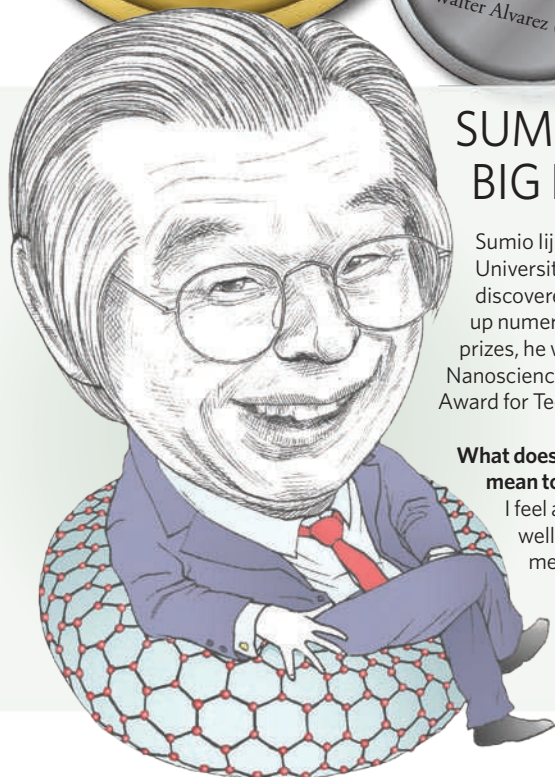
have these opportunities in a single year. Only one thing that I am not satisfied with is that both awards have not been known much in Japanese society.

### What will you do with the money?

I will keep it for myself and my family. Partly because I don't have a good pension programme. However, according to Japanese tax law, nearly one-third of it will be taken as tax. It is too bad!

### What advice do you have for other researchers hoping to be as successful as you?

My suggestion is you should do what you think best. You should believe in yourself. If you are an experimentalist, you should train yourself as the best technician in your field. I like the word challenge.



For more stories from some of the prizewinners, see <http://tinyurl.com/5o9g3m>.



# THE MACHINE MAKER

He did more than anyone to build the Large Hadron Collider. This year he saw it finished — and then break down. **Geoff Brumfiel** profiles the LHC's project leader, *Nature's* newsmaker of the year.

**LYNDON REES EVANS** gets up from his desk and crosses his sparsely furnished office to a shelf filled with notebooks. He pauses before choosing one and bringing it to the table. He opens it as fondly as if it were a family scrapbook, flipping through pages crowded with diagrams, budgets and the business cards of mid-level government bureaucrats. Finally he gets to what he was looking for: a photocopied drawing of a conference table. Most of the writing on the diagram is in Japanese, but around the table's edge someone has written names, including Evans's, in English. The date at the top is also in English: 2 March 1995. "This was it, this was the key meeting," he says. He points to a Japanese character written in a corner. "They even showed where the flowers were."

Most laboratory notebooks — like most family scrapbooks — don't record the place settings at meetings with Japanese parliamentarians. But this is the laboratory notebook, or rather one of many notebooks, of the largest scientific experiment ever constructed: the Large Hadron Collider (LHC), a particle accelerator at CERN, the European high-energy physics laboratory near Geneva, Switzerland. The LHC represents a level of ambition never before seen in physics, an ambition so monumental that its realization required it to become the first truly global experimental undertaking. It consists of hundreds of thousands of tonnes of extremely powerful machinery looped round a tunnel 27 kilometres long. Much of this hardware is chilled to within two degrees of absolute zero by a liquid helium system much larger than any seen before.

For most physicists, the LHC story — a new chapter in their discipline's history — has yet to begin. For Lyn Evans it is almost over. After a decade and a half of daily devotion to getting the machine built, he is due to retire at roughly the same time that the LHC will start to generate data. At 63, he is still never more than a quick recap away from being up to speed on every detail of its design and engineering. At one point he more or less redesigned it single-handedly on his kitchen table. Since he joined the project in 1993 he has built relationships with the world's physicists, politicians and industrialists to ensure its support; he has travelled to factories in Europe, North America and Japan to see its components forged; and he has tackled enormous technical challenges — the most recent and dramatic being a galling accident just weeks after the machine was first turned on. "He's the guy who made the LHC," says Chris Llewellyn Smith, a friend and former director-general of CERN. "That is what's going to be on his tombstone."

## Rise and fall

When Evans left his house in Versoix, France, on 10 September 2008, he was heading for the biggest scientific media event of the year. But that sort of slipped his mind. He didn't even mention to his wife that he would be on television

a little later on. He was entirely focused on the experiment.

At the CERN campus, which sits on the Swiss border about ten kilometres away, the car park by the main entrance was crammed with broadcast trucks and satellite dishes. Soon, the LHC's normally hushed control room was packed with news anchors, past laboratory directors and distinguished scientists. It was 'beam day' — the day on which protons would circulate around the LHC for the first time. "I have rarely been in such a stressful situation," Evans says later; he has a lilting Welsh accent that he has kept during four decades of living in France and Switzerland, and a stutter that becomes more pronounced when he is nervous.

The machine's eight sectors turn on one by one. There's a cheer each time the beam first passes through a sector; but it is the last sector — the one that completes the loop — that really counts. The cameras focus in on Evans's round face as he stares at a wall of flat-screen monitors. "So it will be on the next cycle — in about one minute," he says haltingly to the crowd. He completes the countdown in French: "*Trois ... deux ... un ... et zéro.*" Suddenly, two bright dots appear on a screen, a sign that protons have made it all the way round. The control room bursts into applause. Evans's face slackens into a broad smile. He moves around the consoles, shaking hands with the individual members of his team. "*Merci,*" he tells them all. "Well done."

The circulation of that beam puts the LHC on to more front pages the next day than any scientific event since the sequencing of the human genome. Just circulating the beam, though, is not enough. A second, counter-rotating beam has to be put through the machine. Then the current has to be upped, the acceleration increased, the beams focused to the point at which, when they cross inside vast buried detectors, the head-on collisions between protons are frequent enough to offer up a wealth of data. All that will take weeks, maybe months.

Then, nine days into the process, disaster strikes. On an otherwise quiet Friday morning, physicists in the LHC's control room were slowly pumping up the current in the magnets in the region called sector 3–4 to see whether the magnets would work as designed. Suddenly, their screens lit up with alarms. According to the computer, more than 100 magnets inside the machine had 'quenched' or lost their superconductivity. Uncontrolled quenches can be disastrous. Currents of many thousands of amperes can be handled quite safely by superconductors, but they will turn magnets to slag if they encounter even a little electrical resistance. Those in the control room knew that what had happened in sector 3–4 was serious even before a second set of alarms warned of falling oxygen levels along a subsection of the tunnel. Then, the entire sector's power cut out. The operators were literally in the dark about what was happening five kilometres away, more than a hundred metres below the French countryside.

"There were several clever people, but Lyn was really exceptional."

— Walter Scandale



"I was over in the personnel department haggling about some recruitment problem when I got a call," Evans says. He rushed across the lab to the control room. At first, he says, he couldn't understand how so many magnets would quench simultaneously. But he and others soon realized that the quench was by design. The LHC had automatically brought the magnets out of their superconducting state to protect them. At the same time — and probably for the same reason — it had sprung a leak. The oxygen alarms had been triggered by helium escaping onto the tunnel.

Two months later, sporting jeans and a red Geneva Squash Club sweatshirt, Evans introduces me to the culprit behind both quench and leak. The tops of the Jura mountains to the west are obscured by cloud, the Alps to the south nowhere to be seen. We are in a blocky industrial building on the edge of the campus, where four of the LHC's superconducting magnets are scattered about in various stages of disassembly amid shelves of vacuum flanges and copper

tubing. A handful of technicians move between them.

From afar, the magnets look like 15-metre sections of what might be a Franco-Swiss oil pipeline. Their long steel tubing is painted an evening-sky blue, and some have "LHC dipole" in white lettering on their side. Running through each dipole are the two pipes that carry the colliding proton beams in opposite directions around the machine.

"This is the famous busbar that burned," says Evans, pointing at a small ribbon of niobium-titanium alloy, no wider than his own thick index finger, sticking out of the end of a dipole magnet. To an untrained eye, it is almost indistinguishable from the dozens of other superconducting wires that supply the magnets with current. The busbar, however, is the mainstay of the machine's electrical system. It distributes the primary current between all the magnets in a given sector. During installation, the busbar ribbon leading from each magnet must be connected manually to the next by brazing. Evans and his team now think a bad braze

M. BRICE/CERN





Under repair: dipole magnets hauled out of the LHC's tunnel after the accident.

lay behind the accident. When it came undone, 8,700 amps of current vaporized a half-metre length of the ribbon and punctured the LHC's heavy vacuum insulation. The liquid helium it protected boiled instantaneously. The outer shell gave the gas boiling off nowhere to go; in places the pressure built up to 20 atmospheres, prying magnets loose of their steel anchors. All told some 53 magnets were affected.

Now it all needs to be fixed: the damaged magnets must be replaced, the underlying causes sorted out. If a busbar braise bursts again the team has to be sure it won't fill up the system with high-pressure helium. To that end, relief valves need to be added all through the machine.

Before the accident, Evans had hoped to provide the world's waiting physicists with the LHC's first collisions by November 2008. Now, the machine will not start running again until summer 2009, and probably not do any serious physics until 2010. The frustration is all the worse because the team got so close to getting things to work first time. "This was the last circuit on the last sector, so it was a bitch," Evans says. "Fortunately, I've had some hard problems in the past."

### The antimatter opportunity

The hard problems that established Evans's reputation at CERN came about when the lab took a gamble on an utterly new technique in the 1970s. There was a revolution under way in particle physics, and part of its promise was to confirm a prediction that the electromagnetic force and the weak nuclear force were aspects of the same underlying process. This unification called for new particles, called the Z and W bosons, which were suddenly highly sought after. Unfortunately, no accelerator had remotely enough oomph to produce any of them. The big machines — the Main Ring at the Fermi National Accelerator Laboratory (Fermilab) in Batavia, Illinois (see 'Making it big'), and the Super Proton

Synchrotron (SPS) at CERN — were designed to shine their protons on to fixed targets. In fixed-target physics, only a small fraction of the energy in any of those protons is used to make new particles, and neither the Main Ring nor the SPS had any chance of making the new bosons.

In machines that contained two counter-rotating beams it would be possible to arrange head-on collisions between particles — collisions in which a large fraction of the energy released went into producing new stuff. They could make Ws and Zs. The problem was that proton colliders were hard to build; there had only ever been one, a CERN machine called the Intersecting Storage Rings, or ISR, and it operated at much too low an energy to make Ws and Zs. There seemed no way forward until Carlo Rubbia, a gifted and monumentally ambitious Italian physicist, started touting a cunning plan: turn one of the big proton machines into a collider by putting a beam of antiprotons into the same tube as the protons circulating in the opposite direction. Fermilab balked at this outrageous idea, but CERN — a previously rather humdrum lab keen to up its game — gave it a shot.

The project required all CERN's technical tenacity. Antiprotons had to be made from scratch (contrary to the novels of Dan Brown, CERN does not have stocks of antimatter just lying around) and accumulated over weeks, carefully sequestered from regular matter and 'cooled' into a tight beam. Evans took on the complex calculations needed to describe how the particles in such beams would ricochet off one another as they travelled together around the SPS's ring. He then helped to design a set of magnets that could keep the beam tightly packed. "There were several clever people, but he was really exceptional," says Walter Scandale, a long-time CERN physicist who has worked with Evans throughout his career. "I'm speaking of the top 5% at CERN."

Before the SPS, Evans had not necessarily been committed to a career at CERN. A few years after he arrived in the 1970s he was offered a job at the Joint European Torus, a European fusion experiment at Culham, near Oxford, UK. "I brought the offer home and my wife, for reasons known only to her, decided she wanted to stay here," he says. He was unhappy with the decision. "I didn't see where the next step was going in accelerators." After the proton-antiproton work he could see the next step clearly. The challenge of marshalling beams of powerful particles had bewitched him, and CERN was the best place to put it to work on a truly epic scale.

This speciality of Evans's, accelerator physics, is an odd one. It is scientifically demanding, but to an outsider it sounds like a secondary, almost menial, role: the exciting theory-overturning physics is what comes out the other end. Insiders, though, know that accelerator physicists are absolutely crucial, and CERN's culture reflects that. As Philippe Lebrun, who directs the lab's accelerator technology department, puts it: "The accelerator theorists are a kind of aristocracy."

**"Lyn started working like hell on the accelerator. And he made quite a lot of changes." — Chris Llewellyn Smith**

In his childhood, few would have taken Evans for any sort of aristocrat. He was born in 1945 in the Welsh mining town of Aberdare. His father worked down the pit and died of the lung disease silicosis when Evans was just 11. Evans's mother took a job at a school canteen, struggling to support Lyn and his younger brother Peter. It is not a time that Evans is keen to talk about; but he does say that, although it was difficult, he was "perfectly happy". "I played for the town football team, I played rugby, I had a good social network." He got a place in the local grammar school, but describes himself as an undisciplined student until, around the age of 16, he started to get enthusiastic about science. Trying to remember the appeal, he thinks of newspaper stories of hydrogen bombs and fusion power that was too cheap to meter. "All these things were happening, and that just sort of gelled with my own interests and my abilities," he says. "I found science easy."

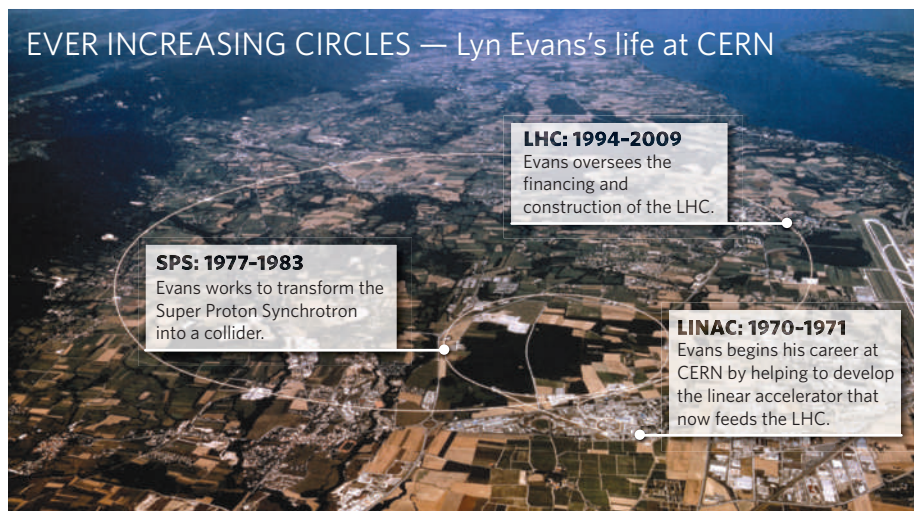
He received top grades in his A-level exams, and went to the University of Wales in Swansea. He started in chemistry but soon switched to physics, staying at Swansea to complete a PhD on fusion energy. On a weekend home in Aberdare he met his wife Lynda, and the couple married in 1967. His adviser, Colyn Grey Morgan, had connections to CERN and convinced the young physicist to apply for a fellowship at the laboratory. Evans had no knowledge of how particle accelerators worked, but his fusion work had focused on stripping gas molecules of their electrons, so he started there, turning hydrogen atoms into protons in a way that suited the accelerator he was working on. "That was my baptism," he says. "I've come all the way from the hydrogen bottle."

The hydrogen bottle led to a linear accelerator, the fixed-target version of the SPS and finally the antiproton work that turned the SPS into a collider. Thanks to Evans and others like him, the gamble that CERN had taken paid off spectacularly. The first *W* and *Z* bosons were found in 1983. A year later, Rubbia got a Nobel prize for the discovery — as did Simon van der Meer, the accelerator physicist whose cooling technique had made it possible. For Evans the real significance of the project was what it suggested might be possible in the future. "For me it was the essential prototype," he says. "Although the LHC was far over the horizon in those days, this is where we learned the physics of intense stored particle beams."

The next machine at CERN, though, was to be different; it would work with electrons, not protons. The Large Electron-Positron collider (LEP) was in some ways technically quite simple; it could manage quite well without superconducting dipoles and the like. But at the same time it was, as the name made clear, large. To be big enough to further the study of *Z*s and *W*s, it had to have much more tunnel than the SPS. And that was a good thing. Rubbia, who became head of CERN in 1989, knew that he would never get the money to build a big proton machine from scratch. Somewhere down the line, though, putting a proton machine into a tunnel that had already been dug might be quite feasible. Before LEP was even finished, Rubbia was forcefully advocating the idea of a similarly vast proton collider as a follow on: the LHC.

CERN started to put more effort into the LHC's design.

## EVER INCREASING CIRCLES — Lyn Evans's life at CERN



CERN

But many European politicians had doubts about actually building it. The United States, stung by its failure to discover the *W*s and *Z*s, was building a much bigger 87-kilometre superconducting supercollider, which would achieve energies three times higher than the proposed LHC. How could CERN's machine be anything other than an also-ran?

### Collide and conquer

In 1993, Llewellyn Smith arrived to replace Rubbia at the same time that Giorgio Brianti, who was leading the LHC project, was planning retirement. Llewellyn Smith needed to appoint a replacement.

"It became pretty clear to me that Lyn was the right guy to do the job," he recalls. In 20 years Evans had worked on practically every accelerator at the laboratory, which would be useful knowledge; several of them would have to be run together into a cascade of pre-accelerators to provide the LHC with its beam. And for all his CERN experience, Evans was only 47 years old. He would be able to see the project through to its completion. Evans accepted the position immediately, and although he was not officially scheduled to take over until 1994, he began a vigorous redesign of the machine. "Lyn started working like hell on the accelerator," Llewellyn Smith recalls. "And he made quite a lot of changes."

In October 1993, as Evans was in the midst of reworking the LHC design, the US Congress dropped a bombshell. Furious with projected cost overruns and poor management at the US supercollider project, it withdrew its funding for the accelerator, even though construction had already begun.

The supercollider's cancellation put the LHC back in the game. In fact, it made it the only game in town. But it could still prove too rich a game for the blood of CERN's member states. Evans trimmed hundreds of millions of Swiss francs from the budget. However, in June 1994, Britain and Germany, two of the most powerful members of CERN's council, balked at the price tag of 2,350 million Swiss francs (US\$1,590 million).

Evans and Llewellyn Smith hatched plan B: a design in which the LHC would initially be built with only two-thirds of its superconducting magnets. In terms of physics it was unthinkable — it would cripple the machine's capabilities — but politically they knew that it might be the only

**"It was a totally crazy scenario. But one that was swallowed by the German government."**  
— Lyn Evans



way to get the CERN council's support. Once they had that support, Evans and Llewellyn Smith could go and get the rest of the money from elsewhere — from Japan, which had been a reluctant partner in the superconducting supercollider, and perhaps also from the humbled Americans.

So Evans found himself the Sunday before a crucial trip to Bonn working furiously at his kitchen table to finalize a design that, he believed, could never produce ground-breaking science. "It was a totally crazy scenario," he says. "But one that was swallowed by the German government." The project won approval from the council in December 1994, and Evans and Llewellyn Smith were given two years to find the money for the full-power machine. Suddenly the shy physicist, who had spent his entire career cloistered at CERN, was thrust into the unexpected role of international diplomat — a role he would find fascinating.

"I was mystified at first," he recalls of his early visits to Japan. "We would have ten courtesy visits in the morning, just in and out, covering all the bases. We drank so much green tea." But Evans is in many ways a natural negotiator. He is quiet and deferential, but also confident and engaging, especially when speaking one-on-one. "He never says what doesn't need to be said," says Peter Limon, a high-energy physicist from Fermilab who worked with Evans on bringing the United States into the project. "That's sort of the definition of a diplomat."

The efforts paid off. In June 1995, some ¥5 billion (US\$50 million) appeared for the project, wrapped up with emergency spending in the wake of the Kobe earthquake. "With no warning at all, we had the announcement of a

**"Evans never says what doesn't need to be said."**  
— Peter Limon

contribution," Evans says. "That started the ball rolling." In the cash-strapped Russian Federation, a complex arrangement was worked out whereby CERN and the Russian government each paid for a third of parts supplied. "The third third, nobody knew where it came from," he says. "It was just cheap labour."

By the end of 1996, CERN had secured contributions from Japan, India, Canada and Russia, and had a strong signal of interest from the US government. Then came the 'kick in the teeth': Britain and Germany announced at the last minute that they would not meet their 1994 commitments. But the council allowed CERN to make up the shortfall with loans from the European Investment Bank. By 1996, construction work on the project had begun — and Evans's role changed yet again, from designer to diplomat to something more like a foreman.

### Organized chaos

You might expect a laboratory based on the border of France and Switzerland that measures the fundamental symmetries of existence to be a supremely orderly and Cartesian sort of place. You would be wrong; it is in fact decidedly higgledy piggledy. Its gently decaying post-war buildings, to take one example, are identified in such a way that numbers 30, 112 and 376 sit side-by-side — half a kilometre away from building 31. Either through force of habit or tradition, the thousands of physicists and engineers from dozens of nations who work at the lab organize themselves in the manner of academics: they set up small and often loose collaborations; when absolutely necessary they will

## Making it big

A machine as ambitious as the LHC could only be undertaken by a vast multinational organization. Other big science projects have come about differently — and with very different characters at the helm.

"Perhaps we were his slaves, but we liked it," declared George Ellery Hale's younger brother, who along with his sister had been recruited to help the teenaged Hale build a substantial laboratory in their Chicago home. "We always had the belief that with him we were going to do things that were mysterious."

That charisma and leadership led Hale to become a driving force in the new science of astrophysics. In 1892, 24-year-old Hale approached Charles Yerkes, a shady financier who had renewed his fortune in Chicago after being run out of Philadelphia. Yerkes had already turned down a request from the recently founded University of Chicago in Illinois to build a biology laboratory, but Hale was evidently more persuasive. Emphasizing that he wanted to build the

biggest telescope in the world, and that it would preserve Yerkes's name for posterity, Hale extracted enough money to build the Yerkes Observatory in rural Wisconsin and get his 102-centimetre refracting telescope up and running by 1897.

Hale later moved to California, where he found prime observing sites in the mountains overlooking Los Angeles, and made contact with a fresh supply of entrepreneurs eager to indulge in grand philanthropic gestures. The result, in the early twentieth century, was a series of what were then the world's greatest telescopes: the 152-centimetre reflector telescope on Mount



**George Hale drove astrophysics in the 1890s.**

Wilson, then the 254-centimetre Mount Wilson telescope — the instrument Edwin Hubble used to discover the expansion of the Universe — and finally the 508-centimetre Mount Palomar telescope, which was completed after Hale died in 1938.

In the late 1920s, meanwhile, a young, South Dakota-born physics professor named Ernest Lawrence also headed west. Feeling hemmed in by Yale's academic atmosphere, Lawrence tied his ambitions with those of the rising University of California, Berkeley. There, after building the first cyclotron in 1931 — a palm-sized machine

that could accelerate protons to 80,000 electronvolts — he immediately hatched plans for larger accelerators. "Lawrence was young, he was bursting with energy, his enthusiasm swept me off my feet," recalled one early collaborator. "He would try to outdo you in seizing the implications and possibilities" of any new idea put to him, said another. Eager young physicists began to show up on his doorstep asking to be put to work. Lawrence also proved adept at charming money out of the nouveau riche of California, seizing on the largely unproven medical benefits of particle beams as a way to attract donations.

One young physicist whose career got an early boost from research funds under Lawrence's control was Robert Wilson, who

put together a committee to decide on a course of action. Paperwork can meet with something approaching deliberate disregard.

Evans's style is much in line with that culture. Understandable, as he has worked there all his life; necessary, too, as imposing any other style might prove impossible; and probably wise, as CERN has brought in groundbreaking mega projects one after the other. True to CERN culture he oversaw the LHC project with a group of around half-a-dozen advisers. The bulk of the daily work was carried out by teams that resemble academic lab groups, each responsible for a subsystem or a sub-subsystem, but overall scheduling remained the preserve of Evans's core team alone. It was an approach seen by some as aloof. Still, when someone ran into a technical problem, Evans would be one of the first on the scene to help. He would get his hands dirty literally and metaphorically; he would take the hours needed to understand a cooling system in the most painstaking detail.

Some at the lab, particularly the engineers, see a downside to Evans's loose, confederate approach. At the start of the project he didn't have all the stringent, quality-control procedures that were needed, says Gerard Bachy, a mechanical



A taste of things to come: Evans with his machine's much sought-after quarry.

engineer who has since retired from the laboratory. "It's not just paperwork at all," he says. "You have to have full traceability for each bit and piece — it's a very complicated machine." And Evans's readiness to mingle on the floor of the machine shop, although often appreciated, left some middle managers feeling out of the loop. There were frayed egos and crossed wires.

A consequence of what one engineer describes as Evans's

F. COFFRIN/AFP/GETTY IMAGES

later became the first director and guiding spirit of the National Accelerator Laboratory (NAL) in Batavia, Illinois, subsequently renamed the Fermi National Accelerator Laboratory (Fermilab).

### More for less

Wilson was something of a swashbuckler, pushing ahead with design changes for the original NAL accelerator that yielded higher particle energies for less than the anticipated cost. Barry Barish, now at the California Institute of Technology in Pasadena, recalls how he and another young Fermilab colleague proposed a new way to make neutrinos — and found that Wilson was not only eager to hear their suggestion, but also willing to take a chance on trying it. "Wilson was very adventurous and had lots of confidence in himself," Barish says. He made mistakes, but always believed he could fix them and move on.

Barish later undertook a big task of his own, overseeing construction

of the US National Science Foundation's Laser Interferometer Gravitational Wave Observatory (LIGO) at two sites, in Louisiana and Washington, during the 1990s. The people who build such one-of-a-kind, sophisticated projects have to be scientists with an aptitude for management, he says. "The hardest thing is to make the instrument as good as you can to meet science goals" within the restrictive setting that government funding and oversight inevitably entails.

Particle physics, with its complex detectors and need for large scientific teams, seems to have become a breeding ground for big-science managers. Jerry Nelson, for instance, left particle physics and returned to an early interest in astronomy because he didn't savour the prospect of working with 50-person teams.

But when he joined a study of the future of ground-based astronomy at the University of California, Santa Cruz, he began advocating a new segmented-mirror design that would make huge mirror diameters both technically feasible and affordable. He then became the project scientist for the Keck Observatory in Hawaii.

Taking a new technology from demonstration projects to a working telescope

brings with it an unavoidable tension between the scientific desire to tinker and improve, and the managerial responsibility to stick to budgets and schedules, says Nelson. For Keck he worked with project manager Jerry Smith, who had overseen several space and astronomy initiatives at NASA's Jet Propulsion Laboratory in Pasadena, California. Nelson says that part of his job was to argue for changes that would

benefit the project, whereas Smith's role was to limit risk. The arrangement "worked very well", Nelson says. Smith could be "tough to get along with, but I always understood his perspective".

Although neither Nelson nor Barish claim any premeditation in their career paths — Barish says he was drawn into big projects because "the most exciting science requires the most complex instruments" — both seem to have settled into a niche that few scientists would aspire to, let alone succeed at. Nelson is now project scientist for the Thirty Meter Telescope, an instrument that will take segmented mirror technology far beyond the 10-metre aperture of the two Keck telescopes. It is due to begin construction in 2009. Barish, although still associated with LIGO, is now director of the global design effort for the International Linear Collider: a proposed electron-positron collider that would be a companion to the Large Hadron Collider.

David Lindley



Ernest Lawrence built the first cyclotron.

NEW YORK TIMES/GETTY IMAGES



“soft control” of the project became apparent towards the end of 2000. Six years after the LHC’s initial approval, CERN’s council wanted a new cost estimate. As auditors looked in more detail at what had already been spent, they realized that the project was likely to run over budget by about 20%. Evans, now the accomplished diplomat, pushed hard for the lab’s director, an Italian particle theorist named Luciano Maiani, to break the news to the member states gently. Instead, Maiani presented the cost overrun to an open council meeting in September 2001, along with a bald request for the inflated budget needed to cover it. The council members were furious. Robert Aymar, a French physicist with a background in nuclear fusion and a long history on large projects was called in to mount a full review of the lab’s management. Evans was an obvious and possibly politically expedient target. “Many people were shooting at Lyn,” recalls Lucio Rossi, who oversaw the making of the LHC’s magnets.

But Aymar did not fire Evans. He was more worried about the generally fragmented culture at CERN, which made it hard for the lab to focus and prioritize, than about Evans’s specific handling of the LHC. Aymar says that although he recognized Evans’s faults, there were many more reasons to keep him on than to fire him: he was popular with the staff and he was willing to work to keep a better track of future costs. Above all he really understood the machine, and could manage the complex relations between its millions of components and the thousands of people and organizations responsible for them.

Evans repaid the confidence. Aymar took over as director-general of CERN in 2004, and soon thereafter the machine was faced with a major crisis: the system that fed liquid helium to the magnets proved too poorly manufactured to be used. After that it was a design flaw in some of the magnets. Then there were problems with the connections between sections of beamline. Every time, Evans’s calm, low-key approach and overall grasp of the project let him reorder the responsibilities of CERN staff and outside contractors, keep the council calm and find the workaround. “He is the one who is able to control the technical part of the project, which is by far the most important,” says Aymar today.

### The Last Hadron Collider?

Although the setbacks were weathered, there were costs to doing so: the problems with the liquid-helium system, for example, delayed completion by nearly a year. The lost year now facing the machine is thus not unprecedented. But it has come about in a much more public way.

Sitting in a kitchen that adjoins the LHC’s control room, Evans maintains his usual upbeat attitude. “When the damn thing works, it will be the scientific tool for really crossing the frontier into new knowledge,” he says. Throughout the winter — during which the LHC would normally be shut down anyway, as electricity costs a lot more — engineers are working double shifts to replace dozens of magnets and to repair those damaged in the incident. Meanwhile, new diagnostic tools are being developed to spot faulty connections before they can cripple the machine.

The first collisions cannot come soon enough for the lab’s frustrated detector physicists, many of whom have had PhD theses and sabbaticals derailed by the accident. Evans has found himself the subject of more than one



Vanishing point: the LHC stretches out into CERN’s future.

ad hominem attack in physics chat rooms and blogs; he knows because he Googles to find out.

If Evans is confident that the LHC can get through this just as it got through earlier slip-ups and crises, he is less certain about CERN’s long-term future. Each generation of accelerators becomes larger and more expensive. The next machine the community wants to build will be an electron machine, like LEP, but linear rather than a loop. If its 30-kilometre rifle barrel is ever built, it is unlikely to be in the suburbs and farms around CERN. There are, currently, no plans for any further proton machines after the LHC, although the LHC itself could be upgraded. The first proton collider was built at CERN: the last one may have been, too. The CERN that Evans came to in the 1970s, about to occupy the commanding heights of particle physics for the rest of the century, is nearing the end of its time. Quite a few of Evans’s younger colleagues have moved from the LHC to the new international fusion project in France, ITER. Evans says that if he were starting now, he might head in the same direction.

But he sees no rush for CERN to diversify out of particle physics. “The flagship for the next 20 years at CERN will be the LHC.” Due to retire in 2010, Evans plans to split the subsequent years between the local golf courses and some part-time work on the upgrade plans. “I kid myself that it’s not going to leave a void,” he says, knowing that it will. “The ability to step away is something that I’m going to have to test myself on.”

Building the LHC has taken his days, his evenings and his weekends. He has so much unused holiday from his years devoted to the machine that he had originally been planning to quit the project next October, months shy of retirement, to use it up. Now he has to face the faint worry that even then it might not be working. It won’t be for lack of effort by him and his team — but it will mean a change of plan.

“If it still isn’t working,” he says matter-of-factly, “I certainly will not take my vacation.” ■

**Geoff Brumfiel is a senior reporter based in London.**

**See Editorial, page 837.**

M. BRICE/CERN

# CORRESPONDENCE

## You're the best man for this job, son. What a coincidence!

SIR — As an Italian PhD student abroad, I agree with your Editorial 'Situations vacant' (*Nature* **456**, 142; 2008), in which you discuss issues influencing the hiring of academic staff in Italy. The day after this was published, details of yet another scandal in the Italian academic world appeared in the Italian newspaper *Corriere della Sera* under the headline 'A single candidate for a research position: the professor's son' (<http://tinyurl.com/5nsd2c>).

The emergence of a single candidate in the *concorso* (national competition) for a position at the University of Messina in Sicily is surprising in itself: such *concorsi* are rarely held, owing to the limited funding available to Italian universities. Even more disturbing is the fact that two other candidates stood down unexpectedly at the last minute, ensuring the victory of the one who remained.

The successful candidate's father had retired from the same faculty, so his alleged reply in an interview by the newspaper's reporter to a question regarding the candidate's identity was perplexing: "Ask the university. How can I know him? This is a national competition!" He apparently added, "If my son is the only candidate, it is because there were no other people that fulfil the requirements", and continued with the disturbing reflection that professors' sons are more suitable for such positions because their home environment has given them the right mentality.

This kind of event is all too familiar in Italy. An example of an 'academic dynasty' was reported last year in the newspaper *La Repubblica* (<http://tinyurl.com/5lqwul>). But the words of a professor who reportedly doesn't recognize the anomaly of the system, while claiming superiority for his offspring, add another distasteful component.

Considering this situation,

I would like to conclude by changing your Editorial's statement into a question. Should Italy's universities be free to hire whom they want?

**Albert Ruggi** Laboratory of Supramolecular Chemistry and Technology, University of Twente, PO Box 217, 7500 AE Enschede, The Netherlands  
e-mail: [a.ruggi@tnw.utwente.nl](mailto:a.ruggi@tnw.utwente.nl)

Readers are welcome to comment at <http://tinyurl.com/5lg42f>.

## Online archives are revealing uncensored history of science

SIR — Search engines are invaluable for finding out about the latest research but, thanks to publishers' efforts to digitize back issues of scientific journals, we can now also search deep into the past. And what turns up isn't necessarily pretty.

In the CAB (Centre for Agricultural Bioscience) abstracts database, for example, I found more than 100 articles written by the discredited Soviet geneticist Trofim Denisovich Lysenko. One of his most astounding reports, in a 1947 issue of the journal *Literaturnaya Gazeta*, declaimed that: "intraspecific competition does not occur... the opposition of bourgeois geneticists to this theory is attributed to their desire to justify capitalist exploitation, which is essentially a struggle within the human species".

Another search, using Web of Knowledge, brought up hundreds of Chinese scientific articles from the decades after Mao Zedong came to power in 1949, with titles such as 'Chairman Mao's brilliant philosophic thought guides me in winning triple cropping with high yield' (*Li K. C. Sci. China Ser. A* **20**, 391-391; 1977).

Also using Web of Knowledge, I came upon 70 research papers by Claus Schilling, the Nazi war criminal who conducted medical experiments on prisoners in Dachau concentration camp. None of

his wartime research is in the database but, as I scrolled through the record of his publications, I found myself looking for the point at which he had gone wrong.

These examples stand in contrast with the high-minded official version of science history that we read in textbooks. As Thomas Kuhn remarked in *The Structure of Scientific Revolutions* (Univ. Chicago Press, 1962), science is like Big Brother's society in George Orwell's 1984 — constantly rewriting history to show itself in the best light.

But will this censorship be possible when every politically motivated, unethical and demonstrably incorrect scientific article breaks out from dusty library storerooms to appear online? How will anyone be able to believe that science is an honest quest for truth, when its inglorious past is a mouse click away?

**William Burns** Diamantina Institute for Cancer, Immunology and Metabolic Medicine, University of Queensland, Princess Alexandra Hospital, Ipswich Road, Woolloongabba, Queensland 4102, Australia  
e-mail: [w.burns@uq.edu.au](mailto:w.burns@uq.edu.au)

## Finding of unusual soil on Mars could stem from tools used

SIR — In your News story 'Phoenix fades away' (*Nature* **456**, 8-9; 2008), you suggest that the polar soil analysed by NASA's Phoenix Lander "was like nothing else tested so far on Mars". But the soils sampled may not be unusual at all. An alternative explanation may lie with the instruments used for the analysis, given that these had never been used before.

The Martian soils were found to be alkaline and to contain trace amounts of perchlorates and carbonates. But they may still be similar to the soils analysed by previous landers. The Phoenix measurement of soil pH (pH 8.3) was carried out by dissolving small amounts of soil in liquid water. Geochemical

modelling indicates that adding water to the ionic composition of the most acidic environment described so far on Mars, Meridiani Planum, should give a pH of 9.2, according to my own calculations. The identification by the Mars Exploration Rover (MER) Opportunity of a set of minerals that could not precipitate in an alkaline solution, including sulphate evaporites, provides information about a post-settlement acidification at Meridiani. This was driven by gaseous carbon dioxide, sulphur dioxide and iron ions, neutralizing the pH-raising capacity of the basaltic minerals in the host rock and allowing the synthesis of acidic minerals.

Also, the discovery of perchlorate as a result of diluting Martian dust in water and searching for the soluble salts it contains is not necessarily a unique characteristic of the Phoenix soils. The inferred presence of chlorides at all Martian landing sites may not be the sole explanation after the identification of chlorine. It has been known since the Viking missions in the seventies that conditions at the Martian surface are strongly oxidizing. This could be due, for example, to chlorine salts such as chlorites, chlorates and perchlorates that originated photochemically in the atmosphere.

Moreover, the signal for calcium carbonate encountered by Phoenix is in fact the same footprint found by Mars Global Surveyor in soils all around the planet in 2003, and by the MER Spirit in Gusev crater in 2004. The only difference is that these previous identifications uncovered magnesium carbonate.

It is, therefore, possible that if the previous landers had incorporated the same analysis capabilities as Phoenix, the results might have been very similar.

**Alberto G. Fairén** Space Science and Astrobiology Division, NASA Ames Research Center, MS 245-3, Moffett Field, California 94035, USA  
e-mail: [afairen@arc.nasa.gov](mailto:afairen@arc.nasa.gov)



## COMMENTARY

# Three rules for technological fixes

Not all problems will yield to technology. Deciding which will and which won't should be central to setting innovation policy, say **Daniel Sarewitz** and **Richard Nelson**.

For some social problems, scientific research and technological innovation deliver significant progress, whereas for others, such activities lead to little if any improvement. Remarkable advances have been made in disease reduction through vaccination efforts, for example. But the story for literacy is different. In the United States, nearly a half century of research, application of new technologies and development of new methods and policies has failed to translate into improved reading abilities for the nation's children<sup>1</sup>.

Although vaccinating children and teaching them to read may seem so different as to make them incommensurable, they are similar in several important respects. Both are carried out by trained professionals in a controlled environment using the standard tools of their respective trades. Notably, each has been, and continues to be, the subject of considerable research. But the reasons why progress has been so uneven point to three simple rules for anticipating when more research and development (R&D) could help to yield rapid social progress. In a world of limited resources, the trick is distinguishing problems amenable to technological fixes from those that are not. Our rules provide guidance in making this distinction, be it for education, disease prevention or even climate change.

## Square peg, round hole

Both vaccinating and teaching involve skilfully produced artefacts. But unlike vaccines, the textbooks and software used in education do not embody the essence of what needs to be done. That is, they don't provide the basic 'go' of teaching and learning. That depends on the skills of teachers and on the attributes of classrooms and students. Most importantly, the effectiveness of a vaccine is largely independent of who gives or receives it, and of the setting in which it is given. A health-care practitioner (unlike a teacher) doesn't usually have to figure out what will work on a case-by-case basis — no matter if the child is rich or poor, if he or she speaks English or Mandarin. The vaccine captures the basic go in a technological



artefact, distinguishing it from the teaching of reading. Thus, our first rule for technological fixes is:

**I. The technology must largely embody the cause-effect relationship connecting problem to solution.**

A key point, well-illustrated by vaccines, is that a technological fix needs to be successful within the context of a complex socio-technical system that is difficult to understand, let alone manage. The health-care system in the United States, for example, is notoriously dysfunctional, inequitable and resistant to successful reform, yet most children manage to get vaccinated. Vaccines offer a clear advantage over other approaches to protecting children from certain infectious diseases. This advantage dampens disagreement about alternative approaches. Such clarity allows policy and operational coordination to emerge among diverse actors and institutions, ranging from doctors and parents to school districts, insurance companies, vaccine manufacturers and regulatory bodies.

Yet in the case of reading, an equally diverse set of actors and institutions remains in a continual state of conflict regarding how best to improve performance, and the education system itself is often blamed for the lack of improvement. Our point is that performance could improve despite system complexities if a broadly effective method of teaching reading were developed. The problem is that decades of effort have not led to such a method<sup>2-4</sup>. Different approaches to improved teaching remain strongly context dependent, and no particular approach confers an obvious advantage over others in all circumstances. Adherents of every approach have citable evidence to back their position, reinforcing their sense that 'the system' is the problem. These observations lead to our second rule:

**II. The effects of the technological fix must be assessable using relatively unambiguous or uncontroversial criteria.**

From their earliest use, vaccines provoked opposition on moral and practical grounds, a trend that continues today. But opposition has not stemmed the long-term advance of vaccines. This is in part because their effectiveness is hard to argue against and because continual improvement has tended to answer objections about efficacy and risk. The situation stands in stark contrast to the teaching of reading, for which no particular method or theory has been able to achieve long-term or widespread dominance and for which compelling evidence of improved efficacy even over timescales of a century is lacking.

For vaccination, the standardized core, the vaccine — first developed more than two centuries ago not through basic research but through empiricism guided by folk wisdom — remains the fulcrum on which cumulative learning and improved practice can be leveraged. This makes it possible to experiment with confidence that what is learned can be applied to standard practice and used by a range of practitioners, and leads to our third rule:

**III. Research and development is most likely to contribute decisively to solving a social problem when it focuses on**



B. MELLOR

**improving a standardized technical core that already exists.**

Scientific understanding related to a standardized core is much easier to apply than science aimed at elucidating the theoretical foundations, causes or dynamics of a problem. When knowledge is not largely embodied in an effective technology, but must instead be applied to practice through, say, training, institutional incentives, organizational structures or public policies, the difficulty of improving outcomes is greatly amplified. Now the task involves moulding, coordinating and governing the activities of practitioners, who themselves must acquire judgement and skill that may not be easily translatable from one context to another. Interpreting the results of management or policy innovations is difficult because of the many variables involved, few of which are directly related to the actual technology deployment. When the results of applying knowledge to practice are uncertain, the value of the new knowledge itself becomes subject to controversy.

**The limits of technology**

In the absence of an existing standardized core, therefore, R&D programmes aimed at solving particular social problems should neither be expected to succeed, nor be advertised as having much promise of succeeding, at least in the short and medium term. They should be understood and described as aiming at the creation of fundamental knowledge and the exploration of new approaches, with success possible only over the long term, and with a significant chance of failure.

We are not, of course, arguing against working hard to address social problems that are not amenable to technological fixes, but we are saying that R&D is unlikely to be the main source of short- or medium-term progress. So long as the teaching of reading, for example, cannot be condensed into an easily deployed technology or tightly specified routine, improvement will mostly come through context-dependent trial and error at the level of public policy and organizational management. This is more a process of effective politics than effective innovation, and typically progress will be slow, hard-fought and uneven. On the other hand, when a standardized technological core relevant to a particular problem is available, appropriate R&D investments have the potential to stimulate rapid progress.

How might these insights help guide innovation policies today? To illustrate the implications of our rules for decision-makers, we turn briefly to climate change.

The global energy system that lies at the heart of the climate-change problem is probably more complex and resistant to successful reform than the health-care and education

systems discussed above. Despite enormous scientific, political and diplomatic efforts over the past two decades, no progress on reducing global greenhouse-gas emissions has been made<sup>5,6</sup>. In the absence of technological fixes, progress towards significant reductions of greenhouse-gas emissions will remain frustratingly slow, uneven and inconclusive.

What are the prospects for a technological fix? In principle, stabilizing atmospheric carbon dioxide concentrations at levels deemed acceptable by climate experts can be achieved through radically reduced emissions or through direct removal of CO<sub>2</sub> from the atmosphere. Most discussion and effort focuses on the former. The suite of promising possibilities for reducing emissions — from nuclear fission, to photovoltaics, to on-site carbon capture and storage — offers attractive targets for R&D investments<sup>7</sup> consistent with Rule III: existing technological capacities can leverage continued improvement. Nevertheless, successful transition to a low-emissions energy system requires effective management across all sectors of society and all uses of CO<sub>2</sub>-emitting technologies. Within this system, no particular technology fully encompasses the go of the process — eliminating CO<sub>2</sub> in the atmosphere — just as no particular teaching technology encompasses the go of teaching children to read. Rule I is violated.

Moreover, because emissions-reducing technologies will compete with existing energy technologies supported by entrenched interests, and because there will be competition between the emerging technologies, we can expect ongoing technical and political debates about efficacy of specific technologies, as seen for biofuels today — a violation of Rule II. System-wide progress is therefore likely to be buffered by political processes similar to the ones that frustrate progress now.

In contrast, direct removal of CO<sub>2</sub> from the atmosphere — air capture<sup>8</sup> — satisfies the rules for technological fixes. Most importantly, air capture embodies the essential cause–effect relations — the basic go — of the climate-change problem, by acting directly to reduce CO<sub>2</sub> concentrations, independent of the complexities of the global energy system (Rule I). There is a criterion of effectiveness that can be directly and unambiguously assessed: the amount of CO<sub>2</sub> removed (Rule II). And although air-capture technologies have been remarkably neglected in both R&D and policy discussions, they nevertheless seem technically feasible (Rule III)<sup>9–11</sup>.

Our rules do not allow us to predict if air-capture technologies will in fact help stabilize

greenhouse-gas concentrations. Certainly these technologies face technical, political and economic obstacles. Our rules do, however, allow us to strongly predict that stabilization is unlikely to be achieved, except in the very long term, without something like air capture. Such technologies should therefore receive much greater attention in energy innovation portfolios.

The climate-change example illustrates an important final point: technological fixes do not offer a path to moral absolution, but to technical resolution. Indeed, one of the key elements of a successful technological fix is that it helps to solve the problem while allowing people to maintain the diversity of values and interests that impede other paths to effective action.

Recognizing when such opportunities for rapid progress are available

should be a central part of innovation policy, and should guide investment choices. ■

**Daniel Sarewitz** is co-director of the Consortium for Science, Policy & Outcomes, and Professor of Science and Society, at Arizona State University, Tempe, Arizona 85287, USA.

e-mail: daniel.sarewitz@asu.edu

**Richard Nelson** is George Blumenthal Professor of International and Public Affairs Emeritus at Columbia University, New York 10027, USA, and visiting professor at the University of Manchester Business School.

e-mail: rrn2@columbia.edu

**"Technological fixes do not offer a path to moral absolution, but to technical resolution."**

1. <http://nces.ed.gov/nationsreportcard/ltr/results2004>
2. Donovan, M. S., Wigdor, A. K. & Snow, C. E. (eds) *Strategic Education Research Partnership* (National Academies Press, 2003).
3. Foray, D. & Hargreaves, D. *Lond. Rev. Edu.* **1**, 7–19 (2003).
4. Murnane, R. & Nelson, R. *Economics of Innovation and New Technology* **16**, 307–327 (2007).
5. Prins, G. & Rayner, S. *Nature* **449**, 973–975 (2007).
6. Sarewitz, D. & Pielke Jr, R. in *Controversies in Science and Technology*, vol. 2: *From Chromosomes to the Cosmos* (eds Kleinman, D. L. & Handelsman, J.) 329–351 (Mary Ann Liebert, 2008).
7. Hoffer, M. I. et al. *Science* **298**, 981–986 (2002).
8. Keith, D. W., Ha-Duong, M. & Stolaroff, J. K. *Climatic Change* **74**, 17–45 (2006).
9. Bacocchi, R., Storti, G. & Mazzotti, M. *Chem. Eng. Process.* **45**, 1047–1058 (2006).
10. Lackner, K. S. *Science* **300**, 1677–1678 (2003).
11. Stolaroff, J. *Capturing CO<sub>2</sub> from Ambient Air: A Feasibility Assessment* (PhD Dissertation, Carnegie Mellon University, 2006).

**To comment on this article and others in our innovation series, visit <http://tinyurl.com/5uolx2>.**

**Correction**

The Commentary 'Towards responsible use of cognitive-enhancing drugs by the healthy' (*Nature* **456**, 702–705; 2008) described views derived from the report *Beyond Therapy* as solely those of Leon Kass. In fact, the work in question was by the President's Council on Bioethics, which at that time Kass chaired.



## BOOKS &amp; ARTS

## A wonderful life by leaps and bounds

Stephen Jay Gould's idea of evolution by bursts was controversial. But it gave the field of palaeontology a long-overdue boost, explains **Steve Jones**.

**Stephen Jay Gould:  
Reflections on His View of Life**

Edited by Warren D. Allmon, Patricia H. Kelley and Robert M. Ross

Oxford University Press: 2009. 416 pp.  
£18.99, \$34.95

Stephen Jay Gould was one of the world's top six snail geneticists, and the other five of us agreed. Unlike his colleagues — and in the tradition of Edgar Allan Poe and his 1839 work *The Conchologist's First Book: Or, a System of Testaceous Malacology* — he followed the iron rule that nobody who works on snails becomes famous until they give it up. His elegant studies on shell shape in Bermudan land molluscs were succeeded by a series of popular books and essays, some of great brilliance, and, again in the footsteps of Poe, by a set of sonorous but increasingly Delphic statements on the revealed truths of life, the Universe and such things.

*Reflections* is a Festschrift of sorts. But among the praise, there is no shortage of negative comment on the hero's work or polemic about just what he was trying to say. A dozen or more of Gould's ex-students and colleagues assess his science, standing and personality, six years after his untimely death. He emerges as a genius of sorts, but — appropriately for his geologist beginnings — with feet not marked by day.

Much of Gould's *oeuvre* descends from Charles Darwin's dictum that "general and popular Treatises are almost as important for the progress of science as original work". Gould was central to today's awakening of public interest in the past. He was also an invaluable ally in the fight against creationism, and spared no effort in opposing the endless attempts to insinuate stupidity into US schools. His influence did not, alas, quite make it across the Atlantic.

Some of his imagery may have creaked a little. Yet only Gould could incorporate a picture of himself pushing a luggage trolley labelled *Metaphors* in a Greek airport to make the point that a metaphor is no more than a means of moving an idea from one place to another. His baseball obsession threatened to become boring — but then his 1996 book *Full House* revealed an unexpected parallel between that baffling sport and life itself. Fans complained that the game was stagnant because batting averages had levelled off, but Gould noticed the equivalent decline in their



U. ANDERSEN/GETTY IMAGES

Gould's accessible books were key in sparking popular interest in evolutionary history.

variance, proof that the game had become leaner and meaner as its players pushed the limits of the physically possible. (Cricket, incidentally, shows no such pattern.) From that he wove a tale that incorporated the history of skyscrapers, his chances of surviving the cancer that darkened his later years, and the whole notion of progress in evolution.

Gould held fast to Darwin's maxim that "All observation must be for or against some view if it is to be of any service", and was among that band who felt that those not for him must be against him — which was not much help in keeping friends. The great biologist John Maynard Smith wrote that most evolutionists saw Gould as "a man whose ideas are so confused as to be hardly worth bothering with, but as one who should not be publicly criticized because at least he is on our side against the creationists".

Gould was hurt by that acidulous statement, which was without doubt unfair. Whatever the importance of sudden leaps in the fossil record, his notorious idea of punctuated equilibria, nicknamed 'punk eek' and referred to as 'evolution by jerks' by some of its critics — their own views characterized by Gould as "evolution by creeps" — gave the fossilized field of palaeontology a much-needed kick in the pants. Gould saw punk eek as a "coordinating centrepiece" that "congealed into a coherent critique" of evolutionary theory. Many biologists, by contrast, insist that what look like palaeontological leaps

can be explained by simple Darwinism. To them, an instant in geology may represent almost an infinity in biology, leaving plenty of time for evolution by natural selection to do its normal job. His other great passion, contingency — the notion that evolution goes on with sudden bangs rather than protracted whimpers — has also not held up particularly well. *Wonderful Life*, Gould's 1989 book on the Burgess Shale, suggests that the obscure fauna of the late pre-Cambrian represents a lost universe wiped out by some unknown disaster, but now we know that they have descendants among modern animals. Even so, scientific ideas often change, and that volume, like most of his others, remains a rattling good read. The fact that nature must build on what it has, and not on what it wants, is still at the centre of evolutionary thinking.

Gould remained a dedicated teacher, which few great researchers can claim, but lost his gloss with the years. The teaching fellows on his course at Harvard University recount in the book how praise mutated into complaints about pomposity and intolerance; and I myself attended several lectures that were hard to follow, went grossly over time and were interspersed with rants about flash photography.

In time Gould was promoted from mere scientist to Thinker, and corresponded with President Jimmy Carter about God. As one ex-student reports, some of his colleagues felt that Gould became a caricature of himself.

Backwards ran his sentences, and some of his ideas were equally opaque. In support of punk eek, for example, he wrote that "species are individuals ... by all vernacular criteria", which is at best obscure, and at worst obscurantist.

As *Reflections* portrays, its hero showed an increasing regard for style over content, and was resistant to the notion that anyone should dare to edit his writings. The pinnacle — the very summit, crown and peak — of his great Olympus of orotundity was his last voluminous volume, *The Structure of Evolutionary Theory*, published in the year of his death. All the authors agree that this is not a book to be lightly tossed aside, but their motives for saying

so vary. Its reviews are quoted with a certain relish: "an elephantine opus"; "pathological logorrhea"; "billowing clouds of verbal flatulence" — but Gould had no doubt of its value. In it he came out with the idea of life as a series of interlocking hierarchies and of a grand unification of its sciences into some post-Darwinian consilience, comprehensible only to the chosen.

Poe was much the same. His last substantial work, *Eureka: A Prose Poem*, published just before his own demise, discusses the relationship of man to God, and to "the Material and Spiritual Universe: of its Essence, its Origin, its Creation, its Present Condition and its Destiny". It was seen by Poe as replacing

Newton's ideas about gravity. Poe wrote that "What I have propounded will (in good time) revolutionize the world of Physical and Metaphysical science". Some see in it a presage of the Big Bang and of modern astronomy, but others ridicule its pretensions, its rambling nature and its overblown prose. Nine decades later, Albert Einstein described *Eureka* as a "beautiful achievement of an unusually independent mind". Perhaps, one day, the same will be said of Gould.

■ **Steve Jones** is professor of genetics at University College London, London WC1E 6BT, UK. His most recent book is *Coral: A Pessimist in Paradise*. e-mail: j.s.jones@ucl.ac.uk

## Does genius breed success?

### Outliers: The Story of Success

by Malcolm Gladwell

Allen Lane/Little, Brown: 2008.  
256 pp/320 pp. £16.99/\$27.99

Thomas Edison's insight more than a century ago that genius is 1% in inspiration and 99% perspiration is often quoted, yet few seem to believe it. The common notion of genius is that we are either born with it or we're not. This seductive idea enables us to hold up successful people as exotic, propelled to triumph by talent alone. More than that, it reinforces the impression that those who are masters of one field are masters of many. Hence the widely held assumption, recently disproved, that financiers who have been successful in one market are expert in all; or that the 76 Nobel science laureates who endorsed Barack Obama's electoral campaign were worth listening to in matters of politics.

Malcolm Gladwell aims in his book *Outliers* to dismantle the idea of innate genius once and for all. His main point is that it is nonsense to explain someone's success solely in terms of their own actions and choices. Culture, family environment, opportunities and, above all, hard work count far more than any inherited quality. "It's not enough to ask what successful people are like," he says. "It is only by asking where they are from that we can unravel the logic behind who succeeds and who doesn't."

Gladwell follows the formula that worked for him in his previous bestsellers *The Tipping Point* and *Blink*, weaving psychological and sociological theory into a compelling narrative. He asserts that few stars of any field succeed without putting in at least 10,000 hours of practice, including 'prodigies' such as Mozart.

Similarly, few make it to the top without being handed a life-changing opportunity early in life, generally one they neither deserved nor earned. Both Bill Joy, founder of Sun Microsystems, and Bill Gates, creator of Microsoft, for example, learned to program computers as a result of attending a university or private school with unrivalled equipment. Gladwell argues those early opportunities enabled Joy and Gates to improve beyond their peers and take advantage of opportunities down the line. They were talented, but they were also fortunate.

Gladwell is convincing — almost too convincing. Psychological and sociological theories of behaviour are never tidy, and the reader may sense that they are being manipulated by clever selection of data. Presumably, Gates and Joy had classmates who spent similar amounts of time in front of computers but never became billionaires. Gladwell claims that the key to The Beatles' success was the time they spent in Hamburg in early 1960s Germany, where they performed 270 five-hour gigs in 18 months. Clearly this improved their technical proficiency, but surely what set The Beatles apart was their songwriting, another skill entirely. Many other musicians put in long playing hours but don't become famous. The question is not so much whether Gladwell's thesis rings true — it does — but whether it is as comprehensive as he makes out, which is unlikely.

The book suffers another flaw, one of structure rather than argument. After 158 pages on the 'ecology' of genius, Gladwell shifts his focus to the effect of culture on people's behaviour. He includes a chapter on how flight crews from cultures that emphasize hierarchy and deference,

such as South Korea and Colombia, are more likely to crash their planes because co-pilots and flight engineers are less inclined to challenge the captain when they think he is making an error. Although this discussion is interesting and broadly about success, it seems to fall some way from where the story began.

*Outliers* is probably Gladwell's most important book yet. Unlike his previous two, it has implications for public life. His demonstration that intelligence, above a certain threshold level, has no bearing on future success should turn university selection policy on its head. To win a Nobel prize, you need to be smart enough to get

into a decent university, nothing more. His most graphic example of how intelligence above a certain level is irrelevant to achievement is an experiment by psychologist Lewis Terman. Terman failed in his attempt to nurture the future elite of the United States by selecting people

for their very high IQ; although many of his 'geniuses' did well, very few went on to become nationally recognized.

Gladwell also asks why Asian students tend to be so much better at maths than their western counterparts. He reckons it is firstly because the regularity of the Asian number system means that basic tasks such as addition can be done more easily, and secondly that Asia's rice-growing culture, involving hours of dedication in the fields, has imbued its people with a dogged attitude essential for tackling mathematical problems. Although that might sound far-fetched, his suggestion that underachieving children in the West could transform their performances if they studied during the holidays makes sense. That's what Gladwell does best: he gives you a new way of seeing the world, and it's worth taking him seriously for that. ■

■ **Michael Bond** is a science writer based in London. e-mail: michael.bond@btinternet.com

**"To win a Nobel prize, you need to be smart enough to get into a decent university, nothing more."**



# The science communicator

**Science and Controversy: A Biography of Sir Norman Lockyer, Founder Editor of *Nature***

by A. J. Meadows

Macmillan Science: 2008. 352 pp.

\$35.00, £24.99

Norman Lockyer, the founder of *Nature* and an important transitional figure between the amateur and the professional scientist, was no stranger to controversy. In addition to his outstanding research skills in astrophysics and meteorology, he acquired a reputation for the pugnacious tenacity with which he fought for the intellectual credit due to him. His personality constituted a rich source of material for fellow scientists who, as was common in the nineteenth century, were also amateur poets.

With the following verse, James Clerk Maxwell, the first head of the Cavendish Laboratory at the University of Cambridge, UK, epitomized and framed the perceptions of Lockyer's persona for the rest of his life:

*And Lockyer, and Lockyer,  
Gets cockier, and cockier;  
For he thinks he's the owner  
Of the solar corona.*

Lockyer's passion for science and the building of institutions to nurture it was not driven by the egotistical pursuit of fame. As someone who was committed to science as a vocation, Lockyer — to use sociologist Max Weber's words on religion and capitalism, written in the same period — was certainly no "specialist without spirit".

Lockyer's organizational skills were deftly deployed when he founded *Nature* in 1869. He mobilized his abilities for social networking to ensure that the fledgling periodical survived against competitors such as *Knowledge* and *Academy*. The founder of *Knowledge*, Richard Proctor, aimed to involve the general public directly in scientific discussions through reader feedback, seeing his role as a 'conductor' rather than as an editor. Lockyer, by contrast, wanted *Nature* to promote a science that was accessible to the public, but that did not involve the public in the scientific discussions themselves. These competing visions of the nature and role of science led to several disputes between Lockyer the editor and Proctor the conductor.

Lockyer's vision for his new journal prevailed. During this period, science was slowly transformed from an amateurish pursuit enjoyed by



Personifying the gentleman scientist, Lockyer (inset, and seated left) helped create observatories in India.

people of means and leisure, to a professional activity. Its results were to be communicated to the public, but its practice would eventually be off limits to non-scientists. Lockyer intended *Nature* to play an active part in reconciling the divergent and the emergent tensions between science and the arts, amateurs and professionals, generalists and specialists. His goal was to capture the public's interest and imagination such that the British government might be persuaded to provide financial support for science. Lockyer's creation of the British Science Guild in 1905 played a similar role until the 1930s, when the organization withered away because, as A. J. Meadows points out, "the main elements of its policy became part of the general vision".

Like gentlemen scientists of the period, Lockyer's scientific interests were diverse, cut-

ting across the disciplinary boundaries that emerged and later became institutionalized. Meadows provides a detailed and riveting account of Lockyer's interests — from the orientation of ancient monuments, such as Stonehenge, to the influence of

the Sun on terrestrial weather — focusing on Lockyer's important contributions to astronomical spectroscopy and astrophysics. The diverse contexts of Lockyer's work in India and Britain, and the controversies surrounding the identification and confirmation of the existence of helium (which Lockyer named) are significant elements of Meadows's absorbing narrative.

A particularly interesting and controversial episode in Lockyer's scientific career was his

attempt to link terrestrial weather to sunspot cycles — a topic of extreme interest to administrators in the British Empire such as William Hunter, the director-general of statistics in India. Confronted by the country's devastating famines that were largely a consequence of specific policies, particularly the Permanent Settlement Act of 1793, administrators were keen to follow up and support Lockyer's conjecture of linking sunspot cycles to drought and famine. Despite all the data that Lockyer gathered and analysed, the claim that sunspot cycles were to blame for famines was scientifically unsustainable. However, his expeditions and observations helped initiate the tradition of international collaboration in the collection of meteorological data, and led to the establishment of several modern astronomical observatories in India.

Despite his key role in the professionalization of science, Lockyer continued to display many attributes of the generalist amateur. This, as Meadows points out, is what makes his life and career so interesting. The book's foreword, written by *Nature*'s editor-in-chief Philip Campbell, highlights the breakthroughs and controversies — such as 'smart' drugs, sequencing of the human genome and Dolly the sheep — in which Lockyer's enduring institutional legacy continues to play a part. Meadows's biography constitutes an important, absorbing and eminently readable narrative of Lockyer's role in transforming the practice and social organization of late Victorian science. ■

**Zaheer Baber** is professor of sociology at the University of Toronto, Ontario M5S 2J4, Canada, and author of *The Science of Empire*. e-mail: zaheer.baber@gmail.com

**"Lockyer wanted *Nature* to promote science that was accessible, but that did not involve the public in scientific discussions."**

# Looking at the face of the Earth

A sixteenth-century Dutch master's carefully orchestrated winter landscape may have benefited from his knowledge of geographers' techniques of the time, explains **Martin Kemp**.

Old-master paintings are now conspicuous among the array of Christmas cards. Museums and galleries vigorously market cards based on their holdings of Madonnas, adorations and winter landscapes. Probably no 'secular' subject is more popular than Pieter Bruegel's great vista of *Winter* (1565), often called *Hunters in the Snow*.

The painting shows the hunters, one bearing the meagre corpse of a fox, trudging heavily across the top of a wooded hill accompanied by weary dogs, all silhouetted against the stark snow. Below, in panoramic array, a landscape unfolds, marked indelibly by human presence and the ordering activity of irrigation and agriculture.

To the left, peasants bring bundles of faggots to a blazing fire outside an inn. The inn sign — "This is the Hart" — hangs askew. It depicts, schematically, St Hubert witnessing his vision of the crucified Christ between the antlers of a stag. Diminutive figures of skaters, curlers and spinners of tops play on the frozen ponds. Black birds punctuate the gloomy skies.

This was a new kind of picture, a new way of looking at Earth and its inhabitants. Fascinatingly, one of Bruegel's great friends was the geographer Abraham Ortelius, whose famous maps disseminated the Renaissance cartographers' new ways of envisaging the world. Ortelius's 1573 epitaph for Bruegel, written four years after the painter's death, leaves us in no doubt about his opinion: "No one except through envy, jealousy or ignorance of that art will ever deny that Peter Bruegel was the most perfect painter of this century." Ortelius suggests that Bruegel's untimely death might be attributed to "Nature's fear that his ingenious artifice in imitation would bring her into contempt".

Ortelius and Bruegel were in related branches of a Ptolemaic project. Ptolemy distinguished between geography and chorography in the second century. The former was concerned with "the mapping of countries", the latter with "smaller divisions". Geography, by analogy, is "concerned with the depiction of the entire head", whereas chorography involves itself with "individual features, such as an eye or ear". Bruegel is the great master of the facial features that characterize Earth.

Bruegel is profoundly involved in acts of articulate seeing. He has perfectly captured the way that the glare of the snow suppresses much of the internal detail of colour and



Pieter Bruegel's wintry scene is testament to his scientific observation of light and geographical features.

surface modelling that normally characterize his peopled landscapes. Medieval optical science stressed that strong brightness and deep darkness distorted perception, as they lay outside the "range of moderateness".

He has meticulously registered what happens as the medieval "species" (images) weaken on their journey through the air. The detail visible in the twiggy trees is systematically graded according to the distance from the viewer's eye. Atmosphere progressively leaches out colour and veils the extreme distance. The silhouetted manikins lose the definition of their limbs as they move farther away. Remarkably, Bruegel notes that the dark reflections below the figures on the ice do not begin exactly at their feet, but are separated by a thin layer of sheen.

These are just the kind of effects mastered by Ibn-al-Haytham, the great student of optics in eleventh-century Egypt. Leonardo da Vinci's writings on the optical effects of glare, shine, contrast, motion, distance and atmosphere depend on the tradition established by al-Haytham. We know little about Bruegel's intellectual engagements, but he had been to Italy and had undoubtedly encountered theorizing artists who sought a science of seeing in pictures. His paintings themselves testify that his profound and systematic observations of light

in nature were no less intense than Leonardo's.

Ortelius, for his part, was no simple map maker. His great atlas, *Theatrum Orbis Terrarum* (Theatre of the Globe of the World, 1570), was deeply concerned with historical, economic and social geography. He used evidence of early maps to chart the biblical lands and historic journeys. He critically collated historical accounts, not least by the great classical writers, of the characters of the lands and their peoples, comparing them to modern observations.

Of the Dutch themselves, he immodestly claims that "as long as anyone respects their homely and plain manners, there is no nation more prone to be civil, courteous and humane, or one in which you will find less cruelty, bad temper or strictness; they are good-natured, plain, devoid of all treachery and guile, and not inclined to notorious vices".

Bruegel brings his analytical eye to bear on his magnificent portraits of the land and its inhabitants. Ortelius brings maps into the orbit of the great historical story of Earth and its peoples. Their friendship clearly went beyond compatible personalities and respect for each other's professional skills. They shared ways of conveying the human condition.

**Martin Kemp** is emeritus professor in history of art at the University of Oxford, Oxford, UK.

PHOTO SCALA, FLORENCE/KUNSTHISTORISCHES MUSEUM, VIENNA



## ESSAY

# Migration: An engine for social change

The movement of people into societies that offer a better way of life is a more powerful driver of cultural evolution than conflict and conquest, say **Peter J. Richerson** and **Robert Boyd**.

As cultural evolutionists interested in how societies change over the long term, we have thought a lot about migration, but only recently tumbled to an obvious idea: migration has a profound effect on how societies evolve culturally because it is selective. People move to societies that provide a more attractive way of life and, all other things being equal, this process spreads ideas and institutions that promote economic efficiency, social order and equality.

Culture is the set of socially acquired ideas, beliefs and values carried by a population of individuals. Various processes change the distribution of cultural variants through time. Some processes act at the individual level as people selectively learn ideas, and those ideas affect an individual's chance of teaching others or of being imitated by them, causing some cultural variants to spread and others to disappear. Theory and much empirical data indicate that individual-level processes can stabilize a vast array of beliefs and institutions.

The existence of stable differences between groups means that competition between them also affects cultural evolution. Indeed, a lot of attention has been focused on what happens when militarily or economically more powerful societies expand at the expense of weaker ones. For example, many European ideas and institutions spread to the rest of the world as a result of colonial conquests.

Less attention has been given by cultural evolutionists to the movement of people from poorer, more chaotic or more unequal societies into richer, more orderly, more just ones — another group-level process that preoccupies much of the developed world today. People migrate to improve their lot. Although their goals and aspirations vary, most prefer wealth to poverty, safety and security to fear and danger, health to illness, and equality to inequality.

If immigrants just took advantage of the social and material benefits that their host countries provided, there would be no cultural evolution. But immigrants, and their descendants, adopt some of the ideas and institutions that make their new homes better places to live and raise families. This integration promotes the spread of ideas and institutions that encourage order, justice and economic efficiency.

We believe that immigration generates

far more cultural evolution today than does conquest. Flows of migrants are often substantial. Foreign-born people, mainly from Latin America and Asia, compose about 11% of the current US population, a figure close to historical averages. The richer countries of Europe, such as Sweden, Norway and Germany, once the source of streams of immigrants to the United States and elsewhere, are now receiving people from Asia, Africa and poorer European countries such as Poland and the Balkan states.

Immigration is not a modern phenomenon. In the 1970s, anthropologist Bruce Knauft described two neighbouring village-scale societies in New Guinea, the Gebusi and the Bedamini. The Gebusi's destructive system of witchcraft trials and executions was leading

Empire. Confucian humanism, with its concern for good government, replaced the predatory and quarrelsome landed elite as the backbone of Chinese society. Hindu tolerance and productive organization of cultural diversity led to one of the world's wealthiest societies in medieval times. Medieval Islam attracted converts spanning from North Africa to southeast Asia because it supported effective statecraft, intellectual advancement and trade on a vast scale.

This way of thinking changes our view of the consequences of conflicts between societies. Focusing on military competition alone predicts that societies may be nice to insiders and rough on outsiders. Powerful societies may exploit their conquered and resist their assimilation. But taking the effects of assimilation into account suggests that conquering empires will be ephemeral unless they induce immigration and integration.

Societies that achieve more order and economic efficiency will grow even if they begin by conquest, because people are attracted to join them. Alexander the Great and Genghis Khan were successful conquerors, but they made a less durable impact on the world than, say, Mohammed, Buddha, Christ and the institution builders they inspired such as Constantine and the Umayyad caliphs. The government envisioned by Confucius, and implemented by Han Dynasty emperors centuries after his death, was the engine of assimilation for the peoples of south China. US revolutionaries and British Commonwealth reformers built societies that have proven highly attractive to incomers.

As long as they vote with their feet and hearts, immigrants are a more powerful engine for social change than armies. ■

**Peter J. Richerson** is in the Department of Environmental Science and Policy, University of California, Davis, California 95616, USA.  
e-mail: [pjricherson@ucdavis.edu](mailto:pjricherson@ucdavis.edu)

**Robert Boyd** is in the Department of Anthropology, University of California, Los Angeles, California 90095, USA.  
e-mail: [rboyd@anthro.ucla.edu](mailto:rboyd@anthro.ucla.edu)

See <http://tinyurl.com/5blvmt> for further reading.  
For more on Being Human, see [www.nature.com/nature/focus/beinghuman](http://www.nature.com/nature/focus/beinghuman).



to their extinction. Some of the Gebusi took advantage of friendship or marriage to join the better-functioning Bedamini. Ethnographers have documented many similar cases.

Likewise, the growth of ancient empires seems to have owed much to the assimilation of border peoples. Conquering elites, such as the Mongols in China, the Mughals in India and the Goths in Rome, largely adapted to their highly successful host culture rather than the other way around. In every case, these durable systems had institutions — the Confucian merit-based bureaucracy, the Hindu system of self-governing castes, Roman law — that endure today in one form or another.

These examples support the idea that societies that attract immigrants tend to have ideas and institutions that cause them to be richer, less violent and less exploitative than the societies that supply them. The Goths were fleeing chaos on the steppe. Christianity, with its concern for the poor and humble, grew mainly by voluntary conversion to eventually become the official religion in the Roman

## MOLECULAR BIOLOGY

# Spliceosome meets telomerase

Sophie Bonnal and Juan Valcárcel

**The spliceosome is best known for shepherding primary messenger RNA transcripts to maturity. This enzyme complex also contributes to the synthesis of an enzyme that maintains chromosome ends.**

When the Stargate Atlantis Expedition Team found Dr Beckett at a distant galactic outpost, they figured that he was a clone of the late Dr Beckett because his telomeres were 30% shorter than expected for his age<sup>1</sup>. That the complex concept of telomere dynamics has permeated popular fiction testifies to their significance. These repetitive DNA sequences are known to have key roles in fundamental processes such as ageing, tissue renewal, cell proliferation and cancer<sup>2</sup>. Nonetheless, many aspects of telomere synthesis and processing remain elusive. On page 910 of this issue, Box *et al.*<sup>3</sup> report the unexpected finding that, at least in a yeast species, telomere synthesis and maintenance depend on the incomplete activity of a molecular machine called the spliceosome, which normally functions in generating mature messenger RNA from the longer primary gene transcripts.

Telomeres protect the ends of chromosomes both from the continuous shrinkage associated with the mechanism of DNA replication, and from being recognized as DNA breaks, which are susceptible to genomic rearrangements. A remarkable enzyme complex known as telomerase maintains and controls telomere length<sup>4</sup>. One component of this molecule is a cellular reverse transcriptase enzyme, which uses another component — an RNA template known as the telomerase RNA — to add telomeric repeats to chromosome ends (Fig. 1a). Previous work in the fission yeast *Schizosaccharomyces pombe* identified *ter1* as the gene encoding telomerase RNA, and demonstrated the existence of transcripts longer than the functional telomerase RNA, which is present in the telomerase enzyme complex<sup>5,6</sup>. The function of these longer transcripts, which, like mRNAs, carry a sequence of adenine nucleotides called a polyadenylate tail, remained unknown.

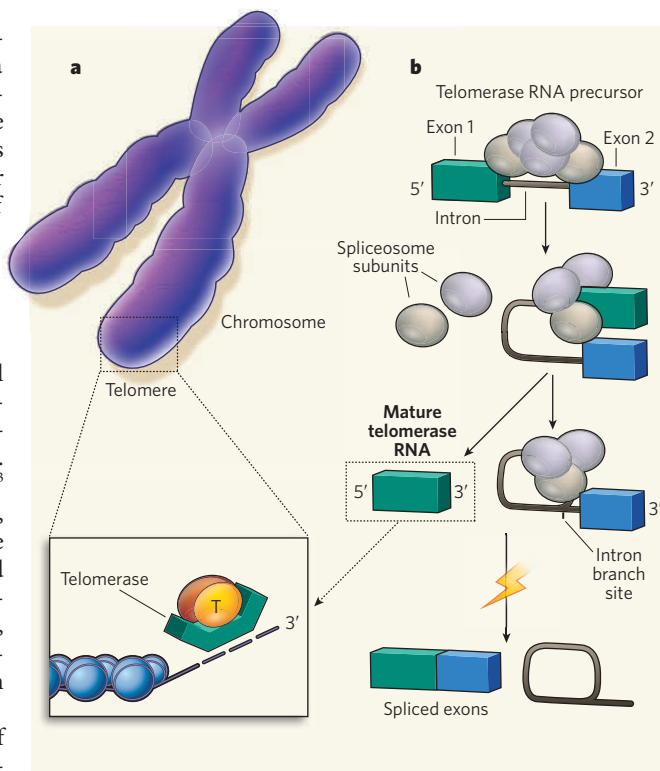


**Figure 1 | Processing of telomerase RNA by the spliceosome.**

**a**, Chromosome ends contain telomeric repeats, which are added to the 3' end of DNA molecules by the telomerase enzyme complex. Telomerase consists of a reverse transcriptase enzyme (T), which uses another component of this complex, the telomerase RNA, as a template for telomere synthesis. **b**, Box *et al.*<sup>3</sup> find that, in fission yeast, telomerase RNA is initially transcribed as a precursor containing an intron. Mature telomerase RNA is then generated by the spliceosome, which cleaves the 5' end of the intron. The second step of the 'standard' splicing reaction catalysed by the spliceosome, which would cleave the intron at the 3' end and mediate the splicing of the exons, is inhibited during maturation of telomerase RNA.

In eukaryotes (organisms such as yeast, plants and animals), the spliceosome processes primary RNA transcripts to mature mRNAs that can be translated into proteins<sup>7</sup>. This process involves the removal of sequences that don't encode proteins (introns) and the splicing together of those that do (exons). Box *et al.*<sup>3</sup> realized that some of the longer polyadenylated telomerase-RNA transcripts in *S. pombe* differ from their shorter, functional counterpart

in having an intron that harbours putative splicing signals at its ends; this observation hinted at a role for the spliceosome in the processing of telomerase RNA.

Indeed, the authors find that mutation of the splicing signals greatly reduced the levels of the shorter telomerase RNA, and consequently compromised telomerase function, leading to telomere shortening. Box *et al.* therefore conclude that splicing of the longer, polyadenylated transcripts is necessary for generating functional telomerase RNA and for telomerase activity. They propose that the longer transcripts act as precursors, which are converted by the spliceosome to functional telomerase RNA.

Normally, the spliceosome removes an intron in two consecutive reactions. First, it cleaves the intron's 5' end, allowing the free 5' phosphate to form a phosphodiester bond with an adenosine nucleotide — known as the branch site — located close to the intron's 3' end (Fig. 1b). Next, the intron is cleaved at its 3' end, and the exons are spliced together. Box and colleagues find that the 3' end of functional telomerase RNA precisely coincides with the 5' boundary of the intron present in the longer transcripts. So it seems that the site-specific cleavage activity of the spliceosome during the first step of the reaction generates the proper 3' end of telomerase RNA.

As essential as the cleavage of the telomerase RNA precursor is, it is equally important that the spliceosome is prevented from completing its normal function of splicing the exons together, because this would lead to a different 3' end for the mature telomerase RNA and so a non-functional molecule (Fig. 1b). Box *et al.* demonstrate that an unusually long distance between the branch site and the 3' end of the intron prevents



efficient completion of the second step, and that this arrangement allows accumulation of what would normally be reaction intermediates. In the case of telomerase RNA, however, one of these intermediates is the final, processed product that functions as part of the telomerase enzyme. It is therefore the incomplete function of the spliceosome — as measured by mRNA-production standards — that is needed for the formation of telomerase RNA.

Telomerase activity is essential for long-term cell proliferation — including stem-cell renewal and cancer-cell immortalization — and increased telomerase activity can delay ageing in cancer-resistant mice<sup>2,8</sup>. So it will be of interest to know whether Box and colleagues' results<sup>3</sup> in *S. pombe* apply to other organisms.

Conceivably, modulation of spliceosome activity — such as changes in the efficiency of the second catalytic step and of the release of splicing intermediates from the spliceosome

complex — could control telomerase function in organisms in which telomerase RNA follows this processing route. Polyadenylated and/or longer telomerase-gene transcripts have been identified in other species, including humans<sup>9,10</sup>, but whether the spliceosome plays a part in the synthesis of telomeric RNA in these organisms remains unknown.

A notable insight comes from Box and colleagues' observation that the spliceosome can generate the proper 3' end of telomerase RNA. It could be that other RNA molecules can similarly exploit this incomplete activity of the spliceosome to generate alternative transcript ends. If so, the expanding world of non-coding RNAs, many of which contain introns, could offer a large inventory of substrates for diversification of the cellular pool of RNA transcripts, adding to the complexity of the still largely hidden genetic program of our genomes<sup>11</sup>. ■

Sophie Bonnal and Juan Valcárcel are at the Centre de Regulació Genòmica and Universitat Pompeu Fabra, Barcelona, Spain. Juan Valcárcel is also at the Institut Català de Recerca i Estudis Avançats, Dr. Aiguader 88, 08003 Barcelona, Spain.  
e-mail: [juan.valcarcel@crg.es](mailto:juan.valcarcel@crg.es)

1. [www.gateworld.net/atlas/s4/transcripts/419.shtml](http://www.gateworld.net/atlas/s4/transcripts/419.shtml)
2. Blasco, M. A. *Nature Chem. Biol.* **3**, 640–648 (2007).
3. Box, J. A., Bunch, J. T., Tang, W. & Baumann, P. *Nature* **456**, 910–914 (2008).
4. Blackburn, E. H. *FEBS Lett.* **579**, 859–862 (2005).
5. Leonardi, J., Box, J. A., Bunch, J. T. & Baumann, P. *Nature Struct. Mol. Biol.* **15**, 26–33 (2008).
6. Webb, C. J. & Zakian, V. A. *Nature Struct. Mol. Biol.* **15**, 34–42 (2008).
7. Will, C. L. & Lührmann, R. in *The RNA World* 3rd edn (eds Gesteland, R. F., Cech, T. R. & Atkins, J. F.) 369–400 (Cold Spring Harbor Laboratory Press, 2005).
8. Tomás-Loba, A. *et al.* *Cell* **135**, 609–622 (2008).
9. Chapon, C., Cech, T. R. & Zaug, A. J. *RNA* **3**, 1337–1351 (1997).
10. Fu, D. & Collins, K. M. *Cell* **11**, 1361–1372 (2003).
11. Mattick, J. S. & Makunin, I. V. *Hum. Mol. Genet.* **15**, R17–R29 (2006).

## QUANTUM PHYSICS

# Don't look now

Alexei Ourjoumtsev

**Before picking up the phone and calling a technician to fix a faulty microwave oven, there are always a few simple things one should check. So far, "stop looking at it" has not been part of the checklist.**

For people with a special kind of imagination, microwave oven manuals contain warnings such as "do not use it to dry animals or as a storage place for books"<sup>1</sup>. For everyone else, the daily operation is basic: dose the door, set the time and press the start button. Now, physicists might be tempted to add "and don't look inside or it won't work". Writing in *Physical Review Letters*, Bernu *et al.*<sup>2</sup> show that the build-up of a microwave inside a resonator can be blocked by just 'watching' it without absorbing the wave's energy. The edge of a very strange quantum world is now one step closer to everyday life.

Nature states firmly that information has a price. The lowest, non-negotiable one is set by quantum physics: measuring something always disturbs something else. Usually, this disturbance goes unnoticed. To detect a microwave, it is generally converted into an electric current by an antenna, or into the heat that cooks your food, so the wave is not only perturbed but destroyed. But even if you were an outstanding experimentalist and you could measure the microwave's intensity at the ultimate quantum level without absorbing a single photon, you would still leave your fingerprint by making its phase completely random. Instead of regular oscillations, the wave would make a sudden jump. This is exactly what happened in Bernu and colleagues' experiment<sup>2</sup>.

Start injecting an empty cavity with a resonant

wave: it builds up and, after a short time (say, a tenth of a second), its amplitude reaches a value  $\alpha$ . Let's see this again in slow motion. First, a small wavelet comes in. At resonance, it makes an integer number of oscillations during a cavity round-trip. Therefore, it remains in phase with the next incoming wavelet, and they simply add up. And so on. After 100 milliseconds, the wave in the cavity is made of  $N$  identical wavelets, all oscillating in phase with the same amplitude  $\alpha/N$ . In a sense, the intracavity field makes  $N$  steps each with a length  $\alpha/N$  in a direction defined by the phase of the wavelets (Fig. 1a).

However, if one now repeats the same procedure but measures the number of photons after each wavelet injection, their phases will become totally random: the field will still 'walk' by steps of  $\alpha/N$ , but in completely random directions (Fig. 1b). As in a usual diffusion phenomenon,  $N$  steps will typically result in an amplitude of  $(\alpha/N) \times \sqrt{N} = \alpha/\sqrt{N}$ , so the final intensity will be only  $\alpha^2/N$  instead of  $\alpha^2$ . If measured more and more often, this attenuation factor  $1/N$  will become smaller and smaller, and eventually the resonator will simply become empty. This so-called quantum Zeno effect, which prevents a system from evolving while observed, has been convincingly demonstrated before, but usually in conjunction with other quantum effects, such as Bose–Einstein condensation or quantum tunnelling<sup>3–8</sup>. The object of interest was

never as simple and classical as the intensity of a microwave in a cavity.

For Bernu and colleagues, the key to success was an incredibly good microwave resonator. Indeed, to measure the exact number of photons, everything they interact with must be under absolute control. Photons must obey two commandments: "You shall not appear in the resonator unless I send you", and "You shall not leave it before I'm done with measuring you". For Bernu *et al.* this meant building a cavity in which tightly confined photons could bounce between two superconducting mirrors about 1 billion times, cooled to a temperature of 0.8 kelvin to prevent undesired thermal photons from appearing. In addition, keeping the cavity on resonance required its frequency to be stabilized with a relative precision of about  $10^{-11}$ . All this led to a clear, fivefold microwave-intensity reduction after a 100-millisecond experimental sequence of alternating-field injections and photon counting.

But how can one count photons without destroying them? In physics, an old trick to measure a weak signal with low disturbance is to observe how it affects the motion of a pendulum. Just choose the right one. Back in 1846, a pendulum the size of a planet (Uranus) was used to detect Neptune. Five years later, just next door to the Ecole Normale Supérieure in Paris, where Bernu and co-workers performed their experiments, Léon Foucault used a smaller, yet still impressive, pendulum to demonstrate the rotation of the Earth.

Bernu *et al.* downsized the pendulum to the atomic scale. They excited individual rubidium atoms to 'Rydberg' states, making an electron oscillate between two orbits far away from the nucleus. These atoms acted as light-sensitive atomic clocks, the 'time' being given by the phase of their oscillations. When they were sent across the resonator, the hands

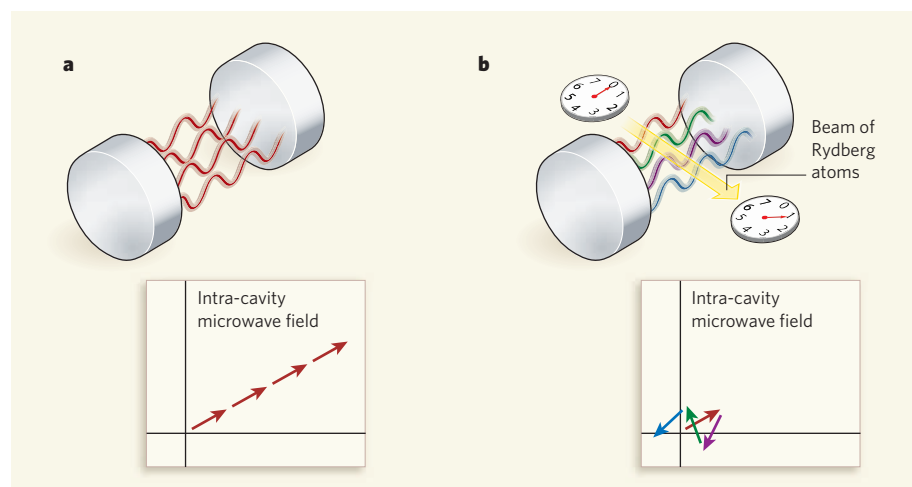


**Figure 1 | Non-destructive intensity measurements.** **a**, The build-up of a resonant wave in an empty cavity corresponds to the consecutive injection of  $N$  identical wavelets, all oscillating with the same amplitude  $\alpha/N$  and the same phase  $\phi$ . They can be represented by small vectors with a length  $\alpha/N$  and an angle  $\phi$ , which respectively define the length and the direction of elementary 'steps' made by the total intra-cavity field. A resonant field 'walks' away from zero always in the same direction and acquires an amplitude  $\alpha$  ( $(\alpha/N) \times N$ ) after  $N$  steps. **b**, Bernu *et al.*<sup>2</sup> use a beam of rubidium Rydberg atoms, which act as a light-sensitive atomic clock, to measure non-destructively the number of photons in the cavity between each wavelet injection. Owing to the quantum back-action of this measurement, the phases of the wavelets become random. The intra-cavity microwave field undergoes a random two-dimensional walk, and after  $N$  measurements its average amplitude is only  $(\alpha/N) \times \sqrt{N} = \alpha/\sqrt{N}$ . Increasing  $N$  decreases this amplitude, and therefore the final intensity of the field.

of these clocks were shifted by the microwave photons, each photon adding a shift of 45°. The electronic state of the atoms was measured outside the cavity by ionizing the most excited ones, and the electric current created

was amplified to become measurable. This last, 'destructive' part of the measurement affected only the atomic probe, leaving the microwave photons intact.

The Zeno effect cannot prevent the irreversible

decay of the microwave's intensity. In an oven with a typical power of 1 kilowatt, one microwave photon is lost every  $10^{-27}$  seconds, much too fast to count the photons left inside the resonator. There is thus no need to rewrite the user manual. But Bernu and colleagues' demonstration that the coherent evolution of a system can be 'frozen' by non-destructive measurements is a significant step forward for quantum control. For instance, one could continuously modify the way of measuring the system to bring it into exotic quantum states that cannot be prepared otherwise. But above all, this work is one of an impressive series<sup>9–11</sup>, demonstrating three essential qualities of Bernu and co-workers: expertise, rigour and a love of fundamental physics. ■

Alexei Ourjoumtsev is at the Max Planck Institute for Quantum Optics, Hans-Kopfermann Strasse 1, Garching D-85748, Germany.  
e-mail: alexei.ourjoumtsev@mpq.mpg.de

1. Daewoo KOC-870T instruction manual, page b (1999).
2. Bernu, J. *et al.* *Phys. Rev. Lett.* **101**, 180402 (2008).
3. Nagels, B., Hermans, L. J. F. & Chapovsky, P. L. *Phys. Rev. Lett.* **79**, 3097 (1997).
4. Itano, W. M., Heinzen, D. J., Bollinger, J. J. & Wineland, D. J. *Phys. Rev. A* **41**, 2295 (1990).
5. Balzer, C., Huesmann, R., Neuhauser, W. & Toschek, P. *Opt. Commun.* **180**, 115–120 (2000).
6. Streed, E. W. *et al.* *Phys. Rev. Lett.* **97**, 260402 (2006).
7. Kwiat, P. G. *et al.* *Phys. Rev. Lett.* **83**, 4725 (1999).
8. Hosten, O. *et al.* *Nature* **439**, 949–952 (2006).
9. Gleyzes, S. *et al.* *Nature* **446**, 297–300 (2007).
10. Guerlin, C. *et al.* *Nature* **448**, 889–893 (2007).
11. Deléglise, S. *et al.* *Nature* **455**, 510–514 (2008).

## CIRCADIAN CLOCKS

# Tips from the tip of the iceberg

Fred W. Turek

**Daily remodelling of histone proteins underlies interactions between circadian clock genes and metabolic genes. This regulatory mechanism could be widespread, affecting other physiological processes.**

If you monitor the precise daily onset of wheel-running behaviour in a mouse kept in an environment devoid of time cues, you can predict that, tomorrow, the animal will start running 23.7 hours — not 23.6 hours, not 23.8 hours — from when it started today. This is because, in organisms as diverse as bread mould, fruitflies, mice and humans, a central circadian clock program coordinates multiple behavioural and physiological processes, including movement, sleep and energy balance, on a daily basis, even when the organism is removed from all external time cues such as the daily light–dark cycle. How such circadian processes are regulated at a molecular level has long fascinated scientists. On page 997 of this issue, Alenghat *et al.*<sup>1</sup> provide a clue: activation of an enzyme that is involved in chemical modification of chromatin (complexes of DNA and histone

proteins) is a central point in the regulation of circadian metabolic processes.

Since the 1970s, studies on the anatomy, neurobiology and function of the mammalian circadian clock have focused on a brain region called the suprachiasmatic nucleus, which has a central role in regulating most, if not all, daily behavioural, physiological and cellular rhythms<sup>2</sup>. It emerged that numerous canonical circadian clock genes (such as *Clock*, *Pers*, *BMAL1* and *Cry*) are expressed in many central and peripheral tissues, and that, *in vitro*, the molecular clock could regulate the diurnal transcription of at least 10% of the genes in any given tissue<sup>3</sup>. These findings led to the realization that the circadian clock is not just central to the overall temporal regulation of behaviour and physiology, but that it perhaps also has a key role in the regulation of many

cellular pathways and networks in various tissues and organs.

Particular attention was paid to how the molecular circadian clock affects processes related to energy homeostasis. There were two main reasons for this. First, mutation of a key circadian gene, *Clock*, leads to obesity and metabolic syndrome — a combination of disorders that increases the risk of diabetes and heart disease<sup>4</sup>. Second, several genes involved in metabolism, including those mediating the formation of fatty tissue and carbohydrate metabolism (such as *Rev-erba*, *Rora* and *Ppara*), show reciprocal regulation with core circadian clock genes<sup>5</sup>.

Alenghat and colleagues' results<sup>1</sup> link these 'chronometabolic' molecular interactions to the cyclic regulation of chromatin through histone acetylation. They show that a specific genetic disruption of the interaction between the nuclear receptor co-repressor 1 (Ncor1) and the chromatin-modifying enzyme histone deacetylase 3 (Hdac3), which is activated by Ncor1, leads to aberrant regulation of clock genes and abnormal circadian behaviour. In turn, the oscillatory expression pattern of several metabolic genes is disrupted, leading to alterations in energy balance. The authors find that mice with loss of function of the Ncor1–Hdac3 complex are leaner than normal,



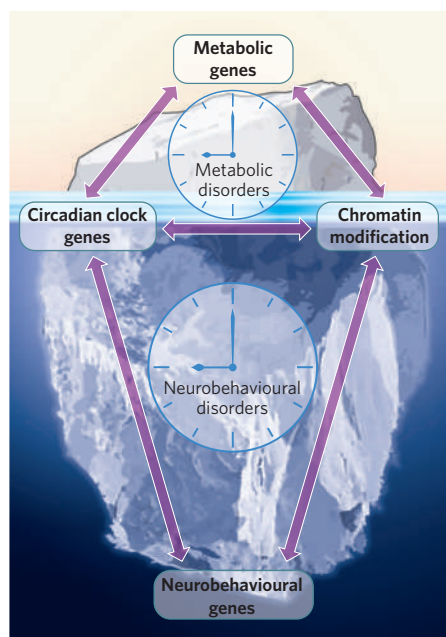


**Figure 1 | Clock genes in health and disease.** Alenghat *et al.*<sup>1</sup> find that activation of the chromatin-modifying enzyme Hdac3 by the Ncor1 protein is a key point of interaction between circadian clock genes and metabolic genes. Deregulation of the diurnal chromatin modifications that control the interplay between these two sets of genes could be central to several metabolic disorders, including cardiovascular disease, diabetes and obesity. Given the influence of the circadian clock on several other physiological systems and behaviours, such interactions could be more widespread, involving neurobehavioural genes, for example. Disruption of interactions between these genes and clock genes could cause various neurobehavioural disorders such as insomnia, depression and addiction. Like an iceberg, the observed chronometabolic epigenetic interactions could be providing only a glimpse of the importance of circadian temporal organization for health and disease.

showing increased sensitivity to the hormone insulin as a result of increased energy expenditure. So, contrary to the common perception that disruption of normal daily rhythms (for example, in shift workers) is metabolically deleterious, these results indicate that alterations of normal circadian physiology could lead to favourable metabolic changes — changes that could combat diseases of nutritional excess, including cardiometabolic disorders.

The fact that the remarkable temporal features of mammalian life depend on interactions between many circadian clock genes and complex gene networks has become apparent over the past decade. Regulation of circadian processes by modulations in the expression of clock genes and clock-controlled genes through rhythmic changes in histone modifications is also well documented<sup>6–8</sup>. What the observations of Alenghat and colleagues highlight is not only that temporal regulation of metabolism is crucial for normal energy balance, but also that the activation of Hdac3

by Ncor1 is central to the epigenetic regulation of circadian and metabolic physiology.

The interrelationship between circadian clock genes, metabolic genes and chromatin modification might have profound implications for cardiometabolic diseases and their treatment (Fig. 1). The precise 24-hour temporal organization that enables a mouse to start its routine behaviour every day 23.7 hours later than the day before might also be important for normal physiology at the tissue and organ level, with the clock — like the conductor of an orchestra — keeping all the different behavioural and physiological components in synchrony. And this need for tight temporal control for cardiometabolic function might represent only the tip of the iceberg.

Although numerous studies have looked for molecular links between circadian and metabolic genes and transcriptional regulation<sup>9</sup>, fewer studies have attempted to examine such links between the core circadian clock genes and the regulatory genes and gene networks underlying other physiological systems. For example, the core molecular clock could involve the activity of neurobehavioural genes and also regulate them through epigenetic mechanisms. Indeed, previous findings indicate that animals with mutations in *Clock* sleep 1–2 hours less each day than do normal animals

and show behaviour associated with bipolar disorder<sup>10,11</sup>. Mental disorders and addiction might also involve epigenetic mechanisms that alter chromatin structures at specific gene promoter sites<sup>12,13</sup>. So, as with an iceberg, whose tip provides only a glimpse (roughly 10%) of what is below the surface, the importance of circadian temporal organization for health and disease could be much more profound than we realize.

Fred W. Turek is at the Center for Sleep and Circadian Biology, Northwestern University, Evanston, Illinois 60208-3520, USA.  
e-mail: fturek@northwestern.edu

1. Alenghat, T. *et al.* *Nature* **456**, 997–1000 (2008).
2. Takahashi, J., Turek, F. & Moore, R. (eds) *Handbook of Behavioural Neurobiology* Vol. 12 (Kluwer Academic/Plenum, 2001).
3. Panda, S. *et al.* *Cell* **109**, 307–320 (2002).
4. Turek, F. *et al.* *Science* **308**, 1043–1045 (2005).
5. Preitner, N. *et al.* *Cell* **110**, 251–260 (2002).
6. Ripperger, J. & Schibler, U. *Nature Genet.* **38**, 369–374 (2006).
7. Doi, M., Hirayama, J. & Sassone-Corsi, P. *Cell* **125**, 497–508 (2006).
8. Etchegaray, J. *et al.* *Nature* **421**, 177–182 (2003).
9. Ramsey, K. *et al.* *Annu. Rev. Nutr.* **27**, 219–240 (2007).
10. Naylor, E. *et al.* *J. Neurosci.* **20**, 8138–8143 (2000).
11. McClung, C. A. *Pharmacol. Ther.* **114**, 222–232 (2007).
12. Renthal, W. & Nestler, E. J. *Trends Mol. Med.* **14**, 341–350 (2008).
13. Sharma, R. *Schizophr. Res.* **72**, 79–90 (2005).

**Competing financial interests:** declared (see online article for details).

## ORGANOMETALLIC CHEMISTRY

# Catalyst takes control to heart

Steven T. Diver

**Some transition-metal catalysts control organic reactions so that, given a choice of two mirror-image products, only one forms. The metal atom in these catalysts has been ignored as a source of control — until now.**

In a classic episode of *The Simpsons*, Homer encounters problems when he enters a three-dimensional world beyond the flat environs of his cartoon existence. Chemists can appreciate his culture shock because, although flat organic molecules are relatively easy to make, three-dimensional molecules are much more challenging — especially those containing chiral carbon atoms, which have four different groups attached. Chiral molecules exist as one of two mirror-image forms (enantiomers), each of which interacts differently with other chiral entities. Because most biological molecules are chiral, it is essential to find ways of making enantiomerically pure compounds for drug discovery and other biochemical applications.

Chiral catalysts are invaluable in this respect, because they churn out chiral organic products as single enantiomers from flat starting materials. Such catalysts contain structures that act as templates for chirality in the products, and are said to be stereogenic. Usually these

catalysts consist of one or two chiral ligand molecules bound to a central metal atom, so the stereogenicity comes from carbon atoms in the ligands. But, reporting on page 933 of this issue, Hoveyda and colleagues<sup>1</sup> demonstrate that 'stereogenic-at-metal' catalysts can also be used effectively to form enantiomerically pure products in a carbon–carbon bond-forming reaction — that is, the source of chirality is a metal atom to which four different ligands are attached. This represents a new way of relaying chiral 'information' to organic molecules.

The ideal catalyst for a particular class of reaction would react with any substrate for that reaction. In practice, it is difficult to find catalysts with such wide scope, and so, for any given reaction, there is often one catalyst that performs better than another. Frustratingly, it isn't always clear in advance which catalyst will be best. It is therefore useful to have several different catalysts (each with their own combinations and/or arrangements of ligands) that can be tested in new reactions to find which

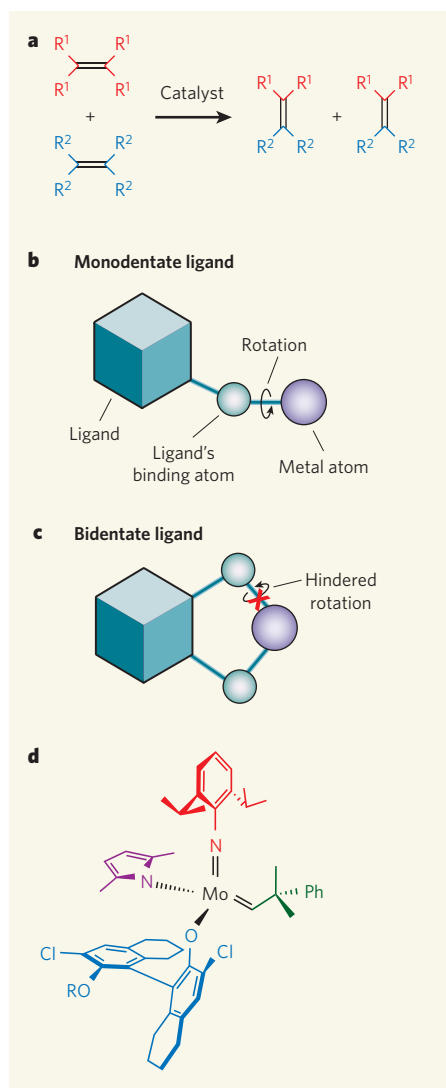


**Figure 1 | Chiral catalysts for olefin metathesis.**

**a**, In the olefin metathesis reaction, carbon–carbon double bonds in olefin reactants are redistributed between the atoms in the molecules. In some cases, a chiral carbon atom is made in one of the groups (here  $R^1$  or  $R^2$ ) attached to the carbon–carbon double bond of the product. Several transition-metal complexes act as metathesis catalysts that produce chiral products as single enantiomers. **b**, Some of these catalysts contain monodentate ligands, which bind to the metal through only one atom. Monodentate ligands can rotate and flex, and tend to distance themselves from reactants when these bind to the metal. Both of these effects reduce the catalyst's control of enantiomer formation. Only one ligand is shown here, but metathesis catalysts usually require four or more. **c**, Bidentate ligands bind to metals through two atoms, restricting rotation of the ligand. But the resulting lack of flexibility can also limit the reactivity of metathesis catalysts. **d**, Hoveyda and colleagues<sup>1</sup> report a metathesis catalyst in which the metal (molybdenum, Mo) atom is a source of chirality, because four different ligands are attached to it; each ligand is shown in a different colour. The monodentate ligands are less rigid than conventional bidentate ligands, and do not move away from the reactants' binding site. These two design features provide the catalyst with excellent control over the enantiomeric outcome of a reaction, even for difficult substrates. Cl is a chlorine atom; Ph is a phenyl group.

one optimizes the yield of products — or, for chiral reactions, which one optimizes the transfer of chiral information from the catalyst to the product.

A case in point is the olefin metathesis reaction. In this process, two olefins (which contain carbon–carbon double bonds,  $C=C$ ) react in the presence of a catalyst so that the  $C=C$  bonds in the reactants break, and new  $C=C$  bonds form between the fragments (Fig. 1a). Metathesis means 'exchange of parts', and the reactants can be thought of as pairs of dancers, who switch partners as if they were taking part in a square dance<sup>2</sup>. The metathesis reaction has become incredibly useful for organic synthesis. Indeed, in 2005 the Nobel Prize in Chemistry was awarded to Robert Grubbs, Richard Schrock and Yves Chauvin for their pioneering work in this area.

There are two main classes of catalyst for olefin metathesis: the molybdenum-containing catalysts devised by Schrock, and the ruthenium-based variety developed by Grubbs. The ruthenium catalysts are most popular because they can be used in the widest range of solvents and are not compromised by most of the chemical groups that are commonly found in organic molecules. The molybdenum

catalysts are more sensitive, and are typically reserved for use with less reactive olefins and for substrates that have few chemical groups that might foul up the catalyst. But they have a useful role in metathesis reactions that yield enantiomeric products, partly because it is easy to incorporate chiral ligands into molybdenum catalysts, and also because these catalysts are fairly good at transferring chiral information from their ligands to reaction products.

The work reported by Hoveyda and colleagues<sup>1</sup> takes molybdenum catalysts to their highest level of performance yet. The authors' new catalyst, with its stereogenic-at-metal design, performs metathesis reactions that provide greater yields than the existing compounds, and also provides higher levels of chiral induction, so that products are obtained as essentially only one enantiomer. This is directly attributable to the ability of the stereogenic molybdenum atom to direct the interactions of  $C=C$  bonds in reactants with the catalyst, controlling the alignment of the bonds so that only one enantiomeric product can form. But there is another unusual aspect of the catalyst's design that is key to its success: the ligands.

The simplest ligands in metal complexes are monodentate — they bind to the metal through

a single atom (Fig. 1b). But monodentate ligands present a design challenge for chiral catalysts, and especially so for metathesis catalysts. In a reaction catalysed by a metal complex, the starting materials form a complex with the metal atom; this brings the starting materials close together so that they can react. The alignment of the reactants in the complex determines the chiral outcome of the reaction, and is governed by the other ligands around the metal, which jostle with the reactants for space. For maximum chiral induction, the ligands should be as close as possible to the newly forming bond between the reactants.

But in ruthenium metathesis catalysts, the monodentate chiral ligand sits on the opposite hemisphere of the intermediate complex to that of the reactants, minimizing the potential for chiral induction. The same problem occurs in catalysts for many other reactions: chiral monodentate ligands tend to move far away from reactant-binding sites. Nevertheless, Grubbs and co-workers have found ways to successfully 'drape' the stereogenic element of monodentate ligands around the central metal atom of a metathesis catalyst towards the reactants, so that products are formed predominantly as one enantiomer<sup>3,4</sup>.

Another problem with monodentate ligands in chiral catalysts is that they tend to rotate around the point of attachment to the metal. Such rotation changes the catalyst's conformation, thus altering the chiral environment around the metal. This is catastrophic, because each conformation has a different reactivity and provides a different degree of chiral induction. Such difficulties are usually overcome by using bidentate ligands, which bind to metals through two atoms (Fig. 1c). These ligands are less floppy than monodentate ones, and have fewer conformations to complicate (or limit) the degree of chiral induction. Bidentate ligands have allowed the successful development of chiral catalysts for alkene metathesis in both the ruthenium<sup>5</sup> and molybdenum<sup>6,7</sup> classes. But bidentate ligands don't always have the flexibility to allow large structural changes around the catalytic metal atom, as is sometimes required for metathesis reactions.

The ligands in Hoveyda and colleagues' catalyst<sup>1</sup> are monodentate (Fig. 1d). This is necessary for efficient chiral induction from the stereogenic molybdenum atom. But, remarkably, the complexes are configurationally stable, preventing the problems usually caused by monodentate ligand rotation. Furthermore, because the flexible monodentate ligands accommodate large structural changes during reactions, the catalyst is more reactive than analogous catalysts that use bidentate ligands. The stereogenic-at-metal design thus yields an exceptionally reactive catalyst that also provides high levels of chiral induction.

The authors use their catalyst in an elegant, short synthesis of a structurally complex, naturally occurring compound, quebrachamine (see Fig. 4 on page 936). They find that the catalyst



distinguishes between three different olefins in the achiral starting material, sequentially reacting only the required two, thus yielding the product essentially as a single enantiomer in high yield. This reaction could not have been achieved using previously available catalysts. Moreover, their catalyst performs the reaction in the presence of a tertiary amine (an organic base containing a nitrogen to which three hydrocarbon groups are attached) in the substrate, which is typically a troublesome motif in metathesis reactions.

Hoveyda and colleagues' stereogenic-at-molybdenum complex has the potential to become an all-purpose chiral catalyst for olefin metathesis reactions. More broadly, the authors have discovered a bold new design for chiral catalysts that will inspire the development of future generations of catalysts, not only

for olefin metathesis, but also for many other catalytic reactions.

Steven T. Diver is in the Department of Chemistry, University at Buffalo, The State University of New York, 572 Natural Sciences Complex, Amherst, New York 14260-3000, USA. e-mail: diver@buffalo.edu

1. Malcomson, S. J., Meek, S. J., Sattely, E. S., Schrock, R. R. & Hoveyda, A. H. *Nature* **456**, 933–937 (2008).
2. [http://nobelprize.org/nobel\\_prizes/chemistry/laureates/2005/animation.html](http://nobelprize.org/nobel_prizes/chemistry/laureates/2005/animation.html)
3. Seiders, T. J., Ward, D. W. & Grubbs, R. H. *Org. Lett.* **3**, 3225–3228 (2001).
4. Funk, T. W., Berlin, J. M. & Grubbs, R. H. *J. Am. Chem. Soc.* **128**, 1840–1846 (2006).
5. Van Veldhuizen, J. J., Garber, S. B., Kingsbury, J. S. & Hoveyda, A. H. *J. Am. Chem. Soc.* **124**, 4954–4955 (2002).
6. Alexander, J. B., La, D. S., Cefalo, D. R., Hoveyda, A. H. & Schrock, R. R. *J. Am. Chem. Soc.* **120**, 4041–4042 (1998).
7. Fujimura, O. & Grubbs, R. H. *J. Org. Chem.* **63**, 824–832 (1998).

histone H3 in mouse and yeast cells, respectively. This mechanism involves enzymatic cleavage of the first 21 amino-acid residues at the N terminus of H3, thus sweeping away en masse all modifications present in this region (Fig. 1).

Despite the evolutionary conservation of this mechanism, there seems to be a striking difference between mice and yeast in the endopeptidase enzyme each organism uses for N-tail cleavage. The 'clipper' in mouse is cathepsin L, which belongs to a class of protease enzymes called cysteine proteases. Cathepsins are found in the cellular organelles called lysosomes, but are also present in the nucleus<sup>5</sup>. The as-yet-unidentified yeast enzyme is likely to be a serine protease<sup>2</sup>. The feature these enzymes share, however, is that they are regulated: cathepsin L is induced during differentiation of embryonic stem cells in mice, whereas the activity of the yeast enzyme is triggered under conditions of nutrient deprivation that lead either to the stationary phase of growth or to sporulation.

The signals that promote the activity of the mouse and yeast proteases are unknown. Both groups<sup>1,2</sup> report, however, that the two enzymes are sensitive to the modification state of the target H3 N tail. The presence of certain marks inhibited the activity of the endopeptidases, whereas other marks increased their activity (Fig. 1). So it could be that enzymatic cleavage of H3 is regulated by an interplay between the endopeptidases and other chromatin-modifying activities.

What are the biological consequences of H3-tail clipping? The role of H3-tail cleavage during differentiation of embryonic stem cells is unknown, although stem cells contain a signature mark of trimethylation on lysines 4 and 27 (H3K4me3/H3K27me3) in the H3 N tail that is altered upon differentiation<sup>6</sup>. By removing this and other modifications during differentiation, H3-tail clipping could set the transcriptional state of a particular cell lineage.

At the cellular level, H3-tail clipping could simply clear all repressive marks from chromatin, thereby allowing the binding of transcription-activator complexes to the affected DNA. Indeed, the results of Santos-Rosa and colleagues<sup>2</sup> support a role for this

## EPIGENETICS

# How to lose a tail

Mary Ann Osley

**Everyone carries some baggage they would like to lose. For the histone protein H3, that baggage is a chunk of its tail, which when clipped off affects the expression of genes with which the histone is associated.**

Chromatin — the complex of DNA and histone proteins — is highly dynamic. The histone constituents of chromatin can be reversibly modified, replaced with related proteins, or cleaved by proteolytic enzymes. Two studies<sup>1,2</sup>, published in *Cell* and *Nature Structural and Molecular Biology*, now show that histone modification by regulated proteolytic cleavage is required during cell differentiation in both mammals and yeast to alter gene expression.

A histone molecule is divided into two distinct regions: a carboxy terminus that organizes DNA on the surface of each unit of the DNA–histone complex (the nucleosome), and a flexible amino terminus dubbed the N tail, which protrudes from the nucleosome. N tails make contact with DNA and with histones in adjacent nucleosomes, thereby enabling chromatin folding. Histone proteins are also typically decorated with a large number and variety of small chemical groups, such as methyl and acetyl groups, and these modifications have a central role in regulating gene transcription<sup>3</sup>. Why so many modifications, and how do they affect transcription?

The prevailing view holds that distinct patterns of N-tail modifications, or 'marks', provide signals for the recruitment of specific transcription factors to chromatin or stimulate the activity of proteins that either modify the chromatin further or disrupt it<sup>3,4</sup>. As a consequence, transcription is turned on or off, depending on whether activating or repressing marks are present. The corollary of this is

that, when the transcriptional status has to be reversed, the N-tail marks must be removed to allow appropriate restructuring of chromatin.

Commonly, marks are actively removed using the opposite reaction to the one that added them; for example, histone deacetylase enzymes remove acetyl marks, which were added by histone acetyltransferases. But what happens if more than one mark must be removed simultaneously? Most enzymes engaged in histone modification show specificity — that is, they only attack single, or several, marks of the same kind. Using this strategy, each type of modification would have to be removed by a different enzyme. Duncan *et al.*<sup>1</sup> and Santos-Rosa and colleagues<sup>2</sup> describe a more dramatic way in which multiple marks are simultaneously removed from the N tail of

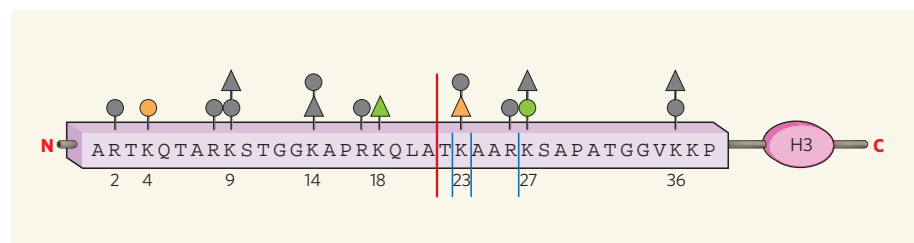


**Figure 1 | Cleavage of the H3 amino-terminal tail.** The amino-acid sequence of the mammalian histone H3 N tail is shown along with the major sites of methylation (circles) and acetylation (triangles) that have been mapped to arginine (R) and lysine (K) residues<sup>3</sup>. Two groups<sup>1,2</sup> find that the enzyme cathepsin L in mouse embryos and a serine protease in yeast cleave H3 after alanine 21 (red line). Minor cleavage sites generated by cathepsin L are also indicated (blue lines). The orange and green symbols indicate modifications that were shown to respectively inhibit or activate the proteases when present on synthetic peptides during *in vitro* cleavage assays.

modification in regulating the selective activation of transcription in yeast, as mutation of the H3 cleavage site impaired expression of several genes normally activated during sporulation or entry into the stationary phase. The authors' work<sup>2</sup> also hints at an additional effect of H3-tail clipping in yeast, involving regulation of nucleosome displacement. Cleavage of the H3 tail precedes loss of nucleosomes at several promoter sequences *in vivo* — an event that exposes promoter DNA and thus enhances the binding of transcription-activator complexes to the promoter during gene activation<sup>7</sup>. Intriguingly, a trimethylation mark, K4me3, which prevents clipping by the yeast endopeptidase *in vitro*, is maintained in chromatin at promoters during gene activation<sup>8</sup>. This observation supports a mechanism in which nucleosomes that do not contain K4me3 are marked for H3 cleavage and subsequent displacement.

Apart from the unknown identity of the

serine protease that clips H3 in yeast, and the mysterious way in which clipper activities in mouse and yeast are regulated, many other questions arise from these fascinating observations<sup>1,2</sup>. The first relates to the unexpected role of lysosomal proteases in chromatin activities. Do other cysteine proteases also have nuclear targets? Second, is N-tail clipping unique to H3, or are other histone proteins also cleaved at their N tails in a regulated manner? There are reports that other histone N tails are proteolytically removed, notably during development in the ciliate *Tetrahymena*, in which many striking observations relating to chromatin structure have been made<sup>9</sup>. Third, could the loss of the N tail affect gene expression not just by removing some marks but also by actively preventing formation of others on N tails? And finally, how is the cleaved H3 molecule replaced with an intact H3, and could this provide a mechanism for substituting one set

of tail marks for another? Just when it seemed that we knew how chromatin structure is regulated, previously unknown pathways emerge to keep this field of research vital and interesting. ■

Mary Ann Osley is in the Department of Molecular Genetics and Microbiology, University of New Mexico School of Medicine, Albuquerque, New Mexico 87131-0001, USA.

e-mail: mosley@salud.unm.edu

1. Duncan, E. M. *et al.* *Cell* **135**, 284–294 (2008).
2. Santos-Rosa, H. *et al.* *Nature Struct. Mol. Biol.* doi:10.1038/nmsb.1534 (2008).
3. Kouzarides, T. *Cell* **128**, 693–705 (2007).
4. Jenuwein, T. & Allis, C. D. *Science* **293**, 1074–1080 (2001).
5. Goulet, B. *et al.* *Mol. Cell* **14**, 207–219 (2004).
6. Bernstein, B. E. *et al.* *Cell* **125**, 315–326 (2006).
7. Lee, C. K., Shibata, Y., Rao, B., Strahl, B. D. & Lieb, J. D. *Nature Genet.* **36**, 900–905 (2004).
8. Liu, C. L. *et al.* *PLoS Biol.* **3**, e328 (2005).
9. Lin, R., Cook, R. G. & Allis, C. D. *Genes Dev.* **5**, 1601–1610 (1991).

## CONDENSED-MATTER PHYSICS

# The eternal triangle

Mark Harris

**The frustration that atomic interactions can undergo is not unlike that occurring when human aims are thwarted. An elegant study offers a way of visualizing the hitherto mysterious dynamics of 'frustrated' systems.**

It is one of the great embarrassments of condensed-matter physics — but also one of its greatest strengths — that we understand so poorly the fundamental interactions inside materials. On the one hand, any elementary textbook will provide simple descriptions of such interactions (ionic, covalent and van der Waals bonds, as well as various magnetic interactions). But on the other hand, wonderfully unexpected and qualitatively new behaviour is invariably observed in real, experimental materials when these same interactions are allowed to mix, match and, especially, 'fight' each other.

The properties of 'frustrated' systems offer a classic example of the end result being greater than the sum of the parts — the geometry of the atomic lattice in such systems prevents the simultaneous minimization of the interaction energies between the neighbouring atoms, precluding the existence of a unique ground state — and explain why they have long been at the forefront of research in the physical sciences. Many commercial materials (such as the ferrite ceramic magnets used in microelectronics) contain strongly frustrated interactions that affect their physical properties. A better understanding of frustration might allow for more subtle 'tuning' of such materials to achieve desirable commercial properties.

One of the long-standing problems in this area is that of the Ising anti-ferromagnet on

the triangular lattice, the archetypal frustrated magnet. This is stunningly simple to conceptualize but surprisingly elusive in nature, with a relative scarcity of experimental realizations. On page 898 of this issue, Han *et al.*<sup>1</sup> describe experiments on a new kind of system, based on non-magnetic colloidal monolayers, that is shown to approximate the triangular Ising anti-ferromagnet in a number of ways. What's more, its dynamics may be visualized directly in real time.

Although Han and colleagues' work involves an entirely non-magnetic soft-matter system, its significance is best appreciated by considering the way magnetic interactions behave on simple two-dimensional atomic lattices (Fig. 1). In the case of the triangular lattice, Gregory Wannier's pioneering study<sup>2</sup> predicted that the lowest-energy state of the system (its ground state) is disordered, and retains finite entropy even at absolute zero temperature. A closely related result<sup>3</sup> was obtained by Philip Anderson in 1973. He considered the case of quantum spins on the triangular lattice and predicted that the ground state is a 'spin-liquid' state, containing strong dynamic correlations but no static order whatsoever, even down to the lowest temperatures. This tantalizing spin-liquid state has preoccupied physicists ever since, especially because it was highlighted as a possible explanation for high-temperature superconductivity.

Research has snowballed exponentially to consider many other types of geometrical frustration and spin-liquid behaviour, such as spin ice, pyrochlores, kagomé lattices and kagomé ice, to name but a few examples<sup>4–8</sup>. Recent work has also pointed to the possibility of fabricating some of the classic frustrated models, for instance using nanoscale magnetic islands in thin-film form<sup>9</sup>. But so far, these techniques have not been exploited to probe the dynamics of the frustrated systems, especially how these systems explore their highly degenerate ground states. One intriguing suggestion has been to test soft-matter colloidal systems in which the interactions between the particles can be tuned<sup>10</sup>, and the results of Han *et al.*<sup>1</sup> demonstrate the enormous potential of these systems.

The experiments were performed on a system of microgel colloidal spheres that self-organize into a buckled triangular lattice. The up- or down-displacements of the spheres are closely analogous to the up- or down-spin states of the Ising anti-ferromagnet. In terms of structure and interactions then, this new system presents a tantalizing approximation to the triangular Ising anti-ferromagnet. Remarkably, the system is fully dynamic, which means that a number of poorly understood issues associated with frustrated systems can be investigated, in particular how individual particles reorganize themselves upon changes in the local environment, how defects arise and travel around the lattice, and how transitions to frozen, glassy states occur.

Han and colleagues' system comes with two further novelties. First, the interactions and dynamics of the system can be carefully fine-tuned (something that is difficult, if not impossible, with magnetic materials) through changes in the diameter of the microgel spheres. This clearly points towards the potential for investigating other statistical-mechanical



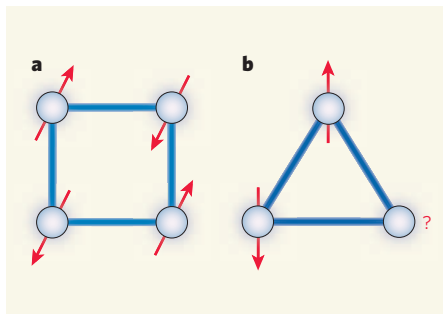


**Figure 1 | Geometric frustration.** In many magnetic materials, the interactions between neighbouring atoms favour anti-parallel alignment of the magnetic moments (or spins), a property known as anti-ferromagnetism. **a**, When the atoms are arranged at the corners of a square lattice, the system can easily find an ordered structure that satisfies anti-ferromagnetism. **b**, When those same atoms are placed at the corners of a triangular lattice, only two out of the three spins can align anti-parallel, while the interactions of the third remain frustrated — the third spin cannot 'decide' which of the other two neighbouring spins to align anti-parallel with. This is the basis of the Ising anti-ferromagnet on a triangular lattice, which is expected to be disordered at all temperatures. Han *et al.*<sup>1</sup> describe a system of diameter-tunable microgel spheres that exhibits properties analogous to those of frustrated anti-ferromagnetic systems.

models of disordered systems. Second, as the spheres are visible under a microscope, the microscopic dynamic properties can be observed in real time.

With all this in mind, Han *et al.* notice interesting differences between the colloidal system and the ideal triangular Ising anti-ferromagnet. In particular, the colloid tends to relieve its frustration as the temperature is lowered by forming partially ordered 'striped' structures. This means that, instead of possessing a finite and extensive entropy — one that scales with the number of particles,  $N$  — at zero temperature, as would be the case in the triangular Ising anti-ferromagnet, the entropy is still finite but 'subextensive', and scales as  $N^{1/2}$ . This subextensive entropy is reflected in the dynamics of the system. In particular, zero-energy modes are expected in the triangular Ising anti-ferromagnet, where certain local configurations can flip from one to the other with no energy cost, even at zero temperature. But the colloid is devoid of such zero-energy modes, and the dynamics of the system is seen to slow down and become more 'glassy' than the Ising anti-ferromagnet as the temperature is lowered. These characteristics relate the colloidal system to many frustrated magnetic materials that also show glassy behaviour.

Indeed, such glassiness at low temperature is a near-ubiquitous feature in experimental frustrated systems, and this is only poorly understood at present. But the fact that the microscopic dynamics of the colloid can be observed directly, and in real time, means that

such microscopic effects can be probed more fully than before. For instance, Han *et al.*<sup>1</sup> were able to see the nucleation, diffusion and annihilation of defects directly, and see their influence on the dynamics of neighbouring particles, knowledge of which has been very limited in frustrated systems so far.

It is still early days for colloidal frustrated systems. There is much to try out, and Han *et al.* generously point the way by suggesting a variety of future experiments, including subjecting the system to probes as diverse as optical tweezers, gravitational and electric fields, or carefully controlled dopants. This diversity of ways in which the colloidal system can be manipulated highlights both its flexibility and its transparency as an experimental test bed of frustrated physics. With such fascinating possibilities for research in view, one would hope

that Han and colleagues' proposals are adopted enthusiastically by frustrated magneticians the world over. ■

Mark Harris is at Oriel College, University of Oxford, Oxford OX1 4EW, UK.

e-mail: mark.harris@oriel.ox.ac.uk

1. Han, Y. *et al.* *Nature* **456**, 898–903 (2008).
2. Wannier, G. H. *Phys. Rev.* **79**, 357–364 (1950).
3. Anderson, P. W. *Mater. Res. Bull.* **8**, 153–160 (1973).
4. Harris, M. J., Bramwell, S. T., McMorrow, D. F., Zeiske, T. & Godfrey, K. W. *Phys. Rev. Lett.* **79**, 2554–2557 (1997).
5. Ramirez, A. P., Hayashi, A., Cava, R. J., Siddharthan, R. & Shastri, B. S. *Nature* **399**, 333–335 (1999).
6. Castelnovo, C., Moessner, R. & Sondhi, S. L. *Nature* **451**, 42–45 (2008).
7. Olariu, A. *et al.* *Phys. Rev. Lett.* **100**, 087202 (2008).
8. Fennell, T., Bramwell, S. T., McMorrow, D. F., Manuel, P. & Wildes, A. R. *Nature Phys.* **3**, 566–572 (2007).
9. Wang, R. F. *et al.* *Nature* **439**, 303–306 (2006).
10. Libál, A., Reichhardt, C. & Olson Reichhardt, C. J. *Phys. Rev. Lett.* **97**, 228302 (2006).

## NEUROSCIENCE

# Greasy proteins of the neuron

Maurine E. Linder

**An analysis of neuronal proteins reveals that many are regulated through covalent attachment of the lipid palmitate. This reversible modification seems to affect the form and function of synaptic junctions.**

Phosphates, lipids, sugars and even small polypeptides covalently attach to proteins, changing a protein's activity, localization or stability. Such modifications can be either reversible or permanent. Reversible modifications allow regulation of protein function, which is essential for cellular responses. Phosphorylation has long been the kingpin of regulatory modifications, and the total pool of cellular proteins (the proteome) that undergo phosphorylation is vast. On page 904 of this issue, Kang *et al.*<sup>1</sup> reveal another regulated proteome — neuronal proteins modified by the 16-carbon fatty acid palmitate.

That the analysis of the palmitoyl-proteome is feasible was first established in yeast<sup>2</sup>. To identify palmitoylated proteins in rat neurons, Kang *et al.* applied the same methods as those used in yeast — they marked palmitoylated proteins with a covalent chemical tag<sup>3</sup>, isolated them and identified them using mass spectrometry. Not only did they detect most of the palmitoylated neuronal proteins identified previously, but they also revealed more than 200 new candidates. As false positives can arise in the analysis, validation of candidate proteins is important. The authors' verification by other methods that 21 of these candidate proteins are indeed palmitoylated underscores the success of their approach.

The neural palmitoyl-proteome features many proteins with roles in the transmission and modulation of signals across synaptic junctions in the nervous system<sup>1</sup>. Among the

new palmitoylated proteins Kang *et al.* identify are: several ion channels; proteins that regulate availability of neurotransmitters at synapses; neurotransmitter receptors; proteins that regulate the growth and retraction of axonal processes; and many cell-surface proteins involved in synaptic adhesion.

One particularly intriguing find is a palmitoylated variant of Cdc42, a GTPase enzyme that regulates cell polarity and the actin cytoskeleton<sup>4</sup>. Like many GTPases, Cdc42 normally associates with membranes through an isoprenoid lipid at its carboxy terminus and was not considered a substrate for palmitoylation. Kang *et al.* demonstrate that a palmitoylated variant of Cdc42 does exist, and that — unlike the canonical isoprenylated isoform, which is expressed ubiquitously — this isoform is brain specific<sup>1,5</sup>.

Cdc42 and its targets are known to have a role in regulating the formation of dendritic processes in neurons<sup>4</sup> — an essential step in the generation of new synapses. Although both isoprenylated and palmitoylated isoforms of this protein are localized in dendrites, palmitoylated Cdc42 is concentrated in dendritic protrusions called spines, which participate in synaptic transmission<sup>1</sup>. Kang *et al.* used RNA interference to selectively block expression of the two Cdc42 isoforms. They find that loss of palmitoylated Cdc42 results in a significant reduction both in extension of dendritic filopodia — the presumed precursors of dendritic spines<sup>4</sup> — and in spine formation; the absence

of the isoprenylated isoform, by contrast, had no effect. These observations make a persuasive case for palmitoylated Cdc42 as the dominant isoform regulating dendritic spine morphology, with palmitoylation being crucial for this function.

Kang *et al.* propose that the functional differences between palmitoylated and isoprenylated Cdc42 could be ascribed to their different membrane localization, governed by their specific lipid modifications. For example, dendritic spines are enriched in cholesterol-sphingolipid membrane microdomains called lipid rafts<sup>6</sup>, and palmitoylated proteins are known to preferentially associate with rafts<sup>7</sup>. Perturbing rafts in neurons leads to a loss of dendritic spines<sup>6</sup>, an effect similar to the consequences of depleting palmitoylated Cdc42 in neurons<sup>1</sup>. It would be interesting to determine whether palmitoylated Cdc42 localizes within membrane microdomains.

If palmitoylation is a bona fide regulatory modification, then a protein's palmitoylation, and thus its function, should change in response to molecular signals. Kang *et al.* show that palmitoylation is a dynamic process — they document rapid changes in the palmitoylation state of selected synaptic proteins in neurons grown in culture in response to treatment with the neurotransmitter glutamate. Not all of the ten proteins examined were affected, however, with those that were affected showing either increased or decreased palmitoylation. So glutamate does not seem to have a general effect on protein palmitoylation in neurons.

As for Cdc42, on treatment with glutamate its palmitoylation decreased, and this GTPase was lost from dendritic spines. A previous study<sup>8</sup> showed that dendritic spines contract and collapse in cultured neurons under the same experimental conditions as those used by Kang and colleagues. This correlative evidence therefore supports the proposal that regulated palmitoylation of Cdc42 contributes to changes in spine morphology in response to synaptic activity. Establishing the broader significance of palmitoylation in regulating communication at synaptic junctions will require an understanding of the functional consequences of dynamic palmitoylation of other synaptic targets identified by the authors.

Characterization of the neural palmitoyl-proteome is a technical tour de force and provides a wealth of data to mine. Many investigators will find their favourite proteins on Kang and colleagues' list and will be challenged to consider how palmitoylation might alter those proteins' function. Moreover, changes in the palmitoylation state of proteins in response to synaptic activity imply that enzymes that add palmitate to, or remove it from, proteins may also be regulated by synaptic activity. The first order of business, however, will be to identify enzymes responsible for reversible palmitoylation of Cdc42 and other synaptic proteins.

Palmitoylation is catalysed by a large family of palmitoyltransferases — enzymes that share an evolutionarily conserved domain with a signature motif of aspartate-histidine-histidine-cysteine amino-acid residues<sup>7,9</sup>. Once animals lacking a specific palmitoyltransferase are engineered, Kang and colleagues' approach can be used both to identify the full spectrum of palmitoylated proteins that are substrates for that enzyme and to examine the functional consequences of ablating specific palmitoylation events *in vivo*. Less is known about enzymes that remove the palmitoyl group from proteins<sup>7</sup>, and their discovery will also be essential for elucidating the pathways that make palmitoylation dynamic. ■

Maurine E. Linder is in the Department of Cell Biology and Physiology, Washington University School of Medicine, St Louis, Missouri 63110, USA. e-mail: mlinder@wustl.edu

1. Kang, R. *et al.* *Nature* **456**, 904–909 (2008).
2. Roth, A. F. *et al.* *Cell* **125**, 1003–1013 (2006).
3. Drisdell, R. C. & Green, W. N. *Biotechniques* **36**, 276–285 (2004).
4. Ethell, I. M. & Pasquale, E. B. *Prog. Neurobiol.* **75**, 161–205 (2005).
5. Marks, P. W. & Kwiatkowski, D. J. *Genomics* **38**, 13–18 (1996).
6. Hering, H., Lin, C. C. & Sheng, M. *J. Neurosci.* **23**, 3262–3271 (2003).
7. Smotryś, J. E. & Linder, M. E. *Annu. Rev. Biochem.* **73**, 559–587 (2004).
8. Halpain, S., Hipolito, A. & Saffer, L. J. *J. Neurosci.* **18**, 9835–9844 (1998).
9. Tsutsumi, R., Fukata, Y. & Fukata, M. *Pflügers Arch.* **456**, 1199–1206 (2008).

## BIOGEOCHEMISTRY

# Nitrous oxide in flux

Sharon A. Billings

**In drought conditions, forest soils can serve as a small but surprisingly persistent sink for the greenhouse gas nitrous oxide. The effect highlights a research avenue necessary for predicting Earth's climate.**

Increasing amounts of reactive nitrogen<sup>1</sup> are entering the environment through human agency. One consequence is increased production of the powerful greenhouse gas nitrous oxide — N<sub>2</sub>O — by microorganisms in soils. We do not understand the intricate dynamics of N<sub>2</sub>O production and consumption in soils, prompting research such as that reported in *Global Change Biology*<sup>2</sup> by Goldberg and Gebauer. They tracked N<sub>2</sub>O fluxes in European spruce-forest soils under experimental conditions of a predicted climate pattern — increasing episodes of drought followed by heavy rainfall.

The burning of fossil fuel, planting of crops associated with bacteria that can capture atmospheric dinitrogen (N<sub>2</sub>), and use of increasing amounts of fertilizer, all result in more nitrogen in Earth's biological cycles<sup>1</sup>. Atmospheric concentrations of N<sub>2</sub>O have risen by 18% since the middle of the eighteenth century, in part because of these activities<sup>3</sup>. In the atmosphere, N<sub>2</sub>O lasts for an average of 114 years before undergoing reactions resulting in its destruction. However, this atmospheric N<sub>2</sub>O sink accounts for only about 71% of known sources, leaving 5.2 million tonnes 'missing' from the atmosphere annually<sup>3</sup>. This discrepancy means that we are either overestimating N<sub>2</sub>O sources or underestimating N<sub>2</sub>O sinks. Goldberg and Gebauer offer evidence that addresses this point. Reports of soil N<sub>2</sub>O fluxes typically describe net emissions to the atmosphere<sup>4</sup>, but Goldberg and Gebauer conclude that forest soils may serve as net N<sub>2</sub>O sinks to a greater extent than previously thought.

Nitrous oxide is both produced and consumed in soils by a complex suite of microbially mediated processes. For example, denitrifiers perform the step-by-step chemical reduction of nitrate (NO<sub>3</sub><sup>-</sup>) to N<sub>2</sub>, producing N<sub>2</sub>O as an intermediate by-product. Some N<sub>2</sub>O escapes from the soil, but under anaerobic conditions some is completely transformed into N<sub>2</sub>. The denitrification pathway is thus associated with both N<sub>2</sub>O production and consumption. Moreover, other groups of microorganisms<sup>4–6</sup> can also transform nitrogen in ways that produce and consume N<sub>2</sub>O.

Moisture availability can promote the production of N<sub>2</sub>O (ref. 7), but investigators often presume that N<sub>2</sub>O consumption — transformation into N<sub>2</sub> — is also highest when soil moisture levels are high because of the anaerobic nature of this process<sup>4</sup>. There are relatively few field studies that report net N<sub>2</sub>O consumption at the soil surface, but those that do describe comparatively small fluxes that show no predictable relationship with soil moisture. These small fluxes are often dismissed as an indication of the challenges of quantifying N<sub>2</sub>O levels near detection levels, and not robust evidence of soil N<sub>2</sub>O sink strength<sup>4</sup>. Thus, the influence of soil moisture on N<sub>2</sub>O production and its ultimate fate — release or consumption — remains unclear.

Goldberg and Gebauer<sup>2</sup> have tackled this issue by inducing soil drought in a spruce forest in Germany, and measuring net N<sub>2</sub>O fluxes at the soil surface and concentrations within the soil profile. They found that net N<sub>2</sub>O consumption at the soil surface was enhanced by drought, and, surprisingly, that it occurred





regions. Advances<sup>8,12</sup> in quantifying the relative abundances of two types of  $^{15}\text{N}_2\text{O}$  ( $^{15}\text{N}^{14}\text{NO}$  and  $^{14}\text{N}^{15}\text{NO}$ ) promise to help in distinguishing between the paths by which  $\text{N}_2\text{O}$  is produced. Such work will help us further constrain the global  $\text{N}_2\text{O}$  budget and, ultimately, understand critical features of the two-way feedbacks between climate and  $\text{N}_2\text{O}$ .

Sharon A. Billings is in the Department of Ecology and Evolutionary Biology, and the Kansas Biological Survey, University of Kansas, 2101 Constant Avenue, Lawrence, Kansas 66047, USA. e-mail: sharonb@ku.edu

1. Galloway, J. N. *et al. Science* **320**, 889–892 (2008).
2. Goldberg, S. D. & Gebauer, G. *Global Change Biol.* doi:10.1111/j.1365-2486.2008.01752.x (2008).
3. Intergovernmental Panel on Climate Change *Climate Change 2007: The Physical Science Basis* (eds Solomon, S. D. *et al.*) (Cambridge Univ. Press, 2007).
4. Chapuis-Lardy, L., Wrage, N., Metay A., Chotte, J.-L. & Bernoux, M. *Global Change Biol.* **13**, 1–17 (2007).
5. Wrage, N., Velthof, G. L., van Beusichem, M. L. & Oenema, O. *Soil Biol. Biochem.* **33**, 1723–1732 (2001).
6. Vieten, B., Conen, F., Seth, B. & Alewell, C. *Biogeosciences* **5**, 129–132 (2008).
7. Davidson, E. A., Ishida, F. Y. & Nepstad, D. C. *Global Change Biol.* **10**, 718–730 (2004).
8. Bol, R. *et al. Rapid Commun. Mass Spectrosc.* **17**, 2550–2556 (2003).
9. Holtgrieve, G. W., Jewett, P. K. & Matson, P. A. *Oecologia* **146**, 584–594 (2006).
10. Baggs, E. M. *Rapid Commun. Mass Spectrosc.* **22**, 1664–1672 (2008).
11. Rodhe, H. *Science* **248**, 1217–1219 (1990).
12. Sutka, R. L., Ostrom, N. E., Ostrom, P. H., Gandhi, H. & Breznak, J. A. *Rapid Commun. Mass Spectrosc.* **17**, 738–745 (2003).

across much of a forest's growing season. Deep within the soil profile, concentrations of  $\text{N}_2\text{O}$  were orders of magnitude greater than atmospheric levels. During drought, soil  $\text{N}_2\text{O}$  concentrations near the surface declined to sub-atmospheric levels, promoting the diffusion of  $\text{N}_2\text{O}$  from the atmosphere into the soil. With rewetting, soils quickly resumed their role as a net source of  $\text{N}_2\text{O}$  to the atmosphere. Both net uptake and production rates of  $\text{N}_2\text{O}$  were small — within the range that other investigators have viewed as unreliably close to zero<sup>4</sup>. However, net  $\text{N}_2\text{O}$  consumption during the drought was sufficient in both magnitude and duration for the soil profile to require almost four months for cumulative fluxes to reflect net  $\text{N}_2\text{O}$  production again.

To help identify the processes governing these  $\text{N}_2\text{O}$  fluxes, Goldberg and Gebauer<sup>2</sup> quantified the rare, stable isotopes  $^{15}\text{N}$  and  $^{18}\text{O}$  in the  $\text{N}_2\text{O}$  within the profile. Because these isotopes are relatively heavy, microbial processing of them tends to be slower than that of the more common, lighter  $^{14}\text{N}$  and  $^{16}\text{O}$ . As a result, quantifying  $^{15}\text{N}_2\text{O}$  and  $\text{N}_2^{18}\text{O}$  can provide clues about the processes governing  $\text{N}_2\text{O}$  production and consumption<sup>8–10</sup>.

Trends in  $\text{N}_2^{18}\text{O}$  were possibly confounded by the exchange of oxygen with soil water, but the  $^{15}\text{N}_2\text{O}$  data are revealing. Near-surface soil  $\text{N}_2\text{O}$  exhibited high amounts of  $^{15}\text{N}_2\text{O}$  relative to deeper values. This is consistent with microbial consumption of  $\text{N}_2\text{O}$  dominating  $\text{N}_2\text{O}$  dynamics throughout the profile, because microorganisms preferentially consume  $^{14}\text{N}_2\text{O}$ , leaving remaining  $\text{N}_2\text{O}$  relatively enriched in  $^{15}\text{N}$ . Importantly, soil drought increased the relative abundance of  $^{15}\text{N}_2\text{O}$  throughout the profile. The authors<sup>2</sup> suggest that

the source strength of  $\text{N}_2\text{O}$  within the profile declined with drought, whereas rates of  $\text{N}_2\text{O}$  transformation into  $\text{N}_2$  remained constant.

Goldberg and Gebauer's study<sup>2</sup> is an example of the kind of research required to understand the global  $\text{N}_2\text{O}$  budget — measurement of  $\text{N}_2\text{O}$  fluxes and soil-profile concentrations, combined with isotopic analyses — but they do not elaborate on the mechanisms governing the isotopic shifts they observed. If, as they suggest,  $\text{N}_2\text{O}$  sources declined and consumption was maintained with drought, the dominant microbial source must have shifted to one that generates greater relative amounts of  $^{15}\text{N}_2\text{O}$ . This could explain increasing  $^{15}\text{N}_2\text{O}$  throughout the profile with drought, because different microbial pathways can generate  $\text{N}_2\text{O}$  exhibiting distinct abundances of  $^{15}\text{N}$ . Alternatively, rates of consumption of  $\text{N}_2\text{O}$  could have increased while the  $\text{N}_2\text{O}$  source strength and path were maintained; such a change would result in a shifting 'front' of  $^{15}\text{N}_2\text{O}$  with drought, similar to that observed.

Studies such as this are essential for predicting Earth's future climate. Atmospheric concentrations of  $\text{N}_2\text{O}$  are low compared with those of carbon dioxide — 319 parts per billion compared with 379 parts per million (figures as of 2005)<sup>3</sup>. On a 100-year timescale, however, each molecule of  $\text{N}_2\text{O}$  has some 300 times the radiative forcing power of  $\text{CO}_2$  (ref. 11), making it an important driver of Earth's climate.

Future research must clarify the mechanisms that generate net soil  $\text{N}_2\text{O}$  uptake in different soil types under varying environmental conditions. Research will particularly need to focus on the influence of soil moisture on  $\text{N}_2\text{O}$  dynamics, given the predicted increase in drought frequency and rainfall variability in many

## Ralph Lewin (1921–2008)

Ralph Lewin, who died on 30 November aged 87, was a marine biologist specializing in algae, and a poet. Here is an example of his verse:

### Toxic Blooms

Toxic blooms, toxic blooms  
Vie with smog and sonic booms.  
Bigger, thicker, redder tides  
Taint the seas with plankticides.  
Toll the tocsins! Tides of doom!  
Woe to us the bloody bloom!

Neurotoxins attack  
Herrings in the Skagerrak,  
Decimating fishes that  
Used to throng the Kattegat,  
Dooming them to dismal fates:  
Death by dinoflagellates.

His poems had a range of topic and tone, but they typically had a thread of gentle humour that also characterized his communications with this journal over editorial standards. Lewin spent most of his long career at the Scripps Institution of Oceanography, California, and — science and poetry apart — will also be remembered as co-translator of A. A. Milne's *Winnie-the-Pooh* into Esperanto. More can be found at <http://tinyurl.com/5kkyyx> and <http://tinyurl.com/58r4le>.

# Snowball prevention questioned

Arising from: W. R. Peltier, Y. Liu & J. W. Crowley *Nature* 450, 813–818 (2007)

The ‘snowball Earth’ hypothesis<sup>1</sup> interprets geological evidence as indicating multi-million-year episodes of global glaciation near the beginning and end of the Proterozoic eon. On the basis of a coupled carbon cycle–climate model, Peltier *et al.*<sup>2</sup> propose that temperature-dependent remineralization of organic carbon in a Neoproterozoic ocean with 100–1,000× more dissolved organic carbon than today<sup>3</sup> could create a negative climate feedback, thereby preventing a snowball Earth. Their results are sensitive to initial conditions and model parameters<sup>4</sup>; moreover, important geological observations and components of the carbon cycle are not considered—notably the absence of sources or sinks of carbon. Their model results<sup>2</sup> fall short of explaining the geological evidence in the absence of global glaciation.

Peltier *et al.*<sup>2</sup> invoke temperature-dependent solubility of O<sub>2</sub> as a negative climate feedback through its control on organic carbon (or dissolved organic carbon) remineralization. Temperature-dependent solubility of CO<sub>2</sub> is ignored. With falling temperature, CO<sub>2</sub> solubility rises more rapidly than that of O<sub>2</sub> (ref. 5), driving a larger fraction of the total pool of dissolved inorganic carbon towards CO<sub>2</sub>(aq.), lowering CaCO<sub>3</sub> saturation. The resulting increase in net dissolution of CaCO<sub>3</sub> turbidites on deep-sea fans<sup>6</sup> creates an additional sink for CO<sub>2</sub>. If CO<sub>2</sub> solubility had been taken into account, the likely result would have been a positive rather than a negative climate feedback.

The model solutions presented<sup>2</sup> exist only for the parameter range  $0 < F_{21} < F_{crit}$  (where  $F_{21}$  is the remineralization flux parameter and  $F_{crit}$  is the critical value where the system changes behaviour from slushball to snowball cycling), implying that variations in the remineralization flux must be less than 1% for the temperature changes involved. This constraint is unlikely to be met in a system with large natural variability.

Sea-ice dynamics must have featured in Neoproterozoic low-latitude glaciation; they raise the characteristic partial pressure of CO<sub>2</sub> at the snowball instability<sup>7</sup>. The model of Peltier *et al.*<sup>2</sup> lacks sea-ice dynamics but assumes that isotopic fractionation associated with organic carbon fixation has a strong dependence on the partial pressure of CO<sub>2</sub> (ref. 2). This dependence is highly nonlinear<sup>8</sup> and might well be negligible if sea-ice dynamics were included.

The modelled isotopic fluctuations<sup>2</sup> accompanying the slushball–interglacial cycle are compared with isotopic data<sup>9</sup> from Neoproterozoic strata. This comparison is likely to be inappropriate because the isotopic fluctuations occur mostly on shallow-water marine carbonate platforms where no deposition occurred during glacioeustatic lowerings.

The palaeogeography used in the model<sup>2</sup> is contrary to what has long been inferred from sedimentological and palaeomagnetic observations (see refs 10, 11 for a summary). In the model<sup>2</sup>, a supercontinent is situated over the South Pole. This would produce a relatively warm climate if CO<sub>2</sub> sources and sinks were included, because low average terrestrial temperatures and moisture would reduce weathering rates, maintaining higher CO<sub>2</sub> levels. Conversely, palaeomagnetically informed geographies<sup>10,11</sup> with fragmented equatorial continents produce cold climates<sup>12</sup>, as are observed.

Peltier *et al.*<sup>2</sup> remark that their point of departure was criticism<sup>13</sup> that a slushball glaciation would not be stable for millions of years, as inferred geologically<sup>14</sup>. The criticism<sup>13</sup> was that “with all the continents

covered in ice, volcanic emissions without chemical weathering would cause atmospheric CO<sub>2</sub> levels to rise. But with ice-free tropical oceans, even a modest rise in CO<sub>2</sub> would cause the tropical glaciation to be short-lived”. Consistent with this claim, it was later shown that the CO<sub>2</sub> required to deglaciate a slushball was ~100× less than for a snowball<sup>15</sup>, implying that its duration should be <1% the length of a snowball glaciation. As the carbon cycle model in the present work<sup>2</sup> has no sources or sinks of carbon, the criticism<sup>13</sup> was never addressed.

The existence of sub-glacial and ice-proximal deposits at sea level close to the palaeoequator, and in carbonate-dominated successions formed in the warmest parts of the surface ocean, provide compelling evidence for two pan-glacial episodes in Cryogenian time. The extent of ice cover on the oceans is indeterminate because of sea-floor subduction and because evidence of open water on glaciated margins is equivocal—deposits could represent initial ice advance or terminal retreat, not maximum extent. However, an ice-covered ocean better explains the duration of the pan-glacial periods<sup>14</sup>, uniquely associated Fe<sub>2</sub>O<sub>3</sub> and MnO<sub>2</sub> ore deposits<sup>1</sup>, and syn-deglacial cap dolostones at all palaeolatitudes<sup>6</sup>.

**Paul F. Hoffman<sup>1</sup>, John W. Crowley<sup>1</sup>, David T. Johnston<sup>2</sup>, David S. Jones<sup>1</sup> & Daniel P. Schrag<sup>1</sup>**

<sup>1</sup>Department of Earth and Planetary Sciences, 20 Oxford Street, Harvard University, Cambridge, Massachusetts 02138, USA.

e-mail: hoffman@eps.harvard.edu

<sup>2</sup>Department of Organismic and Evolutionary Biology, 20 Oxford Street, Harvard University, Cambridge, Massachusetts 02138, USA.

Received 30 January; accepted 17 November 2008.

- Kirschvink, J. L. in *The Proterozoic Biosphere* (eds Schopf, J. W. & Klein, C.) 51–52 (Cambridge Univ. Press, 1992).
- Peltier, W. R., Liu, Y. & Crowley, J. W. Snowball Earth prevention by dissolved organic carbon remineralization. *Nature* 450, 813–818 (2007).
- Rothman, D. H., Hayes, J. H. & Summons, R. E. Dynamics of the Neoproterozoic carbon cycle. *Proc. Natl Acad. Sci. USA* 100, 8124–8129 (2003).
- Crowley, J. W. *Carbon Cycle Dynamics for a Neoproterozoic Climate Model*. B.Sc. thesis, Univ. Toronto (2006); available at (<http://www.snowballearth.org>).
- Murray, C. N. & Riley, J. P. The solubility of gases in distilled water and sea water — IV. Carbon dioxide. *Deep-Sea Res.* 18, 533–541 (1971).
- Hoffman, P. F. *et al.* Are basal Ediacaran (635 Ma) “cap dolostones” diachronous? *Earth Planet. Sci. Lett.* 258, 114–131 (2007).
- Lewis, J. P., Weaver, A. J. & Eby, M. Snowball versus slushball Earth: Dynamic versus nondynamic sea ice? *J. Geophys. Res.* 112, C11014 (2007).
- Kump, L. R. & Arthur, M. A. Interpreting carbon-isotope excursions: Carbonates and organic matter. *Chem. Geol.* 161, 181–198 (1999).
- Hayes, J. M., Strauss, H. & Kaufman, A. J. The abundance of <sup>13</sup>C in marine organic matter and isotopic fractionation in the global biogeochemical cycle of carbon during the past 800 Ma. *Chem. Geol.* 161, 103–125 (1999).
- Trindade, R. I. F. & Macouin, M. Paleolatitude of glacial deposits and paleogeography of Neoproterozoic ice ages. *C.R. Geosci.* 339, 200–211 (2007).
- Li, Z. X. *et al.* Assembly, configuration, and break-up history of Rodinia: A synthesis. *Precamb. Res.* 160, 179–210 (2008).
- Donnadieu, Y., Goddard, Y., Ramstein, G., Nédélec, A. & Meert, J. A ‘snowball Earth’ climate triggered by continental break-up through changes in runoff. *Nature* 428, 303–306 (2004).
- Schrag, D. P. & Hoffman, P. F. Life, geology and snowball Earth. *Nature* 409, 306 (2001).
- Hoffman, P. F., Kaufman, J. A. & Halverson, G. P. Comings and goings of global glaciations on a Neoproterozoic carbonate platform in Namibia. *GSA Today* 8, 1–9 (1998).
- Crowley, T. J., Hyde, W. T. & Peltier, W. R. CO<sub>2</sub> levels required for deglaciation of a “near-snowball” Earth. *Geophys. Res. Lett.* 28, 283–286 (2001).

doi:10.1038/nature07655



# Carbon cycling and snowball Earth

Arising from: W. R. Peltier, Y. Liu & J. W. Crowley *Nature* **450**, 813–818 (2007)

The possibility that Earth witnessed episodes of global glaciation during the latest Precambrian challenges our understanding of the physical processes controlling the Earth's climate. Peltier *et al.*<sup>1</sup> suggest that a 'hard snowball Earth' state may have been prevented owing to the release of CO<sub>2</sub> from the oxidation of dissolved organic carbon (DOC) in the ocean as the temperature decreased. Here we show that the model of Peltier *et al.* is not self-consistent as it implies large fluctuations of the ocean alkalinity content without providing any processes to account for it. Our findings suggest that the hard snowball Earth hypothesis is still valid.

Enhanced oxidation of a DOC reservoir at low temperature would drive the transfer of organic carbon into dissolved inorganic carbon (DIC), which would increase DIC as temperature declines, thereby increasing atmospheric CO<sub>2</sub>. Peltier *et al.* describe a closed carbon cycle and only account for processes occurring in the oceanic and atmospheric reservoirs, while neglecting continental weathering. However, their study spans several million years, a timescale over which this process is the dominant forcing function of climate evolution<sup>2–5</sup>. To keep the carbon model of Peltier *et al.* physically consistent, silicate weathering has to be accounted for, which would heavily affect atmospheric CO<sub>2</sub>.

The partial pressure of atmospheric CO<sub>2</sub> ( $p_{\text{CO}_2}$ ) is dependent on the DIC content of the ocean and on alkalinity. Peltier *et al.* assume that atmospheric carbon content is related to the DIC content of the ocean to the power  $X$  ( $X = 2$  being the standard case; equation (2) in ref. 6). However, Kump and Arthur<sup>6</sup> arrived at this mathematical expression by assuming that sea water was saturated with respect to the mineral calcite. Peltier *et al.* suggest that the ocean DIC content rose markedly in response to the oxidation of a DOC reservoir. Consequently, keeping the validity of the equation of Kump and Arthur implicitly requires that seawater alkalinity also rose drastically (to maintain the saturation with respect to carbonate minerals and to ensure the validity of the key equation of their model). Using equations defining seawater carbonate speciation, we calculated the concomitant change in alkalinity implied by Peltier *et al.* (Fig. 1a). We find that carbonate alkalinity has to rise by 40% when calculated atmospheric CO<sub>2</sub> rises from 100 to 450 parts per million by volume (p.p.m.v). Values other than 2 for  $X$  are meaningless;  $X$  is not a free parameter and depends on the equilibrium constants of the carbonate speciation.

The additional alkalinity cannot come from either the dissolution of seafloor carbonates (because the model of Peltier *et al.* implicitly assumes permanent saturation of seawater with respect to calcite) or from the oxidation of DOC by oxygen (because this process does not supply alkalinity). Anoxic recycling of organic matter may provide alkalinity, but this process is overlooked by Peltier *et al.* This leaves continental weathering as the only remaining source of the additional alkalinity. The weathering of exposed carbonate platforms cannot be the culprit, as sea level also rises by several hundred metres in the model of Peltier *et al.* when CO<sub>2</sub> increases from 100 to 450 p.p.m.v. Carbonate platforms should therefore be water-covered, and this source of alkalinity should actually decrease with rising CO<sub>2</sub> (ref. 7). The ultimate source of alkalinity is continental silicate and intracratonic carbonate weathering which is a function of climate and atmospheric CO<sub>2</sub>.

Using the GEOCLIM numerical model describing continental weathering under Neoproterozoic conditions<sup>4</sup>, we calculated that the fluctuations in continental weathering implicitly required by Peltier *et al.* force the atmospheric CO<sub>2</sub> to fluctuate between 320 and 800 p.p.m.v. (Fig. 1b), markedly above their CO<sub>2</sub> reconstruction. The model of Peltier *et al.* arrives at a paradox. The equation that underpins their study requires that continental weathering changed markedly during their calculated carbon cycle oscillations, whereas Peltier *et al.* state that continental weathering is negligible because air temperature is low and land plants are absent in the Proterozoic. Our

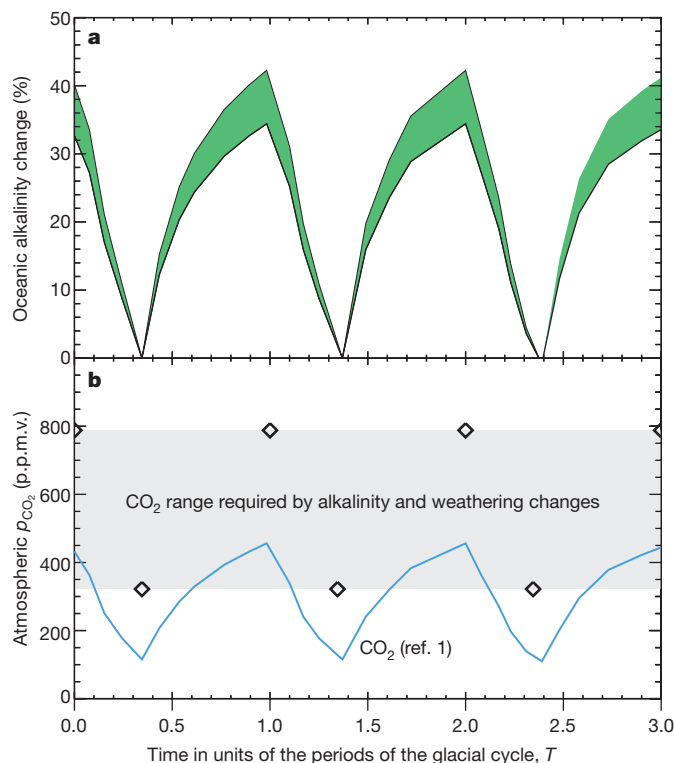


**Figure 1 | Oceanic carbonate alkalinity changes required by the Peltier *et al.* scenario and consequences for the calculated atmospheric CO<sub>2</sub>.** **a**, The increase in carbonate alkalinity concentration in sea water as a function of atmospheric partial pressure of CO<sub>2</sub> ( $p_{\text{CO}_2}$ ) required by the Peltier *et al.*<sup>1</sup> scenario for snowball Earth prevention. It is expressed in percentage increase from the alkalinity content at 100 p.p.m.v. The green shading corresponds to calculations performed at 4 and 25 °C. We use equations defining seawater carbonate speciation when equilibrated with the atmospheric CO<sub>2</sub> level. As boundary conditions, we use the oscillating  $p_{\text{CO}_2}$  of the Peltier *et al.* study<sup>1</sup> (between 100 and 450 p.p.m.v). **b**, Comparison between the atmospheric  $p_{\text{CO}_2}$  calculated by Peltier *et al.* (ref. 1; blue line) and the range of CO<sub>2</sub> change required by the carbonate alkalinity fluctuations implied by the Peltier *et al.* model (grey shaded area; optima are represented by diamonds).

calculations indicate that overly simplistic descriptions of the geological carbon cycle can result in misinterpretations.

Yves Godderis<sup>1</sup> & Yannick Donnadieu<sup>2</sup>

<sup>1</sup>LMTG, CNRS-Observatoire Midi-Pyrénées, 31400 Toulouse, France.

e-mail: godderis@lmtg.obs-mip.fr

<sup>2</sup>LSCE, CNRS-CEA, 91191 Gif-sur-Yvette, France.

Received 28 December 2007; accepted 17 November 2008.

1. Peltier, W. R., Liu, Y. & Crowley, J. W. Snowball Earth prevention by dissolved organic carbon remineralization. *Nature* **450**, 813–818 (2007).
2. Berner, R. A. & Caldeira, K. The need for mass balance and feedback in the geochemical carbon cycle. *Geology* **25**, 955–956 (1997).
3. Donnadieu, Y. *et al.* A GEOCLIM simulation of climatic and biogeochemical consequences of Pangea breakup. *Geochim. Geophys. Geosyst.* **7**, doi:10.1029/2006GC001278 (2006).
4. Donnadieu, Y. *et al.* A 'snowball Earth' climate triggered by continental break-up through changes in runoff. *Nature* **428**, 303–306 (2004).
5. Walker, J. C. G., Hays, P. B. & Kasting, J. F. A negative feedback mechanism for the long term stabilization of Earth's surface temperature. *J. Geophys. Res.* **86**, 9776–9782 (1981).
6. Kump, L. R. & Arthur, M. A. Interpreting carbon-isotope excursions: Carbonates and organic matter. *Chem. Geol.* **161**, 181–198 (1999).
7. Ridgwell, A. J., Kennedy, M. J. & Caldeira, K. Carbonate deposition, climate stability, and Neoproterozoic ice ages. *Science* **302**, 859–862 (2003).

doi:10.1038/nature07653

# Peltier & Liu reply

Replying to: P. F. Hoffman, J. W. Crowley, D. T. Johnston, D. S. Jones & D. P. Schrag *Nature* **456**, doi:10.1038/nature07655 (2008); Y. Godd  ris & Y. Donnadieu *Nature* **456**, doi:10.1038/nature07653 (2008)

The first of several questionable assertions in the Comment of Hoffman *et al.*<sup>1</sup> on our paper<sup>2</sup> is that our results are “sensitive to initial conditions and model parameters”. This references an undergraduate report<sup>3</sup> in which this issue was not addressed. Figure 1 illustrates a sequence of trajectories of the nonlinear system. These are ‘attracted to’ the set of steady state solutions such that, following transient adjustment, the system locks-on to the oscillatory ‘slushball’ solution unless the initial CO<sub>2</sub> concentration is extremely low or  $F_{21}$ , the control variable of the model that determines the sensitivity of the rate of remineralization to temperature changes, is supercritical. This first assertion is therefore misleading.

The second concerns our neglect of CO<sub>2</sub> solubility relative to that of oxygen. Our model assumes a biogeochemically mediated partitioning of CO<sub>2</sub> between atmosphere and ocean that depends solely on ocean dissolved inorganic carbon (DIC; the concentration of which is  $M_1$ ) relative to an equilibrium level ( $M_{1e}$ ), namely:

$$\frac{p_{\text{CO}_2}(t)}{p_{\text{CO}_2e}} = \left[ \frac{M_1(t)}{M_{1e}} \right]^X$$

Here  $p_{\text{CO}_2}$  is the partial pressure of CO<sub>2</sub> and subscript “e” indicates its equilibrium value. With  $X = 2$ , this is from Kump and Arthur<sup>4</sup> and relies on the assumption that the ocean remains saturated with respect to carbonate. This appears to have been overlooked by Hoffman *et al.*<sup>1</sup>. Godd  ris and Donnadieu<sup>5</sup>, in their Comment, question the internal self-consistency of its application but recognize its central importance. Because Neoproterozoic glacial events terminate in massive ‘cap carbonate’ precipitation, the assumption of (super?) saturation for the glacial periods (see also ref. 6) would appear to be well founded. Furthermore, because DIC rises as the system cools, leading to the exhaust of CO<sub>2</sub> into the atmosphere, and because the cooling-induced drawdown of the CO<sub>2</sub> due to solubility also causes DIC to rise, this influence would be self-limiting and thus trumped by the buffering action of biogeochemistry. Oxygen uptake by the oceans is not similarly buffered.

The argument of Godd  ris and Donnadieu focuses on the alkalinity change needed to maintain ocean carbonate saturation given the

predicted variation of  $p_{\text{CO}_2}$  / DIC. The claim is that silicate weathering is the only source of this alkalinity. We would like to point out, however, that: (1) alkalinity is also available from microbial respiratory activity in sub-oxic/anoxic settings (see, for example, ref. 7) which is not accounted for; (2) the assertion that “exposed carbonate platforms cannot be the culprit, as sea level also rises by several hundred metres..... when CO<sub>2</sub> increases from 100 to 450 p.p.m.v.” is incorrect. During the phase of the cycle when CO<sub>2</sub> is increasing (see original Fig. 3), continental ice volume remains high and therefore such platforms remain exposed and susceptible to intense weathering. This source delivers alkalinity when and only when the ocean needs it and involves no net  $p_{\text{CO}_2}$  drawdown. (3) The authors seem to neglect volcanic outgassing entirely. In our view, there is therefore no “paradox” in the scenario we have proposed.

Concerning silicate weathering, our model has been specifically designed to isolate the influence due to temperature dependence of the rate of remineralization of dissolved organic carbon. We assume that the silicate weathering sink precisely balances the volcanic outgassing source, and therefore have not neglected sources and sinks as claimed by Hoffman *et al.*<sup>1</sup>. The impact of imprecision in this balance may be captured qualitatively by noting that the control parameter  $F_{21}$  determines the rate at which the system traverses the hysteresis loop. Assuming that weathering is less efficient at moderating outgassing in the glacial phase leads to relative contraction of the ice-free phase (Fig. 2). The additional concern of Hoffman *et al.*<sup>1</sup> regarding the timescale of glacial episodes is therefore unfounded as weathering continues during them (see also ref. 6).

It will be noted that we have neglected the orbital forcing that would have caused multiple advances and retreats of land ice (see, for example, ref. 8). The suggestion by Hoffman *et al.*<sup>1</sup> that our explicitly predicted low frequency variability should be susceptible to noise misses the point that the variations in flux are in its average over the entire volume of the oceans. Its stability may be tested using newly developed methods<sup>9</sup>.

The assertion by Hoffman *et al.*<sup>1</sup> that dynamic sea-ice processes would eliminate the ‘slushball’ is based on an inconsistent model<sup>10</sup> (no explicit atmospheric dynamics or radiative transfer). In ref. 11, complete Neoproterozoic integrations of the NCAR CSM 1.4 model with dynamic sea ice were performed, starting with fully glaciated

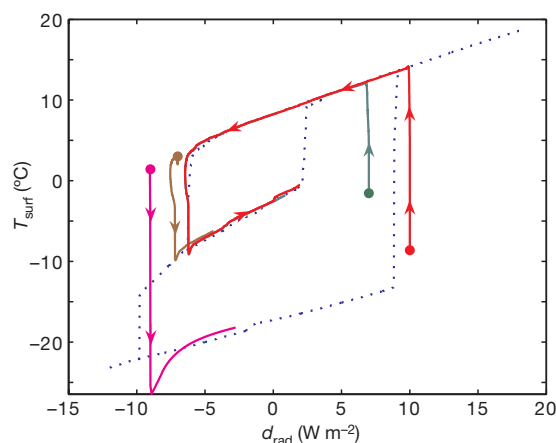


**Figure 1 | Trajectories of the solution for the coupled carbon cycle and climate model started from different initial conditions, indicated by filled circles of different colours.** The dotted line represents the set of steady state solutions of the climate model; this set includes the hysteresis loop on the cold branch of which the ‘slushball’ forms. The parameter  $d_{\text{rad}}$  denotes the increase in infrared radiative forcing at the surface of the Earth due to the increasing concentration of carbon dioxide in the overlying atmosphere. The variable  $T_{\text{surf}}$  is the annual mean surface temperature of the planet.

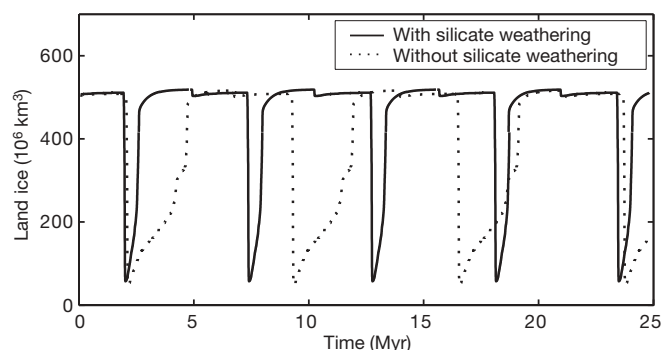


**Figure 2 | Influence of silicate weathering on the evolution of the coupled model.** The influence of weathering is qualitatively simulated by increasing the value of  $F_{21}$  by a factor of 5 from the base value of  $8 \times 10^{-5}$  per °C on the glacial branch of the hysteresis loop to the higher value of  $4 \times 10^{-4}$  per °C on the hot branch. The consequence of this parameterization of the diminished influence of weathering relative to outgassing in the glacial phase of the cycle is that the length of the warm period of the cycle is correspondingly reduced.



continents to optimize the probability of 'hard snowball' development. With a 6% decrease in solar insolation, a Marinoan-like distribution of the continents, and a  $p_{\text{CO}_2}$  of 280 p.p.m.v., the near equilibrium climate maintained significant open water at the Equator.

Concerning the issue of palaeogeography, we note the recent suggestion<sup>12,13</sup> that the appearance of heavy glaciation at sea level in the tropics could have resulted from an inertial interchange true polar wander (IITPW) event. Before the Sturtian ice age, Rodinia was positioned near the north magnetic pole<sup>14</sup>. Subsequently, it came to be positioned near the Equator. If IITPW had occurred, an already glaciated polar supercontinent would have shifted to low latitude. Apparently this possibility is not ruled out by the palaeomagnetic and dating constraints (J. Kirschvink, personal communication to W.R.P.; we note this author has previously argued for a similar IITPW event during the Cambrian<sup>15</sup>). The palaeogeography-based argument could be the ultimate 'red herring' in the snowball debate.

Our carbon cycle coupled climate model has been used to explore the efficacy of a particular negative feedback which was plausibly active during the Neoproterozoic. This feedback may work to prevent the occurrence of hard snowball conditions while allowing very severe glaciation of the continents. It is an influence not previously considered and warrants further analysis. All of us interested in the science of climate variability in deep geological time would be well advised to accept the limitations on our ability to divine the truth due to the paucity and ambiguity of the observational constraints available to us.

**W. R. Peltier<sup>1</sup> & Yonggang Liu<sup>1</sup>**

<sup>1</sup>Department of Physics, University of Toronto, Toronto, Ontario, Canada M5S-1A7.

e-mail: peltier@atmos.physics.utoronto.ca

- Hoffman, P. H., Crowley, J. W., Johnston, D. T., Jones, D. S. & Schrag, D. P. Snowball prevention questioned. *Nature* **456**, 10.1038/nature07655 (2008).
- Peltier, W. R., Liu, Y. & Crowley, J. W. Snowball Earth prevention by dissolved organic carbon remineralization. *Nature* **450**, 813–818 (2007).
- Crowley, J. W. *Carbon Cycle Dynamics for a Neoproterozoic Climate Model*. B.Sc. thesis, Univ. Toronto (2006).
- Kump, L. R. & Arthur, M. A. Interpreting carbon-isotope excursions: Carbonates and organic matter. *Chem. Geol.* **161**, 181–198 (1999).
- Goddéris, Y. & Donnadieu, Y. Carbon cycling and snowball Earth. *Nature* **456**, 10.1038/nature07653 (2008).
- Ridgwell, A. J., Kennedy, M. J. & Caldeira, K. Carbonate deposition, climate stability, and Neoproterozoic ice-ages. *Science* **302**, 859–862 (2003).
- Kaufman, A. J., Corsetti, F. A. & Varni, M. A. The effect of rising atmospheric oxygen on carbon and sulphur isotope anomalies in the Neoproterozoic Johnnie Formation, Death Valley, USA. *Chem. Geol.* **237**, 47–63 (2007).
- Etienne, J. L., Allen, P. A., Rieu, R. & Le Guerroue, E. in *Glacial Sedimentary Processes and Products* (eds Hambrey, M. J., Christoffersen, P., Glasser, N. F. & Hubbard, B.) 343–399 (Special Publication 39, Association of Sedimentologists, 2008).
- Stastna, M. & Peltier, W. R. On box models of the North Atlantic thermohaline circulation: Intrinsic and extrinsic millennial timescale variability in response to deterministic and stochastic forcing. *J. Geophys. Res.* **112**, C10023, doi:10.1029/2006JC003938 (2007).
- Lewis, J. P., Weaver, A. J. & Eby, M. Snowball versus slushball Earth: Dynamic versus nondynamic sea ice? *J. Geophys. Res.* **112**, C11014, doi:10.1029/2006JC004037 (2007).
- Peltier, W. R., Tarasov, L., Vetteretti, G. & Solheim, L. P. in *The Extreme Proterozoic: Geology, Geochemistry and Climate* (eds Jenkins, G. S., McMenamin, M. A., McKay, C. & Sohl, L.) 107–124 (Geophysical Monograph 146, American Geophysical Union, 2004).
- Li, Z. X., Evans, D. V. D. & Zhang, S. A 90° spin on Rodinia: Possible causal links between the Neoproterozoic supercontinent, superplume, true polar wander and low-latitude glaciation. *Earth Planet. Sci. Lett.* **220**, 409–420 (2004).
- Peltier, W. R. in *Treatise on Geophysics* Vol. 9 (ed. Schubert, G.) 243–294 (Elsevier, 2007).
- Li, Z. X. *et al.* Assembly, configuration, and break-up history of Rodinia: A synthesis. *Precamb. Res.* **160**, 179–210 (2008).
- Kirschvink, J. L., Ripperdan, R. L. & Evans, D. A. Evidence for a large scale re-organization of early continental masses by inertial interchange true polar wander. *Science* **277**, 541–545 (1997).

doi:10.1038/nature07656

# Sensing voltage across lipid membranes

Kenton J. Swartz<sup>1</sup>

**The detection of electrical potentials across lipid bilayers by specialized membrane proteins is required for many fundamental cellular processes such as the generation and propagation of nerve impulses. These membrane proteins possess modular voltage-sensing domains, a notable example being the S1–S4 domains of voltage-activated ion channels. Ground-breaking structural studies on these domains explain how voltage sensors are designed and reveal important interactions with the surrounding lipid membrane. Although further structures are needed to understand the conformational changes that occur during voltage sensing, the available data help to frame several key concepts that are fundamental to the mechanism of voltage sensing.**

Most of us appreciate the importance of electricity at a young age. It powers many useful and entertaining man-made devices: a light for seeing the world, a computer for searching the internet, or an omnipresent iPod for listening to music. The concept that living organisms use electricity as a fundamental mechanism for signalling across membranes and between cells is less widely appreciated, even though scientists have been thinking about the biological roles of electricity since the late eighteenth century. Indeed, Galvani's experiments<sup>1</sup> showing that spark generators can elicit contraction of frog muscles were contemporary with key developments in understanding the phenomenon of electricity itself. Today we know a great deal about the biological roles of electrical signals and it would be impossible to overstate their profound importance. In humans, electrical signals are used to complete a computation within the cerebral cortex, to secrete insulin after a meal, or to signal that a sperm has entered an egg and for embryogenesis to commence.

In cells, electrical forces arise from the separation of  $\text{Na}^+$ ,  $\text{K}^+$ ,  $\text{Ca}^{2+}$  and  $\text{Cl}^-$  across a lipid membrane that is intrinsically highly impermeable to these ions. ATP is consumed by pumps to produce concentration gradients across the membrane for these ions, creating a chemical potential that can generate an electrical potential when ion-selective channel proteins open and provide pathways for these ions to move down their concentration gradients. In a quiescent neuron, for example,  $\text{K}^+$  channels most commonly establish an electrical potential, or voltage, that is negative inside relative to outside because the concentration of  $\text{K}^+$  is high inside the cell and low outside it. A cell membrane can be depolarized (less negative inside) when neurotransmitters open ion channels that are permeable to  $\text{Na}^+$  or  $\text{Ca}^{2+}$  because the concentrations of these ions are high outside and low inside. For such electrical potentials to generate action potentials<sup>2</sup>, to trigger neurotransmitter secretion or to initiate muscle contraction, voltage-activated ion channels must sense the voltage across the cell membrane and react by opening or closing an ion conduction pore. In these instances, changes in membrane voltage are detected by voltage sensors that are intrinsic to the ion channel; in most instances the voltage sensors move between 'resting' and 'activated' states to open the pore when membrane voltage becomes depolarized, but there are varieties that trigger pore opening when the membrane becomes hyperpolarized (more negative inside). Investigation into the mechanism of voltage sensing has progressed rapidly since the classical studies of Hodgkin and Huxley on the squid giant axon<sup>2</sup>, with the cloning of the voltage-activated  $\text{Na}^+$  (Nav),  $\text{K}^+$

(Kv) and  $\text{Ca}^{2+}$  (Cav) channels in the late 1980s<sup>3–5</sup> and the first X-ray crystal structure of a Kv channel in 2003 (ref. 6) representing historical landmarks. Although many mechanistic aspects of voltage sensing are debated, this review focuses on the emerging mechanistic concepts for which there is growing consensus. I will begin by discussing the architecture and structure of voltage-sensing domains in Kv channels, where our understanding is most advanced, and will outline four key concepts that emerge from both functional and structural studies. I will end by discussing how voltage sensors might move within the membrane and highlight directions for future research.

## Voltage-sensing domains in membrane proteins

The best understood voltage sensors are found in the voltage-activated ion channels that are so crucial for electrical signalling in the nervous system. When these channels were first cloned, the fourth putative membrane-spanning segment, termed S4, stood out because it contains many basic Arg or Lys residues that are capable of carrying a positive charge<sup>3–5,7,8</sup>. The S4 segment is always found together with three other transmembrane segments (S1–S3) that contain negatively charged acidic residues, and the four segments together collectively form an S1–S4 voltage-sensing domain (Fig. 1a). The concept that S1–S4 is a domain in the formal sense grew out of comparisons of Kv channels and other simpler  $\text{K}^+$  channels that lack the S1–S4 region<sup>9</sup>, experiments identifying important acidic residues in S2 and S3 (ref. 10), and the discovery that tarantula toxins can bind to S1–S4 domains in different types of voltage-activated ion channels<sup>11</sup>. The fact that S1–S4 voltage sensors are functionally independent protein domains was demonstrated by Lu and colleagues when they found that the S1–S4 region of a Kv channel could endow KcsA, a weakly voltage-dependent  $\text{K}^+$  channel from *Streptomyces lividans*, with strong voltage sensitivity<sup>12,13</sup>. Bacteria can synthesize, properly fold and insert isolated S1–S4 voltage-sensing domains into their membranes<sup>6,14</sup>, further supporting the idea that S1–S4 is an independent domain.

For S1–S4 voltage-sensing domains to sense voltage across membranes, they must change conformation between states where charged residues or dipoles have different relative free energies. In principle, this conformational change could result from charges moving through a stationary electric field or the electric field reshaping around fixed charges. An important advance in studying this conformational change was the discovery that the movement of charges relative to the field could be detected electrically as a nonlinear capacitive current, or

<sup>1</sup>Porter Neuroscience Research Center, Molecular Physiology and Biophysics Section, National Institute of Neurological Disorders and Stroke, National Institutes of Health, Bethesda, Maryland 20892, USA.



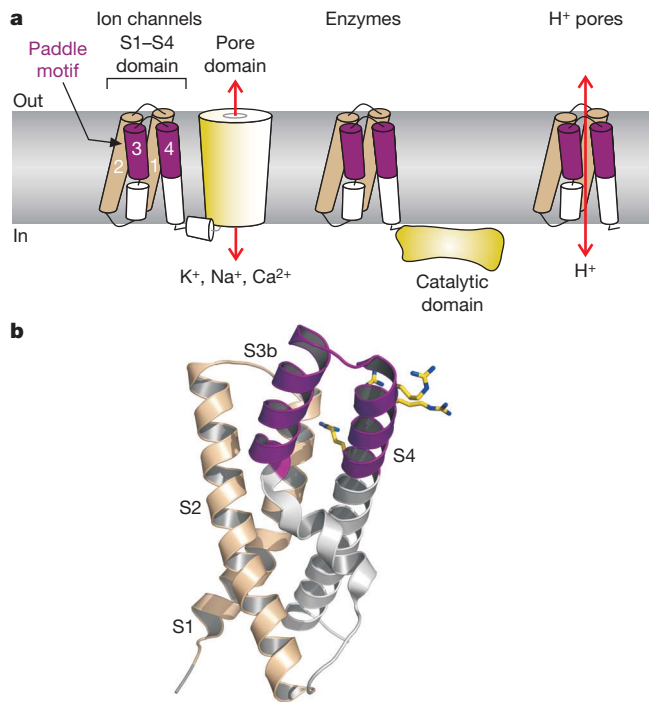


**Figure 1 | Types of membrane proteins that contain S1-S4 voltage-sensing domains and the structure of an S1-S4 domain.** **a**, Cartoon illustration of S1-S4 voltage-sensing domains in different types of membrane proteins. S1-S4 helices are labelled with the paddle motif coloured purple. In voltage-activated ion channels, the S1-S4 domains couple to an ion-selective pore domain (yellow); only one of four S1-S4 domains is shown for clarity. In enzymes such as the Ci-VSP, the S1-S4 domain couples to a soluble phosphatase domain (yellow). In voltage-activated proton channels, protons are thought to permeate the S1-S4 domain directly. **b**, Ribbon representations of the X-ray structure of the S1-S4 domain of KvAP (Protein Data Bank (PDB) accession code: 1ORS) with the paddle motif coloured purple. The outer four Arg residues in S4 are shown as stick representations, with carbon coloured yellow and nitrogen coloured blue. Structural representations in all figures were generated using PyMOL (DeLano Scientific).

gating current<sup>15–17</sup>. Measurements of this sort led to two key conclusions about the conformational change occurring when voltage sensors activate. First, the conformational change involves the movement of 3 to 3.5 elementary charges relative to the full membrane electric field for each S1-S4 voltage sensor<sup>18–22</sup>. Second, the external four Arg residues in S4 (Fig. 1b) carry most of the measured gating charge<sup>19,20,22</sup>. Although reshaping of the electric field may have a role, it is clear that S4 moves outward in channels that activate with membrane depolarization<sup>23–38</sup> (see ‘Voltage sensor motions’ section).

Although S1-S4 voltage-sensing domains were originally thought only to exist in voltage-activated ion channels, Okamura’s group made the seminal discovery that S1-S4 domains exist in proteins that lack associated ion-conducting pores<sup>39</sup>. The *Ciona intestinalis* voltage-sensitive phosphatase (Ci-VSP), for example, uses an S1-S4 domain to control the hydrolysis of membrane phosphoinositides by an associated phosphatase domain<sup>39,40</sup> (Fig. 1a). Another S1-S4 domain protein without a separate pore domain was shown to function as a voltage-activated proton channel (Hv1)<sup>41–43</sup> (Fig. 1a). In this case, the S1-S4 domain seems to contain the proton permeation pathway (see below). One of the interesting differences between voltage-activated ion channels and the other voltage-sensing proteins is the number of S1-S4 domains that they contain. There are four in Kv, Nav and Cav channels<sup>3–6</sup>, two in the proton channel<sup>43,44</sup> and only one in the phosphatase<sup>40</sup>. Although much remains to be learned about

these fascinating new voltage-sensing proteins, key regions can be swapped with Kv channels without disrupting function or pharmacological sensitivities, suggesting that their basic voltage-sensing mechanisms are related<sup>45</sup>.

### Structures of voltage-sensing domains

For many years, the lack of three-dimensional structures of voltage sensors was a barrier to understanding the mechanism of voltage sensing. At present, four X-ray structures have been solved that contain S1-S4 voltage-sensing domains<sup>6,46,47</sup>. As will be discussed later, these structures are probably most relevant for understanding the activated state of voltage sensors that exist at depolarized membrane voltages. The first two structures reported in 2003 by MacKinnon and his colleagues were those of the isolated S1-S4 domain and the full-length channel of KvAP<sup>6</sup>, an archaebacterial Kv channel from *Aeropyrum pernix*. The structure of the isolated S1-S4 domain comprises five helices, with S1, S2 and S4 forming long uninterrupted helices and S3 containing two shorter helices (Fig. 1b), consistent with helix scanning studies in eukaryotic Kv channels<sup>48–51</sup>. Because this domain was crystallized without the pore or the surrounding membrane, it wasn’t obvious how it is oriented with respect to the pore or the surrounding membrane.

The structure of the full-length KvAP channel did not answer this question because the voltage-sensing domains in this structure are distorted<sup>6</sup>. However, comparisons of the structures of the isolated S1-S4 domain and the full-length channel led MacKinnon and colleagues to three important conclusions<sup>6,35</sup>. First, both structures contain a conserved helix–turn–helix motif that is composed of the S3b and S4 helices, termed the voltage-sensor paddle (Fig. 1a, b, purple helices). This motif contains the most crucial S4 Arg residues<sup>19,20</sup> (stick chains in Fig. 1b) and is widely targeted by tarantula toxins<sup>45,51–53</sup> that inhibit voltage-activated ion channels by binding within the membrane<sup>54–56</sup>. Second, the distortions evident in the KvAP full-length structure suggest that S1-S4 domains are inherently flexible and lack tight attachments to the surface of the pore domain. In other words, the ‘malleability’ of voltage sensors reveals an underlying structural flexibility that may be related to how these domains function. Third, the paddle motif moves at the periphery of the channel protein in contact with the surrounding lipid membrane. As wonderful as it was to ‘see’ the first structures of voltage sensors and to ponder these new ideas, many questions remained unanswered. To what extent is the structure of the S1-S4 domain in the full-length KvAP channel distorted? How representative is the structure of the isolated S1-S4 domain of KvAP, and how is this domain oriented with respect to the central pore domain?

The X-ray structure of the eukaryotic Kv1.2 channel provided the first clear perspective of S1-S4 domains in a full-length channel and revealed how they are oriented with respect to the central pore domain and the surrounding lipid membrane<sup>46,57</sup>. Even though the quality of electron density within the S1-S4 domain is relatively weak (mean *B* factor = 162 Å<sup>2</sup>), leaving many residues unresolved, helices S1 to S4 clearly adopt transmembrane orientations and appear loosely attached to the central pore domain. The most recent X-ray structure of the Kv1.2 channel containing the paddle motif from the Kv2.1 channel (paddle-chimaera channel)<sup>47</sup> currently provides the clearest picture of the structure of the voltage sensor in a full-length channel (Fig. 2). The close apposition of the S3b–S4 helices is similar to what is seen for the paddle motif in the KvAP structures: S1 and S4 are positioned adjacent to the pore domain and both S2 and S3 are positioned peripherally. Electron densities for many lipid molecules are also present in the maps for the paddle-chimaera channel, revealing that lipids interact intimately with the channel. Lipids are present between the S1-S4 voltage-sensing domain and the pore domain, between adjacent S1-S4 domains and even intercalating between helices (Fig. 2a, b, teal molecules).

Three important structural features of voltage sensors can be seen if we superimpose the structures of the paddle-chimaera and of the

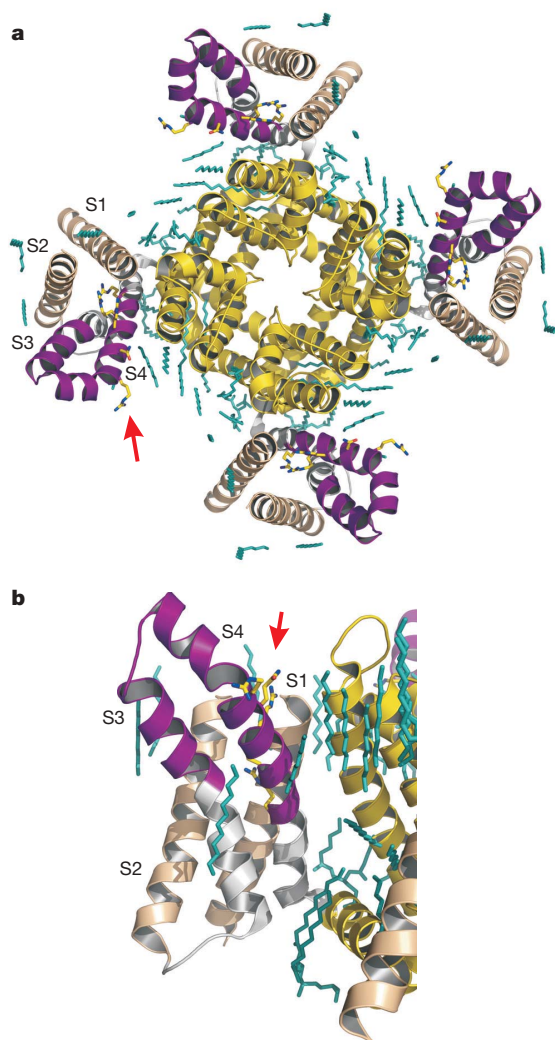


**Figure 2 | Structure of the paddle-chimaera Kv channel.** **a**, Ribbon representation of the X-ray structure of the paddle-chimaera channel viewed from the external side of the membrane. The paddle motif is coloured purple, the pore domain is coloured yellow and lipids are coloured teal. Basic residues in S4 are shown as stick representations, with carbon atoms coloured yellow, oxygen atoms coloured red and nitrogen atoms coloured blue. The PDB accession code is 2R9R. The red arrow identifies outer S4 Arg residues projecting towards the lipid membrane. **b**, Side view of the paddle-chimaera channel focusing on the S1–S4 voltage-sensing domain and its interface with the pore domain.

isolated S1–S4 domain of KvAP (Fig. 3). First, the structures of voltage sensors are well conserved from archaeobacteria to mammals. There are interesting differences in the S3 helix, but overall the folds of the S1–S4 domains of the paddle chimaera and KvAP are remarkably similar. Second, both structures reveal a widespread network of electrostatic interactions between basic residues in S4 and acidic residues in S1, S2 and S3, and in many cases the side chains of these key residues virtually superimpose (Fig. 3). In the activated conformation of the paddle chimaera there are two clusters of acidic residues: an external acidic cluster formed by Glu residues in S1 and S2, and an internal acidic cluster consisting of a Glu in S2 and an Asp in S3a. The residues in the external cluster lie within a large crevice exposed to the external aqueous environment (Fig. 3, green arrow), whereas the internal cluster is largely buried within the protein interior. On the basis of their earlier mutagenic rescue experiments in the Shaker Kv channel, Papazian and colleagues concluded that the inner acidic residues in S2 and S3 form a stabilizing network

with the fifth basic residue in S4 when the voltage sensor is in an activated state<sup>10</sup>, in agreement with the inner network shown in the structure of the paddle chimaera. A third structural feature evident in the comparison is that the outermost Arg residues do not interact with acidic residues, but project out from the domain towards the surrounding membrane (red arrow in Figs 2a, b and 3). Both of these structures were solved in the absence of an electric field, or 0 mV, a voltage at which functional studies on KvAP and the paddle chimaera indicate that their voltage sensors are in activated conformations<sup>47,58</sup>, implying that these two structures are representative of the activated state. The internal S6 gate region within the pore of the paddle chimaera is open, consistent with the voltage sensors being activated, and there are no structural changes in the selectivity filter to suggest that the channel is inactivated<sup>59</sup>. The paddle-chimaera structure is compatible with constraints imposed by metal bridges between S4 and S5 in the activated state<sup>36</sup>, further suggesting that it is representative of the activated conformation.

### Emerging concepts

The available structures of activated voltage sensors represent a remarkable advance and, when considered in the context of other biophysical studies, constrain our thinking about the mechanism of voltage sensing. Although it is clear that structures of voltage sensors in other conformations are needed, such as the resting state that predominates at negative voltages, the available data allow us to frame several key concepts that are fundamental to the mechanism of voltage sensing. Some of these concepts have been central to our thinking for some time, whereas others have their roots in the more recent X-ray structures.

**Charged residues have two important roles.** The external four Arg residues in S4 appear to carry most of the gating charge, thus serving to drive conformational changes in response to changes in membrane voltage<sup>19,20,22</sup>. Although this concept is also supported by extensive evidence that S4 actually moves<sup>23–38</sup>, an untested assumption in many of these studies is that neutralization of charged residues does not alter the position of the S4 helix. If this were to occur, the contribution of residues to gating charge could go undetected. The second important role of charged residues is to stabilize the basic Arg residues in the low dielectric of the membrane interior. Glu and Asp residues in S1–S3 form the external and internal clusters seen in the paddle-chimaera structure and contribute to a network of electrostatic interactions that stabilize some of the S4 Arg and Lys residues within the membrane<sup>10,47</sup> (Fig. 3). The outermost Arg residues do not appear to interact with acidic residues in the external cluster, but project towards the surrounding lipid membrane (see Fig. 3 and below).

**Voltage sensors contain a water-filled permeation pathway.** The first hints that water might penetrate voltage sensors and that the charged Arg residues move within an aqueous pathway came from studies by Horn and others, showing extensive reactivity of water-soluble methanethiosulfonate (MTS) reagents with Cys residues introduced within S4 (refs 23–26). In effect, the Arg residues in S4 can be viewed as tethered ions that move within S1–S4 domains. Remarkably, untethered ions can actually permeate through voltage sensors. Bezanilla and colleagues found that His residues introduced within S4 create a proton pore<sup>28,34</sup>, and Isacoff's group made the discovery that ions as large as guanidinium can permeate S1–S4 domains when the outermost Arg in S4 is truncated<sup>60,61</sup>. The recent discoveries of voltage-activated proton channels containing only an S1–S4 domain<sup>41–43</sup> suggest that this permeation pathway can serve an important biological function. The paddle-chimaera structure shows a large crevice between S1–S4 helices that would be contiguous with the external aqueous phase when the channel is embedded in a membrane. This region of the voltage sensor houses many of the basic and acidic residues (Fig. 3, green arrow), presumably identifying the pathway for ions to permeate voltage sensors<sup>62</sup>. One important implication of water intercalation into voltage sensors is that it would



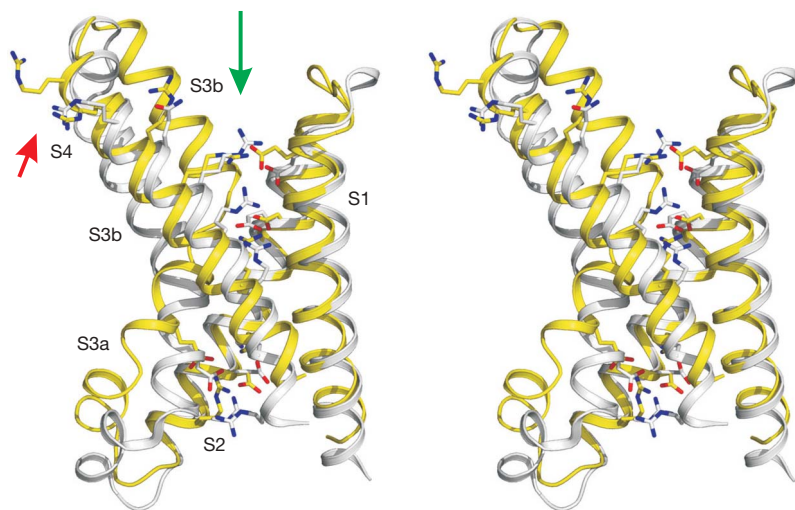


**Figure 3 | Charged amino acids in S1–S4 voltage-sensing domains.** Superposition of the structures of the S1–S4 domains of KvAP (yellow ribbon) and the paddle-chimaera channel (white ribbon) shown as a stereo pair and viewed from the side. The structures were aligned to minimize deviations between the S1 and S2 helices<sup>47</sup>. Basic and acidic residues are shown as stick representations, with carbon coloured yellow or white, oxygen coloured red and nitrogen coloured blue. The green arrow identifies an aqueous crevice within the S1–S4 domain that would be continuous with the external solution, and the red arrow identifies outer S4 Arg residues projecting towards the lipid membrane. The PDB accession code for S1–S4 of KvAP is 1ORS, and that for the paddle-chimaera is 2R9R.

be expected to focus the membrane electric field, allowing movements smaller than the full thickness of the bilayer to translocate charge across the full extent of the electric field. Indeed, focusing of the electric field has been inferred from studies with electrochromic fluorophores<sup>63</sup>, proton permeation mediated by introduced His residues<sup>64</sup> and charged MTS compounds with variable length tethers<sup>65</sup>. **The paddle motif flexes within S1–S4 domains.** The S3b–S4 paddle motif contains the outer four S4 Arg residues that carry most of the gating charge in Kv channels<sup>19,20,22</sup>, and in the X-ray structures this motif is connected to other regions of the protein by means of flexible linkers<sup>6,35</sup>. The accessibility of biotinylated positions in the paddle motif to avidin suggests that it is a uniquely mobile motif within S1–S4 domains<sup>35,37,66</sup>, a feature that also can be seen in electron paramagnetic resonance (EPR) measurements of spin label mobility<sup>14,67</sup>. The paddle motif can be transplanted between proteins with S1–S4 domains, whether they are found in archaeobacterial or eukaryotic Kv channels<sup>45</sup>, Nav channels<sup>68</sup> or voltage-sensing proteins such as Ci-VSP or Hv1 (ref. 45), suggesting that this motif resides in a relatively unconstrained environment and that its function is conserved throughout voltage sensors. Another indicator that the paddle motif is a crucial flexing motif within S1–S4 voltage sensors is that it forms the receptor for tarantula toxins, such as hanatoxin<sup>45,51–53</sup>, which inhibit voltage-sensor activation<sup>52,55</sup>. Many other toxins from spiders and scorpions alter the activity of voltage-activated ion channels by binding to paddle motifs<sup>68</sup>, indicating that nature has targeted this motif throughout evolution.

**Voltage sensors interact intimately with lipids.** The structures of KvAP and Kv1.2 channels discussed previously indicate that the paddle motif is exposed to the surrounding lipids, and the paddle-chimaera structure provides a glimpse of what these interactions might look like because lipid molecules actually crystallize with the channel (Fig. 2). EPR studies on the S1–S4 domain and full-length KvAP channel demonstrate extensive exposure of the voltage sensors to the surrounding lipid membrane<sup>14,67,69</sup>. The interaction of tarantula toxins with paddle motifs also strongly supports the idea that the paddle moves at the protein–lipid interface because these toxins bind to it within the membrane<sup>45,54–56</sup> and the toxin-binding surface projects out towards the surrounding lipid membrane<sup>45</sup>.

Although we are only beginning to learn about the nature of the interactions between lipids and voltage sensors, several recent studies indicate that these lipid–protein interactions may be fundamentally important for voltage-sensor function. MacKinnon and colleagues showed that lipids with phosphate-containing head groups are required for channel function and that they stabilize the voltage sensor in the activated state<sup>70</sup>. One possibility is that the outer S4 Arg residues projecting out towards the surrounding membrane in the structure of the activated state of the paddle-chimaera channel

(red arrows in Figs 2a, b and 3) actually interact directly with phosphate head groups. The outer Arg residues are shown to be exposed to the lipid membrane in EPR studies<sup>14,67,69</sup>, and stabilizing interactions between Arg residues and phosphate head groups can be seen in molecular dynamics simulations<sup>71–73</sup>.

A series of recent studies by Lu and colleagues points to intimate interactions between specific lipids and voltage sensors. They found that extracellular application of sphingomyelinase D, an enzyme that hydrolyses the zwitterionic membrane phospholipid sphingomyelin to the anionic ceramide-1-phosphate, produces a marked stabilization of the activated state of the voltage sensors<sup>74</sup>. The implication is that ionic interactions between positively charged S4 Arg residues and the negatively charged phosphate head group are strengthened when the positively charged choline group is removed. The effects of sphingomyelinase D can only be seen on certain types of Kv channels, suggesting that sphingomyelin may be interacting intimately with those channels that are sensitive to the lipase. In addition, sphingomyelinase D treatment notably alters the stability of hanatoxin bound to voltage-sensor paddles, consistent with an intimate interaction between toxins, lipids and paddle motifs<sup>56</sup>. Treatment of membranes with sphingomyelinase C, which removes the entire head group of the lipid, immobilizes the voltage sensors in a resting state<sup>75</sup>, consistent with the possibility that phosphate-containing lipids help to stabilize the voltage sensors in the activated state. Binding of tarantula toxins to the voltage sensors seems to diminish access of sphingomyelinase C to the channel<sup>75</sup>, suggesting that the interaction between sphingomyelin and voltage sensors are remarkably intimate. All of these studies raise the possibility that lipid interactions with voltage sensors may have crucial roles in the mechanism of voltage sensing.

### Voltage sensor motions

To proceed from these concepts to a more refined understanding of the mechanisms of voltage sensing, we will need to see an actual structure of a voltage-sensing domain in the resting state. The rearrangements within the voltage sensors that occur as the protein moves from an activated state, the structure of which we now know quite a bit about, to the resting state, about which we know relatively little, remains poorly constrained. If we are willing to use broad strokes, however, the emerging concepts can be put together to paint an impressionistic image of voltage-sensor motions. It seems probable that the activated state of the voltage sensor is the stable conformation because this is the state found in the absence of a membrane electric field (0 mV). The domain is organized so that the S3b and S4 helices of the paddle motif reside in a relatively unconstrained and flexible environment, with much of the surface of the motif exposed to the surrounding lipid bilayer (Figs 2 and 3). This includes the outermost Arg residues that probably interact with phosphate lipid head groups

(Fig. 4). The deeper Arg residues are stabilized by interactions with acidic residues in S1, S2 and S3 (Figs 3 and 4), which line a water-filled crevice projecting into the protein from the external aqueous phase. In the case of Kv channels studied so far, the S1–S4 domains have few interactions with the pore domain within the outer half of the bilayer that are required for voltage sensing<sup>46,76</sup>. The existence of Ci-VSP and Hv1 seem to confirm this, in particular because both of these voltage-sensing proteins can function as monomers<sup>40,43</sup>. When membrane voltage becomes negative (inside relative to outside), the paddle motif moves the most, with charged Arg residues in S4 moving towards the internal side of the membrane (Figs 4 and 5). The S3b helix may move in association with S4, or the interface between the two helices may change somewhat, but in either case it seems probable that the S3b helix does not become deeply submerged in the membrane<sup>55,77–79</sup>. The outermost Arg residues probably exchange their interactions with phosphate head groups for acidic residues in the external cluster in an ion-exchange-type mechanism, the middle Arg residues exchange interactions with the external cluster for those in the internal cluster (Fig. 4), and the innermost Arg residues might exchange interactions with the internal cluster for those with phosphate head groups of lipids within the inner leaflet of the bilayer<sup>71</sup>. It is tempting to speculate that the prominent external-facing crevice seen in the paddle-chimaera structure (Fig. 3, green arrow) may largely vanish when the domain adopts a resting conformation and an inward-facing water-filled crevice might emerge<sup>80</sup>.

**Range of motion.** Although this picture captures the key concepts for which there is experimental evidence, we haven't mentioned the nature of the motions within the voltage-sensing domains, and this is where things remain somewhat uncertain. Viewed collectively, most of the evidence is compatible with the notion that the Arg residues in S4 move about 15 Å inward along a trajectory that is approximately perpendicular to the membrane plane as the voltage sensors move from activated to resting states. Tarantula toxins can partition into the outer leaflet of the membrane<sup>54–56</sup> and bind to the paddle motif in both resting and activated states in eukaryotic Kv channels<sup>55</sup>—a constraint suggesting that the motions of the paddle are confined to the outer half of the bilayer. Similarly, fluorescence resonance energy transfer between fluorophores attached near S4 and lipophilic acceptors that flip back and forth across the membrane indicate that motions of S4 are considerably less than the full thickness of the bilayer<sup>81</sup>. One informative estimate of the allowed motions of S4 comes from experiments measuring the reactivity of biotinylated residues in the S1–S4 domain of KvAP with avidin applied to external or internal solutions<sup>35,37</sup>. When the accessibility data are mapped onto the structure of the S1–S4 domain of KvAP, it is evident that the S4 helix must be capable of motions of at least 15 Å (Fig. 5a). Because the structure represents the activated conformation of the

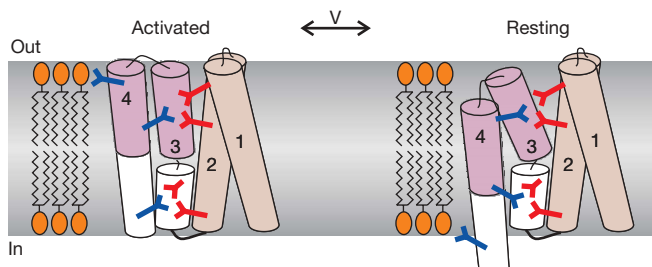


**Figure 4 | Shifting charge interactions during movements of voltage sensors.** The cartoons illustrate shifting interactions between positively charged Arg residues in S4 (blue) and either negatively charged phosphate lipid head groups (orange) or acidic residues (red) in the external and internal acidic residue clusters. The cartoon to the left is for the activated state that occurs at positive membrane voltages and that on the right is for the resting state that occurs at negative voltages. The illustrated motions of helices are not meant to imply anything about the structural changes occurring during voltage-sensor movement.

voltage sensor, the positions towards the external side of the membrane that are accessible to internal avidin (Fig. 5a, yellow and blue spheres) must move to within 10 Å of the internal side of the membrane in the resting state (in the vicinity of the blue spheres towards the internal side of the structure, which are marked by a dashed line). Such a motion is consistent with MTS accessibility experiments<sup>23–26</sup>, His-mediated proton transfer studies<sup>34,64</sup> and mutagenic rescue experiments<sup>82</sup>. Another constraint for S4 motions comes from the recent discovery by Bezanilla and colleagues in the Shaker Kv channel that Cys residues introduced at the outermost Arg in S4 can form disulphide and metal bridges with Cys residues introduced into S1 or S2 when the voltage sensors are in the resting state<sup>38</sup> (Fig. 5b). The distance between Cβ atoms in the X-ray structure of the paddle chimaera is 19 Å for the S4 (green sphere) to S1 (light pink sphere) bridge, and 18.4 Å for the S4 to S2 (magenta sphere) bridge. Although S4 might move somewhat more or less than the 18–19 Å separating these residues (depending on the orientation of the Cys side chains), these bridges indicate that S4 motions in Shaker Kv channels are large, but probably somewhat less than those proposed for KvAP based on the biotin–avidin studies. In contrast to these estimates, most fluorescence distance measurements point to motions on the order of a few ångströms<sup>31,32,83</sup>. A recent fluorescence study on the Shaker Kv channel reporting an extensive number of distance constraints supports larger displacements of S4, on the order of about 10 Å (ref. 84). The question of how far particular regions within S1–S4 move will require further study and it will be important to explore the possibility that the range of motions can vary for different types of voltage-activated ion channels.

**Possible rotational motions.** In addition to translational motions, the S4 helix has been proposed to rotate<sup>7,8</sup>, perhaps as much as 180° (refs 31,32,85). The bridges already discussed between S4 and either S1 or S2 (ref. 38) offer an informative perspective on the question of S4 rotations. If we consider these bridges in the context of the X-ray structure of the activated state of the paddle chimaera (Fig. 5c), it seems that S4 wouldn't need to rotate much for the relevant position (green sphere) to form a bridge with S1 (light pink sphere), but would need to rotate significantly (<90°) to bridge with S2 (magenta sphere). These bridges seem to rule out large rotations of S4, but would be consistent with the possibility that S4 undergoes a modest rigid body rotation relative to S1 and S2. Another scenario put forward on the basis of the X-ray structures of the paddle chimaera<sup>47</sup> and the MlotiK channel<sup>86</sup>, a K<sup>+</sup> channel from *Mesorhizobium loti*, is that S4 undergoes a transition from a standard α-helix with 3.6 residues per turn in the activated state to a more tightly wound 3<sub>10</sub> helix with 3 residues per turn in the resting state. Transitioning from a standard α-helix in the activated state to a 3<sub>10</sub> helix in the resting state would allow the outermost Arg residues to rotate moderately into the S1–S4 domain without necessitating the type of rigid body motion that would require extensive adjustments in packing between S4 and the other helices in the voltage sensor. In the structure of the activated paddle-chimaera channel, the internal region of S4 is also a 3<sub>10</sub> helix, leading to the suggestion of a wave-like transition where the zone of 3<sub>10</sub> secondary structure propagates from the internal to external regions of S4 as the voltage sensor moves from activated to resting states<sup>47</sup>. 3<sub>10</sub> helices are energetically unstable, but in the case of voltage sensors it is possible that the energy necessary to adopt a 3<sub>10</sub> helix could come from the membrane electric field. In this way, the electric field would hold the voltage sensor in an unstable or 'cocked' position at negative membrane voltages, which would readily relax to an energetically more stable conformation once the field dissipates with depolarization of the membrane towards 0 mV.

## Future prospects

The present picture of voltage-sensor structure and motions has evolved considerably since the cloning of the first membrane proteins with S1–S4 voltage sensors, yet many exciting and open questions remain. What does the structure of a voltage sensor look like in the



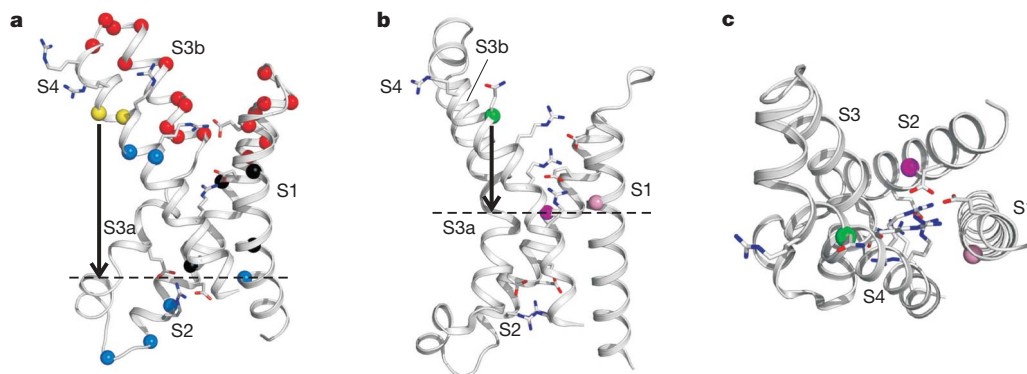


**Figure 5 | Inferring motions from accessibility and bridging experiments.** **a**, Ribbon representation of the structure of the S1–S4 domain of KvAP, showing accessibility of biotinylated positions to avidin with 9 Å and 10 Å tethers<sup>37</sup>. The positions marked by red spheres ( $\alpha$ -carbon) are only accessible to external avidin, those marked by blue spheres are only accessible to internal avidin, and those marked by yellow spheres are accessible to either external or internal avidin. Black spheres mark inaccessible positions. The structure is of an activated voltage sensor, so yellow and blue positions located towards the external side of the membrane must move to within  $\sim 10$  Å of the internal side of the membrane (dashed line) in the resting state,

as indicated by the black arrow. Basic and acidic residues are shown as stick representations. **b**, Ribbon representation of the structure of the S1–S4 domain of the paddle-chimaera channel showing positions that form disulphide or metal bridges in the resting state<sup>38</sup>. The structures shown in **a** and **b** are aligned as in Fig. 3. In the Shaker Kv channel, Cys substituted at Arg 362 in S4 (equivalent to Arg 294 in the paddle chimaera; green sphere) can bridge with either I241C in S1 (Ile 177 in the paddle chimaera; light pink sphere) or I287C in S2 (Ile 230 in the paddle chimaera; magenta sphere) when the voltage sensors are in a resting state. **c**, Bridging positions from **b** viewed from the external side of the membrane.

resting conformation? How does the voltage sensor move during activation? Where exactly is the permeation pathway for ions to permeate S1–S4 domains? How do the interactions of lipids with voltage sensors influence their structure and motions? What does the structure of the lipid membrane look like around voltage sensors? Most structural and biophysical experiments have been done on a relatively small number of voltage-activated ion channels, mostly Shaker, Kv1.2 and KvAP, and at this point we don't know how similar the mechanisms will be for the large family of ion channels and enzymes that contain S1–S4 domains. Indeed, there is precedence from the work of Aldrich and colleagues that gating in some types of Kv channels involves only a subset of the conformational changes thought to occur in Shaker Kv channels<sup>87</sup>. In addition, very little is known about the S1–S4 domains for ion channels such as cyclic-nucleotide-gated channels or transient receptor potential channels. It is unknown whether the S1–S4 domains in these channels have any voltage-sensing functions, and whether they undergo structural changes on binding ligands that might be related to those that occur in voltage sensors. In many respects, we have only recently developed a solid foundation for thinking about how S1–S4 voltage-sensing domains work, and there are many fascinating experiments to be done.

- Galvani, L. De viribus electricitatis in motu musculari. *Bononiensi scientiarum et artium atque instituto academiae commentarii* **7**, 363–418 (1791).
- Hodgkin, A. L. & Huxley, A. F. A quantitative description of membrane current and its application to conduction and excitation in nerve. *J. Physiol. (Lond.)* **117**, 500–544 (1952).
- Noda, M. *et al.* Expression of functional sodium channels from cloned cDNA. *Nature* **322**, 826–828 (1986).
- Tanabe, T. *et al.* Primary structure of the receptor for calcium channel blockers from skeletal muscle. *Nature* **328**, 313–318 (1987).
- Tempel, B. L., Papazian, D. M., Schwarz, T. L., Jan, Y. N. & Jan, L. Y. Sequence of a probable potassium channel component encoded at Shaker locus of *Drosophila*. *Science* **237**, 770–775 (1987).
- Jiang, Y. *et al.* X-ray structure of a voltage-dependent K<sup>+</sup> channel. *Nature* **423**, 33–41 (2003).
- Catterall, W. A. Molecular properties of voltage-sensitive sodium channels. *Annu. Rev. Biochem.* **55**, 953–985 (1986).
- Guy, H. R. & Seetharamulu, P. Molecular model of the action potential sodium channel. *Proc. Natl Acad. Sci. USA* **83**, 508–512 (1986).
- Kubo, Y., Baldwin, T. J., Jan, Y. N. & Jan, L. Y. Primary structure and functional expression of a mouse inward rectifier potassium channel. *Nature* **362**, 127–133 (1993).
- Papazian, D. M. *et al.* Electrostatic interactions of S4 voltage sensor in Shaker K<sup>+</sup> channel. *Neuron* **14**, 1293–1301 (1995).

- Li-Smerin, Y. & Swartz, K. J. Gating modifier toxins reveal a conserved structural motif in voltage-gated Ca<sup>2+</sup> and K<sup>+</sup> channels. *Proc. Natl Acad. Sci. USA* **95**, 8585–8589 (1998).
- Lu, Z., Klem, A. M. & Ramu, Y. Coupling between voltage sensors and activation gate in voltage-gated K<sup>+</sup> channels. *J. Gen. Physiol.* **120**, 663–676 (2002).
- Lu, Z., Klem, A. M. & Ramu, Y. Ion conduction pore is conserved among potassium channels. *Nature* **413**, 809–813 (2001).
- Chakrapani, S., Cuellar, L. G., Cortes, D. M. & Perozo, E. Structural dynamics of an isolated voltage-sensor domain in a lipid bilayer. *Structure* **16**, 398–409 (2008).
- Armstrong, C. M. & Bezanilla, F. Currents related to movement of the gating particles of the sodium channels. *Nature* **242**, 459–461 (1973).
- Schneider, M. F. & Chandler, W. K. Voltage dependent charge movement of skeletal muscle: a possible step in excitation-contraction coupling. *Nature* **242**, 244–246 (1973).
- Keynes, R. D. & Rojas, E. Kinetics and steady-state properties of the charged system controlling sodium conductance in the squid giant axon. *J. Physiol. (Lond.)* **239**, 393–434 (1974).
- Schoppa, N. E., McCormack, K., Tanouye, M. A. & Sigworth, F. J. The size of gating charge in wild-type and mutant Shaker potassium channels. *Science* **255**, 1712–1715 (1992).
- Seoh, S. A., Sigg, D., Papazian, D. M. & Bezanilla, F. Voltage-sensing residues in the S2 and S4 segments of the Shaker K<sup>+</sup> channel. *Neuron* **16**, 1159–1167 (1996).
- Aggarwal, S. K. & MacKinnon, R. Contribution of the S4 segment to gating charge in the Shaker K<sup>+</sup> channel. *Neuron* **16**, 1169–1177 (1996).
- Noceti, F. *et al.* Effective gating charges per channel in voltage-dependent K<sup>+</sup> and Ca<sup>2+</sup> channels. *J. Gen. Physiol.* **108**, 143–155 (1996).
- Ahern, C. A. & Horn, R. Specificity of charge-carrying residues in the voltage sensor of potassium channels. *J. Gen. Physiol.* **123**, 205–216 (2004).
- Yang, N. & Horn, R. Evidence for voltage-dependent S4 movement in sodium channels. *Neuron* **15**, 213–218 (1995).
- Yang, N., George, A. L. Jr & Horn, R. Molecular basis of charge movement in voltage-gated sodium channels. *Neuron* **16**, 113–122 (1996).
- Larsson, H. P., Baker, O. S., Dhillon, D. S. & Isacoff, E. Y. Transmembrane movement of the shaker K<sup>+</sup> channel S4. *Neuron* **16**, 387–397 (1996).
- Yusaf, S. P., Wray, D. & Sivaprasadarao, A. Measurement of the movement of the S4 segment during the activation of a voltage-gated potassium channel. *Pflügers Arch.* **433**, 91–97 (1996).
- Mannuzzu, L. M., Moronne, M. M. & Isacoff, E. Y. Direct physical measure of conformational rearrangement underlying potassium channel gating. *Science* **271**, 213–216 (1996).
- Starace, D. M., Stefani, E. & Bezanilla, F. Voltage-dependent proton transport by the voltage sensor of the Shaker K<sup>+</sup> channel. *Neuron* **19**, 1319–1327 (1997).
- Cha, A. & Bezanilla, F. Characterizing voltage-dependent conformational changes in the Shaker K<sup>+</sup> channel with fluorescence. *Neuron* **19**, 1127–1140 (1997).
- Cha, A. & Bezanilla, F. Structural implications of fluorescence quenching in the Shaker K<sup>+</sup> channel. *J. Gen. Physiol.* **112**, 391–408 (1998).
- Glauner, K. S., Mannuzzu, L. M., Gandhi, C. S. & Isacoff, E. Y. Spectroscopic mapping of voltage sensor movement in the Shaker potassium channel. *Nature* **402**, 813–817 (1999).
- Cha, A., Snyder, G. E., Selvin, P. R. & Bezanilla, F. Atomic scale movement of the voltage-sensing region in a potassium channel measured via spectroscopy. *Nature* **402**, 809–813 (1999).

33. Gandhi, C. S., Loots, E. & Isacoff, E. Y. Reconstructing voltage sensor-pore interaction from a fluorescence scan of a voltage-gated K<sup>+</sup> channel. *Neuron* **27**, 585–595 (2000).
34. Starace, D. M. & Bezanilla, F. Histidine scanning mutagenesis of basic residues of the S4 segment of the Shaker K<sup>+</sup> channel. *J. Gen. Physiol.* **117**, 469–490 (2001).
35. Jiang, Y., Ruta, V., Chen, J., Lee, A. & MacKinnon, R. The principle of gating charge movement in a voltage-dependent K<sup>+</sup> channel. *Nature* **423**, 42–48 (2003).
36. Laine, M. *et al.* Atomic proximity between S4 segment and pore domain in Shaker potassium channels. *Neuron* **39**, 467–481 (2003).
37. Ruta, V., Chen, J. & MacKinnon, R. Calibrated measurement of gating-charge arginine displacement in the KvAP voltage-dependent K<sup>+</sup> channel. *Cell* **123**, 463–475 (2005).
38. Campos, F. V., Chanda, B., Roux, B. & Bezanilla, F. Two atomic constraints unambiguously position the S4 segment relative to S1 and S2 segments in the closed state of Shaker K channel. *Proc. Natl Acad. Sci. USA* **104**, 7904–7909 (2007).
39. Murata, Y., Iwasaki, H., Sasaki, M., Inaba, K. & Okamura, Y. Phosphoinositide phosphatase activity coupled to an intrinsic voltage sensor. *Nature* **435**, 1239–1243 (2005).
40. Kohout, S. C., Ulbrich, M. H., Bell, S. C. & Isacoff, E. Y. Subunit organization and functional transitions in Ci-VSP. *Nature Struct. Mol. Biol.* **15**, 106–108 (2008).
41. Sasaki, M., Takagi, M. & Okamura, Y. A voltage sensor-domain protein is a voltage-gated proton channel. *Science* **312**, 589–592 (2006).
42. Ramsey, I. S., Moran, M. M., Chong, J. A. & Clapham, D. E. A voltage-gated proton-selective channel lacking the pore domain. *Nature* **440**, 1213–1216 (2006).
43. Tombola, F., Ulbrich, M. H. & Isacoff, E. Y. The voltage-gated proton channel Hv1 has two pores, each controlled by one voltage sensor. *Neuron* **58**, 546–556 (2008).
44. Lee, S. Y., Letts, J. A. & MacKinnon, R. Dimeric subunit stoichiometry of the human voltage-dependent proton channel Hv1. *Proc. Natl Acad. Sci. USA* **105**, 7692–7695 (2008).
45. Alabi, A. A., Bahamonde, M. I., Jung, H. J., Kim, J. I. & Swartz, K. J. Portability of paddle motif function and pharmacology in voltage sensors. *Nature* **450**, 370–375 (2007).
46. Long, S. B., Campbell, E. B. & MacKinnon, R. Crystal structure of a mammalian voltage-dependent Shaker family K<sup>+</sup> channel. *Science* **309**, 897–903 (2005).
47. Long, S. B., Tao, X., Campbell, E. B. & MacKinnon, R. Atomic structure of a voltage-dependent K<sup>+</sup> channel in a lipid membrane-like environment. *Nature* **450**, 376–382 (2007).
48. Monks, S. A., Needleman, D. J. & Miller, C. Helical structure and packing orientation of the S2 segment in the Shaker K<sup>+</sup> channel. *J. Gen. Physiol.* **113**, 415–423 (1999).
49. Li-Smerin, Y., Hackos, D. H. & Swartz, K. J.  $\alpha$ -helical structural elements within the voltage-sensing domains of a K<sup>+</sup> channel. *J. Gen. Physiol.* **115**, 33–49 (2000a).
50. Hong, K. H. & Miller, C. The lipid–protein interface of a Shaker K<sup>+</sup> channel. *J. Gen. Physiol.* **115**, 51–58 (2000).
51. Li-Smerin, Y. & Swartz, K. J. Helical structure of the COOH terminus of S3 and its contribution to the gating modifier toxin receptor in voltage-gated ion channels. *J. Gen. Physiol.* **117**, 205–218 (2001).
52. Swartz, K. J. & MacKinnon, R. Hanatoxin modifies the gating of a voltage-dependent K<sup>+</sup> channel through multiple binding sites. *Neuron* **18**, 665–673 (1997a).
53. Li-Smerin, Y. & Swartz, K. J. Localization and molecular determinants of the hanatoxin receptors on the voltage-sensing domain of a K<sup>+</sup> channel. *J. Gen. Physiol.* **115**, 673–684 (2000).
54. Lee, S. Y. & MacKinnon, R. A membrane-access mechanism of ion channel inhibition by voltage sensor toxins from spider venom. *Nature* **430**, 232–235 (2004).
55. Phillips, L. R. *et al.* Voltage-sensor activation with a tarantula toxin as cargo. *Nature* **436**, 857–860 (2005).
56. Milesu, M. *et al.* Tarantula toxins interact with voltage sensors within lipid membranes. *J. Gen. Physiol.* **130**, 497–511 (2007).
57. Long, S. B., Campbell, E. B. & MacKinnon, R. Voltage sensor of Kv1.2: structural basis of electromechanical coupling. *Science* **309**, 903–908 (2005).
58. Ruta, V., Jiang, Y., Lee, A., Chen, J. & MacKinnon, R. Functional analysis of an archaeobacterial voltage-dependent K<sup>+</sup> channel. *Nature* **422**, 180–185 (2003).
59. Yellen, G. The voltage-gated potassium channels and their relatives. *Nature* **419**, 35–42 (2002).
60. Tombola, F., Pathak, M. M. & Isacoff, E. Y. Voltage-sensing arginines in a potassium channel permeate and occlude cation-selective pores. *Neuron* **45**, 379–388 (2005).
61. Sokolov, S., Scheuer, T. & Catterall, W. A. Ion permeation through a voltage-sensitive gating pore in brain sodium channels having voltage sensor mutations. *Neuron* **47**, 183–189 (2005).
62. Freitas, J. A., Tobias, D. J. & White, S. H. A voltage-sensor water pore. *Biophys. J.* **91**, L90–92 (2006).
63. Asamoah, O. K., Wuskell, J. P., Loew, L. M. & Bezanilla, F. A fluorometric approach to local electric field measurements in a voltage-gated ion channel. *Neuron* **37**, 85–97 (2003).
64. Starace, D. M. & Bezanilla, F. A proton pore in a potassium channel voltage sensor reveals a focused electric field. *Nature* **427**, 548–553 (2004).
65. Ahern, C. A. & Horn, R. Focused electric field across the voltage sensor of potassium channels. *Neuron* **48**, 25–29 (2005).
66. Banerjee, A. & MacKinnon, R. Inferred motions of the S3a helix during voltage-dependent K<sup>+</sup> channel gating. *J. Mol. Biol.* **381**, 569–580 (2008).
67. Cuello, L. G., Cortes, D. M. & Perozo, E. Molecular architecture of the KvAP voltage-dependent K<sup>+</sup> channel in a lipid bilayer. *Science* **306**, 491–495 (2004).
68. Bosmans, F., Martin-Eaucclair, M. F. & Swartz, K. J. Deconstructing voltage sensor function and pharmacology in sodium channels. *Nature* **456**, 202–208 (2008).
69. Vamvouka, M., Cieslak, J., Van Eps, N., Hubbell, W. & Gross, A. The structure of the lipid-embedded potassium channel voltage sensor determined by double-electron-electron resonance spectroscopy. *Protein Sci.* **17**, 506–517 (2008).
70. Schmidt, D., Jiang, Q. X. & MacKinnon, R. Phospholipids and the origin of cationic gating charges in voltage sensors. *Nature* **444**, 775–779 (2006).
71. Jogini, V. & Roux, B. Dynamics of the Kv1.2 voltage-gated K<sup>+</sup> channel in a membrane environment. *Biophys. J.* **93**, 3070–3082 (2007).
72. Sands, Z. A. & Sansom, M. S. How does a voltage sensor interact with a lipid bilayer? Simulations of a potassium channel domain. *Structure* **15**, 235–244 (2007).
73. Freitas, J. A., Tobias, D. J., von Heijne, G. & White, S. H. Interface connections of a transmembrane voltage sensor. *Proc. Natl Acad. Sci. USA* **102**, 15059–15064 (2005).
74. Ramu, Y., Xu, Y. & Lu, Z. Enzymatic activation of voltage-gated potassium channels. *Nature* **442**, 696–699 (2006).
75. Xu, Y., Ramu, Y. & Lu, Z. Removal of phospho-head groups of membrane lipids immobilizes voltage sensors of K<sup>+</sup> channels. *Nature* **451**, 826–829 (2008).
76. Soler-Llavina, G. J., Chang, T. H. & Swartz, K. J. Functional interactions at the interface between voltage-sensing and pore domains in the Shaker K(v) channel. *Neuron* **52**, 623–634 (2006).
77. Nguyen, T. P. & Horn, R. Movement and crevices around a sodium channel S3 segment. *J. Gen. Physiol.* **120**, 419–436 (2002).
78. Gandhi, C. S., Clark, E., Loots, E., Pralle, A. & Isacoff, E. Y. The orientation and molecular movement of a K<sup>+</sup> channel voltage-sensing domain. *Neuron* **40**, 515–525 (2003).
79. Darman, R. B., Ivy, A. A., Ketty, V. & Blaustein, R. O. Constraints on voltage sensor movement in the Shaker K<sup>+</sup> channel. *J. Gen. Physiol.* **128**, 687–699 (2006).
80. Islas, L. D. & Sigworth, F. J. Electrostatics and the gating pore of Shaker potassium channels. *J. Gen. Physiol.* **117**, 69–89 (2001).
81. Chanda, B., Asamoah, O. K., Blunck, R., Roux, B. & Bezanilla, F. Gating charge displacement in voltage-gated ion channels involves limited transmembrane movement. *Nature* **436**, 852–856 (2005).
82. Grabe, M., Lai, H. C., Jain, M., Nung Jan, Y. & Yeh Jan, L. Structure prediction for the down state of a potassium channel voltage sensor. *Nature* **445**, 550–553 (2007).
83. Posson, D. J., Ge, P., Miller, C., Bezanilla, F. & Selvin, P. R. Small vertical movement of a K<sup>+</sup> channel voltage sensor measured with luminescence energy transfer. *Nature* **436**, 848–851 (2005).
84. Posson, D. J. & Selvin, P. R. Extent of voltage sensor movement during gating of shaker K<sup>+</sup> channels. *Neuron* **59**, 98–109 (2008).
85. Pathak, M. M. *et al.* Closing in on the resting state of the Shaker K<sup>+</sup> channel. *Neuron* **56**, 124–140 (2007).
86. Clayton, G. M., Altieri, S., Heginbotham, L., Unger, V. M. & Morais-Cabral, J. H. Structure of the transmembrane regions of a bacterial cyclic nucleotide-regulated channel. *Proc. Natl Acad. Sci. USA* **105**, 1511–1515 (2008).
87. Ledwell, J. L. & Aldrich, R. W. Mutations in the S4 region isolate the final voltage-dependent cooperative step in potassium channel activation. *J. Gen. Physiol.* **113**, 389–414 (1999).

**Acknowledgements** I thank J. Diamond, J. Mindell, S. Silberberg and the members of the Swartz laboratory for discussions. I thank R. MacKinnon for providing coordinates for the paddle-chimera and those for the superimposed structures shown in Fig. 3. This work was supported by the Intramural Research Program of the NINDS, NIH.

**Author Information** Reprints and permissions information is available at [www.nature.com/reprints](http://www.nature.com/reprints). Correspondence should be addressed to K.J.S. ([swartzk@ninds.nih.gov](mailto:swartzk@ninds.nih.gov)).



## ARTICLES

# Geometric frustration in buckled colloidal monolayers

Yilong Han<sup>1,2\*</sup>, Yair Shokef<sup>1\*†</sup>, Ahmed M. Alsayed<sup>1</sup>, Peter Yunker<sup>1</sup>, Tom C. Lubensky<sup>1</sup> & Arjun G. Yodh<sup>1</sup>

**Geometric frustration arises when lattice structure prevents simultaneous minimization of local interaction energies. It leads to highly degenerate ground states and, subsequently, to complex phases of matter, such as water ice, spin ice, and frustrated magnetic materials. Here we report a simple geometrically frustrated system composed of closely packed colloidal spheres confined between parallel walls. Diameter-tunable microgel spheres are self-assembled into a buckled triangular lattice with either up or down displacements, analogous to an antiferromagnetic Ising model on a triangular lattice. Experiment and theory reveal single-particle dynamics governed by in-plane lattice distortions that partially relieve frustration and produce ground states with zigzagging stripes and subextensive entropy, rather than the more random configurations and extensive entropy of the antiferromagnetic Ising model. This tunable soft-matter system provides a means to directly visualize the dynamics of frustration, thermal excitations and defects.**

Geometric frustration arises in physical and biological systems<sup>1</sup> that range from water<sup>2</sup> and spin ice<sup>3</sup> to magnets<sup>4,5</sup>, ceramics<sup>6</sup> and high-transition-temperature superconductors<sup>7</sup>. The essence of this phenomenon is best captured in the model of Ising spins arranged on a two-dimensional (2D) triangular lattice and interacting antiferromagnetically<sup>8,9</sup>; two of the three spins on any triangular plaquette within this lattice can be antiparallel to minimize their antiferromagnetic interaction energy, but the third spin is frustrated because it cannot be simultaneously antiparallel to both neighbouring spins (Fig. 1a). Such frustration leads to materials with many degenerate ground states and extensive entropy proportional to the number of particles in the system. Consequently, small perturbations can

introduce giant fluctuations with peculiar dynamics. Traditionally, these phenomena have been explored in atomic materials by ensemble averaging techniques, such as neutron and X-ray scattering, muon spin rotation, nuclear magnetic resonance and measurements of heat capacity and susceptibility<sup>5</sup>. More recently, artificial arrays of mesoscopic constituents have been fabricated to probe geometric frustration at the single-‘particle’ level. Examples include Josephson junctions<sup>10</sup>, superconducting rings<sup>11</sup>, ferromagnetic islands<sup>12–14</sup> and recent simulations<sup>15</sup> of charged colloids in optical traps. But observations in these model systems have been limited to the static patterns into which these systems freeze when cooled. Thus many questions about frustrated systems remain unexplored, particularly those associated with single-particle dynamics. For example, how, when and why do individual particles change states to accommodate their local environments, and what kinetic mechanisms govern transitions to glassy phases?

Here we report the static and dynamic properties of a self-assembled colloidal system analogous to Wannier’s antiferromagnetic Ising model<sup>8</sup>. Densely packed spheres between parallel walls form an in-plane triangular lattice with out-of-plane up and down buckling<sup>16–26</sup>. The up–down states of the spheres produced by buckling are analogous to up–down states of Ising spins (Fig. 1b). Nearest-neighbour excluded volume interactions between particles favour opposite states for neighbouring particles, as do the antiferromagnetic interactions between neighbouring spins in the Ising model. In contrast to engineered mesoscopic systems<sup>10–14</sup>, however, our colloidal system facilitates easy tuning of the effective antiferromagnetic interaction through changes in the diameter of temperature-sensitive microgel spheres<sup>27</sup>. The colloidal system also permits direct visualization of thermal motion at the single-particle level. In the limit of weak confinement, or weak interaction strength, system properties closely follow those predicted for the antiferromagnetic Ising model, but in the limit of strong confinement, they do not. For strong interactions, the lattice deforms to maximize free volume, and the collective nature of the free-volume-dominated free energy characteristic of most soft-matter systems becomes important. We understand these effects

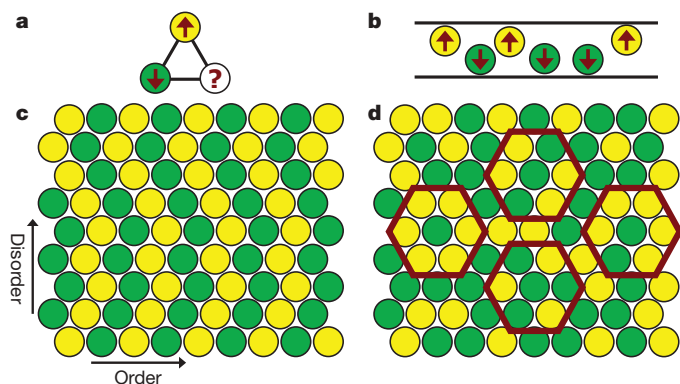


**Figure 1 | Ising ground state.** **a**, Three spins on a triangular plaquette cannot simultaneously satisfy all antiferromagnetic interactions. **b**, For colloids confined between walls separated by a distance of the order 1.5 sphere diameters (side view), particles move to opposite walls in order to maximize free volume. **c**, **d**, Ising ground-state configurations wherein each triangular plaquette has two satisfied bonds and one frustrated bond. **c**, Zigzag stripes generated by stacking rows of alternating up/down particles with random sidewise shifts; all particles have exactly 2 frustrated neighbours. **d**, Particles in disordered configurations have 0, 1, 2 or 3 frustrated neighbours (red hexagons).

<sup>1</sup>Department of Physics and Astronomy, University of Pennsylvania, 209 South 33rd Street, Philadelphia, Pennsylvania 19104, USA. <sup>2</sup>Department of Physics, Hong Kong University of Science and Technology, Clear Water Bay, Kowloon, Hong Kong. <sup>†</sup>Present address: Department of Physics of Complex Systems, Weizmann Institute of Science, Rehovot 76100, Israel. \*These authors contributed equally to this work.

theoretically in terms of tiling of the plane by isosceles triangles. The tiling scheme identifies a ground state consisting of zigzagging stripes with subextensive entropy. Interestingly, in contrast to Ising-model predictions, first measurements of single-particle 'spin-flipping' suggest that flipping dynamics depend not only on the number of nearest-neighbour frustrated 'bonds', but on how these bonds are arranged. Thus we begin to explore connections between frustrated soft matter and hard materials such as frustrated antiferromagnetic media. (Unless otherwise specified, we use 'antiferromagnetic Ising model' to refer to antiferromagnetic spins on a rigid triangular lattice; we will, however, also discuss this model on a deformable lattice.)

### Experimental system

For walls separated by distances of the order of 1.5 sphere diameters, the particles maintain in-plane triangular order but buckle out-of-plane (Fig. 2a, d). This buckling minimizes system free energy,  $F = U - TS$ , where  $U$  is internal energy,  $T$  temperature and  $S$  entropy. The bare interaction potential between our weakly charged<sup>27</sup> particles was measured to be short ranged and repulsive<sup>28</sup>, that is, nearly hard core. Thus the dominant contribution to the free energy is entropic. Spheres will move apart to minimize internal energy and to maximize their free volume and entropy resulting from it. This effect gives rise to multi-body effective interactions between spheres which, for low volume fractions, can be well approximated by a two-body repulsive entropic potential with range of the order of the interparticle spacing<sup>29</sup>. At high volume fraction, many-body contributions to the potential may become important. The effective repulsion causes spheres to move to the top or bottom wall, and nearest neighbours maximize free volume by moving to opposite walls (Fig. 1b). Buckled colloidal monolayers were first observed more than two decades ago<sup>16–18</sup>, and the antiferromagnetic analogy was then suggested<sup>17,30</sup> (note that ref. 30 includes the experimental work reported in ref. 16). However, to date, few quantitative measurements have been performed on this system class, and the themes explored by most early work centred on structural transitions exhibited by colloidal thin films as a function of increasing sample thickness<sup>17–20,22–24</sup>, rather than their connection to frustrated antiferromagnets. The use of temperature-sensitive diameter-tunable NIPA (N-isopropyl acrylamide) microgel spheres<sup>27</sup> also distinguishes our experiments from

earlier work. By varying temperature we change particle size and sample volume fraction and, therefore, vary the strength of the effective antiferromagnetic interparticle interactions.

Samples were prepared at low volume fraction near the melting point to produce 2D crystal domains with  $\sim 10^4$  spheres covering an area of the order of  $60 \mu\text{m}^2$ . Video microscopy measurements were carried out far from grain boundaries on an  $\sim 32 \mu\text{m}^2$  central area ( $\sim 2,600$  spheres) within the larger crystal domain. Particle motions were observed by microscope, recorded to videotape using a CCD camera and tracked by standard image-processing techniques<sup>31</sup>. In most colloid experiments, the important thermodynamic control variable is particle volume fraction. The present experiment achieved substantial variation in sphere diameter using small changes in temperature, which altered thermal energies by less than 1%. Here we monitor and report temperature rather than volume fraction because the interactions between spheres contain a soft 'tail' that introduces some ambiguity into the assignment of a geometric diameter to the particles. Below  $24^\circ\text{C}$ , the system is jammed and no dynamics are observed. Above  $27.5^\circ\text{C}$ , the in-plane crystals melt. Our primary measurements of the frustrated states probe five temperatures from  $24.7^\circ\text{C}$  to  $27.1^\circ\text{C}$  in  $0.6^\circ\text{C}$  steps. In this range, the hydrodynamic diameter of the nearly-density-matched particles decreases linearly with increasing temperature from  $0.89 \mu\text{m}$  to  $0.76 \mu\text{m}$  (see Supplementary Fig. 1), whereas the average in-plane particle separation remains constant (see Supplementary Table 1). The measured in-plane structures are crystalline. To reach thermal equilibration, the sample was annealed near the melting point before the temperature was slowly decreased. (Here 'annealed' means that the sample was left to evolve for several hours near the melting point to relieve possible unbalanced pressure and provide time for defects to move to produce higher quality crystals.) Slow cycling through this temperature range produced no hysteresis.

### Antiferromagnetic order

The images in Fig. 2a, d show roughly half of the spheres as bright because they are in the focal plane of the microscope; the other half, located near the bottom plate, are slightly out-of-focus and appear dark. A histogram, based on image brightness, showing the degree to which particles are 'up' or 'down' is given in Supplementary Fig. 2.

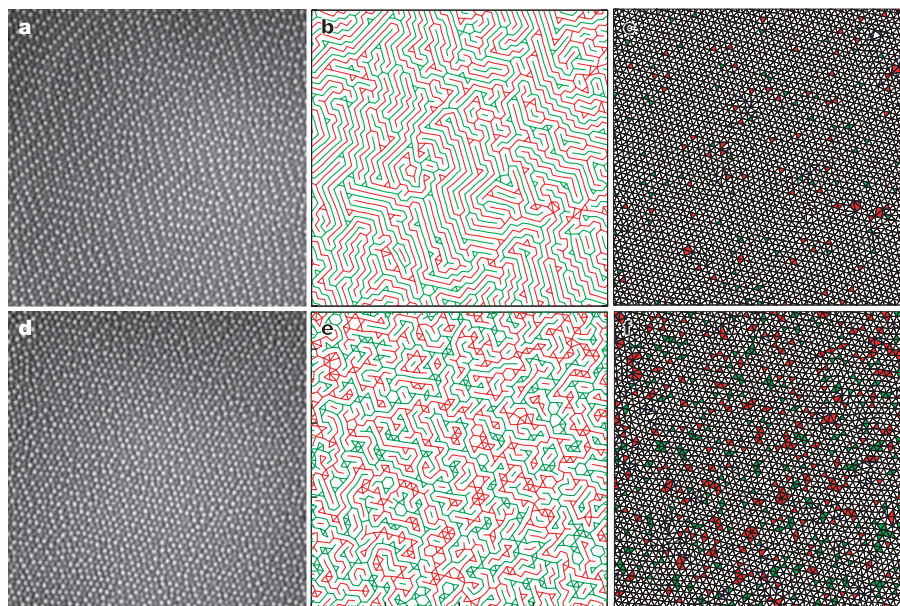


**Figure 2 | Buckled monolayer of colloidal spheres.** Shown are data from an area of  $32 \mu\text{m}^2$  at  $T = 24.7^\circ\text{C}$  (a–c) and  $27.1^\circ\text{C}$  (d–f). **a, d**, Bright spheres, up; dark spheres, down. **b, e**, Labyrinth patterns obtained by drawing only the frustrated up–up (red) and down–down (green) bonds. **c, f**, Corresponding Delaunay triangulations. Blue dots mark defects in the

triangular lattice, that is, particles that do not have exactly six nearest neighbours. Thermally excited triangles with three spheres up/down are labelled by red/green. These snapshots are taken from Supplementary Movies.



The histogram is bimodal, but clearly a range of ‘up’ and ‘down’ is evident in this classical system. The continuous brightness profile was discretized into two ‘Ising’ states with  $s_i = \pm 1$  (here  $s_i$  refers to the state of particle  $i$ ). The brightness cut-off was chosen near the interior minimum so that half the particles are up and half are down. Shifting this cut-off changed structural and dynamical analyses very little (that is, by a few per cent) for shifts of a few per cent in up/down cut-off. The nature of the frustrated states can be exhibited in different ways in processed images. One way focuses on the ‘bonds’ between particles. We refer to pairs of neighbouring particles ( $i$  and  $j$ ) in opposite states ( $s_i s_j = -1$ ) as satisfied bonds (that is, satisfying the effective antiferromagnetic interaction), and to up–up or down–down pairs (with  $s_i s_j = 1$ ) as frustrated bonds. Images show that the frustrated bonds form a nearly single-line labyrinth (Fig. 2b) at low temperature that then nucleates into domains (Fig. 2e) at high temperature. Local antiferromagnetic order is alternatively characterized by the average number of frustrated bonds per particle,  $\langle N_f \rangle$ . In the limit of weak interactions, an Ising system chooses a completely random configuration with half of the six bonds satisfied and half frustrated, leading to  $\langle N_f \rangle = 3$ . In the limit of strong interactions, on the other hand, each triangular plaquette has one frustrated bond (Fig. 1a), a third of the bonds are frustrated, and  $\langle N_f \rangle = 2$ .  $\langle N_f \rangle$  is a linear rescaling of the density of excited triangles (3 up or 3 down) in Fig. 2c, f, which ranges from 0 in the Ising ground state to 0.5 for a random configuration. We find that  $\langle N_f \rangle$  decreased from approximately 2.5 to 2.1 in the temperature interval 27.1–24.7 °C. Detailed statistics of the different local configurations are presented in Supplementary Table 1.

We first consider the static properties of the frustrated samples. In particular, we aim to identify similarities and differences between the colloidal system and the Ising model. As the temperature is lowered to increase particle diameter,  $\langle N_f \rangle$  is observed to approach 2. This behaviour is expected in the Ising-model ground state. However, the vast majority of Ising ground-state configurations are disordered. The colloidal monolayers, by contrast, condense into stripe phases. The stripes are not straight, as could be produced by higher-order inter-particle interactions<sup>32</sup>. Rather, they bend and form zigzag patterns<sup>22–26</sup> (see Fig. 2a and configuration statistics in Supplementary Table 1). In this colloidal zigzag-striped phase, we measured spatial correlations  $\Gamma(i-j) = [\langle s_i s_j \rangle - \langle s \rangle^2] / [\langle s^2 \rangle - \langle s \rangle^2]$  over separations  $|i-j|$ , along the principal lattice directions, of up to 20 particles, and found that they decay exponentially in magnitude with alternating sign (Supplementary Fig. 4).  $\Gamma(i-j)$  is positive for  $i-j$  even and negative for  $i-j$  odd. In contrast,  $\Gamma(i-j)$  averaged over the Ising ground state is positive when  $i-j$  is an integer multiple of 3. Furthermore, for zigzagging stripes each particle has exactly two frustrated neighbours (Fig. 1c), whereas in the fully disordered Ising ground state  $N_f$  can be 0, 1, 2 or 3 (Fig. 1d) and only the average  $\langle N_f \rangle$  is 2. These observations suggest that fluctuations in  $N_f$ , that is,  $\text{Var}(N_f) = \langle N_f^2 \rangle - \langle N_f \rangle^2$ , might be a useful measure for distinguishing the zigzag-stripe phase observed here from the disordered Ising ground state. Figure 3 plots the behaviour of  $\text{Var}(N_f)$  as a function of  $\langle N_f \rangle$  for the Ising model and for data obtained both from experiments and from hard-sphere Monte Carlo simulations (see Supplementary Information). Results from experiment and simulation agree at both low and high volume fraction and differ from those of the Ising model, especially at high volume fraction when interactions are strong. Three length scales affect the physics in this problem: sphere diameter, wall separation, and lattice constant. Therefore, two length ratios can be varied. The simulations showed explicitly (Fig. 3, Supplementary Fig. 5) that the frustration behaviours as functions of sphere diameter for different plate separations were similar as long as the plate separation did not exceed approximately two particle diameters<sup>22,23</sup>.

### Zigzagging stripes

Ideal geometrically frustrated systems, such as the antiferromagnetic Ising model, are highly degenerate with extensive entropy at zero

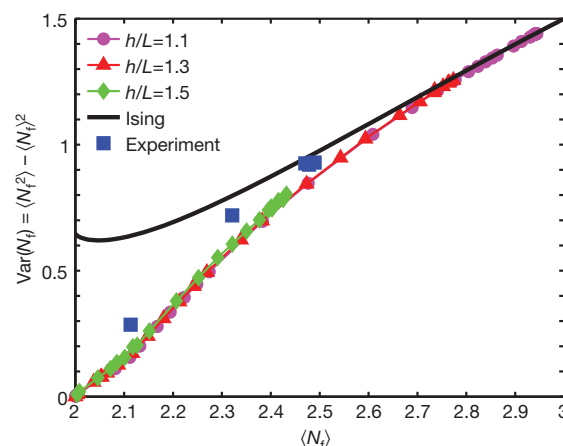


**Figure 3 | Fluctuation in the number of frustrated bonds per particle as a function of its average.** Experiments quantitatively agree with hard-sphere simulations at different plate separations,  $h$ , normalized by the average in-plane lattice constant,  $L$ . Simulations collapse onto a single curve and deviate significantly from the behaviour in the Ising model.

temperature. However, in real materials, subtle effects—for example anisotropic interactions<sup>9</sup>, long-range interactions<sup>32</sup>, boundary conditions<sup>33</sup> and lattice distortions<sup>34–36</sup>—relieve frustration. Our partially ordered zigzag-stripe phase at high volume fraction is an example of frustration relief by lattice distortion. In the colloidal monolayer the triangular packing is self-assembled, and the particles are not forced to remain at fixed positions on the lattice<sup>26</sup>. This deformability and the fact that the free volume of the system is a collective function of all particle positions breaks the mapping to simple Ising models with pair-wise-additive nearest-neighbour interactions. In fact, the positions of the colloidal particles may be thought of as comprising a planar structure that crumples between the two confining planes. This ‘crumpling’ leads to deformations of the planar triangular lattice with satisfied bonds (projected onto the plane) on average 3–4% shorter than frustrated bonds (see Supplementary Table 1). This difference is consistent with the notion that each pair of neighbouring particles prefers to be separated by the same fixed distance in three dimensions (3D), whether or not their connecting bond is satisfied.

A simple tiling argument demonstrates why the colloidal system ground-state configurations of stripes and zigzags pack better than the disordered Ising configurations (Fig. 4). The tiling model shows explicitly that maximal volume fractions of stripe and zigzag phases are the same (see Supplementary Information). Each triangular plaquette in the Ising ground state contains two satisfied bonds and one frustrated bond. Thus, when spheres are close-packed in 3D, the equilateral triangle defined by each such triplet of neighbouring particles is tilted, and when projected onto the 2D plane, it deforms into an isosceles triangle with two short sides along the satisfied bonds and one long side along the frustrated bond (Fig. 4a, b). Subsequently, close-packed configurations of the buckled spheres in 3D are described by tilings of the plane by isosceles triangles. Figure 4c shows the configurations of isosceles triangles for different numbers of frustrated bonds ( $N_f$ ) in the basic hexagonal cell. By summing up the angles around the central vertex, one immediately sees that for  $N_f = 0, 1, 3$ , the triangles cannot close-pack. Only the two configurations with  $N_f = 2$  enable tiling the plane with isosceles triangles, or, equivalently, close-packing of the buckled spheres in 3D. Configuration 2b corresponds to a bend in a stripe, and 2c to a stripe continuing along a straight line. Both have the same maximal volume fraction, thus corroborating observations of zigzagging stripes in the experiments and simulations.

Experiments and simulations suggest a possible preference for the stripes to form straight segments rather than to bend easily and thus to generate randomly zigzagging configurations (Fig. 2a). Zigzagging

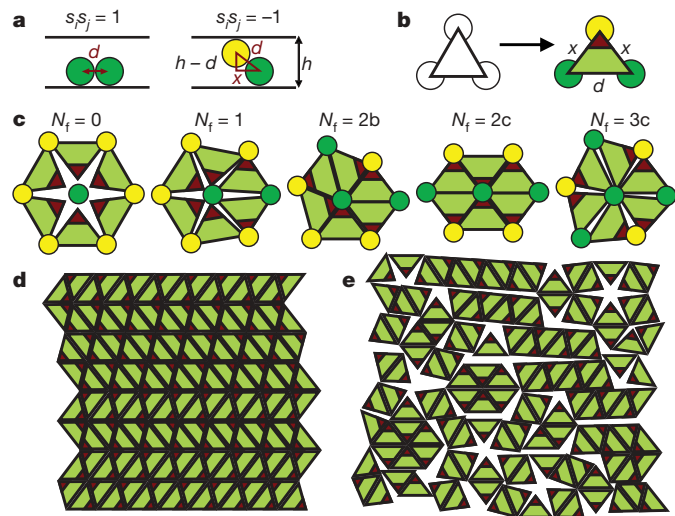


**Figure 4 | Tiling the plane with isosceles triangles.** **a**, Close-packed spheres are separated by one particle diameter  $d$  in 3D. This distance projected on the 2D plane remains  $d$  for a frustrated bond ( $s_i s_j = 1$ ), but is reduced to  $x = \sqrt{d^2 - (h-d)^2}$  for a satisfied bond ( $s_i s_j = -1$ ). **b**, Viewed from above, each plaquette in the lattice tends to deform to an isosceles triangle with one long side ( $d$ ) along the frustrated bond and two short sides ( $x < d$ ) along the satisfied bonds. The angle larger than  $\pi/3$  is marked in red. **c**, All possible in-plane local particle configurations appearing in the Ising ground state. The isosceles triangles can tile the plane without extra space only for  $N_f = 2$ . The 'white space' for  $N_f = 0, 1, 3$  corresponds to additional excluded volume. **d, e**, Tilings corresponding to striped and disordered Ising ground-state configurations, respectively, of Fig. 1c, d.

stripes can be viewed as a random stack of ordered lines of alternating up and down particles (Fig. 1c); thus straight and zigzagging stripes are analogous to the face-centred cubic (f.c.c.) lattice and the random hexagonal-close-packed (r.h.c.p.) structure<sup>20</sup> in 3D. Straight and zigzagging stripes have the same maximal volume fraction in the close-packed limit. However, for smaller volume fractions there may be an order-by-disorder effect<sup>5,37</sup>, giving a small free volume advantage of straight stripes over zigzagging ones, similar to the free volume advantage<sup>38</sup> of f.c.c. over r.h.c.p. in 3D. Indeed, stripes in Fig. 2a persist in the same direction for several particle diameters and the sample appears more ordered than the random zigzag stripes of Fig. 1c.

Instead of an extensive entropy at zero temperature<sup>8</sup>, wherein  $S$  scales linearly with the number of particles in the system ( $N$ ), the buckled system has subextensive entropy. The number of zigzagging striped configurations grows exponentially with the linear dimension of the system (there are two possible ways of placing one row relative to its predecessor in Fig. 1c); hence the entropy scales<sup>39</sup> as  $\sqrt{N}$ . Alternatively, a non-branching single-line labyrinth is dictated by  $\sim \sqrt{N}$  particles on the boundary, and a cluster of order  $\sqrt{N}$  particles should be flipped for the system to rearrange from one zigzag-stripe configuration to another. Subextensive ground-state entropy also appears in related models emulating systems with glassy dynamics<sup>40</sup>. Similar zigzag stripes have been observed in superconducting arrays in external fields<sup>41</sup> and in microscopic Ising models<sup>42</sup>.

### Dynamics

Taken together, these observations have interesting consequences for the ground-state dynamics of frustrated systems. The Ising ground state has a local zero-energy mode, as shown in configuration 3c in Fig. 5a: the central particle can flip without changing the energy of the system, thus rapidly relaxing spin correlations via a sequence of such single spin flips, even at zero temperature. For buckled spheres, on the other hand, the close-packed configurations have only particles with  $N_f = 2$ , and, moreover, even a particle with  $N_f = 3$  in an excited configuration has to cross an energy barrier in order to flip. Thus frustration relief creates a 'glass-like' medium having energy barriers

between the various energy minima. Like the glassy behaviour of an Ising model on a deformable lattice<sup>43,44</sup>, the slow dynamics we observe at low temperature is a consequence of the absence of local zero-energy modes in the bulk.

Our system permits direct visualization of 'spin flipping' and the motions of thermal excitations and defects in frustrated systems (see Supplementary Movies). Thermal excitations labelled as coloured triangles in Fig. 2c, f were typically found to be generated/annihilated in pairs owing to the flipping of a particle shared by the two triangles. Well-isolated thermal excitations, on the other hand, appear to be more stable. To quantify these effects, we first extract the full time trajectory,  $s_i(t)$ , of each particle  $i$  from the movies. In Fig. 5b we plot the single-particle autocorrelation function  $C(t) = [\langle s_i(t)s_i(0) \rangle - \langle s_i \rangle^2] / [\langle s_i^2 \rangle - \langle s_i \rangle^2]$ , averaged over all particles not at lattice defects. As the temperature is lowered, the correlation function develops a stretched exponential form,  $C(t) = \exp[-(t/\tau)^\beta]$ . The measured relaxation time  $\tau$  exhibits a dramatic increase as the particles swell at low temperature, whereas the extracted stretching exponent  $\beta$  decreases, indicating slow dynamics similar to those found in glasses<sup>45</sup>.

To further explore the dynamics of different local configurations (defined in Fig. 5a), Fig. 5c shows the measured flipping rate  $f_i$  of

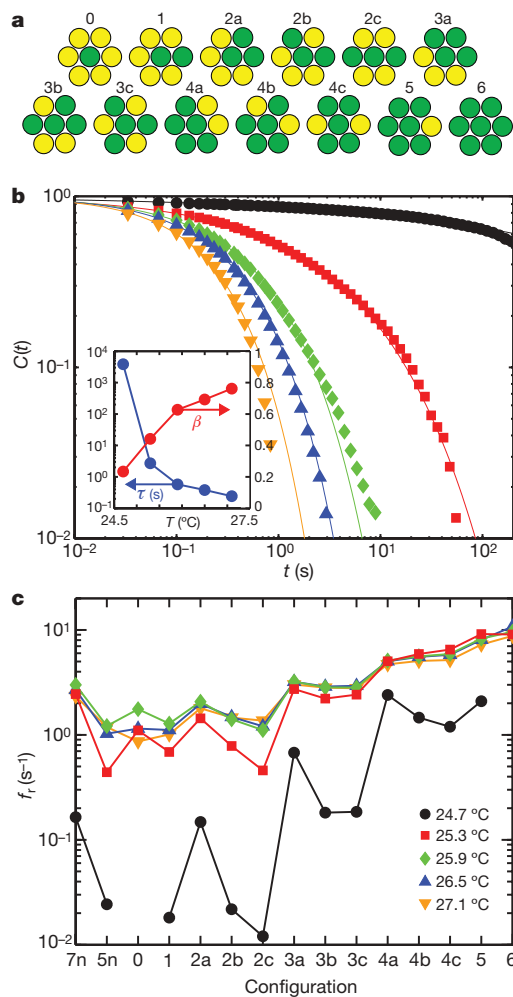


**Figure 5 | Single-particle dynamics.** **a**, Local configurations are labelled by their value of  $N_f$  and an index a, b, c indicating the precise geometrical arrangement of the frustrated neighbours for  $N_f = 2, 3, 4$ . Symmetry under rotation and inversion reduces the  $2^7$  possible configurations to the 13 given here. **b**, Single-particle autocorrelation functions plotted versus decay time. Lines are fits to stretched exponentials  $C(t) = \exp[-(t/\tau)^\beta]$ , with  $\tau$  and  $\beta$  given in the inset. **c**, Flipping rates for the different local environments. Configurations 7n and 5n are defects in the in-plane lattice, with 7 and 5 nearest neighbours.



single particles with a fixed neighbour structure. We measured the probability  $p$  that a particle flips between consecutive images given that the Ising states of its neighbours remained unchanged. The time intervals of  $dt = 1/30$  s between frames were short enough that  $p$  was typically small (0.36 at most) and the flip rate could be approximated by  $f_r = p/dt$ . At high temperature, the behaviour is similar to that of an Ising model undergoing Glauber dynamics:  $f_r \propto \exp(-\Delta E/k_B T)$ , where the energy difference  $\Delta E$  is proportional to the difference in  $N_f$  before and after flipping. As the volume fraction is increased by lowering the temperature, particle dynamics slow by 1–2 orders of magnitude and, more interestingly, significant differences develop between different geometrical configurations with the same  $N_f$ . Such phenomena may not appear in the simple Ising model where the Hamiltonian depends only on  $N_f$ .

Defects in the underlying lattice can strongly affect the properties of frustrated systems. However, detailed knowledge about the role of defects in frustrated systems is very limited. Our experiments permit direct visualization of defects nucleating, annihilating and diffusing (Supplementary Movies). By comparing trajectories containing different numbers and types of defects, initial studies suggest that defects, namely particles that do not have exactly six nearest neighbours, have enhanced in-plane diffusion (Supplementary Fig. 6) and slower flipping dynamics than those averaged over particles with six nearest neighbours.

## Outlook

We have presented experimental measurements of single-particle statics and dynamics in a geometrically frustrated system. Other experimental systems offering ‘single-spin’ resolution are based on lithography<sup>10–12</sup>. An attractive feature of the lithographic systems is that any underlying lattice can be created. Colloidal suspensions in 2D, by contrast, will self-assemble into triangular lattices unless an external potential is applied, and because the colloidal system is entirely self-assembling, it possesses a comparatively rich phenomenology originating from lattice deformability. The colloids also offer the possibility of dynamical studies; the lithography-based arrays, by contrast, are frozen in place.

The 2D colloidal frustrated ‘antiferromagnet’ we have studied provides an ideal platform for future study of the properties of frustrated and glassy systems. Sample dynamics and structure can be microscopically imaged, and the system can be perturbed and manipulated with laser tweezers and other tools. It thus offers hope for deeper insights into the interplay between frustration relaxation and order—for example the formation of phases with lower entropy than the antiferromagnetic Ising ground state—and into the connections between glassy dynamics, frustration and subextensive yet system-size-divergent entropy. Further experiments to address these issues are readily envisaged. For example, potential energy landscapes for the particles can be created using laser tweezers of varying periodicity and strength (including rigid lattices), enabling experimenters to explore the role of lattice deformability in the dynamics and the creation of structure. Optical or magnetic traps can be used to flip and to move individual spins, and video microscopy can be used to probe the resulting system’s responses. Boundaries affect frustration, but they are not well studied; such effects could be created by changing sample cell geometry or by fixing particles to the boundary. Gravity, external fields, and surface treatment can be used to mimic the effects of applied magnetic fields on frustrated magnetic systems. Defects affect frustration but have not been explored at the single-particle level; such effects can be studied by doping with particles having different shapes and interaction potentials. In the theoretical arena, it will be interesting to consider possible modifications to the rigid-lattice Ising model that generate a zigzagged-stripe ground state. This should allow a fuller exploration of the relation between buckled colloidal systems and the compressible Ising model, including the possibility of generating order-by-disorder via thermal fluctuations. It should also

enable the study of glassy dynamics arising from subextensive zero-temperature entropy.

**Note added in proof:** Blunt *et al.*<sup>46</sup> have recently measured motions of excitations in a molecular system which may be mapped onto the triangular-lattice antiferromagnetic Ising model.

Received 11 July; accepted 21 October 2008.

- Moessner, R. & Ramirez, A. R. Geometrical frustration. *Phys. Today* **59**, 24–26 (2006).
- Pauling, L. The structure and entropy of ice and of other crystals with some randomness of atomic arrangement. *J. Am. Chem. Soc.* **57**, 2680–2684 (1935).
- Harris, M. J., Bramwell, S. T., McMorrow, D. F., Zeiske, T. & Godfrey, K. W. Geometrical frustration in the ferromagnetic pyrochlore  $\text{Ho}_2\text{Ti}_2\text{O}_7$ . *Phys. Rev. Lett.* **79**, 2554–2557 (1997).
- Bramwell, S. T. & Gingras, M. J. P. Spin ice state in frustrated magnetic pyrochlore materials. *Science* **294**, 1495–1501 (2001).
- Moessner, R. Magnets with strong geometric frustration. *Can. J. Phys.* **79**, 1283–1294 (2001).
- Ramirez, A. R. Geometric frustration: Magic moments. *Nature* **421**, 483 (2003).
- Anderson, P. W. The resonating valence bond state in  $\text{La}_2\text{CuO}_4$  and superconductivity. *Science* **235**, 1196–1198 (1987).
- Wannier, G. H. Antiferromagnetism. The triangular Ising net. *Phys. Rev.* **79**, 357–364 (1950); erratum *Phys. Rev. B* **7**, 5017 (1973).
- Houtappel, R. M. F. Order-disorder in hexagonal lattices. *Physica* **16**, 425–455 (1950).
- Davidović, D. *et al.* Correlations and disorder in arrays of magnetically coupled superconducting rings. *Phys. Rev. Lett.* **76**, 815–818 (1996).
- Hilgenkamp, H. *et al.* Ordering and manipulation of the magnetic moments in large-scale superconducting  $\pi$ -loop arrays. *Nature* **422**, 50–53 (2003).
- Wang, R. F. *et al.* Artificial ‘spin ice’ in a geometrically frustrated lattice of nanoscale ferromagnetic islands. *Nature* **439**, 303–306 (2006).
- Möller, G. & Moessner, R. Artificial square ice and related dipolar nanoarrays. *Phys. Rev. Lett.* **96**, 237202 (2006).
- Nisoli, C. *et al.* Ground state lost but degeneracy found: The effective thermodynamics of artificial spin ice. *Phys. Rev. Lett.* **98**, 217203 (2007).
- Libál, A., Reichhardt, C. & Reichhardt, C. J. O. Realizing colloidal artificial ice on arrays of optical traps. *Phys. Rev. Lett.* **97**, 228302 (2006).
- Koshikawa, Y. & Hachisu, S. [in Japanese] *Lecture at Colloid Symposium of Japan* (1982).
- Pieranski, P., Strzelecki, L. & Pansu, B. Thin colloidal crystals. *Phys. Rev. Lett.* **50**, 900–903 (1983).
- Van Winkle, D. H. & Murray, C. A. Experimental observation of two-stage melting in a classical two-dimensional screened Coulomb system. *Phys. Rev. Lett.* **58**, 1200–1203 (1987).
- Weiss, J. A., Oxtoby, D. W., Grier, D. G. & Murray, C. A. Martensitic transition in a confined colloidal suspension. *J. Chem. Phys.* **103**, 1180–1190 (1995).
- Pansu, B., Pieranski, P., & Pieranski, P. Direct observation of a buckling transition during the formation of thin colloidal crystals. *J. Phys.* **45**, 331–339 (1984).
- Chou, T. & Nelson, D. R. Buckling instabilities of a confined colloid crystal layer. *Phys. Rev. E* **48**, 4611–4621 (1993).
- Schmidt, M. & Löwen, H. Freezing between two and three dimensions. *Phys. Rev. Lett.* **76**, 4552–4555 (1996).
- Schmidt, M. & Löwen, H. Phase diagram of hard spheres confined between two parallel plates. *Phys. Rev. E* **55**, 7228–7241 (1997).
- Zangi, R. & Rice, S. A. Phase transitions in a quasi-two-dimensional system. *Phys. Rev. E* **58**, 7529–7544 (1998).
- Melby, P. *et al.* The dynamics of thin vibrated granular layers. *J. Phys. Condens. Matter* **17**, S2689–S2704 (2005).
- Osterman, N., Babič, D., Poberaj, I., Dobnikar, J. & Zihnerl, P. Observation of condensed phases of quasiplanar core-softened colloids. *Phys. Rev. Lett.* **99**, 248301 (2007).
- Alsayed, A. M., Islam, M. F., Zhang, J., Collings, P. J. & Yodh, A. G. Premelting at defects within bulk colloidal crystals. *Science* **309**, 1207–1210 (2005).
- Han, Y., Ha, N. Y., Alsayed, A. M. & Yodh, A. G. Melting of two-dimensional tunable-diameter colloidal crystals. *Phys. Rev. E* **77**, 041406 (2008).
- Shokef, Y. & Lubensky, T. C. Stripes, zigzags, and slow dynamics in buckled hard spheres. Preprint at (<http://arxiv.org/abs/0807.4884>) (2008).
- Ogawa, T. A maze-like pattern in a monodisperse latex system and the frustration problem. *J. Phys. Soc. Jpn* **52** (Suppl.), 167–170 (1983).
- Crocker, J. C. & Grier, D. G. Methods of digital video microscopy for colloidal studies. *J. Colloid Interface Sci.* **179**, 298–310 (1996).
- Metcalf, B. D. Ground state spin orderings of the triangular Ising model with the nearest and next nearest neighbor interaction. *Phys. Lett. A* **46**, 325–326 (1974).
- Millane, R. P. & Blakeley, N. D. Boundary conditions and variable ground state entropy for the antiferromagnetic Ising model on a triangular lattice. *Phys. Rev. E* **70**, 057101 (2004).
- Chen, Z. Y. & Kardar, M. Elastic antiferromagnets on a triangular lattice. *J. Phys. C* **19**, 6825–6831 (1986).
- Gu, L., Chakraborty, B., Garrido, P. L., Phani, M. & Lebowitz, J. L. Monte Carlo study of a compressible Ising antiferromagnet on a triangular lattice. *Phys. Rev. B* **53**, 11985–11992 (1996).

36. Lee, S.-H., Broholm, C., Kim, T. H., Ratcliff, W. & Cheong, S.-W. Local spin resonance and spin-Peierls-like phase transition in a geometrically frustrated antiferromagnet. *Phys. Rev. Lett.* **84**, 3718–3721 (2000).
  37. Villain, J., Bidaux, R., Carton, J. P. & Conte, R. Order as an effect of disorder. *J. Phys.* **41**, 1263–1272 (1980).
  38. Mau, S. C. & Huse, D. A. Stacking entropy of hard-sphere crystals. *Phys. Rev. E* **59**, 4396–4401 (1999).
  39. Liebmann, R. *Statistical Mechanics of Periodic Frustrated Ising Systems* (Springer, 1986).
  40. Nussinov, Z. Avoided phase transitions and glassy dynamics in geometrically frustrated systems and non-Abelian theories. *Phys. Rev. B* **69**, 014208 (2004).
  41. Shih, W. Y. & Stroud, D. Two-dimensional superconducting arrays in a magnetic field: Effects of lattice structures. *Phys. Rev. B* **32**, 158–165 (1985).
  42. Nussinov, Z. Commensurate and incommensurate  $O(n)$  spin systems: novel even-odd effects, a generalized Mermin-Wagner-Coleman theorem, and ground states. Preprint at (<http://arxiv.org/abs/cond-mat/0105253>) (2001).
  43. Chakraborty, B., Gu, L. & Yin, H. Glassy dynamics in a frustrated spin system: The role of defects. *J. Phys. Condens. Matter* **12**, 6487–6495 (2000).
  44. Yin, H. & Chakraborty, B. Entropy-vanishing transition and glassy dynamics in frustrated spins. *Phys. Rev. Lett.* **86**, 2058–2061 (2001).
  45. Ediger, M. D. Spatially heterogeneous dynamics in supercooled liquids. *Annu. Rev. Phys. Chem.* **51**, 99–128 (2000).
  46. Blunt, M. O. *et al.* Random tiling and topological defects in a two-dimensional molecular network. *Science* **322**, 1077–1081 (2008).
- Supplementary Information** is linked to the online version of the paper at [www.nature.com/nature](http://www.nature.com/nature).
- Acknowledgements** We thank B. Chakraborty, R. D. Kamien, D. Li, A. J. Liu, C. D. Modes, T.-K. Ng, S. A. Rice, Y. Snir, T. A. Witten and Y. Zhou for discussions. This work was supported primarily by the NSF through MRSEC grant DMR-0520020 and partially by DMR-0804881 (NSF) and by NAG-2939 (NASA).
- Author Contributions** Y.H. and A.M.A. initialized the project. A.M.A. synthesized the particles. Y.H. conducted the experiments. Y.S. performed the simulations and provided the tiling model. Y.H. and Y.S. analysed and explained the experimental data. P.Y. characterized the particles. T.C.L. provided theoretical guidance. A.G.Y. provided experimental guidance. Y.H., Y.S., T.C.L. and A.G.Y. wrote the paper.
- Author Information** Reprints and permissions information is available at [www.nature.com/reprints](http://www.nature.com/reprints). Correspondence and requests for materials should be addressed to Y.S. ([yair.shokef@weizmann.ac.il](mailto:yair.shokef@weizmann.ac.il)) or Y.H. ([yilong@ust.hk](mailto:yilong@ust.hk)).



## ARTICLES

# Neural palmitoyl-proteomics reveals dynamic synaptic palmitoylation

Rujun Kang<sup>1\*</sup>, Junmei Wan<sup>2\*</sup>, Pamela Arstikaitis<sup>1</sup>, Hideto Takahashi<sup>1</sup>, Kun Huang<sup>1</sup>, Aaron O. Bailey<sup>3</sup>, James X. Thompson<sup>3</sup>, Amy F. Roth<sup>2</sup>, Renaldo C. Drisdel<sup>4</sup>, Ryan Mastro<sup>4</sup>, William N. Green<sup>4</sup>, John R. Yates III<sup>3</sup>, Nicholas G. Davis<sup>2\*</sup> & Alaa El-Husseini<sup>1\*‡</sup>

**Palmitoylation regulates diverse aspects of neuronal protein trafficking and function. Here a global characterization of rat neural palmitoyl-proteomes identifies most of the known neural palmitoyl proteins—68 in total, plus more than 200 new palmitoyl-protein candidates, with further testing confirming palmitoylation for 21 of these candidates. The new palmitoyl proteins include neurotransmitter receptors, transporters, adhesion molecules, scaffolding proteins, as well as SNAREs and other vesicular trafficking proteins. Of particular interest is the finding of palmitoylation for a brain-specific Cdc42 splice variant. The palmitoylated Cdc42 isoform (Cdc42-palm) differs from the canonical, prenylated form (Cdc42-prenyl), both with regard to localization and function: Cdc42-palm concentrates in dendritic spines and has a special role in inducing these post-synaptic structures. Furthermore, assessing palmitoylation dynamics in drug-induced activity models identifies rapidly induced changes for Cdc42 as well as for other synaptic palmitoyl proteins, suggesting that palmitoylation may participate broadly in the activity-driven changes that shape synapse morphology and function.**

Recent studies indicate an important role for palmitoylation in modulating neuronal protein trafficking and function<sup>1</sup>. This lipid modification—the attachment of the 16-carbon saturated fatty acid palmitate to cysteines by thioester linkage—functions in tethering proteins to membranes or in the sorting of proteins to particular lipid microdomains such as lipid rafts<sup>1–4</sup>. Like phosphorylation, palmitoylation can be reversible, and can therefore dynamically regulate protein localization. A notable example of palmitoyl regulation in neurons is provided by the scaffolding molecule, postsynaptic density-95 (PSD-95, also known as Dlg4), the activity-directed palmitoylation–depalmitoylation of which regulates AMPA-type glutamate receptor retention at excitatory glutamatergic synapses<sup>5</sup>. Nonetheless, given the technical difficulties hindering palmitoylation analysis, coupled with a lack of palmitoylation consensus sequences for prediction, one expects that the scope of this modification's involvement at the synapse has been underestimated.

## Neural palmitoyl-proteomes

Here we have applied acyl-biotinyl exchange (ABE) proteomic technology<sup>5</sup>, which purifies palmitoylated proteins from complex protein extracts, towards a comprehensive description of rat neural palmitoyl-proteomes. Use of this methodology in the yeast *Saccharomyces cerevisiae* tripled the number of known yeast palmitoyl proteins<sup>6</sup>. This method, based on the previously described ABE chemistry<sup>7</sup>, substitutes biotin for palmitoyl modifications through a sequence of three chemical steps: unmodified cysteine thiols are blocked with *N*-ethyl maleimide; palmitoylation thioester linkages are cleaved with hydroxylamine (HAM); and finally, newly-exposed cysteinyl thiols are marked with a thiol-specific biotinylation reagent. These biotinylated proteins are then affinity-purified with streptavidin-agarose and identified by multidimensional protein identification technology (MudPIT), which is a tandem mass spectrometry-based proteomic methodology<sup>8</sup>.

Proteins from cultured rat embryonic cortical neurons and purified synaptosomal membrane fractions (enriched for both pre- and post-synaptic membranes) extracted from whole adult rat brain tissues were used for this analysis. Application of ABE to cortical neurons purifies a wide spectrum of proteins (Fig. 1a, + HAM). A standard control that allows contaminant proteins to be distinguished involves processing protein extracts through a parallel protocol that omits the hydroxylamine cleavage step<sup>6</sup> (Fig. 1a, – HAM). Four iterations of MudPIT analysis of samples with/without HAM identified 1,643 proteins, including many known palmitoyl proteins. Using spectral count-based quantification<sup>9,10</sup>, identified proteins were plotted by relative plus and minus HAM sample abundance (Fig. 1b and Supplementary Methods). Proteins showing substantial abundances in both the plus and minus HAM samples are probably contaminant proteins, whereas proteins that cluster along the *x*-axis with the known palmitoyl proteins (Fig. 1b, red dots) represent the new palmitoyl-protein candidates. Parallel ABE and MudPIT analysis of synaptosomal membrane fractions yielded a similar collection of known and candidate palmitoyl proteins that overlapped the neuronal collection considerably (Fig. 1c, Supplementary Fig. 1 and Supplementary Tables 1–5).

The combined neuronal and synaptosomal MudPIT data sets were used to assign candidate palmitoyl proteins to a high-confidence group A and a lower-confidence group B. The 64 known palmitoyl proteins identified in these groupings were removed (50 from group A and 14 from group B; 4 known palmitoyl proteins were detected only at low significance levels; known palmitoyl proteins are listed and annotated in Supplementary Table 3). Also removed were proteins that were probably not palmitoylated but were detected by ABE because of their biochemical use of thioester linkages, a category that includes several ubiquitin conjugases/ligases, as well as enzymes using either lipoic acid or phosphopantetheine prostheses

<sup>1</sup>Department of Psychiatry, Brain Research Centre, University of British Columbia, Vancouver V6T 1Z3, British Columbia, Canada. <sup>2</sup>Department of Pharmacology, Wayne State University School of Medicine, Detroit, Michigan 48201, USA. <sup>3</sup>Department of Cell Biology, The Scripps Research Institute, La Jolla, California 10550, USA. <sup>4</sup>Department of Neurobiology, University of Chicago, Chicago, Illinois 60637, USA.

\*These authors contributed equally to this work.

‡Deceased.

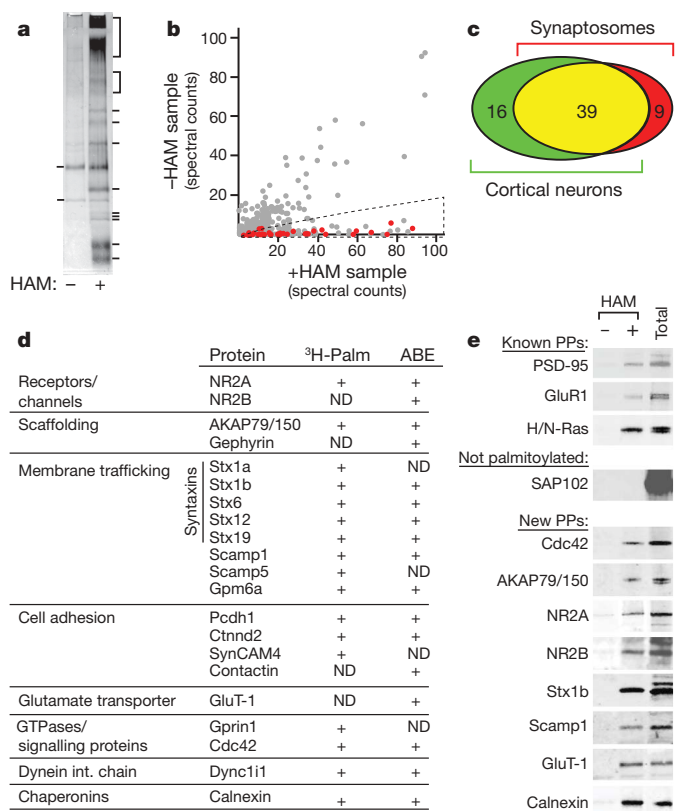


**Figure 1 | Global analysis of neuronal protein palmitoylation.** **a**, ABE purification of palmitoyl proteins from cultured rat cortical embryonic neurons. Proteins purified by parallel ABE protocols, with (+) or without (–) hydroxylamine (HAM) were subjected to SDS–PAGE and silver-staining. Marks at the left show protein species common to both + and – hydroxylamine samples, whereas those at right indicate proteins in which the purification is hydroxylamine-dependent (that is, presumptive palmitoyl proteins). **b**, ABE and MudPIT analysis. The 1,643 different proteins identified from MudPIT analyses of four paired + and – HAM samples are each plotted by their associated averaged + HAM (*x* coordinate) and – HAM (*y* coordinate) spectral counts. The 58 proteins that were known to be palmitoylated before this analysis are shown as red dots. New candidate palmitoyl proteins co-cluster along the *x* axis (region indicated) with the known palmitoyl proteins. **c**, Overlapping identification of known palmitoyl proteins, by the neuronal and synaptosomal proteomic analyses. **d**, Summary of palmitoylation testing. Results are summarized for the 21 candidate proteins that were individually tested for palmitoylation either by [<sup>3</sup>H]palmitate metabolic labelling or by ABE methodologies (see Supplementary Fig. 2). ND, not determined. **e**, Verification of palmitoylation for selected palmitoyl protein (PP) candidates. Proteins, ABE-purified from cultured neurons exactly as for proteomic analysis, both in the presence (+) and absence (–) of HAM, were analysed by western blotting using the indicated specific antibodies. Palmitoylated proteins are expected to show HAM-dependent detection. As a control, a portion of the starting protein sample (before ABE purification) was also screened (total).

(Supplementary Table 6). The 113 group A candidates and 318 group B candidates that remain after these subtractions are listed and annotated in Supplementary Tables 4 and 5, respectively (see Supplementary Methods for analysis details). For 21 of the new candidates, palmitoylation was subsequently confirmed using traditional [<sup>3</sup>H]palmitate metabolic and/or ABE methodologies (Fig. 1d, e and Supplementary Fig. 2).

Many of the new candidate palmitoyl proteins (Box 1 and Supplementary Fig. 1), are hydrophilic proteins, with palmitoylation probably functioning for membrane tethering. However, most of the candidates are predicted transmembrane proteins, in which palmitoylation may provide targeting to specialized membrane microdomains, or perhaps function structurally, modifying the protein's transmembrane architecture. Notable highlights of our list include AKAP79/150

(also known as Akap5) and gephyrin (Gphn) scaffolding proteins, numerous ion channels, voltage-gated Na channels, as well as several transporters for neurotransmitter re-uptake (Box 1). Adding to the list of ionotropic neurotransmitter receptor subunits recently found to be palmitoylated<sup>1,11</sup>, our method identifies the NMDA receptor subunits NR2A (Grin2a) and NR2B (Grin2b), as well as the serotonin receptor subunit 5HT-3C (Htr3c). Numerous SNARE proteins also are prominently detected, including six different syntaxins and three VAMPs. Other important proteins identified include those involved in regulation of growth cone dynamics (semaphorin-4D and latrophilin 1), and synaptic adhesion (protocadherins Pcdh1, 8, 9, 10 and 17, the  $\delta$ -catenin Ctnnd2, synCAM4 (also known as Cadm4 and Necl4) and ephrin receptors).

### A palmitoylated Cdc42 splice variant

Our strong proteomic identification of Cdc42 as a candidate palmitoyl protein was intriguing. Like other Rho GTPases, Cdc42 uses actin cytoskeletal regulation to reshape cellular morphology inducing filipodia in many cell types, and in neurons it has been implicated in inducing axon/dendrite outgrowth, dendritic arborization, and spine formation<sup>12–16</sup>. Although Cdc42 is well known to be prenylated<sup>17</sup>, it has not been shown to be palmitoylated. Furthermore, Cdc42 differs from dually palmitoylated-prenylated G proteins such as H-Ras and N-Ras, in that it lacks cysteines proximal to its carboxy-terminal CaaX prenylation motif (in which C is Cys, a is an aliphatic amino acid, and X is a variety of amino acids) that might act as palmitoyl acceptors. However, a second Cdc42 splice variant has been reported that exchanges in an alternative C-terminal exon, which replaces the prenylation motif with a new C-terminal domain that terminates with the tetrapeptide sequence Cys-Cys-Ile-Phe<sup>18</sup> (Fig. 2a). Using metabolic [<sup>3</sup>H]palmitate labelling, we find that this Cdc42 splice variant (isoform 2) is palmitoylated, whereas the canonical form is not (Fig. 2b). Furthermore, introduction of the Cys-Cys→Ser-Ser mutation (Fig. 2a) eliminates this palmitoylation, implicating these cysteines as the probable palmitoyl acceptors. Notably, although the canonical, prenylated Cdc42 isoform (Cdc42-prenyl) is expressed in all tissues, the variant, palmitoylated form (Cdc42-palm) is expressed only in the brain<sup>18</sup> (Fig. 2c). Quantitative messenger RNA analysis finds the two forms to be expressed at roughly similar levels in brain and neuronal culture (Supplementary Fig. 3).

### Cdc42-palm and dendritic spines

To assess the implications of this neuron-specific Cdc42 palmitoylation, we first examined the effects on localization. The two isoforms show distinct dendritic localizations: whereas Cdc42-prenyl distributes throughout the dendrite to dendritic spine and shaft alike, Cdc42-palm is found to be more heavily concentrated in dendritic spines, a distribution that is abolished by the introduction of the palmitoylation-defective Cys-Cys→Ser-Ser mutation (Fig. 3a). Consistent with this, a neuronal membrane fractionation analysis finds that the two isoforms also show distinctive patterns of fractionation (Supplementary Fig. 4). Cdc42 activity is known to modulate signalling pathways and plasticity-related mechanisms that regulate spine morphology<sup>12–16,19–21</sup>. To determine whether palmitoylation is involved in regulating Cdc42 function at the synapse, we contrasted the effects of the Cdc42 splice variants on spine induction. Constructs expressing constitutively-active (CA) Gly12Val mutant forms of Cdc42(CA)-palm and Cdc42(CA)-prenyl were transfected into developing cultured hippocampal neurons at 7 days *in vitro* (DIV 7), with changes in spine number analysed at DIV 14 (Fig. 3b). Although Cdc42(CA)-prenyl is clearly active in this assay showing a significant induction of dendritic spines, a substantially more robust spine induction is seen for Cdc42(CA)-palm (Fig. 3b). Mutation of the two palmitoyl-accepting cysteines (Cdc42(CA)Cys-Cys→Ser-Ser) abolishes this induction. Similarly, pre-treatment with the general palmitoylation inhibitor 2-bromopalmitate (2BP) blocked spine induction by Cdc42(CA)-palm, but not by



**Box 1 | New palmitoyl-protein candidates**

The proteins with strong proteomic support for palmitoylation are listed by functional category. In the list below, proteins with confirmed palmitoylation (Fig. 1e) are indicated by asterisks. For more complete, annotated listings of both known and newly identified candidate palmitoyl proteins see Supplementary Fig. 1 and Supplementary Tables 3–6.

**Receptors and channels**

The receptors and channels include NR2A\* and NR2B\*, the voltage-gated Na-channel  $\alpha$  subunits Scn1a, Scn2a1, Scn3a and Scn9a, the tweety-like Cl-channels Ttyh1 and Ttyh3, the prostaglandin receptor regulator Ptgfrn, Htr3c and the Ca-activated K-channel Kcnma1.

**Scaffolding proteins**

Scaffolding proteins include AKAP79/150\*, the PSD-95-associated protein Dlgap2 and Gphn (gephyrin)\*.

**Membrane trafficking**

Membrane trafficking proteins include numerous SNARE proteins, the syntaxins Stx1a\*, Stx1b2\*, Stx6\*, Stx7, Stx8, Stx12\* and Stx19\*, and the VAMPs Vamp1, Vamp4 and Vamp7. Other trafficking proteins include Scamp1\*, Scamp3, Scamp5\*, the Rab GTPases Rab1b, Rab3, Rab5, Rab7, Rab10, Rab14, the lysosomal sorting receptor Sort1, the reticulons Rtn1\* and Rtn3 and the proteolipid-protein (PLP)-like Gpm6a (M6a)\*.

**Cell adhesion**

The cell adhesion proteins include Mcam, the ephrin receptors EphA5, EphA3 and EphB2, the ephrin ligand Efnb3, SynCAM4\*, IgSF6 (PGR1; EWI-2), the protocadherins Pcdh1\*, Pcdh8, Pcdh9, Pcdh10, Pcdh17 and Pcdhac2, Ctnnd2 ( $\delta$ -catenin-2)\*, Cxadr (coxsackie and adenovirus receptor), Astn1 (astrotactin-1), Cntn1 (contactin-1), Jam3 (junctional CAM-3), Pkp4 (plakophilin-4), Sema4d (semaphorin-4D), Lphn1 (latrophilin-1), Plxn2 (plexin-B2) and Neo1 (neogenin-1).

**Myelin-associated**

The myelin-associated proteins include Mbp (myelin basic protein and Golli-MBP), Mobp (myelin-associated oligodendrocyte basic protein) and Mog (myelin oligodendrocyte glycoprotein).

**Transporters**

Transporter proteins include the glutamate transporters Slc1a1, Slc1a2 and Slc1a3 (GluT-1)\*, the vesicular GABA transporters Slc6a1 and Slc32a1, the Ca transporters Atp2b1, Atp2b3 and Atp2c1, the Na/Ca exchangers Slc8a1 and Slc8a2, the amino acid transporter Slc3a2 and the choline transporter Slc4a2.

**GTPases and signalling proteins**

GTPases and signalling proteins include Cdc42\*, Rac1, Rras, Rras2, Rala, Ralb, septins Sept3, Sept6 and Sept8, G $\alpha$ -interacting Gprn1\* and Gprn3, the Rho-GDI $\alpha$  Arhgdia, the sprouty-related proteins Spred1 and Spred2, adenylyl cyclases Adcy1, Adcy5, Adcy6 and Adcy9 (palmitoylation has been reported for an adenylyl cyclase previously; however, the isoform identity of the palmitoylated cyclase was not determined<sup>32</sup>), the inositol phosphatase Inpp5a, the FYVE-motif phosphoinositide-binding protein Zfyve28 and the cAMP/cGMP dual phosphodiesterase Pde10a.

**Cytoskeletal proteins**

Cytoskeletal proteins include the actin-binding protein Ablim2 and the dynein intermediate chain Dync1i1\*.

**Chaperones**

Chaperone proteins include calnexin\* and the peptidyl-prolyl isomerase Ppiib.

**Metabolism**

Proteins involved in metabolism include the palmitoyl transferase Zdhc5, Agpat1 (involved in lipid biosynthesis), the calpain Capn5, the gamma-glutamyl transpeptidase Ggt7, the cytochrome b5 reductase Cyb5r3 and the mercaptopyruvate sulphotransferase Mpst.

**Mitochondrial**

Mitochondrial proteins include Cox6c (which acts in the respiratory chain) and the outer membrane porins Vdac1, Vdac2 and Vdac3.

Cdc42(CA)-prenyl. Replication of this analysis in COS-7 cells yielded similar results: a substantially more robust filopodia induction was seen with Cdc42(CA)-palm, with the induction abolished by the Cys-Cys $\rightarrow$ Ser-Ser mutation and severely diminished by 2BP treatment (Supplementary Fig. 5).

To examine the role of endogenously expressed Cdc42, plasmid-based short interfering RNAs (siRNAs) targeting sequences either common or unique to the two Cdc42 isoforms (Supplementary Fig. 6) were transfected into DIV 9 neurons, with spine density analysed on DIV 14 (Fig. 3c). Consistent with a recent siRNA analysis<sup>21</sup>, a construct targeting sequences common to the two isoforms significantly inhibited spine formation (Pan siRNA; Fig. 3c). In terms of individual isoform contributions, a knockdown of Cdc42-prenyl expression showed no discernible effect on spine induction, being indistinguishable from both empty vector or scrambled siRNA controls. In contrast, the Cdc42-palm knockdowns, using either of our two Cdc42-palm-targeted siRNA plasmids, yielded highly significant spine number reductions. Thus, the Cdc42-palm isoform is required for spine induction—a key step of synaptogenesis.

We have used the same siRNA analysis to examine Cdc42 isoform roles in the induction of dendritic filopodia. These filopodia are thought to be spine precursors, extending out from the dendrite to explore the local environment for potential pre-synaptic connections<sup>22</sup>. As we found for spines, filopodia also uniquely rely on the palmitoylated Cdc42 isoform: filopodia numbers are significantly knocked down by the Cdc42-palm-targeted siRNA, but not by the Cdc42-prenyl siRNA (Supplementary Fig. 7c). As a further siRNA-specificity control, we have demonstrated that an overproduced Cdc42-palm, having silent changes in the siRNA target sequence making it siRNA-resistant,

is able to fully rescue the filopodia knockdown (Supplementary Fig. 7a–c). In contrast, Cdc42-prenyl affords only a partial rescue, indicating that Cdc42-prenyl, when similarly overproduced, substitutes only poorly for depleted Cdc42-palm function. Thus, as for spines, Cdc42-palm plays the predominant role in the induction of dendritic filopodia as well.

**Regulatable synaptic palmitoylation**

The functional differences distinguishing the two Cdc42 isoforms must ultimately redound to their different lipid modifications, perhaps reflecting the differential membrane microdomain affinity of the two lipids; palmitoylated proteins typically show increased segregation into raft-like domains<sup>3</sup>, which are known to be enriched in dendritic spines<sup>23</sup>. The two forms also differ with regard to their regulatory potential, with Cdc42-palm potentially controllable by reversible palmitoylation. To examine palmitoyl turnover, a panel of neuronal palmitoyl proteins, including Cdc42, was assessed for palmitate loss after a 5-h period of 2BP-instigated palmitoylation blockade in cultured neurons. In the presence of 2BP, proteins that undergo rapid, constitutive palmitoyl recycling should fail to be repalmitoylated and should therefore be lost from the ABE-purified palmitoyl proteome. Providing proof of principle, we see that PSD-95, which is known to undergo rapid palmitoyl cycling<sup>5</sup>, is indeed largely lost from the 2BP-treated palmitoyl proteome (Fig. 4a, b). The unaltered PSD-95 levels detected in the starting, unpurified protein extracts (Fig. 4a, total panels), indicates this to be palmitoyl turnover, not protein turnover. Significant palmitoyl turnovers were also seen for Cdc42, as well as for two other G proteins, H/N-Ras and Rho-B (Fig. 4a, b). In contrast, the 2BP treatment had little or no effect on other proteins, namely Snap25,

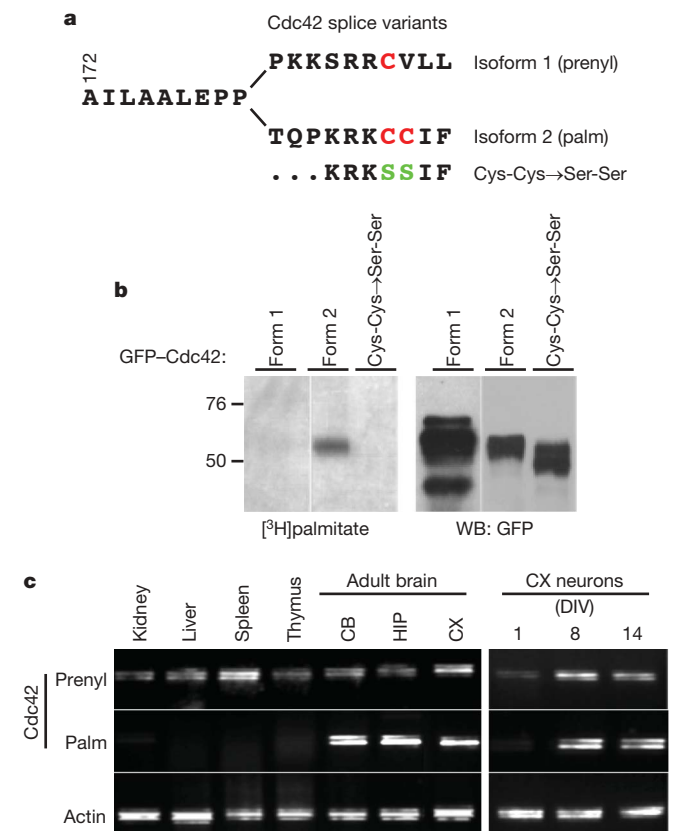


**Figure 2 | Palmitoylation of a brain-specific Cdc42 splice variant.**

**a**, C-terminal amino acid sequences of the two alternatively-spliced Cdc42 isoforms. Isoform 1 is the previously characterized prenylated form of Cdc42 (Cdc42-prenyl), whereas isoform-2 is the variant form, shown in panel **b** to be palmitoylated (Cdc42-palm). The Cys-Cys→Ser-Ser mutation removes the two putative palmitoyl-accepting cysteines from Cdc42-palm. **b**, Cdc42 isoform-2 (Cdc42-palm) is palmitoylated. COS-7 cells transfected by the indicated GFP-Cdc42 constructs were metabolically labelled with [<sup>3</sup>H]palmitic acid. GFP-Cdc42 proteins were immunoprecipitated then subjected either to autoradiography to assess palmitate incorporation, or to western analysis (WB). **c**, Cdc42-palm expression is limited to the brain. Tissue specific expression of the two Cdc42 isoforms was analysed by RT-PCR. RNA was analysed from the indicated organs, brain regions (cerebellum (CB); hippocampus (HIP); cortex (CX)), as well as from developing cultured embryonic cortical neurons.

synaptotagmin 1 (Syt1), Scamp1 and the glutamate transporter GluT-1 (Slc1a3), indicating that the palmitoyl modifications of these proteins are relatively stable under basal conditions; we note that these proteins showing stable palmitoylation are largely presynaptic. The differential palmitoyl-modification stabilities for Cdc42, Snap25, Stx1b and Syt1 have been confirmed by [<sup>3</sup>H]palmitate labelling pulse-chase analysis (Supplementary Fig. 8). We also find that 2BP treatment results in a notable inhibition of endogenous neuronal Cdc42 activity (Supplementary Fig. 9). In addition to affecting Cdc42 palmitoylation, 2BP may also affect upstream components in this pathway, thus potentially affecting Cdc42 activity indirectly.

Regulated palmitoylation may have a role in modulating the cytoskeletal changes that are associated with activity-driven synapse remodelling<sup>24</sup>. To gain insights into how palmitoyl regulation might couple to synaptic activity, we have tracked our test panel of neuronal palmitoyl proteins for rapidly-induced palmitoylation changes in response to a 5-min treatment with 50  $\mu$ M glutamate—a treatment that modulates synaptic activity and spine morphology through the activation of synaptic and extrasynaptic glutamate receptors<sup>25–28</sup>. The effects on palmitoylation are surprisingly broad, with proteins showing both increases and decreases in palmitoylation (Fig. 4c and Supplementary Fig. 10a). The results for Cdc42 are particularly notable, with

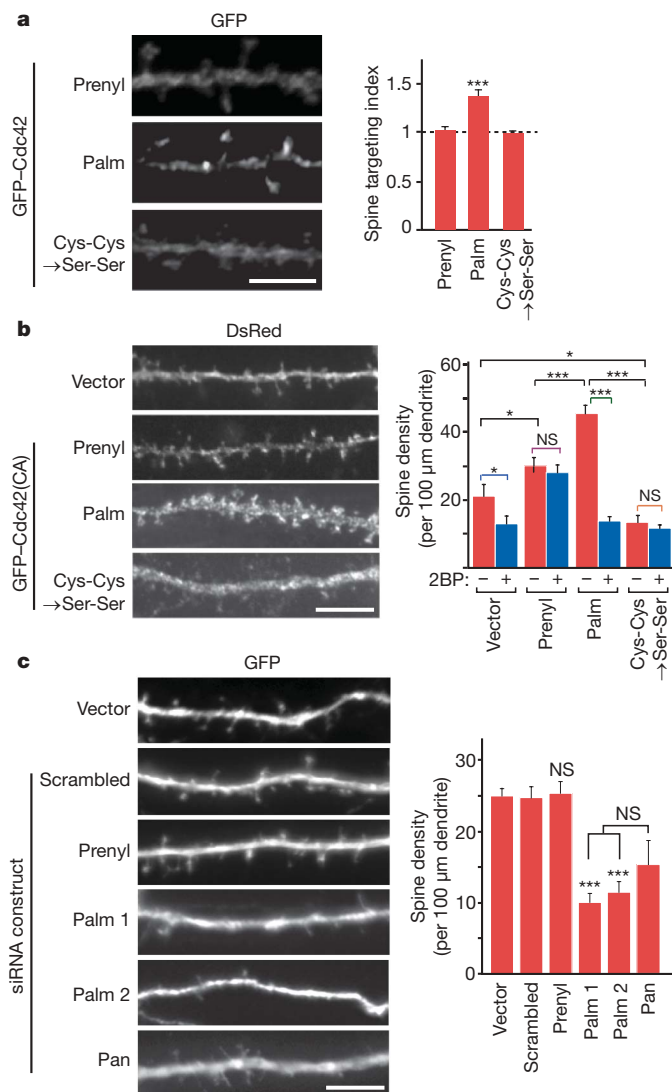


**Figure 3 | Role of Cdc42-palm in dendritic spine induction.** **a**, Different dendritic localizations for Cdc42-palm and Cdc42-prenyl. Hippocampal neurons transfected with the indicated GFP-Cdc42 constructs on DIV 7 were analysed on DIV 14 using anti-GFP immunofluorescence. Relative distribution to dendritic shaft versus spine was analysed with the spine targeting index (STI; see Supplementary Methods). An STI of 1 indicates passive distribution, >1 indicates accumulation of the GFP-Cdc42 construct within spines;  $n = 10$  cells. **b**, Differential spine induction activity for constitutively-active (CA; Gly12Val mutation) versions of the GFP-Cdc42 constructs were co-transfected with a DsRed expression plasmid into hippocampal neurons on DIV 7, with spine density assessed on DIV 14. Parallel cultures were treated with 100  $\mu$ M 2BP for 5 h on DIV 14 to assess effects of palmitoylation inhibition;  $n = 14–24$  cells. The inhibition of spine induction by Cdc42(CA)Cys-Cys→Ser-Ser relative to the vector control is significant, suggesting a dominant-negative action for this mislocalized mutant. **c**, The Cdc42-palm isoform is required for spine development. pSUPER/GFP-based siRNA expression plasmids, targeting sequences specific to either Cdc42-prenyl or Cdc42-palm mRNAs, were transfected into hippocampal neurons on DIV 9, with spine densities assessed on DIV 14. Results for six different knockdown constructs are reported: a prenyl siRNA targeting the Cdc42-prenyl isoform (41 cells analysed); two different palm siRNAs (palm 1 and 2, 25 and 10 cells, respectively) targeting the Cdc42-palm isoform; a Pan siRNA targeting a sequence common to both isoforms (12 cells); a scrambled siRNA of a scrambling of a Pan siRNA target sequences (31 cells); and an empty pSUPER/GFP vector (56 cells). COS-7 cell testing of knockdown efficacy showed that the four knockdown constructs reduced expression of their target isoform by 65–70% (Supplementary Fig. 6). \* $P < 0.05$ , \*\* $P < 0.01$ , \*\*\* $P < 0.001$ ; scale bars, 5  $\mu$ m; error bars, mean and s.e.m.



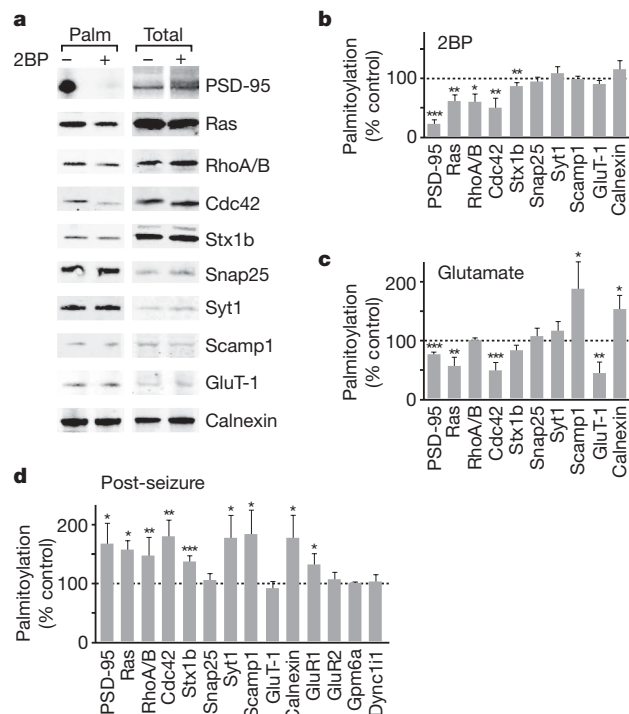


**Figure 4 | Broad modulation of palmitoylation levels in neuronal activity models.** ABE and western analysis were used to follow palmitoylation changes within selected panels of neuronal palmitoyl proteins in response to three treatment regimens: 5-h treatment of cortical neurons with 100  $\mu$ M 2BP to assess constitutive palmitoyl turnover (**a**, **b**), 5-min treatment of cortical neurons with a 50  $\mu$ M glutamate excitatory stimulus (**c**), and after kainic-acid-induced seizures (10 mg kg<sup>-1</sup> kainic acid injected intraperitoneally with brain collected within 30 min of the onset of seizure activity) (**d**). **a**, Example western blots are shown for the 2BP treatment regimen. Total palmitoyl proteins, ABE-purified from the 2BP-treated and -untreated neuronal cultures were blotted with the indicated specific antibodies. To control for 2BP effects on test protein expression levels, the initial unpurified protein extracts were also blotted (total). Western blot data for glutamate- and seizure-induced changes are provided in Supplementary Fig. 10. **b–d**, Quantification of the palmitoylation changes induced by the three treatment protocols. Protein levels measured from the purified palmitoyl-protein samples (palm) were normalized to levels measured from the corresponding unpurified extracts (total). See Supplementary Methods for details. Data are presented from three independent experiments as means and s.e.m.; \* $P < 0.05$ , \*\* $P < 0.01$ , \*\*\* $P < 0.001$ . Note, some antibodies detect several paralogues and/or isoforms: the Cdc42 antibody recognizes both Cdc42-palm and Cdc42-prenyl isoforms; the Ras antibody recognizes H-, N- and K-Ras (only H- and N-Ras are palmitoylated); the Rho A/B antibody recognizes both Rho A and Rho B (only Rho B is palmitoylated).

glutamate inducing rapid depalmitoylation. Correlated with this depalmitoylation, glutamate also results in a rapid dislocation of Cdc42 from dendritic spines (Supplementary Fig. 11). These rapidly induced changes to Cdc42 palmitoylation and localization correlate with, and may contribute to, the rapid spine collapse that accompanies such high-level glutamate treatments in neurons<sup>29</sup>. Thus, the concentration of Cdc42 in spines can be rapidly modified by neuronal activity in a palmitoylation-dependent manner, with dynamic Cdc42 palmitoylation perhaps serving to rapidly regulate synapse architecture in response to changing neuronal activity.

To explore the role of palmitoylation modulation in the *in vivo* brain, we have monitored palmitoylation changes in response to treatment with kainic acid—a drug that enhances neuronal excitability, inducing synchronous neuronal firing, ultimately leading to seizure-like activity<sup>30,31</sup>. Animals were injected with 10 mg kg<sup>-1</sup> kainic acid and tissues were collected within 30 min of seizure activity onset. As with the glutamate-treated neurons (Fig. 4c), we find that surprisingly broad

changes in palmitoylation are induced; in this case, however, increased palmitoylation is the predominant change (Fig. 4d and Supplementary Fig. 10b). These palmitoylation increases suggest actions on pools of non-palmitoylated proteins, with palmitoylation perhaps acting to recruit proteins to synapses. Thus, in brain, as in cultured neurons, changes in neuronal activity result in palmitoylation changes that are rapidly and broadly induced, indicating modulation of palmitoylation to be an early event elicited by changes in neuronal firing. Our proteomic analysis has greatly expanded the neuronal purview of palmitoylation, highlighting a broad role in regulating synaptic function.

## METHODS SUMMARY

Palmitoylation analysis relied in a large part on the ABE purification of palmitoyl proteins *en masse* from whole rat brain, from purified rat synaptosomes, or from cultured embryonic rat neurons. This procedure, which starts with denatured protein extracts, is an *in vitro* chemical exchange of biotin for thioester-linked acyl modifications, with the resulting biotinylated protein being affinity-purified using streptavidin-agarose. Subjecting the purified proteins to MudPIT mass spectral analysis identified the contingent palmitoyl proteins. These purified palmitoyl-proteomic samples were also used to follow individual protein palmitoylation levels in drug-induced neural activity mechanisms, for example, analysing changes after a 5-min treatment of neuronal cultures with 50  $\mu$ M glutamate or the induced changes in the post-seizure brain (kainic acid-induced). For such analysis, purified palmitoyl-proteomic samples from the treated and control conditions were immunoblotted with panels of antibodies specific to individual neuronal palmitoyl proteins; proteins with increased or decreased palmitoylation showed corresponding increased or decreased abundance levels within the purified proteomic samples. Representations within the purified samples were normalized to levels in starting, total protein extracts, eliminating the potential contributions from changes in protein expression or turnover. The localization and function of the two Cdc42 isoforms were assessed in cultured embryonic rat hippocampal neuronal cells transfected with plasmids expressing amino-terminally enhanced green fluorescent protein (EGFP)-tagged versions of the two Cdc42 isoforms (wild-type and mutant forms) or for the knockdown analysis, isoform-specific siRNAs expressed from a plasmid also co-expressing a cytosolic GFP marker. Transfected cells, identified by GFP immunodetection, were analysed for Cdc42 localization and morphology, for example, the number of dendritic filopodia or spines.

Received 28 May; accepted 30 October 2008.

- Huang, K. & El-Husseini, A. Modulation of neuronal protein trafficking and function by palmitoylation. *Curr. Opin. Neurobiol.* **15**, 527–535 (2005).
- Resh, M. D. Palmitoylation of ligands, receptors, and intracellular signaling molecules. *Sci. STKE* **2006**, re14 (2006).
- Smotryns, J. E. & Linder, M. E. Palmitoylation of intracellular signaling proteins: regulation and function. *Annu. Rev. Biochem.* **73**, 559–587 (2004).
- Linder, M. E. & Deschenes, R. J. Palmitoylation: policing protein stability and traffic. *Nature Rev. Mol. Cell Biol.* **8**, 74–84 (2007).
- El-Husseini, A. E.-D. *et al.* Synaptic strength regulated by palmitate cycling on PSD-95. *Cell* **108**, 849–863 (2002).
- Roth, A. F. *et al.* Global analysis of protein palmitoylation in yeast. *Cell* **125**, 1003–1013 (2006).
- Driscoll, R. C. & Green, W. N. Labeling and quantifying sites of protein palmitoylation. *Biotechniques* **36**, 276–285 (2004).
- Link, A. J. *et al.* Direct analysis of protein complexes using mass spectrometry. *Nature Biotechnol.* **17**, 676–682 (1999).
- Liu, H., Sadygov, R. G. & Yates, J. R. III. A model for random sampling and estimation of relative protein abundance in shotgun proteomics. *Anal. Chem.* **76**, 4193–4201 (2004).
- Wan, J. *et al.* Palmitoylated proteins: purification and identification. *Nature Protoc.* **2**, 1573–1584 (2007).
- Hayashi, T., Rumbaugh, G. & Huganir, R. L. Differential regulation of AMPA receptor subunit trafficking by palmitoylation of two distinct sites. *Neuron* **47**, 709–723 (2005).
- Nishimura, T. *et al.* Role of numb in dendritic spine development with a Cdc42 GEF intersectin and EphB2. *Mol. Biol. Cell* **17**, 1273–1285 (2006).
- Negishi, M. & Katoh, H. Rho family GTPases and dendrite plasticity. *Neuroscientist* **11**, 187–191 (2005).
- Choi, J. *et al.* Regulation of dendritic spine morphogenesis by insulin receptor substrate 53, a downstream effector of Rac1 and Cdc42 small GTPases. *J. Neurosci.* **25**, 869–879 (2005).
- Scott, E. K., Reuter, J. E. & Luo, L. Small GTPase Cdc42 is required for multiple aspects of dendritic morphogenesis. *J. Neurosci.* **23**, 3118–3123 (2003).
- Nakazawa, T. *et al.* p250GAP, a novel brain-enriched GTPase-activating protein for Rho family GTPases, is involved in the N-methyl-D-aspartate receptor signaling. *Mol. Biol. Cell* **14**, 2921–2934 (2003).

17. Wilson, A. L. *et al.* Prenylation of Rab8 GTPase by type I and type II geranylgeranyl transferases. *Biochem. J.* **333**, 497–504 (1998).
18. Marks, P. W. & Kwiatkowski, D. J. Genomic organization and chromosomal location of murine Cdc42. *Genomics* **38**, 13–18 (1996).
19. Kreis, P. *et al.* The p21-activated kinase 3 implicated in mental retardation regulates spine morphogenesis through a Cdc42-dependent pathway. *J. Biol. Chem.* **282**, 21497–21506 (2007).
20. Node-Langlois, R., Muller, D. & Boda, B. Sequential implication of the mental retardation proteins ARHGEF6 and PAK3 in spine morphogenesis. *J. Cell Sci.* **119**, 4986–4993 (2006).
21. Wegner, A. M. *et al.* N-wasp and the arp2/3 complex are critical regulators of actin in the development of dendritic spines and synapses. *J. Biol. Chem.* **283**, 15912–15920 (2008).
22. Ethell, I. M. & Pasquale, E. B. Molecular mechanisms of dendritic spine development and remodeling. *Prog. Neurobiol.* **75**, 161–205 (2005).
23. Hering, H., Lin, C. C. & Sheng, M. Lipid rafts in the maintenance of synapses, dendritic spines, and surface AMPA receptor stability. *J. Neurosci.* **23**, 3262–3271 (2003).
24. Fischer, M. *et al.* Rapid actin-based plasticity in dendritic spines. *Neuron* **20**, 847–854 (1998).
25. Ehlers, M. D. Activity level controls postsynaptic composition and signaling via the ubiquitin-proteasome system. *Nature Neurosci.* **6**, 231–242 (2003).
26. Kirov, S. A. & Harris, K. M. Dendrites are more spiny on mature hippocampal neurons when synapses are inactivated. *Nature Neurosci.* **2**, 878–883 (1999).
27. McKinney, R. A. *et al.* Miniature synaptic events maintain dendritic spines via AMPA receptor activation. *Nature Neurosci.* **2**, 44–49 (1999).
28. Soriano, F. X. *et al.* Preconditioning doses of NMDA promote neuroprotection by enhancing neuronal excitability. *J. Neurosci.* **26**, 4509–4518 (2006).
29. Halpain, S., Hipolito, A. & Saffer, L. Regulation of F-actin stability in dendritic spines by glutamate receptors and calcineurin. *J. Neurosci.* **18**, 9835–9844 (1998).
30. Fannjiang, Y. *et al.* BAK alters neuronal excitability and can switch from anti- to pro-death function during postnatal development. *Dev. Cell* **4**, 575–585 (2003).
31. Chen, L. & Toth, M. Fragile X mice develop sensory hyperreactivity to auditory stimuli. *Neuroscience* **103**, 1043–1050 (2001).
32. Mollner, S., Beck, K. & Pfeuffer, T. Acylation of adenylyl cyclase catalyst is important for enzymic activity. *FEBS Lett.* **371**, 241–244 (1995).

**Supplementary Information** is linked to the online version of the paper at [www.nature.com/nature](http://www.nature.com/nature).

**Acknowledgements** This paper is dedicated to the memory of our friend and colleague, Alaa El-Husseini, whose ideas about palmitoylation and plasticity inspired this work (deceased 23 Dec 2007). We thank J. Levinson, M.-F. Lise, C. Jiang and E. Yu for technical assistance. This work was supported by grants to A.E.-H. from the Canadian Institutes for Health Research (CIHR) (A.E.-H., 20R90479 and 20R91909), the Michael Smith foundation for Health Research (A.E.-H., 20R52464), the EJLB Foundation and Neuroscience Canada (A.E.-H., 20R61933), as well as from grants from the National Institutes of Health to N.G.D. (GM65525), J.R.Y. (RR011823) and W.N.G. (NS043782, DA13602 and DA019695), and the Peter F. McManus Trust. H.T. was supported by a research fellowship from the Uehara Memorial Foundation. We thank L. Raymond, Y. T. Wang, K. Gerrow, R. Hines, M. Prior and I. Papanayotou for comments on manuscript.

**Author Contributions** R.K. and J.W. are co-first authors. R.K. was responsible for assessing candidate palmitoyl-protein palmitoylation, siRNA knockdown effects in neurons, and activity-dependent palmitoylation changes. J.W. was responsible for the ABE purifications of samples used for western blotting and mass spectrometry analysis, and for the quantitative northern analysis. P.A. and H.T. analysed filopodia and spine changes in transfected neurons. K.H. analysed palmitoylated proteins using an ABE assay. A.O.B., J.X.T. and J.R.Y. performed the mass spectrometry. N.G.D. analysed, assembled and interpreted the mass spectral data. R.C.D., R.M. and W.N.G. contributed to analysis of some of the palmitoylated proteins. A.F.R. constructed plasmids, particularly those used for the siRNA analysis and rescue. The original co-corresponding authors, A.E.-H. and N.G.D., provided hypothesis development, experimental design input, data interpretation and co-wrote the manuscript. With the passing of A.E.-H., N.G.D. supervised the experimental analyses and rewriting required for the revised manuscript.

**Author Information** Reprints and permissions information is available at [www.nature.com/reprints](http://www.nature.com/reprints). Correspondence and requests for materials should be addressed to N.G.D. ([ndavis@med.wayne.edu](mailto:ndavis@med.wayne.edu)) or R.K. ([rkang@interchange.ubc.ca](mailto:rkang@interchange.ubc.ca)).



## ARTICLES

# Spliceosomal cleavage generates the 3' end of telomerase RNA

Jessica A. Box<sup>1\*</sup>, Jeremy T. Bunch<sup>1\*</sup>, Wen Tang<sup>1,2</sup> & Peter Baumann<sup>1,2</sup>

Telomeres cap the ends of chromosomes and provide a means to complete replication. The DNA portion of telomeres is synthesized by the enzyme telomerase using part of an RNA subunit as a template for reverse transcription. How the mature 3' end of telomerase RNA is generated has so far remained elusive. Here we show that in *Schizosaccharomyces pombe* telomerase RNA transcripts must be processed to generate functional telomerase. Characterization of the maturation pathway uncovered an unexpected role for the spliceosome, which normally catalyses splicing of pre-messenger RNA. The first spliceosomal cleavage reaction generates the mature 3' end of telomerase RNA (TER1, the functional RNA encoded by the *ter1*<sup>+</sup> gene), releasing the active form of the RNA without exon ligation. Blocking the first step or permitting completion of splicing generates inactive forms of TER1 and causes progressive telomere shortening. We establish that 3' end processing of TER1 is critical for telomerase function and describe a previously unknown mechanism for RNA maturation that uses the ability of the spliceosome to mediate site-specific cleavage.

Telomerase controls the proliferative capacity of cells by replenishing terminal sequences that are lost with each cell division<sup>1</sup>. The amount of telomerase in most somatic cells is not sufficient to counteract telomere shortening, causing proliferation to cease after a finite number of divisions. Whereas high levels of telomerase activity are associated with most cancers<sup>2</sup>, several degenerative syndromes including dyskeratosis congenita, aplastic anaemia and idiopathic pulmonary fibrosis have been attributed to mutations in telomerase components<sup>3–7</sup>. At its core, telomerase is comprised of the catalytic protein subunit and an RNA component that provides the template for telomere repeat synthesis. A number of telomerase-associated proteins have been identified, including dyskerin<sup>8</sup>, which is tightly associated with active telomerase<sup>9</sup>.

Consistent with its enzymatic activity, the catalytic subunit telomerase reverse transcriptase shares sequence and structural similarity with other reverse transcriptases<sup>10,11</sup>. Unlike the evolutionarily conserved catalytic subunit, telomerase RNAs vary widely in length and sequence among species—a fact that has complicated the identification of telomerase RNA genes from several important model organisms. Earlier this year, biochemical approaches yielded the *ter1*<sup>+</sup> gene from *S. pombe*<sup>12,13</sup>, a genetically tractable organism that shares many features of its telomere maintenance machinery with mammalian cells<sup>14–18</sup>. The most abundant 3' end of TER1 was mapped to a putative Sm binding site<sup>12,13</sup>, but longer, polyadenylated forms were also identified<sup>12</sup> and amount to approximately 5% of TER1 RNA in the cell. Multiple isoforms have also been reported for budding yeast and human telomerase RNA<sup>19,20</sup>, but whether longer transcripts represent precursors has remained unclear.

## TER1 harbours an intron

In fission yeast predominantly the shortest form of the transcript lacking a poly(A) tail is found in complex with the catalytic subunit of telomerase<sup>12</sup>. While investigating a possible function for the longer polyadenylated forms, we noticed that approximately 5% of these molecules harboured an internal deletion of 56 nucleotides

immediately downstream of the Sm binding site (Fig. 1a). The sequence at the 5' end of the deletion (G/GUAUGU, where '/' marks the beginning of the deletion) closely matched the most common 5' splice site sequence for pre-mRNAs in the *S. pombe* genome (Supplementary Fig. 1). Furthermore, a match for a branch point sequence (UACUAAAC)<sup>21</sup> and 3' splice site were found inside the 56-nucleotide region (Fig. 1b).

To test whether splicing is important for TER1 maturation, we introduced point mutations into both splice sites and the branch point. After propagating cells containing mutant *ter1* for 80 generations, total RNA was isolated and analysed by reverse transcription and polymerase chain reaction (RT-PCR) amplification of an intron-spanning fragment. In the wild type, both unspliced and spliced forms were observed, but splicing was impaired in the mutants (Fig. 1c). A critical function for the intron in TER1 maturation became apparent when total RNA samples were analysed by northern blotting. Mutations in the 5' splice site and branch point resulted in an 8- to 29-fold reduction in the mature form of TER1 (Fig. 1d). These results established that sequences downstream of the mature 3' end are crucial for telomerase activity.

Intriguingly, changing the sequence of the 3' splice site did not interfere with the formation of mature TER1 (Fig. 1d), despite eliminating splicing (Fig. 1c). Cloning and sequencing of telomerase RNA 3' termini from cells harbouring the 3' splice site mutation confirmed that the mature form extended to the same position as the wild type. Consistent with these observations, cells harbouring a 3' splice site mutation maintained normal telomeres, whereas single-nucleotide changes in the 5' splice site or branch point caused telomeres to shorten by 80% over ~80 generations (Fig. 1e). This, and other experiments described below, strongly argued for a precursor-product relationship between the longer unspliced forms and the mature form found in complex with telomerase. We will therefore refer to the slower migrating forms that extend beyond nucleotide 1213 as precursors and the form terminating at nucleotide 1213 as the mature form.

<sup>1</sup>Stowers Institute for Medical Research, Kansas City, Missouri 64110, USA. <sup>2</sup>Department of Molecular and Integrative Physiology, University of Kansas Medical Center, Kansas City, Kansas 66160, USA.

\*These authors contributed equally to this work.

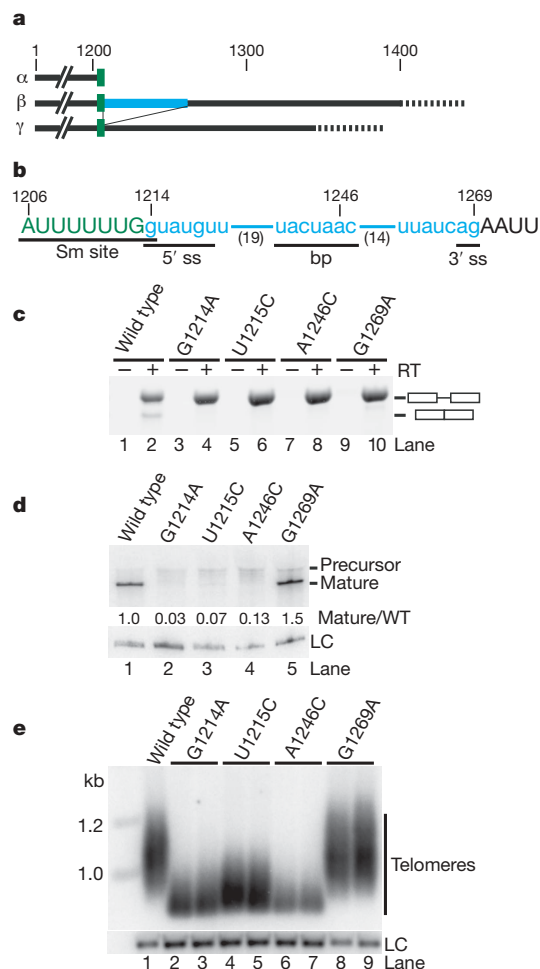


**Figure 1 | An intron in TER1 is essential for RNA maturation.** **a**, TER1 isoforms. Numbers denote positions (in nucleotides) relative to the 5' end of the RNA<sup>31</sup>; the Sm binding site is shown in green, and a blue box represents the 56-nucleotide region missing in the γ form. Dashed lines represent poly(A) tails. **b**, The sequence absent from the γ form (blue) contains consensus 5' and 3' splice sites (ss) and a branch point (bp). Numbers in parentheses indicate nucleotides not shown. Exonic sequences are in uppercase font; the intron in lowercase. **c**, RT-PCR across the intron-containing region. Exons are depicted as boxes, and the intron as a horizontal line. Mutated nucleotides are numbered as in **b**. Reverse transcriptase (RT) was omitted from odd-numbered samples. **d**, Detection of TER1 and snoRNA *snR101* loading control (LC) by northern blot analysis. Precursor and mature forms were assigned on the basis of size, as previously characterized<sup>12</sup>. The term 'mature' signifies a mature 3' end, but the RNA is not necessarily mature in all other features. WT, wild type. **e**, Telomere length was analysed by Southern blotting of EcoRI-digested genomic DNA from two independent isolates for each mutant. Telomere shortening increases the mobility of the terminal EcoRI fragments and decreases hybridization with a telomeric probe relative to a probe against the loading control.

### Partial overlap between the intron and Sm site

Sm proteins participate in RNP biogenesis and are important for the stability and processing of several non-coding RNAs. Deletion of the Sm site in TER1 disrupts maturation and causes telomere shortening in yeast<sup>12,22</sup>. The physical overlap between the Sm site and 5' splice site raised the question of whether the TER1-ΔSm mutant phenotype was caused by the elimination of the 5' splice site. We therefore generated a mutant that disrupts the Sm consensus sequence while retaining the 5' splice site (Fig. 2a). Although the spliced form was detected in this TER1-Sm1 mutant (Supplementary Fig. 2), the mature form was 6-fold less abundant in the mutant cells (Fig. 2b) and consequently telomeres were very short after 100 generations (Fig. 2c). Cloning and sequencing of the 3' end confirmed that the mature form of the TER1-Sm1 RNA

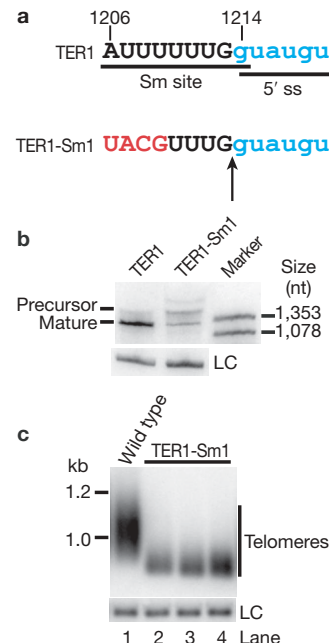


**Figure 2 | Splicing and the Sm binding site.** **a**, The Sm site and 5' splice site (ss) in wild-type TER1 and the TER1-Sm1 mutant. An arrow marks the mature 3' end for wild-type TER1. The TER1-Sm1 3' end was mapped to the same site in 17 out of 18 clones; one clone ended 14 nucleotides further upstream. **b**, Detection of TER1 by northern blotting. HaeIII-digested phiX DNA was run as a marker. **c**, Telomere length analysis on EcoRI-digested genomic DNA.

terminated at the same site as that observed for the wild type (Fig. 2a). The reduced level of mature TER1-Sm1 may reflect a partial impairment of the cleavage reaction. Alternatively, the putative Sm binding site may have a role in regulating RNA stability subsequent to the formation of the mature 3' end.

### The spliceosome functions in TER1 maturation

The presence of splice site and branch point consensus sequences, the detection of spliced product and the phenotypes associated with point mutations in two of the three splice site motifs argued for the spliceosome participating in TER1 maturation. To test this hypothesis directly we turned to an experimental approach that had been used previously to establish the importance of base pairing interactions between the U1 small nuclear RNA (snRNA) and 5' splice sites<sup>23–25</sup>. It was found that a splicing defect caused by a point mutation in a 5' splice site can be rescued by co-expressing a mutant version of the U1 snRNA containing the compensatory nucleotide change. We mutated G1218 in *ter1*<sup>+</sup> to A and C and generated the compensatory versions of *S. pombe* U1 (Fig. 3a). Nucleotide 1217 is the only one of the six nucleotides at the 5' splice site that is not complementary to wild-type U1. Because a change at this position was not expected to impair splicing greatly, a U1217G mutant served as control. The mutant alleles of *ter1* were expressed in a *ter1*<sup>−</sup> strain for ~130 generations before telomere length analysis. As expected, cells harbouring the U1217G mutant maintained wild-type telomeres, whereas the G1218A and G1218C mutations caused an approximately 50% reduction in telomere length (Fig. 3b). Northern blotting of RNA samples from strains expressing the *ter1* mutants revealed that little mature form was produced for G1218A and G1218C (Fig. 3c, lanes 4 and 6). U1 containing the respective compensatory mutation was placed under the control of the *nmt1* promoter and expressed in cells that also contained wild-type U1. Consistent with a direct role for U1 in TER1 maturation, co-expression of the compensatory U1 mutants increased the steady-state level of the mature form by 3.7- and 4.5-fold, respectively, for the two mutations at position 1218 (lanes 5 and 7).



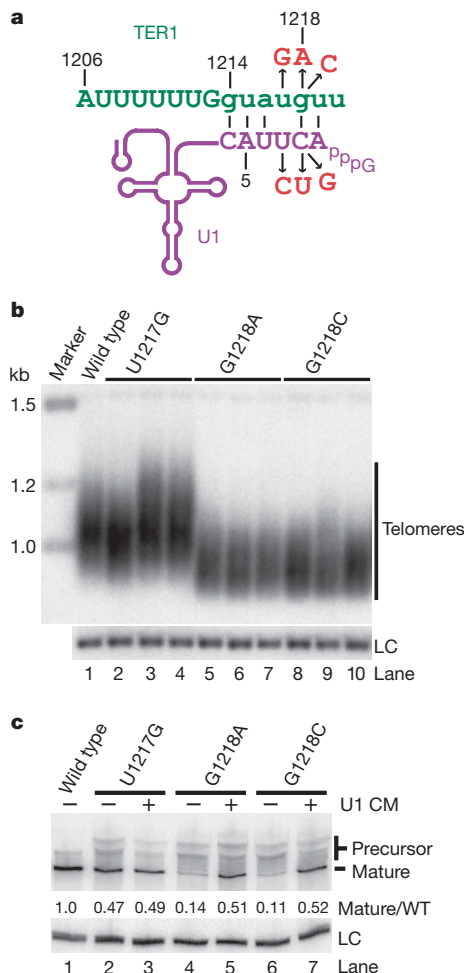


**Figure 3 | A direct role for the U1 snRNA in TER1 maturation.** **a**, Schematic of the 5' splice site (ss) in TER1 (green) paired with the U1 snRNA (purple). Introduced nucleotide replacements are shown in red. **b**, Telomere length analysis as in Fig. 1. Three independent isolates are shown for each mutant. **c**, Northern blot analysis of TER1 and *snR101* as the loading control (LC). RNA was isolated from strains expressing mutant *ter1* alleles alone or in combination with the compensatory mutation (CM) in U1.

Changes in telomere length after long-term co-expression of mutant *ter1*<sup>+</sup> and the compensatory U1 mutant could not be monitored by this experimental approach owing to dominant-negative 'off-target' effects exerted by the mutant U1. Consistent with pleiotropic detrimental effects, many single-nucleotide changes within the first six nucleotides of U1 are lethal or cause a severe growth defect in budding and fission yeast<sup>24,26,27</sup>. Nevertheless, the level of mature TER1 observed in the rescue experiment indicates that sufficient functional telomerase was formed to support telomere maintenance. Furthermore, RT-PCR across the intron indicates that mutations in position 1218 of TER1 reduced splicing, which was restored by the compensatory mutation in U1 (Supplementary Fig. 3). In summary, these experiments argue for a direct role for the spliceosome in the maturation of the telomerase RNA subunit.

### 3' end maturation by spliceosomal cleavage

Our data up to this point suggested that splicing constitutes an essential step in TER1 maturation, with the spliced form representing a short-lived intermediate that is further processed to generate the mature end at position 1213. To test whether absence of the intronic sequence was sufficient to bypass the requirement for splicing, we introduced complementary DNAs corresponding to the unspliced and spliced forms of TER1 into *ter1*<sup>-</sup> cells. Whereas the unspliced cDNA supported wild-type telomere maintenance, cells containing

the spliced cDNA experienced telomere shortening (Fig. 4a). We reasoned that splicing itself was an essential step and speculated that deposition of the exon junction complex on TER1 may be critical for subsequent processing events. Such a model predicts that an intron from another gene would substitute for the TER1 intron. We replaced the *ter1* intron with a heterologous intron (hi) from the protein-encoding *tif212*<sup>+</sup> gene to generate the TER1-hi mutant (Fig. 4b). RT-PCR across the intron revealed that this mutant was spliced efficiently (Fig. 4c, lane 4). Nevertheless, when total RNA was examined by northern blotting, a 30-fold reduction in mature telomerase RNA was observed (Fig. 4d, lane 2) and telomere maintenance was compromised (Fig. 4e, lanes 5 and 6).

The failure of a heterologous intron to substitute for the TER1 intron and the lack of a phenotype associated with the 3' splice site mutation in the endogenous intron were difficult to reconcile with a maturation pathway that included intron removal as an essential step. Intriguingly, the 3' end of the mature form of TER1 maps precisely upstream of the 5' splice site, suggesting that maturation of TER1 may only involve the first step of splicing. This model makes a testable prediction: if the TER1-hi mutant fails to generate mature TER1 because of efficient completion of the second transesterification reaction, mutating the 3' splice site in TER1-hi may rescue TER1 maturation (Fig. 4b and Supplementary Fig. 4). As expected, a 3' splice site mutation compromised splicing, and mostly unspliced TER1-hi\* was detected by RT-PCR (Fig. 4c, lane 6). The small amount of product migrating near the position of the spliced form was attributable to the use of a cryptic splice site downstream (Supplementary Fig. 4). Consistent with a 3' splice site mutation restoring telomerase 3' end processing, mature TER1 accumulated to 6.4-fold higher levels in TER1-hi\* compared with TER1-hi mutants (Fig. 4d), and telomeres were maintained at near wild-type length (Fig. 4e). To confirm that the first transesterification reaction

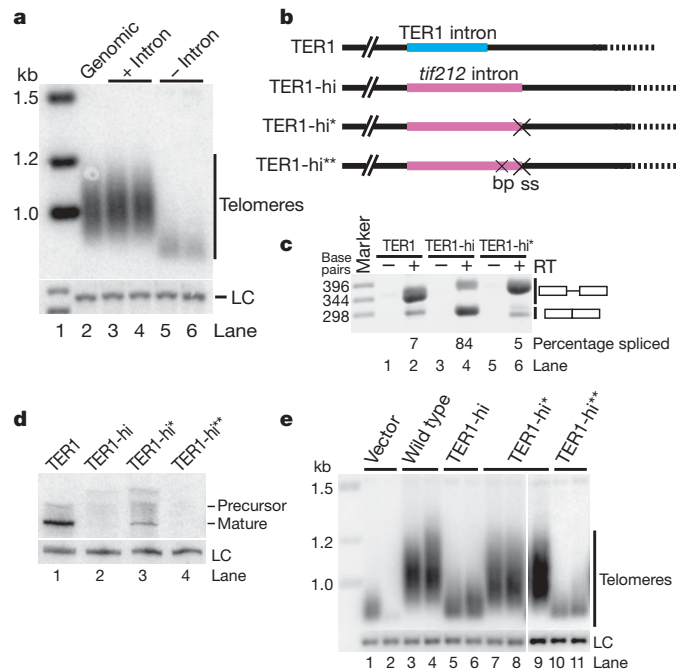


**Figure 4 | The first and second transesterification reactions have opposing effects on TER1 maturation.** **a**, Telomere length analysis of EcoRI-digested genomic DNA from cells expressing unspliced or spliced cDNAs of TER1. **b**, Schematic of constructs used in this experiment. The endogenous TER1 intron (blue) was replaced with the intron from *tif212*<sup>+</sup> shown in pink. The mutated branch point (bp) and 3' splice sites (ss) are indicated by crosses. **c**, RT-PCR across the intron to assess the abundance of the spliced form. **d**, Northern blot for TER1 and the loading control (LC). **e**, Telomere length was analysed after 90 generations. Two or three independent isolates are shown per strain.

was still required in the context of the heterologous intron, we next mutated the branch point in addition to the 3' splice site. Telomerase RNA was undetectable in the resultant TER1-hi\*\* mutant (Fig. 4d) and cells failed to maintain telomeres (Fig. 4e). We concluded that the first step of splicing generates the mature 3' end of TER1 RNA, which is released before exon ligation. The inability of the spliced form to support telomere maintenance further indicates that complete splicing generates an inactive form of TER1 that may be rapidly degraded. Such a mechanism may contribute to the regulation of TER1 levels by favouring the completion of splicing under conditions in which telomerase activity is not required.

With the 5' exon being released as mature TER1, we wondered about the fate of the intron lariat plus 3' exon. Using a probe against the 3' exon, a smear was detected by northern blotting for a *ter1*<sup>+</sup> strain but not for a *ter1*<sup>-</sup> control (data not shown). Detection of a smear rather than a discrete band is consistent with multiple polyadenylation sites in the precursor<sup>12</sup> and the variable length of poly(A) tails. Primer extension can be used to detect lariats and to map the position of branch points because the 2'-5' linkage between the branch point A and the G at the 5' splice site partially blocks reverse transcription<sup>28</sup>. Indeed, a primer extension product terminating one nucleotide downstream of the branch point was detected with a primer complementary to sequences in the 3' exon of TER1 (Fig. 5a). No signal was detected with *ter1*<sup>-</sup> samples and a much stronger signal was observed when TER1 was overexpressed (lanes 7 and 8). Overexpression resulted in a second band corresponding to the adjacent nucleotide, suggesting that either A in CUAAC can act as branch point. A second primer annealing elsewhere in the 3' exon gave identical results (Supplementary Fig. 5a). The intron lariat-3' exon was readily detected when the 3' splice site was mutated, but not when the 5' splice site or branch point were altered (Supplementary

Fig. 5b). Notably, processing of TER1 was not compromised by high-level overexpression from the *nmt1* promoter, as the mature form constituted most TER1 in all strains (Supplementary Fig. 6).

### Spliceosomal cleavage versus splicing

In protein-encoding genes, release of the 5' exon after the first step of splicing would be highly detrimental. The two steps of splicing are therefore tightly coupled to prevent the release of intermediates. It is unknown how TER1 could escape coupling and adapt the first part of intron removal for the purpose of generating the precise 3' end of a non-coding RNA. It seems that the close resemblance of the 5' splice site and branch point to the respective consensus sequences ensures an efficient first step. A weak polypyrimidine tract and the relatively long distance between the branch point and 3' splice site may then compromise the second step. It has been shown that increasing the distance from the branch point to the 3' splice site in a *cdc2* intron severely reduced accumulation of the spliced form<sup>29</sup>. In the TER1 intron, this distance is 22 nucleotides, twice as long as the average distance described for introns in *S. pombe*<sup>21</sup> (Fig. 5b). When we shortened the distance by 14 nucleotides (TER1-55), a strong shift in favour of the spliced form was observed (Fig. 5c). Consequently, little mature form was produced (Fig. 5d) and telomeres shortened (Fig. 5e). It thus appears that a combination of sequence elements that facilitate the first step and attenuate the second step is critical for the function of the spliceosome in TER1 3' end formation. In addition, specific regulatory factors may bind the TER1 RNA and promote the release of the mature form after the first cleavage reaction.

Taken together, our results show that the function of the spliceosome is not limited to intron removal, but that the splicing machinery has an additional role in generating the mature 3' end of the telomerase RNA subunit. To our knowledge this is the first example for which uncoupling of the first and second steps of splicing generates a functional product in a single-step reaction (Fig. 5f). It is not known whether this pathway for 3' end processing has specifically evolved to act in telomerase biogenesis in fission yeast or whether other examples will be uncovered. Longer polyadenylated forms have also been observed for the *S. cerevisiae* telomerase RNA subunit TLC1, but perfect consensus 5' splice site and branch point sequences downstream of the mature 3' end are lacking. However, recent cloning and analysis of telomerase RNA sequences from six *Candida* species revealed two highly conserved sequence motifs downstream of the mature ends (Y. Tzfati and L. Tomaska, personal communication). These correspond to consensus budding yeast 5' splice site and branch point sequences, indicating that the mechanism of 3' end processing is at least conserved among distantly related yeasts. Telomerase aside, previously unknown non-coding RNAs of diverse functions are now being identified almost daily. It would not be surprising if the ability of the spliceosome to generate a precise 3' end in a regulated manner emerges as a more general mechanism of RNA 3' end formation.

### METHODS SUMMARY

The different forms of telomerase RNA were detected by RT-PCR and northern blotting. Telomere length was assessed by Southern analysis of terminal restriction fragments using a telomeric probe. Yeast manipulation and molecular analysis was performed as described<sup>12,30</sup>. Primer extension was used to detect the intron lariat plus 3' exon and to map the branch point.

**Full Methods** and any associated references are available in the online version of the paper at [www.nature.com/nature](http://www.nature.com/nature).

Received 14 August; accepted 10 October 2008.

Published online 3 December 2008.

1. Hug, N. & Lingner, J. Telomere length homeostasis. *Chromosoma* 115, 413–425 (2006).
2. Stewart, S. A. & Weinberg, R. A. Telomeres: cancer to human aging. *Annu. Rev. Cell Dev. Biol.* 22, 531–557 (2006).
3. Mitchell, J. R., Wood, E. & Collins, K. A telomerase component is defective in the human disease dyskeratosis congenita. *Nature* 402, 551–555 (1999).

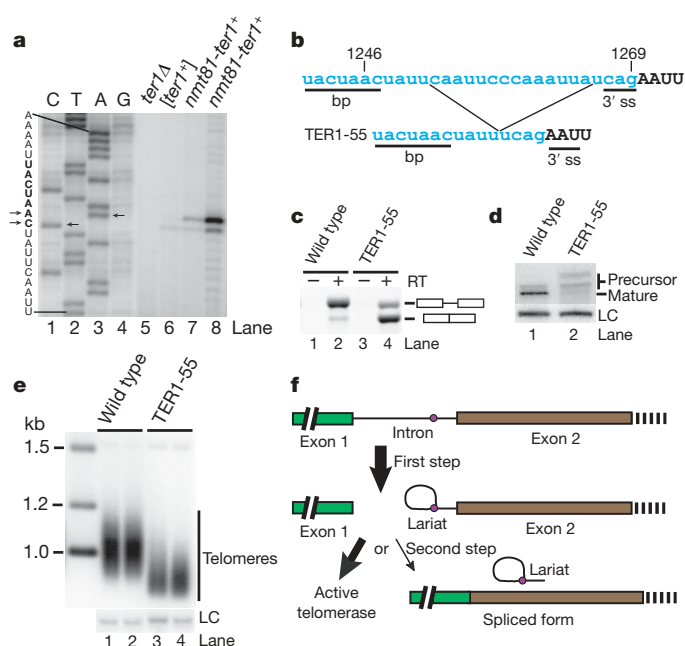


**Figure 5 | Requirements for 3' end processing by the spliceosome.**

**a**, Detection of the lariat plus 3' exon. The branch point was mapped by primer extension at different levels of TER1 expression. RT products were analysed next to sequencing reactions. Arrows mark the position of the RT pause sites; the TER1 sequence surrounding the branch point is shown on the left. **b**, Shortening the distance between the branch point (bp) and the 3' splice site (ss) facilitates exon ligation and compromises TER1 maturation. **c**, RT-PCR across the intron. **d**, Northern blot analysis for TER1 and snR101 (the loading control, LC). **e**, Telomere length analysis for two independent isolates per strain. **f**, Schematic of TER1 3' end processing. Exon 1 (green) corresponds to the mature form of TER1. The branch point is marked by a purple dot.



4. Vulliamy, T. *et al.* The RNA component of telomerase is mutated in autosomal dominant dyskeratosis congenita. *Nature* **413**, 432–435 (2001).
5. Vulliamy, T., Marrone, A., Dokal, I. & Mason, P. J. Association between aplastic anaemia and mutations in telomerase RNA. *Lancet* **359**, 2168–2170 (2002).
6. Armanios, M. Y. *et al.* Telomerase mutations in families with idiopathic pulmonary fibrosis. *N. Engl. J. Med.* **356**, 1317–1326 (2007).
7. Yamaguchi, H. *et al.* Mutations in TERT, the gene for telomerase reverse transcriptase, in aplastic anemia. *N. Engl. J. Med.* **352**, 1413–1424 (2005).
8. Mitchell, J. R., Wood, E. & Collins, K. A telomerase component is defective in the human disease dyskeratosis congenita. *Nature* **402**, 551–555 (1999).
9. Cohen, S. B. *et al.* Protein composition of catalytically active human telomerase from immortal cells. *Science* **315**, 1850–1853 (2007).
10. Lingner, J. *et al.* Reverse transcriptase motifs in the catalytic subunit of telomerase. *Science* **276**, 561–567 (1997).
11. Gillis, A. J., Schuller, A. P. & Skordalakes, E. Structure of the *Tribolium castaneum* telomerase catalytic subunit TERT. *Nature* **455**, 633–637 (2008).
12. Leonardi, J., Box, J. A., Bunch, J. T. & Baumann, P. TER1, the RNA subunit of fission yeast telomerase. *Nature Struct. Mol. Biol.* **15**, 26–33 (2008).
13. Webb, C. J. & Zakian, V. A. Identification and characterization of the *Schizosaccharomyces pombe* TER1 telomerase RNA. *Nature Struct. Mol. Biol.* **15**, 34–42 (2008).
14. Baumann, P. & Cech, T. R. Pot1, the putative telomere end-binding protein in fission yeast and humans. *Science* **292**, 1171–1175 (2001).
15. Chikashige, Y. & Hiraoka, Y. Telomere binding of the Rap1 protein is required for meiosis in fission yeast. *Curr. Biol.* **11**, 1618–1623 (2001).
16. Cooper, J. P., Nimmo, E. R., Allshire, R. C. & Cech, T. R. Regulation of telomere length and function by a Myb-domain protein in fission yeast. *Nature* **385**, 744–747 (1997).
17. Kanoh, J. & Ishikawa, F. spRap1 and spRif1, recruited to telomeres by Taz1, are essential for telomere function in fission yeast. *Curr. Biol.* **11**, 1624–1630 (2001).
18. Miyoshi, T., Kanoh, J., Saito, M. & Ishikawa, F. Fission yeast Pot1–Tpp1 protects telomeres and regulates telomere length. *Science* **320**, 1341–1344 (2008).
19. Chapon, C., Cech, T. R. & Zaug, A. J. Polyadenylation of telomerase RNA in budding yeast. *RNA* **3**, 1337–1351 (1997).
20. Fu, D. & Collins, K. Distinct biogenesis pathways for human telomerase RNA and H/ACA small nucleolar RNAs. *Mol. Cell* **11**, 1361–1372 (2003).
21. Zhang, M. Q. & Marr, T. G. Fission yeast gene structure and recognition. *Nucleic Acids Res.* **22**, 1750–1759 (1994).
22. Seto, A. G., Zaug, A. J., Sobel, S. G., Wolin, S. L. & Cech, T. R. *Saccharomyces cerevisiae* telomerase is an Sm small nuclear ribonucleoprotein particle. *Nature* **401**, 177–180 (1999).
23. Seraphin, B., Kretzner, L. & Rosbash, M. A. U1 snRNA:pre-mRNA base pairing interaction is required early in yeast spliceosome assembly but does not uniquely define the 5' cleavage site. *EMBO J.* **7**, 2533–2538 (1988).
24. Siliciano, P. G. & Guthrie, C. 5' splice site selection in yeast: genetic alterations in base-pairing with U1 reveal additional requirements. *Genes Dev.* **2**, 1258–1267 (1988).
25. Zhuang, Y. & Weiner, A. M. A compensatory base change in U1 snRNA suppresses a 5' splice site mutation. *Cell* **46**, 827–835 (1986).
26. Alvarez, C. J., Romfo, C. M., Vanhoy, R. W., Porter, G. L. & Wise, J. A. Mutational analysis of U1 function in *Schizosaccharomyces pombe*: pre-mRNAs differ in the extent and nature of their requirements for this snRNA *in vivo*. *RNA* **2**, 404–418 (1996).
27. Seraphin, B. & Rosbash, M. Mutational analysis of the interactions between U1 small nuclear RNA and pre-mRNA of yeast. *Gene* **82**, 145–151 (1989).
28. Domdey, H. *et al.* Lariat structures are *in vivo* intermediates in yeast pre-mRNA splicing. *Cell* **39**, 611–621 (1984).
29. Romfo, C. M. & Wise, J. A. Both the polypyrimidine tract and the 3' splice site function prior to the first step of splicing in fission yeast. *Nucleic Acids Res.* **25**, 4658–4665 (1997).
30. Bunch, J. T., Bae, N. S., Leonardi, J. & Baumann, P. Distinct requirements for Pot1 in limiting telomere length and maintaining chromosome stability. *Mol. Cell. Biol.* **25**, 5567–5578 (2005).
31. Box, J. A., Bunch, J. T., Zappulla, D. C., Glynn, E. F. & Baumann, P. A flexible template boundary element in the RNA subunit of fission yeast telomerase. *J. Biol. Chem.* **283**, 24224–24233 (2008).

**Supplementary Information** is linked to the online version of the paper at [www.nature.com/nature](http://www.nature.com/nature).

**Acknowledgements** The authors thank H. Yang and the other members of the Baumann laboratory for help and discussions, Y. Tzfati and L. Tomaska for sharing results before publication, and A. Berglund, M. Blanchette, R. Conaway and T. Cech for discussions and comments on the manuscript. We also thank the Molecular Biology Core Facility for site-directed mutagenesis and sequencing, M. Gogol and R. Voelker for computational analysis, and D. Baumann and R. Helston for proofreading of the manuscript. This work was funded by the Stowers Institute for Medical Research and a Pew Scholars in the Biomedical Sciences Award to P.B.

**Author Contributions** P.B. made the initial observations, oversaw the project and designed the experiments. J.T.B. and P.B. developed protocols for RNA isolation, northern blotting and primer extension analysis. J.A.B. contributed plasmids and strains and performed telomere length analysis and RT-PCR assays. J.T.B. conducted northern blotting and primer extension analysis. W.T. characterized the TER1-Sm1 mutant. All authors contributed to data analysis, and P.B. wrote the manuscript.

**Author Information** Reprints and permissions information is available at [www.nature.com/reprints](http://www.nature.com/reprints). Correspondence and requests for materials should be addressed to P.B. ([peb@stowers-institute.org](mailto:peb@stowers-institute.org)).

## METHODS

**Constructs, strains and DNA analysis.** Mutations in *ter1*<sup>+</sup> were generated in the context of pJW10 (ref. 12) using the QuikChange II XL site-directed mutagenesis kit (Stratagene). Plasmids were sequence verified and introduced into PP407 (*h*<sup>+/−</sup> *ade6-M210/ade6-M216 his3-D1/his3-D1 leu1-32/leu1-32 ura4-D18/ura4-D18 ter1<sup>+</sup> ter1:kan*) by electroporation. Diploid transformants were selected and haploid strains derived as described<sup>31</sup>. After propagating cells for the number of generations indicated for each experiment, genomic DNA was isolated, digested with EcoRI, and telomere length was analysed by Southern blotting<sup>30</sup>. The terminal EcoRI fragments are comprised of 780 base pairs of subtelomeric DNA and a variable number of telomeric repeats for the four arms of chromosomes I and II.

**Splice site sequence analysis.** The sequences of 4,808 annotated introns plus 5 nucleotides of flanking exonic sequences were extracted from GeneDB and aligned in Pictogram<sup>32</sup> to reveal the consensus 5' splice site for *S. pombe*.

**RNA isolation.** Cultures (500 ml) were grown to a density of  $5 \times 10^6$  cells ml<sup>−1</sup> at 32 °C and cells were collected by centrifugation. After two washes in ddH<sub>2</sub>O, cells were resuspended in ddH<sub>2</sub>O and quick-frozen by dripping the cell suspension into liquid nitrogen. Cells were lysed in a 6850 Freezer mill (SPEX SamplePrep) using 8 cycles (2 min) at a rate of 10 per second with 2 min cooling time between cycles. The lysed cell powder was transferred directly into tubes containing 10 ml phenol/chloroform/isoamyl alcohol (25:24:1) and 10 ml sodium acetate (50 mM), 1% (w/v) sodium dodecyl sulphate preheated to 65 °C. RNA was extracted five times with phenol/chloroform/isoamyl alcohol and once with chloroform/isoamyl alcohol. Total RNA was ethanol precipitated and resuspended in 50 mM sodium acetate (pH 5.2). For use in RT-PCR, the RNA was further purified using the RNeasy mini kit from Qiagen following the manufacturer's instructions for DNase digestion and RNA cleanup.

**RT-PCR.** DNase-treated RNA samples (2.5 µg) were combined with oligonucleotide BLoli1275 (CGGAAACGGAATTCAGCATGT, 10 pmol) and dNTP mix (10 nmol). The volume was adjusted to 13 µl with distilled water and samples were heated to 65 °C for 5 min. The volume was increased to 20 µl by the addition of RNasin (40 U, Promega), dithiothreitol (5 mM final), 5× first strand buffer, and Superscript III reverse transcriptase (200 U, Invitrogen). Superscript III was omitted from control reactions to control for DNA contamination. After incubation at 55 °C for 60 min, RNaseH (5 U, NEB) was added and incubation was continued at 37 °C for 20 min. Aliquots (2 µl) of the RT reactions were used for PCR amplification with Taq polymerase (NEB) and oligonucleotide primers BLoli1020 (CAAACAATAATGAACGTCCTG) and BLoli1275 under the following conditions: 5 min at 94 °C followed by 30 cycles of 30 s at 94 °C, 30 s at 57 °C and 60 s at 72 °C, followed by 10 min at 72 °C. PCR products were analysed by electrophoresis on 1.8% agarose gels.

**Primer extension.** The branch point was mapped by primer extension using total RNA from cells expressing *ter1*<sup>+</sup> from the endogenous promoter or at two different levels of overexpression (*nmt81* and *nmt1* promoter<sup>33</sup>). Total RNA (5 µg) was incubated with <sup>32</sup>P-labelled oligonucleotide BLoli1375 (GATGAGCAACCGGTCCTTAC, 1.5 pmol) or BLoli1376 (CGGAAACGGAATTCAGCATG, 1.5 pmol) and dNTPs (10 nmol) in 13 µl of ddH<sub>2</sub>O at 65 °C for 5 min. The reaction volume was increased to 20 µl by the addition of RNase inhibitor (RNasin Plus, 40 U), dithiothreitol (5 mM final), first strand buffer (Invitrogen),

and Superscript III reverse transcriptase (200 U, Invitrogen), and reactions were incubated at 55 °C for 60 min. Reactions were terminated by the addition of 5 µl of stop buffer (100 mM Tris-HCl, pH 7.5, 0.2 M EDTA, 2.5% (w/v) SDS, and 1% (w/v) proteinase K) and incubation at 42 °C for 10 min. Nucleic acids were purified by phenol/chloroform extraction and ethanol precipitation, and solubilised in 3 µl of NaOH (0.1 M) and 7 µl of formamide. Primer extension products were separated on 8% Tris-borate/EDTA (TBE)/7 M urea gels next to a sequencing ladder as marker. Sequencing reactions contained the same primer as the primer extension, cloned *ter1*<sup>+</sup> as template and components of the Sequenase Version 2.0 DNA Sequencing Kit (US Biologicals) as instructed by the manufacturer.

**Northern blotting.** RNA samples (15 µg) were separated on 4% polyacrylamide gels in TBE/7 M urea and transferred to Hybond-N+ nylon membrane (GE Healthcare) at 0.4 A for 1 h in 0.5× TBE buffer. RNA was ultraviolet cross-linked (254 nm, 120 mJ) in a Stratalinker (Stratagene). Hybridizations with radiolabelled probes were carried out in Church-Gilbert buffer<sup>34</sup> at 65 °C (*ter1*<sup>+</sup> probe) or 42 °C (snR101 probe). The TER1 probe was generated by nick-translation of a PCR fragment (nucleotides 17 to 249) in the presence of <sup>32</sup>P-α-dCTP. The snoRNA snR101 (ref. 35; AJ632019) used as loading control was detected with oligonucleotide BLoli1136 (CGCTATTGTATGGGGCCTTTAGATTCTTA) labelled with polynucleotide kinase in the presence of <sup>32</sup>P-γ-ATP. The mature form of TER1 was quantified relative to wild type after normalizing to the signal for the loading control snR101.

**Determination of 3' end sequence.** DNase-treated total RNA samples (2.5 µg) were incubated with poly(A) polymerase (US Biologicals), RNase inhibitor (RNasin, 40 U) and ATP (0.5 mM) in the buffer provided by the manufacturer in 20-µl reactions at 30 °C for 30 min. The reaction volume was increased to 35.5 µl by the addition of the DNA oligonucleotide PBoli560 (GCGGAATTCT<sub>18</sub>, 125 pmol) and dNTP mix (25 nmol), and the reactions were incubated at 65 °C for 3 min followed by slow cooling to room temperature (20 °C). The reaction volume was then adjusted to 50 µl with first strand buffer (Invitrogen), dithiothreitol (5 mM), RNasin (40 U) and Superscript III reverse transcriptase (200 U, Invitrogen), and reactions were incubated at 50 °C for 60 min. RNaseH (5 U, NEB) was added and incubation was continued at 37 °C for 20 min. Aliquots (2.5 µl) of this reaction were used for PCR amplification with Taq polymerase (5 U, NEB), and oligonucleotide primers BLoli1006 (CATTTAAGTGCT-TGTCAGATCACAAACG) and PBoli560 (200 nM each) under the following conditions: 3 min at 94 °C followed by 32 cycles of 30 s at 94 °C, 45 s at 55 °C and 120 s at 72 °C, followed by 7 min at 72 °C. PCR products were separated by electrophoresis on 0.8% agarose gels, and bands of the correct size were excised, purified and cloned into the TOPO TA cloning system (Invitrogen) for sequence analysis.

32. Burge, C. B., Tuschl, T. H. & Sharp, P. A. in *The RNA World* (eds Gesteland, R. F., Cech, T. R. & Atkins, J. F.) 525–560 (Cold Spring Harbor Laboratory Press, 1999).
33. Forsburg, S. L. Comparison of *Schizosaccharomyces pombe* expression systems. *Nucleic Acids Res.* **21**, 2955–2956 (1993).
34. Church, G. M. & Gilbert, W. Genomic sequencing. *Proc. Natl Acad. Sci. USA* **81**, 1991–1995 (1984).
35. Li, S. G., Zhou, H., Luo, Y. P., Zhang, P. & Qu, L. H. Identification and functional analysis of 20 Box H/ACA small nucleolar RNAs (snoRNAs) from *Schizosaccharomyces pombe*. *J. Biol. Chem.* **280**, 16446–16455 (2005).



# SUMOylation regulates Rad18-mediated template switch

Dana Branzei<sup>1</sup>, Fabio Vanoli<sup>1</sup> & Marco Foiani<sup>1,2</sup>

**Replication by template switch is thought to mediate DNA damage-bypass and fillings of gaps. Gap-filling repair requires homologous recombination as well as Rad18- and Rad5-mediated proliferating cell nuclear antigen (PCNA) polyubiquitylation. However, it is unclear whether these processes are coordinated, and the physical evidence for Rad18–Rad5-dependent template switch at replication forks is still elusive. Here we show, using genetic and physical approaches, that in budding yeast (*Saccharomyces cerevisiae*) Rad18 is required for the formation of X-shaped sister chromatid junctions (SCJs) at damaged replication forks through a process involving PCNA polyubiquitylation and the ubiquitin-conjugating enzymes Mms2 and Ubc13. The Rad18–Mms2-mediated damage-bypass through SCJs requires the small ubiquitin-like modifier (SUMO)-conjugating enzyme Ubc9 and SUMOylated PCNA, and is coordinated with Rad51-dependent recombination events. We propose that the Rad18–Rad5–Mms2-dependent SCJs represent template switch events. Altogether, our results unmask a role for PCNA ubiquitylation and SUMOylation pathways in promoting transient damage-induced replication-coupled recombination events involving sister chromatids at replication forks.**

DNA replication is sensitive to damage in the template. Ultraviolet-irradiated cells accumulate gaps in the nascent chains both on the leading and the lagging strands<sup>1–4</sup>. Gap filling is important for cell viability<sup>5</sup>, and two different pathways contribute to this process: genes of the *RAD52* epistasis group that directs recombination repair<sup>6–9</sup>, and genes of the error-free subpathway of postreplicative repair (PRR) coordinated by *RAD6* and *RAD18* (refs 1 and 9–11). Rad18 controls two different modes of PRR, an error-prone mechanism—which uses non-processive translesion polymerases that insert correct or incorrect nucleotides across the damaged site—and another method termed error-free associated with gap-filling repair<sup>3,4,10</sup> (Supplementary Fig. 1)—which is believed to promote a temporary switching to the undamaged sister chromatid<sup>12–14</sup>, in a manner similar to a homologous recombination reaction (Supplementary Fig. 2).

Strand exchange activity is pivotal to all homologous recombination reactions<sup>6,7</sup> but such an activity has not yet been identified in any member of the Rad18 pathway. Ubiquitin modification plays a central role for *RAD6–RAD18*-dependent repair and most factors of the *RAD18* pathway encode ubiquitin-conjugating enzymes (Rad6, and the heterodimer Ubc13–Mms2)<sup>15,16</sup>, or ubiquitin ligases (Rad18 and Rad5)<sup>17–19</sup> (Supplementary Fig. 1). PCNA, a principal replication and repair factor, is a crucial target of the Rad18 pathway<sup>20</sup>. In response to DNA damage, PCNA is monoubiquitylated or polyubiquitylated at the highly conserved lysine residue Lys 164 (ref. 20; Supplementary Fig. 1). Monoubiquitylation of PCNA requires Rad6 and Rad18 and promotes translesion synthesis<sup>21,22</sup>, whereas PCNA modification through Lys 63-linked polyubiquitin chains depends on Ubc13–Mms2 and Rad5 and is required for error-free PRR (Supplementary Fig. 1)<sup>10,11,20</sup>.

Yeast PCNA is also conjugated with SUMO, which primarily targets the same lysine, Lys 164, and to a minor extent, a second site, Lys 127 (Supplementary Fig. 1)<sup>20,23</sup>. SUMO-modified PCNA (PCNA-SUMO) has been proposed to inhibit recombination repair events through its interaction with Srs2 (refs 24 and 25), a helicase that disrupts Rad51

filaments to prevent homologous recombination<sup>26–31</sup>. However, the nature of the recombination events suppressed by PCNA-SUMO and Srs2 remains unknown.

During replication of damaged templates, X-shaped intermediates form and accumulate in certain yeast genetic backgrounds (*sgs1*, *top3*, *rmi1*, *ubc9* and *mms21*)<sup>32–34</sup> (Supplementary Fig. 2). The Sgs1–Top3 complex is required for their resolution<sup>33,35</sup>, and Ubc9–Mms21-dependent SUMOylation was proposed to cooperate with Sgs1 in this process<sup>32</sup>. The homologous recombination protein Rad51 is required for the accumulation of X-shaped intermediates<sup>32–34</sup>. However, the physical evidence implicating Rad5 and Rad18 in generating template switch events at replication forks is missing. Furthermore, it is still unclear whether there is any coordination between the Rad18 pathway and Rad51 in mediating gap-filling repair.

## Rad18–Rad5 promotes sister chromatid junction formation

We investigated the factors implicated in the formation of the cruciform structures formed during replication of damaged templates in a Rad51-dependent manner<sup>32,33</sup>. Such structures were shown to accumulate in *sgs1*, *top3*, *ubc9* and *mms21* cells<sup>32,33</sup>. Damage-induced and Rad51-dependent X-shaped molecules can also be visualized in wild-type cells although the amount is scarce perhaps due to their transient nature (data not shown). We found that the X-shaped structures accumulating in *ubc9-1* have similar biochemical properties against different types of nucleases (T4 endonuclease VII and mung bean) to those of *sgs1* (data not shown), which were suggested to represent pseudo-double Holliday junctions<sup>33</sup>.

We addressed whether Rad18 and Rad5 have any role in the formation/accumulation of these intermediates. Using two-dimensional (2D) gel electrophoresis, we analysed the profile of the replication intermediates formed during replication challenged by methanesulphonate (MMS)-induced damage at *ARS305*, an early efficient origin of replication on chromosome III and its adjacent regions (Supplementary Fig. 3). In contrast with the double mutant *ubc9-1 rad51*

<sup>1</sup>IFOM, the FIRC Institute for Molecular Oncology Foundation, IFOM-IEO Campus, Via Adamello 16, 20139 Milan, Italy. <sup>2</sup>Dipartimento di Scienze Biomolecolari e Biotecnologie, Università degli Studi di Milano, 20133 Milan, Italy.

(ref. 32), *ubc9-1 rad18* (Fig. 1a) and *ubc9-1 rad5* (Supplementary Fig. 4) accumulated a comparable amount of X-molecules to *ubc9-1* at both *ARS305* and its adjacent regions. The X-molecule accumulation in *ubc9-1 rad18* was still dependent on Rad51 (Supplementary Fig. 5). We further analysed the contribution of Rad18–Rad5 to the accumulation of X-molecules in *sgs1* (ref. 33), in which SUMOylation is not defective. *RAD18* deletion reduced the amount of X-molecules in *sgs1* cells (Fig. 1b). The cell-cycle profiles and the ability of the double mutants to activate Rad53 was similar to that of the single *sgs1* mutant, ruling out the possibility that the decrease in X-molecule intermediates in *sgs1 rad18* is due to the inability to fire origins or initiate replication (Supplementary Fig. 6 and data not shown). Thus, Rad18–Rad5 contributes to the formation of X-shaped structures similar to Rad51–Rad52 (ref. 33), but unlike the Rad51 pathway, Rad18 function probably requires Ubc9-dependent SUMOylation.

In addition to Ubc9, which is required for all SUMOylation events, SUMOylation of targets is often facilitated by a specific SUMO ligase<sup>23,36</sup>. In budding yeast, three such activities (Siz1, Siz2 and

Mms21) have been characterized, but only *mms21* mutants accumulate X-molecules at damaged forks<sup>32</sup>. *RAD18* deletion reduced the X-molecule accumulation of *mms21-11* (Fig. 1c) and *mms21-CH* alleles (Supplementary Fig. 7), which both affect the Mms21 SUMO ligase activity<sup>19,32</sup> in a manner similar to its effect in *sgs1* cells (Fig. 1b).

The accumulation of X-molecules at damaged forks in *sgs1*, *mms21* and *ubc9-1* mutants and their differential dependency on Rad18 are also observed at other origins of replication, located on other chromosomes (Supplementary Figs 8 and 9). We conclude that the Rad18–Rad5 function in promoting the formation of damage-induced SCJs is regulated by a SUMOylation pathway different from the pathway mediated by Mms21.

### SCJ formation requires Mms2 and PCNA polyubiquitylation

Mms2–Ubc13-mediated PCNA polyubiquitylation is pivotal for gap-filling repair<sup>10,11,20</sup> (Supplementary Fig. 1). The *mms2* mutation decreased the accumulation of X-molecules in *sgs1* but not in *ubc9-1* cells (Fig. 2a). We examined the genetic relationship between *sgs1* and *rad18*, *rad5* and *mms2* mutations. The *rad18* and *rad5* mutants are much more sensitive to MMS than *sgs1*, whereas *mms2* is mildly sensitive to MMS, to a lesser degree than *sgs1* (Fig. 2b). The double mutants *sgs1 rad18* and *sgs1 rad5* are not more sensitive than *rad18* and *rad5*, respectively, and *sgs1 mms2* is as sensitive as *sgs1* alone (Fig. 2b). These genetic data are congruent with the idea that Sgs1 is acting to resolve the substrates generated by the ubiquitylation action of Rad18 and Mms2.

We also observed that *ubc9-1* suppresses the MMS sensitivity of *rad18* and *rad5* (ref. 32), whereas *mms2* is epistatic to *ubc9-1* (Fig. 2c). Previous genetic data proposed SUMOylation to act upstream of Rad18 and to inhibit certain recombination events<sup>24,25</sup>. Indeed, in *ubc9-1* mutants, Rad18, Rad5 and Mms2 are not required for the accumulation of X-molecules (Figs 1a, 2a and Supplementary Fig. 4), which still form in a Rad51-dependent manner (Supplementary Fig. 5 and ref. 32). Thus, one set of recombination events prevented by SUMOylation are those that are mediated by Rad51 but are independent of Rad18, leading to SCJ formation during damage-bypass replication.

### PCNA SUMOylation is required for Rad18-mediated SCJs

We analysed the effect of the K164R mutation in the *POL30* gene encoding PCNA. The *pol30(K164R)* mutant encodes PCNA that is neither mono/polyubiquitylated, nor SUMOylated at this residue<sup>20</sup> (Supplementary Fig. 1). *pol30(K164R)* had a partial effect on the SCJ accumulation in *sgs1* (Fig. 3a), less notable than that of *rad18* (Fig. 1b) or *mms2* (Fig. 2a). It is possible that Rad18 has other targets, besides PCNA, the ubiquitylation of which is important for the SCJ formation. In that case, the effect of the *pol30(K164R)* mutation should be masked by the effect of *rad18*, that is, *sgs1 rad18 pol30(K164R)* should accumulate a similar amount of X molecules with *sgs1 rad18* (see also Supplementary Fig. 10). Conversely, we found that the *sgs1 rad18 pol30(K164R)* behaved like *sgs1 pol30(K164R)* and not like *sgs1 rad18* in regard to the SCJ accumulation (Fig. 3a). Thus, Rad18 promotes X-molecule formation in *sgs1* but not in *sgs1 pol30(K164R)*. *sgs1 pol30(K164R)* mimicked *ubc9-1* in its requirement for Rad18, thus suggesting that PCNA is the SUMO target required for the downstream activation of the Rad18 ability to promote SCJ formation (Supplementary Fig. 10). SUMOylation of the Lys 164 residue of PCNA requires Siz1 (refs 20, 24 and 25) and if our interpretation were correct, we would similarly expect that in the absence of Siz1-mediated SUMOylation (the *sgs1 siz1* background), the Rad18 pathway would not contribute to the SCJ formation as it does in *sgs1*. These expectations were confirmed by our experimental data (Fig. 3b).

These results do not rule out the possibility that Rad18 and/or Mms2 may have other targets, different from PCNA, the ubiquitylation of which may contribute to SCJ-mediated damage-bypass.

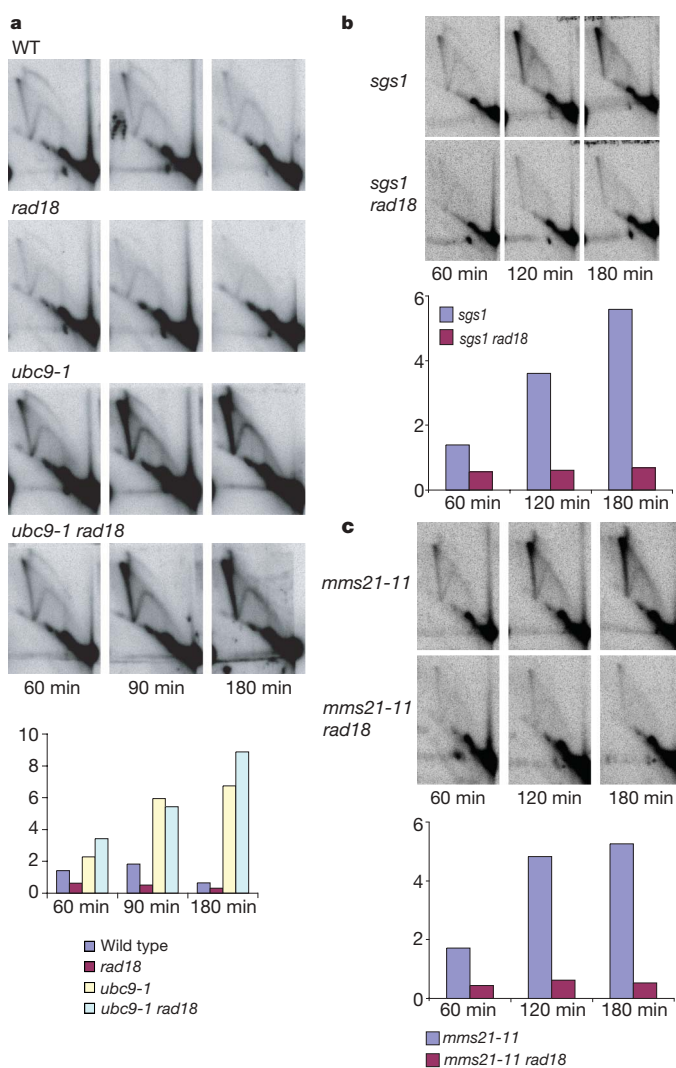


**Figure 1 | Rad18 promotes SCJ formation during replication of damaged templates, but its functionality requires SUMOylation.** **a–c.** The profile of replication intermediates at *ARS305* from **(a)** wild type (WT; Y002), *ubc9-1* (Y0174), *rad18* (HY0520) and *ubc9-1 rad18* (HY0521) mutants, from **(b)** *sgs1* (HY0501) and *sgs1 rad18* (HY0695) mutants, and from **(c)** *mms21-11* (FY1012) and *mms21-11 rad18* (HY0748) mutants. The quantification of the X-molecules is shown in the graphs, where the relative amount of X versus other intermediates is represented on the y axes of the graph for each time point analysed.



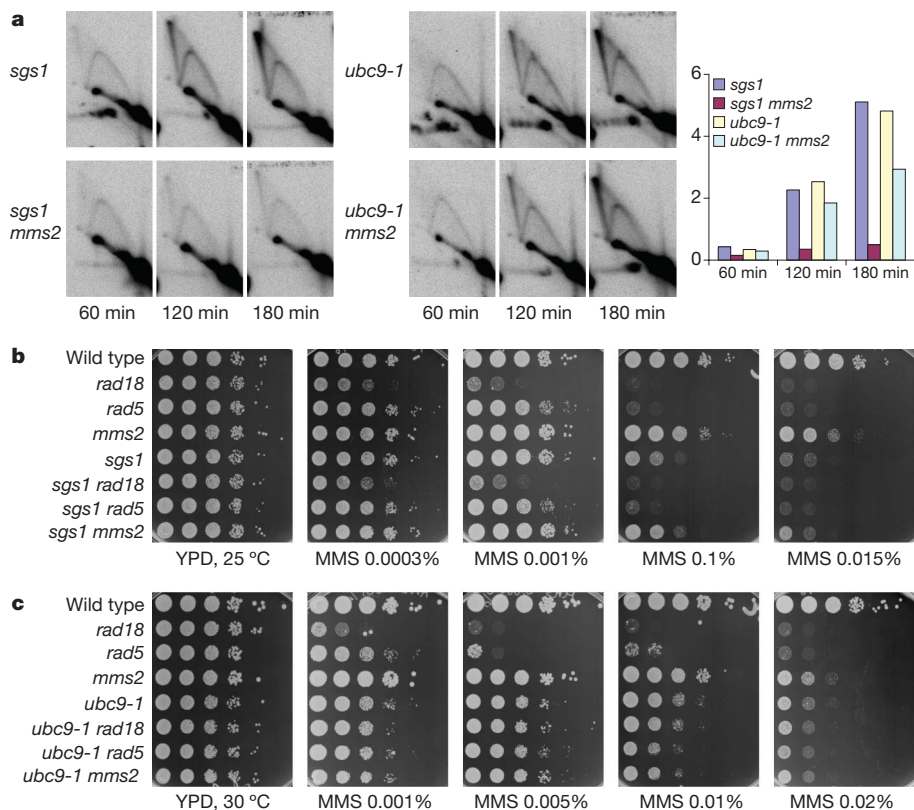


**Figure 2 | Sgs1 functions to resolve the damage-induced SCJs formed by Rad18-Mms2-PCNA polyubiquitylation.** **a**, The 2D gel profile of replication intermediates from *sgs1* (HY0501), *sgs1 mms2* (HY0810), *ubc9-1* (Y0174) and *ubc9-1 mms2* (HY0519) mutants at ARS301 (see Supplementary Fig. 3). The relative amount of X versus other intermediates is represented on the y

axes of the quantification graph for each time point analysed. **b**, **c**, Spot assays of strains wild-type (Y0002), *rad18* (HY0520), *rad5* (HY0516), *mms2* (HY0518), *sgs1* (HY0501), *sgs1 rad18* (HY0695), *sgs1 rad5* (HY0692), *sgs1 mms2* (HY0810), *ubc9-1* (FY0114), *ubc9-1 rad18* (HY0695), *ubc9-1 rad5* (HY0517) and *ubc9-1 mms2* (HY0519).

However, all of these presumptive downstream targets of Rad18 will probably require Siz1-mediated SUMOylation for their ability to promote SCJ formation, as does Rad18 itself.

The data suggest that the role of the Rad18–Rad5–Mms2 pathway in promoting SCJ formation involves PCNA polyubiquitylation but requires previous SUMOylation of PCNA. This model is also in agreement with genetic data. Similar to the *mms2* mutation (Fig. 2b), we found that *pol30(K164R)* is epistatic to *sgs1* (Supplementary Fig. 11 and Fig. 3c), corroborating the idea that Sgs1 is resolving the structures generated by Mms2 and PCNA-Lys 164 polyubiquitylation. The MMS sensitivity of *sgs1 rad18* (equal to that of *rad18*, see also Fig. 2b) is rescued both by the *siz1* and the *pol30(K164R)* mutations (Fig. 3c). These genetic results may reflect the inability of *sgs1 rad18* cells to bypass damage through SCJ formation (Fig. 1b and Supplementary 7), whereas the triple mutants form SCJs (Fig. 3) in a manner now independent of the Rad18 pathway, but dependent on Rad51 (Supplementary Fig. 5 and see later).

## Two pathways of SCJ formation coordinated by PCNA SUMOylation

Our results indicate that there are two pathways leading to SCJ formation during replication and that these are coordinated by PCNA SUMOylation (Fig. 4a). A related model for DNA repair has been suggested on the basis of genetic arguments, in which Siz1 and

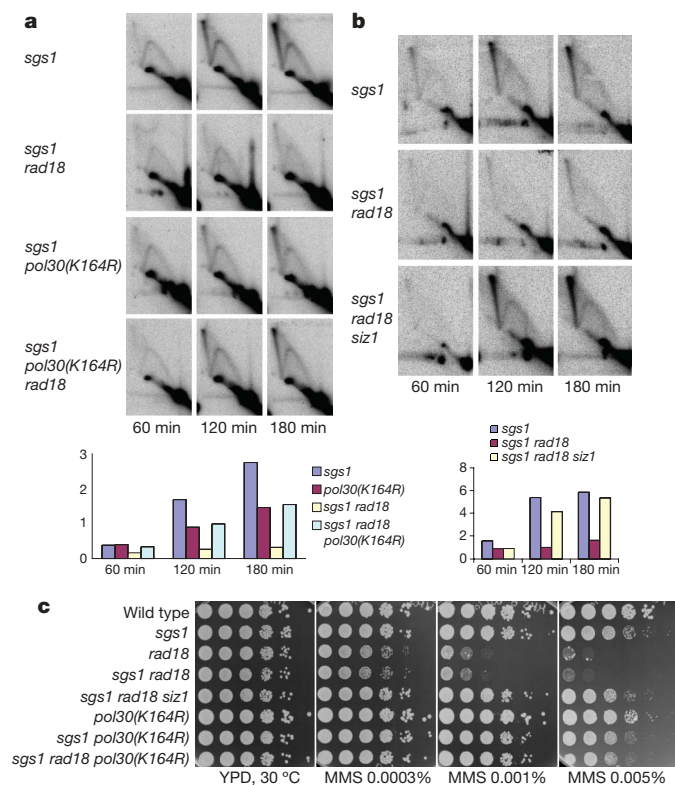


**Figure 3 | The contribution of PCNA SUMOylation in the formation of SCJs accumulating in *sgs1* during replication of damaged templates.** **a**, 2D gel analysis of replication intermediates in *sgs1* (HY0501), *sgs1 rad18* (HY0695), *sgs1 pol30(K164R)* (HY0722) and *sgs1 rad18 pol30(K164R)* (HY0838) mutant strains at the ARS301 region. **b**, Same as in **a** but of strains *sgs1* (HY0501), *sgs1 rad18* (HY0695) and *sgs1 rad18 siz1* (HY0823) at the ARS305 region. The relative amount of X versus other intermediates is represented on the y axes of the quantification graphs for each time point analysed. **c**, Spot assay of strains wild type (Y0002), *sgs1* (HY0501), *rad18* (HY0520), *sgs1 rad18* (HY0695), *sgs1 rad18 siz1* (HY0823), *pol30(K164R)* (FY0103), *sgs1 pol30(K164R)* (HY0722) and *sgs1 rad18 pol30(K164R)* (HY0838).

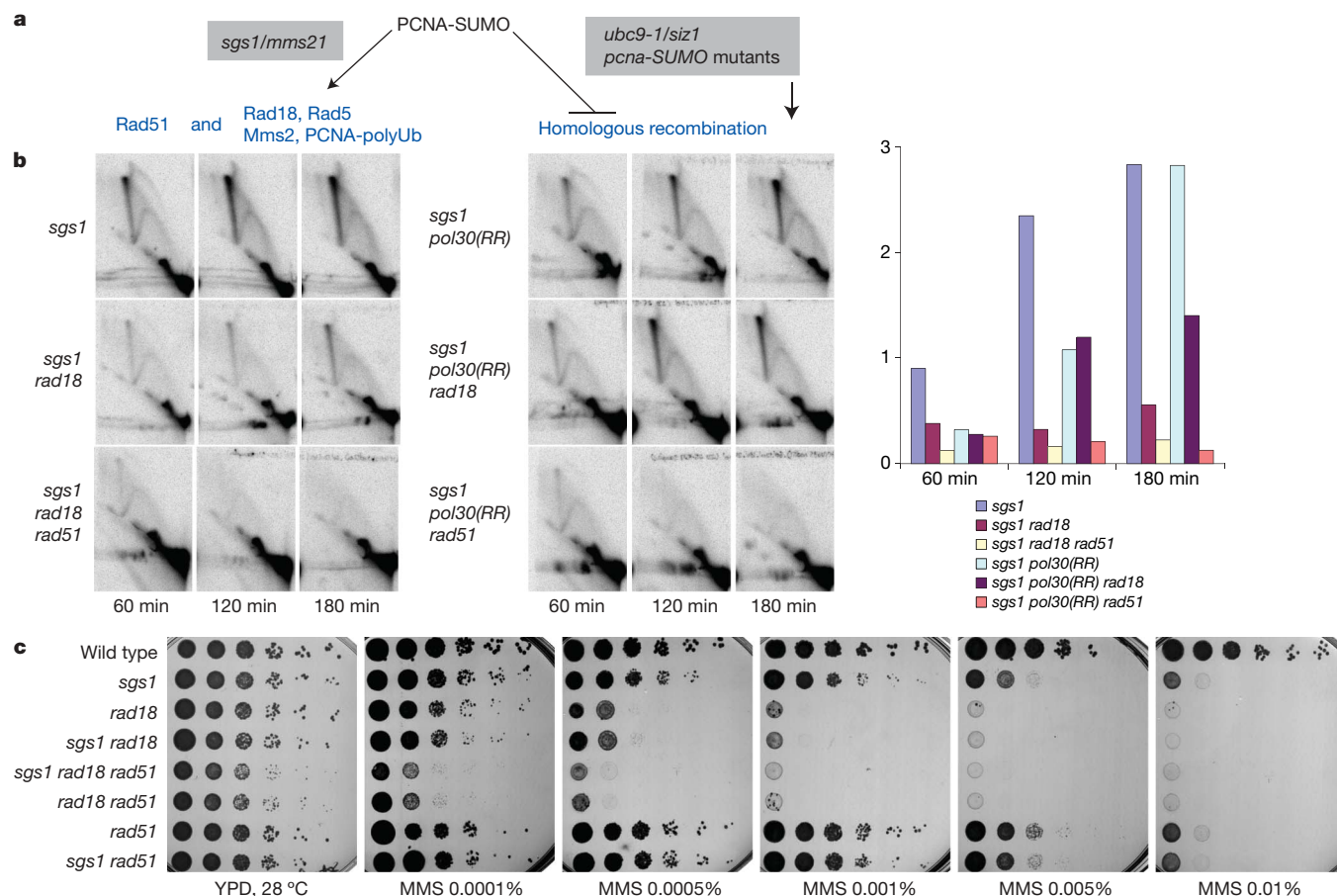


**Figure 4 | Two pathways contributing to SCJ formation.** **a**, Schematic representation of the pathways. Rad18–Rad5–Mms2 cooperates with Rad51 in mediating template switch, but this pathway requires PCNA SUMOylation. In the absence of PCNA SUMOylation, gap-filling occurs in a Rad18-independent manner, solely by means of homologous recombination. **b**, 2D gel analysis of strains *sgs1* (HY0501), *sgs1 rad18* (HY0695), *sgs1 rad18 rad51* (HY0872), *sgs1 pol30(RR)* (HY0724),

*sgs1 pol30(RR) rad18* (HY0840) and *sgs1 pol30(RR) rad51* (HY0874) at ARS305. *sgs1 pol30(RR)* represents *sgs1 pol30(K164R, K127R)*. The relative amount of X versus other intermediates is represented on the y axes of the quantification graph for each time point analysed. **c**, MMS sensitivity of wild-type (FY0113), *sgs1* (HY0985), *rad18* (HY0520), *rad18 sgs1* (HY1007), *rad18 sgs1 rad51* (HY1077), *rad18 rad51* (HY1075), *rad51* (HY0499) and *sgs1 rad51* (HY1049).

SUMOylated PCNA, by means of recruiting Srs2 (refs 24 and 25), were proposed to inhibit recombination events and promote PRR<sup>26–31</sup>.

The data presented here extend this model in several ways. Our results indicate that when PCNA SUMOylation is functional (wild type, *sgs1* and *mms21* backgrounds), SCJ formation at damaged replication forks takes place by a pathway that in addition to Rad51 (refs 32 and 33) requires the functions of Rad18–Rad5–Mms2-mediated PCNA polyubiquitylation (Fig. 1). Furthermore, in *sgs1 rad18* cells, ablation of *RAD51* completely abolishes the X molecules accumulation during replication of damaged templates (Fig. 4b). However, in the absence of PCNA SUMOylation, the damage-bypass process leading to X-molecule formation involves only the homologous recombination pathway (Supplementary Fig. 5, Figs 3 and 4b). Thus, in *sgs1 pol30(K164R)* (Fig. 3a), *sgs1 pol30(K164R, K127R)* in which both residues of PCNA targeted for SUMOylation are mutated (Fig. 4b), *sgs1 siz1* (Fig. 3b) and *ubc9-1* (Fig. 1a) genetic backgrounds, the X-molecule accumulation is Rad18-independent but Rad51-dependent (Supplementary Fig. 5, Fig. 4b and data not shown).

The traditional view holds that the Rad18 and the Rad51 repair pathways are parallel and independent. This was on the basis of genetic arguments showing that the phenotypes (damage sensitivity, and the ability of cells to convert nascent DNA from small to large size after irradiation) of the *rad18 rad51* and *rad18 rad52* double mutants are more severe than the phenotypes of each single mutant<sup>8,19</sup>. These results reflect independent, different roles of Rad18 and Rad51 in DNA repair, but do not rule out a possible overlap between these

two pathways. We propose that damage-bypass replication through SCJs represents a specific repair context in which Rad18 and Rad51 work together to promote replication bypass of the lesion by using the information on the newly synthesized chromatid (Supplementary Figs 2 and 12). We envisage that Sgs1 acts to resolve the SCJs formed by the combined action of Rad18 and Rad51, as well as the ones formed by homologous recombination alone. The genetic data that we found or that were previously reported do not contradict the possibility of such a model. We found that *sgs1* is epistatic to *rad18* (Fig. 2b), and it has been reported that *sgs1* is also epistatic to *rad52* (ref. 37). In line with previous results, we found that *rad18 rad51* double mutants are more sensitive than *rad18* and *rad51* single mutants, and that *rad51* is epistatic to *sgs1* (Fig. 4c). We also find, however, that the *sgs1 rad18 rad51* triple mutant is no more sensitive than *rad18 rad51*, supporting the idea that when Siz1-mediated SUMOylation of PCNA is not affected (Fig. 4a), the repair attempts of Rad18 and Rad51 converge to generate structures that require the same functions or efforts of Sgs1 to be resolved.

## Discussion

Proteins of the error-free branch of PRR are well-conserved and have been implicated in gap-repair, in both yeast and mammalian cells<sup>1,9–11,38–40</sup>. Mutations in *RAD18* and *RAD5* are associated with cancer and genome instability in human cells<sup>39,41</sup>, and with increased gross chromosomal rearrangements, trinucleotide repeat extension<sup>42,43</sup>, and the stability of repetitive sequences in yeast<sup>14,44</sup>.



Here we have shown using physical and genetic evidence that the Rad18–Rad5–Mms2 pathway functions through PCNA polyubiquitylation during replication of damaged templates to promote the formation of cruciform, X-shaped intermediates at replication forks. We propose that these SCJs represent template switch intermediates. Our data bring physical evidence in support of the crossfork template switch model of gap-filling repair<sup>13,14</sup> (Supplementary Fig. 2). The results of this study indicate that Rad18 and Rad51 may cooperate to promote the formation of SCJs at damaged replication forks (Fig. 4a and Supplementary Fig. 12). A backup to this system exists in the cells: when the Rad18 pathway fails to be activated (that is, when Siz1-mediated and PCNA SUMOylation are inhibited) a mechanism leading to SCJ formation occurs that requires the function of homologous recombination proteins (Rad51) but is independent of Rad18 (Fig. 3 and Fig. 4a, b). It is natural to reason that cells are endowed with a mechanism that discourages the use of only homologous recombination in this process. It has been proposed that the role of PCNA SUMOylation during replication is to recruit the Srs2 helicase, which will abolish the access of recombination factors to stalled forks<sup>24,25,45</sup> and thereby halt recombination. Our data indicate that the formation of SCJs by homologous recombination alone represents one type of recombination event suppressed by PCNA SUMOylation and possibly by Srs2 (Supplementary Fig. 12).

Supportive of the idea of an interaction between Rad18 and Rad51 in homologous recombination, studies in chicken DT40 cells have found that deletions of the *RAD51* paralogue *XRCC3*, which has been implicated in repair by homologous recombination<sup>46</sup>, suppresses the genome instability and damage sensitivity of *rad18* mutants<sup>47</sup>. Furthermore, in budding yeast the gross increase in chromosomal rearrangements observed in *rad18* and *rad5* mutants depends on Rad51 (ref. 42). These results indicate that homologous recombination may be toxic in the absence of a functional Rad18 pathway.

Given that the genes of the Rad18–Rad5 pathway govern responses to many damaging agents, and that their mutations have been associated with cancer development, increased mitotic recombination and sister chromatid exchanges in mouse embryonic stem cells and chicken DT40 cells<sup>39,47–50</sup>, understanding how Rad18–Rad5 acts together with the Rad51 set of genes to promote replication completion and limit aberrant recombination events is probably also important for anticancer therapeutic strategies.

## METHODS SUMMARY

**Yeast strains and plasmids.** The yeast strains used in this study are derivatives of DF5 or W303 strains (ref. 32 and references therein), and the relevant genotypes are shown in the Supplementary Table 1.

**Growing conditions, cell cycle arrests and drug treatments.** Unless otherwise indicated, strains were grown at 25 °C in YPD medium. Cells were synchronized by adding nocodazole to a final concentration of 10 µg ml<sup>−1</sup> together with 1% (v/v) dimethylsulphoxide, for about 2 h. The release from nocodazole arrest was performed as previously described, in YPD medium containing 0.033% (v/v) MMS at 30 °C<sup>32</sup>.

**Spot assays of drug sensitivity.** Log-phase cells were counted and tenfold series dilutions were spotted on plates containing various concentrations of MMS and incubated at the indicated temperatures.

**DNA extraction, FACS analysis and 2D gel technique.** Purification of DNA intermediates, FACS analysis and 2D gel procedure were carried out as previously described<sup>32,33</sup>. Quantification of the relative amount of X-shaped intermediates was performed using the IMAGE QUANT software as previously described<sup>32</sup>. The DNA samples were digested with HindIII and EcoRV and analysed by 2D gel with probes against *ARS305* and the flanking region *ARS301*, or alternatively digested with NcoI and analysed with probes recognizing *ARS305*, *ARS306* or *ARS1* (Supplementary Fig. 3).

Received 5 February; accepted 21 October 2008.

- Prakash, L. Characterization of postreplication repair in *Saccharomyces cerevisiae* and effects of *rad6*, *rad18*, *rev3* and *rad52* mutations. *Mol. Gen. Genet.* **184**, 471–478 (1981).
- Lopes, M., Foiani, M. & Sogo, J. M. Multiple mechanisms control chromosome integrity after replication fork uncoupling and restart at irreparable UV lesions. *Mol. Cell* **21**, 15–27 (2006).

- Branzei, D. & Foiani, M. Interplay of replication checkpoints and repair proteins at stalled replication forks. *DNA Repair (Amst.)* **6**, 994–1003 (2007).
- Lehmann, A. R. & Fuchs, R. P. Gaps and forks in DNA replication: Rediscovering old models. *DNA Repair (Amst.)* **5**, 1495–1498 (2006).
- Fabre, F., Chan, A., Heyer, W. D. & Gangloff, S. Alternate pathways involving Sgs1/Top3, Mus81/ Mms4, and Srs2 prevent formation of toxic recombination intermediates from single-stranded gaps created by DNA replication. *Proc. Natl Acad. Sci. USA* **99**, 16887–16892 (2002).
- Symington, L. S. Role of RAD52 epistasis group genes in homologous recombination and double-strand break repair. *Microbiol. Mol. Biol. Rev.* **66**, 630–670 (2002).
- San Filippo, J., Sung, P. & Klein, H. Mechanism of eukaryotic homologous recombination. *Annu. Rev. Biochem.* **77**, 229–257 (2008).
- Gangavarapu, V., Prakash, S. & Prakash, L. Requirement of RAD52 group genes for postreplication repair of UV-damaged DNA in *Saccharomyces cerevisiae*. *Mol. Cell. Biol.* **27**, 7758–7764 (2007).
- Zhang, H. & Lawrence, C. W. The error-free component of the RAD6/RAD18 DNA damage tolerance pathway of budding yeast employs sister-strand recombination. *Proc. Natl Acad. Sci. USA* **102**, 15954–15959 (2005).
- Torres-Ramos, C. A., Prakash, S. & Prakash, L. Requirement of RAD5 and MMS2 for postreplication repair of UV-damaged DNA in *Saccharomyces cerevisiae*. *Mol. Cell. Biol.* **22**, 2419–2426 (2002).
- Haracska, L. et al. Opposing effects of ubiquitin conjugation and SUMO modification of PCNA on replicational bypass of DNA lesions in *Saccharomyces cerevisiae*. *Mol. Cell. Biol.* **24**, 4267–4274 (2004).
- Higgins, N. P., Kato, K. & Strauss, B. A model for replication repair in mammalian cells. *J. Mol. Biol.* **101**, 417–425 (1976).
- Goldfless, S. J. et al. DNA repeat rearrangements mediated by DnaK-dependent replication fork repair. *Mol. Cell* **21**, 595–604 (2006).
- Branzei, D. & Foiani, M. Template switching: from replication fork repair to genome rearrangements. *Cell* **131**, 1228–1230 (2007).
- Jentsch, S., McGrath, J. P. & Varshavsky, A. The yeast DNA repair gene RAD6 encodes a ubiquitin-conjugating enzyme. *Nature* **329**, 131–134 (1987).
- Hofmann, R. M. & Pickart, C. M. Noncanonical MMS2-encoded ubiquitin-conjugating enzyme functions in assembly of novel polyubiquitin chains for DNA repair. *Cell* **96**, 645–653 (1999).
- Ulrich, H. D. & Jentsch, S. Two RING finger proteins mediate cooperation between ubiquitin-conjugating enzymes in DNA repair. *EMBO J.* **19**, 3388–3397 (2000).
- Bailly, V. et al. Specific complex formation between yeast RAD6 and RAD18 proteins: a potential mechanism for targeting RAD6 ubiquitin-conjugating activity to DNA damage sites. *Genes Dev.* **8**, 811–820 (1994).
- Branzei, D. & Foiani, M. Regulation of DNA repair throughout the cell cycle. *Nature Rev. Mol. Cell Biol.* **4**, 297–308 (2008).
- Hoegge, C. et al. RAD6-dependent DNA repair is linked to modification of PCNA by ubiquitin and SUMO. *Nature* **419**, 135–141 (2002).
- Stelter, P. & Ulrich, H. D. Control of spontaneous and damage-induced mutagenesis by SUMO and ubiquitin conjugation. *Nature* **425**, 188–191 (2003).
- Kannouche, P. L., Wing, J. & Lehmann, A. R. Interaction of human DNA polymerase  $\eta$  with monoubiquitinated PCNA: a possible mechanism for the polymerase switch in response to DNA damage. *Mol. Cell* **14**, 491–500 (2004).
- Geiss-Friedlander, R. & Melchior, F. Concepts in sumoylation: a decade on. *Nature Rev. Mol. Cell Biol.* **8**, 947–956 (2007).
- Pfander, B. et al. SUMO-modified PCNA recruits Srs2 to prevent recombination during S phase. *Nature* **436**, 428–433 (2005).
- Papouli, E. et al. Crosstalk between SUMO and Ubiquitin on PCNA Is Mediated by Recruitment of the Helicase Srs2p. *Mol. Cell* **19**, 123–133 (2005).
- Lawrence, C. W. & Christensen, R. B. Metabolic suppressors of trimethoprim and ultraviolet light sensitivities of *Saccharomyces cerevisiae* *rad6* mutants. *J. Bacteriol.* **139**, 866–876 (1979).
- Aboussekhra, A. et al. *RADH*, a gene of *Saccharomyces cerevisiae* encoding a putative DNA helicase involved in DNA repair. Characteristics of *radH* mutants and sequence of the gene. *Nucleic Acids Res.* **17**, 7211–7219 (1989).
- Schiestl, R. H., Prakash, S. & Prakash, L. The *SRS2* suppressor of *rad6* mutations of *Saccharomyces cerevisiae* acts by channeling DNA lesions into the *RAD52* DNA repair pathway. *Genetics* **124**, 817–831 (1990).
- Palladino, F. & Klein, H. L. Analysis of mitotic and meiotic defects in *Saccharomyces cerevisiae* *SRS2* DNA helicase mutants. *Genetics* **132**, 23–37 (1992).
- Krejci, L. et al. DNA helicase Srs2 disrupts the Rad51 presynaptic filament. *Nature* **423**, 305–309 (2003).
- Veaute, X. et al. The Srs2 helicase prevents recombination by disrupting Rad51 nucleoprotein filaments. *Nature* **423**, 309–312 (2003).
- Branzei, D. et al. Ubc9- and Mms21-mediated sumoylation counteracts recombination events at damaged replication forks. *Cell* **127**, 509–522 (2006).
- Liberi, G. et al. Rad51-dependent DNA structures accumulate at damaged replication forks in *sgs1* mutants defective in the yeast ortholog of BLM RecQ helicase. *Genes Dev.* **19**, 339–350 (2005).
- Mankouri, H. W., Ngo, H. P. & Hickson, I. D. Shu proteins promote the formation of homologous recombination intermediates that are processed by Sgs1-Rmi1-Top3. *Mol. Biol. Cell* **18**, 4062–4073 (2007).
- Wu, L. & Hickson, I. D. The Bloom's syndrome helicase suppresses crossing over during homologous recombination. *Nature* **426**, 870–874 (2003).
- Johnson, E. S. Protein modification by SUMO. *Annu. Rev. Biochem.* **73**, 355–382 (2004).

37. Onoda, F., Seki, M., Miyajima, A. & Enomoto, T. Involvement of *SGS1* in DNA damage-induced heteroallelic recombination that requires *RAD52* in *Saccharomyces cerevisiae*. *Mol. Gen. Genet.* **264**, 702–708 (2001).
38. Branzei, D., Seki, M. & Enomoto, T. Rad18/Rad5/Mms2-mediated polyubiquitination of PCNA is implicated in replication completion during replication stress. *Genes Cells* **9**, 1031–1042 (2004).
39. Tateishi, S. *et al.* Dysfunction of human Rad18 results in defective postreplication repair and hypersensitivity to multiple mutagens. *Proc. Natl Acad. Sci. USA* **97**, 7927–7932 (2000).
40. Zhao, G. Y. *et al.* A critical role for the ubiquitin-conjugating enzyme Ubc13 in initiating homologous recombination. *Mol. Cell* **25**, 663–675 (2007).
41. Motegi, A. *et al.* Human SHPRH suppresses genomic instability through proliferating cell nuclear antigen polyubiquitination. *J. Cell Biol.* **175**, 703–708 (2006).
42. Motegi, A. *et al.* Regulation of gross chromosomal rearrangements by ubiquitin and SUMO ligases in *Saccharomyces cerevisiae*. *Mol. Cell. Biol.* **26**, 1424–1433 (2006).
43. Daee, D. L., Mertz, T. & Lahue, R. S. Postreplication repair inhibits CAG•CTG repeat expansions in *Saccharomyces cerevisiae*. *Mol. Cell. Biol.* **27**, 102–110 (2007).
44. Johnson, R. E. *et al.* *Saccharomyces cerevisiae* *RAD5*-encoded DNA repair protein contains DNA helicase and zinc-binding sequence motifs and affects the stability of simple repetitive sequences in the genome. *Mol. Cell. Biol.* **12**, 3807–3818 (1992).
45. Sung, P. & Klein, H. Mechanism of homologous recombination: mediators and helicases take on regulatory functions. *Nature Rev. Mol. Cell Biol.* **7**, 739–750 (2006).
46. Otsuki, M. *et al.* Functional interactions between BLM and XRCC3 in the cell. *J. Cell Biol.* **179**, 53–63 (2007).
47. Szuts, D. *et al.* Role for RAD18 in homologous recombination in DT40 cells. *Mol. Cell. Biol.* **26**, 8032–8041 (2006).
48. Tateishi, S. *et al.* Enhanced genomic instability and defective postreplication repair in *RAD18* knockout mouse embryonic stem cells. *Mol. Cell. Biol.* **23**, 474–481 (2003).
49. Yamashita, Y. M. *et al.* *RAD18* and *RAD54* cooperatively contribute to maintenance of genomic stability in vertebrate cells. *EMBO J.* **21**, 5558–5566 (2002).
50. Shekhar, M. P. *et al.* Rad6 overexpression induces multinucleation, centrosome amplification, abnormal mitosis, aneuploidy, and transformation. *Cancer Res.* **62**, 2115–2124 (2002).

**Supplementary Information** is linked to the online version of the paper at [www.nature.com/nature](http://www.nature.com/nature).

**Acknowledgements** We thank S. Jentsch and H. Ulrich for yeast strains, T. Enomoto for critical reading, and all members of our laboratories for helpful discussions. This work was supported by grants from the Associazione Italiana per la Ricerca sul Cancro to D.B., Association for International Cancer Research and European Community GENICA grant to M.F. and D.B., and partly by European Community DNA Repair grant, Telethon, MIUR, and Ministry of Health to M.F. D.B. was partly supported by the Buzzati-Traverso foundation.

**Author Contributions** D.B. conceived the project, designed and performed the experiments, and wrote the paper. F.V. quantified the 2D gels, performed data analysis and provided technical help. M.F. discussed the results, analysed the data, edited the manuscript and provided scientific advice and financial support.

**Author Information** Reprints and permissions information is available at [www.nature.com/reprints](http://www.nature.com/reprints). Correspondence and requests for materials should be addressed to D.B. ([dana.branzei@ifom-ileo-campus.it](mailto:dana.branzei@ifom-ileo-campus.it)).



# Structure of an argonaute silencing complex with a seed-containing guide DNA and target RNA duplex

Yanli Wang<sup>1</sup>, Stefan Juranek<sup>2</sup>, Haitao Li<sup>1</sup>, Gang Sheng<sup>1</sup>, Thomas Tuschl<sup>2</sup> & Dinshaw J. Patel<sup>1</sup>

Here we report on a 3.0 Å crystal structure of a ternary complex of wild-type *Thermus thermophilus* argonaute bound to a 5'-phosphorylated 21-nucleotide guide DNA and a 20-nucleotide target RNA containing cleavage-preventing mismatches at the 10–11 step. The seed segment (positions 2 to 8) adopts an A-helical-like Watson–Crick paired duplex, with both ends of the guide strand anchored in the complex. An arginine, inserted between guide-strand bases 10 and 11 in the binary complex, locking it in an inactive conformation, is released on ternary complex formation. The nucleic-acid-binding channel between the PAZ- and PIWI-containing lobes of argonaute widens on formation of a more open ternary complex. The relationship of structure to function was established by determining cleavage activity of ternary complexes containing position-dependent base mismatch, bulge and 2'-O-methyl modifications. Consistent with the geometry of the ternary complex, bulges residing in the seed segments of the target, but not the guide strand, were better accommodated and their complexes were catalytically active.

RNA-induced silencing complex (RISC)-associated argonaute (Ago) proteins composed of PAZ- and PIWI-containing modules have a central role in mediating distinct assembly and cleavage steps of the RNA interference (RNAi) catalytic cycle<sup>1–4</sup>. The Ago protein, as the sole component of RISC exhibiting RNA 'slicer' activity<sup>5–7</sup>, is a critical player in the RNAi pathway<sup>8</sup>, effecting transcriptional and post-transcriptional gene regulation in plants and animals<sup>1–4</sup>. In this capacity, Agos have essential roles ranging from maintaining genomic integrity to heterochromatin formation. Some Ago proteins with active endonuclease domains contribute to the maturation of bound short interfering RNAs (siRNAs) by degradative cleavage of the passenger strand and subsequent guide-strand-mediated sequence-specific cleavage of target RNAs<sup>9–12</sup>. An improved understanding at the molecular level of guide-strand recognition in a binary complex with Ago and RNA target recognition and cleavage at the ternary Ago complex level could effect the application of RNAi approaches as a therapeutic modality against diverse human diseases<sup>13,14</sup>.

Bacteria also exhibit Ago-based cleavage activity of target RNAs and hence use the RNAi machinery, although details of the players and pathways at the cellular level are at present poorly understood. Most of the structural research on Ago proteins has initially focused on archaeal and eubacterial thermophilic Agos<sup>4,15–18</sup>. Crystal structures have been reported for archaeal *Pyrococcus furiosus* Ago<sup>5</sup> and eubacterial *Aquifex aeolicus* Ago<sup>19</sup>, both in the free state, thereby defining the relative alignments of the PAZ-containing (N and PAZ domains and linkers L1 and L2) and PIWI-containing (Mid and PIWI) modules. Given that binding and cleavage studies have identified these eubacterial and archaeal Agos to be site-specific DNA-guided endoRNases<sup>19</sup>, our group has recently solved the crystal structure of eubacterial *T. thermophilus* Ago with 5'-phosphorylated 10- and 21-nucleotide guide DNAs<sup>20</sup>, thereby identifying the guide strand-binding channel between the basic PAZ- and PIWI-containing lobes of the bilobal<sup>19</sup> Ago scaffold. This structure established that the 5'-phosphate and 3'-hydroxyl

ends are positioned in their respective binding pockets in the Mid<sup>21,22</sup> and PAZ<sup>23,24</sup> domains of Ago, the 2–10 segment of the bound guide DNA forms a stacked array, such that the solvent-exposed Watson–Crick edges of bases 2 to 6 in the 'seed' segment are positioned for nucleation with target RNA<sup>20</sup>. In addition, the side chain of R548 was inserted between bases 10 and 11, thereby disrupting base stacking, and locking this step in a non-catalytically competent conformation. We now report on the structural characterization of the ternary *T. thermophilus* Ago complex containing target RNA, thereby defining in molecular detail the alignment and pairing of guide and target strands spanning the seed segment and their positioning within the expanded nucleic-acid-binding channel of the bilobal Ago scaffold.

## Structure of ternary complex

The 3.0 Å crystal structure of wild-type *T. thermophilus* Ago complexed with a 5'-phosphorylated (5'-phos-T<sub>1</sub>GAGG<sub>5</sub>TAGTA<sub>10</sub>GGTTG<sub>15</sub>TATAG<sub>20</sub>T) 21-nucleotide guide DNA and its essentially complementary 20-nucleotide target RNA, containing cleavage-preventing A-C and G-U mismatches at the 10 and 11 steps (Fig. 1a), is presented in a stereo view in Fig. 1b, with an alternative perspective shown in Fig. 1c. A movie of the ternary Ago complex is included in Supplementary Movie 1. The Ago protein, in a ribbon representation, is colour-coded by domains and linker elements, with the traceable segments of the guide DNA in red and the target RNA in blue.

The bases of the guide DNA can be traced for the 1–10 segment (electron density map, Supplementary Fig. 1a), in which the 5'-phosphate is inserted into its binding pocket in the Mid domain<sup>21,22</sup> (Supplementary Fig. 2a), and can be traced for the 18/19 to 21 segment (electron density map, Supplementary Fig. 1b, c), in which nucleotides 20 and 21 at the 3' end are inserted into their binding pocket in the PAZ domain (Supplementary Fig. 2b)<sup>23,24</sup>. The observed anchoring of both ends of the guide DNA in the ternary complex with RNA target<sup>2</sup> was unexpected on topological grounds, although we

<sup>1</sup>Structural Biology Program, Memorial-Sloan Kettering Cancer Center, New York, New York 10065, USA. <sup>2</sup>Howard Hughes Medical Institute, Laboratory of RNA Molecular Biology, The Rockefeller University, New York, New York 10065, USA.

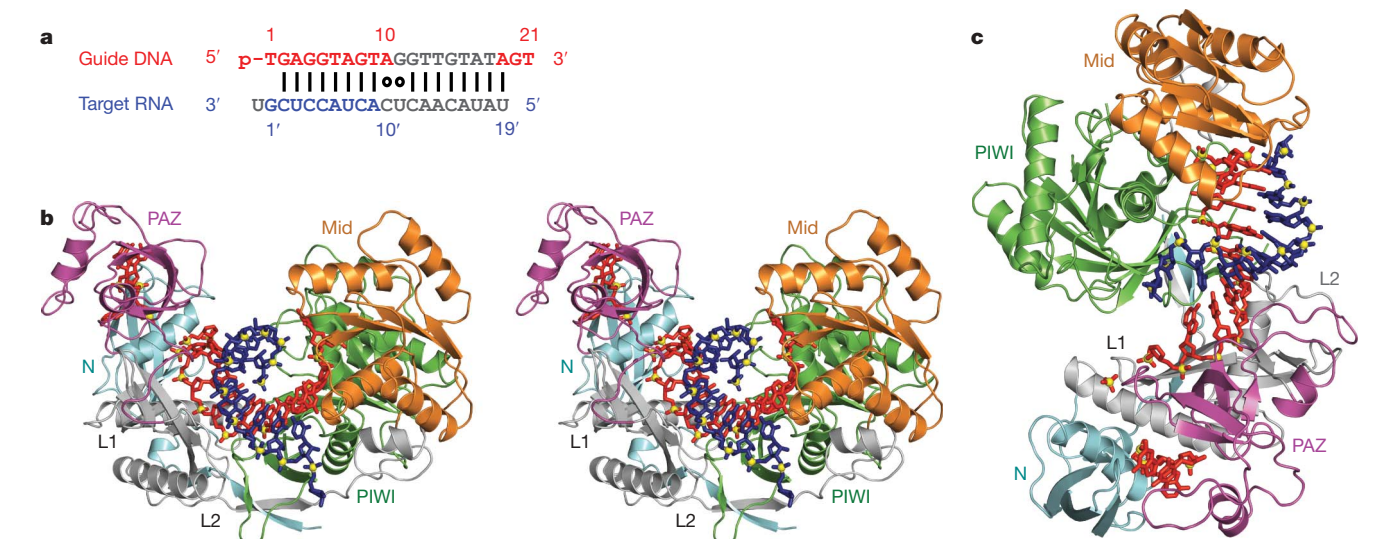


**Figure 1 | Crystal structure of *T. thermophilus* Ago bound to 5'-phosphorylated 21-nucleotide guide DNA and 20-nucleotide target RNA.**

**a**, Sequence of the guide DNA-target RNA duplex. The traceable segments of the bases of the guide DNA and target RNA in the structure of the ternary complex are shown in red and blue, respectively. Disordered segments of the bases on both strands that cannot be traced are shown in grey. **b**, Stereo view of the 3.0 Å crystal structure of the Ago ternary complex. The Ago protein is

colour-coded by domains (N in cyan, PAZ in magenta, Mid in orange and PIWI in green) and linkers (L1 and L2 in grey). The bound 21-nucleotide guide DNA is in red and traced for bases of the 1–10 and 19–21 segments, whereas the bound 20-nucleotide target RNA is in blue and traced for bases of the 1' to 9' segment. Backbone phosphorus atoms are in yellow. **c**, An alternate view of the complex.

anticipate the release of the 3'-end if pairing was to go beyond the seed segment observed in the present structure.

#### Guide-target duplex spanning seed segment

The bases of the target RNA can be traced for the 1'–9' segment (electron density map, Supplementary Fig. 3), with Watson–Crick alignment of the target RNA with the guide DNA, spanning the entire 2–8 seed segment (Fig. 2a). In addition, we can trace the sugar-phosphate backbone of the guide DNA and target RNA strands spanning the mismatch-containing 10–11 step (electron density map, Supplementary Fig. 4), thereby defining the orientation of the mismatch-distorted 10–11 cleavage step on the target RNA relative to the Asp catalytic triad of the RNase H fold of the PIWI domain of Ago (Fig. 2b).

The relative positions of the guide DNA in the binary (1–11 and 18–21, in silver) and ternary (1–10 and 19–21, in red) Ago complexes after superposition of their 5'-phosphate-recognizing Mid binding pockets is shown in Fig. 2c. Although the guide DNA superpositions well for the 1–4 segment, there is an 8.9 Å displacement by position 10 and an 17.1 Å displacement by position 21, suggesting that a noticeable change occurs in the trajectory of the guide strand on proceeding from the binary to the ternary complex.

The 2–8 seed segment formed by the guide DNA-target RNA duplex in the ternary Ago complex superpositions quite well with an A-form helix (Fig. 2d, left panel) and less well with its B-form helical counterpart (Fig. 2d, right panel). The guide-target duplex adopts different trajectories in the *Archaeoglobus fulgidus* Piwi ternary complex reported previously<sup>21,22</sup>, which lacks the PAZ-containing module, and in the *T. thermophilus* Ago ternary complex (stereo view in Supplementary Fig. 5).

#### Conformational transitions

We had previously identified an orthogonal alignment of bases 10 and 11 of the guide DNA as a result of insertion of the R548 side chain into the 10–11 step in the binary Ago complex<sup>20</sup> (Supplementary Fig. 6). In contrast, the side chain of R548 no longer inserts between bases 10 and 11 in the ternary complex (Fig. 2e), as a result of conformational changes on addition of target RNA. Thus, the non-helical conformation at the 10–11 step in the binary Ago complex (Supplementary Fig. 6)—an arrangement that would be detrimental

for catalytic cleavage of target RNA by the RNase H fold of the PIWI domain—is released on ternary Ago complex formation (Fig. 2e).

A single  $Mg^{2+}$  cation can be identified bound to the catalytic Asp residues for one molecule (Fig. 2a and Supplementary Fig. 7a) but not for the other in the asymmetric unit of the ternary complex, with reasonable superposition of the Asp side chains between molecules (biscuit and green colours in Supplementary Fig. 7b). The relative alignments of these catalytic Asp residues changes on proceeding from the binary (in silver, Supplementary Fig. 7c) to the ternary (in green, Supplementary Fig. 7c) Ago complex with added target RNA.

There is a marked conformational change in the relative alignments of the PAZ- and PIWI-containing lobes of the bilobal Ago scaffold on proceeding from the binary *T. thermophilus* Ago complex (with bound guide DNA) to the ternary complex (with added target RNA). This is readily observable on comparing the trajectory of the bound DNA guide strand (silver and red for the binary and ternary complexes, Fig. 2f) and adjacent protein segments (cyan and magenta for the binary and ternary complexes, Fig. 2f; conformational change highlighted by a red arrow) between the two complexes. Specifically, the PAZ- and PIWI-containing lobes move further apart on proceeding from binary (Fig. 3a) to ternary (Fig. 3b) complex formation, resulting in an opening movement that widens the nucleic-acid-binding channel, thereby facilitating insertion, alignment and pairing of the target RNA.

These movements can be tracked (Supplementary Movie 2) and are reinforced in a superpositioned view comparing the binary (in cyan) and ternary (in magenta) Ago complexes (Fig. 3c). The opening movement on ternary complex formation is reflected in a large conformational change in the N (rotation of 18.6° and translation of 0.6 Å) and PAZ (rotation of 23.1° and translation of 1.4 Å) domains (see red arrows in Fig. 3c) after superposition of their PIWI-containing modules (Mid and PIWI domains).

We also note that although bases 20 and 21 are similarly positioned in the PAZ binding pocket, the 18–19 segments of the binary and ternary complexes adopt different trajectories, associated with conformational changes in nearby protein segments (Supplementary Fig. 8).

#### Effect of mismatches and bulges on cleavage

Previous biochemical studies showed RNase H catalytic activity of bacterial Ago proteins loaded with guide DNA<sup>19,20</sup>. To assess the



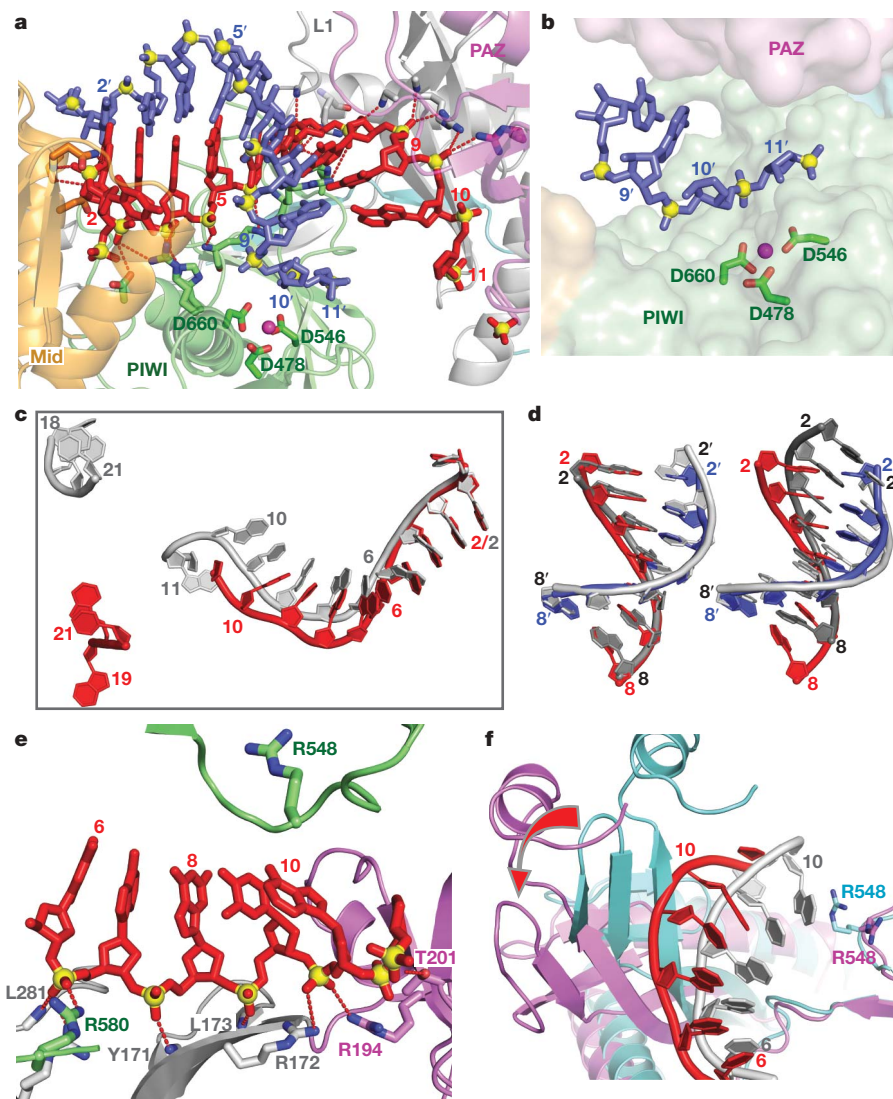


**Figure 2 | Comparison of structural details between the binary Ago complex with bound guide DNA and the ternary complex with added target RNA.** **a**, Expanded view of the ternary complex highlighting the guide DNA (1–10)-target RNA (1'–9') duplex and  $Mg^{2+}$ -coordinated catalytic residues (D478, D546 and D660) of the RNase H fold of the PIWI domain. Intermolecular hydrogen bonds between the Ago protein and the DNA guide strand in red are shown by dashed lines. **b**, Positioning of the sugar-phosphate backbone of the target RNA strand spanning the mismatch-containing 10–11-step relative to the catalytic residues of the PIWI domain. **c**, Comparison of the trajectory of traceable bound guide DNA in the binary (bases 1–11 and 18–21 in silver) and ternary (bases 1–10 and 19–21 in red) Ago complexes after superposition of their 5'-phosphate-binding pockets.

importance of base pairing of the guide DNA to target RNA, we introduced single nucleotide mismatches at positions from 1 to 19 in the 21-nucleotide guide strand (Fig. 4a). Cleavage reactions were carried out by first preincubating the Ago protein with guide DNA strands at 55 °C, followed by the addition of target RNA and further incubation at either 55 or 70 °C; both enhanced cleavage and background hydrolysis were observed at the higher temperature. Single mismatches were fully tolerated in the 3'-guide DNA regions (positions 13–19), and at the very 5' end (position 1), whereas cleavage was either abolished (position 9 and 10) or reduced (positions 11 and 12) by mismatches surrounding the cleavage site at 55 °C. Single mismatches in the seed region (position 2–8) showed reduced cleavage activity.

We next introduced several mismatches in the 3'-region and observed unaltered cleavage activity for up to six contiguous mismatches (positions 13–18) and reduced activity for eight contiguous

**d**, Superposition of the guide DNA (red)-target RNA (blue) duplex spanning the 2–8 seed segment on A-form (left panel) and B-form (right panel) helices (silver) after best-fit superposition of the target RNA strand of the ternary Ago complex with one strand of the A/B-form helices. **e**, Positioning of stacked residues 6–10 of the DNA guide strand relative to R548, with emphasis on intermolecular interactions involving the sugar-phosphate backbone. **f**, Relative positioning of the 6 to 10/11 segment of the bound guide DNA strand and R548 in the binary (guide strand in silver, protein in cyan) and ternary (guide strand in red, protein in magenta) Ago complexes. The conformational change in the protein on proceeding from binary to ternary Ago complexes is indicated by a red arrow.

mismatches (positions 12–19) at both 55 and 70 °C (Fig. 4b). These alterations of catalytic activity as a consequence of mismatches run parallel to earlier structure-function analysis in animals<sup>11,25</sup>, emphasizing the importance of contiguous base pairing for RNase H-mediated cleavage<sup>26</sup> in the 5'-seed segment (positions 2–8), especially near the cleavage site (step 10–11), and minimal contribution of the 3'-half (positions 13–19).

The importance of the seed segment became more apparent when we introduced single nucleotide insertions or deletions into the guide DNA (Fig. 4c). Cleavage was abrogated by a single nucleotide insertion at position 5 in the seed segment, whereas they had little effect when introduced at position 11 adjacent to the cleavage site or at position 14 in the 3' region of the guide strand. This suggests that the seed segment of the guide strand cannot accommodate a bulge nucleotide when paired to the target in the context of a helical duplex geometry, without disruption of the extensive intermolecular interactions that

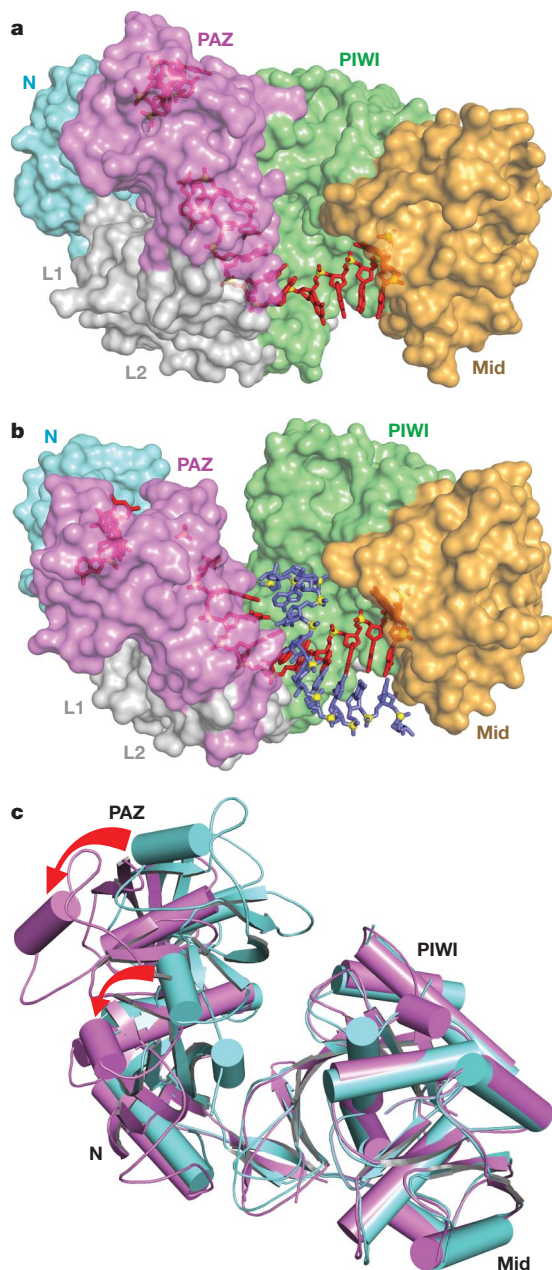


**Figure 3 | Conformational changes within the bilobal Ago scaffold on proceeding from the binary (guide) complex to the ternary (guide + target) complex.** **a, b**, The nucleic acid binding canyon changes width on proceeding from the binary (**a**) to the ternary (**b**) complex. The Ago protein is shown in a space-filling representation with labelled domains and linkers colour-coded as in Fig. 1. The guide DNA (red) and target RNA (blue) are shown in stick representation with backbone phosphorus atoms in yellow. **c**, View of alignment of binary (cyan) and ternary (magenta) Ago complexes, after superpositioning of their PIWI-containing modules. The red arrows indicate the magnitude of the conformational changes on proceeding from binary to ternary complexes.

anchor the guide strand within the Ago scaffold (Fig. 2a; see schematic in Supplementary Fig. 9).

We next assessed the importance of single and double bulges within the target RNA. Unexpectedly, insertion of single bulges opposite positions 4–5 and 5–6 of the guide strand 5′-seed segment had minimal effect on cleavage, but cleavage was reduced after insertion of dual bulges at the same positions (Fig. 4d). In contrast to the guide strand, the sugar-phosphate backbone of the target strand complementary to the seed segment makes no contacts with the Ago scaffold (Supplementary Fig. 10 and Supplementary Movie 3),

and seemingly accommodates single and to a lesser extent double bulges within the paired seed segment. Insertion of double bulges opposite positions 14–15 and 18–19 of the guide strand 3′ region did not impair target RNA cleavage (Fig. 4d), again reinforcing the conclusion that helical imperfections disrupting pairing interactions involving the 3′ region of the guide strand have a minimal effect on cleavage activity.

### Effect of guide length and 2′-O-methyl on cleavage

To investigate the constraints on guide strand length for cleavage activity, we systematically investigated the cleavage activity of guide strands spanning from 7 to 36 nucleotides. At a reaction temperature of 55 °C, cleavage is observed for 5′-phosphorylated guide strand sequences that are as short as 9 nucleotides and as long as 36 nucleotides (Fig. 4e, left panel). Increasing the reaction temperature to 70 °C restricts cleavage to 12–36-nucleotide guide strands (Fig. 4e, right panel). Furthermore, cleavage activity is strictly dependent on the presence of a 5′-phosphate on the guide strand (Supplementary Fig. 11), a dependence not strictly observed for animal Ago complexes<sup>27,28</sup>. The observed cleavage for guide strands as short as 9-nucleotides at 55 °C (Fig. 4e, left panel), which lack residues proximal to the cleavage site that could not be mutated without loss of activity (Fig. 4a), was unanticipated. This suggests that mismatch accommodation introduces steric constraints that interfere with proper placement of the target strand cleavage residues, and that the geometry required for cleavage can also be adopted in the absence of residues 10 and 11 of the guide strand. The absence of cleavage for 9- to 11-nucleotide guide strands at 70 °C (Fig. 4e, right panel) probably reflects the thermodynamic instability of short duplex hybridization at higher temperatures. The observed cleavage activity by guide strands up to 36-nucleotides in length (Fig. 4e) could be rationalized by the guide strand adopting alternate trajectories for its 3′-segment leading into the PAZ pocket. This flexibility is presumably a consequence of fewer intermolecular contacts between the protein side chains and the sugar-phosphate backbone of the 3′-guide strand segment (residues 12–19; Supplementary Fig. 12), which is in contrast to the extensively sugar-phosphate backbone-anchored 5′-seed counterpart (Fig. 2a and Supplementary Fig. 9). In addition, the nucleic-acid-binding channel that encompasses the 3′-segment of the bound guide strand is accessible to the outside and permissive to looping-out longer 3′-segments (Supplementary Fig. 12).

In mammalian systems, altering the guide strand 2′-hydroxyl to 2′-O-methyl was shown to influence the cleavage activity depending on the extent and position of modification<sup>29</sup>. To probe the importance of the 2′-position in the eubacterial guide DNA, we introduced 2′-O-methyl modifications at various positions and monitored cleavage at 55 and 70 °C (Supplementary Fig. 13). We observed that fully modified 2′-O-methylated guide molecules, as reported for mammalian RNAi<sup>30</sup>, abrogated cleavage, whereas substitutions spanning the 5′-half (residues 2–9) or the 3′-half (residues 12–19) severely reduce activity. In contrast, pairwise replacement of DNA residues by 2′-O-methyl had minimal effects on catalytic activity, independent of the position (Supplementary Fig. 13). These results indicate that extensive 2′-O-methyl modifications of the guide strand may introduce cumulative steric constraints that inhibit the adoption of cleavage competent conformations or even interfere with guide strand accommodation into the Ago protein.

Our structural results on the ternary Ago complex have highlighted details of guide-strand-mediated target RNA recognition spanning the seed segment, and the conformational transitions that expand the nucleic-acid-binding channel within the bilobal Ago scaffold, thereby accommodating and aligning the target RNA for eventual site-specific cleavage. We have been unable in the present study to trace the electron density accurately for base 11 of the DNA guide and bases 10′ and 11′ of the RNA target strands of the bound duplex, with the disorder probably due to distortions associated with mismatch incorporation at the 10–11 step.



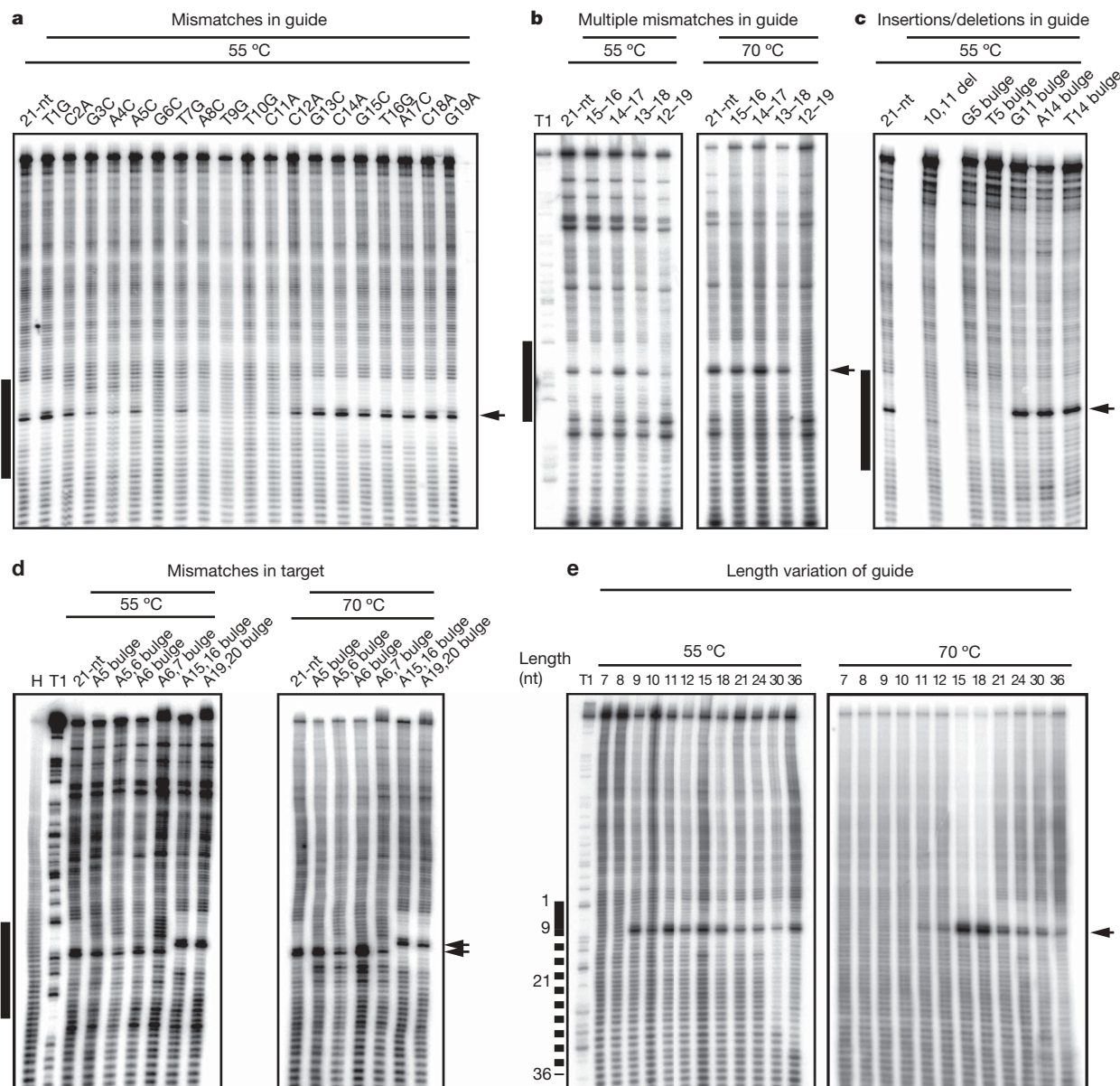


**Figure 4 | Target RNA cleavage activity of *T. thermophilus* Ago loaded with mismatched, bulge-containing or length-altered guide DNA strands.**

Besides Ago-mediated target RNA cleavage, extensive chemical hydrolysis is observed over the entire RNA substrate length, except for a 12-nucleotide (nt) region across guide DNA positions 2 to 13, which was protected from hydrolysis by the interaction with Ago and its guide DNA. Mismatches or bulges in the 5' region reduce protection, and frequently catalysis, because of reduced base-pairing stability and deviation from hydrolysis-protecting helical geometry. The black bar to the left of the images defines the region of the cleavage substrate complementary with the 21-nucleotide (nt) guide DNA (a–d) or the region complementary with the 7-nucleotide guide DNA with the dotted line indicating pairing for 3'-extended guide DNAs (e). Arrows indicate the cleavage site. Del, deletion; H, hydrolysis ladder of

substrate RNA; T1, partial RNase T1 digest of substrate RNA. **a**, Single mismatches were placed in the 21-nucleotide guide, at positions 1 to 19. **b**, Double, quadruple, sextuple and octuple mismatches were introduced in the DNA guide 3' region at indicated positions. **c**, Cleavage assay using DNA guides with a deletion or insertions of bulged nucleotides at indicated positions. **d**, Insertion of bulges in the target RNA. Insertion of nucleotides upstream of the cleavage site leads to shifts in the cleavage site by the number of inserted nucleotides. **e**, DNA guide length was increased from 7 to 36 nucleotides. The sequences of DNA guides and RNA targets are listed in Supplementary Table 2. As evident from increased hydrolysis of the target region recognized by the guide, insertion of bulges seems to destabilize guide–target interactions.

### Functional implications

The biochemical and structural information helps us to understand how microRNA (miRNA)–target RNA duplexes can be accommodated in Ago complexes, and rationalizes how one class of siRNA off-targets<sup>31</sup> requiring extensive base pairing across the cleavage site can be subjected to cleavage. We can now rationalize how single-site alterations in a target RNA within the sequence defined by the seed can be accommodated without interference with cleavage activity, provided that sufficient pairing is retained along the cleavage site. It is also conceivable that miRNA targets with more extensive base pairing

extending outside the seed region, as observed for a subset of miRNA targets, may be subject to direct messenger RNA cleavage, possibly contributing to the general destabilization encountered in miRNA-mediated mRNA targeting.

Our results on eubacterial *T. thermophilus* Ago are similar to the finding that *Drosophila* Piwi proteins<sup>32</sup> and human AGO proteins<sup>33</sup> can accept different size guide strands to mediate target RNA cleavage. In essence, our studies emphasize that Piwi and Ago scaffolds have sufficient plasticity to accommodate different length guide strands, and that the size range of naturally accommodated small

RNA classes are a direct consequence of their distinct biogenesis mechanisms.

It remains unclear at this time whether mammalian Agos will function in a manner suggested by the structure of the eubacterial Ago ternary complex outlined here. Therefore, the recent report on successful insect cell expression of a soluble form of human AGO2 (also known as EIF2C2 protein; ref. 34) opens opportunities and holds promise for future extension of continuing structural research to eukaryotic Ago complexes, thereby expanding on insights from chemical approaches into the molecular basis of target RNA recognition and cleavage by human RISC<sup>35,36</sup>.

## METHODS SUMMARY

Wild-type *T. thermophilus* Ago was overexpressed from *Escherichia coli* and purified by chromatography. The ternary Ago complex was generated in a step-wise manner by initially mixing Ago with 21-nucleotide guide DNA, followed by addition of 20-nucleotide target RNA. Crystals were grown by hanging-drop vapour diffusion. The ternary Ago complex structure was determined by molecular replacement using the domains of the binary Ago complex structure<sup>20</sup> as search models. Cleavage assays were undertaken using guide oligodeoxynucleotides and a longer target RNA. Details of all biochemical and crystallographic procedures are listed in Methods.

**Full Methods** and any associated references are available in the online version of the paper at [www.nature.com/nature](http://www.nature.com/nature).

**Received 5 August; accepted 25 November 2008.**

- Hock, J. & Meister, G. The Argonaute protein family. *Genome Biol.* **9**, 210 (2008).
- Filipowicz, W. The nuts and bolts of the RISC machine. *Cell* **122**, 17–20 (2005).
- Hutvagner, G. & Simard, M. J. Argonaute proteins: key players in RNA silencing. *Nature Rev. Mol. Cell Biol.* **9**, 22–32 (2008).
- Tolia, N. H. & Joshua-Tor, L. Slicer and the argonautes. *Nature Chem. Biol.* **3**, 36–43 (2007).
- Song, J. J., Smith, S. K., Hannon, G. J. & Joshua-Tor, L. Crystal structure of Argonaute and its implications for RISC slicer activity. *Science* **305**, 1434–1437 (2004).
- Liu, J. *et al.* Argonaute2 is the catalytic engine of RNAi. *Science* **305**, 1437–1441 (2004).
- Parker, J. S., Roe, S. & Barford, D. Crystal structure of a PIWI protein suggests mechanisms for siRNA recognition and slicer activity. *EMBO J.* **23**, 4727–4737 (2004).
- Fire, A. *et al.* Potent and specific genetic interference by double-stranded RNA in *Caenorhabditis elegans*. *Nature* **391**, 806–811 (1998).
- Elbashir, S. M., Lendeckel, W. & Tuschl, T. RNA interference is mediated by 21- and 22-nucleotide RNAs. *Genes Dev.* **15**, 188–200 (2001).
- Martinez, J. & Tuschl, T. RISC is a 5'-phosphomonoester-producing RNA endonuclease. *Genes Dev.* **18**, 975–980 (2004).
- Schwarz, D. S., Tomari, Y. & Zamore, P. D. The RNA-induced silencing complex is a Mg<sup>2+</sup>-dependent endonuclease. *Curr. Biol.* **14**, 787–791 (2004).
- Tomari, Y. & Zamore, P. D. Perspective: machines for RNAi. *Genes Dev.* **19**, 517–529 (2005).
- De Fougères, A., Vornlocher, H.-P., Maraganore, J. & Lieberman, J. Interfering with disease: a progress report on siRNA-based therapeutics. *Nature Rev. Drug. Discovery* **6**, 443–453 (2007).
- Kim, D. H. & Rossi, J. J. Strategies for silencing human disease using RNA interference. *Nature Rev. Genetics* **8**, 173–184 (2007).
- Filipowicz, W., Jaskiewicz, L., Kolb, F. A. & Pillai, R. S. Post-transcriptional gene silencing by siRNAs and miRNAs. *Curr. Opin. Struct. Biol.* **15**, 331–341 (2005).
- Hall, T. M. Structure and function of argonaute proteins. *Structure* **13**, 1403–1408 (2005).
- Parker, J. S. & Barford, D. Argonaute: a scaffold for the function of short regulatory RNAs. *Trends Biochem. Sci.* **31**, 622–630 (2006).
- Patel, D. J. *et al.* Structural biology of RNA silencing and its functional implications. *Cold Spring Harb. Symp. Quant. Biol.* **71**, 81–93 (2006).
- Yuan, Y. R. *et al.* Crystal structure of *A. aeolicus* argonaute, a site-specific DNA-guided endoribonuclease, provides insights into RISC-mediated mRNA cleavage. *Mol. Cell* **19**, 405–419 (2005).
- Wang, Y. *et al.* Structure of the guide-strand-containing Argonaute silencing complex. *Nature* **456**, 209–213 (2008).
- Parker, J. S., Roe, S. M. & Barford, D. Structural insights into mRNA recognition from a PIWI domain-siRNA guide complex. *Nature* **434**, 663–666 (2005).
- Ma, J. B. *et al.* Structural basis for 5'-end-specific recognition of guide RNA by the *A. fulgidus* Piwi protein. *Nature* **434**, 666–670 (2005).
- Ma, J. B., Ye, K. & Patel, D. J. Structural basis for overhang-specific small interfering RNA recognition by the Paz domain. *Nature* **429**, 318–322 (2004).
- Lingel, A., Simon, B., Izaurralde, E. & Sattler, M. Nucleic acid 3'-end recognition by the Argonaute2 Paz domain. *Nature Struct. Mol. Biol.* **11**, 576–577 (2004).
- Haley, B. & Zamore, P. D. Kinetic analysis of the RNAi enzyme complex. *Nature Struct. Mol. Biol.* **11**, 599–606 (2004).
- Nowotny, M., Gaidamakov, S. A., Crouch, R. J. & Yang, W. Crystal structures of RNase H bound to an RNA/DNA hybrid: substrate specificity and metal-dependent catalysis. *Cell* **121**, 1005–1016 (2005).
- Schwarz, D. S. *et al.* Asymmetry in the assembly of the RNAi enzyme complex. *Cell* **115**, 199–208 (2003).
- Chen, P. Y. *et al.* Strand-specific 5'-O-methylation of siRNA duplexes controls guide strand selection and targeting specificity. *RNA* **14**, 263–274 (2008).
- Jackson, A. L. *et al.* Position-specific chemical modification of siRNAs reduces "off-target" transcript silencing. *RNA* **12**, 1197–1205 (2006).
- Dorsett, Y. & Tuschl, T. siRNAs: applications in functional genomics and potential as therapeutics. *Nature Rev. Drug Discov.* **3**, 318–329 (2004).
- Jackson, A. L. *et al.* Expression profiling reveals off-target gene regulation by RNAi. *Nature Biotechnol.* **21**, 635–637 (2003).
- Gunawardane, L. S. *et al.* A slicer-mediated mechanism for repeat-associated siRNA 5'-end formation in *Drosophila*. *Science* **315**, 1587–1590 (2007).
- Martinez, J. *et al.* Single-stranded anti-sense siRNAs guide target RNA cleavage in RNAi. *Cell* **110**, 563–574 (2002).
- MacRae, I. J. *et al.* In vitro reconstitution of human RISC-loading complex. *Proc. Natl Acad. Sci. USA* **105**, 512–517 (2008).
- Ameres, S. L., Martinez, J. & Schroeder, R. Molecular basis for target RNA recognition and cleavage by human RISC. *Cell* **130**, 101–112 (2007).
- Rana, T. M. Illuminating the silence: understanding the structure and function of small RNAs. *Nature Rev. Mol. Cell Biol.* **8**, 23–26 (2007).

**Supplementary Information** is linked to the online version of the paper at [www.nature.com/nature](http://www.nature.com/nature).

**Acknowledgements** The research was supported by funds from the National Institutes of Health and the Starr Foundation to D.J.P. and T.T. We would like to thank the staff of NE-CAT beam line at the Advanced Photon Source, Argonne National Laboratory, supported by the US Department of Energy, for assistance with data collection.

**Author Contributions** Y.W. and G.S. expressed and purified *T. thermophilus* Ago, and grew crystals of the ternary complex. H.L. and Y.W. collected X-ray diffraction data on the micro-focus beam line, and Y.W. solved the structure of the ternary complex. The structural studies were undertaken with the supervision of D.J.P. S.J. was responsible for the cleavage assays on Ago with modified guide strands under the supervision of T.T. D.J.P. and T.T. were primarily responsible for writing the paper and all authors read and approved the submitted manuscript.

**Author Information** The structural coordinates of the ternary complex of *T. thermophilus* Ago bound to 5'-phosphorylated 21-nucleotide guide DNA and 20-nucleotide target RNA have been submitted to the Protein Data Bank under accession number 3F73. Reprints and permissions information is available at [www.nature.com/reprints](http://www.nature.com/reprints). Correspondence and requests for materials should be addressed to D.J.P. (pateld@mskcc.org) or T.T. (ttuschl@mail.rockefeller.edu).



## METHODS

**Crystallization and data collection.** Wild-type *T. thermophilus* Ago was prepared as described previously<sup>5</sup>. Oligodeoxynucleotides were purchased from Invitrogen and RNA oligonucleotides were from Dharmacon. For crystallization, *T. thermophilus* Ago was mixed with 5'-phosphorylated 21-nucleotide guide DNA at 1:1.2 molar ratio, followed by addition of 20-nucleotide target RNA at a 1.2 molar ratio to the binary mixture, to form the ternary complex. The ternary Ago complex crystals were grown from 10% (v/v) polyethylene glycerol 400, 50 mM MES, pH 5.6, 0.1 M KCl and 15 mM MgCl<sub>2</sub> at 35 °C.

Diffraction data were collected at 100K on the micro-focus beam line NE-CAT ID-24E, at the Advanced Photon Source (APS), Argonne National Laboratory. Three data sets were integrated and scaled with the HKL2000 suite<sup>37</sup> and data processing statistics are summarized in Supplementary Table 1. The ternary complex belonged to the *P*2<sub>1</sub> space group and diffracted to 3.0 Å.

**Structure determination and refinement.** The structure of complex was solved by molecular replacement with the program PHASER<sup>38</sup>, using the domains of the Ago–21-nucleotide guide DNA binary complex structure<sup>20</sup> as search models. The model contains two molecules in the asymmetric unit. Initial cycles of simulated annealing refinement by the program CNS<sup>39</sup> were carried out whilst maintaining strict twofold non-crystallographic symmetry (NCS) constraints. After rigid body and minimization refinements, the nucleic acid strands were clearly visible in both  $\sigma_A$ -weighted  $F_o - F_c$  and  $2F_o - F_c$  maps. In later stages of the refinement, the symmetry constraints were loosened within the two molecules in one asymmetric unit. The structure of the Ago ternary complex was manually built with COOT<sup>40</sup> and O<sup>41</sup>, cycled with CNS refinement, to a final  $R_{work}$  of 22.5% and  $R_{free}$  of 28.2%. The final figures were created with Pymol (<http://pymol.sourceforge.net/>).

**Cleavage activity assay of *T. thermophilus* Ago.** The 5'-phosphorylated oligodeoxynucleotides were prepared by solid-phase synthesis using standard DNA phosphoramidites (Sigma-Proligo) and chemical phosphorylating reagent (Glen Research) on an ABI 3400 DNA synthesizer. The 2'-*O*-methyl-ribonucleoside-modified oligodeoxynucleotides were synthesized using DNA and 2'-*O*-methyl-ribonucleoside phosphoramidites (Dharmacon) and chemical phosphorylating

reagent (Dharmacon) on a modified ABI 392 DNA/RNA synthesizer. The 177-nucleotide cleavage substrate was prepared by *in vitro* transcription from a PCR template as described previously<sup>33</sup>. Sequence-altered RNA targets were transcribed from PCR templates prepared from plasmid templates mutagenized using Quickchange II XL (Stratagene). Identity of mutated plasmids was confirmed by sequencing. The transcript was dephosphorylated using alkaline phosphatase (Roche) and then 5'-radiolabelled using T4 polynucleotide kinase (Fermentas) and  $\gamma$ -<sup>32</sup>P-ATP.

Recombinant *T. thermophilus* Ago (1  $\mu$ M final concentration) was incubated with a reaction mixture containing 10 mM HEPES-KOH, pH 7.5, 100 mM NaCl, 5 mM MnCl<sub>2</sub>, and 0.5  $\mu$ M guide strand for 30 min at 55 °C in a final volume of 15  $\mu$ l. Next 5'-<sup>32</sup>P-labelled RNA substrate at a final concentration of 0.1  $\mu$ M was added. The incubation was continued for 30 min at either 55 or 70 °C. The reaction was stopped by addition of 185  $\mu$ l proteinase K solution (1 mg ml<sup>-1</sup> proteinase K, 20 mM HEPES-KOH, pH 7.5, 1.5 mM EDTA, 100 mM NaCl, 1.5 mM CaCl<sub>2</sub> and 1.5% SDS), and incubated at 55 °C for 10 min, followed by phenol-chloroform extraction and ethanol precipitation. The cleavage products were resolved on an 8% denaturing polyacrylamide gel, and radioactivity was monitored by phosphorimaging.

Appropriate controls establishing that both DNA guide and Ago are required for cleavage are shown in Supplementary Fig. 14.

37. Otwinowski, Z. & Minor, W. Processing of X-ray diffraction data collected in oscillation mode. *Meth. Enzymol.* **276**, 307–326 (1997).
38. McCoy, A. J. *et al.* Phaser crystallographic software. *J. App. Crystallogr.* **40**, 658–674 (2007).
39. Brunger, A. T. *et al.* Crystallography & NMR system: A new software suite for macromolecular structure determination. *Acta Crystallogr. D* **54**, 905–921 (1998).
40. Emsley, P. & Cowtan, K. Coot: model-building tools for molecular graphics. *Acta Crystallogr. D* **60**, 2126–2132 (2004).
41. Jones, T. A., Zhou, J. Y., Cowan, S. W. & Kjeldgaard, M. Improved methods for building protein models in electron density maps and the location of errors in these models. *Acta Crystallogr. A* **47**, 110–119 (1991).

# A gravitationally lensed water maser in the early Universe

C. M. Violette Impellizzeri<sup>1</sup>, John P. McKean<sup>1</sup>, Paola Castangia<sup>1,2</sup>, Alan L. Roy<sup>1</sup>, Christian Henkel<sup>1</sup>, Andreas Brunthaler<sup>1</sup> & Olaf Wucknitz<sup>3</sup>

Water masers<sup>1–4</sup> are found in dense molecular clouds closely associated with supermassive black holes at the centres of active galaxies. On the basis of the understanding of the local water-maser luminosity function<sup>5</sup>, it was expected that masers at intermediate and high redshifts would be extremely rare. However, galaxies at redshifts  $z > 2$  might be quite different from those found locally, not least because of more frequent mergers and interaction events. Here we use gravitational lensing to search for masers at higher redshifts than would otherwise be possible, and find a water maser at redshift 2.64 in the dust- and gas-rich, gravitationally lensed type-1 quasar MG J0414+0534 (refs 6–13). The isotropic luminosity is  $10,000 L_{\odot}$  ( $L_{\odot}$ , solar luminosity), which is twice that of the most powerful local water maser<sup>14</sup> and half that of the most distant maser previously known<sup>15</sup>. Using the locally determined luminosity function<sup>5</sup>, the probability of finding a maser this luminous associated with any single active galaxy is  $10^{-6}$ . The fact that we see such a maser in the first galaxy we observe must mean that the volume densities and luminosities of masers are higher at redshift 2.64.

Observations of the water  $6_{16}-5_{23}$  transition (rest frequency, 22.23508 GHz) from MG J0414+0534 (Supplementary Information) were made with the 100-m Effelsberg radio telescope at the redshifted frequency of 6.1 GHz during July and September 2007. The radio spectrum (Fig. 1a) shows an emission feature detected with a signal-to-noise ratio of seven, which we identify as a water maser. The emission arises from the amplification of background photons by stimulated emission of water molecules that have been pumped to a long-lived excited state by collisional excitation<sup>4</sup> (Supplementary Information). The line emission cannot be associated with the lensing galaxy at redshift 0.958 or with a nearby 'local' object, because there are no known strong lines at the corresponding rest frequencies (11.975 GHz and 6.116 GHz, respectively).

To confirm the detection of water-maser emission and to match it spatially with the lensed quasar, we made interferometric observations with the Expanded Very Large Array (EVLA) during September and October 2007. We detected a clear emission line with a signal-to-noise ratio of six (Fig. 1b) when the emission was integrated over the position of the two strongest images (A1 and A2) of the lensed quasar (Fig. 2). The maser line was also detected in the separate spectra of A1 and A2, although at a lower signal-to-noise ratio. The EVLA measurements were not sensitive enough to detect the water-maser emission from the two weaker lensed images (B and C). The radial velocities measured with the Effelsberg radio telescope and the EVLA are identical to within their uncertainties (Supplementary Table 1). The water-maser line is also coincident in velocity with the blueshifted peak of carbon monoxide emission and with the strongest H I absorption trough previously reported in

MG J0414+0534 (refs 12, 13) (Fig. 1). There is no evidence of water-maser emission at the velocities of the other known carbon monoxide emission and H I absorption components. Our detection is consistent with a previously reported non-detection that did not reach sufficient sensitivity<sup>16</sup>.

Hitherto, the highest redshift at which water had been observed was 0.66 (ref. 15); the water maser in MG J0414+0534 is at a redshift of 2.639, which is a factor of six more distant (using luminosity distances). The measured maser transition requires gas temperatures in excess of 300 K and particle densities  $n(\text{H}_2) > 10^7 \text{ cm}^{-3}$  (Supplementary Information). The densest gas previously observed

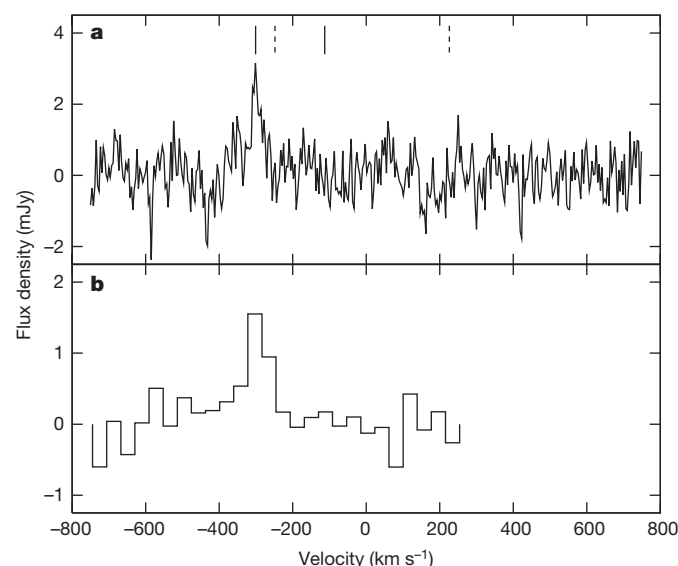


**Figure 1 | The 6.1-GHz water spectra of the lensed quasar MG J0414+0534.** The velocity scale is relative to redshift 2.639 using the optical velocity definition in the heliocentric frame. The vertical solid lines mark the H I absorption components ( $-301 \pm 13 \text{ km s}^{-1}$  and  $-113 \pm 13 \text{ km s}^{-1}$ ) and the vertical dashed lines indicate the peaks of carbon monoxide emission ( $-238 \pm 70 \text{ km s}^{-1}$  and  $+226 \pm 70 \text{ km s}^{-1}$ ). **a**, The combined spectrum taken with the Effelsberg 100-m radio telescope on 16 July and 14 September 2007. The total on-source integration time was 14 h. The spectra were formed with a 1,024-channel autocorrelator, which provided a channel width of  $3.83 \text{ km s}^{-1}$ . The root-mean-square (r.m.s.) noise level of the spectrum is 0.6 mJy per channel. **b**, The spectrum of lensed images A1 and A2 of MG J0414+0534 taken with the EVLA using nine of the upgraded 25-m antennas during 24, 28 and 30 September and 1 and 7 October 2007. The usable observing time was 12 h on-source. The spectrum has 32 channels with a spectral resolution of  $38.4 \text{ km s}^{-1}$  per channel. The r.m.s. noise level is 0.3 mJy per channel.

<sup>1</sup>Max-Planck-Institut für Radioastronomie, Auf dem Hügel 69, D-53121 Bonn, Germany. <sup>2</sup>INAF-Osservatorio Astronomico di Cagliari, Loc. Poggio dei Pini, Strada 54, I-09012 Capoterra (CA), Italy. <sup>3</sup>Argelander-Institut für Astronomie, Auf dem Hügel 71, D-53121 Bonn, Germany.



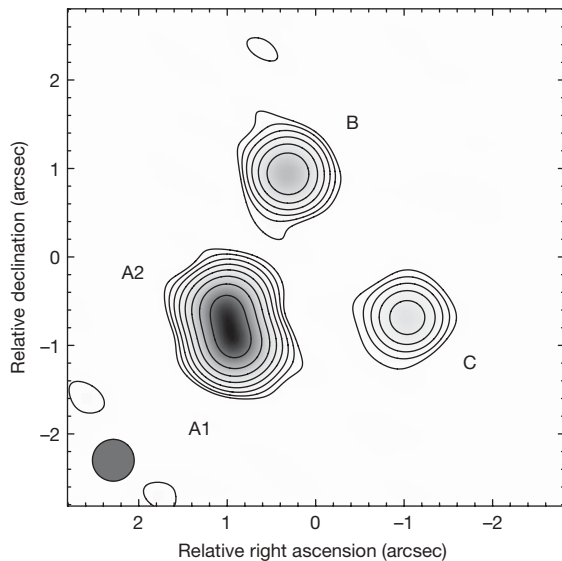


**Figure 2 | The 6.1-GHz EVLA radio continuum image of MG J0414+0534.**

The water-maser emission line shown in Fig. 1 was obtained by integrating over lensed images A1 and A2. The data were taken with the EVLA in BnA configuration during September and October 2007. The observations (25-MHz bandwidth, 32 spectral channels) were amplitude calibrated relative to quasar 3C 48, for which we adopted a flux density of 4.35 Jy, and were band-pass corrected by observing as a calibrator the quasar PKS J0423–0120 approximately every 30 min. Natural weighting was used to increase the sensitivity to the weak line emission during imaging. The spectral line data were averaged over the inner 24 spectral channels to form a continuum data set, which was self-calibrated and then deconvolved using the CLEAN algorithm. The resulting antenna phase solutions were applied to the spectral line data resulting in a line data set which was phase referenced to the continuum. For simplicity, and because the source is unresolved in the east–west direction, the continuum image was restored using a circular Gaussian beam with a full-width at half-maximum of 0.47 arcsec. Note that the synthesized beam of the EVLA has a full-width at half-maximum of  $0.93 \text{ arcsec} \times 0.47 \text{ arcsec}$  at a position angle of  $79^\circ$  east of north. The total radio continuum flux density of the four lensed images is  $0.56 \pm 0.06 \text{ Jy}$ , which is in good agreement with previous measurements<sup>16</sup>. The image contours are  $(-3, 3, 6, 12, 24, 48, 96, 192, 384) \times 0.43 \text{ mJy per beam}$ . The r.m.s. noise is 0.43 mJy per beam.

at high redshift was  $\text{HCO}^+$ , in the Cloverleaf gravitational lens system<sup>17</sup>, tracing a density of  $10^5 \text{ cm}^{-3}$  in star-forming molecular clouds. The apparent unlensed luminosity, assuming that the maser originates in the same region as the continuum core emission and, hence, has approximately the same magnification ( $\sim 35$ ; see ref. 9 and Supplementary Information), is of order  $10,000 L_\odot$ . This luminosity is still extremely high, the most luminous water maser known being in a type-2 quasar at redshift 0.66 and having a luminosity of  $23,000 L_\odot$  (ref. 15). In the event that the water maser is not coincident with the radio continuum, but lies closer to or farther from the lens caustic, the magnification could be higher or, respectively, lower. We note, however, that all luminous (and relatively nearby) water masers studied in detail so far are either associated with the circumnuclear accretion disk or a relativistic jet in its immediate vicinity.

Even without lensing, the water maser in MG J0414+0534 is among those with the highest known apparent luminosities<sup>14,15</sup>. Nevertheless, this discovery was possible only because of the additional amplification provided by the foreground galaxy; it acts as a cosmic telescope reducing the integration time required for the detection by a factor of order 1,000. The probability of a single pointed observation like ours detecting a high-redshift water maser with a luminosity greater than  $10,000 L_\odot$  is only  $10^{-6}$  (Supplementary Information). This detection probability was determined by extrapolating the local water-maser luminosity function<sup>5</sup> to higher luminosities without a cut-off, and assuming that the luminosity function

at high redshift was the same as that locally. Thus, our detection of a water maser in MG J0414+0534 at redshift 2.64 rules out with high probability there being no evolution in the water-maser luminosity function, and requires that the space density of luminous water masers was much larger at high redshift than in the local Universe. However, systematic searches for this population of unmagnified water masers at high redshift will probably require a significant improvement in instrument sensitivity. The proposed Square Kilometer Array radio telescope, which is expected to be operational within a decade, will provide such an improvement<sup>1</sup>.

These apparent lensed and unlensed luminosities have been calculated on the standard assumption of isotropic emission of radiation, for comparison with the luminosity estimates of other masers. However, masers are likely to emit anisotropically<sup>18</sup>. Beaming is expected because differences in the gain path due to irregularities in the cloud shape and velocity coherence cause exponential changes in maser output brightness. Beaming may also occur in some cases because of the alignment of masing clouds occurring only in restricted directions, or because of competitive pumping in saturated masers, in which the stimulated emission in one directional mode dominates that in other directional modes. The resulting beamwidths are uncertain, but arguments have been made for values ranging from  $7^\circ$  (ref. 19) down to as low as milliarcseconds<sup>20</sup>. This expectation is testable using the gravitationally lensed water maser because the light seen in each of the lensed images was emitted in slightly different directions from the background quasar. The angle subtended between image regions A1 and A2, as seen from the quasar, is 0.5 arcsec, and that between image regions A1 and B is 2.3 arcsec. The maser line is seen in the EVLA-observed spectra of both lensed images A1 and A2, so the maser beaming angle is greater than 0.5 arcsec, ruling out milliarcsecond beaming angles for this system. Furthermore, the intrinsic luminosity of the water maser must be greater than  $5 \times 10^{-9} L_\odot$ .

Of the  $\sim 100$  galaxies known to host 22.2-GHz water masers<sup>21</sup>, most are in type-2 Seyfert or LINER (low-ionization nuclear emission-line region) galaxies at redshifts  $< 0.06$  (refs 2–4, 22). The notable exception is a type-2 quasar at redshift 0.66 (ref. 15). This is consistent with unification models<sup>23</sup> in which the type-2 optical spectrum is due to an edge-on orientation of the circumnuclear disk, causing the active nucleus to be hidden behind a large column of dust and gas (Supplementary Information). This geometry provides a long maser gain path length for amplification, so the prevalence of masers in type-2 active galactic nuclei fits naturally with unification models. MG J0414+0534 is an intriguing object as it is one of the few type-1 active galactic nuclei and the only known type-1 quasar to show water-maser activity.

At low redshifts, at least one-third of known water masers are associated with the orbiting molecular clouds of circumnuclear accretion disks<sup>21</sup>. These water masers are typically found within 0.1 to 1.0 pc of the supermassive black hole and tend to have multiple blueshifted, redshifted and systemic velocity components, where individual components have narrow linewidths of  $< 5 \text{ km s}^{-1}$  (refs 19, 24, 25). In three cases, luminous water masers have also been found to be associated with the nuclear parts of relativistic jets that are ejected from some central engines<sup>26–28</sup>. These masers have relatively broad linewidths, of up to  $100 \text{ km s}^{-1}$ , and have velocities that tend to be offset from the systemic velocity of the host galaxy. Whether the water maser in MG J0414+0534 is associated with the circumnuclear accretion disk or is induced by a relativistic jet interacting with a gas cloud cannot be conclusively determined from our data alone. However, given that only a single emission line has been detected, and that it is broad and offset from the systemic velocity by  $\sim 300 \text{ km s}^{-1}$ , the jet–maser hypothesis seems most likely. The type-1 optical spectrum and beamed radio continuum emission of the quasar provide further support for this, as unification models of type-1 objects have the nucleus being viewed from above the plane of the disk. Masers originating from the circumnuclear accretion disk,

however, are preferentially beamed in the plane of the disk. Therefore, disk masers are unlikely to be seen in active galactic nuclei of type 1, whereas masers associated with nuclear jets may be detectable.

Future high-resolution imaging of the water-maser line with very-long-baseline interferometry (VLBI) will provide the exact location of the emission relative to the core-jet radio structure already observed in MG J0414+0534 (refs 9, 29). Resolving such maser component distributions with VLBI would usually be challenging at cosmological redshifts because the angular resolution of global VLBI arrays operating at 6.1 GHz is  $\sim 2$  mas, which corresponds to a spatial resolution of  $\sim 15$  pc at redshift 2.639. However, for MG J0414+0534, the apparent angular extent of the radio structure is increased, owing to the foreground gravitational lens, by a factor of  $\sim 15$  for the two strongest lensed images, A1 and A2 (ref. 9) (see Supplementary Information). Hence, the spatial resolution of a VLBI image will be  $\sim 1$  pc. Furthermore, it will be possible to distinguish water masers separated by  $\sim 0.5$  pc in the background source if each masing component is detected with a signal-to-noise ratio of at least ten, thus matching or even resolving the  $\geq 0.5$  pc outer diameter of known maser disks in the galaxies Circinus and NGC 1068 (refs 28, 30). Thus, VLBI imaging of gravitationally magnified water masers has the potential to trace the sub-parsec-scale structure surrounding accretion disks at cosmological distances.

Received 21 December 2007; accepted 6 October 2008.

- Greenhill, L. J. Extragalactic water masers, geometric estimation of  $H_0$ , and characterization of dark energy. *New Astron. Rev.* **48**, 1079–1084 (2004).
- Morganti, R., Greenhill, L. J., Peck, A. B., Jones, D. L. & Henkel, C. Disks, tori, and cocoons: Emission and absorption diagnostics of AGN environments. *New Astron. Rev.* **48**, 1195–1209 (2004).
- Henkel, C. *et al.*  $H_2O$  megamasers: Accretion disks, jet interaction, outflows or massive star formation? *Astrophys. Space Sci.* **295**, 107–116 (2005).
- Lo, K. Y. Mega-masers and galaxies. *Annu. Rev. Astron. Astrophys.* **43**, 625–676 (2005).
- Henkel, C. *et al.* New  $H_2O$  masers in Seyfert and FIR bright galaxies. *Astron. Astrophys.* **436**, 75–90 (2005).
- Hewitt, J. N., Turner, E. L., Lawrence, C. R., Schneider, D. P. & Brody, J. P. A gravitational lens candidate with an unusually red optical counterpart. *Astron. J.* **104**, 968–979 (1992).
- Lawrence, C. R., Elston, R., Januzzi, B. T. & Turner, E. L. MG 0414+0534: A dusty gravitational lens. *Astron. J.* **110**, 2570–2582 (1995).
- Tonry, J. L. & Kochanek, C. S. Redshifts of the gravitational lenses MG 0414+0534 and MG 0751+2716. *Astron. J.* **117**, 2034–2038 (1999).
- Trotter, C. S., Winn, J. N. & Hewitt, J. N. A multipole-taylor expansion for the potential of the gravitational lens MG J0414+0534. *Astrophys. J.* **535**, 671–691 (2000).
- Elíasdóttir, Á., Hjorth, J., Toft, S., Burud, I. & Paraficz, D. Extinction curves of lensing galaxies out to  $z = 1$ . *Astrophys. J. Suppl. Ser.* **166**, 443–469 (2006).
- Curran, S. J., Darling, J., Bolatto, A. D., Whiting, M. T., Bignell, C. & Webb, J. K. HI and OH absorption in the lensing galaxy of MG J0414+0534. *Mon. Not. R. Astron. Soc.* **382**, L11–L15 (2007).
- Barvainis, R., Alloin, D., Guilloteau, S. & Antonucci, R. Detection of CO (3–2) Emission at  $z = 2.64$  from the gravitationally lensed quasar MG 0414+0534. *Astrophys. J.* **492**, L13–L16 (1998).
- Moore, C. B., Carilli, C. L. & Menten, K. M. Neutral hydrogen 21 cm absorption at redshift 2.6365 toward the gravitational lens MG J0414+0534. *Astrophys. J.* **510**, L87–L90 (1999).
- Koekemoer, A. M. *et al.* A water-vapour giga-maser in the active galaxy TXFS 2226–184. *Nature* **378**, 697–699 (1995).
- Barvainis, R. & Antonucci, R. Extremely luminous water vapor emission from a type 2 quasar at redshift  $z = 0.66$ . *Astrophys. J.* **628**, L89–L91 (2005).
- Wilner, D. J., Bourke, T. L., Ho, P. T. P., Kilean, N. E. B. & Calabretta, M. A search for water masers in the gravitationally lensed quasars H1413+117 and MG 0414+0534. *Astron. J.* **117**, 1139–1142 (1999).
- Riechers, D. A. *et al.* First detection of  $HCO^+$  emission at high redshift. *Astrophys. J.* **645**, L13–L16 (2006).
- Neufeld, D. A., Maloney, P. R. & Conger, S. Water maser emission from X-ray-heated circumnuclear gas in active galaxies. *Astrophys. J.* **436**, L127–L130 (1994).
- Miyoshi, M. *et al.* Evidence for a black hole from high rotation velocities in a sub-parsec region of NGC 4258. *Nature* **373**, 127–129 (1995).
- Tarchi, A., Henkel, C., Peck, A. B. & Menten, K. M. Water maser emission in IC 342. *Astron. Astrophys.* **385**, 1049–1055 (2002).
- Braatz, J. *et al.* in *Astrophysical Masers and their Environments (IAU S242)* (eds Chapman, J. M. & Baan, W. A.) 402–403 (Proc. Internat. Astron. Union Symp. Colloq., Cambridge Univ. Press, 2007).
- Tarchi, A., Henkel, C., Chiaberge, M. & Menten, K. M. Discovery of a luminous water megamaser in the FR II radio galaxy 3C 403. *Astron. Astrophys.* **407**, L33–L36 (2003).
- Antonucci, R. Unified models for active galactic nuclei and quasars. *Annu. Rev. Astron. Astrophys.* **31**, 473–521 (1993).
- Kondratko, P. T., Greenhill, L. J. & Moran, J. M. The parsec-scale accretion disk in NGC 3393. *Astrophys. J.* **678**, 87–95 (2008).
- Herrnstein, J. R. *et al.* A geometric distance to the galaxy NGC 4258 from orbital motions in a nuclear gas disk. *Nature* **400**, 539–541 (1999).
- Claussen, M. J., Diamond, P. J., Braatz, J. A., Wilson, A. S. & Henkel, C. The water masers in the elliptical galaxy NGC 1052. *Astrophys. J.* **500**, L129–L132 (1998).
- Peck, A. B. *et al.* The flaring  $H_2O$  megamaser and compact radio source in Markarian 348. *Astrophys. J.* **590**, 149–161 (2003).
- Gallimore, J. F., Baum, S. A., O'Dea, C. P., Brinks, E. & Pedlar, A.  $H_2O$  and OH masers as probes of the obscuring torus in NGC 1068. *Astrophys. J.* **462**, 740–745 (1996).
- Ros, E. *et al.* VLBI imaging of the gravitational lens MG J0414+0534. *Astron. Astrophys.* **362**, 845–850 (2000).
- Greenhill, L. J. *et al.* A warped accretion disk and wide-angle outflow in the inner parsec of the Circinus galaxy. *Astrophys. J.* **590**, 162–173 (2003).

**Supplementary Information** is linked to the online version of the paper at [www.nature.com/nature](http://www.nature.com/nature).

**Acknowledgements** Our results are based on observations made using the 100-m telescope of the Max-Planck-Institut für Radioastronomie at Effelsberg and the EVLA, which is operated by the National Radio Astronomy Observatory, a facility of the National Science Foundation operated under cooperative agreement by Associated Universities, Inc. The authors are grateful to A. Kraus and M. Claussen, who helped make these observations. J.P.McK. was supported by the European Community's Sixth Framework Marie Curie Research Training Network 'ANGLES'. A.B. and O.W. were supported by the Priority and Emmy-Noether-Programmes of the Deutsche Forschungsgemeinschaft, respectively.

**Author Information** Reprints and permissions information is available at [www.nature.com/reprints](http://www.nature.com/reprints). Correspondence and requests for materials should be addressed to C.M.V.I. ([violette@mpifr-bonn.mpg.de](mailto:violette@mpifr-bonn.mpg.de)).



## LETTERS

# Unconventional superconductivity in $\text{Ba}_{0.6}\text{K}_{0.4}\text{Fe}_2\text{As}_2$ from inelastic neutron scattering

A. D. Christianson<sup>1</sup>, E. A. Goremychkin<sup>2,3</sup>, R. Osborn<sup>2</sup>, S. Rosenkranz<sup>2</sup>, M. D. Lumsden<sup>1</sup>, C. D. Malliakas<sup>2,4</sup>, I. S. Todorov<sup>2</sup>, H. Claus<sup>2</sup>, D. Y. Chung<sup>2</sup>, M. G. Kanatzidis<sup>2,4</sup>, R. I. Bewley<sup>3</sup> & T. Guidi<sup>3</sup>

A new family of superconductors containing layers of iron arsenide<sup>1–3</sup> has attracted considerable interest because of their high transition temperatures ( $T_c$ ), some of which are  $>50$  K, and because of similarities with the high- $T_c$  copper oxide superconductors. In both the iron arsenides and the copper oxides, superconductivity arises when an antiferromagnetically ordered phase has been suppressed by chemical doping<sup>1</sup>. A universal feature of the copper oxide superconductors is the existence of a resonant magnetic excitation, localized in both energy and wavevector, within the superconducting phase<sup>5–9</sup>. This resonance, which has also been observed in several heavy-fermion superconductors<sup>10–12</sup>, is predicted to occur when the sign of the superconducting energy gap takes opposite values on different parts of the Fermi surface<sup>13</sup>, an unusual gap symmetry which implies that the electron pairing interaction is repulsive at short range<sup>14</sup>. Angle-resolved photoelectron spectroscopy shows no evidence of gap anisotropy in the iron arsenides, but such measurements are insensitive to the phase of the gap on separate parts of the Fermi surface<sup>15</sup>. Here we report inelastic neutron scattering observations of a magnetic resonance below  $T_c$  in  $\text{Ba}_{0.6}\text{K}_{0.4}\text{Fe}_2\text{As}_2$ , a phase-sensitive measurement demonstrating that the superconducting energy gap has unconventional symmetry in the iron arsenide superconductors.

Although the first iron arsenide superconductors were based on doped variants of  $\text{RFeAsO}$ , where  $R$  is a rare-earth element, there has been considerable interest in a new series of tetragonal compounds based on  $\text{AFe}_2\text{As}_2$  (where  $A$  is barium, strontium or calcium), in which superconductivity is induced either by doping the  $A$  site with potassium or sodium<sup>16,17</sup> or by applying pressure<sup>18</sup>. These contain the same tetrahedrally coordinated  $\text{Fe}_2\text{As}_2$  planes as the  $\text{LaFeAsO}$  compounds (Fig. 1), separated by planes of the doped  $A$  site, which act as a charge reservoir. So far, the maximum  $T_c$  observed is 38 K (ref. 16), which was seen in  $\text{Ba}_{0.6}\text{K}_{0.4}\text{Fe}_2\text{As}_2$ , the compound we are investigating in this Letter. The antiferromagnetic structure of the undoped parent compound,  $\text{BaFe}_2\text{As}_2$ , is illustrated in Fig. 1 (ref. 19).

Polycrystalline samples of  $\text{Ba}_{0.6}\text{K}_{0.4}\text{Fe}_2\text{As}_2$  were prepared using solid-state synthesis techniques (see Supplementary Information for details). A sharp superconducting transition was observed in magnetic susceptibility at the previously reported temperature of 38 K (ref. 16), and neutron powder diffraction showed no evidence of any impurity phase within the statistical precision of the Rietveld refinement. The inelastic neutron scattering experiments were performed on the recently commissioned time-of-flight MERLIN spectrometer<sup>20</sup> at the ISIS Pulsed Neutron and Muon Facility, UK, using incident energies of 15, 30, 60 and 100 meV. The data were placed on an absolute intensity scale by normalization to a vanadium standard.

Figure 2 shows colour plots of the measured inelastic neutron scattering intensity as a function of momentum transfer,  $Q$  (expressed in units of reciprocal length), and energy transfer,  $\omega$ , below ( $T = 7$  K) and above ( $T = 50$  K) the superconducting transition temperature. The most striking difference between the two temperatures is seen at  $Q \approx 1.15 \text{ \AA}^{-1}$  and an energy transfer of  $\sim 14$  meV. At 7 K, there is clearly a peak that is well defined in both  $Q$  and  $\omega$  and that is not present at 50 K. The value of  $Q$  characterizing this contribution to the magnetic response corresponds to the periodicity of the antiferromagnetic order within each plane of iron spins observed in the undoped parent compound,  $\text{BaFe}_2\text{As}_2$  (ref. 19; see also Fig. 1).

To elucidate the evolution of the magnetic response, we combine measurements below  $T_c$  at three incident energies, in each case using a low-energy cut-off that excludes the tail of strong elastic nuclear scattering. The resulting data are shown in Fig. 3a, where the resonant excitation is seen to peak sharply at  $\omega \approx 14$  meV. We cannot rule out the possibility that there could be a small phononic contribution to the scattering within this energy window, but the strong temperature dependence indicates that it is predominantly magnetic. Figure 3b

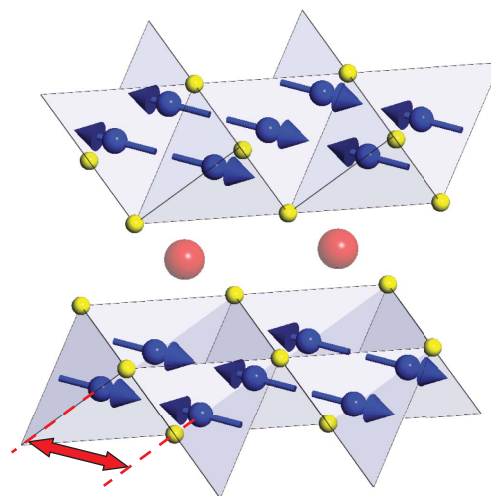


**Figure 1 | The crystal structure of  $\text{Ba}_{0.6}\text{K}_{0.4}\text{Fe}_2\text{As}_2$ .** The unit cell of  $\text{Ba}_{0.6}\text{K}_{0.4}\text{Fe}_2\text{As}_2$  contains two layers of  $\text{Fe}_2\text{As}_2$  tetrahedra (Fe, blue spheres; As, yellow spheres), separated by planes of barium or potassium atoms (red spheres). The blue arrows show the ordering of the iron spins observed in the undoped parent compound  $\text{BaFe}_2\text{As}_2$  (ref. 19). The atomic distance of  $2.77 \text{ \AA}$  that characterizes both the antiferromagnetic modulation and the newly observed resonant excitation is indicated by the red double-headed arrow.

<sup>1</sup>Neutron Scattering Science Division, Oak Ridge National Laboratory, Oak Ridge, Tennessee 37831, USA. <sup>2</sup>Materials Science Division, Argonne National Laboratory, Argonne, Illinois 60439-4845, USA. <sup>3</sup>ISIS Pulsed Neutron and Muon Facility, Rutherford Appleton Laboratory, Chilton, Didcot OX11 0QX, UK. <sup>4</sup>Department of Chemistry, Northwestern University, Evanston, Illinois 60208-3113, USA.

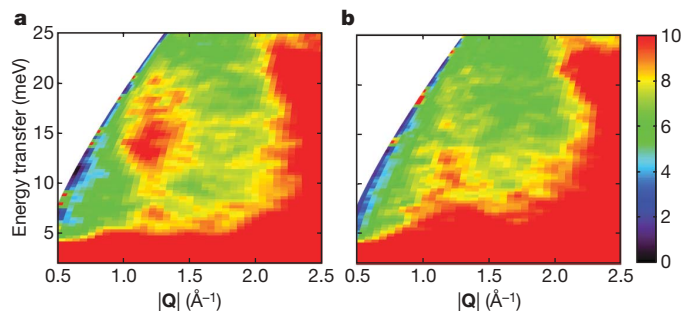


**Figure 2 | Resonant spin excitation in  $\text{Ba}_{0.6}\text{K}_{0.4}\text{Fe}_2\text{As}_2$ .** Inelastic neutron scattering, measured using an incident neutron energy of 60 meV at temperatures below (a, 7 K) and above (b, 50 K)  $T_c$ , shows the development of a magnetic excitation in the superconducting phase at an energy transfer of 14 meV and a momentum transfer of  $1.15 \text{ \AA}^{-1}$ . The strong scattering at low energy transfers arises from the tail of strong elastic nuclear scattering, and the strong increase in scattering at higher values of  $Q$  is due to inelastic phonon scattering. The colour scale indicates scattering intensity in units of millibarns per steradian per millielectronvolt per mole.

shows that spectral weight in the resonant excitation seen below  $T_c$  is transferred to lower energy above  $T_c$ .

We performed a series of shorter measurements to determine the temperature dependence of this resonant excitation. Figure 4 shows data integrated over the  $(Q, \omega)$  region of maximum intensity in the resonant excitation. As also observed in the copper oxide superconductors, the intensity of the resonance falls to zero at  $T_c$ , confirming the strong coupling of this excitation to the superconducting order parameter.

Similar resonant excitations have been observed in other strongly correlated superconductors, such as high- $T_c$  copper oxide<sup>5–9</sup> and heavy-fermion superconductors<sup>10–12</sup>, where they are commonly taken as evidence of an unconventional symmetry of the superconducting order parameter<sup>13</sup>. Below the superconducting transition temperature, the dynamic magnetic susceptibility is predicted to be enhanced at certain values of  $Q$  by a coherence factor, provided that the energy gap has the form  $\Delta_{\mathbf{k}+\mathbf{Q}} = -\Delta_{\mathbf{k}}$  (here  $\mathbf{k}$  and  $\mathbf{k} + \mathbf{Q}$  are wavevectors on different parts of the Fermi surface).

In the copper oxide and heavy-fermion superconductors, this form results from  $d_{x^2-y^2}$  symmetry, which has nodes in the energy gap within a single Fermi surface. In these cases,  $Q$  spans sections of the

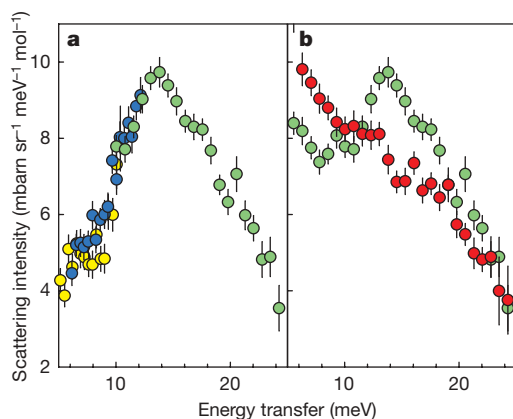


**Figure 3 | Energy dependence of the resonant spin excitation.** a, The inelastic neutron scattering intensity from  $\text{Ba}_{0.6}\text{K}_{0.4}\text{Fe}_2\text{As}_2$  integrated over  $Q$  in the range  $1.0\text{--}1.3 \text{ \AA}^{-1}$  at 7 K, measured using incident neutron energies of 15 meV (yellow circles), 30 meV (blue circles) and 60 meV (green circles). b, Same as in a, but at 7 K (green circles) and 50 K (red circles) using an incident neutron energy of 60 meV. The error bars are derived from the square root of the raw detector counts. The data show a resonant peak at 7 K and the transfer of spectral weight from this peak to lower energies at 50 K, that is, above  $T_c$ .

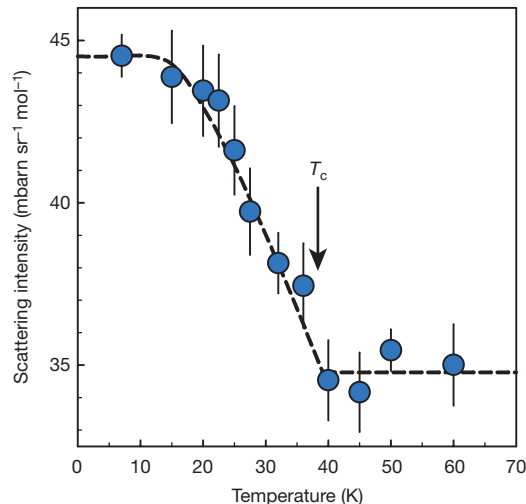


**Figure 4 | Temperature dependence of the resonant spin excitation.** The inelastic neutron scattering intensity from  $\text{Ba}_{0.6}\text{K}_{0.4}\text{Fe}_2\text{As}_2$  integrated over  $Q$  in the range  $1.0\text{--}1.3 \text{ \AA}^{-1}$  and over  $\omega$  in the range  $12.5\text{--}17.5 \text{ meV}$ . The integration range corresponds to the region of maximum intensity of the resonant excitation observed below  $T_c$  (Fig. 2). The error bars are derived from the square root of the raw detector counts. The dashed line is a guide to the eye below  $T_c$  and shows the average value of the integrals above  $T_c$ .

same Fermi surface that are gapped with opposite phases; in the copper oxide superconductors,  $Q = (\pi, \pi)$  is such a wavevector. However, this mechanism seems to be ruled out by results of angle-resolved photoemission spectroscopy (ARPES) of  $\text{Ba}_{0.6}\text{K}_{0.4}\text{Fe}_2\text{As}_2$  that show no evidence of any anisotropy of the energy gap<sup>15</sup>. According to band structure calculations, the Fermi surfaces of the iron arsenide superconductors are predominantly derived from the iron  $d$  electrons, and comprise two small hole pockets centred at the centre of the Brillouin zone and two small electron pockets at the zone boundary<sup>21,22</sup>. ARPES shows there to be isotropic gaps around each of the measured surfaces, apparently ruling out a  $d$ -wave gap symmetry<sup>15</sup>.

A resolution of this apparent discrepancy has been provided by theoretical predictions that the symmetry is not  $d$  wave, but rather extended  $s_{\pm}$  wave<sup>14</sup>, in which the gaps at the hole pockets are isotropic and the gaps at the electron pockets are isotropic but are of opposite sign to those at the hole pockets. This means that magnetic fluctuations are amplified by the coherence factor at values of  $Q$  that couple the hole and electron pockets, as has been confirmed by explicit calculations of the neutron scattering intensities<sup>23,24</sup>. This is precisely where we have observed the resonant excitation, so our measurements, in conjunction with the ARPES data, provide phase-sensitive evidence for the validity of extended  $s_{\pm}$ -wave gap models.

The energy of this resonant excitation is  $\omega_0 \approx 14 \text{ meV}$ . This is equivalent to  $4.3T_c$ , which is just less than the canonical value of  $5T_c$  seen in the copper oxide superconductors<sup>25</sup>. However, it is more appropriate to consider the ratio  $\omega_0/2\Delta_0$ , where  $\Delta_0$  is the maximum value of the gap. This ratio has values ranging from 0.62 to 0.74 in a wide range of materials<sup>11</sup>. From ARPES data on  $\text{Ba}_{0.6}\text{K}_{0.4}\text{Fe}_2\text{As}_2$ ,  $\Delta_0 \approx 12 \text{ meV}$  (ref. 15), giving a ratio of  $\omega_0/2\Delta_0 \approx 0.58$ . It is remarkable that materials with such a divergent range of  $T_c$  (which varies over two orders of magnitude) can be unified by such a simple scaling relation.

Received 24 July; accepted 29 October 2008.

1. Kamihara, Y., Watanabe, T., Hirano, M. & Hosono, H. Iron-based layered superconductor  $\text{La}[\text{O}_{1-x}\text{F}_x]\text{FeAs}$  ( $x = 0.05\text{--}0.12$ ) with  $T_c = 26 \text{ K}$ . *J. Am. Chem. Soc.* **130**, 3296–3297 (2008).
2. Takahashi, H. *et al.* Superconductivity at 43 K in an iron-based layered compound  $\text{LaO}_{1-x}\text{F}_x\text{FeAs}$ . *Nature* **453**, 376–378 (2008).
3. Ren, Z.-A. *et al.* Superconductivity and phase diagram in iron-based arsenic oxides  $\text{ReFeAsO}_{1-\delta}$  ( $\text{Re} = \text{rare-earth metal}$ ) without fluorine doping. *Europhys. Lett.* **83**, 17002 (2008).



4. de la Cruz, C. *et al.* Magnetic order close to superconductivity in the iron-based layered  $\text{LaO}_{1-x}\text{F}_x\text{FeAs}$  systems. *Nature* **453**, 899–902 (2008).
5. Rossat-Mignod, J. *et al.* Neutron scattering study of the  $\text{YBa}_2\text{Cu}_3\text{O}_{6+x}$  system. *Physica C* **185**, 86–92 (1991).
6. Mook, H. A., Yethiraj, M., Aeppli, G., Mason, T. E. & Armstrong, T. Polarized neutron determination of the magnetic excitations in  $\text{YBa}_2\text{Cu}_3\text{O}_7$ . *Phys. Rev. Lett.* **70**, 3490–3493 (1993).
7. Fong, H. F. *et al.* Neutron scattering from magnetic excitations in  $\text{Bi}_2\text{Sr}_2\text{CaCu}_2\text{O}_{8+\delta}$ . *Nature* **398**, 588–591 (1999).
8. Dai, P., Mook, H. A., Aeppli, G., Hayden, S. M. & Dogan, F. Resonance as a measure of pairing correlations in the high- $T_c$  superconductor  $\text{YBa}_2\text{Cu}_3\text{O}_{6.6}$ . *Nature* **406**, 965–968 (2000).
9. He, H. *et al.* Magnetic resonant mode in the single-layer high-temperature superconductor  $\text{Tl}_2\text{Ba}_2\text{CuO}_{6+\delta}$ . *Science* **295**, 1045–1047 (2002).
10. Sato, N. K. *et al.* Strong coupling between local moments and superconducting 'heavy' electrons in  $\text{UPd}_2\text{Al}_3$ . *Nature* **410**, 340–343 (2001).
11. Stock, C., Broholm, C., Hudis, J., Kang, H. J. & Petrovic, C. Spin resonance in the  $d$ -wave superconductor  $\text{CeCoIn}_5$ . *Phys. Rev. Lett.* **100**, 087001 (2008).
12. Stockert, O. *et al.* Magnetism and superconductivity in the heavy-fermion compound  $\text{CeCu}_2\text{Si}_2$  studied by neutron scattering. *Physica B (Amsterdam)* **403**, 973–976 (2008).
13. Chang, J., Eremin, I., Thalmeier, P. & Fulde, P. Theory of magnetic excitons in the heavy-fermion superconductor  $\text{UPd}_2\text{Al}_3$ . *Phys. Rev. B* **75**, 024503 (2007).
14. Mazin, I. I., Singh, D. J., Johannes, M. D. & Du, M. H. Unconventional superconductivity with a sign reversal in the order parameter of  $\text{LaFeAsO}_{1-x}\text{F}_x$ . *Phys. Rev. Lett.* **101**, 057003 (2008).
15. Ding, H. *et al.* Observation of Fermi-surface-dependent nodeless superconducting gaps in  $\text{Ba}_{0.6}\text{K}_{0.4}\text{Fe}_2\text{As}_2$ . *Europhys. Lett.* **83**, 47001 (2008).
16. Rotter, M., Tegel, M. & Johrendt, D. Superconductivity at 38 K in the iron arsenide  $(\text{Ba}_{1-x}\text{K}_x)\text{Fe}_2\text{As}_2$ . *Phys. Rev. Lett.* **101**, 107006 (2008).
17. Sasmal, K. *et al.* Superconducting Fe-based compounds  $(\text{A}_{1-x}\text{Sr}_x)\text{Fe}_2\text{As}_2$  with  $A = \text{K}$  and  $\text{Cs}$  with transition temperatures up to 37 K. *Phys. Rev. Lett.* **101**, 107007 (2008).
18. Park, T. *et al.* Pressure-induced superconductivity in  $\text{CaFe}_2\text{As}_2$ . *J. Phys. Condens. Matter* **20**, 322204 (2008).
19. Huang, Q. *et al.* Magnetic order in  $\text{BaFe}_2\text{As}_2$ , the parent compound of the FeAs based superconductors in a new structural family. Preprint at (<http://arxiv.org/abs/0806.2776v2>) (2008).
20. Bewley, R. I. *et al.* MERLIN, a new high count-rate spectrometer at ISIS. *Physica B (Amsterdam)* **385–386**, 1029–1031 (2006).
21. Liu, C. *et al.* K-doping dependence of the Fermi surface of the iron-arsenic  $\text{Ba}_{1-x}\text{K}_x\text{Fe}_2\text{As}_2$  superconductor using angle-resolved photoemission spectroscopy. *Phys. Rev. Lett.* **101**, 177005 (2008).
22. Yang, L. *et al.* Band structure and electronic signature of the spin density waves in bilayer iron-oxypnictide  $\text{BaFe}_2\text{As}_2$ . Preprint at (<http://arxiv.org/abs/0806.2627v1>) (2008).
23. Korshunov, M. M. & Eremin, I. Theory of magnetic excitations in iron-based layered superconductors. *Phys. Rev. B* **78**, 140509(R) (2008).
24. Maier, T. A. & Scalapino, D. J. Theory of neutron scattering as a probe of the superconducting gap in the iron pnictides. *Phys. Rev. B* **78**, 020514(R) (2008).
25. Hühner, S., Hossain, M. A., Damascelli, A. & Sawatzky, G. A. Two gaps make a high-temperature superconductor? *Rep. Prog. Phys.* **71**, 062501 (2008).

**Supplementary Information** is linked to the online version of the paper at [www.nature.com/nature](http://www.nature.com/nature).

**Acknowledgements** We acknowledge discussions with M. Norman and C. Stock. This work was supported by the Division of Materials Sciences and Engineering Division and the Scientific User Facilities Division of the Office of Basic Energy Sciences, US Department of Energy Office of Science.

**Author Information** Reprints and permissions information is available at [www.nature.com/reprints](http://www.nature.com/reprints). Correspondence and requests for materials should be addressed to R.O. ([rosborn@anl.gov](mailto:rosborn@anl.gov)).

# Highly efficient molybdenum-based catalysts for enantioselective alkene metathesis

Steven J. Malcolmson<sup>1\*</sup>, Simon J. Meek<sup>1\*</sup>, Elizabeth S. Sattely<sup>1</sup>, Richard R. Schrock<sup>2</sup> & Amir H. Hoveyda<sup>1</sup>

Discovery of efficient catalysts is one of the most compelling objectives of modern chemistry. Chiral catalysts are in particularly high demand, as they facilitate synthesis of enantiomerically enriched small molecules that are critical to developments in medicine, biology and materials science<sup>1</sup>. Especially noteworthy are catalysts that promote—with otherwise inaccessible efficiency and selectivity levels—reactions demonstrated to be of great utility in chemical synthesis. Here we report a class of chiral catalysts that initiate alkene metathesis<sup>1</sup> with very high efficiency and enantioselectivity. Such attributes arise from structural fluxionality of the chiral catalysts and the central role that enhanced electronic factors have in the catalytic cycle. The new catalysts have a stereogenic metal centre and carry only monodentate ligands; the molybdenum-based complexes are prepared stereoselectively by a ligand exchange process involving an enantiomerically pure aryloxide, a class of ligands scarcely used in enantioselective catalysis<sup>2,3</sup>. We demonstrate the application of the new catalysts in an enantioselective synthesis of the *Aspidosperma* alkaloid, quebrachamine, through an alkene metathesis reaction that cannot be promoted by any of the previously reported chiral catalysts.

A chiral catalyst may promote a transformation with exceptionally high degrees of efficiency and enantioselectivity if the modes with which it associates with substrate molecules are sterically—as well as electronically—distinct<sup>4,5</sup>. Design of a chiral metal-based catalyst, where stereoelectronic interactions affect the energetics of the catalytic cycle, can lead to consideration of complexes that bear a stereogenic metal centre; stereoselective preparation and preservation of the stereochemical identity of the catalyst then become crucial issues. In the limited number of chiral stereogenic-at-metal catalysts prepared, stereoselective synthesis is addressed through multidentate ligands<sup>6–8</sup>. As stereogenic-at-metal complexes can undergo stereomutation<sup>9</sup>, polydentate ligation ensures minimal erosion of stereochemical integrity. The rigidity of bi- or polydentate ligation may be detrimental, however, if catalyst structural fluxionality gives rise to enhanced activity and/or enantioselectivity. Chiral complexes that bear a stereogenic metal centre and only monodentate ligands, therefore, offer attractive opportunities in enantioselective catalysis<sup>10,11</sup>. Such options are, nonetheless, almost entirely unexplored; it is particularly challenging to design and synthesize enantiomerically pure stereogenic-at-metal catalysts that are devoid of polydentate ligands, do not readily stereomutate and can thus serve as effective chiral catalysts.

The growing list of alkene metathesis transformations that cannot be promoted by the existing metal complexes has underlined the need for more effective classes of catalysts<sup>1,12,13</sup>. One instance that points to such limitations is a key step in an enantioselective synthesis<sup>14</sup> of the adrenergic blocker quebrachamine<sup>15</sup> (Fig. 1): the conversion of achiral **1** to the strained chiral tetracycle **2** by reaction of sterically

hindered alkenes. The results illustrated in Fig. 1, regarding molybdenum alkylidene **3** (refs 12, 16) and ruthenium carbene **4a** (ref. 17), although being somewhat inefficient, represent the optimal among available achiral catalysts. The faster initiating **4b** (ref. 18) proceeds only to 48% conversion, most likely as a result of lower stability of the carbene intermediates. In relation to an enantioselective quebrachamine synthesis, the existing chiral catalysts, represented by **5–7** (ref. 12), are entirely ineffective in promoting the formation of **2** ( $\leq 5\%$  conversion with up to 50 mol% loading after up to 48 h at 22–80 °C). With 16 mol% **8** (ref. 19) at 80 °C, there is approximately 50% conversion, but only *rac*-**2** is generated; related monodentate *N*-heterocyclic chiral ruthenium carbenes<sup>20</sup> are equally ineffective.

As the first step towards identifying a new set of chiral catalysts, we considered reasons for the higher activity of alkylidene **3** in comparison with **5–7**, a variance that exists despite the similar electron-withdrawing ability of the oxygen-based ligands. We surmised that such differences may originate from the structural rigidity of the diolates and the resulting higher energy transition states and intermediates in the catalytic cycle. The O–Mo–O angle in tetrahedral **5a** ( $\angle(\text{O–Mo–O})$ ,  $\sim 127^\circ$  (ref. 21)), compared to that in a related square pyramidal tungstacyclobutane ( $\angle(\text{O–W–O})$ ,  $\sim 99^\circ$  (ref. 22)), supports the hypothesis that structural adjustments within the catalytic cycle may be better accommodated in a less rigid metal complex.

The above considerations imply that a chiral molybdenum catalyst, bearing monodentate ligands—either two that are chiral (identical enantiomers, non-stereogenic-at-Mo; see Fig. 2) or one achiral and one chiral ligand (stereogenic-at-Mo)—would be more active. Recent theoretical studies suggest that high-oxidation-state complexes containing two electronically distinct ligands should be particularly effective promoters of alkene metathesis<sup>4,5</sup> (Fig. 2). According to theoretical explorations, an acceptor ligand (**A** in **I**, Fig. 2) ensures sufficient metal Lewis acidity, necessary for effective binding of the Lewis basic alkene. Efficient alkene coordination, however, requires the presence of a sterically accessible ligation site, made available through alteration of the structure of the initial tetrahedral complex **I** (Fig. 2). It has been proposed that the donor group (**D**) causes **I** to distort dissymmetrically; ligand **D** preferentially interacts with the most available metal orbital such that a trigonal prismatic complex bearing an open ligation site is rendered energetically more accessible. The donor ligand thus occupies an apical site in **II** (the alkylidene, acceptor and imido ligands constitute the basal plane of the trigonal prism), coordinated opposite only to a weakly bound alkene (*trans* effect). The resulting complex, **III**, leads to trigonal bipyramidal **IV**, which undergoes facile cycloreversion (Fig. 2) in which the metallacyclobutane carbons, constituting the alkene being released, are positioned *trans* to **D**, affording **V**. The aforementioned electronic effects thus facilitate formation of complex **V** as well. Such a scenario suggests acceleration at two critical

<sup>1</sup>Department of Chemistry, Merkert Chemistry Center, Boston College, Chestnut Hill, Massachusetts 02467, USA. <sup>2</sup>Department of Chemistry, Massachusetts Institute of Technology, Cambridge, Massachusetts 02139, USA.

\*These authors contributed equally to this work.



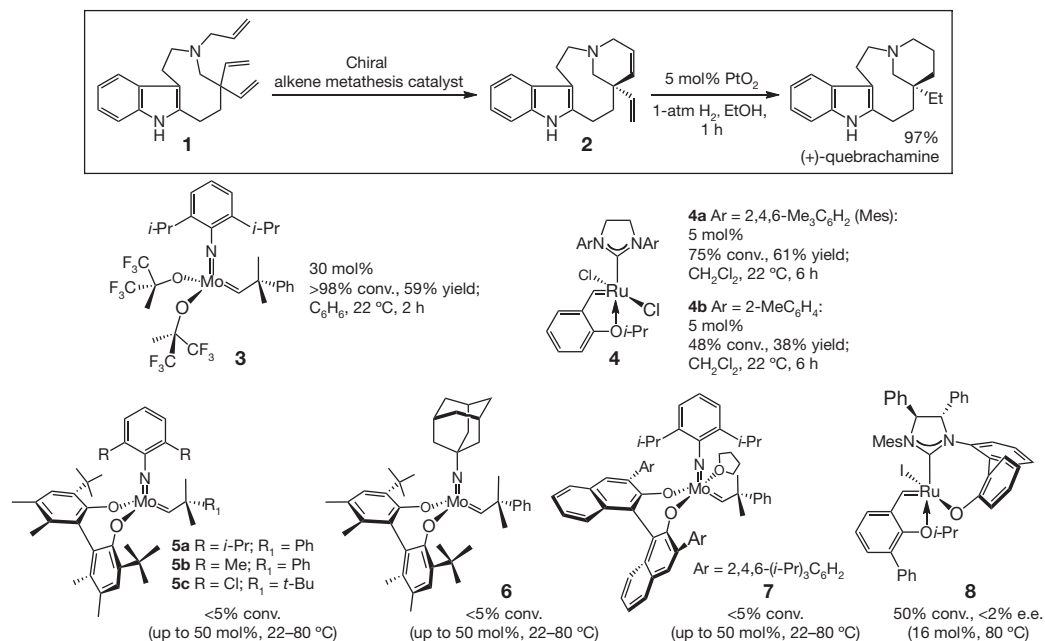


**Figure 1 | Catalytic ring-closing metathesis of triene 1.** This alkene metathesis reaction, required for total synthesis of alkaloid natural product quebrachamine, is not efficiently promoted by the available achiral or chiral

stages of the catalytic cycle: substrate–catalyst association and metallacyclobutane decomposition. The above hypothesis finds support in the efficient reaction shown in Fig. 2: 1 mol% *rac*-9 (ref. 23) promotes formation of *rac*-2 within 1 h. Such a level of activity is in stark contrast to 3 (Fig. 1), a complex with two hexafluoro-*t*-butoxides.

Stereoselective synthesis of stereogenic-at-Mo complexes became our next objective. One approach would involve diastereoselective mono-protonation of bis-pyrrolides 10a and 10b (Fig. 3)<sup>24</sup> with

molybdenum or ruthenium catalysts, indicating that significantly more effective catalysts are needed. Me,  $\text{CH}_3$ ; Et,  $\text{C}_2\text{H}_5$ ; Ph,  $\text{C}_6\text{H}_5$ ; *i*-Pr,  $(\text{CH}_3)_2\text{CH}$ ; and *t*-Bu,  $(\text{CH}_3)_3\text{C}$ . e.e., enantiomeric excess.

1 equiv. of a chiral enantiomerically pure alcohol. Preliminary experiments (T. Pilyugina, A.H.H. and R.R.S., unpublished work), involving chiral diols (for example 5–7, Fig. 1), indicated that pyrrole molecules, released upon alcohol exchange, are not deleterious to catalyst activity. These observations suggested that mono-aryloxides might be prepared and used *in situ*. To this end, we favoured binaphthol-derived alcohols, because this class of ligand possesses several important attributes: (1) ease and low cost of synthesis, (2)

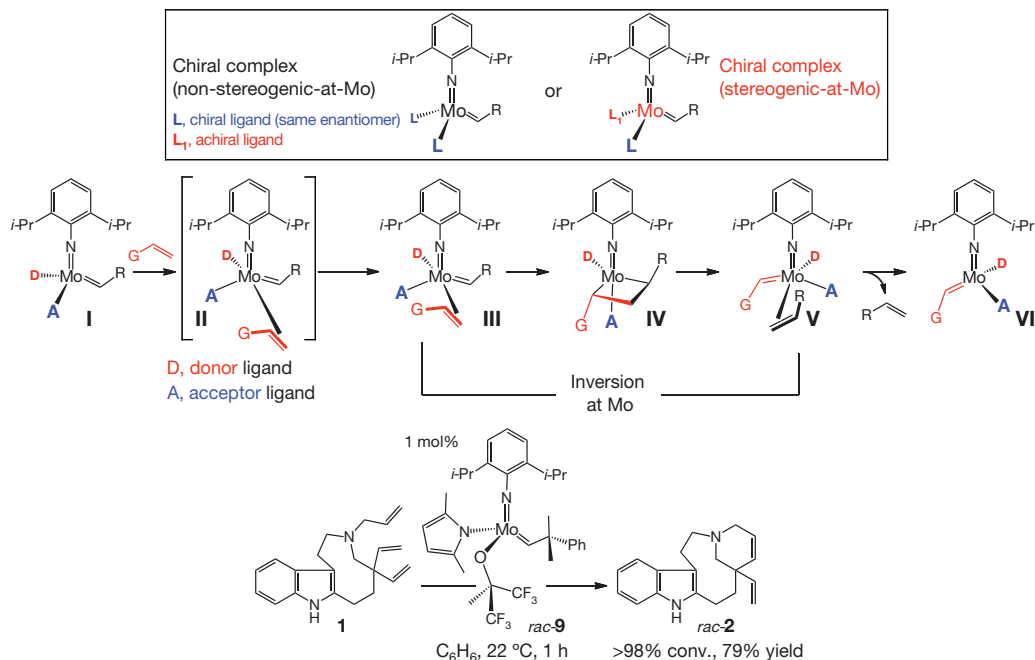


**Figure 2 | Stereoelectronic effects have a critical role in alkene metathesis reactions promoted by a molybdenum complex that bears a donor and an acceptor ligand.** Such a chiral complex distorts dissymmetrically, leading to an open ligation site *trans* to D (see II), thus facilitating catalyst–substrate association; the donor ligand also causes a more facile decomposition of the metallacyclobutane intermediate (IV). These attributes are expected to lead

to a catalyst that is substantially more effective than one that bears two electronically identical acceptor ligands (see the molybdenum complexes illustrated in Fig. 1). The high activity of a complex bearing a donor (pyrrolide) and an acceptor (aryloxide) ligand is illustrated by the efficient conversion of triene 1 to diene 2 (compare with the reaction of molybdenum-based bis-alkoxide 3 shown in Fig. 1). G, functional group.

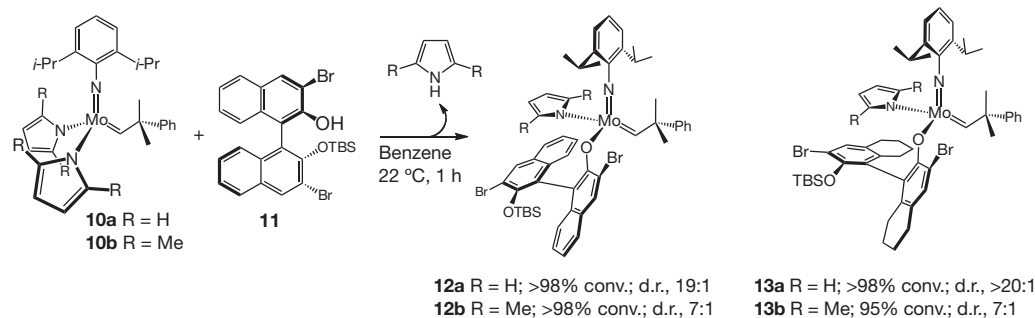


**Figure 3 | Diastereoselective synthesis of stereogenic-at-Mo complexes.** Such processes are achieved by efficient and stereoselective ligand exchange reactions involving enantiomerically pure aryl alcohols, derived from

commercially available binaphthol, and achiral molybdenum-based bis-pyrrolides. TBS, *t*-butyldimethylsilyl; d.r., diastereomeric ratio.

facility of modification and (3) appropriate electron-withdrawing ability.

We subjected bis-pyrrolides **10a** and **10b** to mono-protected diols derived from binaphthol. Treatment of **10a** with 1 equiv. of enantiomerically pure **11** affords **12a** in 19:1 d.r.; with **10b**, **12b** is generated as a 7:1 mixture. Under identical conditions, **13a** and **13b** are obtained with similar selectivity. The identity of the major diastereomer of **13b** was established by X-ray crystallography (Supplementary Information page SI18); assignment of other isomers in Fig. 3 is by inference. The configurational stability of the above complexes is indicated by the absence of detectable variations in the diastereomeric ratios; for example, even after one month, a toluene solution of **13b** remains a 7:1 mixture of the same diastereomers.

Attempts to prepare the mono-aryloxides with the parent ligand lacking the bromides led to a mixture containing bis-aryloxides as well as the unreacted bis-pyrrolides. Synthesis of such complexes can be accomplished with 1 equiv. of the related octahydrobinaphthol, but the process is less stereoselective (d.r., 1–2.5:1) and, unlike the bromides, excess alcohol causes bis-aryloxide formation. In reactions to form **13a** and **13b**, bis-aryloxides are not detected even under relatively forcing conditions (60 °C, 2 h). The bromine atoms are therefore required for efficient and stereoselective formation of **12** and **13** (minimal non-stereogenic-at-Mo bis-aryloxide). Delineation of principles that govern stereoselective ligand exchange reactions is a topic of ongoing investigations.

We then turned our attention to probing the ability of mono-aryloxides to perform as catalysts for enantioselective ring-closing metathesis (RCM). The transformation in Table 1 (**14** → **15**) served as the model process; reactions were performed with complexes prepared and used *in situ*. With 1 mol% **12a** (d.r., 19:1; entry 1, Table 1),

RCM proceeds to 50% conversion, affording (*R*)-**15** in 18% e.e. With **12b** (d.r., 7:1; entry 2, Table 1), complete conversion is achieved and (*S*)-**15** is obtained in 50% e.e. The above trend is again observed in reactions involving **13a** and **13b** (entries 3 and 4, Table 1), but with a wider selectivity gap: with 1 mol% **13a**, RCM proceeds to 54% conversion to afford (*R*)-**15** in 13% e.e., whereas in the presence of **13b** there is >98% conversion and (*S*)-**15** is isolated in 93% e.e. With **13b**, the RCM can be performed in a fume hood at 22 °C with 1 mol% loading (30 min, 96% conversion, 86% yield, 92% e.e.). These results illustrate the significant potential of the new catalysts in practical procedures for enantioselective synthesis. Despite providing slightly lower selectivity, **13b** is more effective than the corresponding optimal molybdenum diolate (5 mol% **5a**: 20 min, 95% conversion, 98% e.e. (ref. 25)).

The reduced reactivity and selectivity in reactions of complexes that are more stereochemically pure (that is, **12a** and **13a**) raises the question of whether the minor diastereomers are more active. To investigate this, a stereochemically pure sample of **13b** (d.r., >25:1) was used to initiate enantioselective RCM of **14** (1 mol%, 22 °C, 30 min): (*S*)-**15** was isolated in 93% e.e. and 94% yield, results identical to those obtained with the 7:1 mixture (entry 4, Table 1). Moreover, by monitoring the reaction progress spectroscopically (400-MHz <sup>1</sup>H NMR) in the presence of **13b**, generated *in situ*, we established that >98% of the major isomer is consumed, presumably through initiation with the alkene substrate, whereas the minor diastereomer remains largely intact (>95%). Related experiments indicate that in the case of binaphtholate **12b**, both isomers are initiated with nearly equal facility, a finding that might explain why the product is obtained with lower selectivity with this complex.

A variety of enantioselective RCM reactions illustrate the special utility of the new catalysts (Table 2). None of the previously reported diolates promotes RCM of secondary allylamine **16** (entry 1, Table 2)<sup>26</sup>; by sharp contrast, with 2.5 mol% **13b**, there is 94% conversion to piperidine **17** within 1 h, furnishing the desired product in 89% yield and 67% e.e. Diolate **7** (see Fig. 1) and **13c** (see Fig. 4 for structure; d.r., 5:1) promote formation of **19** (entry 2, Table 2) with high enantioselectivity (98% and 91% e.e., respectively), but RCM with the mono-aryloxide is significantly more efficient: 3 mol% dichloro-substituted **13c** furnishes 95% conversion to **19** within 1 h, whereas 48 h are required with 10 mol% diolate **7**. Reaction of amine **20** (entry 3, Table 2), which requires 15 mol% **5b**, proceeds to only 75% conversion after 24 h, yielding **21** with low selectivity (e.e., 65:35). By contrast, 1 mol% **13b** is sufficient for >98% conversion within 1 h, affording **21** in >98% yield and 92% e.e. Similarly, enantioselective synthesis of azepine **23** (entry 4, Table 2) is more efficient (1 h versus 20 h) and substantially more selective (81% e.e. versus 40% e.e.) when **13c** is used (versus diolate **5b**). RCM of arylamine **24** (entry 5, Table 2) proceeds with high enantioselectivity when diolate **5a** (ref. 25) or mono-aryloxide **13c** is used; with 1 mol% **13c**, however, there is >98% conversion in 1 h (versus 7 h with 2 mol% **5a**). With enantioselective RCM of silyl ether **26** (entry 6, Table 2), diolate

**Table 1 | Initial examination of the chiral complexes as catalysts for enantioselective RCM**

Entry no.	Chiral complex	Conv. (%)*; Yield (%)†	e.r.‡	e.e. (%); Config.
1	<b>12a</b>	50; ND	41:59	18; ( <i>R</i> )
2	<b>12b</b>	>98; 91	75:25	50; ( <i>S</i> )
3	<b>13a</b>	54; ND	43.5:56.5	13; ( <i>R</i> )
4	<b>13b</b>	>98; 91	96.5:3.5	93; ( <i>S</i> )

The reactions were carried out in purified benzene or toluene under an atmosphere of nitrogen gas (see the Supplementary Information for details). ND, not determined.

\* Conversion measured by analysis of 400-MHz <sup>1</sup>H NMR spectra of unpurified mixtures.

† Yield of isolated product after purification (see the Supplementary Information for details).

‡ The enantiomeric ratio (e.r.) was determined by gas liquid chromatography analysis. See the Supplementary Information for details as well as for proof of product absolute configuration.

§ The e.e. was calculated from the e.r.; the variances of e.e. values are estimated to be between –2% and +2%.

|| Configuration of the major enantiomer.



**Table 2 | Comparison of catalytic enantioselective RCM promoted by chiral molybdenum diolates and chiral aryloxide–pyrrolide complexes**

Entry no.	Substrate	Product	Mo diolate; mol%*	Time (h); Temp. (°C)	Conv. (%)†; Yield (%)‡	e.r. (%); e.e. (%)§	Mo aryloxide; mol%*	Time (h); Temp. (°C)	Conv. (%)†; Yield (%)‡	e.r. (%); e.e. (%)§
1			All available	>36; >40	<5; —	—	<b>13b</b> ; 2.5	1; 22	94; 89	83.5:16.5; 67
2			<b>7</b> ; 10	48; 22	>95; 91	99:1; 98	<b>13c</b> ; 3	1; 22	95; 88	95.5:4.5; 91
3			<b>5b</b> ; 15	24; 22	75; ND	65:35; 30	<b>13b</b> ; 1	1; 22	>98; >98	96:4; 92
4			<b>5b</b> ; 5	20; 22	>98; ND	70:30; 40	<b>13c</b> ; 3	1; 22	95; 86	90.5:9.5; 81
5			<b>5a</b> ; 2	7; 22	>98; 90	97.5:2.5; 95	<b>13c</b> ; 1	1; 22	>98; 86	96.5:3.5; 93
6			<b>5c</b> ; 5	12; 22	>98; 98	97:3; 94	<b>13c</b> ; 1	1; 22	>98; 84	94:6; 88

\* The reactions in entries 1–2 and 4–6 were carried out in purified benzene or toluene under an atmosphere of nitrogen gas (see the Supplementary Information for details); the reaction in entry 3 was performed in pentane.

† Conversion measured by analysis of 400-MHz  $^1\text{H}$  NMR spectra of unpurified mixtures.

‡ Yield of isolated product after purification (see the Supplementary Information for details).

§ The e.r. was determined by high-performance liquid or gas liquid chromatography analysis. See the Supplementary Information for details as well as for proof of product absolute configuration. The e.e. was calculated from the e.r.; the variances of e.e. values are estimated to be between –2% and +2%.

**5c** initiates a slightly more selective ring closure (97:3 e.r. versus 94:6 e.r. with **13c**); with 1 mol% **13c**, conversion of **26** to **27** is complete in 1 h (versus 5 mol% and 12 h with **5c**)<sup>27</sup>. Three points regarding the transformations in Table 2 merit mention. First, in certain cases, dichloro complex **13c** affords similar, but higher, selectivity in comparison with dibromo complex **13b**. Second, the molybdenum centre undergoes two inversions in the course of each catalytic cycle (Fig. 2). The high enantioselectivities observed might suggest that adventitious isomerization occurs at a minimum or not at all, as such isomerizations would furnish the alternative product enantiomers.

Third, chiral ruthenium-based alkene metathesis catalysts developed so far only promote enantioselective RCM of trisubstituted alkenes with high selectivity ( $\geq 80\%$  e.e. or  $\geq 90:10$  e.r.)<sup>20,28,29</sup>.

The most notable demonstration of the attributes of molybdenum mono-aryloxides is in the context of enantioselective synthesis of quebrachamine (Fig. 1). In the presence of 1 mol% **13c**, generated *in situ*, triene **1** is transformed entirely in 1 h to **2** in 84% yield and 96% e.e. (Fig. 4). The target alkaloid is subsequently obtained in high enantiomeric purity and yield (97%). The molybdenum-catalysed process in Fig. 4 thus constitutes the application of a highly effective

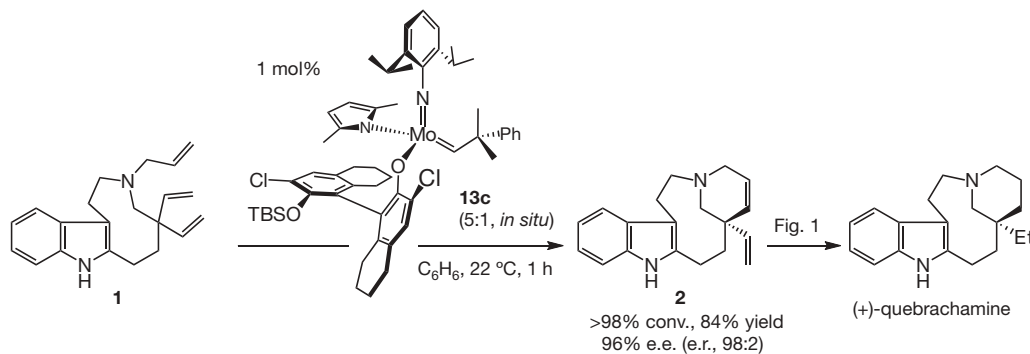


**Figure 4 | Efficient and highly enantioselective synthesis of (+)-quebrachamine.** The new chiral molybdenum aryloxides, represented by **13c**, promote the ring-closing metathesis of **1** to afford **2** with unprecedented efficiency (see Fig. 1 for comparison with previously known catalysts). Moreover, the molybdenum-catalysed ring-closing metathesis of **1**, a process

that cannot be promoted by any of the available chiral molybdenum or ruthenium catalysts, proceeds with exceptionally high enantioselectivity (e.r., 98:2) in the presence of **13c**. Palladium-catalysed hydrogenation of **2** affords the alkaloid natural product quebrachamine in high enantiomeric purity.

catalytic enantioselective RCM (e.r.,  $\geq 95:5$ ) to the total synthesis of a relatively complex natural product<sup>1,12</sup>.

The chiral complexes discovered in this study are examples of configurationally stable, enantiomerically pure, diastereomerically enriched, stereogenic-at-metal catalysts that bear only monodentate ligands. We have demonstrated that constitutionally fluxional stereogenic-at-metal complexes that effectively exploit stereoelectronic factors should be considered as viable and attractive options in future catalyst design.

## METHODS SUMMARY

The general procedure for *in situ* catalyst preparation and catalytic enantioselective alkene metathesis is as follows. An oven-dried (135 °C) 25-mL round-bottom flask, equipped with a magnetic stir bar, is charged with Mo bis-pyrrolide (0.01 equiv.) under N<sub>2</sub> atmosphere (dry box). The flask is sealed with a septum, taped, and brought to a fume hood, in which all manipulations are performed. An 8-mL vial is charged with the alcohol (0.01 equiv.), which is subsequently dried by azeotropic distillation with C<sub>6</sub>H<sub>6</sub>. Toluene (0.02 M) is added to the alcohol and the resulting solution immediately transferred by syringe to the Mo bis-pyrrolide (flask pressurized on addition; that is, no outlet needle). The mixture is allowed to stir for the appropriate period of time at 22 °C. A 20-mL vial is charged with substrate (1 equiv.), which is dried by azeotropic distillation with C<sub>6</sub>H<sub>6</sub>. Toluene (final substrate concentration, 0.2 M) is added and the solution immediately transferred by syringe to the 25-mL flask (flask pressurized on addition); the mixture is allowed to stir for the required period of time. The reaction is quenched by addition of wet diethyl ether and concentrated *in vacuo* (percent conversion determined by 400-MHz <sup>1</sup>H NMR analysis). Purification is performed by silica gel chromatography and enantiomeric purity of the product determined by gas or high-performance liquid chromatography analysis in comparison with authentic racemic material.

Received 30 April; accepted 29 October 2008.

Published online 16 November 2008.

- Hoveyda, A. H. & Zhugralin, A. R. The remarkable metal-catalysed olefin metathesis reaction. *Nature* **450**, 243–251 (2007).
- Hashimoto, S., Komeshima, N. & Koga, K. Asymmetric Diels–Alder reaction catalysed by chiral alkoxyaluminum dichloride. *J. Chem. Soc. Chem. Commun.* 437–438 (1979).
- Tayama, E., Saito, A., Ooi, T. & Maruoka, K. Activation of ether functionality of allyl vinyl ethers by chiral bis(organooaluminum) Lewis acids: application to asymmetric Claisen rearrangement. *Tetrahedron* **58**, 8307–8312 (2002).
- Solans-Monfort, X., Clot, E., Copéret, C. & Eisenstein, O. d<sup>0</sup>-Re-based olefin metathesis catalysts, Re(=CR)(=CHR)(X)(Y): the key role of X and Y ligands for efficient active sites. *J. Am. Chem. Soc.* **127**, 14015–14025 (2005).
- Poater, A., Solans-Monfort, X., Clot, E., Copéret, C. & Eisenstein, O. Understanding d<sup>0</sup>-olefin metathesis catalysts: Which metal, which ligands? *J. Am. Chem. Soc.* **129**, 8207–8216 (2007).
- Brunner, H. & Prommesberger, M. Asymmetric catalysis. Part 127: Enantioselective desymmetrization of 2-*n*-butyl-4,7-dihydro-1,3-dioxepin with (η<sup>6</sup>-arene)ruthenium(II) half-sandwich complexes. *Tetrahedr. Asymm.* **9**, 3231–3239 (1999).
- Faller, J. W., Grimmond, B. J. & D'Allesio, D. G. An application of electronic asymmetry to highly enantioselective catalytic Diels–Alder reactions. *J. Am. Chem. Soc.* **123**, 2525–2529 (2001).
- Noyori, R. Asymmetric catalysis: science and opportunities (Nobel lecture). *Angew. Chem. Int. Ed.* **41**, 2008–2022 (2002).
- Fontecave, M., Hamelin, O. & Ménage, S. Chiral-at-metal complexes as asymmetric catalysts. *Top. Organomet. Chem.* **15**, 271–278 (2005).
- Brunner, H. Optically active organometallic compounds of transition elements with chiral metal atoms. *Angew. Chem. Int. Ed.* **38**, 1194–1208 (1999).
- Brunner, H. & Fisch, K. Catalytic hydrosilylation or hydrogenation at one coordination site of [Cp\*Fe(CO)(X)] fragments. *Angew. Chem. Int. Ed.* **29**, 1131–1132 (1990).
- Schrock, R. R. & Hoveyda, A. H. Molybdenum and tungsten imido alkylidene complexes as efficient olefin-metathesis catalysts. *Angew. Chem. Int. Ed.* **42**, 4592–4633 (2003).
- Grubbs, R. H. *Handbook of Metathesis* (Wiley-VCH, 2003).
- Kozmin, S. A., Iwama, T., Huang, Y. & Rawal, V. H. An efficient approach to *Aspidosperma* alkaloids via [4+2] cycloadditions of aminosiloxenylenes: Stereocontrolled total syntheses of (±)-tabersonine. Gram-scale catalytic asymmetric syntheses of (+)-tabersonine and (+)-16-methoxytabersonine. Asymmetric syntheses of (+)-aspidospermidine and (–)-quebrachamine. *J. Am. Chem. Soc.* **124**, 4628–4641 (2002).
- Deutsch, H. F., Evenson, M. A., Drescher, P., Sparwasser, C. & Madsen, P. Isolation and biological activity of aspidospermine and quebrachamine from an *Aspidosperma* tree source. *J. Pharm. Biomed. Anal.* **12**, 1283–1287 (1994).
- Schrock, R. R. *et al.* Synthesis of molybdenum imido alkylidene complexes and some reactions involving acyclic olefins. *J. Am. Chem. Soc.* **112**, 3875–3886 (1990).
- Garber, S. B., Kingsbury, J. S., Gray, B. L. & Hoveyda, A. H. Efficient and recyclable monomeric and dendritic Ru-based metathesis catalysts. *J. Am. Chem. Soc.* **122**, 8168–8179 (2000).
- Stewart, I. C., Douglas, C. J. & Grubbs, R. H. Increased efficiency in cross-metathesis reactions of sterically hindered olefins. *Org. Lett.* **10**, 441–444 (2008).
- Van Veldhuizen, J. J., Campbell, J. E., Giudici, R. E. & Hoveyda, A. H. A readily available chiral Ag-based N-heterocyclic carbene complex for use in efficient and highly enantioselective Ru-catalyzed olefin metathesis and Cu-catalyzed allylic alkylation reactions. *J. Am. Chem. Soc.* **127**, 6877–6882 (2005).
- Funk, T. W., Berlin, J. M. & Grubbs, R. H. Highly active chiral ruthenium catalysts for asymmetric ring-closing olefin metathesis. *J. Am. Chem. Soc.* **128**, 1840–1846 (2006).
- Alexander, J. B., La, D. S., Cefalo, D. R., Hoveyda, A. H. & Schrock, R. R. Catalytic enantioselective ring-closing metathesis by a chiral biphen-Mo complex. *J. Am. Chem. Soc.* **120**, 4041–4042 (1998).
- Tsang, W. C. P. *et al.* Alkylidene and metalacyclic complexes of tungsten that contain a chiral biphenoxide ligand. Synthesis, asymmetric ring-closing metathesis, and mechanistic investigations. *J. Am. Chem. Soc.* **125**, 2652–2666 (2003).
- Singh, R., Schrock, R. R., Müller, P. & Hoveyda, A. H. Synthesis of monoalkoxide monopyrrolyl complexes of the type Mo(NR')(CHR')(OR')(pyrrolyl). Enyne metathesis with high oxidation state catalysts. *J. Am. Chem. Soc.* **129**, 12654–12655 (2007).
- Hock, A. S., Schrock, R. R. & Hoveyda, A. H. Dipyrrolyl precursors to bisalkoxide molybdenum olefin metathesis catalysts. *J. Am. Chem. Soc.* **128**, 16373–16375 (2006).
- Dolman, S. J., Sattely, E. S., Hoveyda, A. H. & Schrock, R. R. Efficient catalytic enantioselective synthesis of unsaturated amines: preparation of small- and medium-ring cyclic amines through Mo-catalyzed asymmetric ring-closing metathesis in the absence of solvent. *J. Am. Chem. Soc.* **124**, 6991–6997 (2002).
- Sattely, E. S., Cortez, G. A., Moebius, D. C., Schrock, R. R. & Hoveyda, A. H. Enantioselective synthesis of cyclic amides and amines through Mo-catalyzed asymmetric ring-closing metathesis. *J. Am. Chem. Soc.* **127**, 8526–8533 (2005).
- Kiely, A. F., Jernelius, J. A., Schrock, R. R. & Hoveyda, A. H. Enantioselective synthesis of medium-ring heterocycles, tertiary ethers, and tertiary alcohols by Mo-catalyzed ring-closing metathesis. *J. Am. Chem. Soc.* **124**, 2868–2869 (2002).
- Van Veldhuizen, J. J., Gillingham, D. G., Garber, S. B., Kataoka, O. & Hoveyda, A. H. Chiral Ru-based complexes for asymmetric olefin metathesis: Enhancement of catalyst activity through steric and electronic modifications. *J. Am. Chem. Soc.* **125**, 12502–12508 (2003).
- Fournier, P.-A. & Collins, S. K. A highly active chiral ruthenium-based catalyst for enantioselective olefin metathesis. *Organometallics* **26**, 2945–2949 (2007).

**Supplementary Information** is linked to the online version of the paper at [www.nature.com/nature](http://www.nature.com/nature).

**Acknowledgements** This research was supported by the US National Institutes of Health, Institute of General Medical Sciences (grant GM-59426 to A.H.H. and R.R.S.). We are grateful to B. C. Bailey and K. Wampler for assistance in obtaining the X-ray structure of the major diastereomer of molybdenum complex **13b**. We thank A. R. Zhugralin for numerous discussions regarding the mechanistic aspects of these investigations and R. Singh for experimental suggestions. Mass spectrometry facilities at Boston College are supported by the US National Science Foundation (grant DBI-0619576).

**Author Contributions** S. J. Malcolmson and S. J. Meek were involved in the discovery and development of the new catalysts. E.S.S. designed and developed the synthesis route to racemic quebrachamine. A.H.H. and R.R.S. designed and directed the research program. A.H.H. wrote the manuscript.

**Author Information** X-ray crystallographic data have been deposited at the Cambridge Crystallographic Data Centre, UK; CCDC 703841 contains the supplementary crystallographic data for this paper. These data can be obtained free of charge from The Cambridge Crystallographic Data Centre ([www.ccdc.cam.ac.uk/data\\_request/cif](http://www.ccdc.cam.ac.uk/data_request/cif)). Reprints and permissions information is available at [www.nature.com/reprints](http://www.nature.com/reprints). Correspondence and requests for materials should be addressed to A.H.H. ([amir.hoveyda@bc.edu](mailto:amir.hoveyda@bc.edu)).



## LETTERS

# How supercontinents and superoceans affect seafloor roughness

Joanne M. Whittaker<sup>1†</sup>, R. Dietmar Müller<sup>1</sup>, Walter R. Roest<sup>2</sup>, Paul Wessel<sup>3</sup> & Walter H. F. Smith<sup>4</sup>

Seafloor roughness varies considerably across the world's ocean basins and is fundamental to controlling the circulation and mixing of heat in the ocean<sup>1</sup> and dissipating eddy kinetic energy<sup>2</sup>. Models derived from analyses of active mid-ocean ridges suggest that ocean floor roughness depends on seafloor spreading rates<sup>3</sup>, with rougher basement forming below a half-spreading rate threshold of 30–35 mm yr<sup>-1</sup> (refs 4, 5), as well as on the local interaction of mid-ocean ridges with mantle plumes or cold-spots<sup>6</sup>. Here we present a global analysis of marine gravity-derived roughness, sediment thickness, seafloor isochrons and palaeo-spreading rates<sup>7</sup> of Cretaceous to Cenozoic ridge flanks. Our analysis reveals that, after eliminating effects related to spreading rate and sediment thickness, residual roughness anomalies of 5–20 mGal remain over large swaths of ocean floor. We found that the roughness as a function of palaeo-spreading directions and isochron orientations<sup>7</sup> indicates that most of the observed excess roughness is not related to spreading obliquity, as this effect is restricted to relatively rare occurrences of very high obliquity angles (>45°). Cretaceous Atlantic ocean floor, formed over mantle previously overlain by the Pangaea supercontinent, displays anomalously low roughness away from mantle plumes and is independent of spreading rates. We attribute this observation to a sub-Pangaeian supercontinental mantle temperature anomaly<sup>8</sup> leading to slightly thicker than normal Late Jurassic and Cretaceous Atlantic crust<sup>9</sup>, reduced brittle fracturing and smoother basement relief. In contrast, ocean crust formed above Pacific supervents<sup>10</sup>, probably reflecting metasomatized lithosphere underlain by mantle at only slightly elevated temperatures<sup>11</sup>, is not associated with basement roughness anomalies. These results highlight a fundamental difference in the nature of large-scale mantle upwellings below supercontinents and superoceans, and their impact on oceanic crustal accretion.

The relationship between spreading rates and marine basement roughness has predominantly been determined through analysis of near-zero-aged crust on individual profiles across mid-ocean ridges using short-wavelength gravity<sup>3,4</sup> or bathymetry. This relationship was also found to hold for off-axis oceanic crust at all ages<sup>5</sup>. Short-wavelength roughness in gravity anomalies (~20–160 km wavelength) reflects the roughness of oceanic basement topography<sup>4</sup>. Here we use a 2-min gravity anomaly grid downward continued onto the sea floor based on ref. 12 (Supplementary Fig. 1) to create a root mean square (r.m.s.) marine gravity roughness grid (Fig. 1) using a 100-km-wide Gaussian filter with seamounts and oceanic plateaus masked (Supplementary Fig. 2).

Half-spreading rate and sediment cover (Supplementary Fig. 1) strongly influence basement roughness. These factors are removed to examine the role of other potential factors, such as spreading obliquity, mantle temperature and mantle fertility on basement rough-

ness. Each kilometre of sediment<sup>13</sup> results in an ~14% decrease in gravity roughness (Fig. 2a). Global half-spreading rates<sup>7</sup> (1) faster than 35 mm yr<sup>-1</sup> result in low gravity roughness (~7 mGal), (2) between 35–15 mm yr<sup>-1</sup> result in increasingly rough and variable gravity roughness, and (3) slower than 15 mm yr<sup>-1</sup> form high-amplitude gravity roughness (~15 mGal) (Fig. 2b). These results differ from previous findings<sup>4,5</sup> that suggest gravity roughness continues to increase with decreasing half-spreading rates <15 mm yr<sup>-1</sup>.

Our results confirm that the relationship between spreading rate and basement roughness is consistent with the 'magma lens' model of mid-ocean ridge formation<sup>6</sup>, where decreasing spreading rates lead to increasing lens depth and decreased melt production, with a relatively rapid transition from a lens to a no-lens situation. Our global results show that roughness is insensitive to half-spreading rate at rates >35 mm yr<sup>-1</sup> and <15 mm yr<sup>-1</sup>, probably representing lens and no-lens situations, respectively, with a transitional stage occurring as half-spreading rates drop from 30–35 to 15 mm yr<sup>-1</sup>. Crust created at rates <15 mm yr<sup>-1</sup> is approximately twice as rough as crust created at rates >35 mm yr<sup>-1</sup>, consistent with thermo-tectonic cyclicity at slow spreading rates<sup>14</sup>.

Residual roughness (Fig. 3) is calculated by removing spreading rate and sediment thickness effects (Fig. 2) from the r.m.s. gravity roughness grid (Fig. 1) to investigate how spreading obliquity and mantle conditions influence basement roughness. Higher angles of spreading obliquity are related to increasing ridge segmentation<sup>14,15</sup> and seismicity<sup>15</sup>, both due to increased brittle fracturing at higher

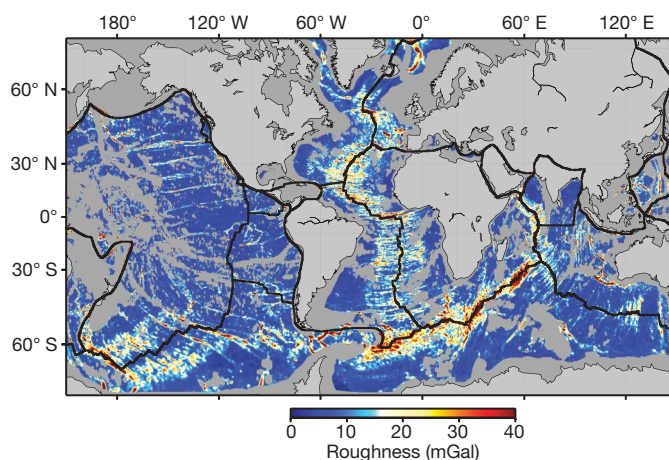


**Figure 1** | Downward-continued gravity r.m.s. roughness calculated using a Gaussian filter with a half-width of 50 km. Plate boundaries shown as heavy black lines, landmasses in light grey, and masked continental shelves, seamounts and large igneous provinces in dark grey.

<sup>1</sup>Earthbyte Group, School of Geosciences, Building F09, The University of Sydney, Sydney, New South Wales 2006, Australia. <sup>2</sup>Ifremer, Centre de Brest, Département des Géosciences Marines, BP 70, 29280 Plouzané, France. <sup>3</sup>Department of Geology and Geophysics, SOEST, University of Hawaii at Mānoa, Honolulu, Hawaii 96822, USA. <sup>4</sup>National Oceanic and Atmospheric Administration, Silver Spring, Maryland 20910, USA. <sup>†</sup>Present address: GETECH, Kitson House, Elmete Hall, Elmete Lane, Leeds LS8 2LJ, UK.

spreading angles<sup>15</sup>. Spreading obliquity has also been found to influence ridge morphology by decreasing effective spreading rates proportionally to  $\cos\theta$  (ref. 16), where  $\theta$  is the angle of obliquity.

To investigate the relationship between spreading obliquity and basement roughness, we create regional 2-min spreading obliquity grids for ten regions (intentionally excluding triple junctions, small/temporary spreading centres, back-arc basins and areas with complex spreading histories; Fig. 3 and Supplementary Figs 5–14) by calculating the difference between the regional plate motion direction and the normal to the regional mid-ocean ridge strike in 5-million-year (5-Myr) stages. Our results show that for spreading obliquities  $<45^\circ$ , variation of residual roughness with spreading obliquity fits a roughness curve that includes the effective reduction in spreading rate caused by oblique spreading (Fig. 3 inset). However, our analysis also reveals that for obliquities  $>45^\circ$ , residual roughness increases much more rapidly, indicating that an additional mechanism, probably brittle fracturing, causes increased roughness at high spreading obliquities.

Analysis of residual roughness is carried out for each selected spreading system (Fig. 4) based on spreading rate, sediment thickness and r.m.s. gravity roughness (see Supplementary Fig. 15 for an example of how the sediment thickness–roughness relationship improves the predicted roughness for individual flanks of the South Atlantic spreading system). Only in the North and South Pacific is basement roughness accurately predicted using spreading rate and sediment thickness. With the additional removal of roughness related to spreading obliquity, the roughness of the Southeast Indian ridge flanks is well predicted, while the misfit for the South American–Antarctic ridge is reduced. However, spreading rate, sediment thickness and spreading obliquity do not accurately predict basement roughness for the remaining regions that exhibit long-term deviations of 5–20 mGal over periods  $>40$  Myr and in many cases  $>60$  Myr (Fig. 4).

Relatively smooth basement is predicted for the Australian–Antarctic discordance (AAD) based on half-spreading rates of  $35\text{--}40\text{ mm yr}^{-1}$  since  $\sim 40$  Myr ago. However, the AAD exhibits basement

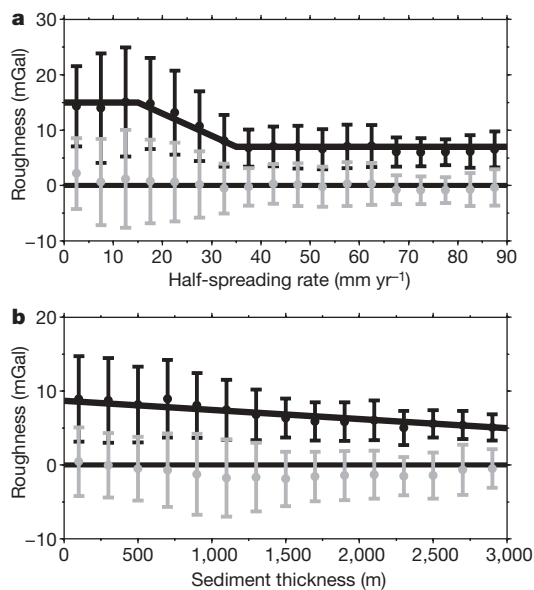


**Figure 2 | Gravity roughness as a function of half-spreading rates and sediment thickness.** Median roughness and its median absolute deviation were calculated in bins sized  $5\text{ mm yr}^{-1}$  for half-spreading rates (a) and 200 m for sediment thickness (b; filled black circles). Dark grey lines on each graph shows line of best fit, which is used to remove the effects of spreading rate and sediment thickness from gravity roughness. Light grey filled circles show variation of residual gravity roughness (see Fig. 3), with spreading rate (a) and sediment thickness (b). Error bars show  $\pm$  median absolute deviation.

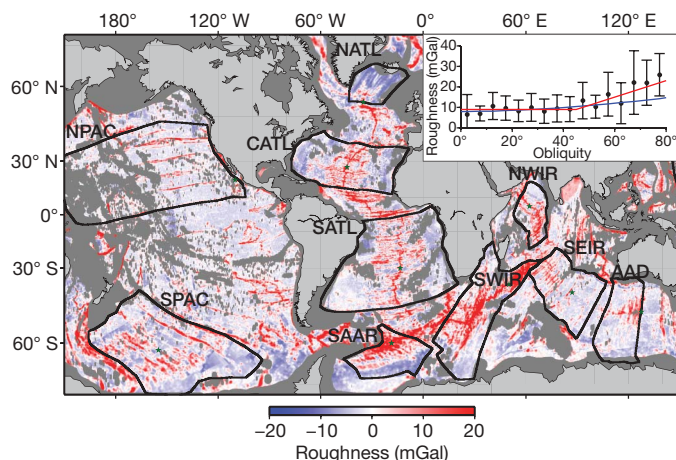


**Figure 3 | Residual roughness, after removing effects of spreading rate and sediment thickness from the r.m.s. roughness grid.** Main panel: black lines, individual spreading systems; green stars, locations where spreading direction through time was calculated for each region. NPAC, North Pacific; SPAC, South Pacific; NATL, North Atlantic; CATL, Central Atlantic; SATL, South Atlantic; SAAR, South American–Antarctic ridge; SWIR, Southwest Indian ridge; NWIR, Northwest Indian ridge; SEIR, Southeast Indian ridge; AAD, Australian–Antarctic discordance. Inset, relationship between roughness and spreading obliquity. Error bars, median absolute deviation; red line, two-stage line of best fit; blue line, basement roughness expected due to the influence of spreading obliquity on spreading rates assuming roughness equals 8 mGal at  $0^\circ$ .

up to 8 mGal rougher than predicted (Fig. 4). Crustal thickness in the AAD is 2–4 km thinner than adjacent crust, implying a  $150^\circ\text{C}$  decrease in mantle temperature<sup>17</sup>. Also, the AAD is located at the site of a palaeosubduction zone, with current lavas probably sourced from depleted magmas derived from subducted oceanic crust<sup>18</sup>. Mantle fertility additionally affects the bulk extent of melting<sup>19,20</sup>, with depleted mantle producing lower melt volumes<sup>21</sup> and thus rougher basement. Both cool mantle temperatures and low mantle fertility have resulted in rough basement in the AAD despite relatively fast spreading rates over the past 15 Myr (ref. 22).

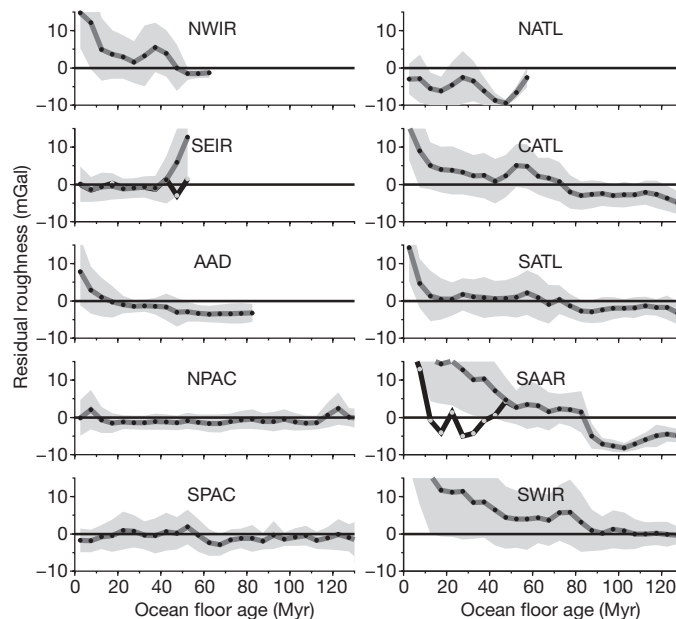


**Figure 4 | Variation of residual roughness in 5-Myr stages for ten selected regions.** Grey line with black dots, residual roughness for regions shown on plots. Grey envelope,  $\pm$  median absolute deviation. Black line with grey dots, residual roughness with roughness attributable to spreading obliquity removed using the relationship shown by the red line in Fig. 3 inset.



We suggest that remaining long-term residual roughness variations, after the removal of roughness caused by variations in spreading rate and sediment cover, are attributable to the temperature and fertility conditions of the underlying mantle. Cretaceous (80–130 Myr old) oceanic crust is smoother than expected, expressed by negative residual roughness ( $-3$  to  $-9$  mGal), mainly in the Central and South Atlantic regions. These regions formed at slow half-spreading rates ( $<30$  mm yr $^{-1}$ ) during the initial stages of continental dispersal and are associated with pre-breakup magmatism that has been suggested to be unrelated to plume activity<sup>8,23</sup>. Smoother than expected crust occurs over a vast spatial and temporal domain (over 9,000 km in length and over  $\sim 50$  Myr), supporting a non-plume-related formation mechanism.

Previously, anomalously thick Cretaceous crust on the North American side of the Atlantic has been attributed to a mantle plume influence<sup>9</sup>. However, our analysis shows that both sides of the Atlantic have Cretaceous crust that is smoother than expected (Supplementary Fig. 16), over an area too vast to be related to hotspot related anomalous mantle. We propose that the majority of preserved Cretaceous oceanic crust accreted from anomalously hot supercontinent mantle following Pangaea break-up. Continental aggregation may cause an enlargement of mantle convection wavelengths leading to mantle temperatures up to 100 °C hotter than normal beneath supercontinents<sup>8</sup>. This mantle thermal anomaly is dissipated through seafloor spreading following supercontinent break-up. The anomalously hot mantle would lead to thicker crust and reduced brittle fracturing even under slow spreading conditions.

The North Pacific is the only region with substantial volumes of preserved 80–130-Myr-old crust that did not form through supercontinent break-up. Here spreading rate and sediment thickness accurately predict basement roughness despite the influence of the Cretaceous North Pacific Darwin rise superswell ( $\sim 120$ – $85$  Myr ago), which may be expected to lead to anomalously smooth basement due to increased heat flow and partial melting<sup>10</sup>. At present the South Pacific is underlain by the similar South Pacific superswell<sup>10</sup>, which also does not lead to smoother (or rougher) than expected basement. Our observations suggest that Pacific superswells, although causing widespread shallowing of the sea floor<sup>10</sup> and widespread, small-scale alkaline volcanism<sup>11</sup>, do not strongly influence accretionary processes at mid-ocean ridges. This may reflect metasomatized Pacific superswell lithosphere underlain by mantle at only slightly elevated temperatures, having a negligible effect on mid-ocean ridge accretionary processes. South Pacific superswell initiation has been suggested to reflect a slab-avalanche event leading to slab detachment at the mantle transition zone<sup>11</sup>. However, a recent plate kinematic model<sup>24</sup> leads to the suggestion that the South Pacific superswell was triggered by the well-mapped Eocene plate reorganization, associated with Izanagi-Pacific ridge subduction and subduction initiation along Tonga-Kermadec and the Marianas. The descending slabs of these newly formed subduction zones probably progressively impeded the southwest flow of sub-Pacific mantle<sup>24</sup>, known to halt at 47 Myr ago<sup>25</sup> and triggering an upper mantle return flow ultimately causing anomalously shallow regional sea floor. Our hypothesis provides a mechanism that explains the ongoing nature of the South Pacific superswell, including a lack of influence on seafloor roughness, as opposed to a temporal, catastrophic mantle avalanche mechanism.

Our results provide observational evidence for a fundamental difference between the long-term mantle evolution below supercontinents and superoceans. Supercontinent assembly may lead to a 100 °C warming of sub-continental mantle, whereas associated sub-oceanic mantle stays relatively constant in temperature<sup>8</sup>. During supercontinent dispersal, newly formed spreading ridges initially sample anomalously hot mantle, whereas normal ocean crust in the antipodal superocean is not similarly affected. Considering that continental break-up occurred in the central North Atlantic at about 175 Myr ago<sup>26</sup>, and that we observe anomalously smooth regional

oceanic basement roughness until 80 Myr ago, it takes nearly 100 Myr for supercontinental mantle warming to dissipate.

Many of the spreading systems analysed here experienced a shift from smoother to rougher than expected basement at  $\sim 70$  Myr ago (central and southern Atlantic systems) and  $\sim 50$  Myr ago (western Indian systems). This may partly reflect the gradual dissipation of a supercontinent-related thermal anomaly, but this alone would not account for a shift to a positive roughness anomaly. Upper mantle depletion is known to reduce melt volumes<sup>21</sup>. The western Indian and central and southern Atlantic mid-ocean ridges are relatively distal to large mantle plumes, resulting in poor upper mantle replenishment because of their dependence on slow, localized mantle upwellings<sup>27</sup>. An unusual geochemical signature indicates that depleted rather than cold mantle is at least partly responsible for anomalously rough basement at the Southwest Indian ridge<sup>21</sup>. We interpret anomalously rough basement formed during the Cenozoic in the Atlantic and western Indian oceans as reflecting a gradual migration of mid-ocean ridges away from major mantle upwellings<sup>28</sup>, depriving spreading centres of asthenospheric replenishment.

Contrary to previous studies, our results demonstrate that mantle temperature/fertility and spreading obliquity can dominate spreading rate effects on oceanic basement roughness. As ocean mixing is strongly influenced by seafloor topography, realistic palaeoceanographic simulations depend on reconstructed ocean basin topography, including palaeo-gateways underlain by now subducted crust. Our model provides a predictive framework for reconstructing more realistic maps of ancient ocean basins—a necessary prerequisite for understanding ocean circulation and mixing through time.

## METHODS SUMMARY

We high-pass filter the downward-continued gravity grid using a Gaussian filter of 100-km width, then calculate a Gaussian-weighted r.m.s. for these residuals with the same filter width (Fig. 1). Short-wavelength roughness in gravity anomalies ( $\sim 20$ – $160$ -km wavelength) reflects the roughness of oceanic basement topography<sup>5</sup>. By computing a roughness grid based on a filter width of 160 km following ref. 5 we find that many basement tectonic features are not well resolved (Supplementary Fig. 4). This reflects the fact that the vast majority of structural features of the sea floor such as abyssal hills, fracture zone troughs and ridges have wavelengths significantly smaller than 160 km. We select a 100-km filter width to better resolve spatial variations in seafloor roughness on relatively small scales (Supplementary Fig. 4). The spreading rate dependence of roughness is analysed here in 5-Myr intervals. Intraplate seamount trails and large igneous provinces, rough features formed by non-accretionary processes, are masked from the basement roughness grid using a mask based on a seamount catalogue<sup>28</sup> and outlines of oceanic plateaux<sup>29</sup>. The mapped seamount radii are multiplied by a factor of 2.5 to mask out flexural effects from seamount emplacement. Without this masking the roughness becomes biased by intraplate volcanism unrelated to mid-ocean ridge processes (Supplementary Fig. 2).

**Full Methods** and any associated references are available in the online version of the paper at [www.nature.com/nature](http://www.nature.com/nature).

Received 9 July; accepted 17 October 2008.

- Polzin, K. L., Toole, J. M., Ledwell, J. R. & Schmitt, R. W. Spatial variability of turbulent mixing in the abyssal ocean. *Science* **276**, 93–96 (1997).
- Gille, S. T., Yale, M. M. & Sandwell, D. T. Global correlation of mesoscale ocean variability with seafloor roughness from satellite altimetry. *Geophys. Res. Lett.* **27**, 1251–1254 (2000).
- Malinverno, A. Inverse square-root dependence of mid-ocean-ridge flank roughness on spreading rate. *Nature* **352**, 58–60 (1991).
- Small, C. & Sandwell, D. T. An abrupt change in ridge-axis gravity with spreading rate. *J. Geophys. Res.* **94** (B12), 17383–17392 (1989).
- Smith, W. H. F. Seafloor tectonic fabric from satellite altimetry. *Annu. Rev. Earth Planet. Sci.* **26**, 697–747 (1998).
- Chen, Y. J. in *Ophiolites and Oceanic Crust: New Insights from Field Studies and the Ocean Drilling Program* (eds Dilek, Y. et al.) 161–179 (Special Paper 349, Geological Society of America, 2000).
- Müller, R. D., Sdrolias, M., Gaina, C. & Roest, W. R. Age, spreading rates and spreading asymmetry of the world's ocean crust. *Geochem. Geophys. Geosyst.* **9**, doi:10.1029/2007GC001743 (2008).
- Coltice, N., Phillips, B. R., Bertrand, H., Ricard, Y. & Rey, P. Global warming of the mantle at the origin of flood basalts over supercontinents. *Geology* **35**, 391–394 (2007).

9. Minshull, T. A. On the roughness of Mesozoic oceanic crust in the western North Atlantic. *Geophys. J. Int.* **136**, 286–290 (1999).
10. McNutt, M. K. Superswells. *Rev. Geophys.* **36**, 211–244 (1998).
11. Finn, C. A., Müller, R. D. & Panter, K. S. A Cenozoic diffuse alkaline magmatic province (DAMP) in the southwest Pacific without rift or plume origin. *Geochem. Geophys. Geosyst.* **6**, Q02005, doi:10.1029/2004GC000723 (2005).
12. Sandwell, D. T. & Smith, W. H. F. Retracking ERS-1 altimeter waveforms for optimal gravity field recovery. *Geophys. J. Int.* **163**, 79–89 (2005).
13. Divins, D. L. *Total Sediment Thickness of the World's Oceans and Marginal Seas* (National Geophysical Data Center, 2004); available at (<http://www.ngdc.noaa.gov/mgg/sedthick/sedthick.html>).
14. Abelson, M. & Agnon, A. Mechanics of oblique spreading and ridge segmentation. *Earth Planet. Sci. Lett.* **148**, 405–421 (1997).
15. de Alteriis, G., Gilg-Capar, L. & Olivet, J. L. Matching satellite-derived gravity signatures and seismicity patterns along mid-ocean ridges. *Terra Nova* **10**, 177–182 (1998).
16. Montesi, L. G. J. & Behn, M. D. Mantle flow and melting underneath oblique and ultraslow mid-ocean ridges. *Geophys. Res. Lett.* **34**, doi:10.1029/2007GL031067 (2007).
17. West, B. P., Sempere, J. C., Pyle, D. G., Phipps Morgan, J. & Christie, D. M. Evidence for variable upper mantle temperature and crustal thickness in and near the Australian-Antarctic Discordance. *Earth Planet. Sci. Lett.* **128**, 135–153 (1994).
18. Ritzwoller, M. H., Shapiro, N. M. & Leahy, G. M. A resolved mantle anomaly as the cause of the Australian-Antarctic Discordance. *J. Geophys. Res.* **108** (B12), 2559–2575 (2003).
19. Langmuir, C. H., Klein, E. M. & Plank, T. in *Mantle Flow and Melt Generation at Mid-Ocean Ridges* (eds Phipps Morgan, J., Blackman, D. K. & Sinton, J. M.) 183–280 (Geophysical Monograph 71, American Geophysical Union, 1992).
20. Klein, E. M. & Langmuir, C. H. Global correlations of ocean ridge basalt chemistry with axial depth and crustal thickness. *J. Geophys. Res.* **92** (B8), 8089–8115 (1987).
21. Meyzen, C. M., Toplis, M. J., Humler, E., Ludden, J. N. & Mevel, C. A discontinuity in mantle composition beneath the southwest Indian ridge. *Nature* **42**, 731–733 (2003).
22. Marks, K. M., Stock, J. M. & Quinn, K. J. Evolution of the Australian-Antarctic discordance since Miocene time. *J. Geophys. Res.* **104** (B3), 4967–4981 (1999).
23. McHone, J. Non-plume magmatism and rifting during the opening of the central Atlantic Ocean. *Tectonophysics* **316**, 287–296 (2000).
24. Whittaker, J. *et al.* Major Australian-Antarctic plate reorganization at Hawaiian-Emperor bend time. *Science* **318**, 83–86 (2007).
25. Tarduno, J. A. *et al.* The Emperor Seamounts: Southward motion of the Hawaiian hotspot plume in Earth's mantle. *Science* **301**, 1064–1069 (2003).
26. Klitgord, K. & Schouten, H. in *The Western North Atlantic Region, DNAG Vol. M* (eds Vogt, P. R. & Tucholke, B. E.) 351–378 (Geological Society of America, 1986).
27. Meyzen, C. M. *et al.* Isotopic portrayal of the Earth's upper mantle flow field. *Nature* **447**, 1069–1074 (2007).
28. Wessel, P. Global distribution of seamounts inferred from gridded Geosat/ERS-1 altimetry. *J. Geophys. Res.* **106** (B9), 19431–19441 (2001).
29. Coffin, M. F. & Eldholm, O. Large igneous provinces: Crustal structure, dimensions, and external consequences. *Rev. Geophys.* **32**, 1–36 (1994).

**Supplementary Information** is linked to the online version of the paper at [www.nature.com/nature](http://www.nature.com/nature).

**Author Contributions** W.H.F.S. contributed to gravity field modelling and the downward continuation. P.W. created the seamount/LIP mask and performed major extensions to *grdfilter* to compute r.m.s. roughness on a Mercator-projected grid. W.R.R. was an initiator of the project who initially explored the effect of both rate and spreading obliquity on roughness. R.D.M. was an initiator of this project, and PhD supervisor of J.M.W., who conceived the idea that supercontinent and superocean effects may drive large-scale roughness anomalies. He and W.R.R. explored workflows to analyse the dependence of seafloor roughness on factors other than spreading rate, and created initial roughness grids, which were improved by the approach implemented by J.M.W. J.M.W. executed the entire project, and combined the various existing ideas and program fragments together into a coherent workflow that allowed systematic testing of ideas and quantification of the supercontinent/superocean hypothesis.

**Author Information** Reprints and permissions information is available at [www.nature.com/reprints](http://www.nature.com/reprints). Correspondence and requests for materials should be addressed to J.M.W. ([jw@getech.com](mailto:jw@getech.com)).



## METHODS

We use a global grid of gravity anomalies based on satellite altimetry, downward continued and draped onto the lowpass of the topo\_8.2.img grid of the sea floor<sup>4,30</sup>, using the filters described in ref. 31 to create a global grid of oceanic basement roughness. Our roughness filter is a variable-width Gaussian filter adjusted to the local scale of the Mercator-projected data, whose half-power point wavelength is 50 km, reflecting gravity anomalies due to uncompensated basement topography, implemented in the Generic Mapping Tools program `grdfilter`. This weighted-average filter is applied to individual points to compute r.m.s. marine gravity roughness. To separate the effects of processes related to seafloor spreading, we mask roughness attributable to intraplate seamount trails and large igneous provinces using masks from refs 28 and 29. The mapped seamount radii are multiplied by a factor of 2.5 to mask out flexural effects from seamount emplacement.

Analysis of the relationship between gravity-derived roughness and spreading rate and sediment thickness were conducted using global grids of sediment thickness<sup>13</sup>, half-spreading rates<sup>7</sup> and oceanic basement roughness. All grids had the same mask of continental crust, seamounts<sup>28</sup> and LIPS<sup>29</sup> applied.

The residual roughness grid was calculated by removing the effects of spreading rate and sediment thickness from the gravity-derived roughness grid. The linear relationships between spreading rate and sediment thickness and gravity-derived roughness (Fig. 2) were used to create a predicted roughness grid, which was then subtracted from the r.m.s. gravity-derived roughness grid.

Ten regions were selected to investigate the relationship between roughness and spreading obliquity. Regions were selected to intentionally exclude triple-junctions, small/temporary spreading centres, back-arc basins and areas with complex spreading histories. The 2-min obliquity grids were computed by calculating the difference between the regional plate motion direction (derived from the plate tectonic model of ref. 7) and the normal to the regional strike of the reconstructed mid-ocean ridge based on ref. 7, in 5-Myr stages. All relevant digital grids can be downloaded from [www.earthbyte.org](http://www.earthbyte.org).

30. Sandwell, D. T. & Smith, W. H. F. Marine gravity anomaly from Geosat and ERS-1 satellite altimetry. *J. Geophys. Res.* **102** (B5), 10039–10054 (1997).

31. Smith, W. H. F. & Sandwell, D. T. Bathymetric prediction from dense satellite altimetry and sparse shipboard bathymetry. *J. Geophys. Res.* **99** (B11), 21803–21824 (1994).

## LETTERS

# Parallel adaptations to high temperatures in the Archaeal eon

Bastien Boussau<sup>1\*</sup>, Samuel Blanquart<sup>2\*</sup>, Anamaria Necșulea<sup>1</sup>, Nicolas Lartillot<sup>2†</sup> & Manolo Gouy<sup>1</sup>

Fossils of organisms dating from the origin and diversification of cellular life are scant and difficult to interpret<sup>1</sup>, for this reason alternative means to investigate the ecology of the last universal common ancestor (LUCA) and of the ancestors of the three domains of life are of great scientific value. It was recently recognized that the effects of temperature on ancestral organisms left 'genetic footprints' that could be uncovered in extant genomes<sup>2–4</sup>. Accordingly, analyses of resurrected proteins predicted that the bacterial ancestor was thermophilic and that Bacteria subsequently adapted to lower temperatures<sup>3,4</sup>. As the archaeal ancestor is also thought to have been thermophilic<sup>5</sup>, the LUCA was parsimoniously inferred as thermophilic too. However, an analysis of ribosomal RNAs supported the hypothesis of a non-hyperthermophilic LUCA<sup>2</sup>. Here we show that both rRNA and protein sequences analysed with advanced, realistic models of molecular evolution<sup>6,7</sup> provide independent support for two environmental-temperature-related phases during the evolutionary history of the tree of life. In the first period, thermotolerance increased from a mesophilic LUCA to thermophilic ancestors of Bacteria and of Archaea–Eukaryota; in the second period, it decreased. Therefore, the two lineages descending from the LUCA and leading to the ancestors of Bacteria and Archaea–Eukaryota convergently adapted to high temperatures, possibly in response to a climate change of the early Earth<sup>1,8,9</sup>, and/or aided by the transition from an RNA genome in the LUCA to organisms with more thermostable DNA genomes<sup>10,11</sup>. This analysis unifies apparently contradictory results<sup>2–4</sup> into a coherent depiction of the evolution of an ecological trait over the entire tree of life.

Investigations into whether the LUCA was a hyperthermophilic (optimal growth temperature (OGT)  $\geq 80^\circ\text{C}$ ), thermophilic (OGT  $50\text{--}80^\circ\text{C}$ ), or mesophilic (OGT  $\leq 50^\circ\text{C}$ ) organism have relied on correlations between the species' OGT and the composition of their macromolecular sequences. In extant prokaryotic species, the G+C content of rRNA stems (that is, double-stranded parts) has been shown to correlate with OGT<sup>12</sup>. Exploiting this correlation, support was obtained for a non-hyperthermophilic LUCA<sup>2</sup>. In contrast, studies based on correlations between the composition of the LUCA's proteins and OGT concluded in favour of a hyperthermophilic LUCA<sup>13,14</sup> and of hyperthermophilic ancestors for both Archaea and Bacteria. The discrepancy between these results could come from some unexplained incongruence between rRNA and proteins, or, as we shall see, from differences between evolutionary models used.

These previous investigations<sup>2,13,14</sup> based their conclusions on comparisons of reconstructed ancestral sequence compositions with extant ones. Accurate modelling of the evolution of compositions is therefore crucial for such approaches. Two of these studies<sup>13,14</sup> relied on homogeneous models of evolution which make the simplifying hypothesis that substitutions occur with constant probabilities over time and across

all lineages. If genomes and proteins had evolved according to a homogeneous model, they would all share the same base and amino acid compositions. Clearly, rRNA<sup>12</sup> and protein sequences<sup>15</sup> do not. Another approach<sup>2</sup> has been to use a branch-heterogeneous model of RNA sequence evolution. Branch-heterogeneous models are computationally more challenging, but more realistic as they allow replacement or substitution probabilities to vary between lineages, and thus explicitly account for compositional drifts<sup>2,6,7,16,17</sup>. Accordingly, they have been shown to accurately reconstruct ancestral sequence compositions<sup>7</sup>.

We recently developed nhPhyML<sup>7</sup>, an efficient program for the branch-heterogeneous modelling of nucleotide sequence evolution in the maximum likelihood framework, and nhPhyloBayes<sup>6</sup>, which implements a site- and branch-heterogeneous Bayesian model of protein sequence evolution. The latter combines the break-point approach<sup>17</sup> to model variations of amino acid replacement rates along branches and the CAT<sup>18</sup> mixture model to account for site-wise variations of these rates. These models have been shown to describe the evolution of real sequences more faithfully than homogeneous ones<sup>6,17</sup>, although neither homogeneous nor heterogeneous models ensure that inferred ancestral sequences are biologically functional. Using nhPhyML and nhPhyloBayes, we can reconstruct ancestral sequences of both rRNAs and proteins with branch-heterogeneous models, and estimate sequence compositions of all nodes of the tree of life, including the LUCA and its descendants. These compositions can be translated into approximate OGTs using the OGT/composition correlations observed in extant sequences<sup>12,15</sup>.

A nucleotide data set of concatenated small- and large-subunit rRNAs—restricted to double-stranded regions—from 456 organisms (1,043 sites), and an amino acid data set of 56 concatenated nearly universal proteins from 30 organisms (3,336 sites), were assembled, each data set sampling all forms of cellular life. Correspondence analyses of the protein data set show that eukaryotes and prokaryotes markedly differ in amino acid compositions and that an effect of temperature on proteomes is detectable only among prokaryotic species (Supplementary Figs 4 and 6b). Similarly, the correlation between rRNA G+C content and OGT has only been documented in prokaryotes<sup>12</sup>. The ability to infer ancestral OGTs from rRNA and protein compositions therefore applies only to prokaryotes. However, eukaryotic sequences were kept in the subsequent analyses because they are part of the tree of life and as such provide useful phylogenetic information for ancestral sequence inferences.

The effect of temperature on prokaryotic proteomes is independent from genomic G+C contents<sup>15</sup>, and was summarized in terms of average content in the amino acids I, V, Y, W, R, E and L (hereafter referred to as IVYWREL). Accordingly, our correspondence analysis identifies two independent factors accounting for most of the variance in amino acid compositions of prokaryotic proteins (Supplementary Fig. 5). The first factor (45.4% of the variance) highly correlates to

<sup>1</sup>Laboratoire de Biométrie et Biologie Evolutive, CNRS, Université de Lyon, Université Lyon I, 43 Boulevard du 11 Novembre, 69622 Villeurbanne, France. <sup>2</sup>LIRMM, CNRS, 161 rue Ada, 34392 Montpellier, France. <sup>†</sup>Present address: Département de Biochimie, Université de Montréal, C.P. 6128, succursale Centre-Ville, Montréal QC H3C3J7, Canada.

\*These authors contributed equally to this work.



genome G+C content ( $r = 0.81$ ); the second (13.8% of the variance) is strongly correlated to OGT ( $r = 0.83$ ) and to IVYWREL content ( $r = 0.73$ , Supplementary Fig. 6). The second factor was therefore used here as a molecular thermometer. The rRNA-based and the protein-based thermometers are thus independent, both because they come from distinct genome parts and because they exploit different effects of temperature on sequence composition. Furthermore, the correlation between rRNA G+C content and OGT is not expected to vary during evolutionary time because it stems from the different thermal stabilities of G–C and A–U RNA base pairs<sup>12</sup>. Thus, assuming that the relationship between temperature and amino acid composition of prokaryotes has also not varied since LUCA, the estimations of rRNA G+C content and amino acid compositions through branch-heterogeneous models provide two independent means to analyse the evolution of thermophily.

For each data set, a phylogenetic tree was inferred and rooted on the branch separating Bacteria from Archaea and Eukaryota (Supplementary Figs 7 and 8). Because the location of the root in the universal tree remains uncertain<sup>19</sup>, the alternative rooting on the eukaryotic branch was also considered. Correlations between G+C content and OGT (Fig. 1a), and between the second axis of the amino

acid correspondence analysis and OGT (Fig. 1b), were used to estimate OGTs for the LUCA and its descendants (Fig. 2).

Proteins and rRNAs support similar patterns of OGT changes for prokaryotes, so the discrepancy between previous rRNA- and protein-based investigations<sup>2,13,14</sup> was not a result of incongruence between these molecules. Protein-derived temperature estimates are generally lower than those based on rRNAs (Fig. 1), although some protein and rRNA-based OGT estimates overlap if confidence intervals of ancestral compositions are taken into account (Supplementary Table 3). Both types of data support key conclusions (Fig. 1). First, the LUCA is predicted to be a non-hyperthermophilic organism, as previously reported<sup>2</sup>. Second, both archaeal and bacterial ancestors, as well as the common ancestor of Archaea and Eukaryota, are estimated to have been thermophilic to hyperthermophilic (Fig. 2). This result is in line with previous studies<sup>3,5</sup>. Third, within the bacterial phylogenetic tree, tolerance to heat decreased (Fig. 2). This last result is congruent with recent estimates of the evolution of OGTs in the bacterial domain based on ancestral reconstructions and characterizations of elongation factor Tu proteins<sup>4</sup>.

Support for the hypothesis of a non-hyperthermophilic LUCA and of subsequent parallel adaptations to high temperatures partly rests on a protein content depleted in IVYWREL for the LUCA and subsequently enriched in these amino acids. This is consistent with a recent report that amino acids IVYEW might be under-represented in LUCA's proteins<sup>20</sup>. This finding has been interpreted as evidence that these five amino acids were a late addition to the genetic code,

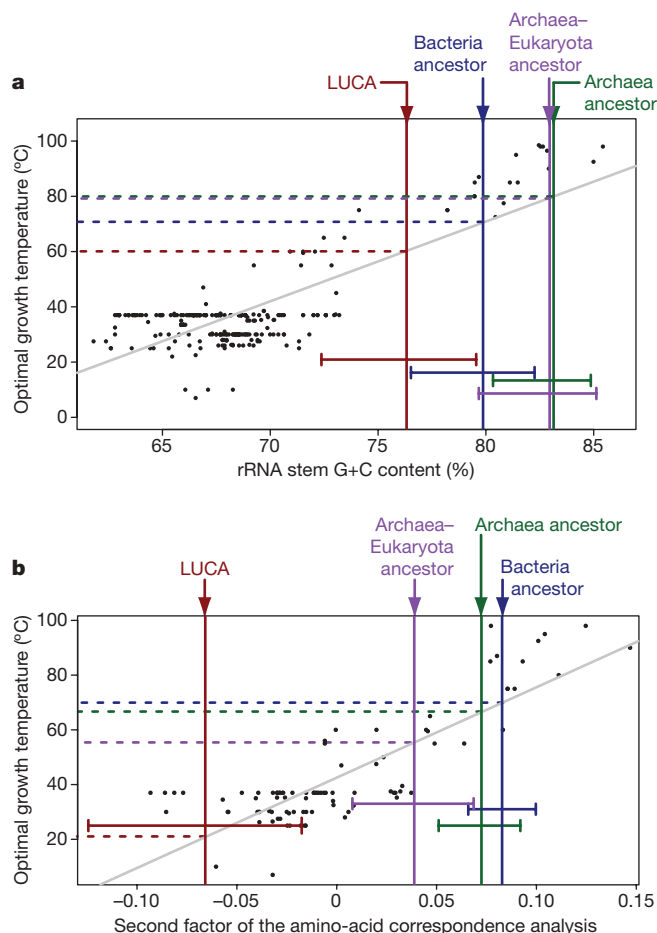


**Figure 1 | Correlations between sequence compositions and OGT, and estimates of key ancestral compositions.** Black dots indicate extant prokaryotes positioned according to their sequence composition and OGT. Dashed coloured lines indicate predicted OGTs for various ancestors. **a**, Correlation between rRNA G+C content and OGT. The vertical coloured bars indicate most likely nhPhyML estimates of ancestral G+C contents with their 95% confidence intervals. **b**, Correlation between the second factor of the correspondence analysis on amino acid compositions and OGT. The vertical coloured bars indicate median ancestral compositions inferred by nhPhyloBayes with their 95% confidence intervals. The LUCA is significantly less thermophilic than its direct descendants ( $P \leq 0.005$ ).

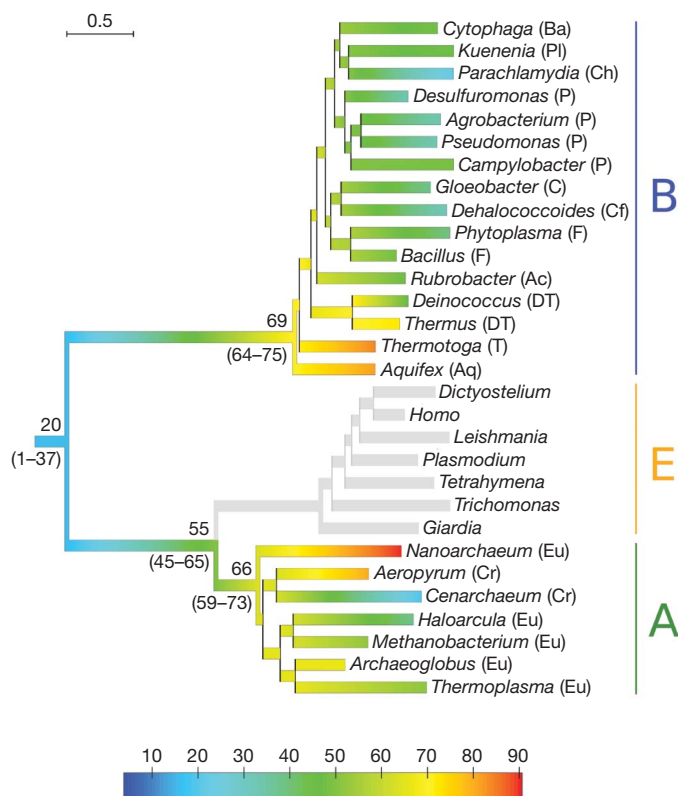


**Figure 2 | Evolution of thermophily over the tree of life.** Protein-derived nhPhyloBayes OGT estimates (and their 95% confidence intervals) for prokaryotic organisms are colour-coded from blue to red for low to high temperatures. Colours were interpolated between temperatures estimated at nodes. The eukaryotic domain, in which OGT cannot be estimated, has been shaded. The colour scale is in °C; the branch length scale is in substitutions per site. A, archaeal; B, bacterial; E, eukaryotic domains. Ac, Actinobacteria; Aq, Aquificae; Ba, Bacteroidetes; C, Cyanobacteria; Cf, Chloroflexi; Ch, Chlamydiae; Cr, Crenarchaeota; DT, Deinococcus/Thermus; Eu, Euryarchaeota; F, Firmicutes; P, Proteobacteria; Pl, Planctomycetes; T, Thermotogae.

and that the proteome of the LUCA had not yet reached compositional equilibrium. Although such interpretation in terms of early genetic code evolution is possible, our hypothesis of parallel adaptations to high temperatures has the advantage of explaining the patterns observed with both rRNAs and proteins.

Additional experiments suggest that the present analyses of rRNA and protein sequences with branch-heterogeneous models of evolution uncover genuine signals of ancient temperature preferences and are not affected by systematic biases.

First, these results are robust to changes in the topology chosen for inference because analyses with alternative topologies yielded virtually identical OGT estimates (Supplementary Fig. 10). Moreover, phylogenetic trees rooted on the eukaryotic branch also suggest that OGT increased between the universal ancestor and the divergence of Archaea and Bacteria (Supplementary Figs 13–15).

Second, taxonomic sampling does not strongly affect these results. With rRNA and protein data sets in which eukaryotic sequences were removed, the signal for OGT increases between the LUCA and the domain ancestors was essentially unchanged (Supplementary Fig. 36). Moreover, both for rRNAs and proteins, two artificially biased data sets containing sequences from either thermophilic or mesophilic prokaryotes were assembled (see Supplementary Information). The signal for parallel increases in OGT is confirmed in all but one of these four data sets: the mesophilic rRNA data set. However, the longest of the two mesophilic alignments, the protein data set, supports the same pattern of OGT changes as the complete data sets (Supplementary Figs 16 and 17). Notably, analysis of the protein mesophilic data set shows that this pattern is independent of the debated position of hyperthermophilic organisms in the tree of life. Furthermore, with all rRNA and protein data sets, even with the sampling limited to thermophilic prokaryotes, the LUCA remains predicted as a non-hyperthermophilic organism (Supplementary Figs 18 and 19).

Third, dependence of the results on models used for ancestral reconstruction was investigated. Additional branch-heterogeneous evolutionary models were applied, two to the rRNA data set, and one to the protein data set (see Supplementary Information). All these alternative branch-heterogeneous models confirm our results (Supplementary Figs 21–23, 29 and 30). Compositional analyses were also conducted using branch-homogeneous models of evolution: GTR<sup>21</sup> for rRNA and proteins, and CAT<sup>18</sup> for proteins. All these models tend to predict parallel adaptations to higher temperatures from the LUCA to its descendants, suggesting the existence of a genuine signal for such a pattern in the data (Supplementary Figs 24, 26 and 28). However, only when models are realistic enough is the LUCA predicted as significantly less thermophilic than its two descendants. For instance, ancestral protein compositions predicted by the GTR model for the LUCA and its two descendants strongly overlap, which may explain previously published results<sup>13</sup>, whereas the CAT model better separates these ancestral node distributions, although less clearly than does the CAT-BP branch-heterogeneous model (Supplementary Figs 26, 28 and 29). These experiments show that as the evolutionary process is more accurately modelled, the support for parallel increases in OGT from the LUCA to its offspring is strengthened.

Fourth, it is known that the base compositions of fast and slowly evolving sites and, particularly, of single- and double-stranded regions of rRNA molecules differ and that this may bias ancestral sequence estimates<sup>16</sup>. To minimize this bias, only double-stranded rRNA regions have been analysed here. Moreover, if fast-evolving sites are removed, estimates still support parallel adaptations to high temperatures (Supplementary Fig. 33).

Fifth, it has been shown that some ancestral reconstruction methods might improperly estimate the frequencies of rare amino acids<sup>22</sup>. To control for that potential bias, the two rarest amino acids, cysteine and tryptophan, were discarded from estimated ancestral sequences: this had essentially no impact on results (Supplementary Fig. 34).

Sixth, the sensitivity of the OGT estimates at the tree root to the prior distribution of ancestral amino acid compositions used for Bayesian analyses was investigated (Supplementary Fig. 35). This prior distribution induces a flat, uninformative distribution over OGTs, whereas the posterior distributions estimated for LUCA and the bacterial ancestor have small variance, and thus reflect a genuine signal in the data, rather than a bias from the prior. Moreover, even with a strongly informative prior distribution that is biased towards high temperature amino acid distributions, the posterior distribution of the LUCA's amino acid composition, although altered, is centred at lower temperatures than that of the bacterial ancestor.

The present use of molecular thermometers requires that evolution of the data sets under analysis can be modelled by a tree structure as far as reconstruction of ancestral compositions is concerned. We emphasize that our protein analyses are based on 56 genes that did not undergo between-domain transfers (see Methods), which precludes that ancestral sequence reconstructions are confounded by such gene exchanges. We do not exclude within-domain lateral transfers of these genes; however, the robustness of the inferred ancestral compositions to alternative domain phylogenies<sup>4,7</sup> (see also Supplementary Figs 10 and 20) suggests that these potential transfers do not fundamentally affect the results for domain ancestors. Finally, because molecular thermometers measure the average environmental temperature of the hosts of ancestral genes, they apply even if ancestral genes of extant prokaryotes originate from diverse organisms<sup>19</sup>.

Thus, all our analyses support the hypothesis of a non-hyperthermophilic LUCA and of transitions to higher environmental temperatures for its descendants. Although these organisms have not yet been anchored in time<sup>23</sup>, a few geological and biological factors may explain observed changes in temperature preferences. It has already been observed<sup>4</sup> that the general trend of decreasing OGTs from the bacterial ancestor to extant species strikingly parallels recent geological estimates of the progressive cooling down of oceans shifting from about 70 °C 3.5 billion years ago to approximately 10 °C at present<sup>24</sup>. The evolution of thermophily in the bacterial domain might therefore stem from the continuous adjustment of Bacteria to ocean temperatures, although the evidence for a hot Archaean climate remains debated<sup>25</sup>. A similar conclusion may apply to Archaea as well, but would require confirmation with additional genome sequences from mesophilic Archaea. A hot Archaean ocean may preclude the existence of a cool 'little pond' where the LUCA could have evolved. Therefore, a non-hyperthermophilic LUCA would suggest that moderate temperatures existed earlier in the history of the Earth.

Geological data about palaeoclimates that old are very scarce. However, some models of Hadean and early Archaean climates (3.5–4.2 billion years ago) suggest that the Earth might have been colder than it is today, possibly covered with frozen oceans<sup>1,26</sup>. Moreover, a hypothesis of brutal temperature changes involving meteoritic impacts that boiled the oceans and therefore nearly annihilated all life forms but the most heat-resistant ones has been proposed<sup>1,8,9</sup>. Huge meteorites probably impacted the Earth at least as late as 3.8–4 billion years ago, most notably during the late heavy bombardment<sup>27</sup> and created a series of brief but very hot climates on Earth<sup>1</sup>. As life may have originated more than 3.7 billion years ago<sup>28</sup>, it is possible that early organisms, namely the LUCA's offspring, experienced such bottlenecks.

Alternatively, under the hypothesis that life originated extra-terrestrially, the transfer of life to the Earth from another planet in ejecta created by meteorite impacts would have also entailed selection of heat-resistant cells<sup>1</sup>. Overall, geological knowledge provides several frames that might fit the predictions of our biological thermometers.

A biological hypothesis could provide an internal mechanism to explain the observed pattern. It posits that the LUCA had an RNA genome, and that its offspring lineages independently evolved the ability to use DNA for genome encoding<sup>10</sup>, possibly by co-opting it from viruses<sup>11</sup>. Although our results do not bring direct evidence in support of this hypothesis, they are compatible with it and could even

help explain such independent acquisitions of DNA in adaptive terms, as DNA is much more thermostable than RNA<sup>29</sup>.

Great care is necessary when attempting a reconstruction of events that took place more than three billion years ago. However, the strong agreement between results obtained using two types of data (proteins and rRNAs), two independent temperature proxies (protein amino acid composition and rRNA G+C content), and independently developed statistical models, is remarkable. This suggests that a similar approach could successfully be used to gain insight into other ecological features of early life. For example, it has been shown that aerobic and anaerobic bacteria differ in the amino acid composition of their proteome<sup>30</sup>; future ancestral sequence reconstructions could reveal the evolution of aerobiosis along the tree of life in relation with the geological record of oxygen atmospheric concentration.

## METHODS SUMMARY

Ribosomal RNA sequences were aligned according to their shared secondary structure. Sites belonging to double-stranded stems were selected to obtain an alignment of 1,043 stem sites for 456 organisms. Protein families with wide species coverage and no or very low redundancy in all species were selected from the HOGENOM database of families of homologous genes. Only sites showing less than 5% gaps were kept, giving an alignment of 3,336 positions for 30 organisms. Phylogenetic trees were inferred using Bayesian or maximum likelihood techniques. Ancestral nucleotide and amino acid compositions were inferred for all tree nodes using the programs nhPhyML<sup>7</sup> and nhPhyloBayes<sup>6</sup>, respectively. The G+C contents of ancestral rRNA sequences were compared to extant rRNA base compositions. The second factor of the correspondence analysis of amino acid compositions of extant prokaryotic proteins was used to estimate ancestral environmental temperatures by adding ancestral amino acid compositions as supplementary rows to the correspondence analysis. These two procedures allowed us to estimate ancestral environmental temperatures with the rRNA and the protein data sets, respectively. Confidence intervals for the estimated environmental temperatures were as follows: in the case of rRNAs, they contained 95% of the distribution obtained by a bootstrap procedure (200 replicates); for Bayesian analyses, regular 95% credibility intervals were computed from a sample of 2,000 points drawn from the posterior distribution.

**Full Methods** and any associated references are available in the online version of the paper at [www.nature.com/nature](http://www.nature.com/nature).

**Received 5 March; accepted 1 September 2008.**

**Published online 26 November 2008.**

- Nisbet, E. G. & Sleep, N. H. The habitat and nature of early life. *Nature* **409**, 1083–1091 (2001).
- Galtier, N., Tourasse, N. & Gouy, M. A nonhyperthermophilic common ancestor to extant life forms. *Science* **283**, 220–221 (1999).
- Gaucher, E. A., Thomson, J. M., Burgan, M. F. & Benner, S. A. Inferring the palaeoenvironment of ancient bacteria on the basis of resurrected proteins. *Nature* **425**, 285–288 (2003).
- Gaucher, E. A., Govindarajan, S. & Ganesh, O. K. Palaeotemperature trend for precambrian life inferred from resurrected proteins. *Nature* **451**, 704–707 (2008).
- Gribaldo, S. & Brochier-Armanet, C. The origin and evolution of archaea: a state of the art. *Phil. Trans. R. Soc. Lond. B* **361**, 1007–1022 (2006).
- Blanquart, S. & Lartillot, N. A site- and time-heterogeneous model of amino-acid replacement. *Mol. Biol. Evol.* **25**, 842–858 (2008).
- Boussau, B. & Gouy, M. Efficient likelihood computations with nonreversible models of evolution. *Syst. Biol.* **55**, 756–768 (2006).
- Sleep, N. H., Zahnle, K. J., Kasting, J. F. & Morowitz, H. J. Annihilation of ecosystems by large asteroid impacts on the early Earth. *Nature* **342**, 139–142 (1989).

- Gogarten-Boekels, M., Hilario, E. & Gogarten, J. P. The effects of heavy meteorite bombardment on the early evolution—the emergence of the three domains of life. *Orig. Life Evol. Biosph.* **25**, 251–264 (1995).
- Mushegian, A. R. & Koonin, E. V. A minimal gene set for cellular life derived by comparison of complete bacterial genomes. *Proc. Natl Acad. Sci. USA* **93**, 10268–10273 (1996).
- Forterre, P. The origin of DNA genomes and DNA replication proteins. *Curr. Opin. Microbiol.* **5**, 525–532 (2002).
- Galtier, N. & Lobry, J. R. Relationships between genomic G+C content, RNA secondary structures, and optimal growth temperature in prokaryotes. *J. Mol. Evol.* **44**, 632–636 (1997).
- Di Giulio, M. The universal ancestor and the ancestor of bacteria were hyperthermophiles. *J. Mol. Evol.* **57**, 721–730 (2003).
- Brooks, D. J., Fresco, J. R. & Singh, M. A novel method for estimating ancestral amino acid composition and its application to proteins of the Last Universal Ancestor. *Bioinformatics* **20**, 2251–2257 (2004).
- Zeldovich, K. B., Berezhovsky, I. N. & Shakhnovich, E. I. Protein and DNA sequence determinants of thermophilic adaptation. *PLoS Comput. Biol.* **3**, 62–72 (2007).
- Gowri-Shankar, V. & Rattray, M. On the correlation between composition and site-specific evolutionary rate: implications for phylogenetic inference. *Mol. Biol. Evol.* **23**, 352–364 (2005).
- Blanquart, S. & Lartillot, N. A Bayesian compound stochastic process for modeling nonstationary and nonhomogeneous sequence evolution. *Mol. Biol. Evol.* **23**, 2058–2071 (2006).
- Lartillot, N. & Philippe, H. A Bayesian mixture model for across-site heterogeneities in the amino-acid replacement process. *Mol. Biol. Evol.* **21**, 1095–1109 (2004).
- Zhaxybayeva, O., Lapierre, P. & Gogarten, J. P. Ancient gene duplications and the root(s) of the tree of life. *Protoplasma* **227**, 53–64 (2005).
- Fournier, G. P. & Gogarten, J. P. Signature of a primitive genetic code in ancient protein lineages. *J. Mol. Evol.* **65**, 425–436 (2007).
- Lanave, C., Preparata, G., Saccone, C. & Serio, G. A new method for calculating evolutionary substitution rates. *J. Mol. Evol.* **20**, 86–93 (1984).
- Williams, P. D., Pollock, D. D., Blackburne, B. P. & Goldstein, R. A. Assessing the accuracy of ancestral protein reconstruction methods. *PLoS Comput. Biol.* **2**, 598–605 (2006).
- Graur, D. & Martin, W. Reading the entrails of chickens: molecular timescales of evolution and the illusion of precision. *Trends Genet.* **20**, 80–86 (2004).
- Robert, F. & Chaussidon, M. A palaeotemperature curve for the Precambrian oceans based on silicon isotopes in cherts. *Nature* **443**, 969–972 (2006).
- Shields, G. A. & Kasting, J. F. Evidence for hot early oceans? *Nature* **447**, E1 (2007).
- Kasting, J. F. & Ono, S. Palaeoclimates: the first two billion years. *Phil. Trans. R. Soc. Lond. B* **361**, 917–929 (2006).
- Gomes, R., Levison, H. F., Tsiganis, K. & Morbidelli, A. Origin of the cataclysmic Late Heavy Bombardment period of the terrestrial planets. *Nature* **435**, 466–469 (2005).
- Rosing, M. T. <sup>13</sup>C-depleted carbon microparticles in >3700-Ma sea-floor sedimentary rocks from West Greenland. *Science* **283**, 674–676 (1999).
- Islas, S., Velasco, A. M., Becerra, A., Delaye, L. & Lazcano, A. Hyperthermophily and the origin and earliest evolution of life. *Int. Microbiol.* **6**, 87–94 (2003).
- Naya, H., Romero, H., Zavala, A., Alvarez, B. & Musto, H. Aerobiosis increases the genomic guanine plus cytosine content (GC%) in prokaryotes. *J. Mol. Evol.* **55**, 260–264 (2002).

**Supplementary Information** is linked to the online version of the paper at [www.nature.com/nature](http://www.nature.com/nature).

**Acknowledgements** This work was supported by Action Concertée Incitative IMPBIO-MODELPHYLO and ANR PlasmExplore. We thank C. Brochier-Armanet and A. Lazcano for help and suggestions, the LIRMM Bioinformatics platform ATGC and the computing facilities of IN2P3.

**Author Contributions** B.B. and S.B. contributed equally to this study, designing and conducting experiments. A.N. performed statistical analyses and retrieved optimal growth temperatures. N.L. and M.G. provided guidance throughout the study, and M.G. gave the original idea. All authors participated in manuscript writing.

**Author Information** Reprints and permissions information is available at [www.nature.com/reprints](http://www.nature.com/reprints). Correspondence and requests for materials should be addressed to M.G. ([mougou@biomserv.univ-lyon1.fr](mailto:mougou@biomserv.univ-lyon1.fr)).



## METHODS

**rRNA data set.** Prokaryotic small (SSU) and large (LSU) subunit rRNAs were retrieved in January 2007 from complete genomes available at the National Center for Biotechnology Information (NCBI). SSU and LSU rRNA sequences from ongoing genome projects or from large genomic fragments of important or poorly represented groups (for example, Archaea or hyperthermophilic bacteria) were added in June 2007. Eukaryotic SSU and LSU rRNA sequences were provided by D. Moreira; 65 slowly evolving sequences were selected from this data set<sup>31</sup>. Sequences were aligned using MUSCLE<sup>32</sup>. Resulting alignments were concatenated and manually improved using the MUST package<sup>33</sup>. Regions of doubtful alignment were removed using the MUST package; 2,239 sites were kept. A distance phylogenetic tree was computed using dnadist (Jukes and Cantor model) and neighbour from the PHYLIP package<sup>34</sup>. The final data set contained 65 eukaryotic, 60 archaeal and 331 bacterial sequences representative of the molecular diversity in each domain. An additional data set of 60 sequences sampling the diversity of the full data set was used in Bayesian analyses. Secondary structure predictions were downloaded from the rRNA database<sup>35</sup>. Sites that were predicted as double-stranded stems in *Saccharomyces cerevisiae*, *Escherichia coli* and *Archaeoglobus fulgidus* were selected to give an alignment of 1,043 sites.

**Protein data set.** Nearly universal protein families with one member per genome were used to avoid ill-defined orthology. Protein families from the HOGENOM database of families of homologous genes (release 03, October 2005, S. Penel and L. Duret, personal communication; <http://pbil.univ-lyon1.fr/databases/hogenom3.html>) that displayed a wide species coverage with no or very low redundancy in all species were selected. Additional sequences from other genomes whose phylogenetic position was interesting were considered. These were downloaded from the Joint Genome Institute (*Desulfuromonas acetoxidans*), The Institute for Genomic Research (*Giardia lamblia*, *Tetrahymena thermophila*, *Trichomonas vaginalis*) or the NCBI (*Kuenenia stuttgartiensis*), and were searched for homologous genes using BLAST<sup>36</sup>; only the best hit was retrieved. The protein families were subsequently aligned using MUSCLE<sup>32</sup> and submitted to phylogenetic analysis using the NJ algorithm<sup>37</sup> with Poisson distances with Phylo\_Win<sup>38</sup>. Proteins from mitochondrial or chloroplastic symbioses and families in which horizontal transfers between Bacteria and Archaea may have occurred were discarded, and so were aminoacyl-tRNA synthetases prone to transfers<sup>39</sup>. In the rare families with two sequences from the same species, the sequence showing the longest terminal branch or whose position was most at odds with the biological classification was discarded. This provided 56 protein families (Supplementary Table 2) for 115 species, which were concatenated using ScaFos<sup>40</sup>. From the 9,218 concatenated sites, 3,336 positions with less than 5% gaps were conserved. The whole data set was used to compute the correspondence analysis and correlations between amino-acid composition and optimal growth temperature. For Bayesian analyses, 30 species among 115 were selected sampling the diversity of cellular life (Supplementary Table 1).

**Multivariate data analyses.** Correspondence analysis<sup>41</sup> was performed on the amino-acid compositions of the protein data set, using the ade4 package<sup>42</sup> of the R environment for statistical computing.

**Phylogenetic tree construction.** An rRNA phylogenetic tree was built from the 456-sequence alignment with both stems and loops with PhyML\_aLRT<sup>43,44</sup> with the GTR model, a gamma law with eight categories and an estimated proportion of invariant sites. The tree for the 60-sequence data set was obtained in the same manner. The phylogenetic trees for the three protein data sets (Supplementary Table 1) were obtained using MrBayes 3.1.1 (ref. 45), using the GTR substitution model and a gamma law with four categories for rates across sites. Chains were run for 1,000,000 generations and samples were collected each 100 generations, a burn-in of 1,000 samples was discarded. The majority rule consensus was computed from the 9,000 remaining samples.

**Identification of fast-evolving rRNA sites.** Posterior probabilities for gamma law rate categories were predicted for each site with PhyML\_aLRT. Site evolutionary rates were obtained by averaging gamma law rate categories weighted by their posterior probabilities. Sites whose evolutionary rate was above the arbitrarily chosen threshold of 2.0 (Supplementary Fig. 2) were discarded, which left 940 sites.

**Estimation of ancestral compositions.** For the maximum likelihood approach, nhPhyML<sup>7</sup> was applied to the rRNA stem sites alignment and the phylogenetic tree described above, and used to estimate all evolutionary parameter values, except tree topology, which was fixed. Site-specific ancestral nucleotide compositions at tree root and at internal node  $j$  descendant of node  $i$  were computed by:

$$p_{\text{root}}(x) = a(x)L_{\text{low}}(x \text{ at root})/L; a(A) = a(T) = (1 - \omega)/2; \\ a(C) = a(G) = \omega/2 \\ p_j(x) = (\sum_y L_{\text{upp}}(y \text{ at node } i) p_{y \rightarrow x} L_{\text{low}}(x \text{ at node } j))/L$$

where  $x$  and  $y$  are in {A, C, G, T},  $L$  is the total tree likelihood at this site,  $L_{\text{low}}$  and  $L_{\text{upp}}$  are site lower and upper conditional likelihoods, respectively<sup>7</sup>,  $\omega$  is the maximum likelihood estimate of root G+C content, and  $p_{y \rightarrow x}$  is the probability of the  $y$  to  $x$  substitution on the  $i$  to  $j$  branch. For Bayesian analyses, nhPhyloBayes<sup>6</sup> was applied to trees described above. Ancestral sequence reconstruction started, for each site, by drawing a state  $x$  at the root:  $x \sim \omega(x)L_{\text{low}}(x \text{ at root})$ , where  $\omega$  was the Markov Chain Monte Carlo<sup>45</sup> (MCMC) estimate of root amino acid or nucleotide frequencies. Then, states  $x$  have been recursively drawn at each node  $j$ :  $x \sim p_{y \rightarrow x}L_{\text{low}}(x \text{ at } j)$ , where  $y$  was the parental node state. Given a realization of the model, this permitted the reconstruction of ancestral sequences at all nodes. Posterior distributions were sampled by 2 (for proteins) or 4 (for rRNA) independent MCMC chains, each with 1,000 to 2,000 realizations. Posterior distributions of sequence compositions combined all realizations of all chains. Protein ancestral compositions were projected on the second axis of the correspondence analysis, and rRNA ancestral compositions were summed up as G+C contents.

**Statistical tests.** In bootstrap analyses, all parameters but topology and branch lengths were estimated under the maximum likelihood criterion for each replicate. In tests of whether the LUCA is less thermophilic than one of its descendants,  $P$  values were the fraction of cases where the temperature estimate for LUCA in a bootstrap replicate or in an iteration of an MCMC chain was above the estimate obtained for its descendant.

- Moreira, D. *et al.* Global eukaryote phylogeny: Combined small- and large-subunit ribosomal DNA trees support monophyly of Rhizaria, Retaria and Excavata. *Mol. Phylogenet. Evol.* **44**, 255–266 (2007).
- Edgar, R. C. MUSCLE: a multiple sequence alignment method with reduced time and space complexity. *BMC Bioinformatics* **5**, 113 (2004).
- Philippe, H. MUST, a computer package of management utilities for sequences and trees. *Nucleic Acids Res.* **21**, 5264–5272 (1993).
- Felsenstein, J. PHYLIP (Phylogeny Inference Package) version 3.6. (Department of Genome Sciences, 2005).
- Wuyts, J., Perrière, G. & Van De Peer, Y. The European ribosomal RNA database. *Nucleic Acids Res.* **32**, D101–D103 (2004).
- Altschul, S. F. *et al.* Gapped BLAST and PSI-BLAST: a new generation of protein database search programs. *Nucleic Acids Res.* **25**, 3389–3402 (1997).
- Saitou, N. & Nei, M. The neighbor-joining method: a new method for reconstructing phylogenetic trees. *Mol. Biol. Evol.* **4**, 406–425 (1987).
- Galtier, N., Gouy, M. & Gautier, C. SEAVIEW and PHYLO-WIN: two graphic tools for sequence alignment and molecular phylogeny. *Comput. Appl. Biosci.* **12**, 543–548 (1996).
- Wolf, Y. I., Aravind, L., Grishin, N. V. & Koonin, E. V. Evolution of aminoacyl-tRNA synthetases—analysis of unique domain architectures and phylogenetic trees reveals a complex history of horizontal gene transfer events. *Genome Res.* **9**, 689–710 (1999).
- Roure, B., Rodriguez-Ezpeleta, N. & Philippe, H. SCAFoS: a tool for selection, concatenation and fusion of sequences for phylogenomics. *BMC Evol. Biol.* **7** (Suppl 1), S2 (2007).
- Hill, M. O. Correspondence analysis: a neglected multivariate method. *Appl. Statist.* **23**, 340–354 (1974).
- Chessel, D., Dufour, A. B. & Thioulouse, J. The ade4 package -I- one-table methods. *R. News* **4**, 5–10 (2004).
- Guindon, S. & Gascuel, O. A simple, fast, and accurate algorithm to estimate large phylogenies by maximum likelihood. *Syst. Biol.* **52**, 696–704 (2003).
- Anisimova, M. & Gascuel, O. Approximate likelihood-ratio test for branches: A fast, accurate, and powerful alternative. *Syst. Biol.* **55**, 539–552 (2006).
- Huelsenbeck, J. P. & Ronquist, F. MrBayes: Bayesian inference of phylogenetic trees. *Bioinformatics* **17**, 754–755 (2001).

## LETTERS

# Successful range-expanding plants experience less above-ground and below-ground enemy impact

Tim Engelkes<sup>1</sup>, Elly Morriën<sup>1</sup>, Koen J. F. Verhoeven<sup>1</sup>, T. Martijn Bezemer<sup>1,2</sup>, Arjen Biere<sup>1</sup>, Jeffrey A. Harvey<sup>1</sup>, Lauren M. McIntyre<sup>3</sup>, Wil L. M. Tamis<sup>4</sup> & Wim H. van der Putten<sup>1,2</sup>

Many species are currently moving to higher latitudes and altitudes<sup>1–3</sup>. However, little is known about the factors that influence the future performance of range-expanding species in their new habitats. Here we show that range-expanding plant species from a riverine area were better defended against shoot and root enemies than were related native plant species growing in the same area. We grew fifteen plant species with and without non-coevolved polyphagous locusts and cosmopolitan, polyphagous aphids. Contrary to our expectations, the locusts performed more poorly on the range-expanding plant species than on the congeneric native plant species, whereas the aphids showed no difference. The shoot herbivores reduced the biomass of the native plants more than they did that of the congeneric range expanders. Also, the range-expanding plants developed fewer pathogenic effects<sup>4,5</sup> in their root-zone soil than did the related native species. Current predictions forecast biodiversity loss due to limitations in the ability of species to adjust to climate warming conditions in their range<sup>6–8</sup>. Our results strongly suggest that the plants that shift ranges towards higher latitudes and altitudes may include potential invaders, as the successful range expanders may experience less control by above-ground or below-ground enemies than the natives.

Range expansion is a key adaptive feature of species in response to changes in climate, habitat availability and other limiting factors<sup>1,2,6–10</sup>. Currently, a number of species are showing rapid range expansion from warmer into previously colder biomes<sup>11</sup>. As not all species have the same range shift capacity, ecological interactions may become disrupted as the community species pool changes<sup>9</sup>. Rapid range expansion and the loss of control by natural enemies are key features of invasive species<sup>12,13</sup>. However, very few studies have actually investigated range expansion in relation to enemy exposure<sup>5,14</sup>. The aim of our study was to examine how rapidly range-expanding plant species are defended against above-ground and below-ground natural enemies in comparison with related plant species that are native to the expansion zone.

Plants are usually attacked by a wide variety of above-ground and below-ground natural enemies<sup>15</sup>. It is well established that invasive exotic plants are less exposed to above-ground and below-ground control by natural enemies than are related natives in the new range<sup>4,16–20</sup>. However, phylogenetically controlled empirical evidence of exotic plant control by natural enemies is scarce<sup>5,21</sup>. Here we compare range-expanding invasive plants of intercontinental origin and intracontinental range-expanding species with congeneric native plant species, all co-occurring in a riverine area. Above ground, we exposed range-expanding exotic plants of inter- and intracontinental origin and congeneric native species to non-coevolved naive polyphagous herbivores, as well as to cosmopolitan polyphagous herbivores. In

the same experiment, we exposed all plants to a general soil community from the invaded range and compared their plant–soil feedback responses<sup>22</sup>. We tested the hypothesis that the plants would not differ in their response to the polyphagous shoot herbivores, as all plants had equal familiarity with them, but that both the inter- and intracontinental range-expanding species would develop soil feedback that is less negative than that of the related natives.

Contrary to our hypothesis, above-ground herbivory influenced plant biomass of range-expanding species differently than it did the native species (plant origin  $\times$  herbivory interaction:  $F_{1,108} = 4.58$ ,  $P = 0.035$ ; Fig. 1a). Herbivores caused significant biomass loss to native plants (the species mean proportional biomass reduction was  $-38.7\%$  and differed from zero:  $t = -2.98$ , d.f. = 8,  $P = 0.017$ ), whereas the effect of herbivory on the range-expanding species was much smaller and not significantly different from zero (effect size was  $-17.3\%$ :  $t = -1.69$ , d.f. = 5,  $P = 0.151$ ; Fig. 2a).

Although the range-expanding species overall had more shoot biomass than the native species ( $P = 0.001$ ), locust survival was significantly lower on the range-expanding species than on the native species ( $F_{2,52} = 9.57$ ,  $P = 0.0003$ ; Fig. 3a). Aphid numbers, on the other hand, were not significantly affected by host plant origin ( $\chi^2 = 4.09$ , d.f. = 2,  $P = 0.129$ ; Fig. 3b). The negative effect of the range-expanding plants on the locusts could not be explained by two general indicators of food quality, namely the carbon/nitrogen ratio (origin effect:  $F_{1,99} = 0.19$ ,  $P = 0.662$ ; origin  $\times$  herbivory interaction:  $F_{1,99} = 1.69$ ,  $P = 0.197$ ) and the nitrogen content of the foliage (origin effect:  $F_{1,101} = 2.65$ ,  $P = 0.107$ ; origin  $\times$  herbivory interaction:  $F_{1,101} = 0.28$ ,  $P = 0.597$ ). We note that the levels of phenolic compounds in the foliage were higher in range-expanding plants with herbivory than in range-expanding plants without herbivory and in the native plants with and without herbivory (interaction effect:  $F_{1,103} = 13.07$ ,  $P = 0.0005$ ; Supplementary Fig. 1). This indicates that range-expanding plants were better than natives in inducing general defences against non-coevolved shoot herbivores. The intercontinental range expanders were slightly less negatively affected by herbivory than were the intracontinental range expanders (range expander origin  $\times$  herbivory interaction:  $F_{1,44} = 4.25$ ,  $P = 0.045$ ; Supplementary Fig. 2a). Nevertheless, the three intracontinental range expanders suffered significantly less from shoot herbivory than did their congeneric natives (origin  $\times$  herbivory interaction:  $F_{1,52} = 6.45$ ,  $P = 0.014$ ). *Bidens* was the only genus to show contrasting effects between native species within a genus (Supplementary Fig. 3a).

Native plant species also suffered more from below-ground biotic interactions in own soil, in comparison with control soil, than did range-expanding plants (plant origin  $\times$  soil interaction:  $F_{1,112} = 4.16$ ,  $P = 0.043$ ; Fig. 1b). The native species experienced significantly

<sup>1</sup>Department of Multitrophic Interactions, Netherlands Institute of Ecology (NIOO-KNAW), PO Box 40, 6666 ZG Heteren, The Netherlands. <sup>2</sup>Laboratory of Nematology, Wageningen University and Research Centre, PO Box 8123, 6700 ES Wageningen, The Netherlands. <sup>3</sup>Departments of Molecular Genetics and Microbiology and Statistics, University of Florida, Gainesville, Florida 32610-1399, USA. <sup>4</sup>Nationaal Herbarium Nederland, Leiden University Branch, PO Box 9514, 2300 RA Leiden, The Netherlands.

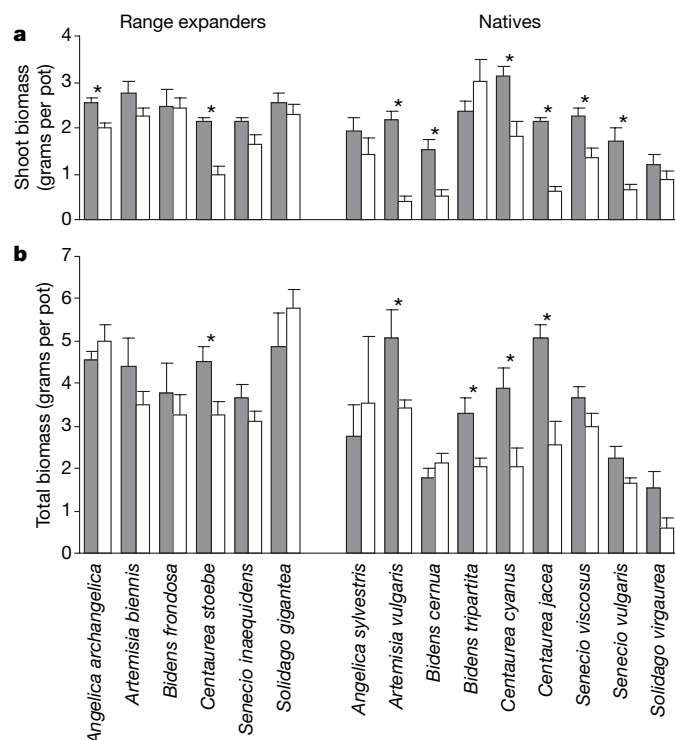


**Figure 1 | Effects of shoot herbivores and soil feedback on plant biomass.**

**a**, Shoot biomass (mean dry weight  $\pm$  s.e.m.) of range-expanding exotic and congeneric native plants without herbivory (grey bars) and plants exposed to above-ground herbivory by the African desert locust, *Schistocerca gregaria*, and the green peach aphid, *Myzus persicae* (white bars), show that most plants experienced a significant biomass loss during three weeks of exposure, but that biomass loss due to herbivory was severest on native plants. **b**, Total biomass (mean dry mass  $\pm$  s.e.m.) in 'control' soil (grey bars) and 'own' soil (white bars) (see Methods) shows that natives are reduced more than range-expanding exotic species in own soil in comparison with control soil. Bars show back-transformed means of log-transformed data. In both panels, an asterisk above a pair of bars indicates statistically significant effects of treatment within plant species ( $t$ -test,  $P < 0.05$ ).

negative soil feedback ( $-12.8\%$ ; difference from zero:  $t = -2.52$ , d.f. = 8,  $P = 0.036$ ), whereas that of the range expanders was much smaller and not different from a neutral effect ( $-3.7\%$ ; difference from zero:  $t = -0.96$ , d.f. = 5,  $P = 0.381$ ; Fig. 2b). The performance in own soil versus control soil did not differ between the intra- and intercontinental range expanders (range expander origin, soil and origin  $\times$  soil interaction: respectively  $F_{1,46} = 0.41$ ,  $P = 0.526$ ;  $F_{1,46} = 2.39$ ,  $P = 0.129$ ;  $F_{1,46} = 0.84$ ,  $P = 0.363$ ; Supplementary Fig. 2b). As observed for above-ground herbivores, a contrasting effect between native species within genus was observed for *Bidens* only (Supplementary Fig. 3b).

Across the herbivory and soil feedback treatments, in 14 out of 18 within-genus comparisons the biomass reduction of the natives was stronger than that of the range expanders (non-parametric sign test:  $M = -5$ ,  $P = 0.031$ ; see Supplementary Information). However, above- and below-ground biotic interactions did not vary in concert with each other; the Spearman's rank-order correlations of the shoot herbivore and soil feedback effects on species within sets of native and range-expanding plant species were not significant ( $P = 0.865$  and  $P = 0.329$ , respectively; see Supplementary Information). We conclude that range-expanding plants were less sensitive to shoot herbivory and negative soil feedback than were natives; however, the rank order in which plants were affected by shoot herbivory differed from the rank order in which they were affected by negative soil feedback.

Our results provide new evidence that plants which are successful in range expansion towards higher latitudes interact differently with

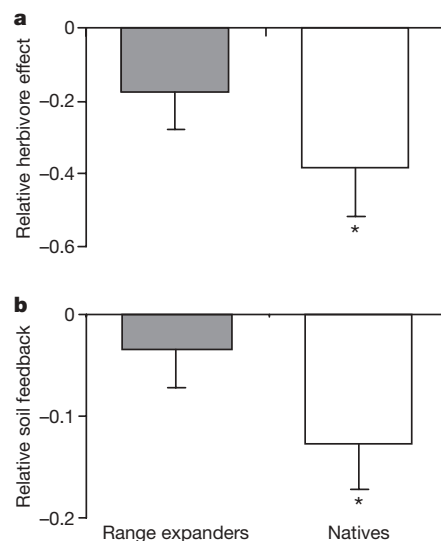


**Figure 2 | Relative change in plant biomass due to shoot herbivores and soil feedback.** **a**, Relative shoot biomass effects of above-ground herbivory by the locust *S. gregaria* and the aphid *M. persicae*, calculated as (shoot biomass with herbivores – shoot biomass without herbivores)/(shoot biomass without herbivores)  $\pm$  s.e.m., on range-expanding exotic plants (grey bars;  $n = 6$  species averages) and related native plants (white bars;  $n = 9$  species averages) using plant species as replicates. **b**, The feedback effect of the soil community, calculated as (total biomass own soil – total biomass control soil)/(total biomass control soil)  $\pm$  s.e.m., based on back-transformed means of log-transformed data using species as replicates. Bar codes are the same as in **a** (see above). Native species on average experienced significant shoot biomass reduction by shoot herbivory and significant negative soil feedback ( $*P < 0.05$ ), whereas exotic range expanding plants did not differ from a neutral response in either case ( $P > 0.05$ ).

shoot herbivores than do congeneric plant species that are native to the invaded range. Although all plant species were equally new to the desert locust, the locusts experienced reduced survival on the successful range expanders, but not on the related native plants. On the other hand, the cosmopolitan aphid was not influenced differentially by plant origin. Our hypothesis predicted no differences; however, the shoot herbivores reduced the biomass of the range-expanding plants less than they did that of the related native plant species. In comparison with the range expanders, the negative soil feedback of the native plants was more in line with our hypothesis. Thus far, studies of enemy exposure to exotic invasive weeds have usually focused either on enemies from the invaded range or on invasive enemies<sup>23</sup>. Our results suggest that the plant species successfully expanding their range towards higher latitudinal riparian areas possess superior defence traits in comparison with related native species. In this respect, these successful range expanders have similarities with invasive exotic plants<sup>21</sup>, which also are superior in short-term resource acquisition<sup>24</sup>, although there was no correlation between the strengths of above- and below-ground enemy effects.

Thus far, most attention has focused on the uncoupling of food-chain interactions due to regional climate warming<sup>14,25,26</sup>. Here we show that some successful range-expanding riparian plant species<sup>11</sup> experience less above-ground and below-ground enemy impacts, even when exposed to non-coevolved and cosmopolitan polyphagous above-ground herbivores. Thus, the successful range expanders differed in defence trait characteristics from the congeneric natives. We focused our sampling strategy on plants successfully expanding their range into northern riparian habitats. Future studies should also explore other habitats, as well as less successful range expanders, to test whether, for example, trees and dry land plant species show similar responses. Poor range shift capacity has been predicted to result in a loss of diversity<sup>6,7</sup>. However, the prediction of consequences of climate warming and other changes that result in range expansion require inputs from different fields in ecology<sup>27</sup>. Our



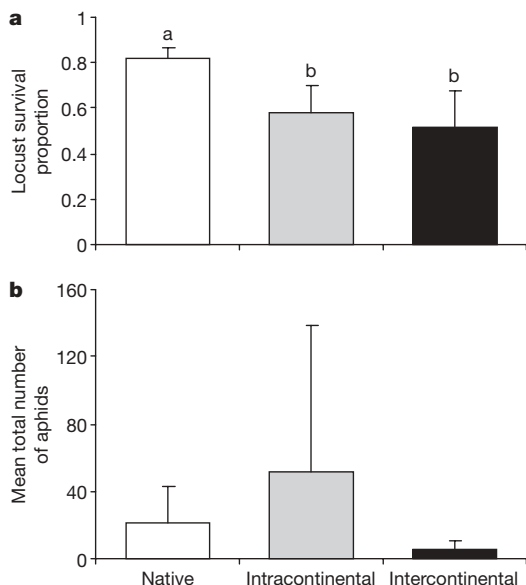


**Figure 3 | Performance of herbivores on native and non-native plants.** **a**, The survival proportion of the naive generalist herbivore *S. gregaria*, which did not have any previous experience with any of the plant species used, on native plants (white bars;  $n = 9$  plant species), intracontinental range expanders (grey bars;  $n = 3$ ) and intercontinental range expanders (black bars;  $n = 3$ ). The survival proportion was calculated as back-transformed means  $\pm$  s.e.m. from arcsine data on numbers recaptured divided by numbers added. The locust survival proportion was on average lower on range expanders from both origins than it was on native host plant species. Different letters above the bars indicate significant differences between bars ( $P < 0.05$ ). **b**, Mean total numbers (per pot)  $\pm$  s.d. of the generalist aphid *M. persicae* after a three-week feeding assay demonstrate that the average population increase did not significantly differ between plant origins ( $P > 0.05$ ) (bar colours as in **a**).

results suggest that successful range-expanding plant species may include species with invasive properties, which is crucial information for the future conservation of biodiversity in temperate and northern latitudes.

## METHODS SUMMARY

We analysed floristic data to identify exotic plant species in riparian areas in the Netherlands, which all have become well established in the twentieth century. We surveyed plants with a strong increase in abundance over the past few decades and congeneric relatives in the same habitat. We obtained seedlings of three intracontinental range expanders, three species that originated from other continents and became naturalized in southern Europe before their northward range expansion, and nine natives (Supplementary Table 1). Three extra native plant species were included to test the sensitivity of our phylogenetic comparison for species-specific effects.

Soil samples were collected from Millingerwaard (an area along the Waal River in the Netherlands), inoculated into sterilized sandy loam soil, placed in four-litre pots and planted with four individuals of one species per pot. After eight weeks in a greenhouse, the plants were harvested and the soils were used for a second growth experiment in order to measure plant–soil feedback effects<sup>22,28</sup>. In this second stage, each plant species was grown in own soil (previously containing individuals of the same species) and control soil (a mixture of soil from all other plant species, excluding species from the same genus). After seven weeks, we placed all pots individually in cages and added above-ground herbivores to half the control-soil pots that had been assigned to the herbivory treatment at the start of the experiment ( $n = 5$ ). We used five-day-old, first-instar locust nymphs of the African desert locust, *Schistocerca gregaria*, which is highly polyphagous throughout all stages of its development and is non-coevolved with any of the tested plant species. We also used the green peach aphid, *Myzus persicae* (Hemiptera: Aphididae), a highly polyphagous herbivore that has a cosmopolitan distribution. Three weeks after adding the herbivores, all plants were harvested, dried, weighed and analysed.

Received 7 December 2007; accepted 25 September 2008.

Published online 19 November 2008.

- Walther, G. R. *et al.* Ecological responses to recent climate change. *Nature* **416**, 389–395 (2002).
- Parmesan, C. & Yohe, G. A globally coherent fingerprint of climate change impacts across natural systems. *Nature* **421**, 37–42 (2003).
- Pearson, R. G. & Dawson, T. P. Predicting the impacts of climate change on the distribution of species: are bioclimate envelope models useful? *Glob. Ecol. Biogeogr.* **12**, 361–371 (2003).
- Klironomos, J. N. Feedback with soil biota contributes to plant rarity and invasiveness in communities. *Nature* **417**, 67–70 (2002).
- Van Grunsven, R. H. A. *et al.* Reduced plant–soil feedback of plant species expanding their range as compared to natives. *J. Ecol.* **95**, 1050–1057 (2007).
- Warren, M. S. *et al.* Rapid responses of British butterflies to opposing forces of climate and habitat change. *Nature* **414**, 65–69 (2001).
- Thomas, C. D. *et al.* Extinction risk from climate change. *Nature* **427**, 145–148 (2004).
- Thomas, J. A. *et al.* Comparative losses of British butterflies, birds, and plants and the global extinction crisis. *Science* **303**, 1879–1881 (2004).
- Lovejoy, T. E. & Hannah, L. *Climate Change and Biodiversity*. (Yale Univ. Press, 2005).
- Brinkhuis, H. *et al.* Episodic fresh surface waters in the Eocene Arctic Ocean. *Nature* **441**, 606–609 (2006).
- Tamis, W. L. M. *et al.* Changes in vascular plant biodiversity in the Netherlands in the 20th century explained by their climatic and other environmental characteristics. *Clim. Change* **72**, 37–56 (2005).
- Levine, J. M. *et al.* Plant–soil feedbacks and invasive spread. *Ecol. Lett.* **9**, 1005–1014 (2006).
- Keane, R. M. & Crawley, M. J. Exotic plant invasions and the enemy release hypothesis. *Trends Ecol. Evol.* **17**, 164–170 (2002).
- Menendez, R. *et al.* Escape from natural enemies during climate-driven range expansion: a case study. *Ecol. Entomol.* **33**, 413–421 (2008).
- van der Putten, W. H. *et al.* Linking above- and belowground multitrophic interactions of plants, herbivores, pathogens, and their antagonists. *Trends Ecol. Evol.* **16**, 547–554 (2001).
- Maron, J. L. & Vila, M. When do herbivores affect plant invasion? Evidence for the natural enemies and biotic resistance hypotheses. *Oikos* **95**, 361–373 (2001).
- Callaway, R. M. *et al.* Soil biota and exotic plant invasion. *Nature* **427**, 731–733 (2004).
- Reinhart, K. O. *et al.* Plant–soil biota interactions and spatial distribution of black cherry in its native and invasive ranges. *Ecol. Lett.* **6**, 1046–1050 (2003).
- Mitchell, C. E. & Power, A. G. Release of invasive plants from fungal and viral pathogens. *Nature* **421**, 625–627 (2003).
- van der Putten, W. H. *et al.* Invasive plants and their escape from root herbivory: a worldwide comparison of the root-feeding nematode communities of the dune grass *Ammophila arenaria* in natural and introduced ranges. *Biol. Invasions* **7**, 733–746 (2005).
- Agrawal, A. A. *et al.* Enemy release? An experiment with congeneric plant pairs and diverse above- and belowground enemies. *Ecology* **86**, 2979–2989 (2005).
- Bever, J. D., Westover, K. M. & Antonovics, J. Incorporating the soil community into plant population dynamics: the utility of the feedback approach. *J. Ecol.* **85**, 561–573 (1997).
- Parker, J. D., Burkepile, D. E. & Hay, M. E. Opposing effects of native and exotic herbivores on plant invasions. *Science* **311**, 1459–1461 (2006).
- Funk, J. L. & Vitousek, P. M. Resource-use efficiency and plant invasion in low-resource systems. *Nature* **446**, 1079–1081 (2007).
- Davis, A. J. *et al.* Making mistakes when predicting shifts in species range in response to global warming. *Nature* **391**, 783–786 (1998).
- Both, C. & Visser, M. E. Adjustment to climate change is constrained by arrival date in a long-distance migrant bird. *Nature* **411**, 296–298 (2001).
- Guisan, A. & Thuiller, W. Predicting species distribution: offering more than simple habitat models. *Ecol. Lett.* **8**, 993–1009 (2005).
- van der Putten, W. H. *et al.* Soil feedback of exotic savanna grass relates to pathogen absence and mycorrhizal selectivity. *Ecology* **88**, 978–988 (2007).

**Supplementary Information** is linked to the online version of the paper at [www.nature.com/nature](http://www.nature.com/nature).

**Acknowledgements** We thank Staatsbosbeheer Regio Oost for giving us permission to work in Millingerwaard; B. Odé, K. Groen, R. van Grunsven, P. Brinkman and the late R. van der Meijden for discussions; M. Houtekamer for carbon and nitrogen determination; T. Vos, M. Vlag, A. Weerheijm and W. Smart for assistance; L. Koopman for providing the locusts; and L. Young and E. J. Bakker for advice on statistics. This study was funded by an ALW-VICI grant to W.H.v.d.P.

**Author Contributions** T.E., E.M., T.M.B., J.A.H. and W.H.v.d.P. designed and analysed the experiment and wrote the manuscript; T.E. and E.M. performed the experiment; W.L.M.T. analysed the long-term floristic dataset and provided the data for selecting plant species; and K.J.F.V., L.M.Mcl. and A.B. carried out the data analysis and were involved in the writing.

**Author Information** Reprints and permissions information is available at [www.nature.com/reprints](http://www.nature.com/reprints). Correspondence and requests for materials should be addressed to W.H.v.d.P. ([w.vanderputten@nioo.knaw.nl](mailto:w.vanderputten@nioo.knaw.nl)).

# Low conservation of gene content in the *Drosophila* Y chromosome

Leonardo B. Koerich<sup>1</sup>, Xiaoyun Wang<sup>2</sup>, Andrew G. Clark<sup>2</sup> & Antonio Bernardo Carvalho<sup>1</sup>

Chromosomal organization is sufficiently evolutionarily stable that large syntenic blocks of genes can be recognized even between species as distantly related as mammals and puffer fish (450 million years (Myr) of divergence)<sup>1–7</sup>. In Diptera, the gene content of the X chromosome and the autosomes is well conserved: in *Drosophila* more than 95% of the genes have remained on the same chromosome arm in the 12 sequenced species (63 Myr of divergence, traversing 400 Myr of evolution)<sup>2,4,6</sup>, and the same linkage groups are clearly recognizable in mosquito genomes (260 Myr of divergence)<sup>3,5,7</sup>. Here we investigate the conservation of Y-linked gene content among the 12 sequenced *Drosophila* species. We found that only a quarter of the *Drosophila melanogaster* Y-linked genes (3 out of 12) are Y-linked in all sequenced species, and that most of them (7 out of 12) were acquired less than 63 Myr ago. Hence, whereas the organization of other *Drosophila* chromosomes traces back to the common ancestor with mosquitoes, the gene content of the *D. melanogaster* Y chromosome is much younger. Gene losses are known to have an important role in the evolution of Y chromosomes<sup>8–10</sup>, and we indeed found two such cases. However, the rate of gene gain in the *Drosophila* Y chromosomes investigated is 10.9 times higher than the rate of gene loss (95% confidence interval: 2.3–52.5), indicating a clear tendency of the Y chromosomes to increase in gene content. In contrast with the mammalian Y chromosome, gene gains have a prominent role in the evolution of the *Drosophila* Y chromosome.

Even in sequenced species little is known about the Y chromosomes because their heterochromatic state precludes sequence assembly into large and easily studied scaffolds, but instead short Y-linked scaffolds must be individually identified<sup>11,12</sup>. In most *Drosophila* species the Y chromosome is essential for male fertility<sup>13</sup>, and genetic data have identified between six and ten Y-linked factors required for this function<sup>14,15</sup>. The paucity of genes and its heterochromatic state suggested that, like the mammalian Y chromosome<sup>16</sup>, the *Drosophila* Y chromosome might be largely a degenerated X chromosome. The conservation of the fertility function in rather distant species fits well with the known conservation of the gene content of *Drosophila* chromosomal arms<sup>6,17</sup>. Therefore sex-chromosome evolutionary theory<sup>8,9</sup>, well-known patterns of chromosome evolution in *Drosophila*, and conservation of biological function all suggest that the *Drosophila* Y chromosome ought to be a degenerated X chromosome, with a few remaining and well-conserved genes. However, the 12 genes identified on the *D. melanogaster* Y chromosome were all acquired through gene duplications from the autosomes, rather than being a relic subset of the X-linked genes<sup>18–22</sup>. Furthermore, a Y-chromosome-autosome fusion in the *D. pseudoobscura* lineage made the ancestral Y chromosome into part of an autosome, and a new Y chromosome arose<sup>23</sup>. Both findings suggest that *Drosophila* Y chromosomes are labile and raise the question of how well conserved is their gene content.

The recent sequencing of 10 further *Drosophila* genomes<sup>24</sup> allows a detailed study of this question. We first identified the putative

orthologues of the 12 known *D. melanogaster* Y-linked genes<sup>18–22</sup> in the remaining species (see Methods). Owing to the low coverage of the Y chromosome<sup>11</sup> and its abundance of repetitive sequences, the sequences of almost all Y-linked genes have large gaps and sequencing errors, and different exons of the same gene are scattered in several scaffolds<sup>19,20</sup> (Supplementary Fig. 1). These problems were corrected by direct sequencing of the products from polymerase chain reaction with reverse transcription (RT-PCR) and rapid amplification of complementary DNA ends (RACE) (see Methods) for all genes. We sequenced ~150 kilobases (kb), and the average gene has one-third of its sequence generated *de novo* (Supplementary Table 1). Notably, we could not find the orthologue of the *Pp1-Y1* gene in *D. mojavensis* or the orthologue of *Ppr-Y* in *D. grimshawi*, even among the raw sequencing traces. Synteny analysis strongly suggests that the *Pp1-Y1* loss is real; degenerate PCR with a primer pair that amplifies *Ppr-Y* in a broad range of species confirmed its loss in *D. grimshawi* (Supplementary Discussion).

Molecular evolutionary analysis, revealing a substantial excess of synonymous over nonsynonymous changes in protein-coding genes, strongly indicates that all of these Y-linked genes are functional (Supplementary Table 2). Orthology was confirmed by phylogenetic analysis of all genes (Supplementary Fig. 2). We then tested their Y-linkage by PCR in males and females. Notably, many of the genes are not Y-linked in several species (Supplementary Fig. 3 and Table 1). The results of *D. pseudoobscura* and *D. persimilis* are expected, given the known Y-autosome fusion that occurred in this lineage<sup>23</sup>. The other linkage changes (Table 1) can be caused by individual movements of genes from the Y chromosome to the other chromosomes or vice versa. Movement direction was unambiguously ascertained by synteny analysis even in the *kl-5* gene, with the data indicating two independent transfers to the Y chromosome (Fig. 1 and Supplementary Fig. 4). Using synteny (Supplementary Figs 4–8) and the known phylogenetic relationships among the sequenced species<sup>24</sup>, we could infer the direction and time of the gene movements, as shown in Fig. 2. Intron positions were conserved in all cases, which rules out retrotransposition and suggests a DNA-based mechanism for the gene movements (Supplementary Discussion). Most or all extant genes were acquired individually by the Y chromosome (as opposed to resulting from large segmental duplications), because they are not adjacent to each other at their original autosomal locations (Supplementary Figs 4–8 and Supplementary Table 3).

It is clear from Fig. 2 that the gene content of the *Drosophila* Y chromosome is highly variable: among the 12 known Y-linked genes of *D. melanogaster*, only three (*kl-2*, *kl-3* and *ORY*) are Y-linked in all sequenced species (we ignored the special case of the Y-chromosome-autosome fusion in the *D. pseudoobscura* lineage because the changes that happened there were not caused by individual gene gain and loss). All other genes (75% of the total) moved onto or off the Y chromosome at least once, or were lost. This contrasts sharply with the remainder of the genome, where it was found that 514 genes out of ~13,000 (4% of

<sup>1</sup>Departamento de Genética, Universidade Federal do Rio de Janeiro, Caixa Postal 68011, CEP 21944-970, Rio de Janeiro, Brazil. <sup>2</sup>Department of Molecular Biology and Genetics, Cornell University, Ithaca, New York 14853, USA.

**Table 1 | Y-linkage across the 12 *Drosophila* species**

Gene	<i>mel</i>	<i>sim</i> <i>sec</i>	<i>ere</i> <i>yak</i>	<i>ana</i>	<i>pse</i> <i>per</i> *	<i>wil</i>	<i>moj</i>	<i>vir</i>	<i>gri</i>
<i>kl-2</i>	+	+	+	+	—	+	+	+	+
<i>kl-3</i>	+	+	+	+	—	+	+	+	+
<i>kl-5</i>	+	+	+	+	—	+	+	+	+
<i>ORY</i>	+	+	+	+	—	+	+	+	+
<i>PRY</i>	+	+	+	+	—	+	—	+	+
<i>Ppr-Y</i>	+	+	+	+	—	+	+	+	0
<i>CCY</i>	+	+	+	+	—	+	—	—	—
<i>ARY</i>	+	+	+	+	—	+	—	—	—
<i>WDY</i>	+	+	+	+	—	—	—	—	—
<i>Pp1-Y1</i>	+	+	+	+	—	—	0	—	—
<i>Pp1-Y2</i>	+	+	+	+	—	—	—	—	—
<i>FDY</i> †	+	0	0	0	0	0	0	0	0

Unabridged species names (in the order of appearance) are: *D. melanogaster*, *D. simulans*, *D. sechellia*, *D. erecta*, *D. yakuba*, *D. ananassae*, *D. pseudoobscura*, *D. persimilis*, *D. willistoni*, *D. mojavensis*, *D. virilis* and *D. grimshawi*. +, Y-linked gene; —, autosomal or X-linked gene; 0, gene absent from the genome.

\* As described in ref 23, the Y chromosome became part of an autosome in the *D. pseudoobscura* lineage.

† The *FDY* gene is a functional duplication to the Y chromosome of the autosomal gene *CG11844*, which happened in the *D. melanogaster* lineage after the split from *D. simulans* (ref. 21; A.B.C. and A.G.C., manuscript in preparation).

the total) moved to different chromosome arms in the same set of species<sup>6</sup>, and may suggest that there is increased gene movement to and from the Y chromosome, as has been observed for the X chromosome<sup>25–27</sup>. However, the rate of gene movements in the Y chromosome is smaller than the rate of similarly sized chromosome arms (Supplementary Discussion), and thus increased gene movement does not seem to be the main cause of the low conservation of Y-linked gene content.

The contrast between the Y chromosome and the other chromosomes seems to reflect their different evolutionary histories: whereas in the ancestor of all sequenced species the large chromosome arms had thousands of genes, the Y chromosome had a very low number of genes (we know of five: *kl-2*, *kl-3*, *Ppr-Y*, *PRY* and *ORY*; Fig. 2). This, coupled with a small number of gene movements in both genomic compartments, would produce the present pattern of low conservation in the Y chromosome and high conservation in the other chromosomes. A possible caveat to this conclusion is that we do not know the full gene content of the *Drosophila* Y chromosome<sup>22</sup>. However, the low conservation of linkage we found should hold for the full gene set of the *D. melanogaster* Y chromosome, because the

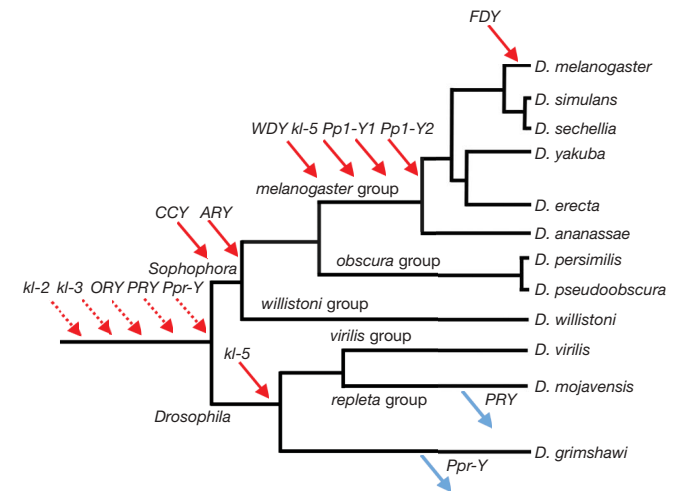


**Figure 2 | Gene movements in the *Drosophila* Y chromosome.** Gene gains (red arrows) and losses (blue arrows) were inferred by synteny. For changes that occurred before the split of the *Drosophila* and *Sophophora* subgenera (genes *kl-2*, *kl-3*, *ORY*, *PRY* and *Ppr-Y*; dashed arrows) there is no close outgroup for inferring the direction (gain versus loss) through synteny. However, all five genes are autosomal or X-linked in *Anopheles*, which suggests that they were acquired by the Y chromosome between 260 (that is, the *Drosophila*–*Anopheles* divergence time<sup>3,5</sup>) and 63 Myr ago.

discovery of the 12 known Y-linked genes did not use any information from the other species (their genomic sequences were not even available at that time). Hence it is safe to conclude that most of the *D. melanogaster* Y-linked genes are recent acquisitions. In contrast, the mammalian Y chromosome mostly contains relic subsets of the X-linked genes, and variation in the Y-linked gene content among species reflects differential loss of these relic genes and some gene acquisitions<sup>28,29</sup>. In *Drosophila* no such relic genes have been found, and variation arises mainly from a continuing process of gene acquisition.

Figure 2 suggests that there are more gene gains than losses in the Y chromosome lineages examined, but these inferences were drawn using genes ascertained in *D. melanogaster*, opening a concern about bias. For example, *D. virilis* probably harbours Y-linked genes that were either acquired after its ancestor split from the *D. melanogaster* lineage, or were lost in the *D. melanogaster* lineage, and such genes would not be detected in the present study. Indeed, direct search in the *D. virilis* genome identified at least two Y-linked genes not shared with *D. melanogaster* (A.B.C. and A.G.C., unpublished data). Given the ascertainment issue, only the rate of gene gain can be estimated in the *D. melanogaster* lineage branches of the phylogeny, and only the rate of gene loss can be estimated in the other branches (Supplementary Fig. 9). This procedure produces an estimate of the raw rate of gene gain by the Y chromosome of 0.1113 genes per Myr (7 gains in 63 Myr), whereas the raw rate of gene loss is 0.0073 genes per Myr (2 losses in 275 Myr). After correcting for an ascertainment bias in the loss rate (Supplementary Methods), and under the assumption that the rates of gene gain and gene loss are homogeneous across the lineages, we found that the rate of gene gain is 10.9 times higher than the rate of gene loss ( $P = 0.003$  under the null hypothesis of equal gain and loss rates), which strongly suggests that the gene content of the Y chromosome has indeed increased.

To explore more fully the consequences of the ascertainment bias of gene content, we performed simulations of gene gain and loss using the observed phylogeny and branch lengths, and made inferences of gene loss conditional on observing the same genes in *D. melanogaster* (identical to the true ascertainment). Approximate Bayesian estimates of the posterior densities of the rates of gene gain and loss were obtained by a rejection-sampling procedure for 1,000 runs (Supplementary Methods). All 1,000 runs had a gene gain rate exceeding the gene loss rate across the phylogeny (Fig. 3 and Supplementary

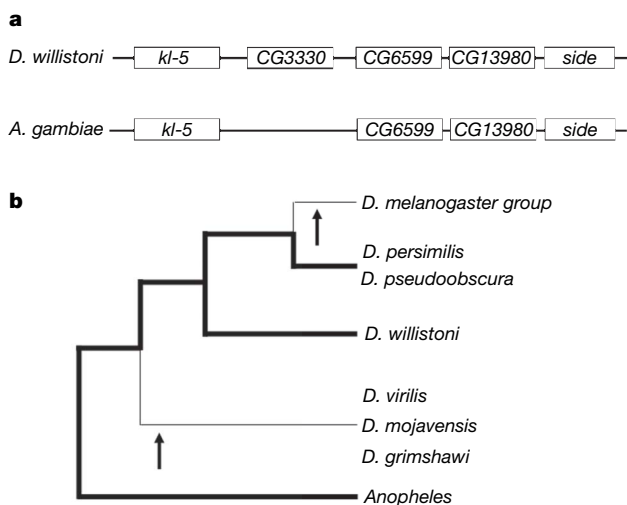


**Figure 1 | Synteny analysis of the *kl-5* gene.** **a**, **b**, The gene is Y-linked in all examined *Drosophila* species except *D. willistoni* (and in *D. pseudoobscura* or *D. persimilis*), which might suggest a Y-chromosome-to-autosome transfer in the *D. willistoni* lineage. However, the conserved synteny between *D. willistoni* and *Anopheles gambiae* (**a**) shows that the autosomal *D. willistoni* location is ancestral (thick lines in **b**). Hence, there were two independent transfers of *kl-5* to the Y chromosome (arrows in **b**). Note that the *Drosophila* *CG3330* gene has no orthologue in *Anopheles*. See Supplementary Fig. 4 for the remaining species.



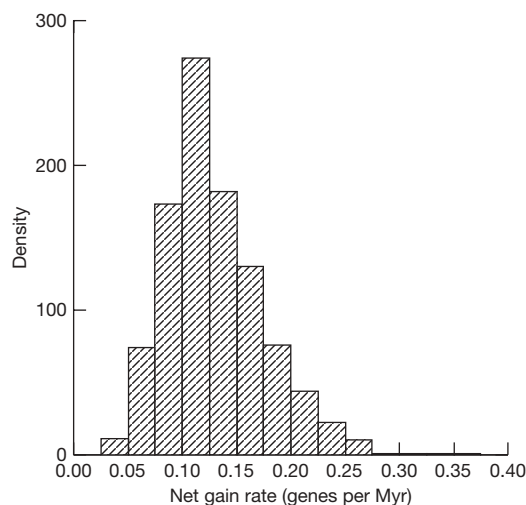


**Figure 3 | Posterior density of the net rate of Y-linked gene gain in the *Drosophila* phylogeny.** A Bayesian rejection sampling procedure was applied (see text) to yield 1,000 estimates of the rates of gene gain and loss conditional on the observed gains and losses of genes on the Y chromosome, and conditional on the genes being observed in *D. melanogaster* (matching the actual ascertainment of Y genes used in this study). The average net gain rate (gain rate minus loss rate) is 0.130 genes per Myr, and all 1,000 simulations had a higher rate of gene gain than loss (range of net gain rate: 0.035 to 0.352).

Fig. 11). Thus both the simulations and the analytical result provide strong evidence that the Y chromosome lineages examined have experienced a net gain in gene number. The origin of the *Drosophila* Y chromosome remains a controversial issue<sup>9,23</sup>; if one assumes that it arose from the degeneration of the X chromosome, then only more recently had gene gains become important after all of its ancestral genes (shared with the X chromosome) had been lost.

Given the restrictive characteristics of the Y chromosome (for example, its heterochromatic state) it is puzzling that genes moved there. Several hypotheses, ranging from neutrality to positive selection, could explain this but our data do not allow definitive support for one model (Supplementary Discussion). The Y-linked gene *Suppressor of Stellate*, which is a recent acquisition in the *D. melanogaster* lineage, may be a case of positive selection<sup>30</sup> (we excluded it because it is multi-copy and RNA-encoding). Whatever its cause, the finding that the Y chromosome has gained genes has interesting consequences. A chromosome that on average has gained genes and yet has few of them must be relatively young. Further Diptera genome sequences may shed light on this issue. But the data in hand already strongly support the conclusion that the gene content of the *Drosophila* Y chromosome is younger than the other chromosomes, and that gene acquisitions have had a prominent role in its evolution.

## METHODS SUMMARY

**Genomic sequences.** We used the WGS3 assembly of *D. melanogaster* (accession AABU000000000), the TIGR assembly of *D. pseudoobscura* (accession AAFS010000000) and the CAF1 assemblies for all other species (available at <http://rana.lbl.gov/drosophila/caf1.html>). Full details of the strains used, sequencing and assembly strategies are described in ref. 24.

**Search of orthologues of *D. melanogaster* Y-linked genes.** We searched for these genes with TblastN<sup>20</sup>, using as queries the protein sequences of the *D. melanogaster* Y-linked genes<sup>18–22</sup> and as databases the genomes of the remaining species. Orthology was confirmed by phylogenetic analysis (Supplementary Fig. 2). Supplementary Table 1 shows the accession numbers of the finished CDS sequences.

**Molecular biology methods.** DNA and RNA were extracted from the same strains used for the genome sequencing<sup>24</sup>. RNA and DNA extractions, PCR and RT-PCR were performed using standard protocols<sup>19,20</sup>. 3' RACE and 5' RACE were performed with the Invitrogen Gene Racer Kit following the instructions of the manufacturer, using testis or whole body total RNA (in the case of *D. grimshawi*) as templates. DNA sequencing was done at Macrogen (Korea) and the Cornell DNA sequencing core facility.

Received 12 June 2008; accepted 26 September 2008.

Published online 16 November 2008.

1. Aparicio, S. et al. Whole-genome shotgun assembly and analysis of the genome of *Fugu rubripes*. *Science* **297**, 1301–1310 (2002).
2. Beverley, S. M. & Wilson, A. C. Molecular evolution in *Drosophila* and the higher diptera II. A time scale for fly evolution. *J. Mol. Evol.* **21**, 1–13 (1984).
3. Zdobnov, E. M. et al. Comparative genome and proteome analysis of *Anopheles gambiae* and *Drosophila melanogaster*. *Science* **298**, 149–159 (2002).
4. Tamura, K., Subramanian, S. & Kumar, S. Temporal patterns of fruit fly (*Drosophila*) evolution revealed by mutation clocks. *Mol. Biol. Evol.* **21**, 36–44 (2004).
5. Yeates, D. K. & Wiegmann, B. M. *The Evolutionary Biology of Flies* 35 (Columbia Univ. Press, 2005).
6. Bhutkar, A., Russo, S. M., Smith, T. F. & Gelbart, W. M. Genome-scale analysis of positionally relocated genes. *Genome Res.* **17**, 1880–1887 (2007).
7. Nene, V. et al. Genome sequence of *Aedes aegypti*, a major arbovirus vector. *Science* **316**, 1718–1723 (2007).
8. Rice, W. R. Evolution of the Y sex chromosome in animals. *Bioscience* **46**, 331–343 (1996).
9. Charlesworth, B. & Charlesworth, D. The degeneration of Y chromosomes. *Phil. Trans. R. Soc. Lond. B* **355**, 1563–1572 (2000).
10. Bachtrog, D., Hom, E., Wong, K. M., Maside, X. & de Jong, P. Genomic degradation of a young Y chromosome in *Drosophila miranda*. *Genome Biol.* **9**, R30 (2008).
11. Carvalho, A. B. et al. Y chromosome and other heterochromatic sequences of the *Drosophila melanogaster* genome: how far can we go? *Genetica* **117**, 227–237 (2003).
12. Hoskins, R. A. et al. Sequence finishing and mapping of *Drosophila melanogaster* heterochromatin. *Science* **316**, 1625–1628 (2007).
13. Ashburner, M., Golic, K. G. & Hawley, R. S. *Drosophila: a Laboratory Handbook* 2nd edn 607–639 (Cold Spring Harbour Laboratory Press, 2005).
14. Kennison, J. A. The genetic and cytological organization of the Y chromosome of *Drosophila melanogaster*. *Genetics* **98**, 529–548 (1981).
15. Hackstein, J. H. & Hochstenbach, R. The elusive fertility genes of *Drosophila*: the ultimate haven for selfish genetic elements. *Trends Genet.* **11**, 195–200 (1995).
16. Skaletsky, H. et al. The male-specific region of the human Y chromosome is a mosaic of discrete sequence classes. *Nature* **423**, 825–837 (2003).
17. Sturtevant, A. H. & Novitski, E. The homologies of the chromosome elements in the genus *Drosophila*. *Genetics* **26**, 517–541 (1941).
18. Gepner, J. & Hays, T. S. A fertility region on the Y chromosome of *Drosophila melanogaster* encodes a dynein microtubule motor. *Proc. Natl Acad. Sci. USA* **90**, 11132–11136 (1993).
19. Carvalho, A. B., Lazzaro, B. P. & Clark, A. G. Y chromosomal fertility factors *kl-2* and *kl-3* of *Drosophila melanogaster* encode dynein heavy chain polypeptides. *Proc. Natl Acad. Sci. USA* **97**, 13239–13244 (2000).
20. Carvalho, A. B., Dobo, B. A., Vibrationovski, M. D. & Clark, A. G. Identification of five new genes on the Y chromosome of *Drosophila melanogaster*. *Proc. Natl Acad. Sci. USA* **98**, 13225–13230 (2001).
21. Carvalho, A. B. & Clark, A. G. Birth of a new gene on the *Drosophila* Y chromosome. *The 44th Annual Drosophila Research Conference, Philadelphia, USA*. Abstract 318C, page 113 (The Genetics Society of America, 2003).
22. Vibrationovski, M. D., Koerich, L. B. & Carvalho, A. B. Two new Y-linked genes in *Drosophila melanogaster*. *Genetics* **179**, 2325–2327 (2008).
23. Carvalho, A. B. & Clark, A. G. Y chromosome of *D. pseudoobscura* is not homologous to the ancestral *Drosophila* Y. *Science* **307**, 108–110 (2005).
24. *Drosophila* 12 Genomes Consortium. Evolution of genes and genomes on the *Drosophila* phylogeny. *Nature* **450**, 203–218 (2007).
25. Betran, E., Thornton, K. & Long, M. Retroposed new genes out of the X in *Drosophila*. *Genome Res.* **12**, 1854–1859 (2002).
26. Emerson, J. J., Kaessmann, H., Betran, E. & Long, M. Extensive gene traffic on the mammalian X chromosome. *Science* **303**, 537–540 (2004).
27. Sturgill, D., Zhang, Y., Parisi, M. & Oliver, B. Demasculinization of X chromosomes in the *Drosophila* genus. *Nature* **450**, 238–241 (2007).
28. Graves, J. A. Sex chromosome specialization and degeneration in mammals. *Cell* **124**, 901–914 (2006).
29. Murphy, W. J. et al. Novel gene acquisition on carnivore Y chromosomes. *PLoS Genet.* **2**, e43 (2006).
30. Hurst, L. D. Is *Stellate* a relict meiotic driver? *Genetics* **130**, 229–230 (1992).

**Supplementary Information** is linked to the online version of the paper at [www.nature.com/nature](http://www.nature.com/nature).

**Acknowledgements** We thank S. Kumar, P. O'Grady, T. Markow, A. J. Bhutkar, S. C. Vaz, E. Betran, A. A. Peixoto, P. H. Krieger and P. Paiva for comments on the manuscript and/or for sharing their unpublished results. We also thank T. Pinhão, A. Bastos and F. Krsticevic for help with the experiments, K. Krishnamoorthy for statistical advice and M. Fetchko for help with GenBank submission. This work was supported by Conselho Nacional de Desenvolvimento Científico e Tecnológico-CNPq, Coordenação de Aperfeiçoamento de Pessoal de Ensino Superior-CAPES, FAPERJ, FIC-NIH grant TW007604-02 (A.B.C.) and NIH grant GM64590 (A.G.C.).

**Author Information** Nucleotide sequence accession numbers are listed in the Supplementary Information. Reprints and permissions information is available at [www.nature.com/reprints](http://www.nature.com/reprints). Correspondence and requests for materials should be addressed to A.B.C. ([bernardo@biologia.ufrj.br](mailto:bernardo@biologia.ufrj.br)).

## LETTERS

# Experience with moving visual stimuli drives the early development of cortical direction selectivity

Ye Li<sup>1\*</sup>, Stephen D. Van Hooser<sup>1\*</sup>, Mark Mazurek<sup>1</sup>, Leonard E. White<sup>1,2</sup> & David Fitzpatrick<sup>1,3</sup>

The onset of vision occurs when neural circuits in the visual cortex are immature, lacking both the full complement of connections<sup>1,2</sup> and the response selectivity that defines functional maturity<sup>3,4</sup>. Direction-selective responses are particularly vulnerable to the effects of early visual deprivation, but it remains unclear how stimulus-driven neural activity guides the emergence of cortical direction selectivity. Here we report observations from a motion training protocol that allowed us to monitor the impact of experience on the development of direction-selective responses in visually naive ferrets. Using intrinsic signal imaging techniques, we found that training with a single axis of motion induced the rapid emergence of direction columns that were confined to cortical regions preferentially activated by the training stimulus. Using two-photon calcium imaging techniques, we found that single neurons in visually naive animals exhibited weak directional biases and lacked the strong local coherence in the spatial organization of direction preference that was evident in mature animals. Training with a moving stimulus, but not with a flashed stimulus, strengthened the direction-selective responses of individual neurons and preferentially reversed the direction biases of neurons that deviated from their neighbours. Both effects contributed to an increase in local coherence. We conclude that early experience with moving visual stimuli drives the rapid emergence of direction-selective responses in the visual cortex.

Direction selectivity is the capacity of neurons to respond more significantly to one principal direction of stimulus motion than any other<sup>5</sup>. In the retino-geniculo-cortical pathway, it is first expressed at the level of columnar circuits in the primary visual cortex (V1), where it is organized into a map of direction preference<sup>6,7</sup>. In ferrets, direction columns emerge shortly after the onset of visual experience in a process that dark-rearing experiments indicate requires visual experience<sup>3</sup>. To gain insight into the mechanisms by which stimulus-driven neural activity shapes the emerging properties of cortical neurons, we asked whether exposure to a moving visual stimulus was sufficient to induce the development of cortical direction columns and, if so, how this experience altered the response properties of individual cortical neurons.

We began by studying the emergence of direction columns using intrinsic signal imaging techniques in juvenile ferrets ( $n = 9$ ; post-natal day 30–35) that had less than one day of visual experience. Consistent with previous reports, the visual cortex of these visually naive ferrets exhibited a well-defined system of orientation columns, but lacked the columnar pattern of direction-selective responses that normally develops to mature levels 7–10 days following eye opening<sup>3</sup> (Fig. 1). To determine whether exposure to a moving visual stimulus was sufficient to induce the emergence of direction-selective responses, animals were exposed to a 'training' stimulus, namely a single sine- or square-wave grating (spatial frequency, 0.06–0.08 cycles per

degree; temporal frequency, 4 Hz) drifting back and forth along an axis of motion orthogonal to the grating orientation. As illustrated in two example cases (Fig. 1b, d), no changes were apparent for the first 8–10 h of stimulation; at later times, however, small domains of directional preference became evident in difference images. This direction difference signal continued to intensify and the number of emergent domains increased across the area of the responsive cortex as the experiments continued. The strength of the direction difference signal was quantified by calculating a direction selectivity index (DSI; see Supplementary Methods), and a notable and progressive increase in DSI accompanied exposure to the training stimulus (Fig. 1e).

Evidence that exposure to the training stimulus was responsible for the rapid emergence of direction selectivity came from experiments, performed following the training period, in which cortical responses to eight directions of motion were examined. Direction-selective responses were evident for stimulus directions that matched that of the training stimulus in seven of nine animals, but were weak or absent for other directions of motion in all animals that were trained (Fig. 1f, g). In comparison with the initial conditions, the average DSI values after training were significantly increased for responses to stimuli whose properties matched the training stimulus ( $t$ -test,  $P < 0.001$ ), but DSI values associated with responses to stimuli orthogonal to the training stimulus were not significantly different from those at the start of training ( $t$ -test,  $P = 0.12$ ). Moreover, at the end of the training period, there was no significant difference in the average response of the trained and untrained orientation columns to a drifting stimulus of the preferred orientation (Supplementary Fig. 1b), indicating that the emergence of direction columns cannot be attributed to a general increase in the activity of the trained columns. Because orientation selectivity is not a prominent feature of precortical sites in the visual pathway (retina, lateral geniculate nucleus)<sup>8–12</sup>, the orientation selectivity of these training effects indicates that the mechanisms responsible for the rapid emergence of direction selectivity must include events that reside at the level of cortical circuits.

To better understand changes at the cellular level that underlie the emergence of direction columns, we used *in vivo* two-photon imaging of calcium signals<sup>13</sup> to explore the direction selective properties of individual layer-2/3 neurons (Fig. 2a). As a first step, we examined the magnitude of single-neuron direction tuning in visually naive animals and compared this to direction tuning in animals that had visual experience sufficient to achieve mature levels of direction selectivity as measured by intrinsic signal imaging. Neurons in visually naive animals were highly responsive and tuned for stimulus orientation, but were at best only weakly selective for direction of motion (Fig. 2b, c). The median direction index value for visually naive animals was 0.15, and only 6% of neurons in visually naive

<sup>1</sup>Department of Neurobiology, Duke University School of Medicine, <sup>2</sup>Department of Community and Family Medicine, Doctor of Physical Therapy Division, Duke University School of Medicine, <sup>3</sup>Duke Institute for Brain Sciences, Duke University, Durham, North Carolina 27710, USA.

\*These authors contributed equally to this work.

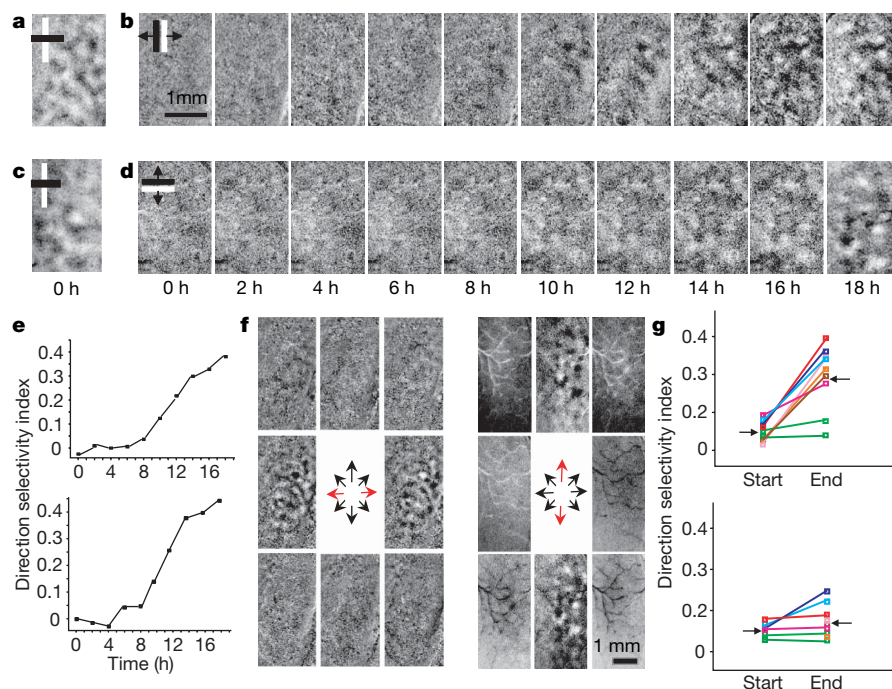


**Figure 1 | Rapid emergence of direction columns with motion training.** **a–d**, Visually naive animals (postnatal days 34, 35) with orientation columns (**a**, **c**) were trained using moving vertical (**b**) or horizontal (**d**) gratings. Direction domains emerged after 8 h. **e**, Time course of training-induced increases in direction selectivity (top, **b**; bottom, **d**). **f**, After training,

direction domains were present only for the trained directions of motion (red arrows) (left, **b**; right, **d**). **g**, Direction selectivity before and after training; colours indicate different animals and arrows indicate median DSI, which increased significantly for trained direction ( $t$ -test,  $P < 0.001$ ; top), but not orthogonal motion directions ( $t$ -test,  $P = 0.12$ ; bottom).

animals exhibited a direction index value of 0.5, which corresponds to a preferred/opposite response ratio of 2:1 (Fig. 2c). By contrast, many neurons in animals with visual experience were well tuned for direction of motion, such that the median value of the direction index was 0.56. Thus, the normal emergence of direction columns that ensues following eye opening in ferrets reflects a significant increase in the percentage of neurons that exhibit strong tuning for direction of motion.

We then examined whether the rapid emergence of direction columns that occurs under the influence of a training stimulus is accompanied by an increase in the direction selectivity of individual cortical neurons. In these experiments, we limited our analysis to 262 cells that had significant orientation tuning (vector test; see Supplementary Methods) and could be unambiguously identified both before and after the training period (Fig. 3a). Because the calcium-sensitive dye generally fades over time, the training period

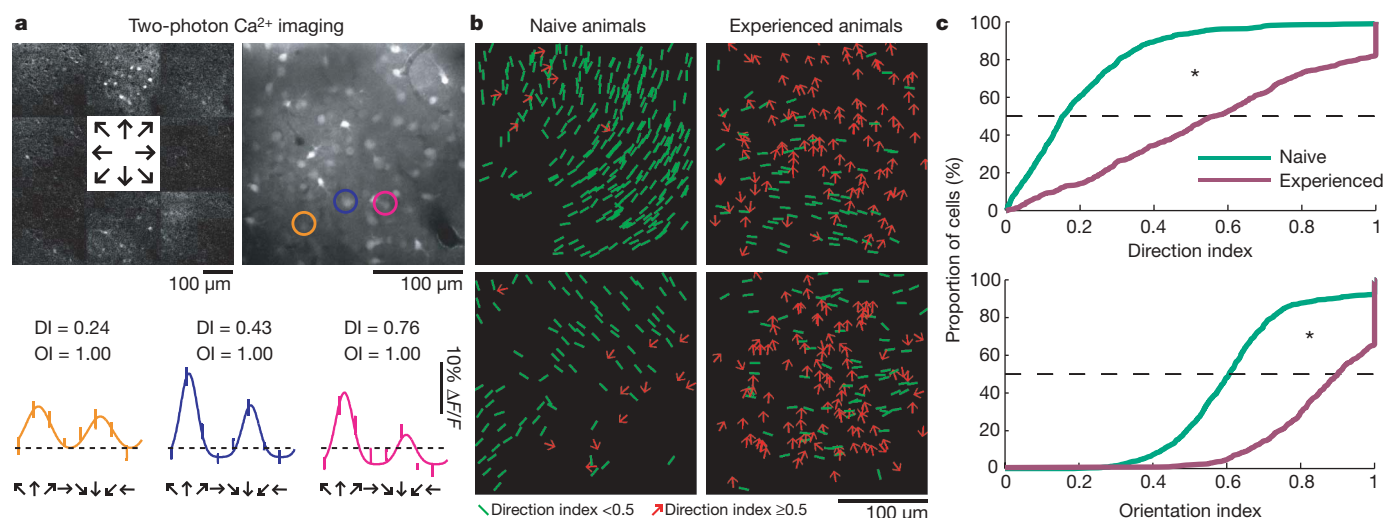


**Figure 2 | Direction selectivity of cells in visually naive and experienced ferrets, demonstrated by two-photon calcium imaging.** **a**, Left, average change in fluorescence ( $\Delta F/F$ ) in response to different directions of motion at 160- $\mu$ m depth in visual cortex of an animal with three weeks of experience; right, cells labelled with Oregon Green 488 BAPTA-1 acetoxymethyl ester, at same depth. Bottom, tuning curves, direction indices (DI) and orientation indices (OI) for cells circled in the right-hand subpanel (dashed lines indicate mean response to grey screen). **b**, Plots of orientation/direction

selective cells in two-photon multi-depth imaging fields from naive and experienced animals. Cells with direction indices  $< 0.5$  are depicted with green bars indicating preferred orientation; cells with direction indices  $\geq 0.5$  are depicted with red arrows indicating preferred direction. **c**, Cumulative histograms of direction index and orientation index for naive and experienced animals. Differences between groups are significant (Kruskal–Wallis test,  $*P < 0.001$ ).



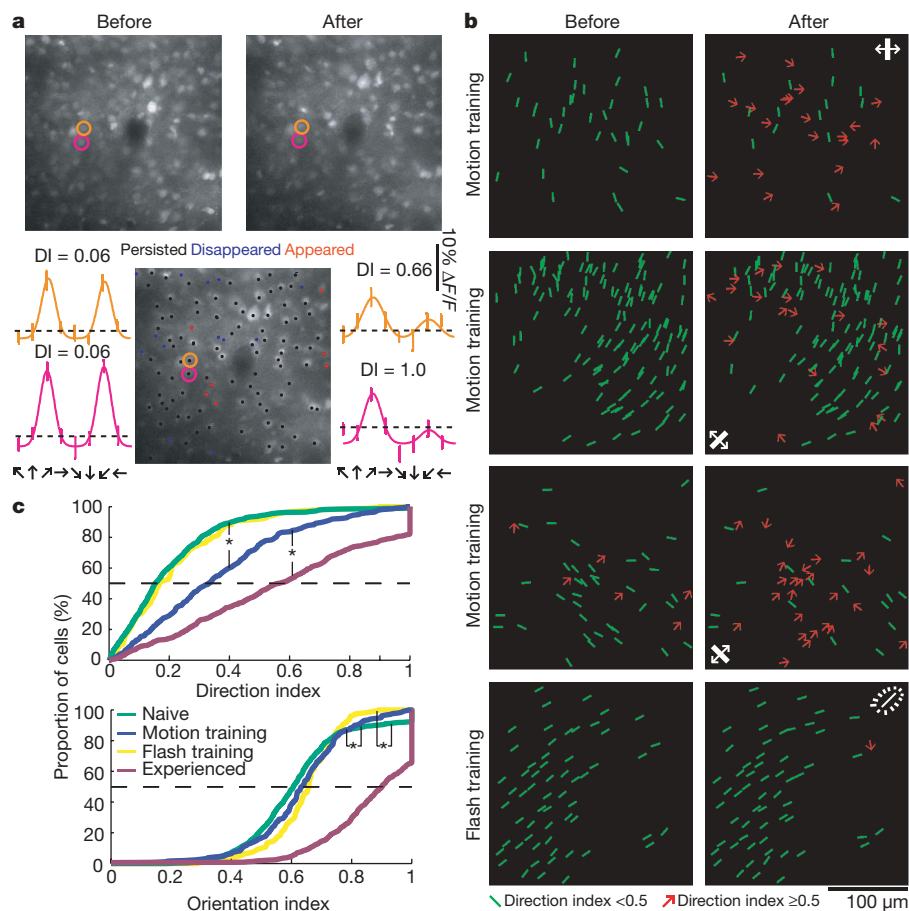


**Figure 3 | Motion training increases direction selectivity in individual cells.** **a**, Representative two-photon images (135-μm depth) showing labelled cells evident before (top left) and after (top right) 6-h motion training. Cell history over the course of training (persisted/disappeared/appeared) is depicted in the bottom-middle panel. Tuning curves and direction index (DI) values for circled cells are shown at bottom left (before training) and bottom right (after training). **b**, Plots of cells from four animals before and after 3–6-h motion or flash training; icons indicate trained directions or orientation of flashing stimulus. **c**, Cumulative histograms of direction index and orientation index for, variously, naive ( $N = 8$ ; cell number, 951), motion-trained ( $N = 5, 262$ ), flash-trained ( $N = 3, 135$ ) and experienced ( $N = 5, 551$ ) conditions. Direction index increased significantly following motion training (Kruskal–Wallis test,  $*P < 0.01$ ), but not after flash training (Kruskal–Wallis test,  $P = 0.27$ ). Orientation index exhibited a small but significant increase following both motion and flash training ( $*P < 0.01$ ).

was shorter (3–6 h) than that used for intrinsic signal imaging so that reliable tuning curves could be measured at the conclusion of training (Supplementary Methods, Supplementary Figures 2–5).

The distribution of direction index values measured after the training period was significantly higher than the values measured in the same neurons before training (Fig. 3b, c; Kruskal–Wallis test,  $P < 0.001$ ): overall, median direction index increased to 0.39, and 36% of cells exhibited direction index values greater than 0.5. On an individual basis, median direction index values increased in all five cases. This training effect was strong enough that statistically significant increases in direction selectivity were observed when the responses of individual cells were compared before and after training (Fig. 3a, Supplementary Figures 2, 3): 59 cells (23%) distributed among four of five animals exhibited a statistically significant increase in direction index over that found before training, and none exhibited a significant decrease in direction selectivity (bootstrap test; see Supplementary Methods).

To test whether motion of the training stimulus was necessary to induce these rapid changes in direction-selective responses, we examined the effects of training with an identical grating stimulus that was flashed (sinusoidal modulation between grating and grey screen, 4 Hz). This stimulus was effective in driving cortical activity (Supplementary Fig. 5a), but no significant increase in direction selectivity was found after flash training (Fig. 3b, c; Kruskal–Wallis test,  $P = 0.27$ ). Both motion and flash training resulted in small increases in the degree of orientation tuning (Kruskal–Wallis test,  $P < 0.001$ ) that were equal in magnitude (Fig. 3c; Kruskal–Wallis test,  $P = 0.29$ ).

These results provide strong evidence that visual experience increases the magnitude of direction selectivity; by itself, this could explain the rapid emergence of columnar structure visualized with intrinsic signal imaging. However, a comparison of the spatial organization of direction preferences in visually naive and experienced

animals suggests that visual experience also has a role in determining which direction of motion is preferred by individual cortical neurons (Fig. 4a). Animals with visual experience exhibited a robust clustering of neurons with similar direction preference, consistent with descriptions of the fine-scale mapping of direction preference in cats<sup>14</sup>. By contrast, in visually naive animals, the spatial organization of direction preferences was weak, and neighbouring neurons often exhibited opposite direction preferences.

To quantify this difference, we developed a measure of local coherence: for each neuron, we calculated the percentage of neighbouring cells with similar direction preferences (within  $45^\circ$ ) minus the percentage with opposite preferences (within  $45^\circ$ ). The direction preference of weakly selective cells is acutely sensitive to trial-to-trial variability; we accounted for this variability in local coherence values by employing the bootstrap technique to create 100 simulations of each cell's responses drawn randomly from the original data with replacement. The median local coherence value from these 100 simulations is reported here. In animals with mature direction selectivity and robust columnar structure, average local coherence values were positive and highest for samples within a radius of 50 μm, falling gradually to near zero at distances of 200–250 μm (Fig. 4b, c). The local coherence values for visually naive animals were significantly lower at all distances; nevertheless, they were significantly different from zero, indicating a weak tendency for nearby neurons in visually naive animals to exhibit similar direction preferences. To determine whether experience with moving stimuli was sufficient to explain increases in the spatial coherence of direction preference, we examined the local coherence indices in animals that had undergone training with a motion stimulus and those that received flash training. Motion training produced a significant increase in local coherence values over that found for visually naive animals (Fig. 4c; Kruskal–Wallis test,  $P < 0.001$ ), whereas flash training produced a significant decrease (Kruskal–Wallis test,  $P < 0.001$ ).

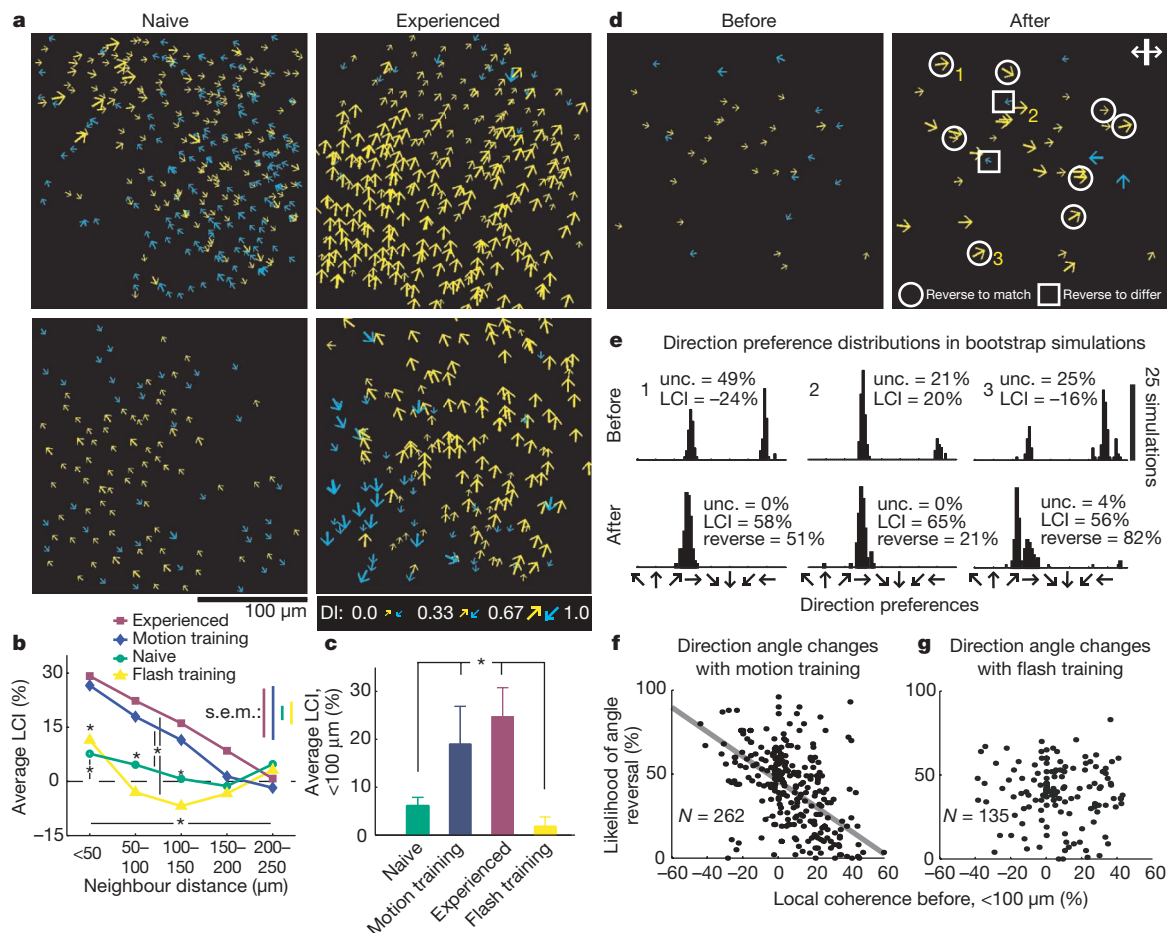


**Figure 4 | Impact of normal experience and motion training on direction preference.** **a**, Plots of direction preference in naive and experienced animals. All cells are represented by arrows, which indicate preferred direction; arrow length indicates magnitude (DI, direction index). Colour differentiates cells with opposite preferences ( $\pm 90^\circ$ ). **b**, **c**, Spatial coherence of direction preference (local coherence index (LCI)) increased—relative to naive ( $N = 8$ ; cell number, 951)—with experience ( $N = 5$ , 551) or motion training ( $N = 5$ , 262), but not with flash training ( $N = 3$ , 135) (s.e.m. calculated across animals). Significant relations among curves and with distance (analysis of variance), and differences from zero in naive and flash traces (sign test) indicated by asterisks. Error bars are s.e.m. calculated across animals. **d**, Direction preference of individual cells before (left) and

after (right) motion training (numbers refer to cells in **e**). Cells in circles and squares appeared to reverse their preference, coming to prefer rightward and leftward motion, respectively. **e**, Distributions of preferred directions in simulations for three cells, after (bottom row) and before (top row) motion training (unc., preference uncertainty; reverse, likelihood of a preference reversal). Some cells (1) initially were uncertain but developed a consistent preference after motion training; other cells exhibited biases that strengthened (2) or reversed (3). **f**, **g**, Influence of initial local coherence index on motion training (**f**) and flash training (**g**) effects. Cells whose preferred direction differed from their neighbours were most likely to reverse (**f**). No systematic relationship was observed with flash training (**g**).

These results imply that as a result of motion training, the direction of motion preferred by individual cortical neurons changes to become more like that of their neighbours. Examination of the preference of individual neurons before and after training revealed a number of examples in which this appeared to be the case (Fig. 4d). However, this conclusion rests on the confidence with which a direction preference can be assigned to the weakly selective neurons in visually naive animals. From our bootstrap simulations, we derived a measure of uncertainty in direction preference, defined to be the percentage of simulations that differed from the mean direction by more than  $90^\circ$ . We observed a wide range of uncertainty in initial direction preferences. The direction preference of some cells was highly uncertain before motion training but became more certain after training (Fig. 4e, left-hand subpanel). For example, 68 cells with uncertainties greater than 25% before motion training exhibited uncertainties that were less than 25% after training. Other cells exhibited moderate direction preference biases at the onset of training that could be either strengthened (Fig. 4e, middle subpanel) or reversed (Fig. 4e, right-hand subpanel). Of the 148 cells that had initial uncertainties less than 25%, 74 were likely to have maintained their initial direction preference (likelihood of reversing,  $<25\%$ ), whereas 20 were more than 75% likely to have reversed their preference.

We then asked whether the diverse effects of motion training produced a more coherent map of direction preference by building on the weak spatial organization that existed at the onset of training. Consistent with this idea, we found a significant correlation between the likelihood of direction preference reversal and local coherence before training (Fig. 4f; regression  $F$ -test,  $P < 0.001$ ,  $R^2 = 0.22$ ), but not with flash training (Fig. 4g; regression  $F$ -test,  $P = 0.34$ ,  $R^2 = 0.006$ ). Thus, in regions with strong local coherence, there was a predictable impact of motion training: cells that were surrounded by neighbouring neurons expressing the opposite direction preference before training (high negative local coherence) were likely to reverse their direction preference, whereas cells whose neighbours expressed the same preference (high positive local coherence) were unlikely to reverse. Furthermore, the impact of motion training on the likelihood of reversal was unpredictable in regions characterized by weak local coherence (local coherence index values near zero). These findings implicate local cortical interactions in the mediation of the effects of motion training on direction preference. This systematic relationship between the likelihood of preference reversal and initial coherence values also rules out the possibility that changes in uncertainty alone are sufficient to explain the increase in local

coherence. Indeed, on average, we estimate that training-induced reversals in direction preference accounted for 53% of the total training-induced increase in spatial coherence, whereas changes in uncertainty accounted for 34%; the remaining 13% was contributed by slight but significant changes in orientation preference that accompanied motion training (Supplementary Methods, Supplementary Figure 4). Although the number of cells that appeared to reverse direction was less than the number of cells that had reduced uncertainty, the impact of a preference reversal on the local coherence index is greater than the impact of a reduction of preference uncertainty.

We conclude that early experience with moving visual stimuli exerts a strong, rapid and selective impact on response properties of developing cortical neurons, transforming a weakly biased array of poorly selective neurons into a more mature state that exhibits stronger direction selectivity and enhanced spatial coherence of direction preference. The rapid time course of these effects and the fact that they are sensitive to the spatio-temporal structure of the stimulus are consistent with activity-dependent mechanisms of synaptic plasticity<sup>15,16</sup>. However, what differentiates these observations from most previous demonstrations of activity-dependent alterations in stimulus preference<sup>17–25</sup> is that the information present in the training stimulus is ambiguous: opposite directions of motion are presented and yet neurons rapidly acquire and/or strengthen their preference for a single direction. Thus, the spatio-temporal cues present in a bidirectional motion training stimulus, which is more consistent with the balanced stimulation an animal might receive in nature, are sufficient to drive the development of cortical circuits that represent each direction of motion. Evidently, sufficient asymmetry in functional architecture exists to facilitate symmetry-breaking and seed the formation of direction columns from stimulus patterns that are equally balanced. Our spatial analysis has identified a constructive mechanism that operates locally and is reflected in the preferences of neighbouring neurons in layer 2/3. This mechanism—possibly mediated by local recurrent or feedforward circuits—effectively disambiguates the bidirectional motion energy of the training stimulus by influencing the probability that a neuron's initial preference will be reinforced or reversed.

Whether the weak direction bias present at the onset of training emerges through visual experience through closed lids<sup>26</sup>, endogenous activity<sup>27,28</sup> or activity-independent mechanisms<sup>29,30</sup> remains unclear. Nevertheless, the evidence presented here indicates that the events preceding eye opening are insufficient to account for either the magnitude of direction selectivity or the preference exhibited by mature cortical neurons, and that early experience with moving stimuli has a significant impact on both features.

## METHODS SUMMARY

Ferrets were anaesthetized with ketamine (50 mg kg<sup>-1</sup>) and isoflurane (2% for surgery, 0.8–1% during imaging). The training protocol consisted of a 5-s stimulation followed by a 10-s interstimulus interval. The protocol continued for 20 min and was followed by 10 min of no stimulation. This entire procedure was repeated for several hours. For intrinsic signal imaging experiments, cortex was illuminated with 610-nm light and data was acquired using the Imager 2001/3001 (Optical Imaging)<sup>3</sup>. For two-photon experiments, Oregon Green 488 BAPTA-1 acetoxymethyl ester (Invitrogen) was pressure injected into cortex and changes in calcium fluorescence were monitored with an Ultima IV two-photon microscope (Prairie Technologies) driven by a mode-locked Chameleon laser (810 nm, Coherent). Stimulation and analysis were performed using custom software for Matlab (Mathworks). See Supplementary Methods for details.

Received 8 May; accepted 11 September 2008.

Published online 22 October 2008.

1. Bourgeois, J. P. & Rakic, P. Changes of synaptic density in the primary visual cortex of the macaque monkey from fetal to adult stage. *J. Neurosci.* **13**, 2801–2820 (1993).
2. Durack, J. C. & Katz, L. C. Development of horizontal projections in layer 2/3 of ferret visual cortex. *Cereb. Cortex* **6**, 178–183 (1996).
3. Li, Y., Fitzpatrick, D. & White, L. E. The development of direction selectivity in ferret visual cortex requires early visual experience. *Nature Neurosci.* **9**, 676–681 (2006).

4. White, L. E. & Fitzpatrick, D. Vision and cortical map development. *Neuron* **56**, 327–338 (2007).
5. Hubel, D. H. & Wiesel, T. N. Receptive fields, binocular interaction and functional architecture in the cat's visual cortex. *J. Physiol. (Lond.)* **160**, 106–154 (1962).
6. Shmuel, A. & Grinvald, A. Functional organization for direction of motion and its relationship to orientation maps in cat area 18. *J. Neurosci.* **16**, 6945–6964 (1996).
7. Weliky, M., Bosking, W. H. & Fitzpatrick, D. A systematic map of direction preference in primary visual cortex. *Nature* **379**, 725–728 (1996).
8. Zhou, Y., Leventhal, A. G. & Thompson, K. G. Visual deprivation does not affect the orientation and direction sensitivity of relay cells in the lateral geniculate nucleus of the cat. *J. Neurosci.* **15**, 689–698 (1995).
9. Tavazoie, S. F. & Reid, R. C. Diverse receptive fields in the lateral geniculate nucleus during thalamocortical development. *Nature Neurosci.* **3**, 608–616 (2000).
10. Krug, K., Akerman, C. J. & Thompson, I. D. Responses of neurons in neonatal cortex and thalamus to patterned visual stimulation through the naturally closed lids. *J. Neurophysiol.* **85**, 1436–1443 (2001).
11. Hubel, D. H. & Wiesel, T. N. Receptive fields of single neurones in the cat's striate cortex. *J. Physiol. (Lond.)* **148**, 574–591 (1959).
12. Cai, D., DeAngelis, G. C. & Freeman, R. D. Spatiotemporal receptive field organization in the lateral geniculate nucleus of cats and kittens. *J. Neurophysiol.* **78**, 1045–1061 (1997).
13. Stosiek, C., Garaschuk, O., Holthoff, K. & Konnerth, A. In vivo two-photon calcium imaging of neuronal networks. *Proc. Natl Acad. Sci. USA* **100**, 7319–7324 (2003).
14. Ohki, K., Chung, S., Ch'ng, Y. H., Kara, P. & Reid, R. C. Functional imaging with cellular resolution reveals precise micro-architecture in visual cortex. *Nature* **433**, 597–603 (2005).
15. Bi, G. Q. & Poo, M. M. Synaptic modifications in cultured hippocampal neurons: dependence on spike timing, synaptic strength, and postsynaptic cell type. *J. Neurosci.* **18**, 10464–10472 (1998).
16. Song, S., Miller, K. D. & Abbott, L. F. Competitive Hebbian learning through spike-timing-dependent synaptic plasticity. *Nature Neurosci.* **3**, 919–926 (2000).
17. Sengpiel, F., Stawinski, P. & Bonhoeffer, T. Influence of experience on orientation maps in cat visual cortex. *Nature Neurosci.* **2**, 727–732 (1999).
18. Schuett, S., Bonhoeffer, T. & Hubener, M. Pairing-induced changes of orientation maps in cat visual cortex. *Neuron* **32**, 325–337 (2001).
19. Engert, F., Tao, H. W., Zhang, L. I. & Poo, M. M. Moving visual stimuli rapidly induce direction sensitivity of developing tectal neurons. *Nature* **419**, 470–475 (2002).
20. Mu, Y. & Poo, M. M. Spike timing-dependent LTP/LTD mediates visual experience-dependent plasticity in a developing retinotectal system. *Neuron* **50**, 115–125 (2006).
21. Meliza, C. D. & Dan, Y. Receptive-field modification in rat visual cortex induced by paired visual stimulation and single-cell spiking. *Neuron* **49**, 183–189 (2006).
22. Yao, H., Shi, L., Han, F., Gao, H. & Dan, Y. Rapid learning in cortical coding of visual scenes. *Nature Neurosci.* **10**, 772–778 (2007).
23. Tanaka, S., Ribot, J., Imamura, K. & Tani, T. Orientation-restricted continuous visual exposure induces marked reorganization of orientation maps in early life. *Neuroimage* **30**, 462–477 (2006).
24. Daw, N. W., Berman, N. E. & Ariel, M. Interaction of critical periods in the visual cortex of kittens. *Science* **199**, 565–567 (1978).
25. Blakemore, C. & Van Sluyters, R. C. Innate and environmental factors in the development of the kitten's visual cortex. *J. Physiol. (Lond.)* **248**, 663–716 (1975).
26. Akerman, C. J., Smyth, D. & Thompson, I. D. Visual experience before eye-opening and the development of the retinogeniculate pathway. *Neuron* **36**, 869–879 (2002).
27. Chiu, C. & Weliky, M. Spontaneous activity in developing ferret visual cortex *in vivo*. *J. Neurosci.* **21**, 8906–8914 (2001).
28. Huberman, A. D., Speer, C. M. & Chapman, B. Spontaneous retinal activity mediates development of ocular dominance columns and binocular receptive fields in v1. *Neuron* **52**, 247–254 (2006).
29. Crowley, J. C. & Katz, L. C. Early development of ocular dominance columns. *Science* **290**, 1321–1324 (2000).
30. Kawasaki, H., Crowley, J. C., Livesey, F. J. & Katz, L. C. Molecular organization of the ferret visual thalamus. *J. Neurosci.* **24**, 9962–9970 (2004).

**Supplementary Information** is linked to the online version of the paper at [www.nature.com/nature](http://www.nature.com/nature).

**Acknowledgements** The authors thank P. Kara, T. Mrcic-Fogel and A. Kerlin for help with two-photon imaging techniques, T. Tucker and J. Heiner for technical assistance and M. Christensson and the members of the Fitzpatrick lab for comments on the manuscript. This work was supported by grants from the Whitehall Foundation to L.E.W. and the US National Institutes of Health to D.F. and S.D.V.H.

**Author Contributions** Y.L. performed intrinsic imaging experiments and analysis. Y.L. and S.D.V.H. performed two-photon experiments, and S.D.V.H., Y.L. and M.M. analyzed the two-photon data. Y.L., S.D.V.H., L.E.W. and D.F. wrote the paper, and all authors discussed the results and commented on the manuscript.

**Author Information** Reprints and permissions information is available at [www.nature.com/reprints](http://www.nature.com/reprints). Correspondence and requests for materials should be addressed to D.F. ([fitzpat@neuro.duke.edu](mailto:fitzpat@neuro.duke.edu)).



# Contact inhibition of locomotion *in vivo* controls neural crest directional migration

Carlos Carmona-Fontaine<sup>1</sup>, Helen K. Matthews<sup>1</sup>, Sei Kuriyama<sup>1</sup>, Mauricio Moreno<sup>1</sup>, Graham A. Dunn<sup>2</sup>, Maddy Parsons<sup>2</sup>, Claudio D. Stern<sup>1</sup> & Roberto Mayor<sup>1</sup>

Contact inhibition of locomotion was discovered by Abercrombie more than 50 years ago and describes the behaviour of fibroblast cells confronting each other *in vitro*, where they retract their protrusions and change direction on contact<sup>1,2</sup>. Its failure was suggested to contribute to malignant invasion<sup>3–6</sup>. However, the molecular basis of contact inhibition of locomotion and whether it also occurs *in vivo* are still unknown. Here we show that neural crest cells, a highly migratory and multipotent embryonic cell population, whose behaviour has been likened to malignant invasion<sup>6–8</sup>, demonstrate contact inhibition of locomotion both *in vivo* and *in vitro*, and that this accounts for their directional migration. When two migrating neural crest cells meet, they stop, collapse their protrusions and change direction. In contrast, when a neural crest cell meets another cell type, it fails to display contact inhibition of locomotion; instead, it invades the other tissue, in the same manner as metastatic cancer cells<sup>3,5,9</sup>. We show that inhibition of non-canonical Wnt signalling abolishes both contact inhibition of locomotion and the directionality of neural crest migration. Wnt-signalling members localize at the site of cell contact, leading to activation of RhoA in this region. These results provide the first example of contact inhibition of locomotion *in vivo*, provide an explanation for coherent directional migration of groups of cells and establish a previously unknown role for non-canonical Wnt signalling.

Neural crest (NC) cells cultured *in vitro* move away from each other, dispersing quickly<sup>10</sup>. *Xenopus* NC explants revealed that only the leading-edge cells were polarized, having large lamellipodia at the front as shown by scanning electron microscopy (arrowheads in Fig. 1a–c) or in a live NC explant expressing membrane-localized green fluorescent protein (GFP) (Fig. 1d). Time-lapse analysis revealed that edge cells had a higher persistence in the direction of migration than cells in the interior of the explant (Fig. 1d'). To establish whether these differences in polarity and migration correspond to two different cell populations or whether they are due to cell–cell contact, we dissociated NC explants into single cells and then re-aggregated them into small or large clusters. Peripheral cells in small or large clusters rapidly became polarized and migrate away from each other (Fig. 1e), whereas internal cells moved randomly (Supplementary Fig. 2 and Supplementary Movie 1), similarly to those in non-dissociated explants. In addition, the randomly migrating internal cells of these explants became polarized when made to have a free edge by wounding or removal of their neighbours (Supplementary Fig. 3). These results suggest that the differential behaviour of leading versus internal cells in explants is due not to intrinsic cell differences but to interactions between neighbouring cells. Furthermore, the average persistence of the leading cells (defined by their position at the border of an explant) in a

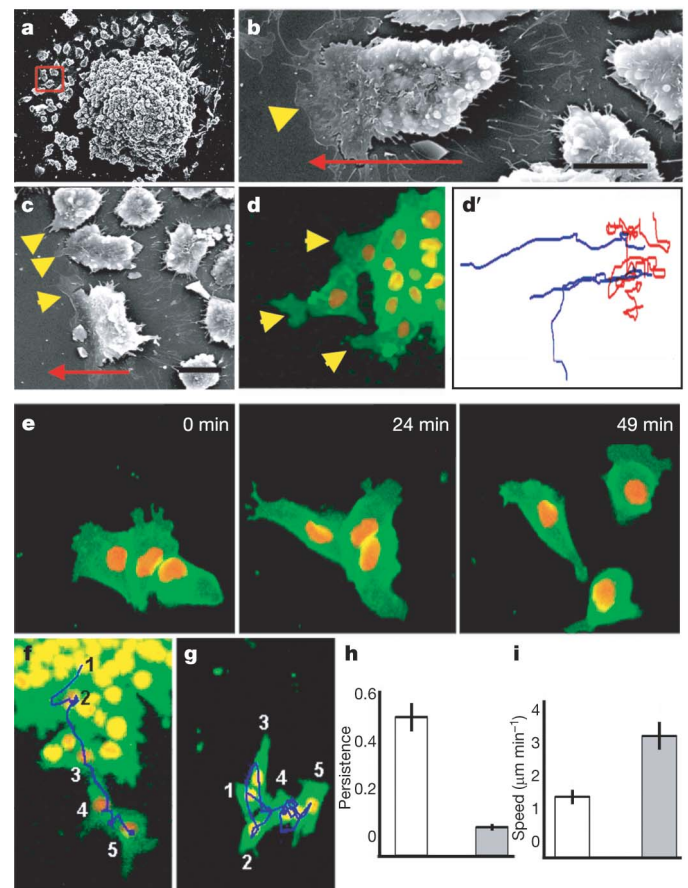


**Figure 1 | Cell-cell contacts polarize migrating NC cells *in vitro*.** **a–g**, NCs were cultured *in vitro* and analysed by scanning electron microscopy (**a–c**) or time-lapse microscopy of cells expressing membrane-GFP and nuclear-RFP (**d–g**). The red square in **a** indicates leading cells (defined by its position at the edge of migration; higher magnifications of other leading cells are shown in **b** and **c**). Arrowheads indicate lamellipodia (note their presence only in the leading cells, either by scanning electron microscopy (**c**); or fluorescence (**d**)); the arrow indicates the direction of migration. Scale bars in **b**, **c**, 50  $\mu$ m. **d'**, Tracks of leading (blue) and trailing (red) cells shown in **d**. **e**, Three frames of a time-lapse movie for dissociated and re-aggregated NC cells. **f**, **g**, Temporal projection to compare the migration of a group of NC cells (**f**) with that of individual cells (**g**). Numbers indicate the position of the same cell at different time frames 10 min apart. The track is shown as a blue line. **h**, **i**, Persistence (**h**) and speed of migration (**i**) for the migration as a group (white bars) or as an individual cell (grey bars) ( $P < 0.005$ ,  $n = 60$ ). Error bars show s.d.

<sup>1</sup>Department of Anatomy and Developmental Biology, University College London, London WC1E 6BT, UK. <sup>2</sup>Randall Division of Cell and Molecular Biophysics, King's College London, London SE1 1UL, UK.

non-dissociated cluster was much higher than that of individual cells; the latter often made little progress and moved in circles, although their overall speed of migration was greater (Fig. 1f–i and Supplementary Movie 2). A similar phenomenon has been reported for cell types showing contact inhibition of locomotion<sup>1</sup>. Taken together, these results indicate that the directional migration of cultured NC cells is dependent on cell–cell contact, which is likely to inhibit the formation of cell protrusions, leading to cell polarization.

To study the behaviour of NC cells when confronted with other cells, we developed an explant-confrontation assay<sup>1,11</sup>. Two NC explants were cultured in close proximity such that their leading cells would encounter cells from the other explant migrating in the opposite direction (Fig. 2A). We found that cells from NC explants aggressively invaded mesodermal (Fig. 2E) and ectodermal (not shown) explants, but never invaded other NC explants (Fig. 2C, Supplementary Fig. 4a–c and Supplementary Movie 3). Confocal microscopic analyses showed that whereas NC cells stopped migrating when confronted with other NC cells, they engulfed the mesoderm explant, with some cells penetrating deep layers of this tissue (Fig. 2D, F and Supplementary Fig. 4d–i). These observations suggest

that contact inhibition of locomotion occurs between NC cells (homotypic) but not between NC cells and other cell types (heterotypic), in the same way as with some malignant cells<sup>4,5,9</sup>.

It is tempting to speculate that such homotypic contact inhibition of locomotion could function in guiding the migration of NC cells in normal development. To determine whether this is true we developed a confrontation assay *in vivo* and found that NC cells can invade the tissue of an adjacent *Xenopus* embryo lacking NC (Fig. 2O) but this invasion is blocked when the host NC is present (Fig. 2N). This result is compatible with contact inhibition of locomotion having this function, but it does not directly demonstrate that NC cells show contact inhibition of locomotion. We therefore performed time-lapse analysis in the explant-confrontation assay, focusing on individual cells. When a NC cell came into contact with a cell from the opposite group, its lamellipodium collapsed and the direction of its migration changed (Fig. 2G and Supplementary Movie 4). This is described precisely by Abercrombie's original definition of contact inhibition of locomotion as “the phenomenon of a cell ceasing to continue moving in the same direction after contact with another cell”<sup>15</sup>. So far, contact inhibition of locomotion has been

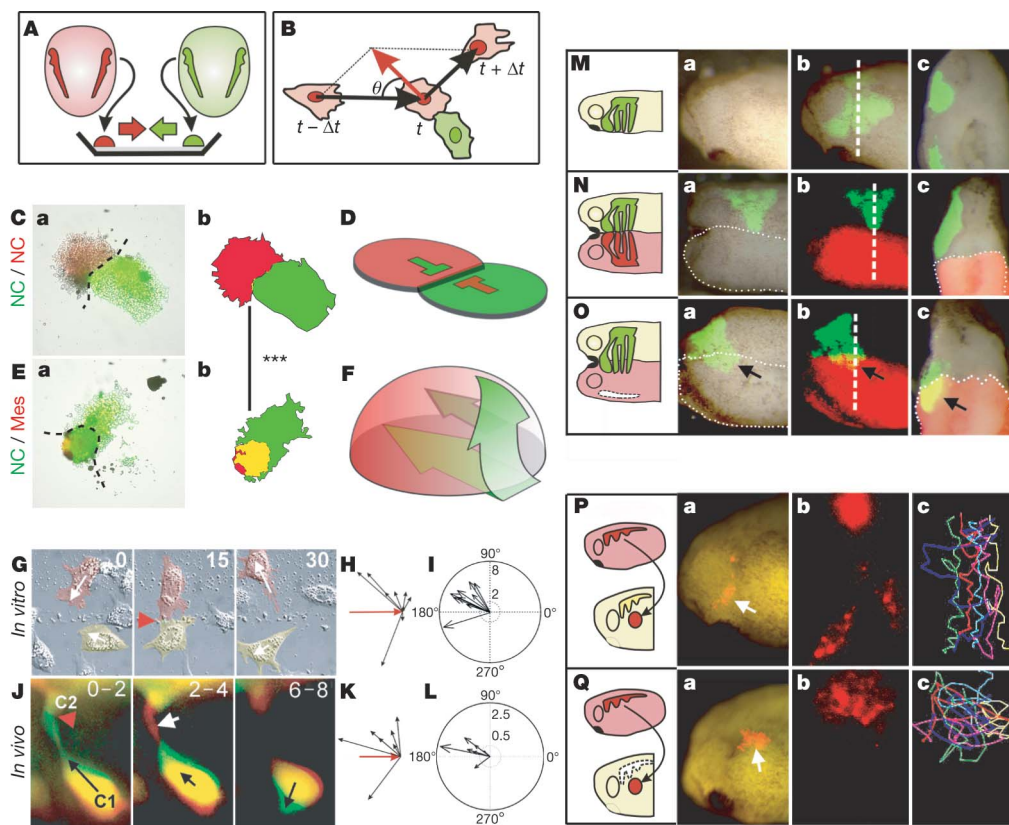


**Figure 2 | Contact inhibition of locomotion in NC cells *in vitro* and *in vivo*.**

**A**, Experimental design. **B**, Analysis of contact inhibition of locomotion. Mean velocities were measured  $\Delta t$  minutes before and after the collision. Acceleration (red) was calculated for each cell. The angle of collision,  $\theta$ , was calculated after initial trajectory alignment. **C–F**, Invasion of confronted explants *in vitro*. **C**, There is no invasion in NC/NC confrontations (**a**), outlines in (**b**), overlapping area in yellow; shown schematically in **F**. **D**, NC explants completely invade and cover mesodermal (mes) explants (**a**), outlines in (**b**), overlapping area in yellow; shown schematically in **F**. Green arrows in **F** indicate the NC path of invasion (see Supplementary Fig. 3 for supporting confocal images). Three asterisks in **b** show a significant difference in the overlapping area (yellow),  $P < 0.005$  ( $n = 5$  for each condition). **G–L**, Contact inhibition of locomotion. **G**, Collision between two pseudocoloured NC cells *in vitro*. Time is shown in minutes. White arrows indicate the direction of migration; the red arrowhead indicates collision. **H**, Velocity vectors for NC *in vitro*; the red arrow indicates the initial velocity vector. **I**, Acceleration vectors for NC collisions *in vitro*. They are clustered

after the collision ( $P < 0.005$ ,  $n = 10$ ). **J**, Collision of two NC cells (C1 and C2) *in vivo* shown as the difference between two consecutive 2-min frames. Green, new area; red, collapsing area; black arrow, direction of migration; red arrowhead, cell contact; white arrow, collapsing protrusion. **K**, *In vivo* velocity vectors. **L**, *In vivo* acceleration. They are clustered after the collision ( $P < 0.01$ ,  $n = 10$ ). **M–O**, NC invasion *in vivo*. **a**, **b**, lateral view; **c**, transverse section along the dashed line shown in **b**. **M**, Labeled and transplanted NC cells in control embryos migrate normally. **N**, **O**, NC cells are not able to invade an adjacent embryo that has NC (**N**; 0% of invasion,  $n = 15$ ), but they can invade an embryo without NC (**O**; arrow, 80% of invasion,  $n = 10$ ). **P**, **Q**, Cell directionality *in vivo*. A small group of nuclear-RFP-labelled NC cells were grafted into a normal embryo (**P**) or into an embryo from which the NC had previously been removed (**Q**). Note that grafted cells migrated directionally in the intact embryo (persistence  $0.6 \pm 0.04$  (mean  $\pm$  s.d.),  $n = 30$ ), but not when the host NCs were removed (persistence  $0.2 \pm 0.02$  (mean  $\pm$  s.d.),  $n = 20$ ).



described only *in vitro*. To address whether it also occurs *in vivo*, we used two Sox10–GFP transgenic zebrafish lines, one expressing GFP in the cytoplasm<sup>12</sup> and the other in the membrane of NC cells, and analysed their migration using live-imaging techniques. Similarly to the observations *in vitro*, whenever two NC cells made contact, they changed their direction of migration and their protrusions collapsed (Fig. 2J, Supplementary Fig. 5 and Supplementary Movies 5–7). Contact inhibition of locomotion can be measured by the change in velocity after cell–cell contact<sup>4,11</sup>. Large changes in the direction of cell migration were seen after each cell collision (Fig. 2B and Supplementary Methods) both *in vitro* and *in vivo* (velocity is shown in Fig. 2H, K, acceleration in Fig. 2I, L). The changes were not stochastic but were strongly biased in the opposite direction to the collision ( $P < 0.005$ ), as predicted by Abercrombie<sup>5,11</sup>. Similarly, in *Xenopus*, grafted NC cells integrated into the endogenous migratory pathway and migrated directionally (Fig. 2P). However, grafted NC lost their directional migratory behaviour when the host NC was removed (Fig. 2Q), suggesting that the directionality of NC migration depends on interactions with other NC cells and supporting our conclusion that contact inhibition of locomotion is required for normal NC migration *in vivo*.

We next explored the molecular mechanisms underlying contact inhibition of locomotion in NC cells. Previous studies have shown that the Wnt planar cell polarity (PCP, or non-canonical) pathway is

required for NC migration in *Xenopus* and zebrafish embryos, whereas canonical Wnt signalling is not<sup>13,14</sup>. To determine whether PCP signalling is involved in contact inhibition of locomotion, we analysed cells expressing a dominant-negative form of *dishevelled* (*DshDep*<sup>+</sup>), which specifically inhibits the PCP pathway<sup>15</sup>. In control explants, only the leading cells were highly polarized, extending cell protrusions at the front, whereas trailing cells were not (Fig. 1a–c). In contrast, *DshDep*<sup>+</sup> cells were not polarized but extended large protrusions in all directions (Fig. 3a–c). Live imaging showed that cells expressing *DshDep*<sup>+</sup> crawled on top of one another, extending protrusions between the neighbour cells, a characteristic of some metastatic cancer cells<sup>3,5,9</sup> (Fig. 3d, e, and Supplementary Movie 8). All *DshDep*<sup>+</sup> (leading and trailing) cells behaved similarly to trailing control cells on the basis of their low persistence of migration and the angles at which they changed direction (Fig. 3f–i). No difference in persistence and speed of migration was observed between dissociated control and *DshDep*<sup>+</sup> cells: both behaved like trailing cells (Fig. 3j–m and Supplementary Movie 9). This indicates that the effect of PCP signalling on NC migration requires cell–cell contact.

To test whether contact inhibition of locomotion is dependent on PCP signalling *in vivo*, we measured the speed of cell migration before and after cell collision in control embryos and in embryos in which PCP signalling had been disrupted (either by expressing *DshDep*<sup>+</sup>, by a dominant-negative form of the PCP ligand Wnt11 or by antisense morpholinos against the PCP pathway members *strabismus* (*Stb*; ref. 16) or *prickle1* (*Pk1*; ref. 17)). The lamellipodia of PCP-inhibited cells failed to collapse when they collide with each other *in vivo*, even after 1 h of contact (control, Supplementary Fig. 6a; PCP disrupted, Supplementary Fig. 6b, c; Supplementary Movie 10). In contrast to control cells (Fig. 4a, g), these cells did not significantly change their direction of migration (Fig. 4b–d), and as shown by the small acceleration vectors, cell velocity was hardly affected by cell–cell contact ( $P \gg 0.05$ ; Fig. 4h–j). Rather, PCP-inhibited cells migrated on top of one another, remaining in close contact (Supplementary Movie 10). Similar observations were made *in vitro* after inhibition of PCP signalling by the expression of *DshDep*<sup>+</sup>, by a dominant-negative form of Wnt11 (*dnWnt11*)<sup>15</sup>, by a morpholino against a protein closely related to mammalian Wnt11 (*Wnt11R*)<sup>18,19</sup> or by a mixture of *dnWnt11* and *Wnt11R* (Fig. 4e, f, k, l, and Supplementary Fig. 7e, f), where PCP inhibited cells did not collapse their protrusions after the collision (Supplementary Fig. 7a–c). Moreover, when control cells and *DshDep*<sup>+</sup>-expressing cells were confronted, only control cells collapsed their lamellipodia and moved away from the *DshDep*<sup>+</sup> cells (Supplementary Fig. 7d and Supplementary Movie 11), indicating that PCP/Dsh signalling is required only in the responding cell.

Activation of the PCP pathway is typically accompanied by membrane localization of Dishevelled (Dsh)<sup>20</sup>. We therefore analysed the subcellular localization of Dsh during NC migration *in vitro* and *in vivo*. In both premigratory NC cells and NC cells cultured on poly-(L-lysine, a non-permissive substrate for NC migration<sup>21</sup>, Dsh was seen in cytoplasmic dots (Supplementary Fig. 8a, b). In contrast, clear membrane localization of Dsh was observed at cell–cell contacts of NC cells grown on a permissive fibronectin substrate (Fig. 4o). For the leading cell, the region of cell–cell contact, and therefore the region of Dsh accumulation, was at the trailing end of the cell *in vitro* (Supplementary Fig. 8c). When two leading cells collided, Dsh became relocalized at the point of cell–cell contact, with a subsequent change in the direction of migration (Fig. 4p and Supplementary Movie 12). Similar observations on Dsh localization at cell–cell contacts between NC cells and at the trailing end of a leading cell were made *in vivo* (Supplementary Fig. 8e, f). A lack of PCP signalling led to a loss of Dsh accumulation in the cell contact (Supplementary Fig. 9). This membrane-localized Dsh is reminiscent of the foci described after activation of Dsh in mesodermal cells<sup>22</sup>. We also observed a redistribution of Wnt11 and the receptor Fz7 at cell–cell contacts *in vitro* (Fig. 4m, n) and *in vivo* (Supplementary Fig. 8g, and not

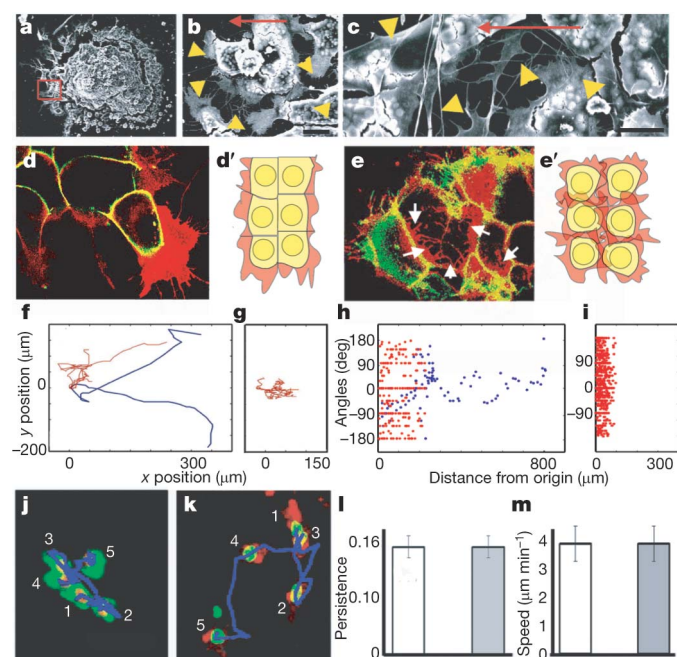


**Figure 3 | Effect of PCP signalling on cell contacts.** **a–c**, Scanning electron microscopy of *Xenopus* cultured NC expressing *DshDep*<sup>+</sup>. The red square indicates leading cells. Higher magnifications of other leading cells are shown in **b** and **c**. Arrowheads indicate cell protrusions; the arrow indicates the direction of migration. Scale bars, 25  $\mu$ m (**b**), 50  $\mu$ m (**c**). **d, e**, Two-plane confocal image to show cell protrusions (red) and cell shape (green). Cell protrusions are produced only at the border of the control explant (**d**), whereas they are observed between the *DshDep*<sup>+</sup> cells (arrows in **e**). **d'**, **e'**, Schematic representations of **d** and **e**, respectively. **f–i**, Analysis of tracks of migrating NC cells. Blue, leading cells; red, trailing cells. **f, g**, Tracks of control (**f**) and *DshDep*<sup>+</sup> (**g**) cells. **h, i**, Plots of distribution of angles of migration for leading (blue) and trailing (red) control (**h**) and *DshDep*<sup>+</sup> (**i**) cells against the distance from the origin. **j–m**, Analysis of migration of dissociated NC cells. **j, k**, Five frames taken every 10 min were overlapped for a control cell (**j**) and a *DshDep*<sup>+</sup> cell (**k**). Numbers indicate consecutive positions of the cell. The blue lines shows the tracks. **l, m**, Persistence (**l**) and speed of migration (**m**) were calculated for control (white bars) and *DshDep*<sup>+</sup> (grey bars) cells ( $P < 0.05$ ;  $n = 62$ ). Error bars show s.d.



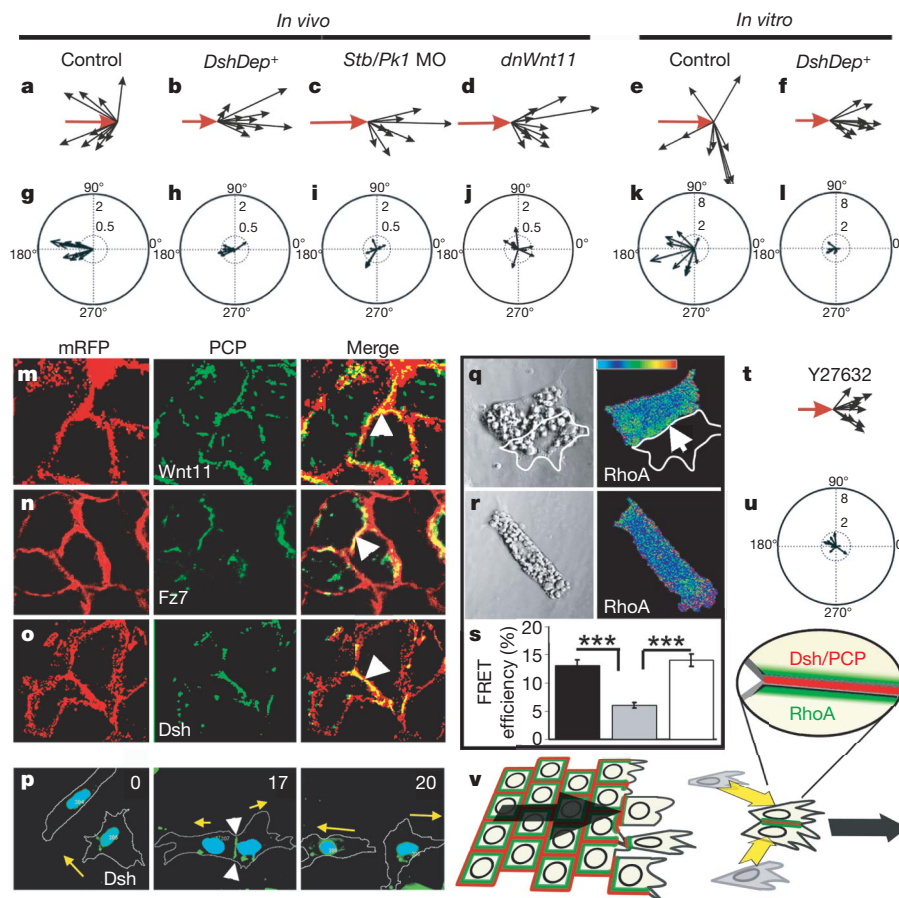


**Figure 4 | Contact inhibition of locomotion: requirement of PCP and RhoA activities.** **a–l**, Cell collisions were analysed *in vivo* (**a–d**, **g–j**) and *in vitro* (**e**, **f**, **k**, **l**). Velocities (**a–f**) and accelerations (**g–l**) were measured after the indicated treatments. MO, morpholino. The scales are the same for all panels. The change of velocity was significantly clustered in the controls ( $P < 0.005$ ,  $n = 10$ ). No significant change was observed in any of the PCP treatments ( $P \gg 0.05$ ,  $n = 10$  for all cases). **m–p**, Different PCP components are localized at the cell–cell contact (arrowheads). mRFP, membrane-RFP. **m**, Wnt11–YFP (yellow fluorescent protein). **n**, Fz7–YFP. **o**, Dsh–GFP. **p**, Cells expressing Dsh–GFP were analysed during a cell collision. The outline of the cell is taken from the differential interference contrast images. Time is shown in minutes. The arrow indicates the direction of migration;

the arrowhead indicates cell contact showing Dsh localization. **q–u**, Role of RhoA. **q–s**, FRET analysis of RhoA activity. **q**, Two NC cells in contact showing RhoA activity localized at the cell contact (arrow). **r**, Single NC cell. **s**, RhoA FRET efficiency. Black bar, cells in contact; grey bar, single cell; white bar, single cell in which PCP has been activated by the expression of Dsh $\Delta$ N. Three asterisks,  $P < 0.005$  ( $n = 12$  for each condition). Error bars show s.d. **t**, **u**, Cell collisions were analysed in the presence of the Rock inhibitor Y27632. **t**, Velocity vectors; **u**, acceleration vectors. No significant change in velocity was observed ( $P \gg 0.05$ ,  $n = 10$ ). **v**, Contact inhibition of locomotion is controlled by localization of PCP elements (red) and RhoA activity (green) at the cell contact, leading to directional migration (arrows).

shown); both became co-localized at the trailing end of the leading cell (Supplementary Fig. 8d). Our results suggest that cell–cell contacts polarize the cell by regulating the accumulation of ligands, receptors and intracellular element of the PCP signalling pathways.

It is well established that small GTPases are important in cell polarity and cell migration. One of them, RhoA, is a known downstream effector of PCP/Dsh during NC migration<sup>14</sup>. To examine a possible role for RhoA in contact inhibition of locomotion, we analysed the levels of RhoA activity in isolated and colliding cells by fluorescence resonance energy transfer (FRET). A significant increase in RhoA activity was detected during cell collision, with the highest activity in regions of cell–cell contact (Fig. 4q–s). When PCP signalling was activated in individual cells by expressing Dsh $\Delta$ N<sup>13,15</sup> a similar increase in RhoA activity was observed (Fig. 4s and Supplementary Fig. 10a–c). Finally, inhibition of Rock, a downstream target of RhoA, led to a complete loss of contact inhibition of locomotion (Fig. 4t, u, Supplementary Fig. 10d and Supplementary Movie 13). These results implicate RhoA as downstream effector of the PCP in contact inhibition of locomotion.

Although contact inhibition of locomotion was described for cultured cells more than 50 years ago<sup>1,2</sup>, we present the first evidence that it occurs *in vivo* and has a key function in the directional migration of

NC cells. We show that the PCP (non-canonical) Wnt pathway is involved in the process. The data are consistent with a model (Fig. 4v) in which cell–cell contact leads to the localized activation of the PCP signalling in the region of cell contact, which is required for the activation of RhoA. The localization of RhoA at the cell contact directs the collapse of cell protrusions and the change in cell polarity. It is commonly believed that directional cell migration during embryogenesis involves the localized production of molecules that attract migrating cells (chemotaxis)<sup>23–25</sup>. Although we do not rule out chemoattraction, we suggest that contact inhibition of locomotion could be sufficient for NC directional migration. This mechanism could also direct the coherent migration of groups of cells (for example mesoderm<sup>26</sup> or lateral line primordium<sup>27</sup>) and the efficient occupation by one cell population of another's territory during metastasis or development (including NC, angioblasts and neurons<sup>28,29</sup>). Most cells migrating *in vivo* maintain close proximity and move in groups. Accordingly, the inhibition of cell protrusions between these clustered cells is equivalent to the process of contact inhibition of locomotion. Their typical coherent directional migration is accomplished through a 'tip-toe' movement in which front cells can move only towards the NC-free zone; that is, forwards. This opens a little space where trailing cells move, and so on (Supplementary Fig. 1).

NC cells behave similarly to some cancer cells in that they display contact inhibition of locomotion towards like, but not towards unlike, cell types<sup>3,5–9</sup>. We propose that homotypic contact inhibition of locomotion confers cells with directionality during migration and that the lack of heterotypic contact inhibition allows them to invade other tissues.

## METHODS SUMMARY

*Xenopus* NC was labelled with nuclear-red fluorescent protein (RFP)/membrane-GFP or membrane-RFP/nuclear-GFP. *In vitro* analysis of NC migration was performed with *Xenopus* NCs cultured on fibronectin-coated plates. For *in vivo* studies we used *Xenopus* embryos grafted with labelled NC or zebrafish transgenic-line embryos expressing cytoplasm or membrane-GFP under the NC promoter *sox10*. Time-lapse photography was performed with differential interference contrast or fluorescent/confocal microscopy. FRET analysis was performed as described in ref. 14. Full methods are given in Supplementary Methods.

Received 17 July; accepted 19 September 2008.

Published online 10 December 2008.

- Abercrombie, M. & Heaysman, J. E. M. Observations on the social behaviour of cells in tissue culture. I. Speed of movement of chick heart fibroblasts in relation to their mutual contacts. *Exp. Cell Res.* **5**, 111–131 (1953).
- Abercrombie, M. & Heaysman, J. E. M. Observations on the social behaviour of cells in tissue culture: II. 'Monolayering' of fibroblasts. *Exp. Cell Res.* **6**, 293–306 (1954).
- Abercrombie, M. & Heaysman, J. E. Invasiveness of sarcoma cells. *Nature* **174**, 697–698 (1954).
- Paddock, S. W. & Dunn, G. A. Analysing collisions between fibroblasts and fibrosarcoma cells: fibrosarcoma cells show an active invasionary response. *J. Cell Sci.* **81**, 163–187 (1986).
- Abercrombie, M. Contact inhibition and malignancy. *Nature* **281**, 259–262 (1979).
- Hendrix, M. J. *et al.* Reprogramming metastatic tumour cells with embryonic microenvironments. *Nature Rev. Cancer* **7**, 246–255 (2007).
- Kulesa, P. M. *et al.* Reprogramming metastatic melanoma cells to assume a neural crest cell-like phenotype in an embryonic microenvironment. *Proc. Natl Acad. Sci. USA* **103**, 3752–3757 (2006).
- Kuriyama, S. & Mayor, R. Molecular analysis of neural crest migration. *Phil. Trans. R. Soc. B* **363**, 1349–1362 (2008).
- Heaysman, J. E. Non-reciprocal contact inhibition. *Experientia* **26**, 1344–1345 (1970).
- Davis, E. M. & Trinkaus, J. P. Significance of cell-to-cell contacts for the directional movement of neural crest cells within a hydrated collagen lattice. *J. Embryol. Exp. Morphol.* **63**, 29–51 (1981).
- Dunn, G. A. & Paddock, S. W. Analysing the motile behaviour of cells: a general approach with special reference to pairs of cells in collision. *Phil. Trans. R. Soc. Lond. B* **299**, 147–157 (1982).
- Carney, T. J. *et al.* A direct role for Sox10 in specification of neural crest-derived sensory neurons. *Development* **133**, 4619–4630 (2006).
- De Calisto, J. *et al.* Essential role of non-canonical Wnt signalling in neural crest migration. *Development* **132**, 2587–2597 (2005).
- Matthews, H. *et al.* Directional migration of neural crest cells in vivo is regulated by Syndecan-4/Rac1 and non-canonical Wnt signaling/RhoA. *Development* **135**, 1771–1780 (2008).
- Tada, M. & Smith, J. C. *Xwnt11* is a target of *Xenopus* Brachyury: regulation of gastrulation movements via Dishevelled, but not through the canonical Wnt pathway. *Development* **127**, 2227–2238 (2000).
- Park, M. & Moon, R. T. The planar cell-polarity gene *stbm* regulates cell behaviour and cell fate in vertebrate embryos. *Nature Cell Biol.* **4**, 20–25 (2002).
- Carreira-Barbosa, F. *et al.* Prickle 1 regulates cell movements during gastrulation and neuronal migration in zebrafish. *Development* **130**, 4037–4046 (2003).
- Garriock, R. J., D'Agostino, S. L., Pilcher, K. C. & Krieg, P. A. Wnt11-R, a protein closely related to mammalian Wnt11, is required for heart morphogenesis in *Xenopus*. *Dev. Biol.* **279**, 179–192 (2005).
- Matthews, H., Broders-Bondon, F., Thiery, J. P. & Mayor, R. *Wnt11r* is required for cranial neural crest migration. *Dev. Dyn.* **237**, 3404–3409 (2008).
- Axelrod, J. D. *et al.* Differential recruitment of Dishevelled provides signaling specificity in the planar cell polarity and Wingless signaling pathways. *Genes Dev.* **12**, 2610–2622 (1998).
- Alfandari, D. *et al.* Integrin  $\alpha 5 \beta 1$  supports the migration of *Xenopus* cranial neural crest on fibronectin. *Dev. Biol.* **260**, 449–464 (2003).
- Witzel, S. *et al.* Wnt11 controls cell contact persistence by local accumulation of Frizzled 7 at the plasma membrane. *J. Cell Biol.* **175**, 791–802 (2006).
- Condeelis, J., Singer, R. H. & Segall, J. E. The great escape: When cancer cells hijack the genes for chemotaxis and motility. *Annu. Rev. Cell Dev. Biol.* **21**, 695–718 (2005).
- Devreotes, P. N. & Zigmond, S. H. Chemotaxis in eukaryotic cells—a focus on leukocytes and *Dictyostelium*. *Annu. Rev. Cell Biol.* **4**, 649–686 (1988).
- Raz, E. Primordial germ-cell development: The zebrafish perspective. *Nature Rev. Genet.* **4**, 690–700 (2003).
- Keller, R. Cell migration during gastrulation. *Curr. Opin. Cell Biol.* **17**, 533–541 (2005).
- Lecaudey, V. & Gilmour, D. Organizing moving groups during morphogenesis. *Curr. Opin. Cell Biol.* **18**, 102–107 (2006).
- Risau, W. & Flamme, I. Vasculogenesis. *Annu. Rev. Cell Dev. Biol.* **11**, 73–91 (1995).
- Ayala, R., Shu, T. & Tsai, L. H. Trekking across the brain: the journey of neuronal migration. *Cell* **128**, 29–43 (2007).

**Supplementary Information** is linked to the online version of the paper at [www.nature.com/nature](http://www.nature.com/nature).

**Acknowledgements** We thank M. Tada, M. Tawak, J. Clarke, C.-P. Heisenberg, R. Kelsh, L. Dale and S. Fraser for reagents, constructs and fish lines; C. F. Riaz for scanning electron microscopy images; and M. Bronner-Fraser, M. Raff, J. Green and A. Ridley for comments on the manuscript. This study was supported by grants to R.M. from the Medical Research Council (MRC) and the Biotechnology and Biological Sciences Research Council. H.K.M. and C.C.-F. are MRC and Boehringer Ingelheim Fonds PhD scholarship holders, respectively, and M.M. is an EMBO postdoctoral fellow.

**Author Contributions** C.C.-F. and R.M. designed the experiments. C.C.-F., H.K.M. and R.M. performed most of the experiments. C.C.-F. and R.M. did the movie analysis. C.C.-F., G.A.D. and R.M. planned and performed the statistical analysis. M.P., S.K., C.C.-F., H.K.M. and R.M. conducted the FRET analysis. M.M. made some of the constructs and the zebrafish transgenic. M.M., C.C.-F., H.K.M. and R.M. performed the PCP localization experiments. C.C.-F., C.S. and R.M. wrote the paper.

**Author Information** Reprints and permissions information is available at [www.nature.com/reprints](http://www.nature.com/reprints). Correspondence and requests for materials should be addressed to R.M. ([r.mayor@ucl.ac.uk](mailto:r.mayor@ucl.ac.uk)).

## LETTERS

# Generation of cell polarity in plants links endocytosis, auxin distribution and cell fate decisions

Pankaj Dhonukshe<sup>1</sup>, Hirokazu Tanaka<sup>2\*</sup>, Tatsuaki Goh<sup>3\*</sup>, Kazuo Ebine<sup>3\*</sup>, Ari Pekka Mähönen<sup>1\*</sup>, Kalika Prasad<sup>1</sup>, Ikram Blilou<sup>1</sup>, Niko Geldner<sup>4,5</sup>, Jian Xu<sup>1</sup>, Tomohiro Uemura<sup>3</sup>, Joanne Chory<sup>5</sup>, Takashi Ueda<sup>3</sup>, Akihiko Nakano<sup>3,6</sup>, Ben Scheres<sup>1</sup> & Jiří Friml<sup>2</sup>

Dynamically polarized membrane proteins define different cell boundaries and have an important role in intercellular communication—a vital feature of multicellular development. Efflux carriers for the signalling molecule auxin from the PIN family<sup>1</sup> are landmarks of cell polarity in plants and have a crucial involvement in auxin distribution-dependent development including embryo patterning, organogenesis and tropisms<sup>2–7</sup>. Polar PIN localization determines the direction of intercellular auxin flow<sup>8</sup>, yet the mechanisms generating PIN polarity remain unclear. Here we identify an endocytosis-dependent mechanism of PIN polarity generation and analyse its developmental implications. Real-time PIN tracking showed that after synthesis, PINs are initially delivered to the plasma membrane in a non-polar manner and their polarity is established by subsequent endocytic recycling. Interference with PIN endocytosis either by auxin or by manipulation of the *Arabidopsis* Rab5 GTPase pathway prevents PIN polarization. Failure of PIN polarization transiently alters asymmetric auxin distribution during embryogenesis and increases the local auxin response in apical embryo regions. This results in ectopic expression of auxin pathway-associated root-forming master regulators in embryonic leaves and promotes homeotic transformation of leaves to roots. Our results indicate a two-step mechanism for the generation of PIN polar localization and the essential role of endocytosis in this process. It also highlights the link between endocytosis-dependent polarity of individual cells and auxin distribution-dependent cell fate establishment for multicellular patterning.

The plant signalling molecule auxin acts as a versatile trigger in many aspects of plant development and mediates different cellular responses on the basis of its graded distribution between cells. Establishment and maintenance of these auxin gradients requires local auxin biosynthesis<sup>9,10</sup> and directional cell-to-cell transport that depends on PIN auxin transporters<sup>11</sup>. PINs have a polar plasma membrane localization that determines the direction of intercellular auxin flow<sup>8</sup>. Thus, the mechanisms underlying PIN polarity belong to central aspects of auxin-mediated plant development. Polar PIN localization is dynamic; PIN proteins constitutively undergo cycles of clathrin-dependent endocytosis<sup>12</sup> and ARF-GEF (guanine-nucleotide exchange factors for ADP-ribosylation factor GTPases)-dependent recycling<sup>13</sup>. The role of this constitutive cycling is unclear but it might account for rapid changes in PIN polarity<sup>14</sup> in response to different cues such as gravity<sup>15</sup>. Also, PIN phosphorylation controlled by PINOID kinase/PP2A phosphatase<sup>16,17</sup> and membrane sterol

composition<sup>18</sup> are important components of polar PIN localization. However, it remains unresolved how PIN polarity is initially generated. In mammalian epithelia, segregation of membrane proteins into apical and basolateral plasma membrane domains is mainly achieved by polar exocytosis of newly synthesized proteins, or by non-polar exocytosis followed by endocytosis and polarized recycling<sup>19</sup>. Here we demonstrate an endocytosis-dependent mechanism for PIN polarity generation, and its importance for plant development.

To test the initial delivery of PINs to the plasma membrane, we photobleached pre-existing yellow fluorescent protein (YFP)-tagged PIN1 from a group of cells and analysed its recovery at the plasma membrane by *de novo* synthesis. This fluorescence recovery after photobleaching (FRAP) experiment showed an initial non-polar PIN1 localization followed by a gradual polarization of PIN1–YFP to the lower cell side (Fig. 1a, b). Using a complementary approach, we followed localization after conditional ectopic expression of PIN1. In inducible *XVE-PIN1* transgenic lines<sup>1</sup> 1 h after induction, PIN1 localizes strongly to intracellular compartments (presumably Golgi) and faintly throughout the plasma membrane in a non-polar manner. Over time, the intracellular PIN1 pool is reduced and non-polar PIN1 localization at the plasma membrane becomes stronger. About 3 h after induction PIN1 polarity is established showing predominant localization at the lower (basal) cell side (Fig. 1c). These observations suggest that, after *de novo* synthesis, PINs get targeted to the plasma membrane initially in a non-polar fashion and PIN polarity is generated in the subsequent step.

Next we tested the contribution of lateral diffusion within the plasma membrane for PIN polarity attainment. Locally photoconverted PIN2-EosFP displays limited lateral diffusion as compared to another plasma membrane-resident protein PIP2-EosFP, which shows much higher lateral diffusion (Supplementary Fig. 1). This suggests that lateral diffusion does not contribute considerably to asymmetric distribution of PINs at the plasma membrane. Therefore, we addressed the possibility that PIN polarity is generated from the original non-polar state by endocytic recycling (Fig. 1d). In this model, the inhibition of PIN endocytosis should interfere with PIN polarity generation. Auxin inhibits PIN internalization<sup>20</sup> and, accordingly, auxin treatment delays PIN1–YFP polarization after photobleaching (compare Fig. 1a, b and Supplementary Fig. 2a, b). Furthermore, endogenous or exogenously manipulated increases in cellular auxin levels correlate with decreased PIN polarity in corresponding cells (see Supplementary Information and Supplementary Fig. 2). These findings favour the hypothesis that after the original

<sup>1</sup>Department of Biology, Faculty of Science, Utrecht University, Padualaan 8, 3584 CH, Utrecht, The Netherlands. <sup>2</sup>Department of Plant Systems Biology, VIB, and Department of Molecular Genetics, Ghent University, Technologiepark 927, 9052 Gent, Belgium. <sup>3</sup>Department of Biological Sciences, Graduate School of Science, University of Tokyo, Bunkyo-ku, Tokyo 113-0033, Japan. <sup>4</sup>Department of Plant Molecular Biology (DBMV), University of Lausanne, UNIL-Sorge, Biophore Building, 1015 Lausanne, Switzerland. <sup>5</sup>Plant Biology Laboratory, The Salk Institute for Biological Studies, La Jolla, California 92037, USA. <sup>6</sup>Molecular Membrane Biology Laboratory, RIKEN Advanced Science Institute, Wako, Saitama 351-0198, Japan.

\*These authors contributed equally to this work.



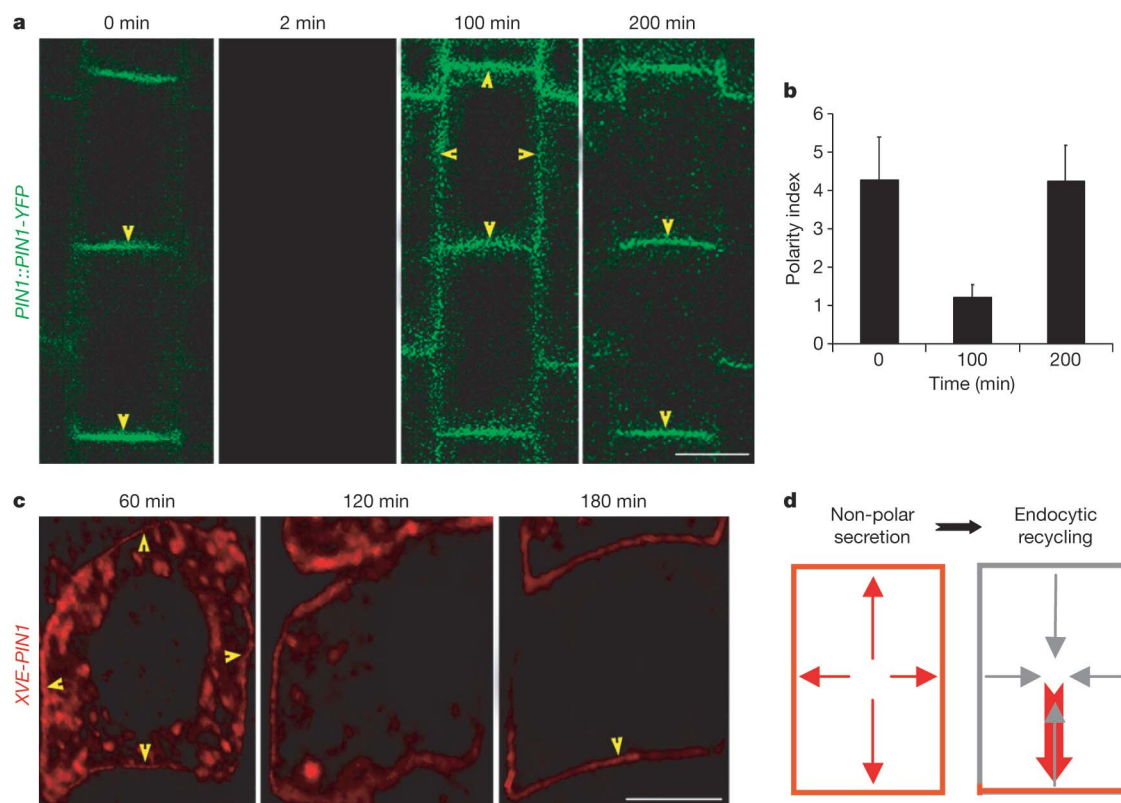


**Figure 1 | Endocytic recycling-based two-step mechanism generates PIN polarity.** **a**, Targeting of newly synthesized PIN1-YFP to the plasma membrane after its complete photobleaching. Note PIN1-YFP localization (yellow arrowheads) at the plasma membrane in a non-polar manner (third panel) before becoming polar (fourth panel). **b**, Quantitative polarity index (ratio of polar to lateral PIN1-YFP intensity) for FRAP experiments. Data are mean and s.d.;  $n = 15$ . **c**, Inducible overexpression of PIN1 in *XVE-PIN1* epidermal cells shows PIN1 localization (yellow arrowheads) in the

intracellular compartments and weak non-polar localization at the plasma membrane (first panel) after 1 h. At later time points, PIN1 shows gradually reduced intracellular signal and establishment of polar plasma membrane localization (third panel). **d**, A two-step mechanism for PIN polarity generation is shown. First, there is default non-polar secretion to the plasma membrane, followed by endocytic recycling establishing polarity. All are root cells. Scale bars are 5  $\mu\text{m}$ .

non-polar PIN targeting the polarity is generated by PIN internalization and subsequent recycling.

To investigate further the role of endocytosis in PIN polarity generation we sought to genetically interfere with endocytosis, allowing us to examine the so far elusive developmental role of this process in plants. An intensively studied Rab5 GTPase pathway has been shown to have a pivotal role for endocytosis in mammalian cells<sup>21</sup>. As two Rab5 homologues (namely Ara7 and Rha1) have been identified in *Arabidopsis* and localize to endosomes<sup>22</sup>, we characterized single and double *ara7* and *rha1* mutants, as well as mutants for their common activator Rab5-GEF AtVps9a. *ara7* and *rha1* do not have noticeable phenotypic defects, whereas the *ara7 rha1* double mutant is gametophytic lethal (data not shown). In addition, the full knockout of *AtVps9a* (*atvps9a-1*) is embryonic lethal and the partial loss-of-function allele (*atvps9a-2*) is viable and shows phenotypic aberrations (see Supplementary Information and Supplementary Fig. 3). We also used another strategy by exploiting *Arabidopsis* lines expressing a dominant negative Rab5 version (*DN-Ara7*) in which Rab5 is locked in its inactive state. Interference with the Rab5 pathway in *Arabidopsis* inhibited endocytosis (as monitored by an uptake of the fluorescent lipophilic dye FM4-64) without comparably influencing recycling or structure-dynamics of various subcellular compartments (see Supplementary Information and Supplementary Figs 4–7). Thus, the manipulation of the *Arabidopsis* Rab5 pathway provides a tool for investigating the role of endocytosis for diverse cellular and developmental processes in plants including its function in PIN polarity generation.

In *Arabidopsis* roots, PIN1 is localized preferentially at the basal (root tip-facing) side of stele cells<sup>23</sup> (Fig. 2a) and PIN2 is at the apical

(shoot tip-facing) side of epidermis cells (Fig. 2b) and located basally in young cortex cells (Fig. 2b)<sup>24</sup>. In *atvps9a-2* mutants, or after short-term (4 h) induction of *DN-Ara7* expression, PIN1 and PIN2 show less polar plasma membrane distribution (Fig. 2a–d). The effect of *DN-Ara7* on polar PIN2 localization is more pronounced in the cortex than in the epidermis (Fig. 2b; see also the insets for cortical PIN2 localization). After the ectopic expression of PIN1 in *XVE-PIN1* lines, freshly synthesized PIN1 arrives at the plasma membrane in a non-polar manner, in wild type (Fig. 1c) as well as after pre- and co-induction of *DN-Ara7* expression (Fig. 2e). However, whereas PIN1 subsequently polarizes in the wild type (Fig. 1c and 2e) it sustains its initial non-polar localization in *DN-Ara7* (Fig. 2e). Taking into account the fact that interference with the Rab5 pathway does not visibly influence PIN secretion or recycling, we conclude that Rab5-mediated endocytosis is required for acquisition of PIN polar localization. Furthermore, the mostly unaltered polar localization of another polar marker auxin influx carrier AUX1 (ref. 25) in *DN-Ara7* (Supplementary Fig. 8) suggests that there is a certain specificity of the Rab5-dependent endocytic mechanism for PIN polarization. This is consistent with previous findings that PIN and AUX1 use distinct polarity pathways<sup>26</sup>.

Next we assessed the developmental importance of Rab5-mediated endocytosis by analysing PIN polarity, auxin distribution and development in *DN-Ara7* and *atvps9a-1* embryos. In embryos expressing *DN-Ara7* under the control of a strong embryonic RPS5A promoter<sup>27</sup> and in *atvps9a-1* embryos PIN1 (Fig. 3a) and PIN4 (data not shown) lose their basal polar localization, resulting in a largely non-polar distribution. Because patterning during embryogenesis requires PIN-dependent asymmetric auxin distribution (auxin gradients)<sup>3</sup>, we next

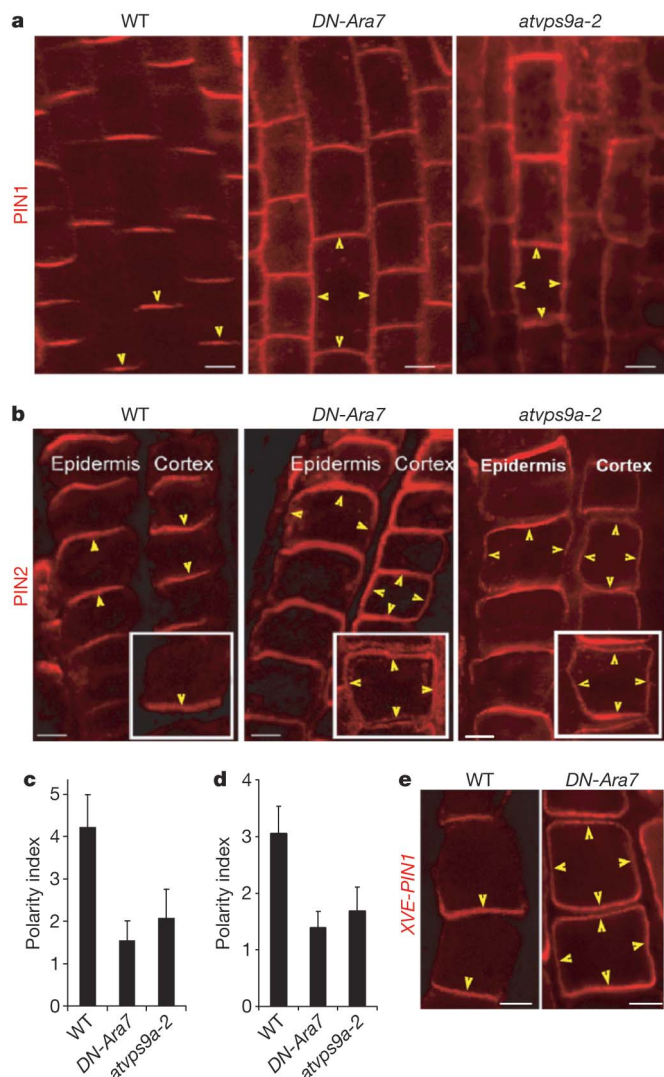


**Figure 2 | Rab5-mediated endocytosis is required for PIN polarization.** **a, b**, PIN1 (**a**) and PIN2 (**b**) polarity is defective in *DN-Ara7* and *atvps9a-2*. Note the polar localization of PINs in wild type (WT; left panels, yellow arrowheads) and their largely non-polar localization in *DN-Ara7* and *atvps9a-2* (middle and right panels, yellow arrowheads). **c, d**, Quantitative evaluation of PIN1 (**c**) and PIN2 (**d**) polarity defects. Data are mean and s.d.;  $n = 63$  and  $38$  (**c** and **d**, respectively). **e**, Post-induction (3 h) XVE-PIN1 localization in wild type and in *DN-Ara7*. Note that in wild type (WT) induced PIN1 becomes polar (left panel, yellow arrowheads), whereas in *DN-Ara7* seedlings it remains largely non-polar (right panel, yellow arrowheads). All are root cells. Scale bars are  $5\ \mu\text{m}$ .

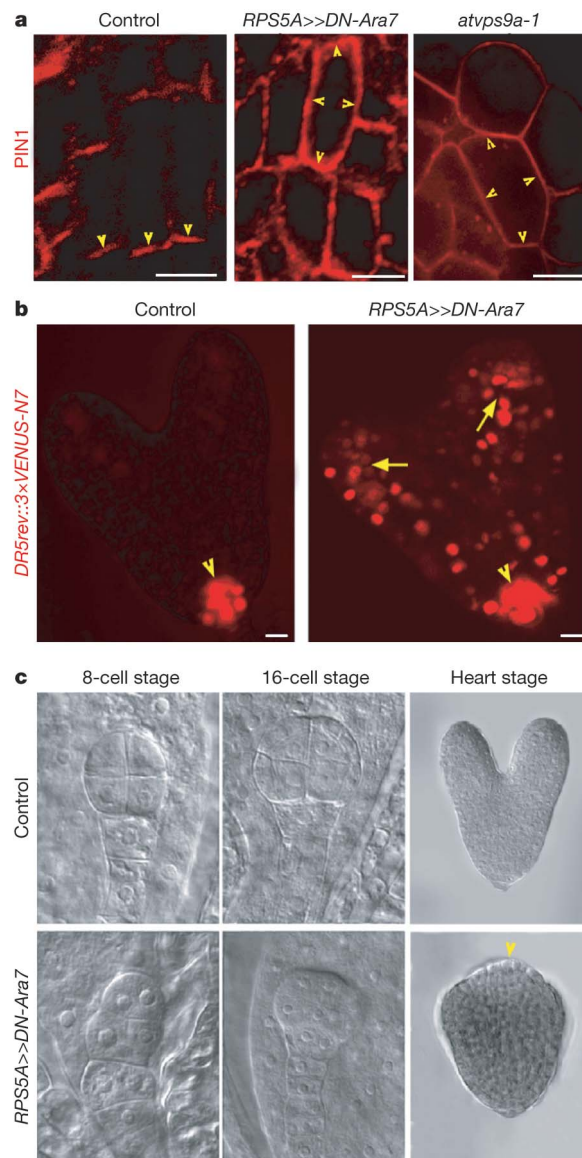


**Figure 3 | Manipulation of the Rab5 pathway during embryogenesis leads to defects in PIN polarity, auxin response distribution and embryo development.** **a**, PIN1 polarity (yellow arrowheads) defects in the heart-shaped embryos in *RPS5A>>DN-Ara7* and in the embryo-lethal *atvps9a-1* mutant as compared to control. Note that PIN1 is localized basally in control (left) and is largely non-polar in both *RPS5A>>DN-Ara7* (middle) and *atvps9a-1* (right) mutants. **b**, Distribution of auxin response (visualized by *DR5rev::3xVENUS-N7*) is altered in the *RPS5A>>DN-Ara7* heart-shaped embryo. Note pronounced DR5 maxima at the root pole in control (left panel, yellow arrowhead) and *RPS5A>>DN-Ara7* embryos and further strong DR5 maxima in cotyledons (right panel, yellow arrows) of *RPS5A>>DN-Ara7* embryos. **c**, Embryonic defects from the 8-cell stage up to the heart-shaped stage in *RPS5A>>DN-Ara7* as compared to control. Note apical embryonic defects (bottom right, yellow arrowhead) in *RPS5A>>DN-Ara7*. All are embryonic cells. Scale bars are  $10\ \mu\text{m}$ .

tested the consequences of PIN polarity defects for spatial distribution of auxin activity and for embryonic patterning. In controls, auxin activity as monitored by the auxin responsive reporter *DR5* shows its normal pattern<sup>3</sup> with strong maxima at the root pole and weaker maxima at the cotyledon tips (Fig. 3b). In contrast, in *atvps9a-1* (data not shown) or *RPS5A>>DN-Ara7* (Fig. 3b) embryos, the *DR5* maxima are less clearly defined with ectopically increased *DR5* activity in developing cotyledons. Analysis of embryo development showed that control embryos have typical developmental stage-specific phenotypes, whereas in *RPS5A>>DN-Ara7* embryos phenotypic abnormalities occur from octant stage onwards and they become more pertinent from the globular stage onwards (Fig. 3c and Supplementary Fig. 9). Typically, cell division planes are altered at the root pole, the cotyledons are occasionally fused and a new outgrowing structure appears in the apical region (Fig. 3c and Supplementary Fig. 9). Similar although less pronounced defects are also observed in *atvps9a-1* embryos (data

not shown). These results indicate that the failure of PIN polarization, resulting from the inhibition of Rab5-mediated endocytosis, leads to perturbation in asymmetric auxin distribution and embryo development.

We next analysed the postembryonic consequences of interference with the Rab5-mediated endocytosis. As the full *atvps9a* knockout is embryo lethal, we analysed the postembryonic development in *RPS5A>>DN-Ara7* seedlings. In parallel, to bypass the early embryonic development, we created RNA interference (RNAi)-based *AtVps9a* silencing lines under the control of the CaMV35S promoter



(Supplementary Fig. 12), which is only weakly active in early embryogenesis<sup>28</sup>. *RPS5A>>DN-Ara7* seedlings remain small compared to controls and show pronounced root and cotyledon defects (Fig. 4a). Notably, in approximately 15% of the seedlings (31 out of 200), cotyledons develop new, chlorophyll-free structures at their tips

(see inset in Fig. 4a and Supplementary Fig. 10). Morphologically these structures clearly differ from occasional cases of necrotic tissue and mostly resemble young root primordia. In rare cases these root-like structures emerging from the cotyledon tips develop further to form normally appearing growing roots (Fig. 4b). Similar although less frequent (17 out of 165 T<sub>1</sub> plants) developmental aberrations, including the ectopic appearance of root-like structures, were observed in *AtVps9a(RNAi)* (inset in Fig. 4a and Supplementary Fig. 12). In later development of both *RPS5A>>DN-Ara7* and *AtVps9a(RNAi)* seedlings, the cotyledon-derived, root-like structures terminally differentiate and these seedlings are not viable (data not shown).

To examine further the identity of the root-like structures, we analysed cell morphologies at scanning electron microscopy (SEM) resolution. Control cotyledons and hypocotyls show cells interspersed with stomata (Fig. 4c, d and Supplementary Fig. 10). In contrast, the root-like structures have distinct narrower rectangular epidermal cells devoid of stomata resembling root epidermis (Fig. 4d). In addition, transformed and growing root-like structures develop root hairs similar to the main root (Fig. 4b). Notably, molecular identity markers confirm the root identity of the root-like structures. We detected ectopic expression of root-specific quiescent cell marker QC25 (ref. 23) at the tips of *RPS5A>>DN-Ara7* cotyledons and also in seedlings that do not show morphologically distinguishable root-like structures (Supplementary Fig. 11). Furthermore, root-like structures in *AtVps9a(RNAi)* seedlings express the root-specific PIN2 protein<sup>7</sup> (Supplementary Fig. 12). Thus, both morphological and molecular markers confirm homeotic transformation of leaves to roots in seedlings perturbed for the Rab5 pathway.

Next we addressed the mechanism by which inhibition of the Rab5-dependent pathway can lead to transformation of organ identities. As the formation of root-like structures spatially coincides with elevated auxin response at cotyledons during embryogenesis, the most straightforward explanation is that this increased auxin response triggers a root-specific developmental programme. An obvious candidate for a mediator of such a change is one of the auxin response-dependent master regulators of root formation, the transcription factor PLT1 (ref. 29). Indeed, we detected strong, ectopic expression of PLT1 in postglobular *RPS5A>>DN-Ara7* embryos at positions of auxin maxima (Fig. 4e). The ectopic expression of other markers, such as root cap-specific PIN3 (ref. 15) and a root quiescent centre-specific WOX5 (ref. 30), is also detected at these positions in addition to their normal expression at the root pole (Fig. 4e). These data show that in *RPS5A>>DN-Ara7* and in *AtVps9a(RNAi)* lines cotyledon identity changes to root identity at positions of increased auxin response maxima during embryogenesis. It seems that timing is particularly important in this case. Although embryonic cells are still competent for such marked alterations in developmental programs, when we impaired the Rab5 pathway during post-germination development (in tamoxifen-inducible *DN-Ara7* lines) we failed to observe any organ identity aberrations although we did detect defects in other auxin-related processes such as root gravitropism and lateral root formation (Supplementary Fig. 13).

A plausible mechanism underlying the observed homeotic organ transformations is that defects in endocytosis cause failure of PIN polarization leading to ectopic auxin accumulation at the place of auxin synthesis in the cotyledons<sup>9,10</sup>, in which downstream PLT expression ultimately leads to transformation of cotyledon fates into root fates. It is surprising, however, that interference with Rab5-dependent endocytosis, which affects several plasma membrane-localized proteins (Supplementary Fig. 4), would show apparently specific auxin-related patterning defects. To more directly address the link between PIN polarity, auxin distribution and organ identity, we used *RPS5A::PIN1-GFP2* that shows strong expression and largely non-polar localization of PIN1-GFP2 in embryos (Supplementary Fig. 14). In wild-type *RPS5A::PIN1-GFP2* seedlings, the cotyledon-originated root-like structure phenotype was observed at lower

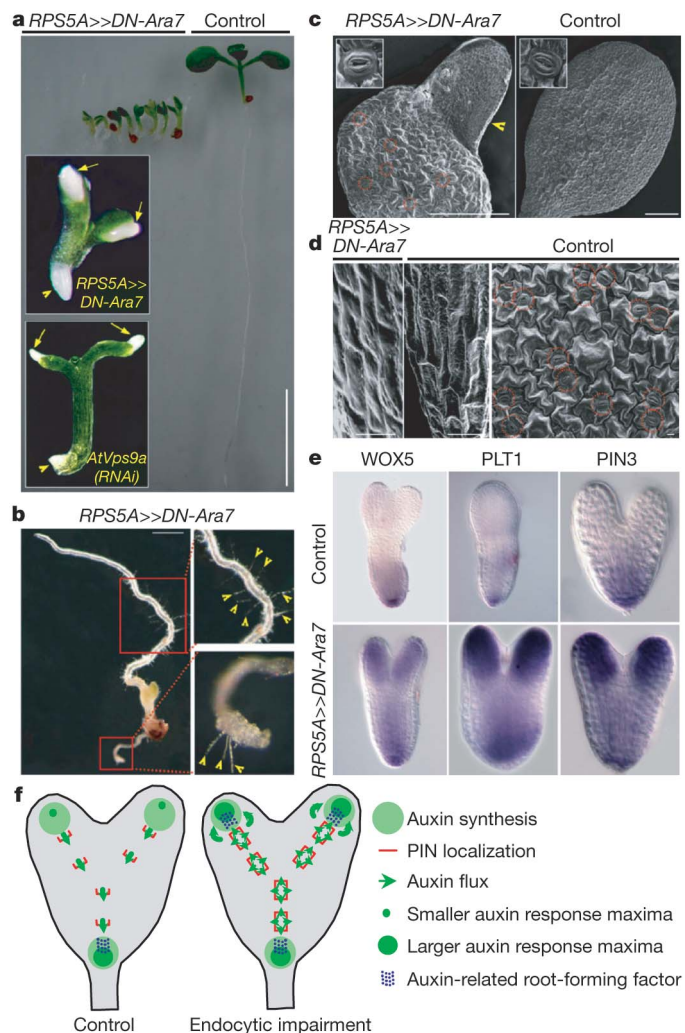


**Figure 4 | Manipulation of Rab5 pathway leads to homeotic leaf-to-root transformation.** **a**, Phenotypic comparison of 6-day-old control and *RPS5A>>DN-Ara7* seedlings. Insets show root-like structures emerging from the embryonic leaves (cotyledons) in *RPS5A>>DN-Ara7* and in *35S::AtVps9a(RNAi)* seedlings. Yellow arrows represent the root-like structures emerging from the embryonic leaves, whereas yellow arrowheads represent the main root. **b**, Two separate growing roots in *RPS5A>>DN-Ara7* 3-week-old seedling. One root emerges from the root pole and another from the position of cotyledon. Note that both roots have root hairs (root-specific epidermal structures highlighted by yellow arrowheads). **c**, **d**, SEM analysis of *RPS5A>>DN-Ara7* and control cotyledons. Stomata, a non-root cell type (red dotted circles, enlarged in insets) are absent from the root-like structure (yellow arrowhead, **c**). Epidermal cells of root-like structure (left panel, **d**), with narrow rectangular cell files, are clearly distinct from cotyledon pavement cells of control (right panel, **d**) and resemble main root epidermal cells of control (middle panel, **d**). **e**, *In situ* hybridization reveals ectopic expression of the root-specific transcription factor PLT1 and the root meristem-identity markers WOX5 and PIN3 in cotyledons of *RPS5A>>DN-Ara7* heart-stage embryos. Note that expression of these markers is restricted to the root pole of control embryos. **f**, A schematic representation depicting enhanced auxin response maxima at the cotyledon regions resulted from non-polar PIN localization. This increased auxin response at the cotyledon regions leads to expression of auxin-induced root-forming regulators and triggers cell fate changes resulting in homeotic leaf-to-root transformation. Scale bars: 4 mm (**a**), 1 mm (**b**), 250  $\mu$ m (**c**) and 10  $\mu$ m (**d**).



frequency (4 out of 129 in the  $T_2$  generation). However, in multiple *pin* mutant background (*pin 1<sup>+/-</sup> 2347<sup>+/-</sup>*), with limited extent of endogenous polarized PINs, this homeotic transformation was already detected in the  $T_1$  generation at markedly increased frequency (23 out of 26; Supplementary Fig. 14). Furthermore, as observed in *RPS5A*  $\gg$  *DN-Ara7* embryos (Fig. 3b), *RPS5A::PIN1-GFP2* embryos showed increased auxin response at cotyledon regions apparently marking the positions of later-emerging root structures (Supplementary Fig. 14). These results strongly indicate that the homeotic leaf-to-root transformation in Rab5-defective plants can be largely attributed to the failure of PIN polarization and to the resulting changes in auxin distribution. Our data further highlight the important role of endocytosis in PIN polarization and its connection to auxin-dependent establishment of cell fates for plant patterning.

Our studies suggest an endocytosis-dependent, two-step mechanism for PIN polarity generation. We show that PINs are first targeted to the plasma membrane without apparent asymmetry, and they then attain polarity by subsequent endocytic recycling. The endocytic step is crucial for the polarity establishment because interference with PIN internalization, for example by increasing auxin amounts or interfering with the Rab5-based endocytic pathway, sustains initial non-polar PIN localization leading to polarity defects. The failure of PIN polarization during embryogenesis apparently disrupts auxin flow from developing cotyledons to the root pole, and consequently auxin levels here increase from auxin production, leading to the establishment of ectopic auxin response maxima at cotyledon positions. Embryonic cells are competent at this stage to interpret the increased auxin response as a positional signal for root formation and accordingly they express the root fate-promoting transcription factor PLT1 that sets up the initiation of roots at the positions of embryonic leaves (Fig. 4f). These results demonstrate important cellular and developmental roles for endocytosis in plants and highlight the morphogenetic features of transport-dependent auxin distribution in plant patterning processes.

## METHODS SUMMARY

**Materials and growth conditions.** *Arabidopsis* seedlings (Columbia ecotype) were grown on vertical 0.5 MS agar plates at 25 °C. FM4-64, BFA (both Molecular Probes), tamoxifen and estradiol (both Sigma) were used from dimethylsulphoxide stock solutions (1 mM for FM4-64, 50 mM for BFA, 3 mM for tamoxifen and 1 mM for estradiol) and added (at 1:1,000 dilution) either to the liquid 0.5 MS growth medium or to the 0.5 MS growth medium plates for the indicated periods of time.

**Immunodetection.** Immunofluorescence analysis in *Arabidopsis* roots was carried out as described previously<sup>12</sup>.

**Embryo and *in situ* analysis.** Embryo and *in situ* analysis was performed as described previously<sup>3,24</sup>.

**Microscopy.** For SEM, seedlings were fixed, dehydrated and then critical point dried. The dried seedlings were mounted onto stubs, sputter coated with platinum and then viewed in a Joel JSM-5310 LV microscope. Live cell microscopy, FRAP analysis and EosFP green-to-red photoconversion analysis were performed as described previously<sup>12</sup>.

**Full Methods** and any associated references are available in the online version of the paper at [www.nature.com/nature](http://www.nature.com/nature).

Received 11 June; accepted 4 September 2008.

Published online 26 October 2008.

1. Petrasek, J. *et al.* PIN proteins perform a rate-limiting function in cellular auxin efflux. *Science* **312**, 914–918 (2006).
2. Galweiler, L. *et al.* Regulation of polar auxin transport by AtPIN1 in *Arabidopsis* vascular tissue. *Science* **282**, 2226–2230 (1998).
3. Friml, J. *et al.* Efflux-dependent auxin gradients establish the apical-basal axis of *Arabidopsis*. *Nature* **426**, 147–153 (2003).
4. Benkova, E. *et al.* Local, efflux-dependent auxin gradients as a common module for plant organ formation. *Cell* **115**, 591–602 (2003).
5. Reinhardt, D. *et al.* Regulation of phyllotaxis by polar auxin transport. *Nature* **426**, 255–260 (2003).

6. Heisler, M. G. *et al.* Patterns of auxin transport and gene expression during primordium development revealed by live imaging of the *Arabidopsis* inflorescence meristem. *Curr. Biol.* **15**, 1899–1911 (2005).
7. Luschig, C., Gaxiola, R. A., Grisafi, P. & Fink, G. R. EIR1, a root-specific protein involved in auxin transport, is required for gravitropism in *Arabidopsis thaliana*. *Genes Dev.* **12**, 2175–2187 (1998).
8. Wisniewska, J. *et al.* Polar PIN localization directs auxin flow in plants. *Science* **312**, 883 (2006).
9. Stepanova, A. N. *et al.* TAA1-mediated auxin biosynthesis is essential for hormone crosstalk and plant development. *Cell* **133**, 177–191 (2008).
10. Zhao, Y. The role of local biosynthesis of auxin and cytokinin in plant development. *Curr. Opin. Plant Biol.* **11**, 16–22 (2008).
11. Tanaka, H., Dhonukshe, P., Brewer, P. B. & Friml, J. Spatiotemporal asymmetric auxin distribution: a means to coordinate plant development. *Cell. Mol. Life Sci.* **63**, 2738–2754 (2006).
12. Dhonukshe, P. *et al.* Clathrin-mediated constitutive endocytosis of PIN auxin efflux carriers in *Arabidopsis*. *Curr. Biol.* **17**, 520–527 (2007).
13. Geldner, N., Friml, J., Stierhof, Y. D., Jurgens, G. & Palme, K. Auxin transport inhibitors block PIN1 cycling and vesicle trafficking. *Nature* **413**, 425–428 (2001).
14. Kleine-Vehn, J. *et al.* ARF GEF-dependent transcytosis and polar delivery of PIN auxin carriers in *Arabidopsis*. *Curr. Biol.* **18**, 526–531 (2008).
15. Friml, J., Wisniewska, J., Benkova, E., Mendgen, K. & Palme, K. Lateral relocation of auxin efflux regulator PIN3 mediates tropism in *Arabidopsis*. *Nature* **415**, 806–809 (2002).
16. Friml, J. *et al.* A PINOID-dependent binary switch in apical-basal PIN polar targeting directs auxin efflux. *Science* **306**, 862–865 (2004).
17. Michniewicz, M. *et al.* Antagonistic regulation of PIN phosphorylation by PP2A and PINOID directs auxin flux. *Cell* **130**, 1044–1056 (2007).
18. Men, S. *et al.* Sterol-dependent endocytosis mediates post-cytokinetic acquisition of PIN2 auxin efflux carrier polarity. *Nature Cell Biol.* **10**, 237–244 (2008).
19. Mostov, K., Su, T. & ter Beest, M. Polarized epithelial membrane traffic: conservation and plasticity. *Nature Cell Biol.* **5**, 287–293 (2003).
20. Paciorek, T. *et al.* Auxin inhibits endocytosis and promotes its own efflux from cells. *Nature* **435**, 1251–1256 (2005).
21. Bucci, C. *et al.* The small GTPase rab5 functions as a regulatory factor in the early endocytic pathway. *Cell* **70**, 715–728 (1992).
22. Ueda, T., Uemura, T., Sato, M. H. & Nakano, A. Functional differentiation of endosomes in *Arabidopsis* cells. *Plant J.* **40**, 783–789 (2004).
23. Friml, J. *et al.* AtPIN4 mediates sink-driven auxin gradients and root patterning in *Arabidopsis*. *Cell* **108**, 661–673 (2002).
24. Blilou, I. *et al.* The PIN auxin efflux facilitator network controls growth and patterning in *Arabidopsis* roots. *Nature* **433**, 39–44 (2005).
25. Swarup, R. *et al.* Localization of the auxin permease AUX1 suggests two functionally distinct hormone transport pathways operate in the *Arabidopsis* root apex. *Genes Dev.* **15**, 2648–2653 (2001).
26. Kleine-Vehn, J., Dhonukshe, P., Swarup, R., Bennett, M. & Friml, J. Subcellular trafficking of the *Arabidopsis* auxin influx carrier AUX1 uses a novel pathway distinct from PIN1. *Plant Cell* **18**, 3171–3181 (2006).
27. Weijers, D. *et al.* An *Arabidopsis* Minute-like phenotype caused by a semi-dominant mutation in a RIBOSOMAL PROTEIN S5 gene. *Development* **128**, 4289–4299 (2001).
28. Benfey, P. N. & Chua, N. H. The cauliflower mosaic virus 35S promoter: combinatorial regulation of transcription in plants. *Science* **250**, 959–966 (1990).
29. Aida, M. *et al.* The PLETHORA genes mediate patterning of the *Arabidopsis* root stem cell niche. *Cell* **119**, 109–120 (2004).
30. Sarkar, A. K. *et al.* Conserved factors regulate signalling in *Arabidopsis thaliana* shoot and root stem cell organizers. *Nature* **446**, 811–814 (2007).

**Supplementary Information** is linked to the online version of the paper at [www.nature.com/nature](http://www.nature.com/nature).

**Acknowledgements** We thank M. Bennett, T. Gaude, L. Jiang, G. Jürgens, C. Luschig, E. Meywerowitz, W. Michalke, R. Offringa, D. Robinson, K. Schumacher, J. Wiedenmann and D. Weijers for sharing published material and RIKEN, SALK and NASC *Arabidopsis* stock centres for providing mutant lines and the RNAi construct. We thank W. Muller for assistance with SEM and F. Kindt and R. Leito for photography. We acknowledge the Center for Plant Molecular Biology (ZMBP), University of Tübingen, Germany for the facilities during the initial phase of the project. This work was supported by VolkswagenStiftung (P.D. and J.F.), EMBO Long Term Fellowship and Netherlands Organization for Scientific Research (NWO)-VENI grant (P.D.), EMBO Young Investigator Program and Odysseus program of FWO (J.F.), HFSP fellowship (H.T.), EMBO Long Term Fellowship and HFSP fellowship (A.P.M.), EMBO Long Term Fellowship (K.P.), NWO-VIDI grant (I.B.), HFSP fellowship and Swiss National Science Foundation (N.G.), HHMI, USDA and NIH (J.C.), NWO-Spinoza award (B.S.) and Grants-in-Aid for Scientific Research from the Ministry of Education, Culture, Sports, Science and Technology of Japan (T.U. and A.N.).

**Author Information** Reprints and permissions information is available at [www.nature.com/reprints](http://www.nature.com/reprints). Correspondence and requests for materials should be addressed to P.D. (P.B.Dhonukshe@uu.nl) or J.F. (jiri.friml@psb.ugent.be).

## METHODS

**Cloning details and *Arabidopsis* transgenic lines.** A 6.1 kb genomic fragment of *AtVps9a* containing promoter, exons, introns and the 3'-flanking region was fused to *GFP* to have a carboxy-terminal *GFP*-fusion which was used for complementation and localization analyses. The complemented line was again transformed with *mRFP-ARA7* and used for colocalization analysis. Construction of *DN-Ara7* by site-directed mutagenesis of wild-type *Ara7* (by replacing S24N) has been described before<sup>31</sup>. For transactivation approach *DN-Ara7* was cloned under the *UAS* promoter and transferred to binary vector *pGreenII* that was used for transformation. The *AtVps9a(RNAi)* construct was obtained from the NASC *Arabidopsis* stock centre. *GFP* complementary DNA was fused to the genomic fragment of *SYP43* containing promoter (2,039 base pairs (bp)), exons, introns and the 3'-flanking region (782 bp) to have an amino-terminal *GFP*-fusion. This chimaeric construct was transformed into the *syd43* mutant line in which the T-DNA is inserted at the second intron and also in *atvps9a-2*. For cloning *RPS5A::PIN1-GFP2*, the *RPS5A* promoter was amplified from a recombinant construct *pGII/K RPS5A t-NOS*<sup>27</sup> and *PIN1-GFP2* was amplified from a *pG2NBL-PIN1::PIN-EGFP* plasmid<sup>32</sup>. *RPS5A::PIN1-GFP2* was then introduced into *pGreenII* binary vector using Multisite Gateway technology (Invitrogen). The root cap-specific *PIN2-EGFP* line was generated from *PIN2::PIN2-EGFP*<sup>33</sup>, by cloning the *PIN2-EGFP* fusion (from ATG to the stop codon) into *pGREENII-0229* between a 3.3 kilobase (kb) promoter fragment of the *At1g79580* gene and the *NOS* terminator. Construction of *PIP2-EosFP* has been described earlier<sup>12</sup>.

The following mutant and transgenic *Arabidopsis* lines have been described previously: *PIN1-YFP*<sup>32</sup>, *PIN2-GFP*<sup>32</sup>, *RPS5A* activator<sup>27</sup>, *pINTAM* activator<sup>16</sup>, *XVE-PIN1* (ref. 1), *PIN2-EosFP*<sup>12</sup>, *DR5rev::ER-GFP*<sup>3</sup>, *DR5rev::3×VENUS-N7* (ref. 6), *VPS29-RFP*<sup>34</sup>, *SNX1-RFP*<sup>34</sup>, *GNOM-Myc*<sup>35</sup>, *GNL1-YFP*<sup>36</sup>, *VHAa1-RFP*<sup>37</sup>, *AUX1-YFP*<sup>38</sup>, *QC25-GUS*<sup>39</sup> and *pin*<sup>+/-</sup>12347<sup>+/-</sup> (ref. 24). Isolation and the initial characterization of *atvps9a* mutants is described elsewhere<sup>40</sup>. *ara7* (WiscDsLox355B06), *rha1* (SAIL\_596-A03) and *syd43* (SALK\_144268) are obtained from the ABRC.

Construction of fusion proteins and *Arabidopsis* transgenic lines for *NPSN12-YFP*, *PIP1-YFP*, *NIP1-YFP*, *RabA5d-YFP*, *SYP32-YFP*, *RabD2B-YFP*, *RabG3f-YFP* and *VAMP711-YFP* will be described elsewhere (N.G. and J.C., unpublished observations). Information on these lines is available at [http://www.unil.ch/dbmv/page49637\\_en.html](http://www.unil.ch/dbmv/page49637_en.html). These lines were crossed with *pINTAM* *DN-Ara7* line for analysing effect of *DN-Ara7* on localization and BFA sensitivity of these markers. Sequences of the primers used are mentioned in Supplementary Table 1.

**Immunodetection.** The following antibodies were used: anti-PIN1 (1:400)<sup>3</sup>, anti-PIN2 (1:1,000)<sup>41</sup>, anti-PIN4 (1:400)<sup>23</sup>, anti-SCAMP1 (1:200)<sup>42</sup>, anti-plasma-membrane-ATPase (1:1,000)<sup>43</sup>, anti- $\gamma$ -COP (1:1,000)<sup>44</sup> and anti-GFP (1:400). Fluorochrome-conjugated secondary antibodies (Dianova) were used at the following concentrations: anti rabbit-FITC (1:300); anti-rabbit-Cy3 (1:500) and anti-mouse-FITC (1:300). The same microscope settings were used

for different experiments and pixel intensities were taken into account when comparing the images. All experiments were performed at least three times using at least 20 roots on each occasion.

**Quantification of PIN polarity.** The mean fluorescence intensity of the PIN signal at the lateral and polar sides of cells was measured using the quantification tool of Leica confocal software (LCS Lite Version 2.61). This tool provides the opportunity to draw lines on the lateral or polar cell side. It also enables the value of mean pixel intensity of the area covered by the drawn line to be obtained. Using this procedure, the mean pixel intensities from the polar and lateral cell sides of individual cells were obtained. They were then used to determine the polarity index—the ratio of PIN intensity at polar versus lateral sides. The mean and s.d. of the polarity index were determined for the number of samples analysed for the condition tested.

31. Dhonukshe, P. *et al.* Endocytosis of cell surface material mediates cell plate formation during plant cytokinesis. *Dev. Cell* **10**, 137–150 (2006).
32. Xu, J. *et al.* A molecular framework for plant regeneration. *Science* **311**, 385–388 (2006).
33. Xu, J. & Scheres, B. Dissection of *Arabidopsis* ADP-RIBOSYLATION FACTOR 1 function in epidermal cell polarity. *Plant Cell* **17**, 525–536 (2005).
34. Jaillais, Y. *et al.* The retromer protein VPS29 links cell polarity and organ initiation in plants. *Cell* **130**, 1057–1070 (2007).
35. Geldner, N. *et al.* The *Arabidopsis* GNOM ARF-GEF mediates endosomal recycling, auxin transport, and auxin-dependent plant growth. *Cell* **112**, 219–230 (2003).
36. Richter, S. *et al.* Functional diversification of closely related ARF-GEFs in protein secretion and recycling. *Nature* **448**, 488–492 (2007).
37. Dettmer, J., Hong-Hermesdorf, A., Stierhof, Y. D. & Schumacher, K. Vacuolar H<sup>+</sup>-ATPase activity is required for endocytic and secretory trafficking in *Arabidopsis*. *Plant Cell* **18**, 715–730 (2006).
38. Swarup, R. *et al.* Structure-function analysis of the presumptive *Arabidopsis* auxin permease AUX1. *Plant Cell* **16**, 3069–3083 (2004).
39. Sabatini, S. *et al.* An auxin-dependent distal organizer of pattern and polarity in the *Arabidopsis* root. *Cell* **99**, 463–472 (1999).
40. Goh, T. *et al.* VPS9a, the common activator for two distinct types of Rab5 GTPases, is essential for the development of *Arabidopsis thaliana*. *Plant Cell* **19**, 3504–3515 (2007).
41. Abas, L. *et al.* Intracellular trafficking and proteolysis of the *Arabidopsis* auxin-efflux facilitator PIN2 are involved in root gravitropism. *Nature Cell Biol.* **8**, 249–256 (2006).
42. Lam, S. K. *et al.* Rice SCAMP1 defines clathrin-coated, trans-golgi-located tubular-vesicular structures as an early endosome in tobacco BY-2 cells. *Plant Cell* **19**, 296–319 (2007).
43. Langhans, M. *et al.* Immunolocalization of plasma-membrane H<sup>+</sup>-ATPase and tonoplast-type pyrophosphatase in the plasma membrane of the sieve element-companion cell complex in the stem of *Ricinus communis* L. *Planta* **213**, 11–19 (2001).
44. Movafeghi, A., Happel, N., Pimpl, P., Tai, G. H. & Robinson, D. G. *Arabidopsis* Sec21p and Sec23p homologs. Probable coat proteins of plant COP-coated vesicles. *Plant Physiol.* **119**, 1437–1446 (1999).

# G protein $G\alpha_i$ functions immediately downstream of Smoothed in Hedgehog signalling

Stacey K. Ogden<sup>1</sup>, Dennis Liang Fei<sup>1</sup>, Neal S. Schilling<sup>1</sup>, Yashi F. Ahmed<sup>2,4</sup>, John Hwa<sup>1,3</sup> & David J. Robbins<sup>1,4</sup>

The hedgehog (Hh) signalling pathway has an evolutionarily conserved role in patterning fields of cells during metazoan development, and is inappropriately activated in cancer<sup>1,2</sup>. Hh pathway activity is absolutely dependent on signalling by the seven-transmembrane protein smoothed (Smo), which is regulated by the Hh receptor patched (Ptc). Smo signals to an intracellular multi-protein complex containing the Kinesin related protein Costal2 (Cos2), the protein kinase Fused (Fu) and the transcription factor Cubitus interruptus (Ci)<sup>3</sup>. In the absence of Hh, this complex regulates the cleavage of full-length Ci to a truncated repressor protein, Ci<sub>75</sub>, in a process that is dependent on the proteasome and priming phosphorylations by Protein kinase A (PKA)<sup>4</sup>. Binding of Hh to Ptc blocks Ptc-mediated Smo inhibition, allowing Smo to signal to the intracellular components to attenuate Ci cleavage. Because of its homology with the Frizzled family of G-protein-coupled receptors (GPCR)<sup>5</sup>, a likely candidate for an immediate Smo effector would be a heterotrimeric G protein. However, the role that G proteins may have in Hh signal transduction is unclear and quite controversial<sup>6–10</sup>, which has led to widespread speculation that Smo signals through a variety of novel G-protein-independent mechanisms. Here we present *in vitro* and *in vivo* evidence in *Drosophila* that Smo activates a G protein to modulate intracellular cyclic AMP levels in response to Hh. Our results demonstrate that Smo functions as a canonical GPCR, which signals through  $G\alpha_i$  to regulate Hh pathway activation.

To examine whether a G protein is involved in Hh signalling, we targeted a series of G proteins by double-stranded RNA (dsRNA)-mediated knockdown. *Drosophila* clone-8 (Cl8) cells were treated with control or  $G\alpha$ -subunit-specific dsRNA and assayed for changes in Hh-mediated induction of a *ptc-luciferase* reporter construct<sup>11</sup>. Whereas  $G\alpha_s$  (also called *G-sz60A*) and  $G\alpha_o$  (also called *G-ox47A*) dsRNAs do not significantly alter Hh-induced reporter activation (Supplementary Fig. 1a, b),  $G\alpha_i$  knockdown is able to trigger a decrease in Hh-dependent reporter gene expression (Fig. 1a). Although not as effective as Smo knockdown in silencing Hh reporter gene activation (Supplementary Fig. 1c),  $G\alpha_i$  (also called *G-ix65A*) dsRNA specific to the coding sequence, or 3' untranslated region (UTR), reduces Hh-induced reporter activity by approximately 70% (Fig. 1a), supporting a role for  $G\alpha_i$  in the Hh pathway. To confirm the specificity of  $G\alpha_i$  dsRNA effects, we established the functional IC<sub>50</sub> of  $G\alpha_i$  3' UTR dsRNA (Supplementary Fig. 1e), then attempted to rescue reporter activity through ectopic expression of wild-type  $G\alpha_i$  or constitutively active  $G\alpha_i^{Q205L}$ . Hh-stimulated reporter activity can be restored by both wild-type and constitutively active  $G\alpha_i$  (Fig. 1b), confirming the specificity of our  $G\alpha_i$  dsRNA-mediated effects. Western blot analyses of Cl8 lysates reveal that cells treated with  $G\alpha_i$  dsRNA show attenuated stabilization of Ci (Fig. 1c, compare lanes 2 and 4) and decreased Fu phosphorylation (Supplementary Fig. 1d, compare lanes 2 and 4) in response to Hh.

Hh-induced Smo phosphorylation is maintained in the presence of  $G\alpha_i$  dsRNA (Fig. 1c, arrow), suggesting that  $G\alpha_i$  functions downstream of Smo and upstream of Fu and Ci.

To determine whether  $G\alpha_i$  can modulate Hh pathway activity *in vivo*,  $G\alpha_i$  constructs were expressed in wing imaginal discs using

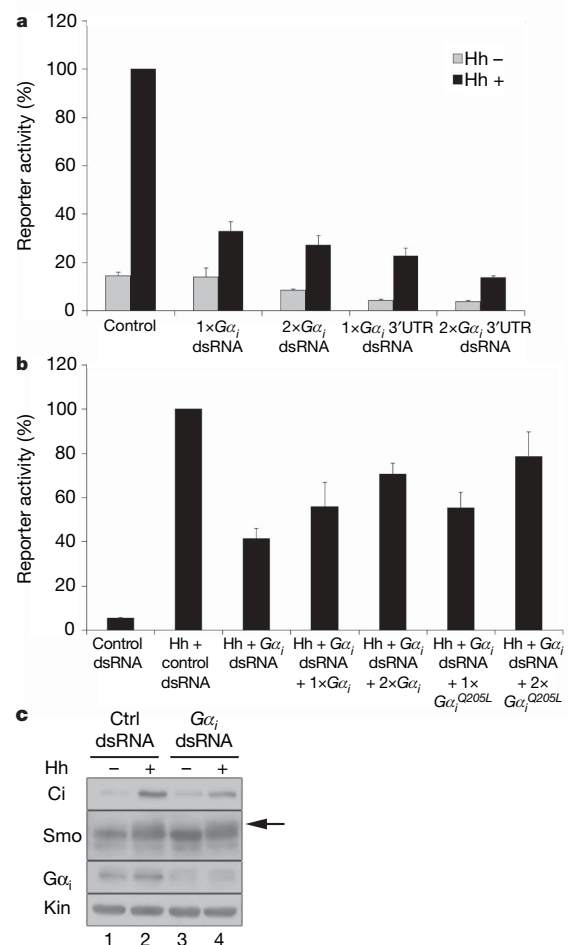


**Figure 1 |  $G\alpha_i$  is required for Hh signalling.** **a, b**, Cl8 cells were transfected with *ptc-luciferase*, *act-renilla*, *hh* expression vector or empty vector control, and the indicated dsRNA and/or  $G\alpha_i$  expression vectors. Percentage reporter expression relative to maximal Hh activity for control dsRNA is shown. Error bars indicate s.e.m. **c**, Cl8 cells were transfected with control or  $G\alpha_i$  dsRNA and *hh* expression vector or empty vector control. Cell lysates were analysed by immunoblotting with the indicated antibodies. The arrow marks the phosphorylation-induced mobility shift. Kinesin (Kin) serves as a loading control.

<sup>1</sup>Department of Pharmacology and Toxicology, <sup>2</sup>Department of Genetics, <sup>3</sup>Department of Medicine (Cardiology), Dartmouth Medical School, Hanover, New Hampshire 03755, USA. <sup>4</sup>Norris Cotton Cancer Center, Dartmouth Medical School, Lebanon, New Hampshire 03756, USA.



*MS1096-Gal4* or *C765-Gal4*. Expression of an inactive  $G\alpha_i$  mutant ( $G\alpha_i^{G204A}$ ) or wild-type  $G\alpha_i$  has little effect on wing vein patterning (Fig. 2a–c). However, expression of constitutively active  $G\alpha_i^{Q205L}$  (ref. 12) results in widening of longitudinal vein LV3–LV4 spacing and ectopic vein material on LV2 and LV3 (Fig. 2, compare panels d and a–c). The severity of this phenotype is dose-dependent, as higher-level expression of *UAS-G $\alpha_i^{Q205L}$*  triggers more severe ectopic vein material anterior to LV3, and further widening of LV3–LV4 spacing (Fig. 2e). Expression of  $G\alpha_i^{Q205L}$  in wing imaginal discs also results in over-growth of the wing pouch, along with expansion of full-length Ci (left panel of Fig. 2g, arrow, compared to left panel of Fig. 2f, no driver). This Ci expansion triggers ectopic expression of the Hh target gene *decapentaplegic* (*dpp*)<sup>13,14</sup> in the wing pouch, as shown by a *dpp-lacZ* reporter gene (compare middle panel of Fig. 2g with middle panel of Fig. 2f).  $G\alpha_i$ -mediated ectopic expression of *dpp* is consistent with the ectopic veins observed in wings expressing  $G\alpha_i^{Q205L}$  (Fig. 2e, arrows)<sup>15</sup>. Taken together, these results support a role for activation of  $G\alpha_i$  in regulating the stability of Ci, and link  $G\alpha_i$  to regulation of a known Hh target gene.

To determine whether  $G\alpha_i$  functions downstream of Smo *in vivo*, we analysed the ability of  $G\alpha_i$  to modulate Hh pathway activity in a *smo* sensitized background. As previously demonstrated, expression of a dominant-negative *smo* transgene, *UAS-Smo5A*, results in severe

disruption of LV3–LV4 wing patterning (Fig. 2h and ref. 16). Expression of wild-type  $G\alpha_i$  in this *smo* sensitized background allows for partial rescue of wing vein structures in the LV3/LV4 zone (Fig. 2i). Expression of constitutively active  $G\alpha_i^{Q205L}$  results in a more complete rescue of the Hh loss-of-function phenotype, allowing for near total restoration of LV3/LV4 patterning (Fig. 2j). As a control, *UAS-GFP* was co-expressed with *Smo5A*, and found to have no effect on the *Smo5A*-induced phenotype (data not shown).

To examine the ability of  $G\alpha_i^{Q205L}$  to modulate Ci stability and Hh target gene activation in the *smo* sensitized background, wing imaginal discs were immunostained with antibodies that recognize full-length Ci and the target gene product Ptc. *UAS-Smo5A* expression results in decreased *ptc* expression and disruption of the Ci gradient (Supplementary Fig. 2, compare panels b and a). Expression of constitutively active  $G\alpha_i^{Q205L}$  in this *smo* sensitized background results in partial restoration of the Ci gradient and a near-complete rescue of *ptc* expression at the anterior/posterior border (Supplementary Fig. 2c). These results support the model that  $G\alpha_i$  contributes to the regulation of Hh target gene expression and Ci stability. Furthermore, the fact that this regulation occurs when Smo function is compromised suggests that  $G\alpha_i$  affects Hh signalling at a level downstream of Smo.

To determine whether  $G\alpha_i$  is required for Hh signalling *in vivo*, we examined Hh target gene expression in clones of cells homozygous for  $G\alpha_i$  mutation. The null allele  $G\alpha_i^{P20}$  removes the entire coding region of the  $G\alpha_i$  gene, and is homozygous lethal<sup>17</sup>.  $G\alpha_i^{P8}$  is a putative hypomorph, which removes the bulk of exons 1 and 2, but leaves the transcriptional start site intact and produces a transcript (Supplementary Fig. 3b). Flies that are homozygous for the  $G\alpha_i^{P8}$  mutation are viable, but weak<sup>17</sup>. Mosaic analysis reveals that expression of the Hh target gene *dpp* is decreased in both  $G\alpha_i^{P20}$  (Fig. 3a) and  $G\alpha_i^{P8}$  (Fig. 3b) mutant clones, supporting a role for  $G\alpha_i$  in activation of Hh target genes *in vivo*. To confirm that the effects on *dpp* expression are due to loss of  $G\alpha_i$ , we attempted to rescue  $G\alpha_i^{P20}$  null clones with *UAS-G $\alpha_i$* . Ectopic expression of  $G\alpha_i$  is able to rescue *dpp* reporter gene expression in  $G\alpha_i^{P20}$  clones (Fig. 3c), consistent with decreased *dpp* expression resulting from disruption of  $G\alpha_i$ .

To determine whether compromised  $G\alpha_i$  activity alters Hh-dependent patterning, we used the viable mutant allele  $G\alpha_i^{P8}$  and an additional viable allele described to be a null or strong hypomorph<sup>18</sup>,  $G\alpha_i^{57}$ . Whereas homozygous  $G\alpha_i^{P8}$  and  $G\alpha_i^{57}$  mutants do not have vein fusions that are typical of strong Hh loss of function, their wings are smaller than wild-type wings (Fig. 3d and Supplementary Fig. 3c). Small wing size might result from altered *dpp* expression in anterior cells of the wing pouch, as Dpp regulates wing blade size<sup>19,20</sup>. Additionally, both  $G\alpha_i^{P8}$  and  $G\alpha_i^{57}$  mutant flies demonstrate varying degrees of incomplete thorax closure, as shown by mild to severe thoracic clefts (middle panel of Fig. 3e, arrow, compared to left panel, and Supplementary Fig. 3, arrows). This phenotype is also consistent with decreased *dpp* expression, in that Dpp, in conjunction with JNK signalling, controls spreading of the anterior edge of wing imaginal discs to initiate thorax closure<sup>21,22</sup>. To confirm that this phenotype results from decreased Hh signalling, we expressed *ptc* in the notum and dorsal compartment of the wing imaginal disc. *ptc* expression triggers the formation of a thoracic cleft when expressed under control of *pannier* and *apterous* promoters (right panel of Fig. 3e, arrow, compared to left and middle panels, and data not shown), suggesting that the thoracic phenotype we observe in  $G\alpha_i$  flies results from compromised Hh signalling. Because  $G\alpha_i^{P20}$  null mutant animals are not viable, we could not examine their wings or thoraces. However, attenuation of Hh signalling by expressing dominant-negative *Smo5A* is enhanced in  $G\alpha_i^{P20}$  heterozygotes, as shown by disruption of LV3 (Supplementary Fig. 3, panels d and d').

Our *in vitro* and *in vivo* data suggest that loss of  $G\alpha_i$  might compromise Ci stabilization in Hh-receiving cells. When we examined Ci and Smo levels in  $G\alpha_i$  mutant clones, we found that both appear to be increased in a cell-autonomous manner (Supplementary Fig. 3e, f). These results are consistent with the modest stabilization of Smo and

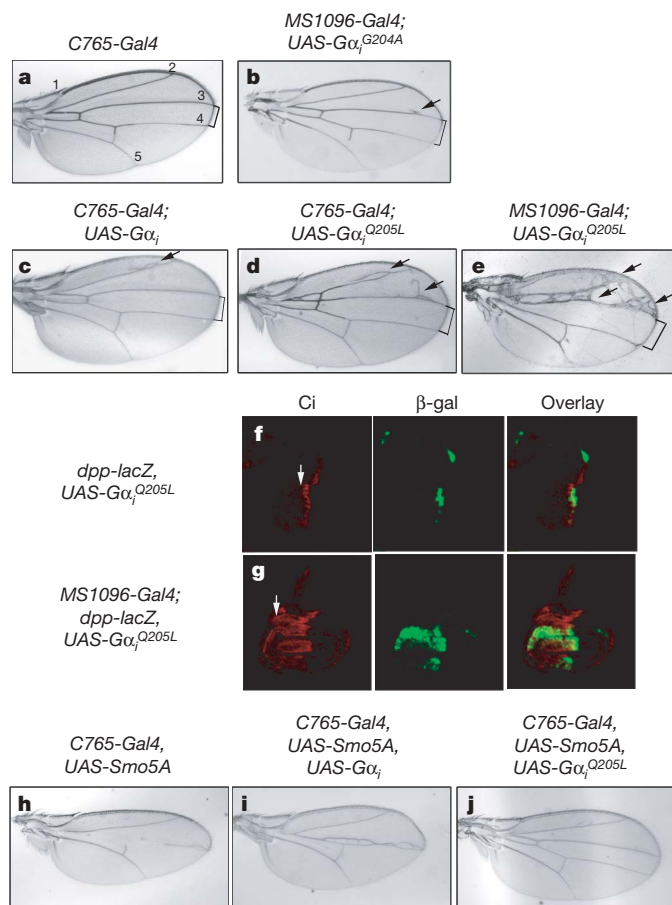


**Figure 2 |  $G\alpha_i$  expression results in ectopic Hh signalling.** **a**, Longitudinal veins are numbered. **a–e**, Wings from *MS1096-Gal4; UAS-G $\alpha_i^{G204A}$*  (**b**), *C765-Gal4; UAS-G $\alpha_i$*  (**c**) and *UAS-G $\alpha_i^{Q205L}$*  (**d**, **e**) flies demonstrate ectopic veins (arrows) and LV3–LV4 widening (brackets), as compared to control (**a**). **f**, **g**, Wing discs from *dpp-lacZ*, *UAS-G $\alpha_i^{Q205L}$*  (**f**) and *MS1096-Gal4; dpp-lacZ*, *UAS-G $\alpha_i^{Q205L}$*  (**g**) larvae were immunostained for Ci (red) and  $\beta$ -galactosidase (green). Overlays are shown in the right column. Anterior is left and dorsal is up. **h–j**, Expression of wild-type  $G\alpha_i$  partially rescues, and  $G\alpha_i^{Q205L}$  fully rescues, the phenotype induced by dominant negative *UAS-Smo5A* (compare **i** and **j** to **h**).

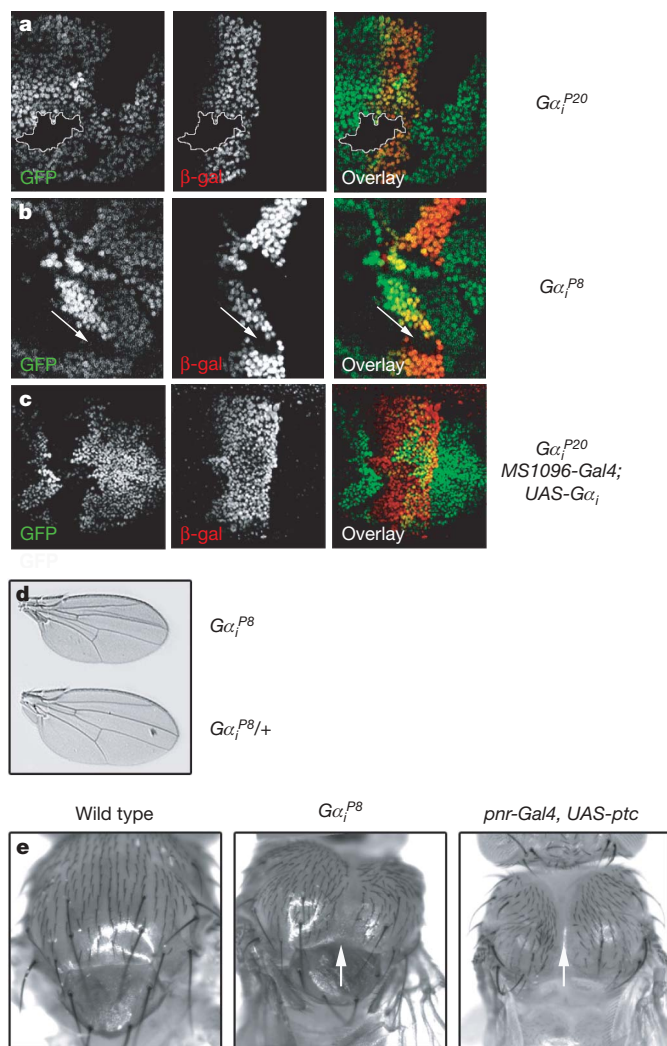


**Figure 3** |  $G\alpha_i$  is required for Hh signalling *in vivo*. **a–c**, Mitotic clones were generated with the  $G\alpha_i^{P20}$  null (**a**, **c**) or  $G\alpha_i^{P8}$  hypomorphic (**b**) alleles. Wing discs were stained for the *dpp-lacZ* gene product  $\beta$ -gal (red). Loss of GFP expression (green) marks  $G\alpha_i$  mutant clones. **c**,  $G\alpha_i^{P20}$  null clones were generated in MS1096-Gal4; UAS- $G\alpha_i$  wing discs. **d**, **e**,  $G\alpha_i$  phenotypes are consistent with decreased Hh signalling. **d**, Homozygous  $G\alpha_i^{P8}$  mutant flies have a small wing phenotype. **e**,  $G\alpha_i^{P8}$  (middle panel) and *pnr*-Gal4, UAS-*ptc* flies (right panel) have thoracic clefts (arrows), as compared to wild type (left panel).

Ci on *in vitro*  $G\alpha_i$  knockdown in non-Hh-treated cells (Fig. 1c, compare lanes 1 and 3). Although these results are unexpected, as  $G\alpha_i$  loss is predicted to increase PKA activity and Ci degradation, previous studies have demonstrated that PKA functions to regulate Hh signalling both positively and negatively<sup>23</sup>. Phosphorylation of Smo by PKA has a positive role in pathway activation<sup>24</sup>, and might account for the modest stabilization of Ci that we observe.

If Smo signals through  $G\alpha_i$  it should be able to induce  $G\alpha_i$  activation rapidly in response to Hh stimulation. To assay for Hh-mediated activation of  $G\alpha_i$ , we treated Cl8 cells with conditioned media containing the amino-terminal Hh signalling molecule (HhN) or control conditioned media, then assayed for Hh-induced changes in intracellular cAMP. Within 5–10 min, HhN treatment reduces the basal intracellular cAMP concentration by approximately 50% (Fig. 4a). To confirm that the Hh-induced decrease in intracellular cAMP is dependent on Hh signalling through Smo and  $G\alpha_i$ , we treated cells with *smo*,  $G\alpha_i$  or control dsRNA, then assayed for a Hh-induced decrease in cAMP (Fig. 4b). Whereas cells transfected with control dsRNA maintain the ability to decrease intracellular cAMP in response to HhN, cells transfected with either *smo* or  $G\alpha_i$  dsRNA are attenuated in their ability to do so. Taken together, these results

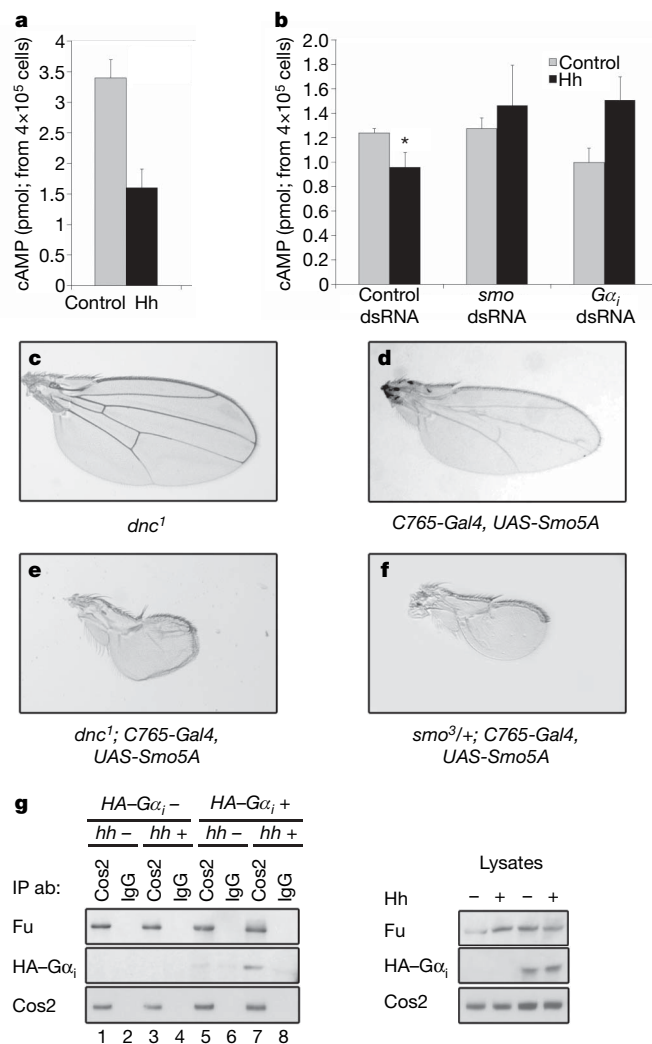


**Figure 4** | Hh regulates  $G\alpha_i$  activity and association with Cos2. **a**, Cl8 cells were treated with control or HhN conditioned media. Error bars indicate s.e.m. **b**, Cl8 cells were transfected with control, *smo* or  $G\alpha_i$  dsRNA, and treated with HhN or control conditioned media. Error bars indicate s.e.m. The asterisk indicates  $P < 0.05$ . **c–f**, Wings from hemizygous *dnc*<sup>1</sup> (**c**), C765-Gal4, UAS-Smo5A (**d**), *dnc*<sup>1</sup>; C765-Gal4, UAS-Smo5A (**e**) and *smo*<sup>3/+</sup>; C765-Gal4, UAS-Smo5A (**f**) flies are shown. Introduction of *dnc*<sup>1</sup> enhances the Smo5A phenotype in approximately 50% of flies ( $n = 57$ ). **g**, Cl8 cells were transfected with HA- $G\alpha_i$  and *hh* expression vectors, as indicated. Immunoprecipitations were performed from cell lysates using anti-Cos2 or IgG control antibodies.

support the idea that  $G\alpha_i$  is activated rapidly, in a Smo-dependent manner, in order to modulate cAMP levels in response to Hh.

To determine whether modulation of cAMP can alter Hh signalling *in vivo*, we used a hypomorphic mutant allele of the cAMP-specific phosphodiesterase *dunce* (*dnc*<sup>1</sup>)<sup>25</sup> to raise intracellular cAMP levels in a Hh-independent manner. Hemizygous *dnc*<sup>1</sup> animals are viable with no obvious Hh defects (Fig. 4c). However, introduction of the *dnc*<sup>1</sup> mutation into a *smo* sensitized background enhances the Smo loss-of-function phenotype, resulting in wings with near complete elimination of wing vein patterning (Fig. 4, compare panels e and d). This enhanced Hh loss-of-function phenotype is similar to the phenotype obtained on decreasing *smo* gene dosage by one-half in the same *smo* sensitized background (Fig. 4, compare panels f with e and d). Along with our *in vitro* cAMP assays, these results indicate that Hh activates Smo to modulate intracellular cAMP, via  $G\alpha_i$ , and that this function is important for proper pathway activity *in vivo*.

Cos2 associates with membranes, microtubules, PKA, Smo, Fu and Ci (refs 26, 27). To determine whether Cos2 facilitates the coupling of



G $\alpha_i$  with these Hh signalling components, we prepared lysates from cells expressing HA-G $\alpha_i$ , and then immunoprecipitated Cos2 (Fig. 4g). We find that G $\alpha_i$  associates with the Cos2 complex, and that this association is enriched in response to Hh (Fig. 4g, left panel, compare lanes 7 and 5). The binding of Fu to Cos2 is not altered by Hh, suggesting that the recruitment of G $\alpha_i$  to this protein complex is regulated. This result suggests that Cos2 facilitates the coupling of Smo with G $\alpha_i$  and additional downstream effectors necessary to transduce the Hh signal.

We have shown a requirement for G $\alpha_i$  in the Hh signalling pathway. We have demonstrated Hh-mediated recruitment and activation of G $\alpha_i$  that results in decreased intracellular cAMP, indicating that Hh may regulate PKA through modulation of the intracellular cAMP concentration. We have also demonstrated that G $\alpha_i$  can modulate Hh pathway activity *in vitro* and *in vivo*, and seems to do so at a level downstream of Smo. Furthermore, loss of G $\alpha_i$  alters Hh signalling *in vivo*, supporting the idea that G $\alpha_i$  is a requisite member of the Hh pathway.

## METHODS SUMMARY

All cell-based assays described here were performed in clone-8 (Cl8) cells, which are a Hh-responsive wing imaginal disc cell line. T7 DNA templates were generated from G $\alpha$  cDNAs by PCR using Vent polymerase (NEB) as described<sup>28</sup>. Cells were lysed 72 h after dsRNA transfection<sup>29</sup> and post-nuclear lysates analysed by immunoblotting, using the indicated antibodies. Reporter assays were performed in cells transfected with the indicated agents, along with a *ptc-luciferase* reporter construct<sup>11</sup> and *act-venilla* transfection control<sup>29</sup>. cAMP levels were determined from cells treated with or without HhN-conditioned media for 5–10 min, using a [<sup>3</sup>H]cAMP receptor competition assay<sup>30</sup>. Measured cAMP levels were then compared to a standard curve to determine intracellular cAMP. For G $\alpha_i$  and Smo knockdown effects on cAMP production, cells were transfected with control, *smo*- or G $\alpha_i$ -specific dsRNA 72 h before treatment with HhN or control conditioned media. A Student's *t*-test was used to determine *P* values. Error bars indicate standard error of the mean.

Fly stocks were maintained on standard yeast-cornmeal molasses media. For *dnc*<sup>1</sup> enhancement of the Smo5A phenotype, crosses were begun at 25 °C, then moved to 22 °C for pupation. All other crosses were performed at 25 °C with the exception of mosaic analyses, which were performed at room temperature. Mutant clones were marked by loss of GFP expression. Imaginal discs were dissected and immunostained as described previously<sup>29</sup>. Adult wings were mounted on glass microscope slides using DPX mounting media. Wing images were collected using a Zeiss Axioskop2 microscope. All images were processed using Adobe Photoshop 6.0. The G $\alpha_i$ <sup>78</sup> breakpoint, as well as expression of the other G $\alpha_i$  alleles, was determined using standard molecular biology techniques.

**Full Methods** and any associated references are available in the online version of the paper at [www.nature.com/nature](http://www.nature.com/nature).

Received 15 August; accepted 26 September 2008.

Published online 5 November 2008; corrected 18 December 2008 (details online).

- Mullor, J. L., Sanchez, P. & Altaba, A. R. Pathways and consequences: Hedgehog signaling in human disease. *Trends Cell Biol.* **12**, 562–569 (2002).
- Ingham, P. W. & McMahon, A. P. Hedgehog signaling in animal development: paradigms and principles. *Genes Dev.* **15**, 3059–3087 (2001).
- Robbins, D. J. *et al.* Hedgehog elicits signal transduction by means of a large complex containing the kinesin-related protein costal2. *Cell* **90**, 225–234 (1997).
- Price, M. A. & Kalderon, D. Proteolysis of the Hedgehog signaling effector Cubitus interruptus requires phosphorylation by Glycogen Synthase Kinase 3 and Casein Kinase 1. *Cell* **108**, 823–835 (2002).
- Alcedo, J., Ayzenzon, M., Von Ohlen, T., Noll, M. & Hooper, J. E. The *Drosophila* smoothened gene encodes a seven-pass membrane protein, a putative receptor for the hedgehog signal. *Cell* **86**, 221–232 (1996).
- DeCamp, D. L., Thompson, T. M., de Sauvage, F. J. & Lerner, M. R. Smoothened activates G $\alpha_i$ -mediated signaling in frog melanophores. *J. Biol. Chem.* **275**, 26322–26327 (2000).
- Low, W. C. *et al.* The decoupling of Smoothened from G $\alpha_i$  proteins has little effect on Gli3 protein processing and Hedgehog-regulated chick neural tube patterning. *Dev. Biol.* **321**, 188–196 (2008).
- Kasai, K. *et al.* The G12 family of heterotrimeric G proteins and Rho GTPase mediate Sonic hedgehog signalling. *Genes Cells* **9**, 49–58 (2004).
- Riobo, N. A., Saucy, B., Dilizio, C. & Manning, D. R. Activation of heterotrimeric G proteins by Smoothened. *Proc. Natl Acad. Sci. USA* **103**, 12607–12612 (2006).

- Murone, M., Rosenthal, A. & de Sauvage, F. J. Sonic hedgehog signaling by the patched-smoothened receptor complex. *Curr. Biol.* **9**, 76–84 (1999).
- Chen, C. H. *et al.* Nuclear trafficking of Cubitus interruptus in the transcriptional regulation of Hedgehog target gene expression. *Cell* **98**, 305–316 (1999).
- Schaefer, M., Petronczki, M., Dörner, D., Forte, M. & Knoblich, J. A. Heterotrimeric G proteins direct two modes of asymmetric cell division in the *Drosophila* nervous system. *Cell* **107**, 183–194 (2001).
- Muller, B. & Basler, K. The repressor and activator forms of Cubitus interruptus control Hedgehog target genes through common generic gli-binding sites. *Development* **127**, 2999–3007 (2000).
- Methot, N. & Basler, K. Hedgehog controls limb development by regulating the activities of distinct transcriptional activator and repressor forms of Cubitus interruptus. *Cell* **96**, 819–831 (1999).
- Capdevila, J. & Guerrero, I. Targeted expression of the signaling molecule decapentaplegic induces pattern duplications and growth alterations in *Drosophila* wings. *EMBO J.* **13**, 4459–4468 (1994).
- Collins, R. T. & Cohen, S. M. A genetic screen in *Drosophila* for identifying novel components of the hedgehog signaling pathway. *Genetics* **170**, 173–184 (2005).
- Yu, F., Cai, Y., Kaushik, R., Yang, X. & Chia, W. Distinct roles of G $\alpha_i$  and G $\beta$ 13F subunits of the heterotrimeric G protein complex in the mediation of *Drosophila* neuroblast asymmetric divisions. *J. Cell Biol.* **162**, 623–633 (2003).
- Hampel, B., Hoeller, O., Bowman, S. K., Dunican, D. & Knoblich, J. A. *Drosophila* Ric-8 is essential for plasma-membrane localization of heterotrimeric G proteins. *Nature Cell Biol.* **7**, 1099–1105 (2005).
- Affolter, M. & Basler, K. The Decapentaplegic morphogen gradient: from pattern formation to growth regulation. *Nature Rev. Genet.* **8**, 663–674 (2007).
- Aegerter-Wilmsen, T., Aegerter, C. M., Hafen, E. & Basler, K. Model for the regulation of size in the wing imaginal disc of *Drosophila*. *Mech. Dev.* **124**, 318–326 (2007).
- Martin-Blanco, E., Pastor-Pareja, J. C. & Garcia-Bellido, A. JNK and decapentaplegic signaling control adhesiveness and cytoskeleton dynamics during thorax closure in *Drosophila*. *Proc. Natl Acad. Sci. USA* **97**, 7888–7893 (2000).
- Pena-Rangel, M. T., Rodriguez, I. & Riesgo-Escovar, J. R. A misexpression study examining dorsal thorax formation in *Drosophila melanogaster*. *Genetics* **160**, 1035–1050 (2002).
- Ohlmeier, J. T. & Kalderon, D. Dual pathways for induction of wingless expression by protein kinase A and Hedgehog in *Drosophila* embryos. *Genes Dev.* **11**, 2250–2258 (1997).
- Apionishev, S., Katanayeva, N. M., Marks, S. A., Kalderon, D. & Tomlinson, A. *Drosophila* Smoothened phosphorylation sites essential for Hedgehog signal transduction. *Nature Cell Biol.* **7**, 86–92 (2005).
- Davis, R. L. & Kiger, J. A. Jr. Dunc mutants of *Drosophila melanogaster*: mutants defective in the cyclic AMP phosphodiesterase enzyme system. *J. Cell Biol.* **90**, 101–107 (1981).
- Ogden, S. K., Ascano, M. Jr, Stegman, M. A. & Robbins, D. J. Regulation of Hedgehog signaling: a complex story. *Biochem. Pharmacol.* **67**, 805–814 (2004).
- Jia, J. & Jiang, J. Decoding the Hedgehog signal in animal development. *Cell. Mol. Life Sci.* **63**, 1249–1265 (2006).
- Stegman, M. A. *et al.* The Kinesin-related protein Costal2 associates with membranes in a Hedgehog-sensitive, Smoothened-independent manner. *J. Biol. Chem.* **279**, 7064–7071 (2004).
- Ogden, S. K. *et al.* Smoothened regulates activator and repressor functions of Hedgehog signaling via two distinct mechanisms. *J. Biol. Chem.* **281**, 7237–7243 (2006).
- Stitham, J., Stojanovic, A., Ross, L. A., Blount, A. C. Jr & Hwa, J. Clusters of transmembrane residues are critical for human prostacyclin receptor activation. *Biochemistry* **43**, 8974–8986 (2004).

**Supplementary Information** is linked to the online version of the paper at [www.nature.com/nature](http://www.nature.com/nature).

**Acknowledgements** This work was supported by National Institutes of Health grants CA82628 (D.J.R.) and HL074190 (J.H.). We are grateful to J. Knoblich for the G $\alpha_i$  antibody and G $\alpha_i$  flies; X. Yang and W. Chia for G $\alpha_i$  flies; D. Casso and T. Kornberg for Ptc antibody and UAS-Smo5A flies; J. Hooper for UAS-G $\alpha_i$  and UAS-G $\alpha_i$ <sup>Q2051</sup> flies; K. Basler, D. Kalderon and P. Ingham for *smo* alleles; and L. Lum for Smo antibody. All additional fly stocks were provided by the Bloomington Stock Center. G $\alpha_i$  and G $\alpha_i$  cDNAs were obtained from the *Drosophila* Genomics Resource Center, Bloomington. E. Lee provided G $\alpha_i$  cDNA. We thank the Dartmouth microscopy core for their assistance. We would also like to thank K. Black for technical assistance and members of the Robbins laboratory, E. Lee, J. Hutchinson, R. Taussig, R. Ostrom and C. Pikielny for thoughtful discussion during the course of this work.

**Author Contributions** S.K.O. was involved in the design, execution and analysis of experiments, and in writing the manuscript. D.L.F. assisted in design and execution of dsRNA experiments and sequencing of G $\alpha_i$  alleles. J.H. was involved in design and execution of cAMP assays. N.S.S. assisted in execution of cAMP assays. Y.F.A. consulted on design and interpretation of genetic experiments. D.J.R. was involved in design and analysis of experiments and writing the manuscript.

**Author Information** Reprints and permissions information is available at [www.nature.com/reprints](http://www.nature.com/reprints). Correspondence and requests for materials should be addressed to D.J.R. ([david.j.robbins@dartmouth.edu](mailto:david.j.robbins@dartmouth.edu)).



## METHODS

**RNA interference.** T7 DNA templates were generated from  $G\alpha$  cDNAs by PCR using Vent polymerase (NEB) as described<sup>28</sup>. dsRNA was generated from these T7 templates using the Megascript T7 kit (Ambion) following the manufacturer's instructions.  $G\alpha$ -subunit-specific dsRNAs were generated from the following regions of the indicated G protein cDNAs:  $G\alpha_i$ , base pairs 219–966 or 14–538 of the 3' UTR;  $G\alpha_o$ , base pairs 213–964; and  $G\alpha_s$ , base pairs 208–1059. BLAST queries were performed to confirm that designed dsRNAs were subunit specific for the intended  $\alpha$  subunit.  $G\alpha_i$  cDNA was obtained from the *Drosophila* Genomics Resource Center (DGRC),  $G\alpha_o$  cDNAs were provided by the DGRC and T. Kornberg (UCSF), and  $G\alpha_s$  cDNA was provided by E. Lee. Semi-quantitative RT–PCR was performed to confirm  $G\alpha_o$  and  $G\alpha_s$  knockdown. RNA was purified using TriReagent (MRC) following the manufacturer's instructions. cDNA was generated from 5  $\mu$ g total RNA using random primers and Superscript II reverse transcriptase (Invitrogen). One-twentieth of the cDNA was used for PCR of G proteins and Actin loading control. Reverse transcriptase minus reactions were used as a control.

To examine the effects of  $G\alpha_i$  and/or Smo knockdown on the Hh signalling pathway, Cl8 cells were lysed 72 h after dsRNA transfection as previously described<sup>29</sup>. Post-nuclear lysates were analysed by SDS–PAGE and western blot using the following published antibodies: Ci (ref. 31), Cos2 (ref. 32), Fu (ref. 33),  $G\alpha_i$  (ref. 12) and Kinesin as a loading control (Cytoskeleton, Inc.). To generate the Smo antibody used for western blot analysis, rats were injected with a peptide corresponding to amino acids 1010–1030 of the Smo carboxy-terminal tail. Antibodies were then affinity purified from sera over a peptide column. Peptides and antibodies were produced and purified using the Covance custom antibody service.

**Reporter assays.** Clone-8 (Cl8) cells were transfected with  $G\alpha_i$  dsRNA, *ptc-luciferase* reporter construct<sup>11</sup> and *act-venilla* transfection control<sup>29</sup> using Cellfectin transfection reagent (Invitrogen). Relative luciferase activity was determined 72 h after transfection using the Dual Luciferase Assay System (Promega). Each assay was performed a minimum of three times, in duplicate. Values were averaged to determine *ptc-luciferase* activity relative to *venilla* transfection control. Error bars indicate standard error of the mean.

**Fly crosses and transgenes.** Fly stocks were maintained on standard yeast-cornmeal molasses media. For *dnc<sup>1</sup>* enhancement of the Smo5A phenotype, crosses were begun at 25 °C, then moved to 22 °C for pupation. All other crosses were performed at 25 °C with the exception of mosaic analyses, which were performed at room temperature. The following genotypes were used for generation of  $G\alpha_i^{P20}$  and  $G\alpha_i^{P8}$  mitotic clones: *w<sup>hs-flp</sup>; G $\alpha_i^{P20}$  FRT2A/Ubi-GFP FRT2A* and *w<sup>hs-flp</sup>; G $\alpha_i^{P8}$  FRT2A/Ubi-GFP FRT2A*. The following genotype was used for  $G\alpha_i^{P20}$  clone rescue experiments: *MS1096-Gal4/yw<sup>hs-flp</sup>; dpp-lacZ/UAS-G $\alpha_i$ ; G $\alpha_i^{P20}$  FRT2A/Ubi-GFP FRT2A*. Recombination was induced by incubation at 37 °C for 1 h, 48 h after egg laying<sup>34</sup>. Null mutant clones were marked by loss of GFP expression. Generation of *UAS-G $\alpha_i^{G204A}$*  transgenic flies was performed by the Duke Model Systems Genomics Core Injection service. *UAS-G $\alpha_i$*  and *UAS-G $\alpha_i^{Q205L}$*  flies were provided by J. Hooper. *C765-Gal4*, *UAS-Smo5A* flies were provided by D. Casso and T. Kornberg. *smo* alleles were provided by D. Kalderon, K. Basler and P. Ingham.  $G\alpha_i$  alleles were provided by X. Yang, W. Chia and J. Knoblich. *dnc<sup>1</sup>*, *dpp-lacZ*, *hsFLP*, *Ubi-GFP*, *FRT2A*, *pannier-Gal4* and *MS1096-Gal4* flies were obtained from the Bloomington *Drosophila* Stock Center.

**PCR and sequencing.** To sequence the  $G\alpha_i^{P8}$  breakpoint, one adult fly was homogenized in 50  $\mu$ l SB buffer (10 mM Tris (pH 8.2), 25 mM NaCl, 1 mM EDTA, 0.2 mg ml<sup>−1</sup> protease K) and incubated for 30 min at 37 °C, followed by an additional 10 min at 85 °C. Lysates were centrifuged for 5 min at 2,000g.

Four microlitres of the supernatant was used as template for PCR with forward primer (GGATCATATGAGTGGCATTCAAGC) located −245 to −222, relative to the  $G\alpha_i$  transcription start site, and reverse primer (CTGATAGC-GCGACGCAGAAG), base pairs +6197 to +6216 relative to the transcription start site. Ten nanograms of PCR product was used for sequencing. The  $G\alpha_i^{P8}$  mutation deletes base pairs +29 to +6104 with respect to the  $G\alpha_i$  transcription start site. For semi-quantitative RT–PCR analysis, three adult wild-type or  $G\alpha_i^{P8}$  flies were homogenized in 200  $\mu$ l Tri Reagent and RNA was extracted as per the manufacturer's instructions (Molecular Research Center). Approximately 2  $\mu$ g of RNA was used for reverse transcription reactions, using random hexamer oligonucleotides and SuperScript II reverse transcriptase (Invitrogen), or RT-minus control reactions.

**Immunostaining and microscopy.** Imaginal discs were dissected and immunostained as described previously<sup>29</sup>. Discs were stained using Ci (2A1)<sup>31</sup>, Ptc<sup>15</sup>, En<sup>35</sup>,  $G\alpha_i^{12}$ , Smo<sup>36</sup> and  $\beta$ -galactosidase (Promega) primary antibodies and Alexa-fluor-conjugated secondary antibodies (Molecular Probes), as described<sup>29</sup>. Adult wings were mounted on glass microscope slides using DPX mounting media. Wing images were collected using a Zeiss Axioskop2 microscope and processed with Adobe Photoshop 6.0.

**Immunoprecipitation.** Cl8 cells were transfected with pAct-HA- $G\alpha_i$ , pAct-hh or empty vector control. Cells were lysed 48 h after transfection and lysates were immunoprecipitated using Cos2 antisera as previously described<sup>32,37</sup>. HA antibody was obtained from GeneTex, Inc.

**cAMP assay.** Cl8 cells were treated with HhN or control S2 conditioned media for 10 min before lysis by boiling in 50 mM Tris-HCl, 4 mM EDTA, pH 7.9. Cell lysates were cleared of nuclei and cellular debris by centrifugation at 2,000g for 10 min at 4 °C. cAMP levels in cell lysates were determined by a radio-receptor competition assay as previously described<sup>30</sup>. Lysates were compared against a known standard curve similar to Supplementary Fig. 4 to determine intracellular cAMP. For Hh-mediated effects on intracellular cAMP, the assay was performed two times in duplicate, and all data were averaged. For  $G\alpha_i$  and Smo knockdown effects on cAMP production, cells were transfected with control, *smo*- or  $G\alpha_i$ -specific dsRNA 72 h before treatment with HhN or control conditioned media. After treatment with conditioned media for 5–10 min, cells were lysed and analysed as described above. Assays were performed two times in triplicate for  $G\alpha_i$  and three times in triplicate for Smo. A representative assay is shown. A Student's *t*-test was used to determine *P* values. Error bars indicate standard error of the mean.

31. Motzny, C. K. & Holmgren, R. The *Drosophila* cubitus interruptus protein and its role in the wingless and hedgehog signal transduction pathways. *Mech. Dev.* **52**, 137–150 (1995).
32. Stegman, M. A. *et al.* Identification of a tetrameric hedgehog signaling complex. *J. Biol. Chem.* **275**, 21809–21812 (2000).
33. Ascano, M. Jr, Nybakken, K. E., Sosinski, J., Stegman, M. A. & Robbins, D. J. The carboxyl-terminal domain of the protein kinase fused can function as a dominant inhibitor of hedgehog signaling. *Mol. Cell. Biol.* **22**, 1555–1566 (2002).
34. Brand, A. H. & Perrimon, N. Targeted gene expression as a means of altering cell fates and generating dominant phenotypes. *Development* **118**, 401–415 (1993).
35. Patel, N. H., Kornberg, T. B. & Goodman, C. S. Expression of engrailed during segmentation in grasshopper and crayfish. *Development* **107**, 201–212 (1989).
36. Lum, L. *et al.* Hedgehog signal transduction via Smoothened association with a cytoplasmic complex scaffolded by the atypical kinesin, Costal-2. *Mol. Cell* **12**, 1261–1274 (2003).
37. Ogden, S. K. *et al.* Identification of a functional interaction between the transmembrane protein Smoothened and the kinesin-related protein Costal2. *Curr. Biol.* **13**, 1998–2003 (2003).

# Suppression of Myc oncogenic activity by ribosomal protein haploinsufficiency

Maria Barna<sup>1</sup>, Aya Pusic<sup>2\*</sup>, Ornella Zollo<sup>2\*</sup>, Maria Costa<sup>2</sup>, Nadya Kondrashov<sup>1</sup>, Eduardo Rego<sup>3</sup>, Pulivarthi H. Rao<sup>4</sup> & Davide Ruggero<sup>2</sup>

The *Myc* oncogene regulates the expression of several components of the protein synthetic machinery, including ribosomal proteins, initiation factors of translation, RNA polymerase III and ribosomal DNA<sup>1,2</sup>. Whether and how increasing the cellular protein synthesis capacity affects the multistep process leading to cancer remains to be addressed. Here we use ribosomal protein heterozygote mice as a genetic tool to restore increased protein synthesis in *Eμ-Myc/+* transgenic mice to normal levels, and show that the oncogenic potential of *Myc* in this context is suppressed. Our findings demonstrate that the ability of *Myc* to increase protein synthesis directly augments cell size and is sufficient to accelerate cell cycle progression independently of known cell cycle targets transcriptionally regulated by *Myc*. In addition, when protein synthesis is restored to normal levels, *Myc*-overexpressing precancerous cells are more efficiently eliminated by programmed cell death. Our findings reveal a new mechanism that links increases in general protein synthesis rates downstream of an oncogenic signal to a specific molecular impairment in the modality of translation initiation used to regulate the expression of selective messenger RNAs. We show that an aberrant increase in cap-dependent translation downstream of *Myc* hyperactivation specifically impairs the translational switch to internal ribosomal entry site (IRES)-dependent translation that is required for accurate mitotic progression. Failure of this translational switch results in reduced mitotic-specific expression of the endogenous IRES-dependent form of Cdk11 (also known as Cdc2l and PITSLRE)<sup>3–5</sup>, which leads to cytokinesis defects and is associated with increased centrosome numbers and genome instability in *Eμ-Myc/+* mice. When accurate translational control is re-established in *Eμ-Myc/+* mice, genome instability is suppressed. Our findings demonstrate how perturbations in translational control provide a highly specific outcome for gene expression, genome stability and cancer initiation that have important implications for understanding the molecular mechanism of cancer formation at the post-genomic level.

Deregulation of *Myc* activity is one of the most frequent oncogenic lesions underlying human cancers<sup>6,7</sup>. *Myc* has an evolutionarily conserved role in the control of cell size and protein synthesis rates, which in *Drosophila* confers a cell survival advantage<sup>1,8,9</sup>. When d*Myc*-induced protein synthesis is restrained in a *minute* mutant background, which is haploinsufficient for ribosomal protein function, cells no longer possess a competitive advantage<sup>10,11</sup>. So far, the relevance of *Myc*-dependent increases in protein synthesis and cell growth in the multistep process leading to cancer remain unknown.

To restore protein synthesis rates in *Myc*-overexpressing cells to normal, we used mouse *minute* mutants that are haploinsufficient for

ribosomal protein function. Haploinsufficiency in certain ribosomal proteins decreases the overall protein synthesis rates to an extent that is compatible with overall cellular and tissue homeostasis. *L24*<sup>+/-</sup> mice are viable<sup>12</sup> and do not show any overt differences in B-lymphocyte development, growth and cell division (Fig. 1 and

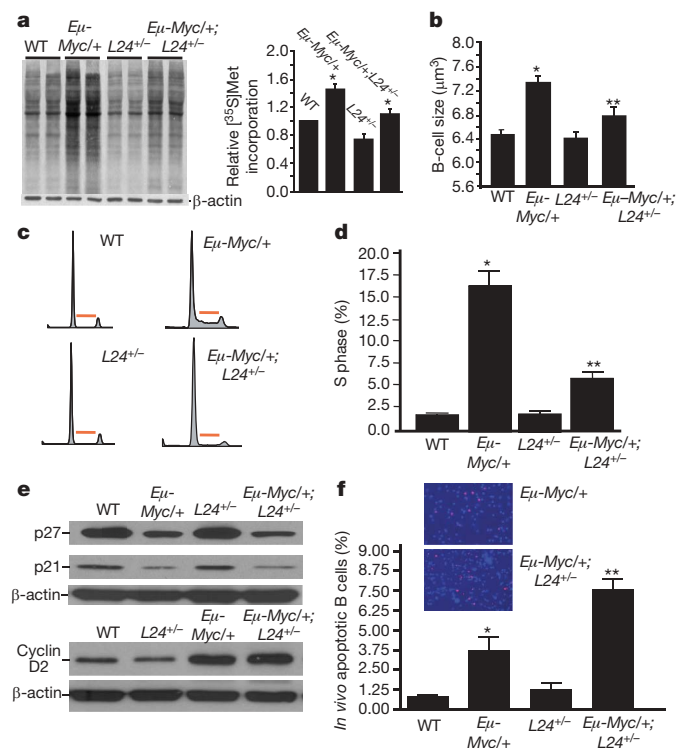


**Figure 1 | Myc-induced increases in protein synthesis regulates B-lymphocyte size, division and apoptosis before lymphomagenesis.**

**a**, Protein synthesis rates assessed by [<sup>35</sup>S] methionine incorporation and densitometry analysis; \**P* < 0.01; *n* = 3. **b**, Cell size analysis; *n* = 3, \**P* < 0.001 for *Eμ-Myc/+* versus wild type (WT), \*\**P* < 0.01 for *Eμ-Myc/+* versus *Eμ-Myc/+;L24*<sup>+/-</sup>. **c**, **d**, Cell cycle distribution (**c**) and quantification of the percentage of cells in S phase (**d**); *n* = 3; \**P* < 0.01, \*\**P* < 0.05. The red bar in **c** indicates S phase. **e**, Western blot analysis for cell cycle targets transcriptionally regulated by *Myc*. **f**, *In situ* TUNEL analysis; *n* = 3. Insets (original magnification ×20) are representative pictures of TUNEL analysis comparing *Eμ-Myc/+* and *Eμ-Myc/+;L24*<sup>+/-</sup> samples; \**P* < 0.05, \*\**P* < 0.05. All experiments (**a–e**) were performed on freshly isolated B-lymphocytes. Error bars, s.d.

<sup>1</sup>Department of Biochemistry & Biophysics, University of California San Francisco, Rock Hall Room 384C, 1550 Fourth Street, San Francisco, California 94158-2517, USA. <sup>2</sup>School of Medicine and Department of Urology, Helen Diller Family Comprehensive Cancer Center, University of California San Francisco, Byers Hall Room 308E, 1700 Fourth Street, San Francisco, California 94158-2517, USA. <sup>3</sup>Center for Cell Based Therapy, Fundação Hemocentro de Ribeirão Preto, University of São Paulo, 14048-900 Brazil. <sup>4</sup>Department of Pediatrics, Baylor College of Medicine, Houston, Texas 77030, USA.

\*These authors contributed equally to this work.

Supplementary Fig. 1). We intercrossed Myc transgenic mice, in which Myc is overexpressed in the B-cell compartment (*Eμ-Myc/+*)<sup>13</sup>, with *L24<sup>+/-</sup>* mice (Supplementary Fig. 2). By lowering the threshold of protein production in *L24<sup>+/-</sup>* mice, the increased protein synthesis rates and cell size in *Eμ-Myc/+* cells<sup>14</sup> were restored to normal levels in *Eμ-Myc/+;L24<sup>+/-</sup>* mice (Fig. 1a, b). Therefore, this genetic approach shows that Myc-induced increases in general protein synthesis rates are responsible for augmented cell growth. Moreover, *Eμ-Myc/+;L24<sup>+/-</sup>* mice are an important genetic model for selectively rescuing increased protein synthesis rates and cell growth downstream of oncogenic Myc signalling.

During cell cycle progression, cell growth normally precedes cell division and it has been suggested that cells must reach a critical cell size or 'setpoint' to facilitate G1–S progression<sup>15</sup>. In mammalian cells, it remains undetermined whether an increase in cell growth is coupled to an increase in cell division upon Myc hyperactivation. The percentage of *Eμ-Myc/+* cells in S phase is markedly increased compared to wild-type cells (Fig. 1c, d). Notably, in *Eμ-Myc/+;L24<sup>+/-</sup>* mice the augmented number of cells in S phase is restored to normal levels (Fig. 1c, d). The rate of cell cycle progression in *Eμ-Myc/+* B-lymphocytes was also monitored by BrdU incorporation (BrdU<sup>+</sup> cells per h, wild-type  $0.16 \pm 0.04$  versus Myc  $5.77 \pm 1.78$ ,  $P < 0.005$ ) and was similarly restored to normal levels in *Eμ-Myc/+;L24<sup>+/-</sup>* cells (BrdU<sup>+</sup> cells per h,  $0.11 \pm 0.02$ ,  $P < 0.02$ ). Important cell cycle targets that are transcriptionally regulated by Myc such as p27 (also known as Cdkn1b; ref. 16), p21 (Cdkn1a; ref. 17) and cyclin D2 (Ccn2; ref. 18), were expressed at similar levels in *Eμ-Myc/+* and *Eμ-Myc/+;L24<sup>+/-</sup>* cells (Fig. 1e and Supplementary Fig. 3). Thereby, the overall protein synthetic capacity of the cell may dictate cell cycle progression independently from the cell cycle program established at the transcriptional level by Myc hyperactivation. These results strongly suggest that Myc-induced cell growth is dependent on the ability of Myc to regulate protein synthesis and is coupled to uncontrolled cell cycle progression in cancer.

Non-immortalized cells counteract Myc overexpression by undergoing programmed cell death as a tumour suppressive response, and inhibition of cell death downstream of Myc activation accelerates lymphoma initiation<sup>7</sup>. The percentage of dying cells in *Eμ-Myc/+;L24<sup>+/-</sup>* mice was more than double that of *Eμ-Myc/+* mice before lymphoma onset (Fig. 1f). Therefore, the tumour suppressive response elicited by Myc overexpression is strongly enhanced in the background of normal protein synthesis and these findings suggest that clonal derivatives of precancerous cells may be more efficiently eliminated by programmed cell death in *Eμ-Myc/+;L24<sup>+/-</sup>* mice.

The restoration of normal protein synthesis downstream of Myc in *Eμ-Myc/+;L24<sup>+/-</sup>* mice is first associated with a marked reduction in splenomegaly—the earliest manifestation of Myc-induced lymphomagenesis (Fig. 2a). We next scored for lymphoma formation in each cohort of mice (Fig. 2b). The onset of lymphomas in the *Eμ-Myc/+;L24<sup>+/-</sup>* mice is markedly delayed compared to *Eμ-Myc/+* mice (Fig. 2b). In addition, a significant percentage of *Eμ-Myc/+;L24<sup>+/-</sup>* mice do not develop lymphomas even after 1.5 years of age (Fig. 2b). A second mouse *minute* line, heterozygous for the ribosomal protein L38 (M.B., manuscript in preparation), was intercrossed with *Eμ-Myc/+* mice. *Eμ-Myc/+;L38<sup>+/-</sup>* mice also show a marked rescue in cell growth and cell division as well as an increase in cell death of precancerous cells compared to *Eμ-Myc/+* cells (Supplementary Figs 1 and 4). Notably, lymphoma initiation in the *Eμ-Myc/+;L38<sup>+/-</sup>* mice was markedly suppressed, as in the *Eμ-Myc/+;L24<sup>+/-</sup>* mice (Supplementary Fig. 5). The suppression of lymphomagenesis was specific to the direct effect of Myc signalling on protein synthesis, as ribosomal protein haploinsufficiency in the context of the *p53<sup>-/-</sup>* background did not have any effect on tumour formation (Fig. 2c). These genetic results demonstrate that the ability of Myc to augment protein synthesis is necessary for its oncogenic potential.

To understand further the molecular mechanisms by which unrestrained increases in global protein synthesis can lead to tumorigenesis,

we analysed protein synthesis control during specific phases of the cell cycle in *Eμ-Myc/+* B-lymphocytes. Unexpectedly, wild-type and *Eμ-Myc/+* cells synchronized in S phase did not show any differences in protein synthesis rates (Fig. 3a). During mitosis, cap-dependent protein synthesis is normally decreased to facilitate cap-independent translation of a subset of messenger RNAs required for accurate mitotic progression<sup>19</sup>. On the contrary, *Eμ-Myc/+* cells show increased protein synthesis rates during mitosis; this is cap-dependent as the increased protein synthesis rates are restored to normal levels after rapamycin treatment (Supplementary Fig. 6) and in *Eμ-Myc/+;L24<sup>+/-</sup>* cells (Fig. 3a, b). Moreover, increased activity of a cap-dependent luciferase reporter gene is observed in Myc-overexpressing cells synchronized in mitosis and this is restored to normal when Myc is overexpressed in the *L24<sup>+/-</sup>* background (Fig. 3c).

Accurate mitotic progression relies on a very precise and orderly switch in translational control through a general decrease in cap-dependent translation and a switch to IRES-dependent translation initiation<sup>19</sup>. We next addressed whether a persistent enhancement of cap-dependent translation during mitosis downstream of Myc overexpression would be unfavourable to an IRES-dependent translational switch. The expression of a bicistronic reporter construct harbouring the hepatitis C virus IRES element (HCV IRES)—a molecular readout of IRES-dependent translation<sup>20</sup>—is impaired in mitotically synchronized Myc-overexpressing cells and restored to normal when Myc is overexpressed in the *L24<sup>+/-</sup>* background (Fig. 3d). Notably, *L24<sup>+/-</sup>* cells do not show differences in IRES-dependent translation

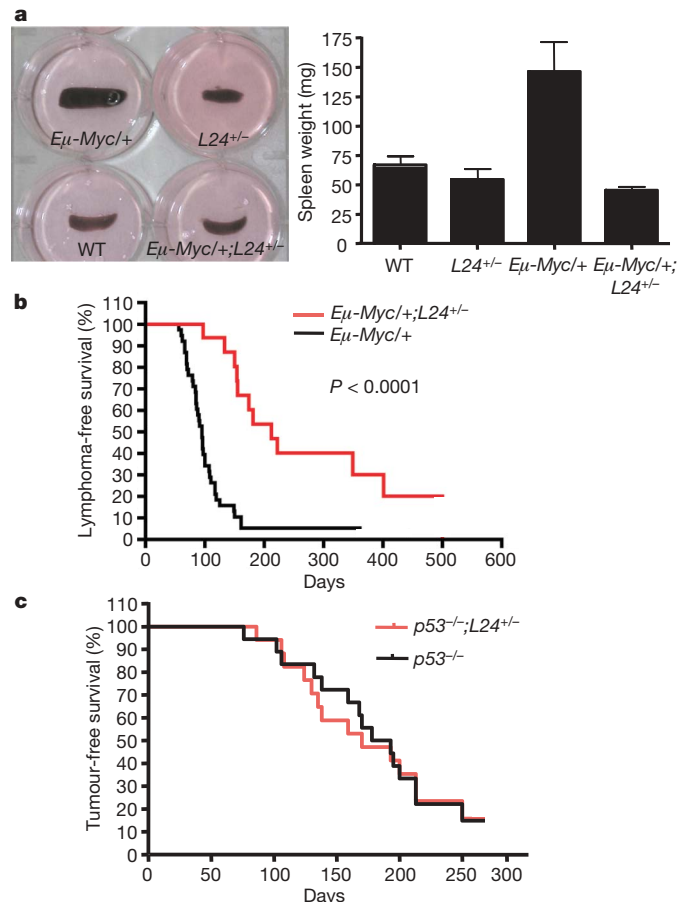


**Figure 2 | The ability of Myc to augment protein synthesis is necessary for its oncogenic potential.** **a**, Representative photographs of spleens (left) and average spleen weight (right); WT, wild type;  $n = 6$  per genotype, 4 weeks of age; error bars, s.d. **b**, Kaplan–Meier curves showing lymphoma-free survival of *Eμ-Myc/+* and *Eμ-Myc/+;L24<sup>+/-</sup>* mice;  $n = 30$  per genotype. **c**, Kaplan–Meier curves showing tumour-free survival of *p53<sup>-/-</sup>* and *p53<sup>-/-</sup>;L24<sup>+/-</sup>* mice;  $n = 25$  per genotype.



compared to wild-type cells (Fig. 3d), suggesting that the rescue in IRES-dependent translation downstream of Myc hyperactivation in the  $L24^{+/-}$  background is the result of restoring cap-dependent translation to normal levels (Fig. 3c). Taken together, these data demonstrate that aberrant and continuous stimulation of cap-dependent protein synthesis by Myc perturbs the mitotic switch to IRES-dependent translation.

We next monitored the expression of a well-characterized endogenous mRNA that is only translated during mitosis by an IRES

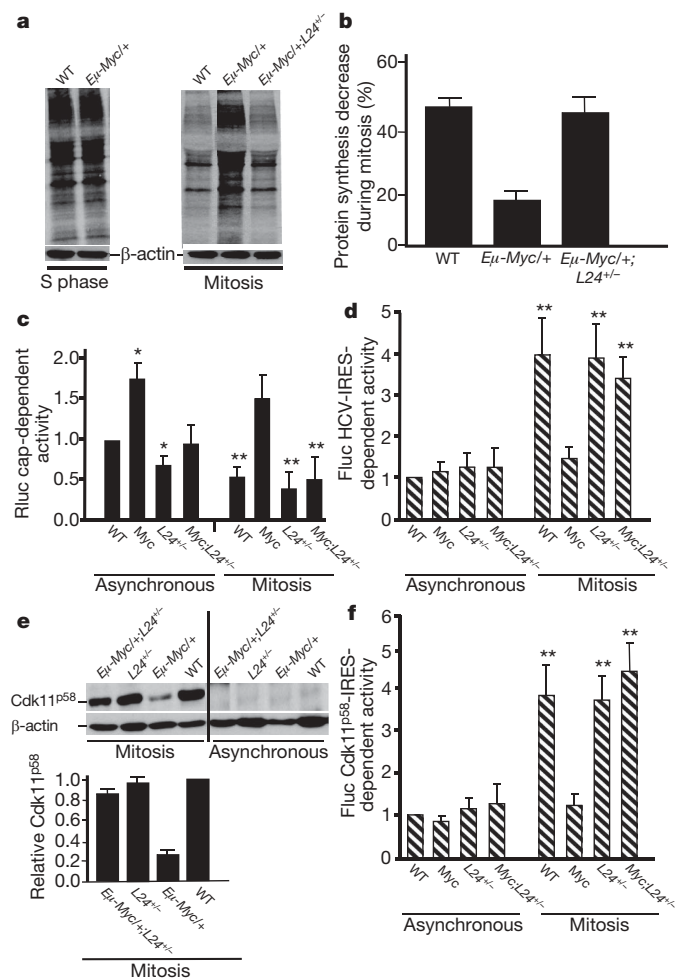


**Figure 3 | Myc hyperactivation impairs the translational switch from cap- to IRES-dependent translation control during mitosis and blocks mitotic translation of the Cdk11 kinase.** **a, b.** [ $^{35}\text{S}$ ]methionine incorporation in B lymphocytes synchronized in S phase and mitosis. Densitometry analysis ( $n = 3$ ) comparing protein synthesis levels in S phase and mitotically arrested B lymphocytes is shown. **c.** Cap-dependent activity of the *Renilla* luciferase (Rluc) reporter mRNA in asynchronous and mitotically synchronized MEFs;  $n = 6$  experiments performed in triplicate,  $*P < 0.001$  compared to wild type (WT),  $**P < 0.005$  compared to asynchronous values. **d.** HCV-IRES-dependent activity of the Firefly luciferase (Fluc) reporter mRNA;  $n = 6$  experiments performed in triplicate in asynchronous and mitotically synchronized MEFs;  $**P < 0.001$  compared to asynchronous values. **e.** Representative western blot of the endogenous Cdk11<sup>p58</sup> kinase in asynchronous and mitotically synchronized primary B lymphocytes. Note that expression of Cdk11<sup>p58</sup> is only present in mitotically synchronized cells (left), and not asynchronous cells (right) via an IRES-element positioned in its 5' UTR. Densitometric analysis is shown at the bottom;  $n = 3$ . **f.** Cdk11<sup>p58</sup>-IRES-dependent activity of firefly luciferase reporter mRNA transfected in asynchronous and mitotically synchronized cells;  $n = 4$  experiments performed in triplicate;  $**P < 0.001$  compared to asynchronous values. Average steady state wild-type values in **c**, **d** and **f** were set to 1. The y-axes show the fold change. Error bars, s.d. A tamoxifen-inducible Myc vector was expressed in a wild-type and  $L24^{+/-}$  background in **c**, **d** and **f**.

element. Cdk11 (also known as Cdc2l and PITSLRE) is a member of the Cdc2-like protein kinase family that undergoes cap-independent translation from an IRES element during mitosis to produce a 58-kDa Cdk11 isoform, Cdk11<sup>p58</sup>, that facilitates accurate mitotic progression<sup>3,4</sup>. Notably, deletions containing the *Cdk11* locus are found in non-Hodgkin's lymphoma<sup>21</sup> and other cancers<sup>22,23</sup>, strongly suggesting that Cdk11 may act as a tumour suppressor gene<sup>24</sup>. The expression of Cdk11<sup>p58</sup> was markedly reduced in mitotically synchronized  $E\mu\text{-Myc}^{+/-}$  cells (Fig. 3e and Supplementary Fig. 7) but was rescued to normal levels in  $E\mu\text{-Myc}^{+/-};L24^{+/-}$  cells (Fig. 3e). Moreover, expression of a reporter gene directed by the *Cdk11*<sup>p58</sup> IRES element is also impaired in mitotically synchronized Myc-overexpressed cells and restored to normal levels when Myc is overexpressed in the  $L24^{+/-}$  background (Fig. 3f). These findings indicate that the general increase in cap-dependent translation downstream of Myc activation prevents the accurate mitotic switch to IRES-dependent translation that regulates Cdk11<sup>p58</sup> expression.

Decreased Cdk11<sup>p58</sup> expression during mitosis impairs accurate cytokinesis, resulting in a binucleated cell phenotype<sup>5</sup> that is associated with aneuploidy<sup>25</sup>. We observed that Myc-overexpressing mouse embryonic fibroblasts (MEFs) display cytokinesis defects and have a significant increase in the number of binucleated cells, a hallmark of Cdk11<sup>p58</sup> loss of function<sup>5</sup> (Fig. 4a). Notably, restoring accurate mitotic Cdk11<sup>p58</sup> expression in Myc-overexpressing cells was sufficient to revert all of these cytokinesis defects (Fig. 4a–c). These findings strongly suggest that the decreased IRES-dependent translation of Cdk11<sup>p58</sup> downstream of oncogenic Myc signalling may be an early event in tumorigenesis that underlies the subsequent development of genomic instability<sup>26</sup>.

We therefore assessed whether  $E\mu\text{-Myc}^{+/-}$  lymphocytes have supernumerary centrosomes, an early characteristic of genome instability. We observed a large percentage of  $E\mu\text{-Myc}^{+/-}$  cells showing centrosome duplications. These duplications are the result of aberrant protein synthesis control downstream of Myc activation because  $E\mu\text{-Myc}^{+/-};L24^{+/-}$  cells show normal centrosome numbers (Fig. 4d). We next directly monitored genomic instability by using comparative genomic hybridization (CGH) analysis. All of the lymphomas analysed from  $E\mu\text{-Myc}^{+/-}$  mice had chromosomal abnormalities, but  $E\mu\text{-Myc}^{+/-};L24^{+/-}$  tumours either showed no chromosomal abnormalities or showed them at a lower frequency (Fig. 4e). These findings establish a direct and previously unrecognized molecular connection between the aberrant control of protein synthesis downstream of Myc activation and the accumulation of genetic lesions in tumours.

In our study, we have used ribosomal protein haploinsufficiency as a genetic tool to restore protein synthesis to normal levels downstream of oncogenic Myc activation. It is worth noting that subsets of ribosomal proteins act as tumour suppressors in Zebrafish<sup>27</sup>. However,  $L24^{+/-}$  and  $L38^{+/-}$  mice used in this study do not show cancer susceptibility (D.R., unpublished observations). Our findings provide genetic evidence that increased global protein synthesis downstream of Myc activation is a rate-limiting determinant of cancer initiation, and delineate how deregulations in protein synthesis control confer oncogenic potential (Fig. 4f). This strongly suggests that oncogenic signals may monopolize the translational machinery to elicit cooperative effects on cell growth, cell cycle progression and cell survival (Fig. 4f). Moreover, Myc-overexpressing cells have cytokinesis defects, supernumerary centrosomes and genomic instability as a consequence of augmented cap-dependent translation, demonstrating a previously unrecognized molecular connection between aberrant protein synthesis control and genome instability in cancer (Fig. 4f).

We have identified a specific translational impairment as a consequence of increasing protein synthesis downstream of oncogenic signalling (Fig. 4f). The failure to suppress cap-dependent translation during mitosis in Myc-overexpressing cells prevents the critical switch to IRES-dependent translation that is required for accurate

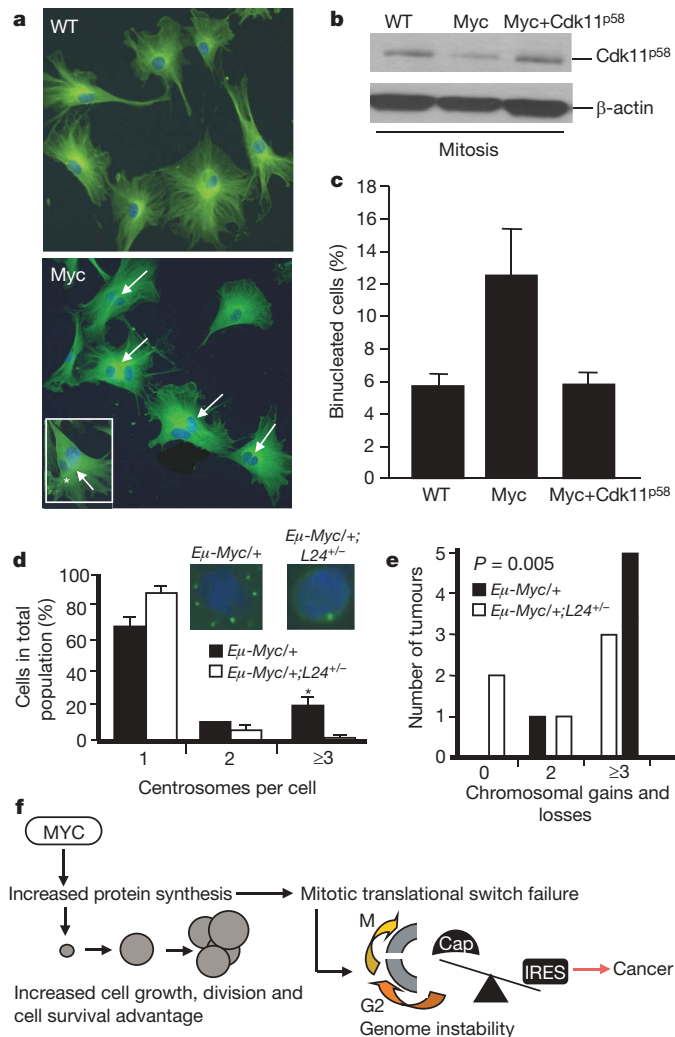


**Figure 4 | Aberrant translation control downstream of Myc activation underlies cytokinesis defects and genome instability.** **a**, Myc-overexpressing MEFs (original magnification  $\times 20$ ) show increased numbers of binucleated cells (arrows). Inset (original magnification  $\times 40$ ) illustrates dysmorphic and variably sized nuclei frequently observed in Myc overexpressing MEFs. WT, wild type. **b**, Western blot of mitotic Cdk11<sup>p58</sup> expression showing decreased expression in MEFs expressing a Myc inducible vector. Myc+p58 cells express a retroviral Cdk11<sup>p58</sup> cDNA. **c**, The increased number of binucleated cells in Myc-overexpressing cells is restored to normal level when Cdk11<sup>p58</sup> is reintroduced;  $n = 4$ , at least 500 cells were scored per experiment. Error bars, s.d. **d**, Percentages of cells with normal (1 and 2) and aberrant (3) centrosome numbers in freshly isolated B-lymphocytes;  $n = 6$ , at least 300 cells per experiment;  $*P < 0.001$ . Insets show representative immunofluorescence staining with a centrosome marker. **e**, CGH analysis of tumours;  $n = 6$ ; error bars, s.d. **f**, Proposed model for how deregulations in translation control downstream of Myc activation lead to cancer initiation. Myc-dependent increases in protein synthesis augment cell growth and this effect is coupled to increased cell cycle progression and a cell survival advantage. Increasing cap-dependent translation downstream of Myc-activation also gives rise to a specific molecular impairment in the modality of translation initiation used during mitosis that leads to cytokinesis defects associated with genome instability.

expression of mitotically expressed mRNAs and suggests that many IRES-containing mRNAs, such as *Cdk11*, may be deregulated at the translational level in Myc-overexpressing cells. Defects in the mitotic translational switch are directly relevant for tumorigenesis, as we have shown that impairments in IRES-dependent translation of Cdk11<sup>p58</sup> result in cytokinesis failure, an early event in cancer that underlies the subsequent development of genomic instability<sup>5,25,28</sup> and which can be reverted in Myc-overexpressing cells by restoring

accurate Cdk11<sup>p58</sup> mitotic expression (Fig. 4a–c). A question remains as to why an increase in cap-dependent translation downstream of Myc activation would decrease IRES-dependent translation. An aberrant increase in cap-dependent translation during mitosis may cause preferential recruitment of translational components (ribosomes and translation initiation factors) to the cap structure at the expense of IRES elements that govern accurate expression of a subset of mRNAs<sup>29</sup>. Several tumour suppressor genes possess an IRES-element and defects in IRES-dependent translation underlie the cancer susceptibility syndrome Dyskeratosis Congenita<sup>30</sup>. Therefore, IRES-containing mRNAs may be preferentially affected as a consequence of deregulations in translational control and may contribute to tumorigenesis. Our data strongly suggest that alterations in quantitative as well as qualitative translational control downstream of oncogenic signalling provide a highly specific and rapid response that may overshadow the effect of the transcriptosome towards cellular transformation.

## METHODS SUMMARY

**Mice.** *Em-Myc/+*, *L24<sup>+/+</sup>*, *L38<sup>+/+</sup>* and *p53<sup>-/-</sup>* mice were all maintained on a C57/BL6 background. Mice were monitored twice a week for signs of morbidity and tumour development. Myc tumour initiation was scored by peripheral lymph node palpation. Moribund mice or mice with obvious tumours were killed, and tumours and different organs were analysed by histology or processed for further analysis.

**Cell culture and analysis of IRES-dependent translation in mitosis.** Primary B-lymphocytes were isolated from spleen or bone marrow from 4–5-week-old mice using an autoMACS separator (Miltenyi Biotec). Primary B-lymphocytes and MEFs were synchronized in mitosis by thymidine and aphidicolin block, respectively. Bicistronic vectors, HCV IRES and Cdk11<sup>p58</sup> IRES were transfected as RNAs. IRES-dependent expression of the endogenous Cdk11<sup>p58</sup> was assessed by western blot using anti-Cdk11<sup>p58</sup> (Abcam).

**Analysis of global protein synthesis.** Equal numbers of freshly isolated or cultured primary B-lymphocytes synchronized in S phase or mitosis were incubated in methionine-free DMEM and then 50  $\mu$ Ci per well (25  $\mu$ Ci ml<sup>-1</sup>) of [<sup>35</sup>S] methionine was added to the cultures for 35 min. Radiolabelled proteins were visualized by exposure to X-ray film and quantified by densitometry analysis.

**Cellular and molecular analysis of B-lymphocytes.** Freshly isolated and cultured B-lymphocytes from 4–5-week-old mice were fixed and stained with the following combination of monoclonal antibodies conjugated with fluorescein isothiocyanate (FITC) or phycoerythrin (PE): CD19-PE and CD3-FITC, CD4-PE and CD8-FITC, and CD43-PE and CD45R-B220-FITC. Cell volume measurements were performed using a Coulter Model Z2 (Beckman Coulter).

**CGH and cytokinesis analysis.** Genomic DNA extracted from lymphomas of *Em-Myc/+* and *Em-Myc/+;L24<sup>+/+</sup>* mice was subjected to CGH analysis by standard methods. For cytokinesis analysis, primary MEFs were stably transfected with a Myc-oestrogen receptor chimera (*MycER*) harbouring puromycin resistance or with *p58* cDNA plus *MycER* via a Phoenix viral vector and cultured. After release from aphidicolin, Myc was activated by the addition of hydroxytamoxifen (OHT). At the 20 h time point, cells were fixed and stained. Binucleated cells were scored used automated segmentation routines.

**Full Methods** and any associated references are available in the online version of the paper at [www.nature.com/nature](http://www.nature.com/nature).

Received 23 July; accepted 16 September 2008.

Published online 16 November 2008.

- Gomez-Roman, N. *et al.* Activation by c-Myc of transcription by RNA polymerases I, II and III. *Biochem. Soc. Symp.* **73**, 141–154 (2006).
- Ruggero, D. & Pandolfi, P. P. Does the ribosome translate cancer? *Nature Rev. Cancer* **3**, 179–192 (2003).
- Cornelis, S. *et al.* Identification and characterization of a novel cell cycle-regulated internal ribosome entry site. *Mol. Cell* **5**, 597–605 (2000).
- Petretti, C. *et al.* The PITSLRE/CDK11<sup>p58</sup> protein kinase promotes centrosome maturation and bipolar spindle formation. *EMBO Rep.* **7**, 418–424 (2006).
- Wilker, E. W. *et al.* 14-3-3 $\sigma$  controls mitotic translation to facilitate cytokinesis. *Nature* **446**, 329–332 (2007).
- Boxer, L. M. & Dang, C. V. Translocations involving c-myc and c-myc function. *Oncogene* **20**, 5595–5610 (2001).
- Pelengaris, S., Khan, M. & Evan, G. c-MYC: more than just a matter of life and death. *Nature Rev. Cancer* **2**, 764–776 (2002).
- Grewal, S. S., Li, L., Orian, A., Eisenman, R. N. & Edgar, B. A. Myc-dependent regulation of ribosomal RNA synthesis during *Drosophila* development. *Nature Cell Biol.* **7**, 295–302 (2005).

9. Johnston, L. A., Prober, D. A., Edgar, B. A., Eisenman, R. N. & Gallant, P. *Drosophila myc* regulates cellular growth during development. *Cell* **98**, 779–790 (1999).
10. Moreno, E. & Basler, K. dMyc transforms cells into super-competitors. *Cell* **117**, 117–129 (2004).
11. de la Cova, C., Abril, M., Bellosta, P., Gallant, P. & Johnston, L. A. *Drosophila myc* regulates organ size by inducing cell competition. *Cell* **117**, 107–116 (2004).
12. Oliver, E. R., Saunders, T. L., Tarle, S. A. & Glaser, T. Ribosomal protein L24 defect in belly spot and tail (*Bst*), a mouse *Minute*. *Development* **131**, 3907–3920 (2004).
13. Harris, A. W. *et al.* The *Eμ-myc* transgenic mouse. A model for high-incidence spontaneous lymphoma and leukemia of early B cells. *J. Exp. Med.* **167**, 353–371 (1988).
14. Iritani, B. M. & Eisenman, R. N. c-Myc enhances protein synthesis and cell size during B lymphocyte development. *Proc. Natl Acad. Sci. USA* **96**, 13180–13185 (1999).
15. Thomas, G. An encore for ribosome biogenesis in the control of cell proliferation. *Nature Cell Biol.* **2**, E71–E72 (2000).
16. Yang, W. *et al.* Repression of transcription of the *p27<sup>Kip1</sup>* cyclin-dependent kinase inhibitor gene by c-Myc. *Oncogene* **20**, 1688–1702 (2001).
17. Wu, S. *et al.* Myc represses differentiation-induced *p21CIP1* expression via Miz-1-dependent interaction with the *p21* core promoter. *Oncogene* **22**, 351–360 (2003).
18. Bouchard, C. *et al.* Direct induction of cyclin D2 by Myc contributes to cell cycle progression and sequestration of p27. *EMBO J.* **18**, 5321–5333 (1999).
19. Pyronnet, S. & Sonenberg, N. Cell-cycle-dependent translational control. *Curr. Opin. Genet. Dev.* **11**, 13–18 (2001).
20. Hellen, C. U. & Sarnow, P. Internal ribosome entry sites in eukaryotic mRNA molecules. *Genes Dev.* **15**, 1593–1612 (2001).
21. Dave, B. J. *et al.* Deletion of cell division cycle 2-like 1 gene locus on 1p36 in non-Hodgkin lymphoma. *Cancer Genet. Cytogenet.* **108**, 120–126 (1999).
22. Nelson, M. A. *et al.* Abnormalities in the *p34<sup>cdc2</sup>*-related PITSRE protein kinase gene complex (CDC2L) on chromosome band 1p36 in melanoma. *Cancer Genet. Cytogenet.* **108**, 91–99 (1999).
23. Lahti, J. M. *et al.* Alterations in the PITSRE protein kinase gene complex on chromosome 1p36 in childhood neuroblastoma. *Nature Genet.* **7**, 370–375 (1994).
24. Chandramouli, A. *et al.* Haploinsufficiency of the *cdc2l* gene contributes to skin cancer development in mice. *Carcinogenesis* **28**, 2028–2035 (2007).
25. Fujiwara, T. *et al.* Cytokinesis failure generating tetraploids promotes tumorigenesis in *p53*-null cells. *Nature* **437**, 1043–1047 (2005).
26. Wade, M. & Wahl, G. M. c-Myc, genome instability, and tumorigenesis: the devil is in the details. *Curr. Top. Microbiol. Immunol.* **302**, 169–203 (2006).
27. Amsterdam, A. *et al.* Many ribosomal protein genes are cancer genes in zebrafish. *PLoS Biol.* **2**, e139 (2004).
28. Ganem, N. J., Storchova, Z. & Pellman, D. Tetraploidy, aneuploidy and cancer. *Curr. Opin. Genet. Dev.* **17**, 157–162 (2007).
29. Svitkin, Y. V. *et al.* Eukaryotic translation initiation factor 4E availability controls the switch between cap-dependent and internal ribosomal entry site-mediated translation. *Mol. Cell Biol.* **25**, 10556–10565 (2005).
30. Yoon, A. *et al.* Impaired control of IRES-mediated translation in X-linked dyskeratosis congenita. *Science* **312**, 902–906 (2006).

**Supplementary Information** is linked to the online version of the paper at [www.nature.com/nature](http://www.nature.com/nature).

**Acknowledgements** We thank F. McCormick, G. Evan and P. O'Farrell for critically reading the manuscript; J. Testa for support and critical discussion during early stages of this work; W. Xu and R. Adamo for technical assistance; J. Copley for editing the manuscript, S. Cornelis for the Cdk11 IRES bicistronic vector. This work was supported by the NIH (D.R.) and the Sandler Foundation (M.B.).

**Author Contributions** M.B. and D.R. conceived the experiments. M.B. designed and M.B., A.Y., O.Z., M.C. and N.K. performed experiments and collected data. E.R. analysed the lymphoid compartment of ribosomal protein heterozygote mice. P.H.R. designed, performed and interpreted CGH experiments. M.B. and D.R. analysed the data and wrote the manuscript.

**Author Information** Reprints and permissions information is available at [www.nature.com/reprints](http://www.nature.com/reprints). Correspondence and requests for materials should be addressed to M.B. ([maria.barna@ucsf.edu](mailto:maria.barna@ucsf.edu)) or D.R. ([Davide.Ruggero@ucsf.edu](mailto:Davide.Ruggero@ucsf.edu)).



## METHODS

**Mice.** *Eμ-Myc*<sup>+</sup> transgenic mice, *L24*<sup>+/-</sup>, *L38*<sup>+/-</sup> and *p53*<sup>-/-</sup> mice were all maintained on a C57/BL6 background and their offspring were bred in accordance with protocols approved by the committee for animal research at the University of California, San Francisco, to obtain the genotypic combinations described in this paper. In all cases, *Eμ-Myc*<sup>+</sup> transgenic mice were maintained and studied on a heterozygote background. Mice were monitored twice a week for signs of morbidity and tumour development. Myc tumour initiation was scored by peripheral lymph node palpation as previously described<sup>31</sup>. Moribund mice (*Eμ-Myc*<sup>+</sup>, *Eμ-Myc*<sup>+</sup>; *L24*<sup>+/-</sup>, *Eμ-Myc*<sup>+</sup>; *L38*<sup>+/-</sup>, *p53*<sup>-/-</sup>, *p53*<sup>-/-</sup>; *L24*<sup>+/-</sup>) or mice with obvious tumours were killed, and tumours and different organs were analysed by histology or processed for further analysis.

**Cell culture and analysis of IRES dependent translation in mitosis.** Primary B-lymphocytes were isolated from spleen or bone marrow from 4–5-week-old mice using an autoMACS separator (Miltenyi Biotec) according to the manufacturer's instructions. To synchronize primary B-lymphocytes in mitosis,  $2 \times 10^6$  cells ml<sup>-1</sup> were plated in culture medium (RPMI-1640 supplemented with 10% fetal bovine serum (FBS), 1% penicillin/streptomycin, 0.5% β-mercaptoethanol, 5 μg ml<sup>-1</sup> CD40 and 15 μg ml<sup>-1</sup> IL-4). After 24 h, cells were resuspended in fresh culture medium supplemented with 2.5 mM thymidine and incubated for 18 h to arrest cells in S phase. Cells were released from the thymidine block by washing in PBS plus 2% FBS and incubated in fresh culture medium for 6 h. Thymidine (2.5 mM) was then added to the medium for 24 h. The cells were released from the second thymidine block as described above and incubated in fresh culture medium containing 1.5 μM nocodazole for 16 h to arrest cells in mitosis. Mouse embryonic fibroblasts (MEFs) were isolated from wild-type and *L24*<sup>+/-</sup> 13–14 days post coitum embryos and infected with MycER<sup>32</sup>. Cells were transfected at steady state and in mitosis. For the steady state condition, MEFs were plated in 6-well culture plates at  $\sim 5 \times 10^5$  cells per well and allowed to grow overnight to  $\sim 50\%$  confluency. Transfection and subsequent steps were performed concurrently in both steady state and mitosis. Synchronization in mitosis was performed as previously described<sup>33</sup>. In brief, after release from the aphidicolin block, MEFs were transfected with the HCV IRES or Cdk11<sup>p58</sup> IRES RNA bicistronic vector as previously described<sup>30</sup>. At this time MycER was activated by the addition of OHT. Cells were collected 12 h in mitosis and Firefly and Renilla activities were quantified using the Glomax luminometer. Bicistronic messenger RNA levels were normalized by quantitative PCR (qPCR) using Rluc 5'-AACGCGGCTCTTCTTATTT-3'; 5'-ATTGCTGATTTGCCATA-3' and Fluc 5'-GAGGTTCCATCTGCAGTA-3'; 5'-CCGGTATCCAGATCCACAAAC-3' primers. IRES-dependent expression of endogenous Cdk11<sup>p58</sup> was performed by western blot using rabbit polyclonal anti-CDK11<sup>p58</sup> from Abcam. Expression of β-actin was detected to confirm equal loading.

**Analysis of global protein synthesis.** Equal numbers of freshly isolated or cultured primary B-lymphocytes (synchronized in S phase or mitosis) from 4–5-week-old mice were incubated in methionine-free DMEM for 45 min and then 50 μCi per well (25 μCi ml<sup>-1</sup>) of [<sup>35</sup>S] methionine (Perkin Elmer) was added to the cultures for 35 min. Whole cell lysates were prepared with protein extraction buffer (50 mM Tris-HCl, pH 7.5, 150 mM NaCl, 1 mM dithiothreitol, 1 mM EDTA, 1% Triton X-100, 1× protease inhibitor cocktails) by freezing in dry ice for 3 min and thawing at 37 °C for 3 min. Thirty micrograms of protein was loaded on a 4–20% Tris-HCl gradient gel (Bio-Rad) and transferred onto a nitrocellulose membrane. In certain experiments, cells were pretreated with 200 nM rapamycin (Sigma) and incubated for 45 min at 37 °C<sup>34</sup>. Thirty microcuries of <sup>35</sup>S was added to each well and incubated for 90 min at 37 °C. Radiolabelled proteins were visualized by exposure to X-ray film at -80 °C for 16 h. The radioactivity of each lane was quantified by densitometry analysis.

**Cellular and molecular analysis of lymphocytes.** Freshly isolated and cultured B-lymphocytes from 4–5-week-old mice were fixed in 95% ethanol, labelled with propidium iodide and cell cycle analysed using a BD Biosciences FACSCalibur system. For *in vivo* analysis of cell cycle rates, mice (4–6 weeks old) were administered 1 mg of BrdU (BD Biosciences BrdU Flow Kit) by intraperitoneal (i.p.) injection 6 h before being killed. Spleenocytes were washed with PBS containing 3% FBS and 0.09% NaN<sub>3</sub> and B-lymphocytes were labelled with pacific blue-conjugated rat-anti mouse B220 (BD Biosciences). BrdU staining was performed using the BD Biosciences BrdU Flow Kit following manufacturer's instructions. Samples were analysed using a BD Biosciences LSRII flow cytometer and the BD Biosciences FACSDiva software. The percentage of BrdU-positive B-lymphocytes was determined using the FlowJo 8.7.1 software. For the immunophenotypic analysis of blood and spleen from *L24*<sup>+/-</sup> and *L38*<sup>+/-</sup> mice, 100 μl of peripheral blood and splenic cell suspensions obtained by mechanical disruption of the spleen, were processed and stained with the following combination of monoclonal antibodies conjugated with FITC or PE: CD19-PE and CD3-FITC,

CD4-PE and CD8-FITC, and CD43-PE and CD45R-B220-FITC. Fluorochrome-conjugated isotypic antibodies of irrelevant specificity were used as negative controls. Red blood cells were lysed immediately after labelling by incubation with 2 ml of FACS lysis solution (BD Biosciences) as recommended by the manufacturer. A minimum of 10,000 events per tube were acquired with a BD Biosciences LSRII flow cytometer. Mononuclear cells were gated and the percentage of each cell subset was determined using the CellQuest software (BD Biosciences). TUNEL assay (Roche) was performed on freshly isolated lymphocytes by following the manufacturer's instructions. Cell volume measurements were performed using a Coulter Model Z2 (Beckman Coulter). Cells were diluted in Isoton II (Beckman Coulter) at 100,000 cells ml<sup>-1</sup> in 10 ml. A 1-ml sample was analysed according to the manufacturer's instructions. Fifty-thousand sorted cells were resuspended in 6 ml of Isoton II, and 1 ml was analysed. Centrosome analysis was performed on cell cytospins fixed in cold methanol for 10 min and then briefly incubated in ice-cold acetone. The antibodies used for immunofluorescence staining were anti-mouse γ-tubulin (T-6557 Sigma; 1:1,000) and 4,6-diamidino-2-phenylindole (DAPI). For western blot analysis total proteins were extracted in buffer A (150 mM NaCl, 20 mM NaH<sub>2</sub>PO<sub>4</sub>, 2 mM EGTA, 2 mM EDTA, 0.5 % Triton X-100, 1 mM dithiothreitol and Complete Protease Inhibitor Cocktail Tablets (Roche)), and 30 μg of proteins were used. The membrane was probed with the appropriate antibody; anti-mouse p27 (BD Biosciences), anti-rabbit cyclin D2 (Santa Cruz) and anti-mouse p21 (BD Biosciences). Expression of β-actin was detected to confirm equal loading.

**CGH analysis.** Genomic DNA extracted from lymphomas of six *Eμ-Myc*<sup>+</sup> transgenic mice and six *Eμ-Myc*<sup>+</sup>; *L24*<sup>+/-</sup> mice was subjected to CGH array analysis. High-molecular-mass mouse DNA was extracted from mutant mice and normal tissue by standard methods and subjected to CGH according to the previously published method with some modifications<sup>35</sup>. In brief, the test DNA and reference DNA were labelled by nick-translation with fluorescein-12-dUTP and Texas Red-5-dUTP (NEN-DuPont), respectively. Equal amounts of test and reference DNA were coprecipitated along with 10 mg of mouse *Cot-1* DNA (GIBCO/BRL) and resuspended in the hybridization mix before *in situ* hybridization to mouse metaphase chromosome spreads on hybridization. The chromosomes were counterstained with DAPI to allow their identification. Then, 10 to 15 separate metaphases were captured for each case using a cooled charge-coupled devices (CCD) camera attached to a Nikon Eclipse 800 microscope. Copy number changes were detected on the basis of the variance of the red:green ratio profile from the standard of one. Ratio values of 1.20 and 0.80 were used as upper and lower thresholds to define gains and losses, respectively.

**Cytokinesis analysis.** A full-length *Cdk11*<sup>p58</sup> cDNA was generated from mitotically synchronized B cells using PCR with reverse transcription (RT-PCR) with the following primers: 5'-GAATTCTGAGGAAATGAGTGAAGATGAAGAC-3' and 5'-GTCGACGACCTCAGAACTTGAGGCTGAA-3'. *p58* PITSRE cDNA was cloned in retroviral pBABE construct harbouring hygromycin resistance. Primary MEFs were stably transfected with *MycER* harbouring puromycin resistance or with *Cdk11*<sup>p58</sup> cDNA plus *MycER* via a Phoenix viral vector and cultured in DMEM containing 10% FBS. Wild type, *MycER* and *p58*; *MycER* cells were each plated in chamber slides at  $2 \times 10^{-4}$  cells per well. Synchronization in mitosis was performed as previously described<sup>33</sup>. After release from aphidicolin, Myc was activated by the addition of OHT. At the 20 h time point, cells were fixed in 4% paraformaldehyde and stained with an antibody against α-tubulin (Sigma) and with DAPI. Binucleated cells were scored from more than four independent experiments with a minimal of 500 cell counts each. The slides were scanned using a motorized XY stage and acquired images were processed using the taxonomy features in Nikon Elements software V3 to quantify the number of binucleated cells for each well.

**Semi-quantitative and quantitative RT-PCR.** Total RNA from B-lymphocytes was extracted using Trizol (Invitrogen) and purified using RNeasy (Qiagen) following the manufacturer's instructions. From each sample, 3 μg RNA was treated with DNase (Turbo DNA Free, Ambion). Then, 1 μg was used for cDNA synthesis with the SuperScript III First-Strand Synthesis System (Invitrogen) following manufacturer's instructions and using 2.5 μg random primers (Promega), 0.5 mM dNTPs and 400 U SuperScript III in a reaction volume of 100 μl. From each sample, 1 μg RNA was used as negative control by the omission of reverse transcriptase. For PCR, 1/10 (v/v) of cDNA was used with 300 nM of the specific primers in a reaction volume of 25 μl. qPCR was used for the analysis of *p21* and *p27* expression. SYBR GREEN PCR Master Mix (Applied Biosystems) was used and the thermal profiles were: pre-denaturation for 10 min at 95 °C, followed by 42 cycles of denaturation at 95 °C for 20 s, annealing at 57 °C for 30 s and extension at 72 °C for 30 s. Reactions were performed in duplicate in an Applied Biosystems 7300 thermocycler and the 7300 software system v1.4.0 was used for analysis. At the end of each PCR reaction, dissociation curves were generated to verify the formation of a specific amplicon.

Primer sequences used were: *p21*, 5'-GACAGTGAGCAGTTGCG-3', 5'-CTCA-GACACCAGAGTGC-3'; *p27*, 5'-TCAAACGTGAGAGTGTCTAACGG-3';  $\beta$ -*actin*, 5'-CCTAGCACCATGAAGATCAAG-3', 5'-ATCGTACTCCTGCTT-GCTG-3'. Forward and reverse primers used for *Gadd45a* qPCR were purchased from SuperArray (PPM02927B). As a positive control for cellular stress and induction of *Gadd45a* mRNA expression, 3T3 cells were incubated with 100  $\mu$ g ml<sup>-1</sup> methyl methanesulphonate in culture medium (DMEM, 10% FBS and 1% streptomycin/penicillin) for 4 h and total RNA was extracted using Trizol. Semi-quantitative PCR was used for the analysis of cyclin D2 expression. GoTaq Master Mix (Promega) was used and the thermal profiles were: pre-denaturation for 3 min at 94 °C, followed by 25 cycles (denaturation for 30 s at 94 °C, annealing for 30 s at 53 °C (for *cyclin D2*), and 57 °C (for  $\beta$ -*actin*), elongation for 1 min at 72 °C) and final elongation for 10 min at 72 °C. Primer sequences were: *cyclin D2*, 5'-GTTCTGCAGAACCTGTTGAC-3', 5'-ACAGCT-TCTCCTTTTGCTGG-3';  $\beta$ -*actin*, 5'-GTATGGAATCCTGTGGCATC-3', 5'-AA-GCACTTGCGGT GCACGAT-3'. Amplicons were resolved in 1.5% agarose gel containing 40 mM Tris-acetate, 1 mM EDTA, pH 8.0, and 0.5  $\mu$ g ml<sup>-1</sup> ethidium bromide. Gels were photographed by ultraviolet transillumination using an AlphaInnotech camera and software. Relative expression ratios were obtained by densitometry using the ImageJ software.

31. Ruggero, D. L. *et al.* The translation factor eIF-4E promotes tumor formation and cooperates with c-Myc in lymphomagenesis. *Nature Med.* **10**, 484–486 (2004).
32. Lenahan, M. K. & Ozer, H. L. Induction of c-myc mediated apoptosis in SV40-transformed rat fibroblasts. *Oncogene* **12**, 1847–1854 (1996).
33. Ferguson, A. M., White, L. S., Donovan, P. J. & Piwnicka-Worms, H. Normal cell cycle and checkpoint responses in mice and cells lacking Cdc25B and Cdc25C protein phosphatases. *Mol. Cell Biol.* **25**, 2853–2860 (2005).
34. Beretta, L., Gingras, A. C., Svitkin Y.V., Hall M. N. & Sonenberg, N. Rapamycin blocks the phosphorylation of 4E-BP1 and inhibits cap-dependent initiation of translation. *Embo J.* **15**, 658–664 (1996).
35. Kallioniemi, O. P. *et al.* Optimizing comparative genomic hybridization for analysis of DNA sequence copy number changes in solid tumors. *Genes Chromosom. Cancer* **10**, 231–243 (1994).

## LETTERS

# A structural explanation for the binding of endocytic dileucine motifs by the AP2 complex

Bernard T. Kelly<sup>1\*</sup>, Airlie J. McCoy<sup>1\*</sup>, Kira Späte<sup>2†</sup>, Sharon E. Miller<sup>1</sup>, Philip R. Evans<sup>3</sup>, Stefan Höning<sup>2</sup> & David J. Owen<sup>1</sup>

Most transmembrane proteins are selected as transport-vesicle cargo through the recognition of short, linear amino-acid motifs in their cytoplasmic portions by vesicle coat proteins. For clathrin-coated vesicles, the motifs are recognized by clathrin adaptors. The AP2 adaptor complex (subunits  $\alpha$ ,  $\beta_2$ ,  $\mu_2$  and  $\sigma_2$ ) recognizes both major endocytic motifs: Yxx $\Phi$  motifs<sup>1</sup> (where  $\Phi$  can be F, I, L, M or V) and [ED]xxxL[LI] acidic dileucine motifs. Here we describe the binding of AP2 to the endocytic dileucine motif from CD4 (ref. 2). The major recognition events are the two leucine residues binding in hydrophobic pockets on  $\sigma_2$ . The hydrophilic residue four residues upstream from the first leucine sits on a positively charged patch made from residues on the  $\sigma_2$  and  $\alpha$  subunits. Mutations in key residues inhibit the binding of AP2 to 'acidic dileucine' motifs displayed in liposomes containing phosphatidylinositol-4,5-bisphosphate, but do not affect binding to Yxx $\Phi$  motifs through  $\mu_2$ . In the 'inactive' AP2 core structure<sup>3</sup> both motif-binding sites are blocked by different parts of the  $\beta_2$  subunit. To allow a dileucine motif to bind, the  $\beta_2$  amino terminus is displaced and becomes disordered; however, in this structure the Yxx $\Phi$ -binding site on  $\mu_2$  remains blocked.

In clathrin-coated vesicles (CCVs), cargo is selected mainly through the recognition of one of three types of signal by clathrin adaptors: the short, linear, transplantable peptide motifs that are widely found on general cargo; covalently attached ubiquitin molecules (reviewed in ref. 4); and the folded determinants on SNAP receptor (SNARE) proteins<sup>5,6</sup>. The two major classes of transplantable motif used in CCVs are the Yxx $\Phi$  and acidic dileucine motifs. The latter can be divided into two further classes: the [ED]xxxL[LI] motifs, which, along with Yxx $\Phi$  motifs, are recognized by the heterotetrameric AP clathrin adaptor complexes on numerous different pathways (reviewed in ref. 7), and the DxxLL motifs, recognized by GGAs (Golgi-localizing,  $\gamma$ -adaptin ear homology domain, ARF-interacting proteins) for transport from the *trans*-Golgi network to endosomes<sup>8,9</sup>. AP2 has a pivotal function in regulating the formation of endocytic CCVs destined for early endosomes. Although the mechanism of Yxx $\Phi$  motif binding by APs has been characterized at the molecular level, there is no mechanistic insight into [ED]xxxL[LI] binding, although several recent studies have indicated that the binding site resides on the  $\alpha$ - $\sigma_2$  heterodimer<sup>10,11</sup>. Eight different 'acidic dileucine' peptides were tried in co-crystallization experiments with the 200-kDa AP2 core, and several produced poorly diffracting crystals. However, co-crystallization with the peptide RM(phosphoS)QIKRLLE (Q peptide) from the T-cell cell-surface antigen protein CD4, and a variant of this peptide (RM(phosphoS)EIKRLLE) (E peptide), resulted in crystals that diffracted to resolutions of 3.0 and 3.4 Å respectively. The structure

of the Q peptide complex was solved by molecular replacement by using models derived from the closed structure<sup>3</sup> (Fig. 1). Rebuilding of the  $\alpha$  and  $\beta_2$  helical solenoids was required because of alterations in their overall curvature (see below), but even in the initial electron density maps the 'dileucine peptide' could be seen clearly. The identity and orientation of the peptide was confirmed as described in Methods.

The structure shows that the peptide binds in an extended conformation near the  $\alpha$ -subunit binding site for phosphatidylinositol-4,5-bisphosphate (PtdIns(4,5)P<sub>2</sub>), which is replaced here by two sulphate ions (Fig. 1 and Supplementary Fig. 3). The LL moiety at positions L0 and L+1 (for nomenclature see ref. 7 and Supplementary Fig. 1b) binds in two adjacent hydrophobic pockets

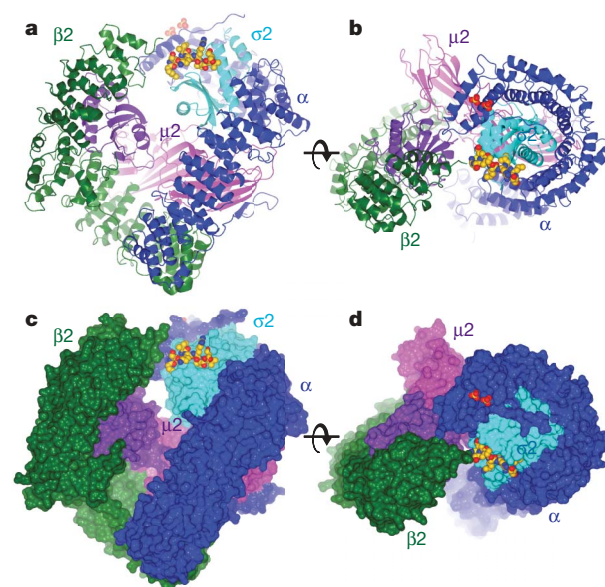


**Figure 1 | Structure of the AP2 adaptor core in complex with the dileucine peptide from CD4.** Orthogonal views of the dileucine motif liganded AP2 complex in ribbon (**a, b**) and in molecular surface (**c, d**) representations. In **a** and **c** the membrane is parallel to the upper face of the complex, and in **b** and **d** the complex is viewed through the membrane, with the membrane interacting surface facing upwards. The  $\alpha$  subunit is coloured dark blue,  $\beta_2$  green,  $\sigma_2$  pale blue, N- $\mu_2$  purple and C- $\mu_2$  mauve. Atoms in the dileucine motif peptide are shown as spheres, with carbons coloured gold. The two sulphate groups bound to the  $\alpha$  subunit in the PtdIns(4,5)P<sub>2</sub> site are shown.

<sup>1</sup>Cambridge Institute for Medical Research and Department of Clinical Biochemistry, University of Cambridge, Addenbrooke's Hospital, Hills Road, Cambridge CB2 0XY, UK. <sup>2</sup>Institute of Biochemistry I and Center for Molecular Medicine Cologne, University of Cologne, Joseph-Stelzmann-Strasse 52, 50931 Cologne, Germany. <sup>3</sup>Medical Research Council Laboratory of Molecular Biology, Hills Road, Cambridge CB2 0QH, UK. <sup>†</sup>Present address: Max Planck Institute for Experimental Medicine, Hermann-Rein-Strasse 3, 37075 Göttingen, Germany. \*These authors contributed equally to this work.



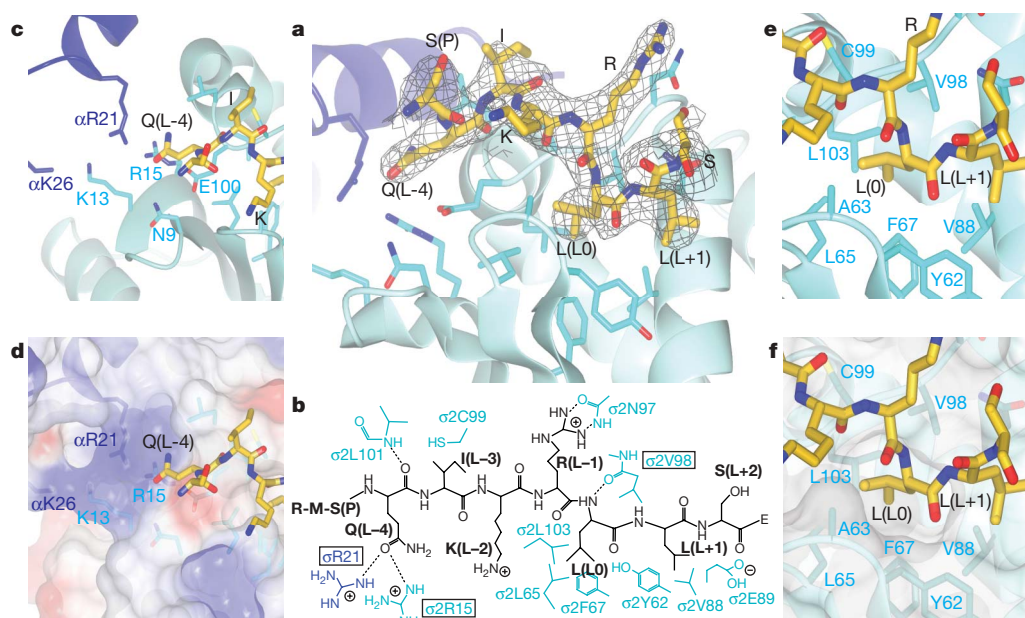


**Figure 2 | Details of binding of the CD4 dileucine signal by the  $\sigma 2$  and  $\alpha$  subunits of AP2.** **a**, The dileucine peptide is bound mainly by the pale blue  $\sigma 2$  subunit near its interface with the  $\alpha$  subunit (dark blue). The peptide is shown in its final  $2mF_o - DF_c$  electron density (cropped around the peptide and contoured at  $0.11\text{e}\text{\AA}^{-3}$ ). **b**, Schematic representation of the dileucine peptide with the principal side chains involved in its binding. Mutants in the boxed residues were analysed kinetically. **c**, Details of the polar Q(L-4)

binding pocket. **d**, As **c**, with a semi-transparent electrostatic surface representation (coloured from red at  $-0.5\text{ V}$  to blue at  $+0.5\text{ V}$ ), showing the positive charge principally due to  $\alpha R21$ ,  $\sigma 2K13$  and  $\sigma 2R15$ . **e**, Details of the deep and shallow pockets on  $\sigma 2$  involved in recognizing the leucine residues at positions L0 and L+1. **f**, As **e**, with a molecular surface. Labelled side chains are in the  $\sigma 2$  subunit unless otherwise indicated.

on the small  $\sigma 2$  subunit that are lined by several hydrophobic residues (Fig. 2), most of which are conserved in all  $\sigma$  subunits from APs 1–4 in species from yeast to mammals (Fig. 3 and Supplementary Information). Mutation of several of these to hydrophilic residues ( $\sigma 2L65S$ ,  $\sigma 2V88D$ ,  $\sigma 2V98S$  or  $\sigma 2L103S$ ), or filling in the pocket by replacement of  $\sigma 2A63$  or  $\sigma 2N92$  with tryptophan, strongly inhibited the binding of recombinant AP2 core complexes to different dileucine motifs displayed on PtdIns(4,5) $P_2$ -containing liposomes (Supplementary Table 2, Methods and ref. 12). The  $K_d$  for the binding of wild-type AP2 to the CD4 dileucine motif was  $0.85\text{ }\mu\text{M}$ , whereas the  $\sigma 2V88$  and  $\sigma 2L103$  mutations decreased binding to below detectable levels. A double mutant in  $\sigma 2R15$  and  $\alpha R21$  decreased binding to the dileucine motif by around an order of magnitude, with the  $K_d$  for  $\sigma 2R15S/\sigma 2R21E$  double mutant decreasing to  $7.8\text{ }\mu\text{M}$ . In contrast, the binding of wild-type and mutant AP2 cores to PtdIns(4,5) $P_2$  and to Yxx $\Phi$  was unaffected, with  $K_d$  values for binding to the TGN38 Yxx $\Phi$  motif between  $0.31$  and  $0.38\text{ }\mu\text{M}$ , indicating that all recombinant core variants were correctly folded and functional (Fig. 3).

The L-4 position of AP2-binding dileucine motifs is most commonly occupied by the acidic residues glutamate or aspartate; however, other residues are possible, such as glutamine (as in the human CD4 dileucine motif used here), histidine (in feline CD4) or arginine (in GLUT4) (reviewed in ref. 7). The binding of the residue in the L-4 position occurs on a hydrophilic patch with an overall positive charge. The electron density for its side chain is not as strong as that for the two leucine residues or the peptide backbone, indicating some degree of flexibility in binding. Indeed, simultaneous mutation of two basic residues in the patch ( $\alpha R21$  and  $\sigma 2R15$ ) were necessary to decrease dileucine motif binding significantly (Fig. 3). In the E peptide, where the L-4 position is the more commonly found glutamate<sup>7</sup>, the electron density is similar to that for the corresponding glutamine in the Q peptide complex (see Supplementary Information). The use of general electrostatic complementarity rather than a specific interaction between side chains is supported

by the fact that exchange of a motif's L-4 glutamate to a shorter aspartate has little effect on the binding of dileucine motifs to AP2 (ref. 11). This general electrostatic interaction probably assists in correctly orienting the peptide, a proposal supported by the observations that mutation of the L-4 acidic residue to alanine significantly weakens binding but does not abolish it, whereas mutation to a positively charged arginine abrogates binding altogether in the context of the sequence EDEPLL<sup>11</sup>. Consistent with this was our observation of a slightly weaker binding of AP2 to the Q peptide than to the E peptide (see data in Supplementary Table 3). However, in GLUT4 transporters (RRTPSLL) the L-4 and L-5 positions of the internalization motifs are arginine residues (reviewed in ref. 7); suggesting that AP2 might possess alternative modes of dileucine motif binding that would probably use the same dileucine-moiety binding pocket but could place the remainder of the peptide in a different location. Taken together, these structural and mutagenesis data explain the inhibition of the endocytosis of dileucine-motif-containing cargoes when the key L[LI] and [ED] residues are mutated<sup>11,13,14</sup>.

Point mutation and motif swapping indicates that the identity of the residues in the L-1 to L-3 positions have some effect on motif binding<sup>10,11</sup>. In the structure presented here, the arginine in the L-1 position interacts with  $\sigma 2N97$ . A proline, often found at this position, would increase the strength of binding by favouring the conformation of the peptide backbone observed in the bound peptide<sup>14</sup>. In this AP2-CD4 peptide complex the amino-acid residue side chains at the -2 and -3 positions point into solvent, away from the AP2 surface. *In vivo*, however, the conformational context of the motif may be affected by these and other surrounding residues, as has been proposed for the L-5 position phosphorylated serine residue, which has no visible electron density for the phosphate in the structures presented here, despite its presence as confirmed by mass spectrometry (data not shown). The apparent lack of sequence specificity for residues other than the L[LI] moiety—manifested in the increased tolerance of AP2 for alterations in residues adjacent to the L[LI] in comparison with AP1 and AP3 (ref. 11)—is reflected in the lack of

strong contacts between non-L[LI] residues of the motif and AP2 shown here. Such comparatively broad specificity, as is demonstrated by the similar binding affinities displayed by AP2 for several different 'acidic dileucine' motifs (Supplementary Table 3), may ensure the efficient internalization of dileucine-motif-containing proteins that arrive at or mis-sort to the cell surface. The ability of the other AP complexes to discriminate between different L[LI] signals may be

necessary to 'fine tune' the directing of cargoes to different intracellular compartments.

In the closed and therefore inactive conformation of AP2 (ref. 3), the hydrophobic L[LI] binding pockets are occupied by side chains from residues in the N-terminal extension to the first helix of the  $\beta 2$  subunit.  $\beta 2F7$  occupies the deep L0 pocket, whereas  $\beta 2Y6$  lies in the broader and shallower L+1 L[LI] pocket (Fig. 4 and Supplementary Fig. 8c). Phosphorylation of  $\beta 2Y6$  by EGFR<sup>15</sup> would inhibit the binding of  $\beta 2Y6$  in the L+1 pocket and therefore would greatly weaken the interaction between the N terminus of  $\beta 2$  and  $\sigma 2$ . In the overall structure of the heterotetrameric complex, the helical solenoids of the  $\alpha$  and  $\beta 2$  chains form a puckered ring around  $\sigma 2$  and the N-terminal domain of  $\mu 2$  (N- $\mu 2$ ), which together make a bowl for the carboxy-terminal domain of  $\mu 2$  (C- $\mu 2$ ). Comparing this dileucine-motif-liganded, unlocked structure with the 'inactive' conformation, the  $\alpha/\beta 2$  ring splits approximately as two rigid bodies,  $\alpha(1-400)-\sigma 2$  and  $\alpha(401-\text{end})\beta 2/\text{N}-\mu 2$ , with a relative rotation of about  $20^\circ$  around a point near residue  $\alpha 400$ . This widens the opening of the ring at the N terminus of  $\beta 2$ , and the N-terminal extension swings away into solvent, thus exposing the peptide-binding site. C- $\mu 2$  forms a third rigid body, bridging between  $\alpha$  and  $\beta 2$ , and roughly preserving its contacts with both  $\alpha$  and  $\beta 2$ , such that the Yxx $\Phi$ -binding site on  $\mu 2$  remains blocked by  $\beta 2V365$  and  $\beta 2Y405$ . In AP1, and very probably therefore also in AP2, it has been proposed that the binding of either

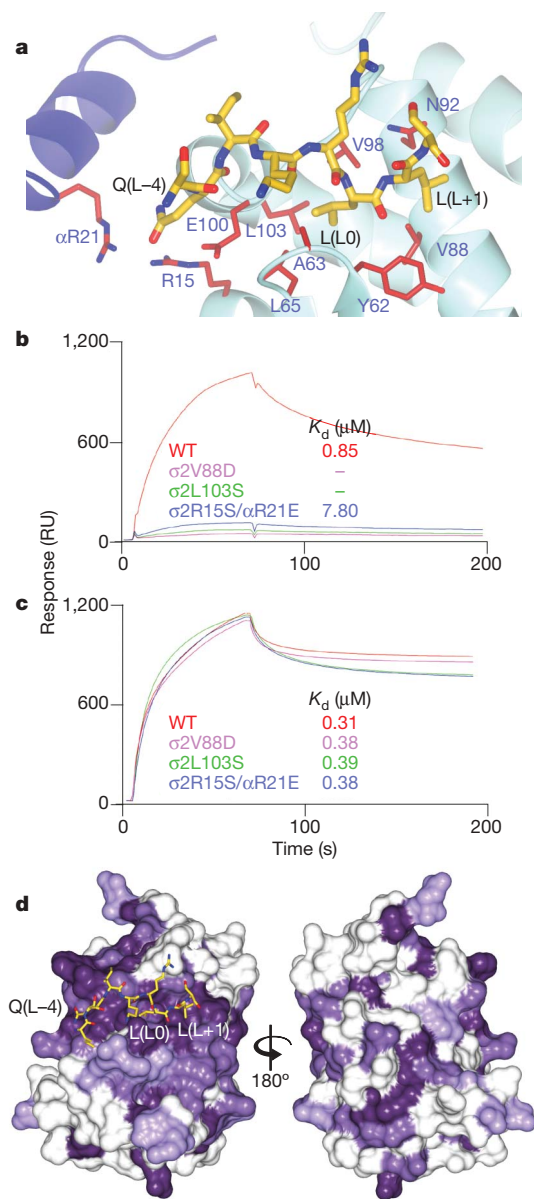


**Figure 3 | Confirmation of location and conservation among different  $\alpha$  subunits of the dileucine-motif-binding site.** **a**, The dileucine-peptide-binding site with residues whose mutation strongly inhibit dileucine peptide binding while not affecting Yxx $\Phi$  motif binding are coloured red (see Supplementary Table 1 and Supplementary Fig. 8). **b**, **c**, Sensorgrams and  $K_d$  values for binding of wild-type AP2 core and three mutants thereof that strongly inhibit the binding of AP2 to PtdIns(4,5) $P_2$ -containing liposomes displaying the CD4 Q peptide motif (**b**) but do not affect binding to PtdIns(4,5) $P_2$ -containing liposomes displaying the TGN38 Yxx $\Phi$  motif (**c**). WT, wild-type; RU, resonance units. **d**, Mammalian  $\sigma 2$ ,  $\sigma 1a$ ,  $\sigma 3$  and  $\sigma 4$  were aligned by using ClustalW (Supplementary Fig. 7) and the residue conservation was plotted from dark purple (absolute conservation) to white (no conservation) onto the surface of mammalian  $\sigma 2$  in two views related by a rotation of  $180^\circ$ . The binding site for the dileucine-motif peptide is the outstanding feature of surface residue conservation.

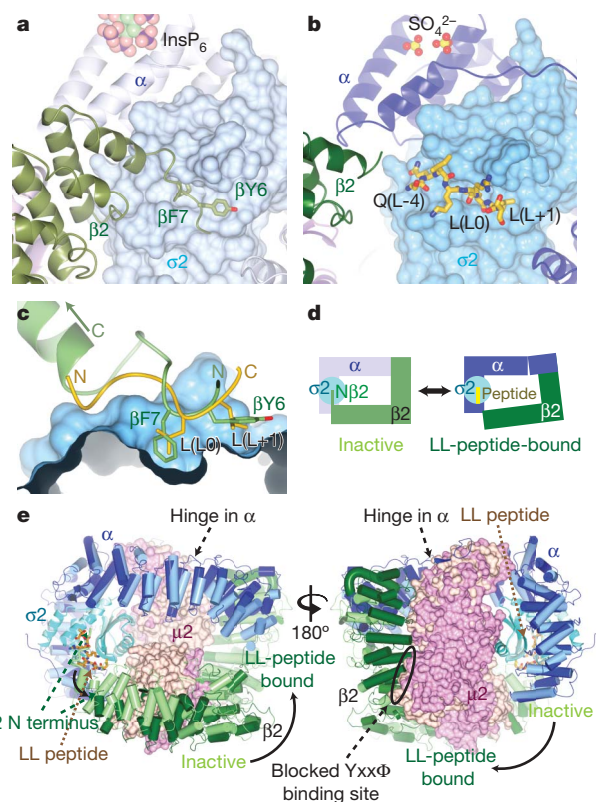


**Figure 4 | A conformational change in AP2 is required for dileucine peptide binding.** **a**, In the  $IP_6$ -liganded inactive conformation the N terminus of  $\beta 2$  is held in place by  $\beta 2F7$  and  $\beta 2Y6$  sitting in the L0 and L+1 pockets. **b**, For dileucine motifs to bind, the N terminus of  $\beta 2$  is displaced from the surface of  $\sigma 2$ . **c**, Close-up of the dileucine-binding site: the dileucine peptide (gold) runs in the opposite direction to the N terminus of  $\beta 2$  (green). **d**, Schematic representation of the conformational change: a  $20^\circ$  hinge movement in  $\alpha$  moves the N terminus of  $\beta 2$  out of the dileucine-binding site, allowing the motif to bind. The  $\mu 2$  subunit has been omitted for clarity. **e**, Front and back views of the conformational change: the  $IP_6$ -liganded inactive conformation is shown in pale colours, the unlocked dileucine-peptide-bound conformation in dark colours. The Yxx $\Phi$  site on  $\mu 2$  remains blocked, and is remote from the dileucine-binding site.



an acidic dileucine or a YxxΦ motif drives a conformational change that favours the binding of the other motif<sup>16</sup>. A further conformational change must therefore occur so as to produce a fully active conformation that is able to bind both types of motif and PtdIns(4,5)P<sub>2</sub> simultaneously. The failure to attain a fully active 'open' conformation is driven by a combination of factors including crystal packing, the lack of a YxxΦ peptide to compete out the auto-inhibitory binding of β2 to μ2, and the high concentration of ammonium sulphate in the crystallization conditions, increasing the apparent strength of the interaction between β2V365 and the C-μ2 Φ-residue binding pocket and also helping to stabilize the interaction of β2 residues 350 and 500 with C-μ2.

The binding site on σ2 used by AP2 to bind acidic dileucine motifs is not the same as that used by other proteins with σ-like or 'longin domain' folds to bind their cognate ligands: these include the SNAREs Sec22b<sup>17</sup> and Vamp7 (ref. 5) and the signal recognition particle SRα subunit<sup>18</sup>. However, the hydrophobic L[LI]-binding pocket, but not the acidic-residue-binding patch at the -4 position, is largely conserved in the ζCOP subunit of the βγδζ subcomplex of COPI that is homologous in structure to AP complexes (PDB 2HF6 and Supplementary Information), pointing to a possible conservation of function in the binding of a di-hydrophobic motif, candidates for which would include the FF motif of the COPI cargoes, the p24 family and ERGIC-53 (ref. 19) and the N terminus of β-COP.

The mechanism of the binding of a dileucine motif by the AP2 clathrin adaptor complex conforms to the established model of a CCV-cargo interaction. The peptide is bound in an extended conformation by a folded adaptor domain, with specificity arising from a few residue side chains fitting into compatible pockets. The mode of binding is therefore superficially similar to the binding of DxxLL motifs by the VHS domains of GGAs<sup>8,9</sup>, but the design of the LL and acidic-residue recognition pockets, their spacing and the structures underlying them are completely different (Supplementary Fig. 9). The interaction between the two isolated components, a dileucine-motif-containing peptide molecule and a single AP2 complex, is dynamic, with a K<sub>d</sub> in the micromolar range (1–3 μM)<sup>12</sup>, and buries about 1,100 Å<sup>2</sup> of solvent-accessible surface area. These values are both similar to those shown for other cargo-clathrin adaptor interactions<sup>6</sup>. When the signal is presented in, and so simultaneously recognized with, a PtdIns(4,5)P<sub>2</sub>-containing membrane, the apparent strength of the interaction with AP2 is increased: the K<sub>d</sub> decreases to the high nanomolar range, as shown here, and it is this coincident detection of PtdIns(4,5)P<sub>2</sub> and acidic dileucine motif that allows the signal to out-compete the N terminus of β2 for binding to σ2. The need for sorting signals to be presented in a PtdIns(4,5)P<sub>2</sub>-containing membrane for efficient AP2 binding also prevents inappropriate recognition of similar sequences in cytoplasmic proteins.

## METHODS SUMMARY

Recombinant AP2 cores were expressed and purified as in ref. 3. Crystals of the CD4-AP2-core complexes were grown over a period of three weeks by hanging-drop vapour diffusion against a reservoir containing 1.7–2.2 M ammonium sulphate, sodium citrate pH 6.5 and 5 mM dithiothreitol from a mixture of 10 mg ml<sup>-1</sup> AP2 core and 7 mg ml<sup>-1</sup> peptide. Crystals were of space group P4<sub>3</sub>2<sub>1</sub>2, with two molecules in the asymmetric unit, and diffracted to a best resolution of 3.0 Å. After cryoprotection, data were collected at 100 K on Diamond beamline I03 and the structure was solved by molecular replacement with PHASER<sup>20</sup>. A complete explanation of the structure determination and of work performed to confirm the identity and orientation of the peptide is given in Methods. Mutant versions of AP2 core were sequenced throughout and the surface plasmon resonance (SPR)-based liposome binding assay was performed as in ref. 12, with the peptides described in Methods.

**Full Methods** and any associated references are available in the online version of the paper at [www.nature.com/nature](http://www.nature.com/nature).

**Received 8 July; accepted 4 September 2008.**

**Published online 2 November 2008; corrected 18 December 2008 (details online).**

- Owen, D. J. & Evans, P. R. A structural explanation for the recognition of tyrosine-based endocytotic signals. *Science* **282**, 1327–1332 (1998).
- Pitcher, C., Honing, S., Fingerhut, A., Bowers, K. & Marsh, M. Cluster of differentiation antigen 4 (CD4) endocytosis and adaptor complex binding require activation of the CD4 endocytosis signal by serine phosphorylation. *Mol. Biol. Cell* **10**, 677–691 (1999).
- Collins, B. M., McCoy, A. J., Kent, H. M., Evans, P. R. & Owen, D. J. Molecular architecture and functional model of the endocytic AP2 complex. *Cell* **109**, 523–535 (2002).
- Hurley, J. H., Lee, S. & Prag, G. Ubiquitin-binding domains. *Biochem. J.* **399**, 361–372 (2006).
- Pryor, P. R. *et al.* Molecular basis for the sorting of the SNARE VAMP7 into endocytic clathrin-coated vesicles by the ArfGAP Hrb. *Cell* **134**, 817–827 (2008).
- Miller, S. E., Collins, B. M., McCoy, A. J., Robinson, M. S. & Owen, D. J. A SNARE-adaptor interaction is a new mode of cargo recognition in clathrin-coated vesicles. *Nature* **450**, 570–574 (2007).
- Bonifacino, J. S. & Traub, L. M. Signals for sorting of transmembrane proteins to endosomes and lysosomes. *Annu. Rev. Biochem.* **72**, 395–447 (2003).
- Shiba, T. *et al.* Structural basis for recognition of acidic-cluster dileucine sequence by GGA1. *Nature* **415**, 937–941 (2002).
- Misra, S., Puertollano, R., Kato, Y., Bonifacino, J. S. & Hurley, J. H. Structural basis for acidic-cluster-dileucine sorting-signal recognition by VHS domains. *Nature* **415**, 933–937 (2002).
- Chaudhuri, R., Lindwasser, O. W., Smith, W. J., Hurley, J. H. & Bonifacino, J. S. Downregulation of CD4 by human immunodeficiency virus type 1 Nef is dependent on clathrin and involves direct interaction of Nef with the AP2 clathrin adaptor. *J. Virol.* **81**, 3877–3890 (2007).
- Doray, B., Lee, I., Knisely, J., Bu, G. & Kornfeld, S. The γ/σ1 and α/σ2 hemicomplexes of clathrin adaptors AP-1 and AP-2 harbor the dileucine recognition site. *Mol. Biol. Cell* **18**, 1887–1896 (2007).
- Honing, S. *et al.* Phosphatidylinositol-(4,5)-bisphosphate regulates sorting signal recognition by the clathrin-associated adaptor complex AP2. *Mol. Cell* **18**, 519–531 (2005).
- Letourneau, F. & Klausner, R. D. A novel di-leucine motif and a tyrosine-based motif independently mediate lysosomal targeting and endocytosis of CD3 chains. *Cell* **69**, 1143–1157 (1992).
- Doray, B., Knisely, J. M., Wartman, L., Bu, G. & Kornfeld, S. Identification of acidic dileucine signals in LRP9 that interact with both GGAs and AP-1/AP-2. *Traffic*. (in the press).
- Huang, F., Jiang, X. & Sorkin, A. Tyrosine phosphorylation of the β2 subunit of clathrin adaptor complex AP-2 reveals the role of a di-leucine motif in the epidermal growth factor receptor trafficking. *J. Biol. Chem.* **278**, 43411–43417 (2003).
- Lee, I., Doray, B., Govero, J. & Kornfeld, S. Binding of cargo sorting signals to AP-1 enhances its association with ADP ribosylation factor 1-GTP. *J. Cell Biol.* **180**, 467–472 (2008).
- Mancias, J. D. & Goldberg, J. The transport signal on Sec22 for packaging into COPII-coated vesicles is a conformational epitope. *Mol. Cell* **26**, 403–414 (2007).
- Schwartz, T. & Blobel, G. Structural basis for the function of the β subunit of the eukaryotic signal recognition particle receptor. *Cell* **112**, 793–803 (2003).
- Bethune, J. *et al.* Coatamer, the coat protein of COPI transport vesicles, discriminates endoplasmic reticulum residents from p24 proteins. *Mol. Cell. Biol.* **26**, 8011–8021 (2006).
- McCoy, A. J., Grosse-Kunstleve, R. W., Storoni, L. C., Adams, P. D. & Read, R. J. PHASER crystallographic software. *J. Appl. Crystallogr.* **40**, 658–674 (2007).

**Supplementary Information** is linked to the online version of the paper at [www.nature.com/nature](http://www.nature.com/nature).

**Acknowledgements** We thank the protein crystallography beamline staff at Diamond, especially E. Duke, K. McAuley and R. Flaig, for their support and assistance. D.J.O., B.T.K. and S.E.M. are funded by a Wellcome Trust Senior Research Fellowship to D.J.O. S.H. and K.S. are supported by grants from the Deutsche Forschungsgemeinschaft (SFB635 and SFB670).

**Author Information** Atomic coordinates and structure factors have been deposited with the Protein Data Bank under accession numbers 2jkr for the Q peptide complex and 2jkt for the E peptide complex, respectively. Reprints and permissions information is available at [www.nature.com/reprints](http://www.nature.com/reprints). Correspondence and requests for materials should be addressed to D.J.O. (djo30@cam.ac.uk).



## METHODS

**Expression, crystallization and structure solution.** The four subunits of the AP2 core (1–621 mouse  $\alpha$ -adaptin; 1–591 human  $\beta$ 2-adaptin; 1–435 rat  $\mu$ 2-adaptin, 1–143 mouse  $\sigma$ 2-adaptin) were co-expressed in *Escherichia coli* from two bicistronic plasmids of different (ampicillin and kanamycin) antibiotic resistances as in ref. 3 in *E. coli* BL21DE3 pLysS cells at 22 °C. Protein expression was allowed to continue for 14 h; the cells were harvested and lysed with a Cell Disrupter (Constant Cell Disruption Systems), and insoluble material was removed by centrifugation. AP2 was purified throughout in 10 mM Tris pH 8.7, 250 mM NaCl, 1 mM dithiothreitol (DTT). The complex was bound to glutathione-Sepharose (Pharmacia), the column was extensively washed and the complex was eluted by cleavage overnight at 20 °C with bovine thrombin (Sigma). The resulting AP2 complex was bound to Ni<sup>2+</sup>-nitrilotriacetate-agarose (Qiagen), the column was extensively washed and the complex was eluted with buffer containing 0.3 M imidazole. The complex was then purified by gel filtration on Superdex S200 (Pharmacia) and finally passed back down a glutathione-Sepharose column to remove any remaining uncleaved glutathione S-transferase (GST)–AP2 complex. The yield was 1–2 mg of purified AP2 per litre of culture.

Crystals of the CD4 peptide/AP2 core complexes were grown over a period of three weeks by hanging-drop vapour diffusion against a reservoir containing 1.7–2.2 M ammonium sulphate, 100 mM sodium citrate pH 6.5 and 5 mM DTT from a mixture of 10 mg ml<sup>-1</sup> AP2 core and 7 mg ml<sup>-1</sup> peptide. The best crystals had dimensions of about 200  $\mu$ m and diffracted to a best resolution of 3.0 Å. Crystals were cryoprotected with 1.8–2.3 M ammonium sulphate, 100 mM sodium citrate pH 6.5, 17% glycerol and 7 mg ml<sup>-1</sup> CD4 dileucine peptide. Data were collected at 100 K on Diamond beamline I03, integrated with Mosflm<sup>21</sup> and scaled with Scala<sup>22</sup>. The crystals belong to space group *P*<sub>4</sub><sub>3</sub><sub>2</sub><sub>1</sub>, with two molecules in the asymmetric unit. The structure was solved by molecular replacement by using Phaser<sup>20</sup>, with models derived from the IP<sub>6</sub>-liganded ‘inactive’ AP2 core structure (ref. 3; PDB code 2VGL). Extra electron density representing the peptide bound to the  $\sigma$ 2 subunit was clear from the first maps after molecular replacement (Supplementary Fig. 1). The final model refined at 3.0 Å resolution comprises residues 3–623 of  $\alpha$  (lacking 1–2 and including a final two residues from the cloning linker), 12–582 of  $\beta$ 2 (lacking 1–11 and 583–591), 1–142 of  $\sigma$ 2 (lacking none), and residues 1–141 and 159–435 of  $\mu$ 2 (lacking 142–158, as well as the loop 223–231, which are also missing from the structure of isolated C- $\mu$ 2), the dileucine peptide, sulphates and waters. For statistics relating to the data collection and structure solution see Supplementary Table 1 and for a sample of typical electron density see Supplementary Fig. 2.

The orientation and registration of the RMS(P)QIKRLLE peptide in this density was decided as follows. First, there were clearly two pockets for hydrophobic residues, one deep and one shallow. Electron density consistent with leucine side chains could be seen in each pocket, but the orientation of the backbone connecting them could be in either direction. Second, the electron density for the peptide extends for about four or five residues on one side of the deep pocket, but not more than one or two on the other side of the shallow pocket; because the LL sequence is only two residues from the C terminus of the peptide, the longer part of the density must be N-terminal to the LL sequence. This places the invariant first L in the deep pocket, and the conserved second L (which can also be I or M) in the shallower pocket. With this model of the peptide, the structure refined well, showing good density for the residues SQIKRLLS (see Fig. 2), but no density for the phosphate moiety of the phosphoserine (S(P)) side chain, which was therefore modelled as a serine, although mass spectrometry of a sample of peptide incubated in crystallization conditions for two weeks confirmed that the serine residue remained phosphorylated. The lack of density for the phosphate is likely to be caused by static disorder of the phosphate group. The structure was refined with Phenix.refine<sup>23</sup>, with default tight non-crystallographic symmetry restraints between the two molecules, and rebuilt with Coot<sup>24</sup>. Large positive difference density peaks close to Arg or Lys side chains were interpreted as SO<sub>4</sub><sup>2-</sup> ions, given the crystallization conditions in 2 M (NH<sub>4</sub>)<sub>2</sub>SO<sub>4</sub>, and a few well-resolved waters were added to the model (Supplementary Fig. 3). TLS (translation-libration-screw) group assignment used the TLSMD server (<http://skuld.bmsc.washington.edu/~tmsmd/>)<sup>25</sup> splitting the  $\alpha$  chain into six groups, the  $\beta$ 2 chain into five groups, the  $\mu$ 2 chain into two groups and the  $\sigma$ 2 chain as one group. Refinement without TLS gave slightly higher *R* factors (*R*<sub>work</sub> = 0.222, *R*<sub>free</sub> = 0.266) but little difference in the maps (map correlation 0.99, 0.93 at 3 Å resolution). Ramachandran analysis of the final model showed 86% of residues in the most favoured region, 96% in ‘allowed’ regions.

The structure of a complex between the AP2 core and a version of the CD4 acidic dileucine motif peptide termed ‘E-peptide’ in which the L–4 Q residue

was replaced with an E (that is, RMSpEIKRLLE) was also solved. The ‘E-peptide’ data set was of lower quality than the best Q-peptide data set. The crystal used to collect the Q-peptide data set gave better diffraction than the many others that were tried, and also had the serendipitous advantage of rotating approximately around the long *c* axis, which reduced the spot overlap compared with rotation around an axis roughly perpendicular to the long axis, as for the E-peptide crystal. The final model from the Q-peptide after the Q to E substitution was refined against the E-peptide data, with and without the peptide; as expected, the map quality was poorer than for the Q-peptide, but there was no significant difference in the structure. The electron density for the peptide shows no evidence of any difference in conformation (Supplementary Fig. 4), nor are the residues contacting the E side chain noticeably different: in particular, the side-chain density for  $\alpha$ R21 is still very weak. The lack of crystallizability of other AP2 core:dileucine motif peptide complexes is likely to be explained by the packing interaction that occur in the crystal between the L–1 position arginine in the peptide and the side chain of  $\beta$ 2Glu157 and the backbone amide of  $\beta$ 2Q154.

**Peptide sequences, conjugation of peptides to lipid and liposome and analyte preparation.** The following peptides were coupled to lipid for incorporation into liposomes, which were then used in the SPR-based binding experiments: TGN38\*, CKVTRRPKASDYQRL; phosphorylated CD4 Q peptide, CHRRRQA-ERM(SP)QIKRLLESEK; phosphorylated CD4 E peptide, CHRRRQAERM(SP)EIKRLLESEK; limp-II, CRGQGSTDEGTADERAPLIRT; tyrosinase\*, CKK-QPQERQLLMDKDDYHSLLYQSHL; TRP1\*, CRSRSTKNEANQPLLDH-YQRYAED; LRP\*, CKVTRRPKASEDEPLLS.

Peptides with an asterisk were also synthesized with mutations in their critical sorting-relevant amino-acid residues (Y→A in TGN38 and pairs of alanine residues substituting for the two leucine residues in dileucine-containing peptides) and served as negative controls.

Coupling of peptides to 1,2-dipalmitoyl-*sn*-glycero-3-phosphoethanolamine-*N*-(4-(*p*-maleimidophenyl) butyramide) (MPB-PE) and the subsequent incorporation into liposomes were performed as described in ref. 12. In brief, peptides were linked covalently through their N-terminal cysteine to MPB-PE (Avanti). The lipid-linked peptide was subsequently incorporated into 100 nm liposomes that were composed of 60% phosphatidylcholine (PC), 20% phosphatidylethanolamine (PE), 10% PtdIns(4,5)P<sub>2</sub> and 10% peptide-lipid. The efficiency of peptide coupling was determined by mass spectrometry, and the integrity of the liposomes was controlled by dynamic light scattering. The average variation of the PtdIns(4,5)P<sub>2</sub> content between different liposome preparations was less than 3% as determined by binding of the ENTH domain of epsin1 (see Supplementary Fig. 5).

Peptide-liposomes were used to generate a stable ‘membrane mimic’ on an L1 sensor surface of a BIAcore 3000 SPR biosensor (BIAcore AB). The system was first equilibrated in 10 mM Tris pH 8.7, 250 mM NaCl, 1 mM DTT, which was used as the running buffer, followed by priming with two injections of 20 mM CHAPS for 1 min (flow rate 10  $\mu$ l min<sup>-1</sup>) and injection of the liposomes (0.25 mM final concentration) for 4 min at 5  $\mu$ l min<sup>-1</sup>. Loosely bound liposomes were removed by two pulse injections of 50 mM sodium hydroxide for 30 s at 30  $\mu$ l min<sup>-1</sup>. This procedure resulted in an increase of the baseline by about 9500 resonance units (RU) with less than 4% variation between the four flow cells. After liposome capture, wild-type and mutant AP2 cores were injected at concentrations ranging from 50 nM to 1  $\mu$ M at a flow rate of 30  $\mu$ l min<sup>-1</sup> for 1 min (association) followed by buffer flow for 4 min (dissociation). All protein that did not dissociate within this period from the membrane was stripped off by a 20-s pulse injection of 50 mM NaOH. In a typical experiment the sensor surface was derivatized with basic liposomes (PC/PE) in flow cell 1, PC/PE plus PtdIns(4,5)P<sub>2</sub> in flow cell 2, PC/PE plus PtdIns(4,5)P<sub>2</sub> plus TGN38 peptide in flow cell 3, and PC/PE plus PtdIns(4,5)P<sub>2</sub> plus phosphoCD4 peptide in flow cell 4. This setup allowed us to differentiate between background binding to PC/PE liposomes, binding to PtdIns(4,5)P<sub>2</sub> and binding to PtdIns(4,5)P<sub>2</sub> together with a sorting-signal-containing peptide. In other experiments, TGN38 and LRP dileucine sorting signal containing peptide-liposomes were compared with liposomes containing mutant versions of both peptides in which the critical tyrosine or both leucine residues had been replaced with alanine. This setup was used to control binding of AP2 to a mutated sorting signal in a membrane containing PtdIns(4,5)P<sub>2</sub> (not shown). The kinetic analysis of binding was performed exactly as described<sup>26</sup> and rate constants were calculated with the evaluation software supplied by the manufacturer (BIAcore evaluation software<sup>27</sup>). All GST–AP2 complexes used in the SPR binding assay were expressed to similar levels and were checked for intactness and folding by SDS–PAGE and circular dichroism before use. A typical Coomassie-blue-stained SDS–PAGE gel of AP2 cores used in the SPR-based assay is shown in Supplementary Fig. 5. The samples were actually those used in the determination of *K*<sub>d</sub> values shown in Fig. 3 in the main text.

21. Leslie, A. G. The integration of macromolecular diffraction data. *Acta Crystallogr. D* **62**, 48–57 (2006).
22. Evans, P. Scaling and assessment of data quality. *Acta Crystallogr. D* **62**, 72–82 (2006).
23. Adams, P. D. *et al.* PHENIX: building new software for automated crystallographic structure determination. *Acta Crystallogr. D* **58**, 1948–1954 (2002).
24. Emsley, P. & Cowtan, K. Coot: model-building tools for molecular graphics. *Acta Crystallogr. D* **60**, 2126–2132 (2004).
25. Painter, J. & Merritt, E. A. Optimal description of a protein structure in terms of multiple groups undergoing TLS motion. *Acta Crystallogr. D* **62**, 439–450 (2006).
26. Ricotta, D., Conner, S. D., Schmid, S. L., von Figura, K. & Honing, S. Phosphorylation of the AP2  $\mu$  subunit by AAK1 mediates high affinity binding to membrane protein sorting signals. *J. Cell Biol.* **156**, 791–795 (2002).
27. Jonsson, U. *et al.* Real-time biospecific interaction analysis using surface plasmon resonance and a sensor chip technology. *Biotechniques* **11**, 620–627 (1991).

## LETTERS

# MicroRNA-21 contributes to myocardial disease by stimulating MAP kinase signalling in fibroblasts

Thomas Thum<sup>1,2\*</sup>, Carina Gross<sup>3\*</sup>, Jan Fiedler<sup>1,2</sup>, Thomas Fischer<sup>3</sup>, Stephan Kissler<sup>3</sup>, Markus Bussen<sup>5</sup>, Paolo Galuppo<sup>1</sup>, Steffen Just<sup>6</sup>, Wolfgang Rottbauer<sup>6</sup>, Stefan Frantz<sup>1</sup>, Mirco Castoldi<sup>7,8</sup>, Jürgen Soutschek<sup>9</sup>, Victor Koteliensky<sup>10</sup>, Andreas Rosenwald<sup>4</sup>, M. Albert Basson<sup>11</sup>, Jonathan D. Licht<sup>12</sup>, John T. R. Pena<sup>13</sup>, Sara H. Rouhanifard<sup>13</sup>, Martina U. Muckenthaler<sup>7,8</sup>, Thomas Tuschl<sup>13</sup>, Gail R. Martin<sup>5</sup>, Johann Bauersachs<sup>1</sup> & Stefan Engelhardt<sup>3,14</sup>

MicroRNAs comprise a broad class of small non-coding RNAs that control expression of complementary target messenger RNAs<sup>1,2</sup>. Dysregulation of microRNAs by several mechanisms has been described in various disease states<sup>3–5</sup> including cardiac disease<sup>6–10</sup>. Whereas previous studies of cardiac disease have focused on microRNAs that are primarily expressed in cardiomyocytes, the role of microRNAs expressed in other cell types of the heart is unclear. Here we show that microRNA-21 (*miR-21*, also known as *Mirn21*) regulates the ERK–MAP kinase signalling pathway in cardiac fibroblasts, which has impacts on global cardiac structure and function. *miR-21* levels are increased selectively in fibroblasts of the failing heart, augmenting ERK–MAP kinase activity through inhibition of sprouty homologue 1 (*Spry1*). This mechanism regulates fibroblast survival and growth factor secretion, apparently controlling the extent of interstitial fibrosis and cardiac hypertrophy. *In vivo* silencing of *miR-21* by a specific antagomir in a mouse pressure-overload-induced disease model reduces cardiac ERK–MAP kinase activity, inhibits interstitial fibrosis and attenuates cardiac dysfunction. These findings reveal that microRNAs can contribute to myocardial disease by an effect in cardiac fibroblasts. Our results validate *miR-21* as a disease target in heart failure and establish the therapeutic efficacy of microRNA therapeutic intervention in a cardiovascular disease setting.

In a transgenic mouse model of cardiac failure<sup>11</sup>, we found that the cardiac microRNA expression signature was progressively deregulated with increasing severity of the disease, with *miR-21* expression being most strongly affected<sup>12–14</sup> (Fig. 1a, b). Similarly, we observed robust upregulation of *miR-21* in other models of cardiac disease<sup>15,16</sup> (Fig. 1c), as well as in human heart failure (Fig. 1d). The finding of increased expression of the *miR-21* precursor (*pre-miR-21*), as assessed by northern blotting (Fig. 1d), suggested a transcriptional mechanism.

Using *in situ* hybridization, we detected only weak *miR-21* signals in normal myocardium, whereas in failing myocardium the hybridization signal was greatly enhanced. At high magnification, the hybridization signal was restricted primarily to small interstitial cells (Fig. 2a), presumably cardiac fibroblasts. Consistent with our *in situ* hybridization data, when we isolated cell fractions from hearts (Fig. 2b), *miR-21* expression was detected predominantly in cardiac

fibroblasts; expression was highest in fibroblasts from the failing heart, but was low in cardiomyocytes (Fig. 2c and data not shown).

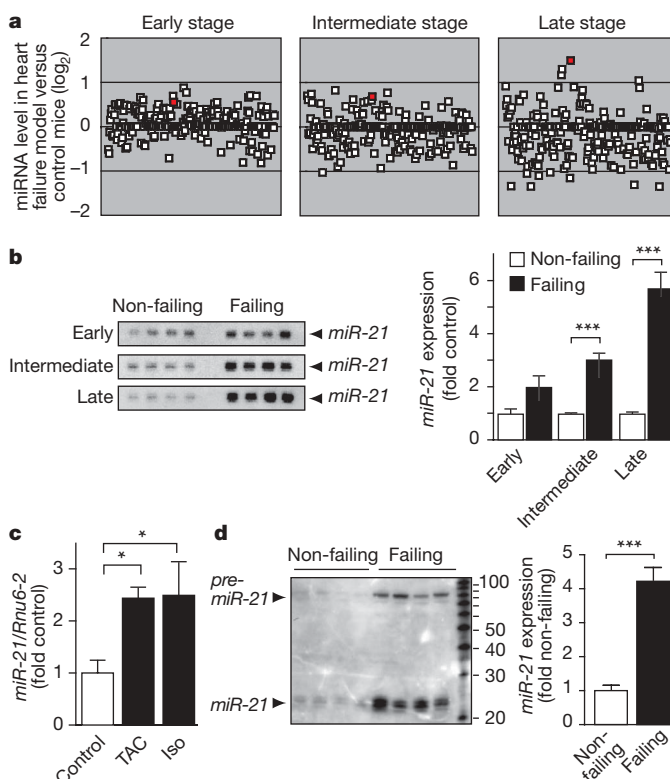


**Figure 1 | Deregulation of *miR-21* expression in cardiac disease.**

**a**, MicroRNA expression in left ventricular myocardium from control and  $\beta_1$ -adrenergic receptor transgenic mice at various disease stages. *miR-21* is marked in red. **b**, Northern blot analysis of *miR-21* expression in mice from **a**. **c**, *miR-21* expression in left ventricular myocardium from mice subjected to TAC or isoproterenol (Iso) infusion. U6 small nuclear (*Rnu6-2*) was used as a control. **d**, Northern blot analysis of *miR-21* in non-failing and failing human left ventricular myocardium. Data are mean and s.e.m.; \* $P < 0.05$ , \*\*\* $P < 0.005$ .  $n = 3–5$  per experiment per group.

<sup>1</sup>Department of Medicine I, <sup>2</sup>Junior Research Group, Interdisziplinäres Zentrum für Klinische Forschung (IZKF), <sup>3</sup>Rudolf Virchow Center, Deutsche Forschungsgemeinschaft (DFG) Research Center for Experimental Biomedicine, <sup>4</sup>Institute of Pathology, University of Würzburg, 97080 Würzburg, Germany. <sup>5</sup>Department of Anatomy, University of California, San Francisco, California 94158, USA. <sup>6</sup>Department of Internal Medicine III, <sup>7</sup>Department of Pediatric Hematology, Oncology and Immunology, <sup>8</sup>Molecular Medicine Partnership Unit, University of Heidelberg, 69120 Heidelberg, Germany. <sup>9</sup>Regulus Therapeutics, Carlsbad, California 92008, USA. <sup>10</sup>Alnylam Pharmaceuticals, Cambridge, Massachusetts 02142, USA. <sup>11</sup>Department of Craniofacial Development, King's College, London SE1 9RT, UK. <sup>12</sup>Northwestern University Feinberg School of Medicine, Chicago, Illinois 60611, USA. <sup>13</sup>Laboratory of RNA Molecular Biology, Rockefeller University, New York, New York 10065, USA. <sup>14</sup>Institute of Pharmacology and Toxicology, Technische Universität München (TUM), 80802 München, Germany.

\*These authors contributed equally to this work.



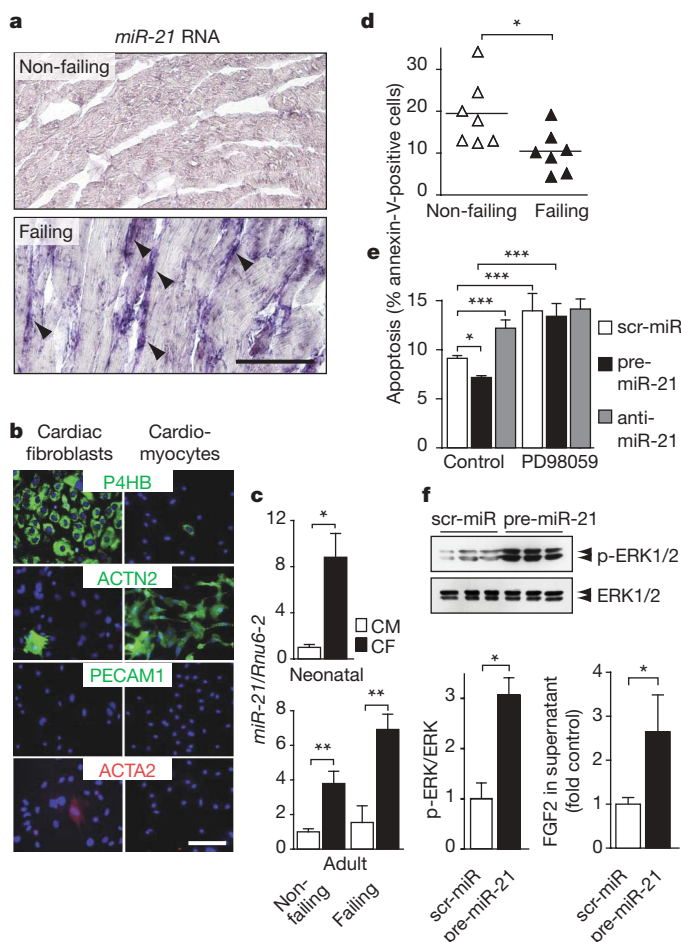


**Figure 2 | *miR-21* promotes ERK-MAP-kinase-mediated cell survival in cardiac fibroblasts.** **a**, *In situ* hybridization of *miR-21* in non-failing and failing myocardium. Scale bar, 100  $\mu$ m. **b**, Cell fractions from rat hearts stained with DAPI and antibodies against prolyl 4-hydroxylase (P4HB),  $\alpha$ 2-actinin (ACTN2), CD31 (PECAM1) and smooth muscle  $\alpha$ 2-actin (ACTA2). Scale bar, 100  $\mu$ m. **c**, *miR-21* expression in cardiomyocytes (CM) and cardiac fibroblasts (CF) isolated from neonatal rat or adult mouse hearts. **d**, Percentage apoptotic cells in the cardiac fibroblast fraction isolated from individual non-failing (wild-type) and failing (intermediate stage  $\beta_1$ -adrenergic receptor transgenic) mouse hearts. Horizontal bars indicate the mean. **e**, Percentage apoptotic primary rat cardiac fibroblasts after treatment with scrambled-miR (scr-miR), synthetic miR-21 (pre-miR-21), miR-21 antagonists (anti-miR-21) and the ERK-MAP kinase inhibitor PD98059. **f**, Western blot assay for ERK1/2 and phospho-ERK1/2 (p-ERK1/2), and ELISA of secreted FGF2. Data are mean and s.e.m.; \* $P < 0.05$ , \*\* $P < 0.01$ , \*\*\* $P < 0.005$ .  $n = 3-7$  animals per experiment.

When cardiac fibroblast fractions were assayed for cell death, we found fewer apoptotic cells in the population isolated from failing than from non-failing mouse hearts (Fig. 2d). When *miR-21* function was inhibited using a synthetic antagonist, the percentage of apoptotic fibroblasts increased, whereas *miR-21* overexpression decreased the percentage of apoptotic cells (Fig. 2e).

This *miR-21*-mediated protection from apoptotic cell death was sensitive to the extracellular signal-regulated kinase-mitogen-activated protein kinase (ERK-MAP kinase) inhibitor PD98059 (ref. 17, Fig. 2e). Consistent with these findings, transfection of synthetic *miR-21* precursor molecules into mouse 3T3 fibroblasts or rat cardiac fibroblasts led to a significant increase in ERK-MAP kinase activation (Fig. 2f, and data not shown). Thus, *miR-21* seems to be a critical regulator of ERK-MAP kinase activity in cardiac fibroblasts. In line with the known effects of ERK-MAP kinase signalling on cell survival and fibroblast activation<sup>17,18</sup>, transfection of primary cardiac fibroblasts with a

synthetic *miR-21* precursor led to a significant increase in fibroblast growth factor 2 (FGF2) secretion (Fig. 2f).

Our expression data showing that *miR-21* expression in cardiomyocytes is low and does not increase in failing hearts (Fig. 2c) indicate that *miR-21* does not have a significant function in cardiomyocytes. Neither enhancement nor suppression of *miR-21* levels affected the morphology, size or number of primary rat cardiomyocytes under resting or hypertrophy-inducing conditions (Supplementary Fig. 1). We also generated transgenic mice overexpressing *miR-21* in cardiomyocytes (Supplementary Fig. 2a), but detected no notable differences in myocardial structure or function, either with age or when subjected to cardiac pressure overload (Supplementary Fig. 2a, b). Moreover, very few differences were detected by transcriptional profiling or by determination of protein expression of predicted *miR-21* targets in left ventricular myocardium from such *miR-21* transgenic mice and their wild-type littermates (Supplementary Fig. 2c and data not shown). Likewise, we found few transcriptome changes in primary cardiomyocytes transfected with *miR-21* precursors and controls (Supplementary Fig. 2d). Although it has recently been suggested that overexpression of *miR-21* alters cardiomyocyte morphology<sup>14</sup>, our data provide strong evidence that *miR-21* exerts its effects on the heart primarily in cardiac fibroblasts.

Using bioinformatic algorithms to predict *miR-21* targets, we identified SPRY1, a potent inhibitor of the Ras/MEK/ERK pathway<sup>19,20</sup>, as a candidate messenger RNA target (Supplementary Table 1). The 3' untranslated region (UTR) of *Spry1* mRNA contains several predicted microRNA-binding sites, of which only one corresponds to a microRNA highly upregulated during cardiac disease (that is, *miR-21*). We also identified a few other potential *miR-21* targets, but these were unaffected or only moderately downregulated on *miR-21* expression in fibroblasts (Supplementary Fig. 3). Transfection of primary cardiac fibroblasts with *miR-21* precursors had no detectable effect on the *Spry1* mRNA level (data not shown), but resulted in strong repression of SPRY1 protein expression (Fig. 3a), indicating that *miR-21* affects *Spry1* expression by repressing translation. When we fused the *Spry1* 3' UTR to a luciferase reporter gene and determined luciferase activity in cells transfected with synthetic *miR-21* precursors, *miR-21* significantly repressed luciferase activity, whereas neither *miR-133a* nor *miR-206* had any effect (Fig. 3a). These experiments identify *Spry1* as a direct target of *miR-21*.

We next determined the *Spry1* expression pattern in the heart. *In situ* hybridization on sections of neonatal wild-type heart showed that within the myocardium *Spry1* mRNA localized to interstitial cells and the smooth muscle of the coronary vessels, but was not detected in cardiomyocytes (data not shown). We generated an allele of mouse *Spry1* (*Spry1*<sup>lacZ</sup>) in which the *lacZ* gene replaces part of the *Spry1* coding sequence (Supplementary Fig. 4). Assays for *lacZ* expression in 3-week-old *Spry1*<sup>lacZ/+</sup> animals indicated that *Spry1* is expressed in smooth muscle cells in the coronary vessels and in interstitial cells, but not in cardiomyocytes (Fig. 3b and data not shown). Co-staining of sections through the left ventricular myocardium of a *Spry1*<sup>lacZ/+</sup> heart with antibodies against  $\beta$ -galactosidase and vimentin, a fibroblast marker, demonstrated that many of the *lacZ*-expressing cells were fibroblasts (Fig. 3b). Together, our data show that *miR-21* and its target, *Spry1*, are co-expressed in cardiac fibroblasts and not in cardiomyocytes. Supporting this conclusion, SPRY1 expression was unchanged in the myocardium from transgenic mice overexpressing *miR-21* specifically in cardiomyocytes (data not shown).

Next we investigated whether the effects of *miR-21* expression on cardiac fibroblasts described above (Fig. 2e, f) are mediated by *Spry1*. If so, it is predicted that inhibiting *Spry1* expression would have the same effect as overexpressing *miR-21*. Knockdown of *Spry1* expression by lentiviral vectors encoding a short hairpin RNA directed against *Spry1* (sh-*Spry1*) led to a marked increase in ERK-MAP kinase activity, FGF2 secretion and cell survival (Fig. 3c). Furthermore, we found that co-transfection of fibroblasts with

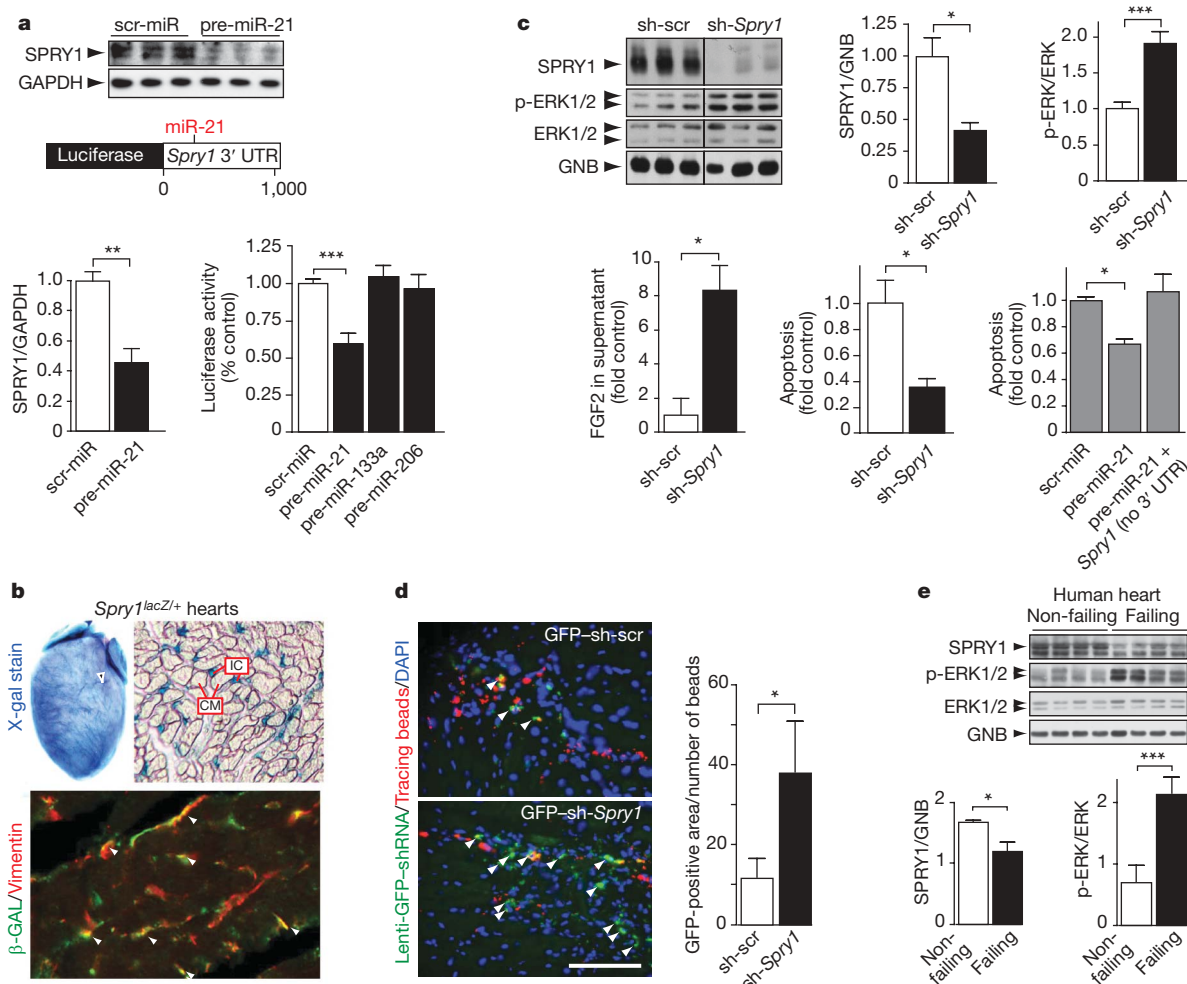


**Figure 3 | *miR-21* derepresses ERK signalling and enhances fibroblast survival by inhibiting *SPRY1* expression.** **a**, *SPRY1* protein expression in primary rat cardiac fibroblasts and activity of a luciferase reporter construct comprising the 3' UTR of *Spry1* mRNA after transfection of synthetic microRNAs. GAPDH, glyceraldehyde dehydrogenase. **b**, Detection of *Spry1* expression (blue staining) in coronary vessels (arrowhead) and in cells throughout the myocardium of *Spry1*<sup>lacZ/+</sup> mice. CM, cardiomyocytes; IC, interstitial cells; X-gal, 5-bromo-4-chloro-3-indolyl-β-D-galactoside. β-galactosidase (β-GAL)-positive (*Spry1*-expressing) cells co-expressing vimentin are indicated (white arrowheads). **c**, *SPRY1* expression, ERK activity, FGF2 secretion and apoptosis in fibroblasts infected with a control

lentiviral vector (GFP-sh-scr) or a vector expressing a short hairpin RNA directed against *Spry1* (GFP-sh-*Spry1*). Bottom right: co-expression of a *miR-21*-resistant *Spry1* cDNA devoid of its 3' UTR (no 3' UTR) prevents the anti-apoptotic effect of pre-*miR-21*. GNB, G-protein β subunits. **d**, Transplantation of control and *SPRY1*-deficient fibroblasts into left ventricular myocardium along with fluorescent tracing beads (red). Scale bar, 100 μm. **e**, Western blot analysis of *SPRY1*, ERK1/2 and phospho-ERK1/2 in non-failing and failing human left ventricular myocardium. Data are mean and s.e.m.; \**P* < 0.05, \*\**P* < 0.01, \*\*\**P* < 0.005. *n* = 3–6 individuals per experiment per group.

*miR-21* precursors and a *Spry1* complementary DNA lacking the 3' UTR completely abolished the anti-apoptotic effect of *miR-21* (Fig. 3c), indicating that this *miR-21*-resistant mutant of *Spry1* is capable of overcoming the effect of *miR-21*. Together our data provide strong evidence that the effects of *miR-21* on cardiac fibroblasts are mediated by *Spry1*.

To determine whether reducing *Spry1* expression would increase the survival of fibroblasts in the native myocardial environment, we transplanted fibroblasts infected with lentiviral vectors expressing green fluorescent protein (GFP)-sh-*Spry1* (*SPRY1*-deficient cells) or a scrambled GFP-shRNA (control cells) into the left ventricular myocardium of immunocompromised mice. We found significantly more fibroblasts in which endogenous *Spry1* expression had been silenced than control fibroblasts, indicating that *SPRY1*-deficient cells had a higher survival rate in the native myocardial environment than control cells (Fig. 3d).

On the basis of these data, we propose that abnormal expression of *miR-21* in cardiac fibroblasts inhibits *SPRY1* protein expression, resulting in augmentation of ERK–MAP kinase activity. In turn, this

enhances cardiac fibroblast survival and thereby the interstitial fibrosis and cardiac remodelling that is characteristic of the failing heart. This model (summarized in Fig. 4g) presents a new paradigm in that it assigns a primary role to cardiac fibroblast activation in myocardial disease, rather than regarding fibrosis as secondary to cardiomyocyte damage.

Consistent with this hypothesis, left ventricular cardiac tissue samples from patients with end-stage heart failure showed greatly enhanced *miR-21* levels, significantly repressed *SPRY1* protein, and ERK–MAP kinase activation (Figs 1d and 3e). One prediction of this model is that loss of *Spry1* function in mice should result in cardiac fibrosis and hypertrophy. This is in fact observed in eight-month-old *Spry1* null animals (data not shown). However, the cause of such fibrosis is currently unknown and might conceivably be due to abnormalities in kidney function<sup>21</sup> or other organs, or due to structural defects in *Spry1* null hearts. Studies involving tissue-specific knockout of *Spry1* will be required to resolve this issue.

Another prediction of this hypothesis is that blocking *miR-21* expression in a cardiac disease model should prevent fibrosis. To test this

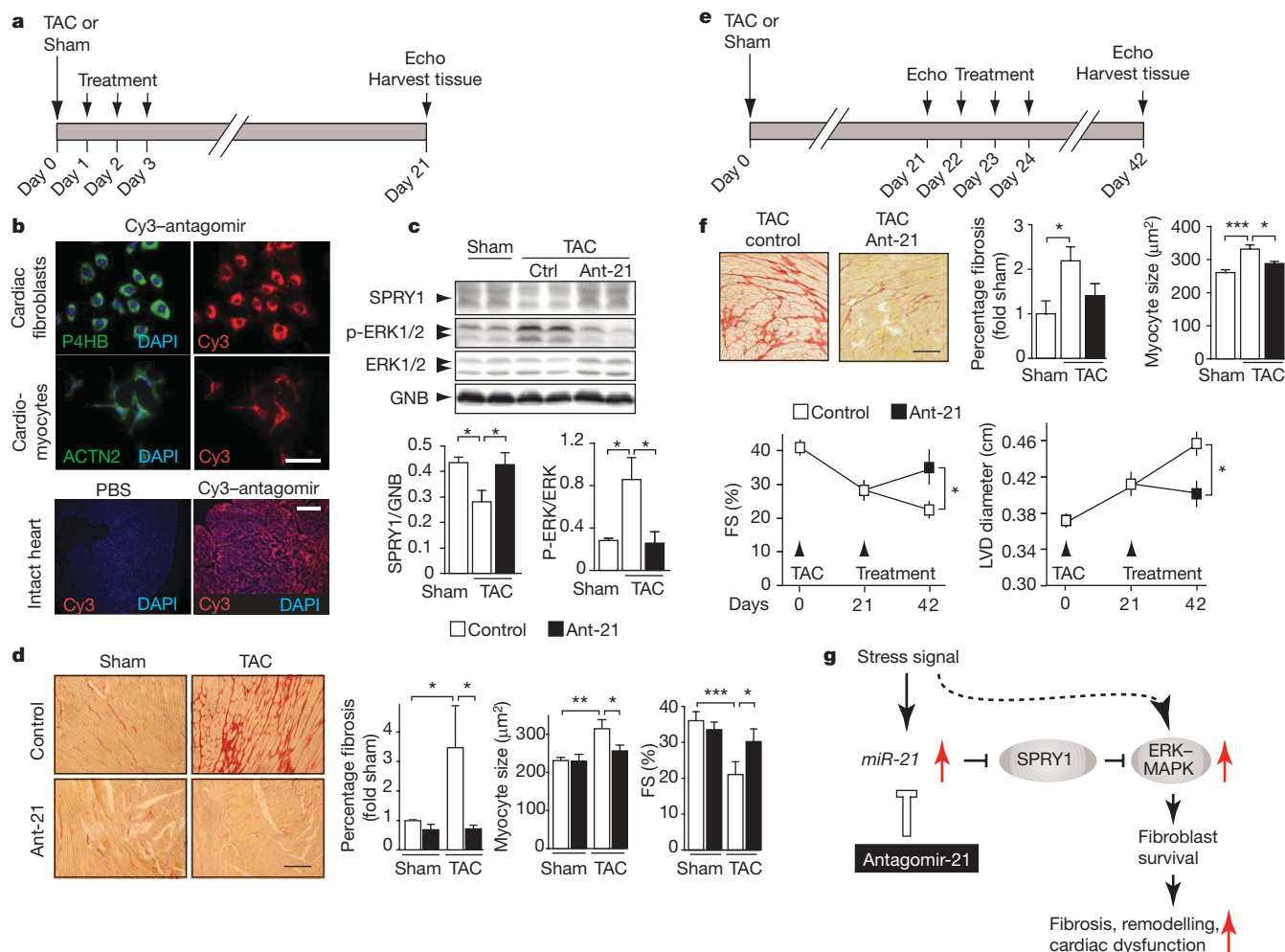


**Figure 4 | Efficacy of *miR-21* silencing in preventing and treating cardiac disease.** **a**, Design of prevention study. Echo, echocardiography. **b**, Uptake of Cy3-labelled antagomirs in cultured cells and the intact heart. Top scale bar, 50  $\mu\text{m}$ ; bottom scale bar, 500  $\mu\text{m}$ . **c**, SPRY1 expression and ERK-MAP kinase activity in mice after sham operation or TAC followed by treatment with control (Ctrl, PBS) or antagomir-21 (Ant-21). **d**, Percentage myocardial fibrosis (Sirius red staining), cardiomyocyte size and fractional shortening (FS). Scale bar, 100  $\mu\text{m}$ . **e**, Design of therapy study. **f**, Myocardial fibrosis, cardiomyocyte size and cardiac function (LVD, left ventricular diastolic).  $P = 0.07$  for percentage fibrosis in mice after TAC treated with

Ant-21 versus mice after TAC treated with control. Scale bar, 100  $\mu\text{m}$ . Data are mean and s.e.m.; \* $P < 0.05$ , \*\* $P < 0.01$ , \*\*\* $P < 0.005$ .  $n = 4-7$  animals per experiment per group. **g**, Proposed mechanism underlying the derepression of cardiac ERK signalling and abnormal fibroblast survival through *miR-21*, which inhibits the expression of SPRY1 protein, an antagonist of ERK-MAPK activation. Cardiac stress can also increase ERK-MAPK activity by other routes (dashed arrow). The increase in ERK-MAPK activity results in an increase in cardiac fibroblast survival, which in turn causes fibrosis, remodelling and cardiac dysfunction.

prediction we performed an experiment in which a chemically modified antisense oligonucleotide<sup>22</sup> specific for *miR-21* (antagomir-21) was injected into mice subjected to pressure overload of the left ventricle by transverse aortic constriction (TAC) or into sham-operated mice (Fig. 4a). *In vitro* studies using an antagomir fluorescently labelled with Cy3 revealed efficient uptake in both cardiac fibroblasts and cardiomyocytes, and intravenous injection of a Cy3-labelled antagomir by a jugular vein catheter resulted in strong Cy3 staining throughout the left ventricular myocardium (Fig. 4b).

When mice subjected to TAC were treated with antagomir-21 or a control for three consecutive days, cardiac *miR-21* expression was repressed for up to three weeks, as shown by northern blot and real-time polymerase chain reaction (PCR) analysis (Supplementary Fig. 5a). In the myocardium, antagomir-21 treatment completely reversed changes in SPRY1 expression, MAP kinase activation (Fig. 4c) and FGF2 protein expression (Supplementary Fig. 5b). Global transcriptome analysis revealed that the expression of various genes that are deregulated after TAC was normalized by antagomir-21 treatment (Supplementary Fig. 6). Specifically, genes encoding collagens and extracellular matrix molecules that are highly upregulated during

cardiac fibrosis, were reduced after specific inhibition of *miR-21*, but increased after knockdown of endogenous *Spry1* (Supplementary Table 2). Furthermore, interstitial fibrosis, cardiomyocyte size and heart weight were significantly increased three weeks after TAC in mice treated with the control, but this effect was strongly attenuated by antagomir-21 treatment (Fig. 4d and Supplementary Fig. 7a). Treatment of sham-operated mice with antagomir-21 had no notable effect on heart weight or myocardial structure.

Analysis of cardiac function by echocardiography revealed that antagomir-21 treatment prevented left ventricular dilatation and normalized fractional shortening (Fig. 4d and Supplementary Fig. 7b). Similar results were obtained with antagomir-21 treatment in an isoproterenol-induced cardiac disease model (Supplementary Fig. 8). Intravenously injected antagomirs were also effectively taken up into other organs such as the liver. Analysis of liver morphology and function showed that both were normal (Supplementary Fig. 9).

To test the curative potential of silencing *miR-21* in cardiac disease, we subjected mice to pressure overload of the left ventricle for three weeks before treatment with antagomir-21. During this period the animals displayed significant left ventricular hypertrophy, fibrosis



and impaired cardiac function. We then treated mice with antago-mir-21 and followed the disease for another three weeks (Fig. 4e). Whereas animals treated with control displayed progressive impairment of left ventricular function as well as interstitial fibrosis and cardiac hypertrophy, animals treated with antagomir-21 showed significant attenuation of the impairment of cardiac function as well as regression of cardiac hypertrophy and fibrosis (Fig. 4f and Supplementary Fig. 7c). Thus, our study demonstrates therapeutic efficacy for silencing of miR-21 by antagomirs in a cardiac disease setting.

To our knowledge, this is the first report of a role for *miR-21* in cardiac disease by affecting ERK–MAP kinase signalling in cardiac fibroblasts. Our data suggest that stimuli or procedures that induce cardiac stress result in miRNA-mediated activation of ERK–MAP kinase activity by means of an effect on SPRY1, which in turn positively regulates cardiac fibroblast survival, leading to fibrosis, hypertrophy and cardiac dysfunction (Fig. 4g). In contrast to the traditional view, in which fibrosis is regarded as a secondary phenomenon, indicative of a primary effect on cardiomyocytes, our results indicate a primary role for cardiac fibroblast activity in myocardial disease. This study represents the first example of microRNA therapeutics in a cardiovascular disease model. Specifically, we show that antagonizing *miR-21* can prevent and even cure structural and functional deterioration in a mouse model of heart failure. These findings suggest a new therapeutic entry point for cardiac disease and illustrate the broad therapeutic potential of microRNA modulation.

## METHODS SUMMARY

**Array analysis.** For microRNA array analysis, 5 µg total RNA was labelled with a Cy3-conjugated RNA linker (Dharmacon) and hybridized to microarrays using the miChip platform as described<sup>23</sup>. Hybridization signal intensities were quantified using the Axon scanner (4000B, Molecular Dynamics) with identical photomultiplier settings. Gene array analysis was performed according to the manufacturer's instructions (GeneChip 430 2.0 and 230 2.0, Affymetrix) followed by data analysis as described<sup>24</sup>.

**microRNA target prediction.** The microRNA databases and target prediction tools miRBase (<http://microrna.sanger.ac.uk/>), PicTar (<http://pictar.mdc-berlin.de/>) and TargetScan (<http://www.targetscan.org/index.html>) were used to identify potential microRNA targets.

**Mouse models of cardiac disease.** The mouse models of cardiac dysfunction used in this study were  $\beta_1$ -adrenergic receptor transgenic mice at early (3 months), intermediate (6 months) and late (12 months) stages of the disease<sup>11</sup>, animals subjected to TAC<sup>15,25</sup>, or animals subjected to infusion with isoproterenol by subcutaneously implanted osmotic minipumps (Alzet, 30 µg isoproterenol per g per day). All animal studies were performed in accordance with the relevant guidelines and regulations of the responsible authorities.

**Injection and detection of antagomirs.** A jugular vein catheter was inserted in male C57/BL6 mice (10–12 weeks old) before TAC was performed. Twenty-four hours (prevention study) or three weeks (therapy study) post-TAC, antagomir-21 (80 mg per kg body weight) or PBS was injected daily for three days through the jugular vein catheter.

**Full Methods** and any associated references are available in the online version of the paper at [www.nature.com/nature](http://www.nature.com/nature).

Received 19 January; accepted 3 October 2008.

Published online 30 November 2008.

1. Ambros, V. The functions of animal microRNAs. *Nature* **431**, 350–355 (2004).
2. Bartel, D. P. MicroRNAs: genomics, biogenesis, mechanism, and function. *Cell* **116**, 281–297 (2004).
3. Mi, S. *et al.* MicroRNA expression signatures accurately discriminate acute lymphoblastic leukemia from acute myeloid leukemia. *Proc. Natl Acad. Sci. USA* **104**, 19971–19976 (2007).
4. He, L. *et al.* A microRNA component of the p53 tumour suppressor network. *Nature* **447**, 1130–1134 (2007).
5. Huang, J. *et al.* Cellular microRNAs contribute to HIV-1 latency in resting primary CD4<sup>+</sup> T lymphocytes. *Nature Med.* **13**, 1241–1247 (2007).

6. Care, A. *et al.* MicroRNA-133 controls cardiac hypertrophy. *Nature Med.* **13**, 613–618 (2007).
7. van Rooij, E. *et al.* Control of stress-dependent cardiac growth and gene expression by a microRNA. *Science* **316**, 575–579 (2007).
8. Yang, B. *et al.* The muscle-specific microRNA miR-1 regulates cardiac arrhythmogenic potential by targeting GJA1 and KCNJ2. *Nature Med.* **13**, 486–491 (2007).
9. Zhao, Y. *et al.* Dysregulation of cardiogenesis, cardiac conduction, and cell cycle in mice lacking miRNA-1-2. *Cell* **129**, 303–317 (2007).
10. Sayed, D., Hong, C., Chen, I. Y., Lypow, J. & Abdellatif, M. MicroRNAs play an essential role in the development of cardiac hypertrophy. *Circ. Res.* **100**, 416–424 (2007).
11. Engelhardt, S., Hein, L., Wiesmann, F. & Lohse, M. J. Progressive hypertrophy and heart failure in  $\beta_1$ -adrenergic receptor transgenic mice. *Proc. Natl Acad. Sci. USA* **96**, 7059–7064 (1999).
12. Cheng, Y. H. *et al.* MicroRNAs are aberrantly expressed in hypertrophic heart — do they play a role in cardiac hypertrophy? *Am. J. Pathol.* **170**, 1831–1840 (2007).
13. Tatsuguchi, M. *et al.* Expression of microRNAs is dynamically regulated during cardiomyocyte hypertrophy. *J. Mol. Cell. Cardiol.* **42**, 1137–1141 (2007).
14. Sayed, D. *et al.* MicroRNA-21 targets Sprouty2 and promotes cellular outgrowths. *Mol. Biol. Cell* **19**, 3272–3282 (2008).
15. Rockman, H. A. *et al.* Segregation of atrial-specific and inducible expression of an atrial natriuretic factor transgene in an *in vivo* murine model of cardiac hypertrophy. *Proc. Natl Acad. Sci. USA* **88**, 8277–8281 (1991).
16. Kudej, R. K. *et al.* Effects of chronic  $\beta$ -adrenergic receptor stimulation in mice. *J. Mol. Cell. Cardiol.* **29**, 2735–2746 (1997).
17. Dudley, D. T., Pang, L., Decker, S. J., Bridges, A. J. & Saltiel, A. R. A synthetic inhibitor of the mitogen-activated protein kinase cascade. *Proc. Natl Acad. Sci. USA* **92**, 7686–7689 (1995).
18. Pages, G. *et al.* Mitogen-activated protein kinases p42mapk and p44mapk are required for fibroblast proliferation. *Proc. Natl Acad. Sci. USA* **90**, 8319–8323 (1993).
19. Hanafusa, H., Torii, S., Yasunaga, T. & Nishida, E. Sprouty1 and Sprouty2 provide a control mechanism for the Ras/MAPK signalling pathway. *Nature Cell Biol.* **4**, 850–858 (2002).
20. Casci, T., Vinos, J. & Freeman, M. Sprouty, an intracellular inhibitor of Ras signaling. *Cell* **96**, 655–665 (1999).
21. Basson, M. A. *et al.* Sprouty1 is a critical regulator of GDNF/RET-mediated kidney induction. *Dev. Cell* **8**, 229–239 (2005).
22. Krutzfeldt, J. *et al.* Silencing of microRNAs *in vivo* with 'antagomirs'. *Nature* **438**, 685–689 (2005).
23. Castoldi, M. *et al.* A sensitive array for microRNA expression profiling (miChip) based on locked nucleic acids (LNA). *RNA* **12**, 913–920 (2006).
24. Thum, T. *et al.* MicroRNAs in the human heart: a clue to fetal gene reprogramming in heart failure. *Circulation* **116**, 258–267 (2007).
25. Buitrago, M. *et al.* The transcriptional repressor Nab1 is a specific regulator of pathological cardiac hypertrophy. *Nature Med.* **11**, 837–844 (2005).

**Supplementary Information** is linked to the online version of the paper at [www.nature.com/nature](http://www.nature.com/nature).

**Acknowledgements** We thank N. Hemmrich, U. Keller, J. Schittl, C. Dienesch, S. Thum, A. Leupold, M. Kümmel, S. Schraut, A. Lauer, S. Marquart, E. Leich and A. Horn for technical assistance. We acknowledge the contribution of V. Benes and S. Schmidt (miChip microarray Platform, EMBL), D. Fraccarollo and K. Hu (*in vivo* studies), S. Leierseder and X. Loyer (primary fibroblast preparation), C. Sohn-Lee (*in situ* hybridization experiments) and M. Manoharan, R. Braich and B. Bhat (antagomir oligonucleotides). We also thank L. Field, T. Brand and M. Gessler for discussions. This work was supported in part by grants from the IZKF (E-31 to T. Thum), the Deutsche Forschungsgemeinschaft (DFG TH903/7-1 to T. Thum and J.B.), the Rudolf Virchow Center/DFG Research Center for Experimental Biomedicine (S.E., S.K.), the Bavarian Ministry of Technology, ProCorde and Sanofi-Aventis (S.E.), and the US NIH (R01 CA78711 to G.R.M.). M.C. is supported by an Excellence Fellowship of The Medical Faculty of the University of Heidelberg, M.U.M. by a Cancer Research Net grant (BMBF (NGFN) 201GSO450), and M.B. by the Leopoldina Academy (BMBF-LPD 9901/8-141).

**Author Contributions** T. Thum, C.G., J.F., T.F., S.K., M.B., P.G., S.J., M.C. and S.E. performed experiments. M.A.B. and J.D.L. provided the Spry/LacZ mouse line. J.T.R.P., S.H.R. and T. Tuschl contributed the *in situ* hybridization experiments. T. Thum, C.G., J.F., W.R., S.F., J.S., V.K., A.R., M.M., G.R.M., J.B. and S.E. analysed data. T. Thum, J.B. and S.E. designed the study. T. Thum, G.R.M., J.B. and S.E. wrote the manuscript. J.B. and S.E. contributed equally as joint senior authors to the study.

**Author Information** Reprints and permissions information is available at [www.nature.com/reprints](http://www.nature.com/reprints). The authors declare competing financial interests: details accompany the full-text HTML version of the paper at [www.nature.com/nature](http://www.nature.com/nature). Correspondence and requests for materials should be addressed to J.B. ([j.bauersachs@medizin.uni-wuerzburg.de](mailto:j.bauersachs@medizin.uni-wuerzburg.de)) and S.E. ([stefan.engelhardt@tum.de](mailto:stefan.engelhardt@tum.de)).

## METHODS

**Expression analyses.** For extraction of total RNA the RNeasy Mini Kit (Qiagen) was used according to the manufacturer's instructions. MicroRNAs were isolated by Trizol (Invitrogen) or a miRNA isolation kit (mirVana, Ambion). The integrity of the isolated RNA was verified using denaturing agarose gel electrophoresis or capillary electrophoresis (Bioanalyzer 2100; Agilent Technologies) as described<sup>26</sup>. For real-time PCR we used target-specific stem loop structure and reverse transcription primers, and after reverse transcription used specific TaqMan hybridization probes to quantify *miR-21* expression (TaqMan miR-21 microRNA assay, Applied Biosystems). The small RNA molecule U6 small nuclear (*Rnu6-2*) was amplified as a control. For northern blot analysis, total RNA was loaded onto 15% acrylamide, 8 M urea TBE (Tris/borate/EDTA (ethylenediaminetetraacetic acid)) gels alongside an appropriate marker. After electrophoresis, RNA was transferred to a nylon membrane (Qiabrane Nylon, Qiagen) and pre-hybridized for 1 h at 65 °C in hybridization buffer (ULTRAhyb-Oligo hybridization buffer, Ambion). Locked nucleic acid oligonucleotides (miRCURY LNA Array detection probes, Exiqon) were labelled with T4 kinase (Ambion) and <sup>32</sup>P-ATP, and hybridized to the membranes overnight (for 12 h) at 42 °C. After a washing step, membranes were exposed on a phosphorimager.

**Western blotting.** Protein lysates were prepared as described<sup>25</sup>. We used primary antibodies against SPRY1 (sc-30048, Santa Cruz), ERK1/2 (9102, Cell Signaling), phospho-ERK1/2 (9101, Cell Signaling), FGF2 (clone 3, 610870, Becton Dickinson), G  $\beta$  subunits 1–4 (GNB, sc-378, Santa Cruz) and glyceraldehyde dehydrogenase (GAPDH, ab8245, Abcam), as well as appropriate secondary antibodies.

**In situ hybridization and assay for  $\beta$ -galactosidase activity.** *In situ* hybridization was carried out on non-failing (wild type) and failing (intermediate stage,  $\beta_1$ -adrenergic receptor transgenic) myocardium using DIG-labelled locked nucleic acid probes directed against miR-21 (J. Pena and T. Tuschl, manuscript in preparation).

To assay for  $\beta$ -galactosidase activity in *Spry1*<sup>lacZ+</sup> mice, hearts were fixed for 2 h in PBS containing 2% formaldehyde and 0.05% glutaraldehyde. Subsequently, the hearts were rinsed four times for 30 min in 0.01% sodium-desoxycholate, 0.02% Nonidet P-40, 2 mM MgCl<sub>2</sub> and 2 mM EGTA in PBS, and then incubated in rinsing solution containing 0.5 mg ml<sup>-1</sup> X-gal, 10 mM K<sub>3</sub>Fe(CN)<sub>6</sub> and 10 mM K<sub>4</sub>Fe(CN)<sub>6</sub> at 37 °C for 18–24 h.

For histological analysis, the hearts stained in whole mount were dehydrated in isopropanol, cleared in xylene, transferred to paraffin, and sectioned at 10  $\mu$ m. For immunofluorescence analysis, three-week-old *Spry1*<sup>lacZ+</sup> hearts were first perfused with PBS supplemented with 2 mM EGTA, followed by a perfusion with Histochoice (Electron Microscopy Science) fixative. The hearts were then post-fixed for 12 h with Histochoice and finally dehydrated through an alcohol series followed by paraffin embedding and sectioning (10  $\mu$ m). Antigen retrieval was performed in 0.05% citraconic anhydride (Pierce), pH 7.5, for 10 min in a boiling water bath. Immunofluorescence assays to detect  $\beta$ -galactosidase protein were performed on sections of the left ventricular myocardium using a rabbit antibody (MP Biomedicals, 55976) and the ABC system from Vectorlabs in combination with a tyramide signal amplification system (PerkinElmer, NEL701). The sections were co-stained with a mouse antibody that detects vimentin (Abcam, ab8978) and an anti-mouse Alexa Fluor 568 secondary antibody (Invitrogen/Molecular Probes).

**Isolation of cardiac fibroblasts and cardiomyocytes.** Hearts were removed from newborn rats (day 0), put into calcium- and bicarbonate-free HEPES-buffered Hanks' medium, cut into pieces and digested with trypsin (Becton Dickinson) under constant stirring. The collected primary cells were passed through a cell strainer (40  $\mu$ m) and then seeded onto uncoated plastic dishes and incubated for 60 min at 37 °C. The supernatant (containing the cardiomyocytes) was collected and the adherent cells were washed several times, and then cultured in minimal essential medium (MEM) containing 5% fetal calf serum (FCS). These cultures contained almost exclusively primary cardiac fibroblasts, as >95% of the cells were stained with antibodies directed against the fibroblast-specific antigen prolyl-4-hydroxylase (P4HB, clone 6-9H6, Acris), and >95% of the cells were negative for the cardiomyocyte-specific marker  $\alpha_2$ -actinin (ACTN2, clone EA-53, Sigma), the endothelial cell marker platelet/endothelial cell adhesion molecule (CD31 antigen) (PECAM1, ab24590, Abcam), as well as smooth muscle  $\alpha_2$ -actin (ACTA2, ab15734, Abcam). The cells in the supernatant that was collected were plated in MEM containing vitamin B<sub>12</sub>, NaHCO<sub>3</sub> and 5% FCS. This cell population was almost exclusively cardiomyocytes, as >95% of the cells stained positive for  $\alpha_2$ -actinin.

Cardiac fibroblasts and cardiomyocytes from adult mice were obtained from Langendorff-perfused hearts as described (<http://www.signaling-gateway.org/reports/v1/CM0005/CM0005.htm>). Separation of cardiomyocytes was achieved by sedimentation at room temperature (22 °C) for 10 min followed by a preplating

step to further deplete fibroblasts. The supernatant of the sedimentation step contained fibroblasts that were pelleted by low-speed centrifugation (250g for 10 min). The resulting preparation was seeded on tissue culture dishes and vigorously washed after 2 h. These cultures contained >95% fibroblasts, based on stainings for cell-type-specific markers.

**Assays for apoptosis, FGF2 secretion, collagen deposition and cell size.** The percentage of cells undergoing apoptosis in cultures of fibroblasts was determined by staining with annexin V and propidium iodide followed by FACS analysis (annexin-V-FLUOS kit, Roche). FGF2 protein level in the culture medium was determined using the Quantikine FGF Basic Immunoassay kit 3 days after transfection or infection of the cells and 24 h after medium change (R&D Systems).

For analysis of collagen deposition, paraffin sections of the left ventricular myocardium were stained with Sirius red and picric acid. Collagen content was calculated as the percentage of the area in each section that was stained with Sirius red.

Cardiomyocyte surface area was determined from digitally recorded images of cell cultures stained with antibodies directed against ACTN2 or of sections (5  $\mu$ m) of the left ventricular myocardium stained with haematoxylin and eosin or wheat germ agglutinin coupled to Alexa488. Images were analysed using the AxioVision (Zeiss) and Metamorph (Molecular Devices) software packages.

**Luciferase assays.** HEK293 cells were transfected with 0.25  $\mu$ g p-MIR-report plasmid (Ambion) containing the 3' UTR of mouse *Spry1* RNA and 50 nM of miR-precursor using Lipofectamine 2000 (Invitrogen). Forty-eight hours later luciferase activity was measured in cell lysates using a luciferase assay kit (Promega).

**Transfection and lentivirus infection.** Rat cardiac fibroblasts and cardiomyocytes, and mouse 3T3 fibroblasts (obtained from the DSMZ, Braunschweig, Germany (DSMZ number ACC 173)), were transfected with precursor and inhibitors of miR-21 (50–100 nM, Ambion) using Lipofectamin 2000 (Invitrogen).

A shRNA sequence targeting *Spry1* for gene silencing by RNA interference was cloned into the lentiviral vector pLBM (S.K., unpublished). pLBM is a modified version of pLB<sup>27</sup> in which the shRNA is expressed from a miR-30 motif incorporated into the 3' UTR of the GFP reporter. The shRNA target sequence was as follows: sh-*Spry1*, CTCCAACACTGTCTATTGTAAG. Lentiviral particles (GFP-sh-*Spry1* or GFP-sh-scr) were produced as described previously<sup>27</sup> and concentrated by ultracentrifugation. 3T3 cells were infected with control pLBM virus (scrambled shRNA) or with *Spry1*-targeting pLBM virus.

**Transplantation of *Spry1*-deficient fibroblasts into left ventricular myocardium.** Thirty-thousand 3T3 fibroblasts infected with a lentiviral vector expressing GFP-sh-*Spry1* (SPRY1-deficient cells) or GFP-scrambled shRNA were injected into the left ventricular myocardium of anaesthetized mice (NOD-SCID, Harlan). Red fluorescent tracing beads (1  $\mu$ m diameter; FluoSpheres, Invitrogen) were co-injected with the fibroblasts to facilitate identification of the injection site. Seven days after transplantation, the hearts were removed and cryosectioned from the base to the top. Photographs of sections containing local accumulations of fluorescent beads were subjected to semi-automated image analysis. The GFP-positive area was then taken as a measure of GFP-positive transplanted cells, and related to the number of beads present.

**Human heart samples.** Approval for studies on human tissue samples was obtained from the ethics committee of the University of Wuerzburg, Germany. We examined cardiac tissue from patients undergoing heart transplantation because of end-stage heart failure due to dilatative cardiomyopathy and, for comparison, healthy heart samples.

**Myh6-promoter-miR-21 transgenic mice.** Transgenic mice overexpressing *miR-21* in a cardiomyocyte-specific manner were generated by pronuclear injection of fertilized oocytes from FVB/N mice with a transgene construct containing the mature *miR-21* sequence, flanked by 154 base pairs (bp) upstream and 136 bp downstream of the native *miR-21* precursor sequence under the control of the mouse myosin heavy chain  $\alpha$  (*Myh6*) promoter (Supplementary Fig. 2).

**Production of the *Spry1*<sup>lacZ</sup> allele.** To construct the targeting vector for producing a *Spry1*<sup>lacZ</sup> allele, we screened a 129/Sv mouse genomic bacterial artificial chromosome library (Incyte Genomics, Palo Alto) by PCR and identified two bacterial artificial chromosomes containing the *Spry1* gene. We excised an 11.5 kb EcoRI fragment containing all three *Spry1* exons and cloned it into pBluescript (pBS-SPRY1). A 4.6 kb NotI-BspEI fragment of pBS-SPRY1, spanning from 5' of the first exon to 444 bp downstream of the start codon in the *Spry1* open reading frame, was excised and inserted into a pSP73 vector, upstream of an XhoI-XbaI fragment containing an IRES-*lacZ* cassette<sup>28</sup> followed by a *loxP*-flanked PGK-*neo* cassette (provided by T. Lufkin). We then excised the NotI-XbaI fragment, which encodes the first 148 amino acids of the SPRY1 protein followed by the IRES-*lacZ* and PGK-*neo* cassettes, from that clone and used it to replace a 5,719 bp EcoRI-PacI fragment of the pBS-*Spry1* construct. In the resulting targeting vector, the sequences encoding the carboxy-terminal domain of the SPRY1 protein that is

required for function were replaced with an IRES-*lacZ*-PGK-*neo*<sup>fllox</sup> cassette (Supplementary Fig. 4a).

The targeting vector, linearized by digestion with NotI, was electroporated into R1 embryonic stem cells (provided by A. Nagy). G418 resistant embryonic stem cell colonies were isolated and Southern blotting was performed on genomic DNA digested with SpeI, using a fragment located 5' of the sequences in the targeting construct as a probe. Twenty-seven out of a total of 96 screened clones had undergone homologous recombination as evidenced by the presence of a 10 kb fragment in SpeI digests, in addition to the 16.6 kb wild-type band (Supplementary Fig. 4b). Two clones were injected into C57BL/6 blastocysts (K. Kelley). Chimaeric males were mated with C57BL/6J females and pups derived from 129/SvJ embryonic stem cells were screened for the presence of the targeted allele by PCR of genomic DNA using the primers described in the legend to Supplementary Fig. 4.

Mice carrying the targeted allele were bred with  $\beta$ -actin-Cre deleter mice<sup>29</sup> on an FVB/N genetic background (Jackson Laboratory) to remove the PGK-*neo* cassette. Successful deletion was confirmed by PCR. X-gal staining of embryos and embryonic tissues confirmed that *lacZ* activity faithfully represented *Spry1* gene expression as detected by *in situ* hybridization.

**TAC model and antagomir application.** TAC was performed on male C57BL/6 mice (10–12 weeks old) from Charles River Laboratories essentially as described<sup>15</sup>. During the same operation, a jugular vein catheter was implanted by standard surgical procedures. Antagomirs were synthesized as described<sup>22</sup> and were directed against miR-21 and miR-181a. Antagomir-181a was additionally labelled with Cy3 at the 5' end of the oligonucleotide. Treatment started 24 h (prevention study) or 3 weeks (therapy study) after TAC, and animals received PBS or antagomir-21 injections by means of an implanted jugular vein catheter (three consecutive days, jugular vein injections of 0.2 ml PBS only or containing antagomir-21 (80 mg per kg body weight)). As a positive control for effective cardiac delivery, Cy-3-labelled antagomir-181a (80 mg per kg body weight) was injected into the jugular vein catheter and the heart was removed three hours later, fixed and Cy3-staining observed by fluorescence microscopy.

**Cardiac functional analysis.** Cardiac dimensions and function were analysed by pulse-wave Doppler echocardiography essentially as described<sup>30</sup>.

**Statistical analysis.** Average data are presented as mean and s.e.m. Statistical analysis was carried out using the Prism software (GraphPad) or StatView (SAS Institute) package. For statistical comparison of two groups, we used unpaired, two-tailed Student's *t*-test; for the comparison of three or more groups, we used ANOVA followed by Fisher's post-test. Differences were considered significant when *P* < 0.05. In the figures, *P* values are indicated by one, two or three asterisks.

26. Thum, T. & Borlak, J. Mechanistic role of cytochrome P450 monooxygenases in oxidized low-density lipoprotein-induced vascular injury: therapy through LOX-1 receptor antagonism? *Circ. Res.* **94**, e1–e13 (2004).
27. Kissler, S. *et al.* *In vivo* RNA interference demonstrates a role for Nramp1 in modifying susceptibility to type 1 diabetes. *Nature Genet.* **38**, 479–483 (2006).
28. Li, X., Wang, W. D. & Lufkin, T. Dicistronic LacZ and alkaline phosphatase reporter constructs permit simultaneous histological analysis of expression from multiple transgenes. *Biotechniques* **23**, 874–878 (1997).
29. Lewandoski, M., Meyers, E. N. & Martin, G. R. Analysis of *Fgf8* gene function in vertebrate development. *Cold Spring Harb. Symp. Quant. Biol.* **62**, 159–168 (1997).
30. Merkle, S. *et al.* A role for caspase-1 in heart failure. *Circ. Res.* **100**, 645–653 (2007).



# X-ray structure of NS1 from a highly pathogenic H5N1 influenza virus

Zachary A. Bornholdt<sup>1</sup> & B. V. Venkataram Prasad<sup>1,2</sup>

The recent emergence of highly pathogenic avian (H5N1) influenza viruses, their epizootic and panzootic nature, and their association with lethal human infections have raised significant global health concerns<sup>1,2</sup>. Several studies have underlined the importance of non-structural protein NS1 in the increased pathogenicity and virulence of these strains<sup>3,4</sup>. NS1, which consists of two domains—a double-stranded RNA (dsRNA) binding domain<sup>5,6</sup> and the effector domain<sup>7</sup>, separated through a linker—is an antagonist of antiviral type-I interferon response in the host<sup>8,9</sup>. Here we report the X-ray structure of the full-length NS1 from an H5N1 strain (A/Vietnam/1203/2004) that was associated with 60% of human deaths in an outbreak in Vietnam<sup>1,2</sup>. Compared to the individually determined structures of the RNA binding domain and the effector domain from non-H5N1 strains, the RNA binding domain within H5N1 NS1 exhibits modest structural changes, while the H5N1 effector domain shows significant alteration, particularly in the dimeric interface. Although both domains in the full-length NS1 individually participate in dimeric interactions, an unexpected finding is that these interactions result in the formation of a chain of NS1 molecules instead of distinct dimeric units. Three such chains in the crystal interact with one another extensively to form a tubular organization of similar dimensions to that observed in the cryo-electron microscopy images of NS1 in the presence of dsRNA. The tubular oligomeric organization of NS1, in which residues implicated in dsRNA binding face a 20-Å-wide central tunnel, provides a plausible mechanism for how NS1 sequesters varying lengths of dsRNA, to counter cellular antiviral dsRNA response pathways, while simultaneously interacting with other cellular ligands during an infection.

NS1 of influenza virus is a multifunctional protein associated with a number of regulatory functions during a viral infection<sup>10</sup>, including conferring resistance to antiviral interferon (IFN) induction<sup>3,4</sup>. Although the mechanisms for how NS1 antagonizes IFN response remains to be fully understood, both the RNA binding domain (RBD)<sup>11,12</sup> and the effector domain (ED)<sup>13–15</sup> have been implicated in this activity. Our goal was to determine the X-ray structure of the full-length NS1 protein to provide a more complete structural framework for understanding the functional aspects of NS1, including the effects of various mutations in H5N1 strains. In contrast to RBD and ED, which were individually amenable for crystallographic analysis<sup>6,7</sup>, full-length NS1 readily aggregates and precipitates at the concentrations needed for crystallographic studies. We determined that two mutations, R38A and K41A, completely abrogated aggregation and allowed full-length NS1 to be sufficiently concentrated for crystallographic studies. The H5N1 NS1 structure was determined using molecular replacement techniques with previously reported structures of the RBD<sup>6</sup> and ED<sup>7</sup> as search models (see Methods and Supplementary Table 1).

In the full-length H5N1 NS1 monomer structure, the RBD and ED are formed by residues 1–72 and residues 84–220, respectively

(Fig. 1). The density corresponding to the five residues (75–79) in the linker region is not well defined, indicating the flexible nature of the linker. The electron density is relatively weak for residues 67–74, and these residues exhibit higher than average temperature factors ( $\sim 70 \text{ Å}^2$ ). The proposed connectivity between RBD and ED (Fig. 1),

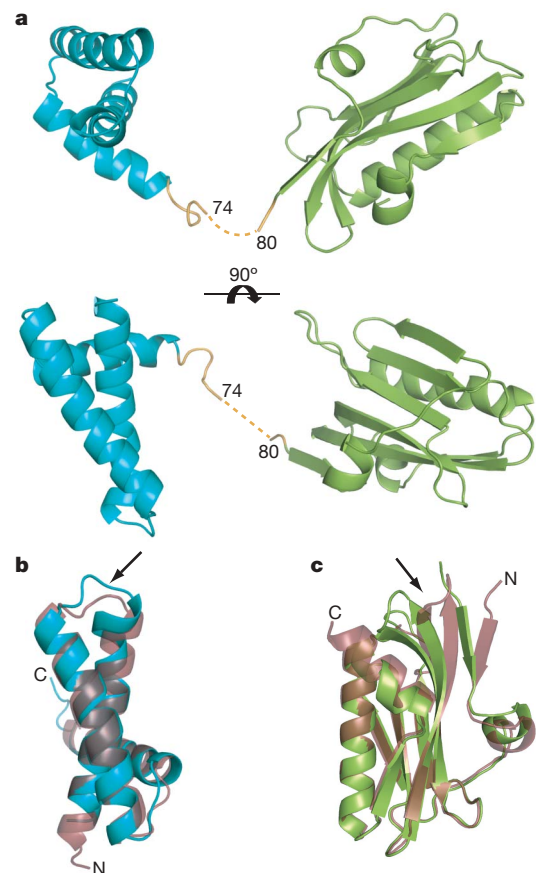


**Figure 1 | H5N1 NS1 structure.** **a**, Cartoon representation of the H5N1 NS1 structure as viewed looking across (top) and down onto (bottom) the main  $\alpha$ -helix of the RBD (aquamarine) that is implicated in dsRNA binding. The ED is coloured green, and the linker region orange; shown as orange dashed lines are 5 residues (75–79) not well defined in the electron density map. **b**, Structural alignment of H5N1 NS1 RBD (aquamarine) with H3N1 NS1 RBD<sup>6</sup> (ruby: PDB ID, 1AIL), and **c**, alignment of the H5N1 NS1 ED (green) with H1N1 NS1 ED<sup>7</sup> (ruby: PDB ID, 2GX9). In both **b** and **c** the alignments are oriented to display the areas of greatest deviation, namely the V22F conformational change in a loop region observed in the H5N1 RBD (**b**), and the movement of the  $\beta$ -sheets in the H5N1 ED (**c**), both indicated by black arrows.

<sup>1</sup>Department of Molecular Virology and Microbiology, <sup>2</sup>Department of Biochemistry and Molecular Biology, Baylor College of Medicine, One Baylor Plaza, Houston, Texas 77030, USA.

although not entirely unequivocal (see Supplementary Fig. 1 for an alternative possibility), is based on reappearance of the density in the  $2F_o - F_c$  and  $F_o - F_c$  maps after removing these residues. The H5N1 NS1 RBD consists of three large  $\alpha$ -helices connected by short loops, as seen in the A/Udm/72 H3N2 NS1 RBD structure<sup>5,6</sup>. The amino acid sequences in the RBD of these two strains show differences at 9 positions (Supplementary Fig. 2). One of the changes in the sequence, V22F, appears to have resulted in a minor but noticeable structural alteration. F22, located at the carboxy terminus of the first  $\alpha$ -helix, causes a slight movement of the loop that connects this  $\alpha$ -helix and the second main  $\alpha$ -helix (Fig. 1b). Except for this minor alteration, the two structures are invariant, with a root mean square (r.m.s.) deviation of 1.2 Å, including that at the locations where the two mutations, R38A and K41A, were introduced to make the protein behave well for crystallographic studies.

The overall polypeptide fold in the H5N1 ED, with seven  $\beta$ -strands and three  $\alpha$ -helices, is similar to the  $\alpha$ -helix  $\beta$ -crescent fold<sup>7</sup> observed in the previously reported structure of the A/PR8/34 H1N1 ED, despite sequence differences in 15 positions and a C-terminal truncation in the H5N1 ED at residue 220 (Supplementary Fig. 2). The r.m.s. deviation of 1.6 Å between the two ED structures is slightly higher than that observed for the RBD, indicating more pronounced structural changes in the ED than those observed in the RBD. These structural changes, although not correlated specifically with any amino acid change, include an en masse shift in three  $\beta$ -strands (by about 8.0 Å at the point of greatest deviation) formed by residues 83–86, 121–132 and 135–146 (Fig. 1c). These three  $\beta$ -strands in the H5N1 NS1 ED, compared to H1N1 ED<sup>7</sup>, are more twisted towards the centre of the ED monomer, and shifted away from the ED dimeric interface.

In the crystal structure of the full-length H5N1 NS1, both RBD and ED participate in dimeric interactions, as expected from the individual crystal structures of these domains from non-H5N1 strains<sup>6,7</sup>. However, in the full-length crystal structure, surprisingly, the two domains of each NS1 molecule—instead of participating in a dimeric interaction with another NS1 molecule to form a single dimeric unit—separately interact with their respective domains from the neighbouring NS1 molecules, related by crystallographic two-fold axes. This results in the formation of a chain of NS1 molecules with alternating RBD and ED dimers (Fig. 2a, Supplementary Fig. 3). The orientation of the subunits and their interactions in the H5N1 RBD dimer are, remarkably, similar to those observed in the previously reported structure of the H3N1 RBD<sup>6</sup>, despite differences in the crystallization conditions and crystal forms (Fig. 2b). Formation of such a structurally conserved RBD dimer is consistent with the observation that RBD dimerization is critical for dsRNA binding activity of the NS1 (ref. 16).

The ED dimer in our full-length H5N1 structure exhibits a large buried surface area of  $\sim 1,600$  Å<sup>2</sup>, which is similar to that observed in the previously published H1N1 ED dimer<sup>7</sup>. However, despite some resemblance, the H5N1 ED dimer exhibits substantial differences when compared to H1N1 NS1 ED dimer<sup>7</sup>. The superposition of these two ED dimers indicates that the protomeric subunits in the full-length ED dimer are significantly more twisted with respect to each other (Fig. 2c). As a result, the dimeric interface of the H5N1 NS1 ED consists of a series of electrostatic interactions, in contrast to the dimeric interactions observed in the H1N1 NS1 ED, which consist of primarily hydrophobic interactions. The residues that participate in the dimeric interactions of the H5N1 NS1 ED dimer are conserved within H1N1 NS1 and vice versa. Thus, one distinct possibility is that the conformational difference in the H5N1 NS1 ED dimer is due to the presence of the RBD and the formation of the RBD dimer. It appears that without the RBD, the ED can adopt alternative dimeric states, as shown by the recent structural analysis of ED from an avian H12N5 strain<sup>17</sup>.

In addition to the constraints imposed by the RBD dimerization, another important factor that influences the extent of the

conformational changes, or the degree of twisting between the subunits in the ED dimer, may be the length of the linker between RBD and ED in the full-length NS1. Compared to either H1N1 or H3N2 NS1, H5N1 NS1 has a shorter linker due to a five residue deletion<sup>18</sup>. As a result of the shorter linker, greater stress is induced within the full-length H5N1 NS1 structure upon RBD dimerization. Thus, the amino termini of the ED subunits in the dimer are pulled towards their respective RBD, causing more pronounced twisting between the ED subunits. In contrast, the additional five residues contained in the linker within H1N1 or other non-H5N1 strains may limit the stress induced and thus the degree of ED twisting upon RBD dimerization.

An unexpected and novel observation from our crystallographic analysis of full-length H5N1 NS1, which has implications for the function of this protein, is the formation of long chains of NS1 molecules with alternating RBD and ED dimers. Despite the involvement of crystallographic two-fold axes in the formation of these dimers, conservation of the RBD dimeric interactions, as mentioned above, and the large buried surface area in the ED dimer, which is typical of protein homodimers, strongly suggest that such a chain formation is more a consequence of the intrinsic ability of NS1 molecules to oligomerize than crystal packing. In the crystal, three such chains related by the crystallographic 3<sub>1</sub>-screw axis parallel to the *c* axis interact with one another to form a  $\sim 65$ -Å-wide tubular organization with a 20-Å central tunnel (Fig. 3a, b). This tubular organization can be described as a helical structure with a pitch of 69.6 Å (unit cell dimension along *c* axis), consisting of three NS1

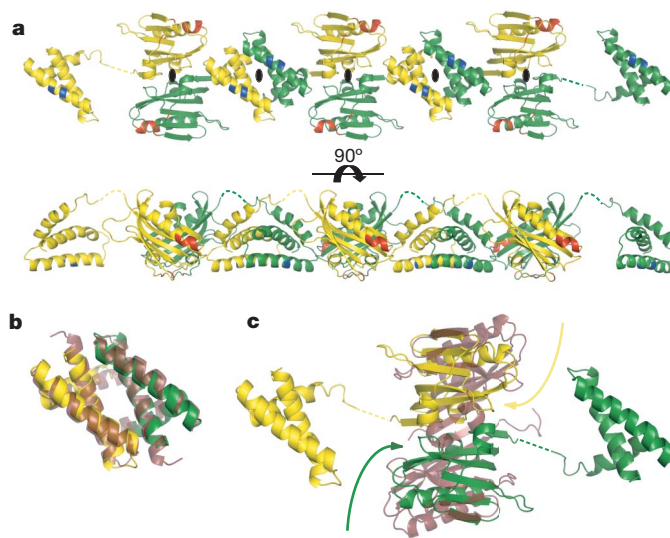


**Figure 2 | RBD and ED dimer formation, and the NS1 chain.** **a**, The RBD and ED of each NS1 molecule separately interact with their respective domains from the neighbouring NS1 molecules, related by crystallographic two-fold axes (perpendicular to plane of the paper indicated the black ovals), resulting in the formation of a chain of NS1 with alternating RBD and ED dimers. The two-fold related NS1 molecules are coloured separately in yellow and green. The residues critical to dsRNA (residues 38 and 41)<sup>16</sup> and CPSF (conserved residues F103, M106 and GLEWN183–187) binding<sup>14,15,19</sup> are coloured in blue and red, respectively. **b**, Superposition of H5N1 RBD dimer with the H3N2 RBD<sup>6</sup> dimer (in ruby; PDB ID, 1AIL); each protomeric subunit in the H5N1 RBD dimer is coloured differently in yellow and green. **c**, Structural alignment of the H5N1 dimer and H1N1 NS1 ED<sup>7</sup> dimer (in ruby; PDB ID, 2GX9), demonstrating the twisting motion (curved arrows) of the H5N1 ED monomers, with respect to H1N1 ED, towards their RBDs. Each monomer in the H5N1 NS1 dimer is coloured as in **a**. The dimeric interface of the H5N1 NS1 ED consists of a series of electrostatic interactions: a salt bridge between K131 and E97, hydrogen-bonding involving the side chains of T91 and R193, E196 and R200, E152 and the amide group of L95, as well as a back-bone hydrogen bond between the E96 amide group and the E152 carbonyl group. In contrast, the dimeric interactions in the H1N1 NS1 ED consist primarily of strong hydrophobic interactions along the continuous anti-parallel  $\beta$ -sheet involving residues L90, V136 and L141 (ref. 7).



dimers in one turn of the helix. The tubular NS1 organization is stabilized by inter-chain interactions involving ED dimers interlocking into saddle-like depressions between the RBD and ED dimers from other NS1 chains (Fig. 3c). The RBD dimers within the tubular structure are positioned such that the conserved residues, R38 and K41, implicated in the dsRNA binding<sup>16</sup> would project into the tunnel to interact with dsRNA (Fig. 3b, Supplementary Fig. 4), whereas all the known ligand binding sites including a conserved Trp residue critical for binding cleavage and polyadenylation specificity factor (CPSF)<sup>14,15,19</sup> are clearly surface-exposed (Fig. 3c).

At present it is not known how NS1 interacts with dsRNA. One mechanism that has been proposed for the IFN-antagonist activity of the NS1 RBD is the sequestration of dsRNA that would otherwise activate the IFN-inducing PKR<sup>12,20</sup> and 2'-5'-oligoadenylate synthetase/RNase L<sup>11</sup> pathways. It has been shown that during a viral infection, dsRNA of at least 30 base pairs (bp) is required to activate these pathways, with maximum activation occurring with a dsRNA greater than 80 bp (ref. 21). Thus, NS1 must be able to sequester varying lengths of dsRNA, and completely prevent exposure of the dsRNA to any interactions with cellular dsRNA binding proteins involved in activating the type-I IFN response in the cell. Previous mutational analysis has implicated both K41 and R38 of NS1 as essential to

dsRNA binding<sup>16</sup>. Whereas mutation K41A lowers dsRNA affinity, mutation R38A completely abrogates the binding of dsRNA<sup>16</sup>. Elimination of ED is shown to significantly alter the dsRNA binding affinity of NS1, suggesting the involvement of this domain in the dsRNA interaction<sup>22</sup> as well.

A plausible model that emerges from our crystallographic analysis for the dsRNA binding activity of full-length NS1 is that NS1 cooperatively oligomerizes in the presence of dsRNA to form a tubular structure completely encasing any length of dsRNA within the observed central tunnel. The ability of full-length NS1 to form chains through ED and RBD dimerization, instead of individual dimeric units, provides a robust mechanism not only to completely protect the dsRNA but also to adapt to any structural variations in dsRNA, including changes in the helical pitch, using the inherent flexibility in the linker between the ED and RBD domains. In this model, the orientation of the RBD with R38 projecting into the central tunnel, and the involvement of ED are consistent with previous mutational studies<sup>16,22</sup> mentioned above.

Cryo-electron microscopy images of native full-length NS1 (A/PR8/34) in the presence of dsRNA further substantiate the tubular model for how NS1 sequesters dsRNA. These images show formation of smooth tubular structures of similar width to that observed in the crystal structure (Fig. 3d). As mentioned earlier, the native full-length NS1 precipitates readily, but in presence of dsRNA it remains in solution, forming such tubular structures. However, based on our crystallographic analysis, full-length NS1 with R38A and K41A mutations mimics formation of the tubular structure even in the absence of dsRNA, indicating thereby that these charged residues in the native protein need to be neutralized by the bound dsRNA or mutated to uncharged residues for the native protein to remain in solution and form tubular structures. The formation of the tubular structure by the mutated full-length protein is concentration dependent, which is consistent with the suggestion that NS1 cooperatively binds to dsRNA depending on its length. At lower concentrations, as shown by size exclusion chromatography, mutated H5N1 NS1 is a dimer (Supplementary Fig. 5), and with increasing concentrations it forms higher order oligomers, as indicated by dynamic light scattering (data not shown).

Our crystallographic and cryo-electron microscopy studies on full-length NS1 bring a novel perspective to the structure–function relationship of NS1. Formation of chains of NS1 and their association to form a tubular structure provides an attractive model for how NS1 could effectively compete with cellular dsRNA-binding proteins to sequester varying lengths of dsRNA. Such a tubular organization does not preclude interactions with other host proteins, as all of the binding sites for the known cellular proteins remain exposed on the outer surface of the NS1 tubular structure. Our model also provides an explanation for recent perplexing data, which indicate that despite overlapping binding sites, NS1 simultaneously interacts with both dsRNA and  $\alpha$ -importin<sup>23</sup>. The cooperative interactions leading to NS1 tubular formation in the presence of dsRNA could allow for a free RBD, which is not involved in either a dimeric interaction or interactions with dsRNA, at either end of the tubular structure to bind  $\alpha$ -importin. Remarkably, a consistent feature in a majority of the recent H5N1 strains is the deletion of  $\sim 5$  residues in the region of NS1 that links RBD and ED<sup>18</sup>. It is possible that this linker region (depending on its length, residue composition, and flexibility) allows modulation of NS1 affinity for dsRNA by influencing the positioning and spacing of the RBD dimers in our proposed model for dsRNA sequestration. Considering also that the observed conformational changes in the ED dimeric interface in our crystal structure of the full-length NS1 could have resulted from a shortened linker, further studies could test the hypothesis that this shortening of the linker region in H5N1 NS1 contributes to increased virulence, either by modulating its dsRNA binding affinity or its interaction with host proteins.

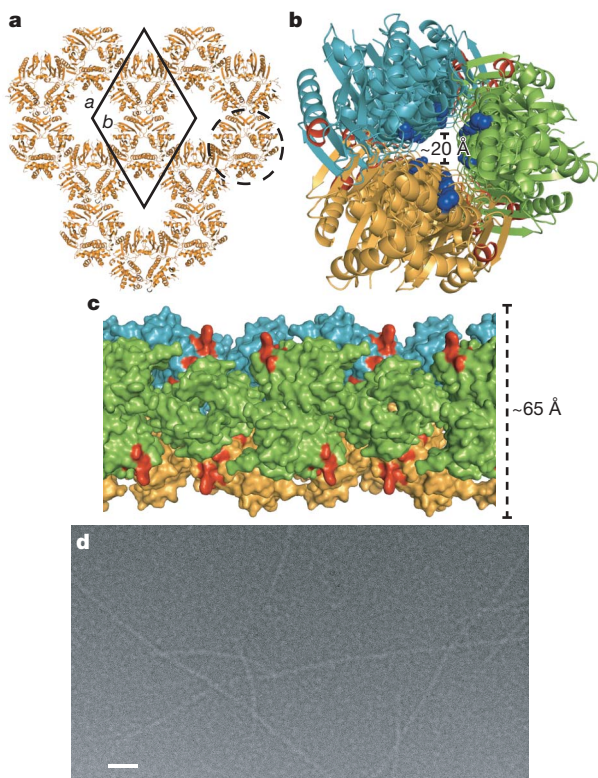


**Figure 3 | NS1 tubular structure.** **a**, A thin slice of the crystal packing of H5N1 NS1 molecules (orange) as viewed along the crystallographic *c* axis. The crystallographic unit cell (solid black diamond) along with the *a* and *b* axes are shown for reference. One of the tubular structures formed by the interaction of three NS1 chains related by the crystallographic  $3_1$ -screw axis (perpendicular to the plane of the paper) is shown surrounded by a dashed circle. **b**, NS1 tubular structure (diameter  $\sim 65$  Å) as viewed down its long axis, showing the  $\sim 20$ -Å-wide tunnel. Each of the three chains is coloured differently in green, orange and light blue. The residues 38 and 41 critical for dsRNA binding<sup>16</sup> are shown as blue spheres, demonstrating their location within the central tunnel, and the residues critical to CPSF binding<sup>14,15,19</sup> are coloured red. **c**, A surface representation of the tubular structure (diameter  $\sim 65$  Å) viewed across its long axis. The CPSF binding sites coloured in red are surface-exposed. Each chain is coloured as in **b**. **d**, A cryo-electron micrograph of native H1N1 NS1 in the presence of dsRNA. Long tubular structures of diameter  $\sim 70$  Å can be clearly visualized. Scale bar,  $\sim 500$  Å.



## METHODS SUMMARY

The expression of H5N1 NS1 was done using a construct containing the mutations R38A and K41A, in BL-21 *Escherichia coli* cells. The clarified lysate was then bound to Qiagen-NTA agarose beads using the batch method. Once eluted, the protein was filtered and put through an HQ column followed by size exclusion chromatography with a 50 mM NaCl, 10 mM Hepes pH 8.0 column buffer. Crystals of the H5N1 NS1 were grown via the hanging drop method using a 1:1 ratio of well solution to protein at 5–8 mg ml<sup>-1</sup>. The well solution was 17% PEG 3350, 225–275 mM KSCN, 100 mM Hepes pH 6.8–7.2. Hexagonal crystals were seen after 2–3 weeks, reaching a maximum size of 0.1–0.2 mm after a month. Data were collected at the Argonne National Laboratory using the SBC-19-ID beamline. Diffraction data were merged and scaled using D\*TREK<sup>24</sup> with an  $R_{\text{merge}}$  of 10% (Supplementary Table 1). Although crystals diffracted to ~2.2 Å, the diffraction intensities were weak between this resolution and 2.7 Å with  $I/\sigma < 2$ . The crystals belong to the primitive hexagonal space group ( $P6_322$ ), as confirmed by analysing the unmerged data in P1 using POINTLESS<sup>25</sup>. The structure of H5N1 NS1 was determined by molecular replacement techniques with PHASER<sup>26</sup> using the H1N1 ED<sup>7</sup> and the H3N2 RBD<sup>6</sup> subunits as search models, and refined using REFMAC5<sup>27</sup> as implemented in the CCP4<sup>28</sup> package. The specimen for cryo-electron microscopy imaging was prepared by incubating dsRNA with a saturating amount of purified A/PR8/34 H1N1 NS1 for 45 min at room temperature followed by size exclusion chromatography to separate NS1 bound to dsRNA from the unbound NS1.

**Full Methods** and any associated references are available in the online version of the paper at [www.nature.com/nature](http://www.nature.com/nature).

Received 28 July; accepted 23 September 2008.

Published online 5 November 2008.

- Abdel-Ghaffar, A. N. *et al.* Update on avian influenza A (H5N1) virus infection in humans. *N. Engl. J. Med.* **358**, 261–273 (2008).
- Beigel, J. H. *et al.* Avian influenza A (H5N1) infection in humans. *N. Engl. J. Med.* **353**, 1374–1385 (2005).
- Seo, S. H., Hoffmann, E. & Webster, R. G. The NS1 gene of H5N1 influenza viruses circumvents the host anti-viral cytokine responses. *Virus Res.* **103**, 107–113 (2004).
- Seo, S. H., Hoffmann, E. & Webster, R. G. Lethal H5N1 influenza viruses escape host anti-viral cytokine responses. *Nature Med.* **8**, 950–954 (2002).
- Chien, C. Y. *et al.* A novel RNA-binding motif in influenza A virus non-structural protein 1. *Nature Struct. Biol.* **4**, 891–895 (1997).
- Liu, J. *et al.* Crystal structure of the unique RNA-binding domain of the influenza virus NS1 protein. *Nature Struct. Biol.* **4**, 896–899 (1997).
- Bornholdt, Z. A. & Prasad, B. V. X-ray structure of influenza virus NS1 effector domain. *Nature Struct. Mol. Biol.* **13**, 559–560 (2006).
- Garcia-Sastre, A. *et al.* Influenza A virus lacking the NS1 gene replicates in interferon-deficient systems. *Virology* **252**, 324–330 (1998).
- Wang, X. *et al.* Influenza A virus NS1 protein prevents activation of NF-kappaB and induction of alpha/beta interferon. *J. Virol.* **74**, 11566–11573 (2000).
- Kochs, G., Garcia-Sastre, A. & Martinez-Sobrido, L. Multiple anti-interferon actions of the influenza A virus NS1 protein. *J. Virol.* **81**, 7011–7021 (2007).
- Min, J. Y. & Krug, R. M. The primary function of RNA binding by the influenza A virus NS1 protein in infected cells: Inhibiting the 2'-5' oligo (A) synthetase/RNase L pathway. *Proc. Natl Acad. Sci. USA* **103**, 7100–7105 (2006).
- Lu, Y., Wambach, M., Katze, M. G. & Krug, R. M. Binding of the influenza virus NS1 protein to double-stranded RNA inhibits the activation of the protein kinase that phosphorylates the eIF-2 translation initiation factor. *Virology* **214**, 222–228 (1995).
- Hale, B. G. *et al.* Influenza A virus NS1 protein binds p85beta and activates phosphatidylinositol-3-kinase signaling. *Proc. Natl Acad. Sci. USA* **103**, 14194–14199 (2006).
- Nemeroff, M. E. *et al.* Influenza virus NS1 protein interacts with the cellular 30 kDa subunit of CPSF and inhibits 3' end formation of cellular pre-mRNAs. *Mol. Cell* **1**, 991–1000 (1998).
- Twu, K. Y. *et al.* The CPSF30 binding site on the NS1A protein of influenza A virus is a potential antiviral target. *J. Virol.* **80**, 3957–3965 (2006).
- Wang, W. *et al.* RNA binding by the novel helical domain of the influenza virus NS1 protein requires its dimer structure and a small number of specific basic amino acids. *RNA* **5**, 195–205 (1999).
- Hale, B. G., Barclay, W. S., Randall, R. E. & Russell, R. J. Structure of an avian influenza A virus NS1 protein effector domain. *Virology* **378**, 1–5 (2008).
- Li, K. S. *et al.* Genesis of a highly pathogenic and potentially pandemic H5N1 influenza virus in eastern Asia. *Nature* **430**, 209–213 (2004).
- Noah, D. L., Twu, K. Y. & Krug, R. M. Cellular antiviral responses against influenza A virus are countered at the posttranscriptional level by the viral NS1A protein via its binding to a cellular protein required for the 3' end processing of cellular pre-mRNAs. *Virology* **307**, 386–395 (2003).
- Diebold, S. S. *et al.* Viral infection switches non-plasmacytoid dendritic cells into high interferon producers. *Nature* **424**, 324–328 (2003).
- Wang, Q. & Carmichael, G. G. Effects of length and location on the cellular response to double-stranded RNA. *Microbiol. Mol. Biol. Rev.* **68**, 432–452 (2004).
- Li, W. X. *et al.* Interferon antagonist proteins of influenza and vaccinia viruses are suppressors of RNA silencing. *Proc. Natl Acad. Sci. USA* **101**, 1350–1355 (2004).
- Melen, K. *et al.* Nuclear and nucleolar targeting of influenza A virus NS1 protein: Striking differences between different virus subtypes. *J. Virol.* **81**, 5995–6006 (2007).
- Pflugrath, J. W. The finer things in X-ray diffraction data collection. *Acta Crystallogr. D* **55**, 1718–1725 (1999).
- Evans, P. Scaling and assessment of data quality. *Acta Crystallogr. D* **62**, 72–82 (2006).
- McCoy, A. J. *et al.* Phaser crystallographic software. *J. Appl. Crystallogr.* **40**, 658–674 (2007).
- Murshudov, G. N., Vagin, A. A. & Dodson, E. J. Refinement of macromolecular structures by the maximum-likelihood method. *Acta Crystallogr. D* **53**, 240–255 (1997).
- The CCP4 suite: Programs for protein crystallography. *Acta Crystallogr. D* **50**, 760–763 (1994).

**Supplementary Information** is linked to the online version of the paper at [www.nature.com/nature](http://www.nature.com/nature).

**Acknowledgements** We thank P. Palese for providing us clones of A/Vietnam/1203/2004 H5N1 and A/PR8/34 (H1N1) NS1. This work was supported by the NIH (AI36040) and the Robert Welch Foundation (to B.V.V.P.). Z.A.B. acknowledges support from an NIH virology training grant (AI07471). We thank P. Palese, A. Rice, M. Schmid and B. Carrillo for discussions and comments on the manuscript and H. Chen for technical assistance with cryo-EM. We acknowledge the use of cryo-EM facilities at the National Center for Macromolecular Imaging (Baylor College of Medicine) supported by the National Institutes of Health (RR002250 to W. Chiu); we also acknowledge the Center for Advanced Microstructures & Devices (CAMD), Baton Rouge, Los Angeles, and H. Bellamy, and the SBC-CAT 19ID beam line at the Advanced Photon Source (supported by the US Department of Energy, Basic Energy Sciences, Office of Science, under contract no.W-31-109-Eng-38) and its staff for their help during data collection.

**Author Information** Atomic coordinates and structure factors for the reported crystal structure have been deposited with the Protein Data Bank under the accession number 3EU6. Reprints and permissions information is available at [www.nature.com/reprints](http://www.nature.com/reprints). Correspondence and requests for materials should be addressed to B.V.V.P. ([vprasad@bcm.tmc.edu](mailto:vprasad@bcm.tmc.edu)).

## METHODS

**Protein expression and purification.** Expression of H5N1 NS1 was done using a construct containing the mutations R38A and K41A, placed in pET-46 Ek/LIC (Novagen) with an engineered thrombin site to remove the HIS tag. The construct was expressed in BL-21 *E. coli* cells at 25 °C overnight at an  $A_{600}$  of 0.6–0.8 with 0.5 mM IPTG. Each bacterial pellet was resuspended in 20 ml of lysis buffer, and lysed using a microfluidizer. The clarified lysate was then bound to 2–3 ml of Qiagen-NTA agarose beads using the batch method. The beads were then washed twice within a 50 ml conical tube with a 50 mM  $\text{NaH}_2\text{PO}_4$ , 300 mM NaCl, 30 mM imidazole wash buffer, and then washed 3 times with 50 mM NaCl, 10 mM Hepes pH 8.0 buffer. The beads were then resuspended in 20 ml of 50 mM NaCl, 10 mM Hepes pH 8.0 buffer, and treated with thrombin at room temperature overnight on a rocker to cut H5N1 NS1 off the beads. The protein was then filtered and put through HQ column to remove the thrombin, then size exclusion chromatography was performed with a 50 mM NaCl, 10 mM Hepes pH 8.0 column buffer which was the final crystallization buffer.

**Crystallization.** Crystals of the H5N1 NS1 were grown by the hanging drop method by using a 1:1 ratio of well solution to protein at 5–8 mg ml<sup>-1</sup>. The well solution was 17% PEG 3350, 225–275 mM KSCN, 100 mM Hepes pH 6.8–7.2. Hexagonal crystals were seen after 2–3 weeks, reaching a maximum size of 0.1–0.2 mm after a month.

**Data collection and processing.** Crystals of H5N1 NS1 were cryoprotected by shock soaking for ~10 s in 35% sucrose, 17% PEG 3350, 225–275 mM KSCN, 100 mM Hepes pH 6.8–7.2. The crystals were then flash frozen in liquid nitrogen and shipped to the synchrotron facility. Data were collected at the Argonne National Laboratory using SBC-19-ID beamline using a 1.0° oscillation angle. Diffraction data were merged and scaled using D\*TREK<sup>24</sup> with an  $R_{\text{merge}}$  of 10% (Supplementary Table 1). Although crystals diffracted to ~2.2 Å, the diffraction intensities were weak between this resolution and 2.7 Å with  $I/\sigma < 2$ . The crystals belong to the primitive hexagonal space group ( $P6_522$ ), as confirmed by analysing the unmerged data in P1 using POINTLESS<sup>25</sup>, with unit cell dimensions of  $a = 106.12$  Å,  $b = 106.12$  Å,  $c = 69.63$  Å,  $\alpha = 90^\circ$ ,  $\beta = 90^\circ$ ,  $\gamma = 120^\circ$ .

**Structure determination and refinement.** The structure of H5N1 NS1 was determined by molecular replacement techniques with PHASER<sup>26</sup> as implemented in the CCP4<sup>28</sup> package using the H1N1 ED<sup>7</sup> and the H3N2 RBD<sup>6</sup> subunits as search models. Some of the missing regions in the model were identified by computing composite-omit maps computed using CNS<sup>29</sup>. Following iterative cycles of model building using COOT<sup>30</sup>, the model was refined using Refmac5<sup>27</sup> (Supplementary Table 1). A 5% of the reflections were set aside for  $R_{\text{free}}$  (ref. 31) calculations. The final structure has an  $R_{\text{free}}$  of 29% and a final  $R$ -factor of 27% using all the data to 2.7 Å resolution. During the course of the refinement, and following the final refinement, stereochemistry of the structure was checked using PROCHECK<sup>32</sup>. The buried surface area for the dimer complex was

calculated with CNS<sup>29</sup>. The structural alignments and calculations of r.m.s. deviation were carried out using PyMOL (<http://pymol.sourceforge.net>), which was also used for making all the figures.

**Cryo-electron microscopy (cryo-EM).** Single stranded, complementary RNA, 12 bases in length (GAGAGAGAGAGA and CUCUCUCUCUCU) were ordered from Dharmacon Products. The strands of RNA were then deprotected, mixed together in equal amounts, and boiled for 1 min. The reaction was then allowed to cool overnight to allow for annealing and formation of dsRNA. The chosen sequence of the complimentary strands with GA and CU repetitions allows for the formation of long dsRNA strands, which would be suitable for cryo-EM visualization following addition of NS1. The dsRNA mixture was then mixed with a saturating amount of purified A/PR8/34 H1N1 NS1. Expression of H1N1 NS1 (A/PR8/34) was done using pET-46 Ek/LIC (Novagen) vector with N-terminal 6 × His tag. The construct was expressed in BL-21 *E. coli* cells at 25 °C overnight at an  $A_{600}$  of 0.6–0.8 with 0.5 mM IPTG. Each bacterial pellet was resuspended in 20 ml of lysis buffer, and lysed using a microfluidizer. The clarified lysate was then bound to 2–3 ml of Qiagen-NTA agarose beads using the batch method. The beads were then washed twice within a 50 ml conical tube with a 50 mM  $\text{NaH}_2\text{PO}_4$ , 300 mM NaCl, 30 mM imidazole wash buffer (pH 8.0), and then eluted with a 50 mM  $\text{NaH}_2\text{PO}_4$ , 300 mM NaCl, 250 mM imidazole elution buffer (pH 8.0). The NS1-dsRNA binding reaction was done in the elution buffer, was incubated for 45 min, and then NS1 bound to dsRNA was separated from unbound NS1 via size exclusion chromatography before preparing the specimen for cryo-EM imaging. Specimen for cryo-EM was embedded in vitreous ice on holey carbon films using standard procedures<sup>33</sup>, and was imaged on a JEOL1200 EX transmission electron microscope operated at ×30,000 magnification using 100-kV electrons and a beam dose of ~5 electrons Å<sup>-2</sup>. Several attempts to duplicate this procedure using A/Vietnam/1203/2004 H5N1 NS1 were unsuccessful due to noticeably accelerated aggregation rate of the wild-type protein when compared to A/PR8/34 H1N1 NS1. The increased instability of the wild-type H5N1 NS1 is probably a result of the observed five amino acid deletion within the linker domain.

29. Brunger, A. T. *et al.* Crystallography & NMR system: A new software suite for macromolecular structure determination. *Acta Crystallogr. D* **54**, 905–921 (1998).
30. Emsley, P. & Cowtan, K. Coot: Model-building tools for molecular graphics. *Acta Crystallogr. D* **60**, 2126–2132 (2004).
31. Brunger, A. T. Free R value: A novel statistical quantity for assessing the accuracy of crystal structures. *Nature* **355**, 472–475 (1992).
32. Laskowski, R. A., MacArthur, M. W., Moss, D. S. & Thornton, J. M. PROCHECK: A program to check the stereochemical quality of protein structures. *J. Appl. Crystallogr.* **26**, 283–291 (1993).
33. Dubochet, J. *et al.* Cryo-electron microscopy of vitrified specimens. *Q. Rev. Biophys.* **21**, 129–228 (1988).

# Structural recognition and functional activation of Fc $\gamma$ R by innate pentraxins

Jinghua Lu<sup>1</sup>, Lorraine L. Marnell<sup>2</sup>, Kristopher D. Marjon<sup>2</sup>, Carolyn Mold<sup>2</sup>, Terry W. Du Clos<sup>2,3</sup> & Peter D. Sun<sup>1</sup>

Pentraxins are a family of ancient innate immune mediators conserved throughout evolution. The classical pentraxins include serum amyloid P component (SAP) and C-reactive protein, which are two of the acute-phase proteins synthesized in response to infection<sup>1,2</sup>. Both recognize microbial pathogens and activate the classical complement pathway through C1q (refs 3 and 4). More recently, members of the pentraxin family were found to interact with cell-surface Fc $\gamma$  receptors (Fc $\gamma$ R) and activate leukocyte-mediated phagocytosis<sup>5–8</sup>. Here we describe the structural mechanism for pentraxin's binding to Fc $\gamma$ R and its functional activation of Fc $\gamma$ R-mediated phagocytosis and cytokine secretion. The complex structure between human SAP and Fc $\gamma$ RIIa reveals a diagonally bound receptor on each SAP pentamer with both D1 and D2 domains of the receptor contacting the ridge helices from two SAP subunits. The 1:1 stoichiometry between SAP and Fc $\gamma$ RIIa infers the requirement for multivalent pathogen binding for receptor aggregation. Mutational and binding studies show that pentraxins are diverse in their binding specificity for Fc $\gamma$ R isoforms but conserved in their recognition structure. The shared binding site for SAP and IgG results in competition for Fc $\gamma$ R binding and the inhibition of immune-complex-mediated phagocytosis by soluble pentraxins. These results establish antibody-like functions for pentraxins in the Fc $\gamma$ R pathway, suggest an evolutionary overlap between the innate and adaptive immune systems, and have new therapeutic implications for autoimmune diseases.

The pentraxin family is divided into two subclasses, the classical short-chain pentraxins, C-reactive protein (CRP) and SAP, and the long-chain pentraxins<sup>3</sup>. Both SAP and CRP recognize various pathogenic bacteria, fungi and yeasts<sup>3</sup>, and activate the classical complement pathway through C1q (ref. 4). Long-chain pentraxins such as PTX3, which contain an additional amino-terminal domain, are produced by macrophages and myeloid dendritic cells in response to proinflammatory stimuli<sup>9,10</sup>. Humans have three classes of activating Fc $\gamma$  receptors—Fc $\gamma$ RI, Fc $\gamma$ RIIa and Fc $\gamma$ RIII—and one inhibitory receptor, Fc $\gamma$ RIb<sup>11</sup>. In addition to activating phagocytosis through Fc $\gamma$ R<sup>5–8</sup>, both SAP and CRP also induce protective immune responses<sup>12</sup>, and high levels of CRP protect mice from endotoxin shock through Fc $\gamma$ R<sup>13,14</sup>. Although pentraxins can both activate and regulate immune responses, the molecular mechanisms and the balance of these antibody-like functions remain unresolved. Here we present structural and functional evidence for the involvement of pentraxins in the activation of Fc $\gamma$ R and suggest their potential role in modulating antibody-mediated inflammatory responses.

Although immune complexes are known to activate Fc $\gamma$ R, leading to phagocytosis and cytokine secretion, it is not clear whether pentraxins induce similar Fc $\gamma$ R activation<sup>7,8</sup>. To investigate whether Fc $\gamma$ R recognize pathogens through pentraxin opsonization, we examined the engulfment of pentraxin-opsonized zymosan by

human monocyte-derived macrophages (MDMs). Zymosan particles labelled with Texas red were efficiently internalized by MDMs on opsonization with human SAP, CRP or IgG in comparison with unopsonized particles (Fig. 1a). The cup-shaped enrichment of Fc $\gamma$ RIIa (labelled green) surrounding the zymosan particles bound to SAP and CRP indicates the involvement of Fc $\gamma$ R in phagocytosis. The addition of soluble IgG decreased the phagocytosis of SAP-opsonized zymosan by 90% from  $3.8 \pm 0.5$  to  $0.4 \pm 0.2$  (means  $\pm$  s.e.m.) zymosan particles per MDM, further confirming the role of Fc $\gamma$ R. We then investigated cytokine secretion as a result of SAP–Fc $\gamma$ R interaction. To avoid activation mediated by zymosan and endotoxin, CD14<sup>+</sup> monocytes were treated with purified SAP in either an aggregated or monomeric form without zymosan and in the presence of polymyxin B. Treatment with SAP resulted in dose-dependent secretion of interleukin (IL)-10, IL-8 and IL-6 by monocytes (Fig. 1b), and only the aggregated SAP, not the monomeric SAP, stimulated cytokines, suggesting a requirement for receptor crosslinking by SAP in cytokine production (Fig. 1c). Cytokine secretion was markedly decreased if SAP was pretreated with bead-bound proteinase K or precleared with phosphoethanolamine (PE)-conjugated Sepharose (Fig. 1d). In addition, antibodies against Fc $\gamma$ R as well as a *Syk* inhibitor, piceatannol, which blocks Fc $\gamma$ R signalling, significantly inhibited cytokine secretion, confirming the involvement of Fc $\gamma$ R (Fig. 1e, f). To assess the contribution of potential contaminating lipopolysaccharide and/or peptidoglycan in the SAP sample to cytokine secretion, bone-marrow-derived macrophages (BMDMs) from *Myd88*<sup>−/−</sup> and *RIP2*<sup>−/−</sup> mice were treated with SAP and assayed for cytokine production. Similar or higher levels of IL-6 and CCL2 were detected in SAP-treated but not PBS-treated BMDMs from *Myd88*<sup>−/−</sup> mice compared with wild-type BMDMs (Fig. 1g). Tumour necrosis factor (TNF)- $\alpha$  production was lower in SAP-treated *Myd88*<sup>−/−</sup> BMDMs than in wild-type BMDMs but remained 10–20-fold higher than after treatment with PBS. Similarly, comparable amounts of cytokines were released in BMDMs from the *RIP2*<sup>−/−</sup> and wild-type mice in response to SAP. The results show that BMDMs from both *Myd88*<sup>−/−</sup> and *RIP2*<sup>−/−</sup> mice produce cytokines on stimulation with SAP, independently of Toll-like receptor (TLR) and nucleotide-binding oligomerization domain-like (NOD) receptor pathways. However, a partial decrease in TNF- $\alpha$  level from the *Myd88*<sup>−/−</sup> compared with the wild-type mice indicates a potential synergistic activation between Fc $\gamma$ R and TLR.

To investigate the structural mechanism for pentraxin-mediated Fc $\gamma$ R activation, we determined the crystal structure of human SAP in complex with the extracellular domain of Fc $\gamma$ RIIa to 2.8 Å resolution, with final *R*-factors of 20.7% and 27.9% for *R*<sub>cryst</sub> and *R*<sub>free</sub> respectively (Supplementary Table 1). The refined ( $2F_o - F_c$ ) density map was continuous throughout the complex except for one SAP loop, residues 140–146, that was disordered in four of the five SAP

<sup>1</sup>Structural Immunology Section, Laboratory of Immunogenetics, National Institute of Allergy and Infectious Diseases, National Institutes of Health, Rockville, Maryland 20852, USA. <sup>2</sup>Department of Internal Medicine and Department of Molecular Genetics and Microbiology, University of New Mexico, Albuquerque, New Mexico 87131, USA. <sup>3</sup>VA Medical Center, Albuquerque, New Mexico 87108, USA.



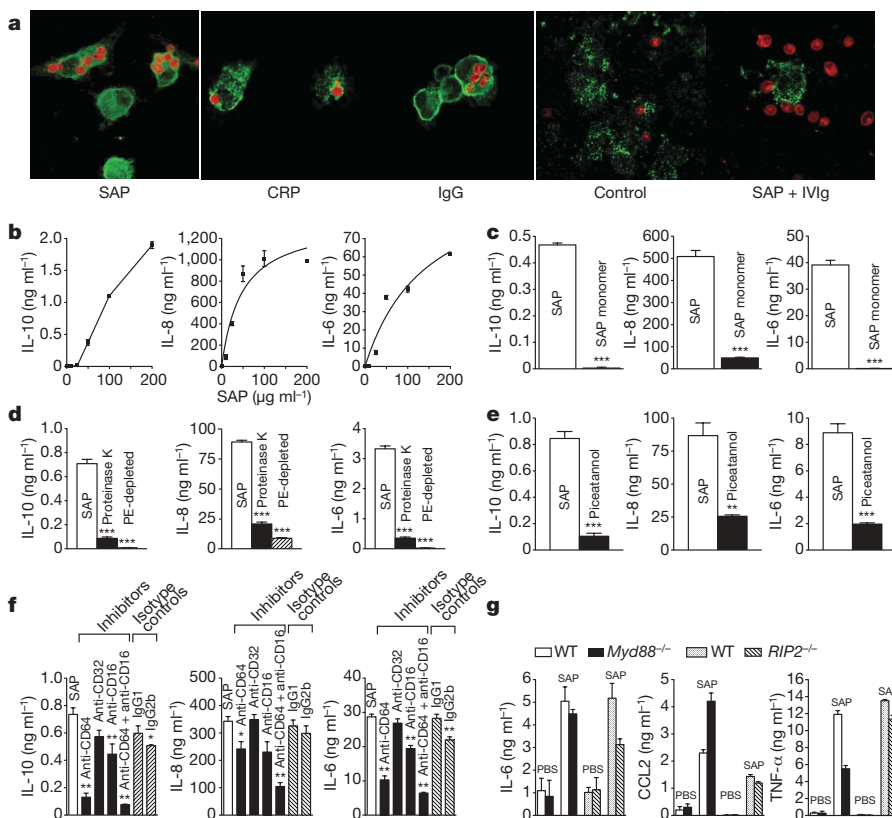


**Figure 1 | Activation of Fc $\gamma$ R by pentraxin results in phagocytosis and cytokine release.** **a**, Zymosans opsonized with SAP and CRP are phagocytosed by human macrophages through Fc $\gamma$ RIIa. MDMs incubated with zymosan (red) opsonized with (from left to right) SAP, CRP, IgG, PBS control or SAP in the presence of 10 mg ml<sup>-1</sup> intravenous immunoglobulin (IVIg). **b–f**, Production of IL-10, IL-8 and IL-6 by CD14<sup>+</sup> monocytes in response to different concentrations of aggregated SAP (**b**), 50  $\mu$ g ml<sup>-1</sup> aggregated or monomeric SAP (**c**), SAP pretreated with proteinase K or precleared with PE-Sepharose (**d**) and SAP in the presence of 25  $\mu$ g ml<sup>-1</sup> piceatannol (**e**), and SAP treatment in the presence of Fc $\gamma$ R specific antibodies or control Ig (**f**). **g**, Cytokine release by BMDMs from wild-type, *Myd88*<sup>-/-</sup> and *RIP2*<sup>-/-</sup> mice stimulated with SAP. Results are means and s.e.m. for triplicate wells in two or three experiments. Significance levels: asterisk,  $P < 0.05$ ; two asterisks,  $P < 0.01$ ; three asterisks,  $P < 0.001$ .

subunits. Each asymmetric unit contained one Fc $\gamma$ RIIa molecule bound to the effector face of one SAP pentamer with the D1 and D2 domains of the receptor spanning diagonally over SAP and contacting the A and C subunits of the pentraxin, respectively (Fig. 2). This diagonal spanning of Fc $\gamma$ RIIa over the SAP pentamer ensures a 1:1 stoichiometry in SAP–Fc $\gamma$ RIIa recognition, thus setting the need for the binding of multivalent pathogens in Fc receptor aggregation. The conformations of the receptor-contacting subunits A and C of SAP do not differ significantly from the other three non-receptor contacting subunits nor from those of receptor-free SAP<sup>15</sup> (Fig. 2d). In fact, the entire SAP pentamer of the current complex, despite the lack of bound Ca<sup>2+</sup> ions and small ligands, can be superimposed on that of receptor-free, Ca<sup>2+</sup>-bound SAP with a root mean squared (r.m.s.) deviation of 0.8 Å. Similarly, the structure of Fc $\gamma$ RIIa in the complex is nearly identical to that of ligand-free Fc $\gamma$ RIIa, with r.m.s. differences of 0.9 Å for 171 C $\alpha$  atoms<sup>16</sup>, suggesting rigid body docking between SAP and the receptor. The only conformational change in the receptor involved a movement of roughly 3 Å in the N-terminal BC loop (residues 28–35) of the Fc $\gamma$ RIIa towards the A subunit of SAP (Fig. 2d).

The complex buries a total of about 1,962 Å<sup>2</sup> of solvent-accessible surface area, equally distributed between the A and C subunits of SAP, and has a shape complementarity index ( $S_c$ ) of 0.58 (ref. 17), similar to those between the T-cell antigen receptor (TCR) and the major histocompatibility complex, between KIR and HLA ( $S_c = 0.5–0.6$ ) but less than those between antibodies and antigens ( $S_c > 0.7$ )<sup>18,19</sup>. Both the A and C subunits of SAP use their ridge helices (Pro 166 to Gln 174), especially Tyr 173 and Gln 174, and the carboxy-terminal residues (Pro 200 to Pro 204) to contact the D1 and D2 domains of Fc $\gamma$ R (Fig. 3), thus highlighting these residues as functional hotspots on SAP. On the receptor side, both the D1 and D2 domains use their topological equivalent BC, C'E loops and the C strand to contact SAP, and the binding site is away from the predicted N-linked glycosylation sites. The D1–A interface consists of a salt bridge between Asp 35 of Fc $\gamma$ RIIa and Arg 38 of SAP, four hydrogen bonds, and van der Waals interactions involving Tyr 173 and Gln 174 from the ridge helix of SAP

(Fig. 3a and Supplementary Table 2). The D2–C interface, in contrast, is entirely mediated by van der Waals interactions (Fig. 3b and Supplementary Table 2). Residues at the D1–A interface are more

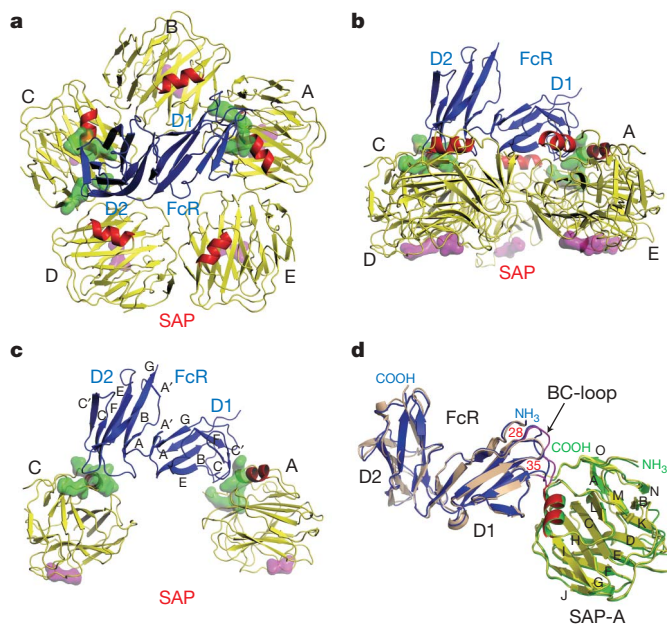


**Figure 2 | Crystal structure of SAP–Fc $\gamma$ RIIa complex.** **a–c**, The view is from the face (**a**) and sides (**b**, **c**) of SAP; in **c** only the receptor contact A and C subunits are highlighted. The five SAP subunits are shown in yellow with ridge helices in red, and Fc $\gamma$ RIIa is coloured blue. The interface is represented by a molecular surface in green. The Ca<sup>2+</sup>-binding and ligand-binding sites on SAP are highlighted in magenta. **d**, Comparison between the free (green) and receptor-bound (yellow) SAP, and between the free (wheat) and SAP-bound (blue) Fc $\gamma$ RIIa structures. For clarity, only the A subunit is shown from the superposition of SAP pentamer. The BC loop (residues 28–35) of the D1 domain is indicated.

conserved across the species than those at the D2–C interface (Supplementary Fig. 1).

The critical receptor contact region of SAP involves the ridge helix and its pentameric assembly, which are conserved features of the pentraxin family. Similarly, the structure of Fc $\gamma$ RIIa showing only 1.2 Å r.m.s. deviation between the C $\alpha$  atoms from Fc $\gamma$ RIII is well conserved; significant interface sequence homology is shared between Fc $\gamma$ Rs (Supplementary Fig. 1). This suggests the possibility of a broader recognition between pentraxins and Fc $\gamma$ R<sup>5,7,8</sup>. Using BIAcore binding, we showed that SAP, CRP and PTX3 all recognized Fc $\gamma$ Rs with affinities ranging from 10 to 0.1  $\mu$ M, similar to those between isoforms of IgG and Fc $\gamma$ R<sup>20</sup> (Supplementary Table 3 and Supplementary Fig. 2). SAP bound most tightly to Fc $\gamma$ RI, with a dissociation constant ( $K_d$ ) of 0.48  $\mu$ M, and more weakly to Fc $\gamma$ RIIa, Fc $\gamma$ RIIb and Fc $\gamma$ RIII ( $K_d$  1–3  $\mu$ M). CRP had similar affinities (2–4  $\mu$ M) for all four Fc $\gamma$ R isoforms. PTX3 recognized only Fc $\gamma$ RIII. SAP and CRP, but not PTX3, recognized the inhibitory Fc receptor, Fc $\gamma$ RIIb, suggesting a potential regulatory function for these pentraxins.

The structural conservation and broad pentraxin–Fc $\gamma$ R recognition suggest that the complex structure is a prototypic model for pentraxin recognition by Fc $\gamma$ R. To test this, we modelled the CRP structure into the current SAP–Fc $\gamma$ RIIa complex. Although SAP and CRP differ in their relative monomer orientations with respect to the pentamer by about 25° (refs 21, 22), they use common residues at the pentameric interface, and CRP can be placed at the Fc $\gamma$ RIIa interface in the model without serious steric hindrance (Supplementary Fig. 3). To verify the CRP–Fc $\gamma$ RIIa model, three putative interface residues of CRP, including the salt-bridge-forming residue His 38 and two ridge-helix residues, Tyr 175 and Leu 176, were mutated and the binding of mutant CRP to Fc $\gamma$ R was measured by BIAcore. Whereas wild-type CRP binds Fc $\gamma$ RIIa with 1.9  $\mu$ M affinity, H38A, Y175L and L176A mutations resulted in a 2–8-fold decrease in the binding affinity in solution (Supplementary Table 3). These mutational results, together with the earlier mutagenesis studies<sup>23</sup>, indicate that Fc $\gamma$ R recognition is conserved between SAP and CRP. A similar decrease in affinity was also observed between the CRP mutants and Fc $\gamma$ RIII, indicating a further structural preservation in Fc $\gamma$ RIII recognition. The mutations did not affect the recognition of Fc $\gamma$ RI by CRP, indicating a variation in CRP–Fc $\gamma$ RI interaction potentially attributed to the presence of an additional domain in Fc $\gamma$ RI.

Polymorphism at residue 131 of Fc $\gamma$ RIIa affects its recognition of immunoglobulins<sup>24–26</sup>. This polymorphism also affected CRP binding<sup>27</sup>. By isothermal titration calorimetry, CRP bound the arginine and histidine isoforms of Fc $\gamma$ RIIa with about 4  $\mu$ M and less than 10  $\mu$ M affinities, respectively (Supplementary Fig. 4). The side chain

of Arg but not His 131 could form hydrogen bonds with the main chains of Gly 178 and Pro 179 from CRP.

Because Fc $\gamma$ RIIa recognized both SAP and IgG, we then examined whether the receptor's binding to SAP affected its binding to immunoglobulins. Unexpectedly, the overlay of the SAP–Fc $\gamma$ RIIa structure on the Fc–Fc $\gamma$ RIII structure showed that the IgG binding site on the Fc receptor partly overlapped with that for SAP<sup>28</sup> (Fig. 4). Both SAP and IgG interact with the BC and FG loops as well as the C and C' strands of the Fc $\gamma$ R D2 domain, creating a steric clash between the C<sub>H</sub>2 domain of IgG and the C and D subunits of SAP. The shared recognition predicts competition between IgG and SAP for Fc $\gamma$ R binding. Indeed, with a BIAcore binding assay, the association between SAP and Fc $\gamma$ RIIa was effectively competed off by increasing concentrations of IgG1 (Fig. 4c). Furthermore, soluble SAP blocks, in a dose-dependent manner, the phagocytosis of IgG-opsonized sheep red blood cells (Eig) by human MDMs (Fig. 4d). Similarly, binding of CRP to Fc receptors (Fc $\gamma$ RIIa, Fc $\gamma$ RIIb and Fc $\gamma$ RIII) was

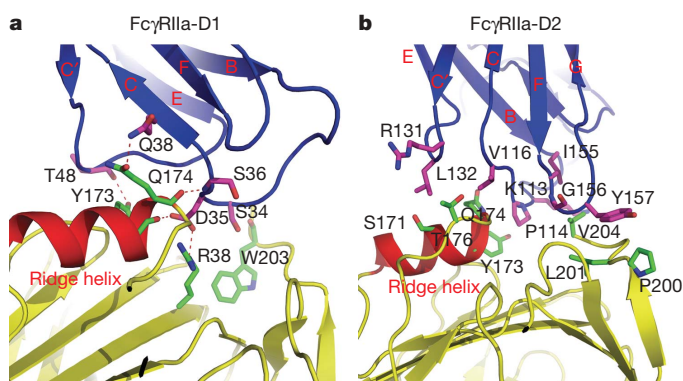


**Figure 3 | The binding interfaces between SAP and Fc $\gamma$ RIIa.** **a**, The interface between the D1 domain of Fc $\gamma$ RIIa (blue and magenta) and the A subunit of SAP (yellow and green) is shown, with participating side residues shown as sticks. Hydrogen-bond interactions are represented by red dashed lines. **b**, The interface between the D2 domain of Fc $\gamma$ RIIa and the C subunit of SAP.

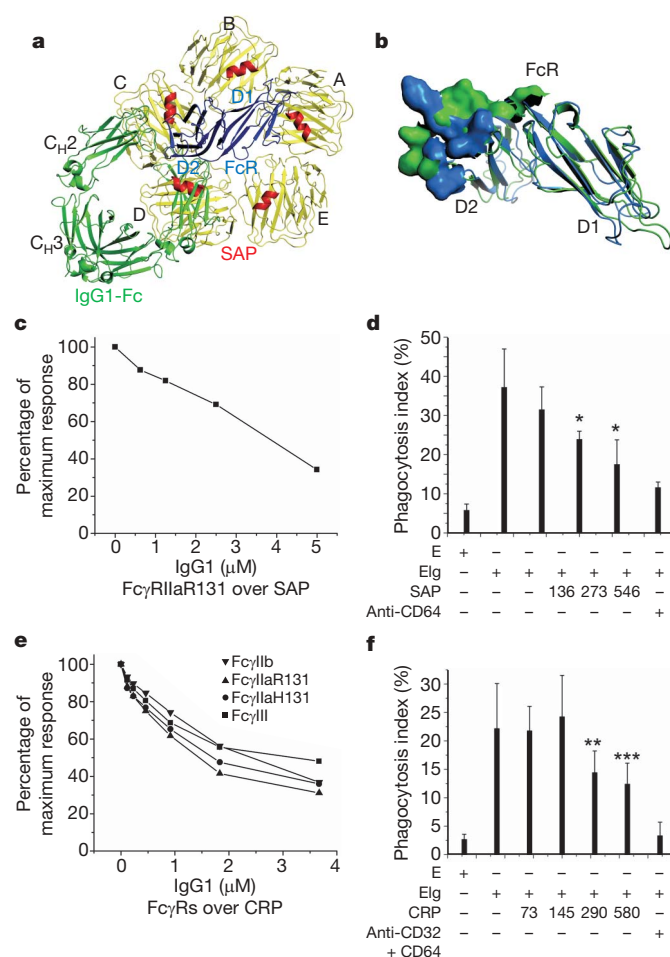


**Figure 4 | Competition between human IgG1 and SAP or CRP for binding to Fc $\gamma$  receptors.** **a**, Superposition of Fc $\gamma$ R between SAP–Fc $\gamma$ RIIa and Fc–Fc $\gamma$ RIII complexes with Fc $\gamma$ RIIa, the Fc portion of IgG1 and SAP shown in blue, green and yellow, respectively. **b**, The interface residues of SAP–Fc $\gamma$ RIIa and Fc–Fc $\gamma$ RIII complexes depicted by molecular surface representations on Fc $\gamma$ RIIa (blue) and Fc $\gamma$ RIII (green), respectively. **c**, **e**, Competition binding between SAP (**c**), CRP (**e**) and human IgG1 using SAP or CRP immobilized CM5 sensor chips. The analytes consisted of a mixture of the stated Fc $\gamma$ R at 5  $\mu$ M (**c**) and 2  $\mu$ M (**e**) with various concentrations of human IgG1. **d**, **f**, SAP (**d**) and CRP (**f**) inhibit IgG-mediated phagocytosis. Human MDMs were incubated with E or Eig in the presence of various concentrations ( $\mu$ g ml<sup>-1</sup>) of CRP or SAP, or of blocking antibodies against Fc $\gamma$ RI (25  $\mu$ g ml<sup>-1</sup>) and Fc $\gamma$ RII (25  $\mu$ g ml<sup>-1</sup>). Results are means and s.d. for triplicate wells in two or three experiments. Significance levels: asterisk,  $P < 0.05$ ; two asterisks,  $P < 0.01$ ; three asterisks,  $P < 0.001$ .



also inhibited by IgG1 in a dose-dependent manner (Fig. 4e), and CRP inhibited the IgG-mediated phagocytosis of EIG (Fig. 4f). The similarity between CRP and SAP in competing with the binding of IgG to FcγR further supports their conserved receptor recognition structure. As the plasma concentration of CRP but not SAP may reach more than 200 μg ml<sup>-1</sup> during the acute phase<sup>2</sup>, the inhibition of IgG-mediated phagocytosis by CRP suggests a potential down-regulation of antibody-mediated FcγR activation by CRP in the late stage of the acute phase, when an excess amount of soluble CRP is available.

Thus we have shown, through structural and functional studies, that pentraxins directly recognize FcγR, activate phagocytosis and induce cytokine secretion. Although pentraxins recognized FcγR with variable affinity and specificity, they probably share a conserved receptor recognition. The overlapping SAP-binding and IgG-binding sites on FcγR blocked antibody-mediated phagocytosis by soluble pentraxins. Taken together, these results provide structural and functional evidence for the involvement of pentraxins in FcγR-mediated immune functions. Thus, pentraxins possess similar functions to those of antibodies that activate both the complement and Fc receptor pathways. This parallel between pentraxins and antibodies suggests that pentraxins were ancient antibodies in evolution, and that they function as antibodies in more primitive organisms. The competition in FcγR binding between IgG and pentraxins suggests potential novel strategies for treating autoimmune diseases on the basis of soluble pentraxins rather than intravenous immunoglobulin.

## METHODS SUMMARY

Recombinant ectodomains of FcγRIIa and IIb1 (residues 1–171) were expressed in *Escherichia coli* and refolded by using a pET30a vector with a C-terminal His<sub>6</sub> tag. SAP and CRP were purified from human plasma or pleural fluid. CRP mutants were expressed in baculovirus system. For confocal and fluorescence microscopy, human MDMs were incubated with SAP, CRP, rabbit anti-zymosan IgG or PBS-opsonized zymosan (conjugated with Texas red) at 37 °C for 30 min. The samples were stained with an anti-CD32 monoclonal antibody and an Alexafluor 488-conjugated goat anti-mouse F(ab')<sub>2</sub>. For inhibition, soluble IgG was added during the phagocytosis. For phagocytosis of sheep red blood cells (sRBCs or E), fresh sRBCs were opsonized with a rabbit anti-sRBC IgG and mixed with MDMs by centrifugation at a ratio of 20:1 and incubation at 37 °C for 2 h in the presence or absence of SAP, CRP, anti-CD32 or anti-CD64. For cytokine release experiments, purified CD14<sup>+</sup> monocytes were incubated with 50 μg ml<sup>-1</sup> (or otherwise indicated) concentrations of aggregated SAP (Supplementary Fig. 5) for 24 h, and cytokines were measured by ELISA. Monomeric SAP was isolated on a Superdex 200 column in the presence of 10 mM methyl-β-D-galactopyranoside. SAP was degraded by a bead-bound proteinase K or depleted by PE-conjugated Sepharose. Anti-FcγR blocking antibodies or isotype controls were added at 5 μg ml<sup>-1</sup> before the addition of SAP. Bone marrow cells from *Myd88*<sup>-/-</sup>, *RIP2*<sup>-/-</sup> and wild-type mice were differentiated to BMDMs and then incubated with 50 μg ml<sup>-1</sup> aggregated SAP for cytokine release. The complex crystals were grown from 2.0 M (NH<sub>4</sub>)<sub>2</sub>SO<sub>4</sub>, 5% isopropanol by hanging-drop vapour diffusion; X-ray data were collected to 2.8 Å resolution at SER-CAT beamlines and processed with HKL2000. The complex structure was solved by a molecular replacement method with the Phenix package. Model building and refinement were performed with O and CNS.

**Full Methods** and any associated references are available in the online version of the paper at [www.nature.com/nature](http://www.nature.com/nature).

Received 20 August; accepted 26 September 2008.

Published online 16 November 2008.

1. Steel, D. M. & Whitehead, A. S. The major acute phase reactants: C-reactive protein, serum amyloid P component and serum amyloid A protein. *Immunol. Today* **15**, 81–88 (1994).
2. Pepys, M. B. *et al.* Comparative clinical study of protein SAP (amyloid P component) and C-reactive protein in serum. *Clin. Exp. Immunol.* **32**, 119–124 (1978).
3. Garlanda, C., Bottazzi, B., Bastone, A. & Mantovani, A. Pentraxins at the crossroads between innate immunity, inflammation, matrix deposition, and female fertility. *Annu. Rev. Immunol.* **23**, 337–366 (2005).
4. Kaplan, M. H. & Volanakis, J. E. Interaction of C-reactive protein complexes with the complement system. I. Consumption of human complement associated with the

- reaction of C-reactive protein with pneumococcal C-polysaccharide and with the choline phosphatides, lecithin and sphingomyelin. *J. Immunol.* **112**, 2135–2147 (1974).
5. Bharadwaj, D., Stein, M. P., Volzer, M. A., Mold, C. & Du Clos, T. W. The major receptor for C-reactive protein on leukocytes is Fcγ receptor II. *J. Exp. Med.* **190**, 585–590 (1999).
6. Marnell, L. L., Mold, C., Volzer, M. A., Burlingame, R. W. & Du Clos, T. W. C-reactive protein binds to FcγRI in transfected COS cells. *J. Immunol.* **155**, 2185–2193 (1995).
7. Bodman-Smith, K. B. *et al.* C-reactive protein-mediated phagocytosis and phospholipase D signalling through the high-affinity receptor for immunoglobulin G (FcγRI). *Immunology* **107**, 252–260 (2002).
8. Bharadwaj, D., Mold, C., Markham, E. & Du Clos, T. W. Serum amyloid P component binds to Fcγ receptors and opsonizes particles for phagocytosis. *J. Immunol.* **166**, 6735–6741 (2001).
9. Alles, V. V. *et al.* Inducible expression of PTX3, a new member of the pentraxin family, in human mononuclear phagocytes. *Blood* **84**, 3483–3493 (1994).
10. Han, B. *et al.* TNFα-induced long pentraxin PTX3 expression in human lung epithelial cells via JNK. *J. Immunol.* **175**, 8303–8311 (2005).
11. Ravetch, J. V. & Bolland, S. IgG Fc receptors. *Annu. Rev. Immunol.* **19**, 275–290 (2001).
12. Bickerstaff, M. C. *et al.* Serum amyloid P component controls chromatin degradation and prevents antinuclear autoimmunity. *Nature Med.* **5**, 694–697 (1999).
13. Xia, D. & Samols, D. Transgenic mice expressing rabbit C-reactive protein are resistant to endotoxemia. *Proc. Natl Acad. Sci. USA* **94**, 2575–2580 (1997).
14. Mold, C., Rodriguez, W., Rodic-Polic, B. & Du Clos, T. W. C-reactive protein mediates protection from lipopolysaccharide through interactions with FcγR. *J. Immunol.* **169**, 7019–7025 (2002).
15. Emsley, J. *et al.* Structure of pentameric human serum amyloid P component. *Nature* **367**, 338–345 (1994).
16. Maxwell, K. F. *et al.* Crystal structure of the human leukocyte Fc receptor, FcγRIIa. *Nature Struct. Biol.* **6**, 437–442 (1999).
17. Lawrence, M. C. & Colman, P. M. Shape complementarity at protein/protein interfaces. *J. Mol. Biol.* **234**, 946–950 (1993).
18. Boyington, J. C., Motyka, S. A., Schuck, P., Brooks, A. G. & Sun, P. D. Crystal structure of an NK cell immunoglobulin-like receptor in complex with its class I MHC ligand. *Nature* **405**, 537–543 (2000).
19. Ysern, X., Li, H. & Mariuzza, R. A. Imperfect interfaces. *Nature Struct. Biol.* **5**, 412–414 (1998).
20. Hulett, M. D. & Hogarth, P. M. Molecular basis of Fc receptor function. *Adv. Immunol.* **57**, 1–127 (1994).
21. Shrive, A. K. *et al.* Three dimensional structure of human C-reactive protein. *Nature Struct. Biol.* **3**, 346–354 (1996).
22. Thompson, D., Pepys, M. B. & Wood, S. P. The physiological structure of human C-reactive protein and its complex with phosphocholine. *Structure* **7**, 169–177 (1999).
23. Bang, R. *et al.* Analysis of binding sites in human C-reactive protein for FcγRI, FcγRIIa, and C1q by site-directed mutagenesis. *J. Biol. Chem.* **280**, 25095–25102 (2005).
24. Tax, W. J., Willems, H. W., Reekers, P. P., Capel, P. J. & Koene, R. A. Polymorphism in mitogenic effect of IgG1 monoclonal antibodies against T3 antigen on human T cells. *Nature* **304**, 445–447 (1983).
25. Clark, M. R., Stuart, S. G., Kimberly, R. P., Ory, P. A. & Goldstein, I. M. A single amino acid distinguishes the high-responder from the low-responder form of Fc receptor II on human monocytes. *Eur. J. Immunol.* **21**, 1911–1916 (1991).
26. Parren, P. W. *et al.* On the interaction of IgG subclasses with the low affinity FcγRIIa (CD32) on human monocytes, neutrophils, and platelets. Analysis of a functional polymorphism to human IgG2. *J. Clin. Invest.* **90**, 1537–1546 (1992).
27. Stein, M. P. *et al.* C-reactive protein binding to FcγRIIa on human monocytes and neutrophils is allele-specific. *J. Clin. Invest.* **105**, 369–376 (2000).
28. Radaev, S., Motyka, S., Fridman, W. H., Sautes-Fridman, C. & Sun, P. D. The structure of a human type III Fcγ receptor in complex with Fc. *J. Biol. Chem.* **276**, 16469–16477 (2001).

**Supplementary Information** is linked to the online version of the paper at [www.nature.com/nature](http://www.nature.com/nature).

**Acknowledgements** We thank D. Klinman, G. Cheng, P. W. Dempsey and S. Bolland for providing the bone marrow from the *Myd88*<sup>-/-</sup>, *RIP2*<sup>-/-</sup> and wild-type C57BL/6 mice, respectively; M. Pancera and B. Dey for technical support in the isothermal titration calorimetry experiments; V. Deretic and S. Master for assistance with confocal microscopy; and B. Bottazzi for providing PTX-3. The X-ray SER-CAT beamlines ([www.ser-cat.org/members.html](http://www.ser-cat.org/members.html)) at the Advanced Photon Source is supported by the US Department of Energy, Basic Energy Sciences, Office of Science, under contract no. W-31-109-Eng-38. This work was supported by intramural research funding from the National Institute of Allergy and Infectious Diseases, National Institutes of Health, and by RO1 AI28358 and by the Department of Veterans Affairs.

**Author Information** Atomic coordinates for the SAP–FcγRIIa complex have been deposited in the PDB data bank under accession number 3D50. Reprints and permissions information is available at [www.nature.com/reprints](http://www.nature.com/reprints). Correspondence and requests for materials should be addressed to P.D.S. ([psun@nih.gov](mailto:psun@nih.gov)).



## METHODS

**Confocal and fluorescence microscopy.** Human MDMs were differentiated on glass coverslips in 24-well plates as described previously<sup>29</sup>. Opsonized zymosan was prepared by incubating Texas red-conjugated zymosan (Molecular Probes) for 30 min at 37 °C with CRP or SAP at 100 µg ml<sup>-1</sup> in HBSS (with Ca<sup>2+</sup> and Mg<sup>2+</sup>) or rabbit anti-zymosan IgG (Molecular Probes), and added to cells at a final concentration of 10<sup>6</sup> particles per well and incubated for 30 min at 37 °C in X-vivo medium. Coverslips were fixed with 2% paraformaldehyde, permeabilized with 0.25% Triton X-100 in PBS, and stained with 5 µg ml<sup>-1</sup> IV.3 monoclonal antibody and Alexafluor 488-conjugated goat anti-mouse F(ab')<sub>2</sub> (Caltag). Confocal images of optical sections 1 µm thick were collected with a Zeiss LSM 510 META system. For inhibition of phagocytosis through FcγR, soluble IgG (10 mg ml<sup>-1</sup> intravenous immunoglobulin; Baxter) was added for 60 min before the addition of opsonized zymosan, and random field images were collected with a Zeiss Axioskop 2 plus fluorescent microscope.

**Cytokine release experiments.** CD14<sup>+</sup> monocytes were purified from peripheral blood mononuclear cells by using CD14 MACS beads and LS columns (Miltenyi), incubated with 50 µg ml<sup>-1</sup> or otherwise indicated concentrations of purified SAP (Supplementary Fig. 5) for 24 h in 96-well plates at a concentration of 5 × 10<sup>5</sup> cells per well in 200 µl of complete RPMI medium (containing 10% FBS, 50 µg ml<sup>-1</sup> gentamicin and 10 µg ml<sup>-1</sup> polymyxin B). Cytokine levels were measured by ELISA with BD BioSciences reagents<sup>30</sup>. Aggregated SAP (200–500 kDa) was prepared by the removal of serum during purification. Addition of 0.5 M salt reverted the aggregates to pentameric SAP, which was dissociated into monomers by the addition of 100 mM methyl-β-D-galactopyranoside (Sigma-Aldrich) and isolated on a Superdex 200 column in 10 mM HEPES, pH 7.4, 0.15 M NaCl, 10 mM methyl-β-D-galactopyranoside, 2 mM CaCl<sub>2</sub>. The endotoxin level of purified SAP was estimated by the Limulus assay (Lonza) as 83 pg ml<sup>-1</sup>. To remove SAP proteolytically, 100 µl of 1 mg ml<sup>-1</sup> SAP was incubated for 30 min at 40 °C with 0.2 mg of bead-bound proteinase K (Sigma). The digested material was filtered and added to cells with an amount of SAP equivalent to 50 µg ml<sup>-1</sup>. SAP was also removed by incubation with 50 µl of PE-conjugated Sepharose in the presence of 2 mM calcium. Piceatannol was added to monocytes at 25 µg ml<sup>-1</sup>, with 2.5% ethanol as the vehicle control, for 30 min at 37 °C before the addition of SAP. For antibody-blocking experiments, cells were pretreated for 30 min with 5 µg ml<sup>-1</sup> monoclonal antibody specific for FcγR or isotype controls before adding SAP. Antibodies were purchased as follows: anti-human CD64 (clone 10.1), mouse IgG1 (Ancell), anti-human CD32 (clone FL18.26) and mouse IgG2b (BD Biosciences), and anti-human CD16 (clone 3G8; Medarex). Anti-human CD32 (clone IV.3) was purified from a hybridoma cell line (ATCC). Bone marrow cells from wild-type C57BL/6 and two 3-month-old MyD88-knockout mice were plated, and adherent cells were differentiated for 6 days in DMEM medium containing 20% FBS, 30% L-cell supernatant, 25 mM HEPES and 5 µg ml<sup>-1</sup> streptomycin and penicillin. Bone marrow cells from two 3-month-old RIP2-deficient mice and control, ten-times-backcrossed, C57BL/6N mice were differentiated similarly. BMDMs were incubated for 24 h with 50 µg ml<sup>-1</sup> aggregated SAP in 10% FBS containing DMEM in the absence of polymyxin B and assayed for cytokine release as described above, with mouse cytokine ELISA kits (R&D Systems). Results are means ± s.e.m. for triplicate wells in two or three experiments. Significance levels: asterisk, *P* < 0.05; two asterisks, *P* < 0.01; three asterisks, *P* < 0.001.

**Purification, crystallization and structural determination.** Recombinant ectodomains of FcγRIIa and IIB1 (1–171) were expressed in *E. coli* and refolded using a pET30a vector with a C-terminal His<sub>6</sub>-tag<sup>31</sup>. SAP and CRP were purified from human plasma or pleural fluid as described (Supplementary Fig. 5)<sup>8,32</sup>. Mutant CRP proteins were expressed in the baculovirus system as previously described<sup>23</sup>. For crystallization of the complex, SAP pentamer was first dissociated into monomers by urea-chelation<sup>33</sup>. After dialysis to remove urea, SAP was mixed

with FcγRIIa in a 1:1 (monomeric SAP to FcγRIIa) molar ratio in 10 mM HEPES, pH 7.4, 0.05 M NaCl, and 0.01% NaN<sub>3</sub>, and concentrated to a final OD<sub>280</sub> of 12. The complex crystals were grown from 2.0 M (NH<sub>4</sub>)<sub>2</sub>SO<sub>4</sub>, 5% isopropanol by hanging drop vapour diffusion. The X-ray data were collected to 2.8 Å resolution at SER-CAT beamlines using flash cooled crystals and processed with HKL2000 (ref. 34) (Supplementary Table 1). The structure of the SAP–FcγRIIa complex was solved by a molecular replacement method with the program Phaser<sup>35</sup> from the Phenix package<sup>36</sup> using either the poly-alanine SAP subunit (1SAC) or CRP (1GNH) subunit and FcγRIIa (1H9V) as search models. Model building and refinement were carried out using O<sup>37</sup> and CNS<sup>38</sup>. Hinge angles were calculated using HINGE<sup>39</sup>. Docking of CRP to SAP–FcγRIIa complex was done using Hex 5.0 with standard parameters<sup>40</sup>. All structure figures were generated with Pymol<sup>41</sup>.

**Phagocytosis of sRBC.** Human monocytes (2.5 × 10<sup>5</sup>) were differentiated into MDMs for 6 days in RPMI-1640 medium supplemented with 10 ng ml<sup>-1</sup> granulocyte-macrophage colony-stimulating factor, 10% FBS, 20 µM glutamine, and penicillin and streptomycin. Fresh sRBCs were opsonized with a rabbit anti-sRBC IgG (1:48,000 dilution; Cappel) in PBS for 1 h at 4 °C. Phagocytosis was initiated by centrifuging IgG-opsonized sRBCs onto MDMs at a ratio of 20:1 and incubating them at 37 °C for 2 h, and was terminated by lysis of the non-ingested sRBCs twice in water for 30 s. SAP, CRP, anti-CD32 or anti-CD64 was added for 30 min before the addition of opsonized sRBCs. The phagocytic index (per cent) was quantified by counting the total number of internalized sRBCs as a proportion of the total number of MDMs in eight random fields (about 200 cells per field) with an Olympus IX70 microscope. The results represent at least three independent experiments with more than 1,000 cells counted per experiment and are presented as means ± s.d. Significance levels: asterisk, *P* < 0.05; two asterisks, *P* < 0.01; three asterisks, *P* < 0.001.

29. Mold, C., Baca, R. & Du Clos, T. W. Serum amyloid P component and C-reactive protein opsonize apoptotic cells for phagocytosis through Fcγ receptors. *J. Autoimmun.* **19**, 147–154 (2002).
30. Mold, C. & Du Clos, T. W. C-reactive protein increases cytokine responses to *Streptococcus pneumoniae* through interactions with Fcγ receptors. *J. Immunol.* **176**, 7598–7604 (2006).
31. Sondermann, P. & Jacob, U. Human Fcγ receptor IIb expressed in *Escherichia coli* reveals IgG binding capability. *Biol. Chem.* **380**, 717–721 (1999).
32. Du Clos, T. W. C-reactive protein reacts with the U1 small nuclear ribonucleoprotein. *J. Immunol.* **143**, 2553–2559 (1989).
33. Potempa, L. A., Siegel, J. N., Fiedel, B. A., Potempa, R. T. & Gewurz, H. Expression, detection and assay of a neoantigen (Neo-CRP) associated with a free, human C-reactive protein subunit. *Mol. Immunol.* **24**, 531–541 (1987).
34. Otwinowski, Z. M. W. processing of X-ray diffraction data collected in oscillation mode. *Methods Enzymol.* **276**, 307–326 (1997).
35. Read, R. J. Pushing the boundaries of molecular replacement with maximum likelihood. *Acta Crystallogr. D* **57**, 1373–1382 (2001).
36. Adams, P. D. et al. PHENIX: building new software for automated crystallographic structure determination. *Acta Crystallogr. D* **58**, 1948–1954 (2002).
37. Jones, T. A., Zou, J. Y., Cowan, S. W. & Kjeldgaard, M. Improved methods for building protein models in electron density maps and the location of errors in these models. *Acta Crystallogr. A* **47**, 110–119 (1991).
38. Brunger, A. T. et al. Crystallography & NMR system: A new software suite for macromolecular structure determination. *Acta Crystallogr. D* **54**, 905–921 (1998).
39. Snyder, G. A., Brooks, A. G. & Sun, P. D. Crystal structure of the HLA-Cw3 allotype-specific killer cell inhibitory receptor KIR2DL2. *Proc. Natl Acad. Sci. USA* **96**, 3864–3869 (1999).
40. Mustard, D. & Ritchie, D. W. Docking essential dynamics eigenstructures. *Proteins* **60**, 269–274 (2005).
41. Delano, W. L. The PyMOL Molecular Graphics System <<http://www.pymol.org>> (2002).

# Endonucleolytic RNA cleavage by a eukaryotic exosome

Alice Lebreton<sup>1,2,3\*</sup>, Rafal Tomecki<sup>4,5\*</sup>, Andrzej Dziembowski<sup>4,5</sup> & Bertrand Séraphin<sup>1,2,3</sup>

The exosome is a major eukaryotic nuclease located in both the nucleus and the cytoplasm that contributes to the processing, quality control and/or turnover of a large number of cellular RNAs<sup>1–6</sup>. This large macromolecular assembly has been described as a 3'→5' exonuclease<sup>1</sup> and shown to contain a nine-subunit ring structure evolutionarily related to archaeal exosome-like complexes and bacterial polynucleotide phosphorylases. Recent results have shown that, unlike its prokaryotic counterparts, the yeast and human ring structures are catalytically inactive. In contrast, the exonucleolytic activity of the yeast exosome core was shown to be mediated by the RNB domain of the eukaryote-specific Dis3 subunit<sup>7–9</sup>. Here we show, using *in vitro* assays, that yeast Dis3 has an additional endoribonuclease activity mediated by the PIN domain located at the amino terminus of this multidomain protein. Simultaneous inactivation of the endonucleolytic and exonucleolytic activities of the exosome core generates a synthetic growth phenotype *in vivo*, supporting a physiological function for the PIN domain. This activity is responsible for the cleavage of some natural exosome substrates, independently of exonucleolytic degradation. In contrast with current models, our results show that eukaryotic exosome cores have both endonucleolytic and exonucleolytic activities, mediated by two distinct domains of the Dis3 subunit. The mode of action of eukaryotic exosome cores in RNA processing and degradation should be reconsidered, taking into account the cooperation between its multiple ribonucleolytic activities.

The exosome complex, first identified as a 3'→5' exonuclease necessary for the 3'-end processing of the yeast 5.8S ribosomal RNA<sup>1</sup>, was later implicated in the 3'-end processing of many stable RNA species<sup>2</sup>, in messenger RNA turnover<sup>3</sup>, in various mRNA surveillance pathways<sup>4</sup> and in the degradation of cryptic unstable transcripts (CUTs)<sup>5</sup>. The exosome is therefore a major eukaryotic 3'→5' exonuclease with pleiotropic functions<sup>6</sup>.

Eukaryotic exosomes consist of a conserved core interacting with nuclear or cytoplasmic specific subunits, and pathway-specific cofactors. The core consists of a ring structure formed by nine subunits<sup>9,10</sup>, similar to the archaeal exosome and bacterial phosphorolytic nucleases, and the Dis3 protein (also called Rrp44), which contains a catalytic RNB domain responsible for the activity of hydrolytic RNase II/R family members<sup>11–13</sup>. Association of Dis3 with the ring structure seems stable in yeast but may be more labile in other species<sup>6</sup>. Recent studies indicated that eukaryotic ring structures are devoid of nuclease activity and that only the Dis3 RNB domain is a functionally active 3'→5' exonuclease<sup>7,8</sup>. In yeast, the non-essential 3'→5' exoribonuclease nuclear-specific subunit Rrp6 cooperates with Dis3 (ref. 14).

In addition to the RNB domain and three OB-fold nucleic-acid-binding domains present in all RNase II/R family members<sup>11–13</sup>, Dis3

harbours a highly conserved N-terminal PIN domain (Fig. 1a and Supplementary Fig. 1). PIN domains have been shown to adopt a RNase H fold, some of which are endowed with nuclease activity<sup>15,16</sup>. An alignment of Dis3 PIN domain sequences with those of PIN domains of known structure reveals that all acidic residues essential for the coordination of divalent cations, and thus putatively involved in catalysis, are conserved (Supplementary Fig. 1). To test whether the N-terminal PIN domain of Dis3 is endowed with ribonucleolytic activity, we assayed RNA degradation by Dis3<sub>D551N</sub>, a recombinant Dis3 mutant of the RNB domain devoid of exoribonucleolytic activity<sup>7</sup>. Dis3<sub>D551N</sub> slowly degraded a short 5'-end-labelled oligoribonucleotide 17-A<sub>14</sub> (CCCCACCACCAUCACUUA<sub>14</sub>) in a divalent-cation-dependent manner (Mg<sup>2+</sup>, Mn<sup>2+</sup> or Zn<sup>2+</sup>; Fig. 1b). Higher concentrations of divalent cations (1–3 mM) were required than were optimal for exoribonucleolytic activity<sup>7</sup>. To determine whether the PIN domain was responsible for the activity observed with Dis3<sub>D551N</sub>, we purified mutant proteins (Dis3<sub>D171N,D551N</sub> and Dis3<sub>D198N,D551N</sub>) with additional single asparagine substitutions of conserved aspartic residues in the predicted PIN-domain catalytic centre (Fig. 1a and Supplementary Fig. 1). We obtained comparable quantities of the single-mutant and double-mutant proteins with equivalent degrees of purity (Supplementary Fig. 2a). The ability of Dis3<sub>D551N</sub> to degrade the 5'-labelled RNA substrate in the presence of divalent cations was lost in the double mutants (Fig. 1b), showing that this RNase activity requires an intact Dis3 PIN domain. In addition, recombinant PIN domain alone (Dis3 amino-acid residues 1–241), but not D171N or D198N mutants of this domain, was able to degrade the same RNA substrate (Supplementary Fig. 3), showing that the PIN activity acts independently of the other Dis3 domains. The Dis3<sub>D551N</sub> activity was highest with Mn<sup>2+</sup> and lowest with Mg<sup>2+</sup>, in good agreement with results obtained for another PIN domain<sup>16</sup>. Degradation intermediates observed with the 5'-end-labelled substrate were consistent with either a 3'→5' exonucleolytic activity or an endonucleolytic one. The degradation of a 3'-end-labelled substrate by Dis3<sub>D551N</sub>, but not by the double mutants, revealed a complementary profile of intermediates (Supplementary Fig. 4), indicating that the activity was most probably endonucleolytic.

Comparison of the activities of the wild-type protein with single and double mutants of the PIN and RNB domains at different concentrations of divalent cations demonstrated endonucleolytic degradation in the context of an exonucleolytically active protein and indicated cooperation of the two activities (Supplementary Fig. 5). Moreover, the wild-type protein, but not the mutants of the PIN domain (Dis3<sub>D171N</sub> or Dis3<sub>D198N</sub>), was able to digest a circular RNA molecule (Fig. 1c). Taken together, these results show that the Dis3 PIN domain is responsible for a previously unidentified endoribonucleolytic activity of the yeast exosome. The Dis3 protein

<sup>1</sup>Equipe Labellisée La Ligue, Centre de Génétique Moléculaire, CNRS UPR 2167, 91198 Gif-sur-Yvette, France. <sup>2</sup>Université Paris-Sud, 91405 Orsay, France. <sup>3</sup>Université Pierre et Marie Curie-Paris 6, 75005 Paris, France. <sup>4</sup>Department of Genetics and Biotechnology, Faculty of Biology, University of Warsaw, 02-106 Warsaw, Poland. <sup>5</sup>Institute of Biochemistry and Biophysics, Polish Academy of Sciences, 02-106 Warsaw, Poland.

\*These authors contributed equally to this work.

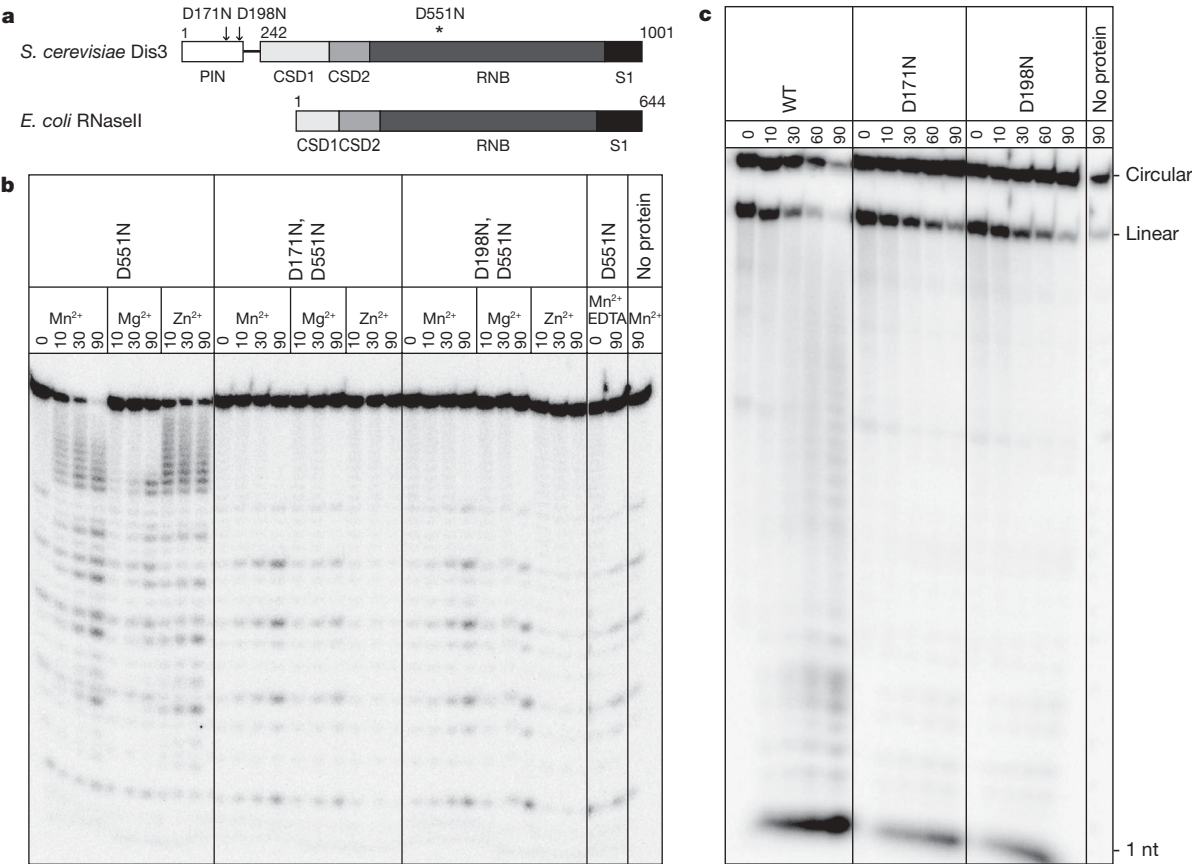


**Figure 1 | Endonucleolytic activity of the Dis3 PIN domain *in vitro*.** **a**, Domain organization and amino-acid numbering of yeast Dis3 and *E. coli* RNase II: RNB domains have exoribonucleolytic activity, OB-folds (CSD1, CSD2 and S1) are RNA-binding domains, and the N-terminal PIN domain is unique to Dis3. Sites mutated in this study are indicated. **b**, Mutations of conserved aspartates of the Dis3 PIN domain abolish its endoribonucleolytic activity. Gel-electrophoresis analysis of products generated by the incubation of the 5'-labelled 17-A<sub>14</sub> oligoribonucleotide (5'-P; 3'-OH) with

various Dis3 versions, in the presence of various divalent cations, for the durations indicated (minutes). Preferential cleavage at adenine residues was observed for this particular substrate but was not investigated further. **c**, The Dis3 PIN domain degrades circular RNA substrates. Wild-type (WT) Dis3 or PIN-domain mutants were incubated with a circularized oligoribonucleotide in the presence of 3 mM MnCl<sub>2</sub> for the durations indicated (minutes). Linear substrate molecules result from spontaneous cleavage or breakage during handling before the reaction.

therefore possesses two distinct nuclease domains that cooperate for RNA degradation, and their respective contributions *in vitro* depend on the assay conditions.

To test the physiological relevance of the PIN activity, we introduced wild-type or mutated *dis3* versions, fused to the protein A tag, on centromeric plasmids in a strain in which the essential chromosomal *DIS3* copy was under the control of a doxycyclin-repressible promoter<sup>17</sup>. We tested the growth phenotypes in the presence or absence of doxycyclin at various temperatures (Fig. 2). After repression of the wild-type *DIS3* allele, the D171N PIN mutant showed a modest growth defect at elevated temperatures. Growth of the exonucleolytically inactive mutant D551N was impaired, as reported<sup>7</sup>. Finally, Dis3<sub>D171N,D551N</sub> was much more profoundly affected than each single mutant. Mutant phenotypes did not result from protein instability or inability to assemble into exosome cores (Supplementary Fig. 6). As the growth phenotype paralleled the relative nuclease activities observed *in vitro* (Supplementary Fig. 5), this result indicates that both nuclease activities of Dis3 are physiologically relevant. The D171N mutation also exacerbated the growth phenotype of the *rrp6Δ* mutant, further supporting the functional implication of PIN in exosome function (Supplementary Fig. 7). In the absence of doxycyclin, the *DIS3*<sub>D171N,D551N</sub> allele generated a weak dominant-negative phenotype at 37 °C, indicating that this inactive protein is expressed and probably blocks exosome function.

Analysis of total RNA by northern blotting with an oligonucleotide probe complementary to the 3' end of the 5'-external transcribed spacer (ETS) by-product of rRNA processing, a known exosome

substrate<sup>2</sup>, revealed that both the D171N and D551N mutants accumulated this species, with a stronger effect for *dis3*<sub>D551N</sub> (Fig. 3a, top panel). The double mutant accumulated even higher amounts of this RNA, its levels reaching those observed in the absence of Dis3. A series of discrete 5'-ETS degradation intermediates was detected in the D551N mutant. These species were no longer visible for *dis3*<sub>D171N,D551N</sub>, suggesting that the PIN endonucleolytic activity was involved in their generation.

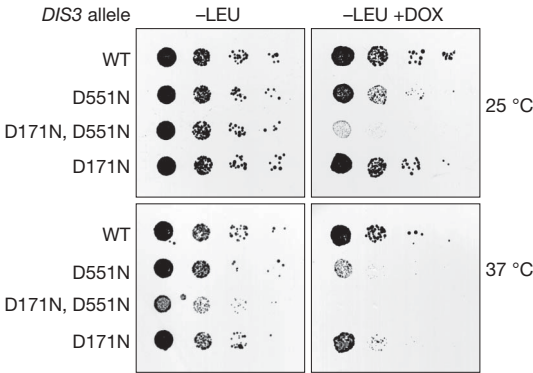


**Figure 2 | Synthetic cell-growth phenotypes of PIN mutants.** Growth phenotypes resulting from expression of plasmid-borne *DIS3*, *DIS3*<sub>D551N</sub>, *DIS3*<sub>D171N,D551N</sub> or *DIS3*<sub>D171N</sub> alleles were assessed in the presence (repressed chromosomal *DIS3*) or absence (expressed chromosomal *DIS3*) of doxycyclin (DOX) after incubation for 50 h at 25 or 37 °C. -LEU, without leucine.



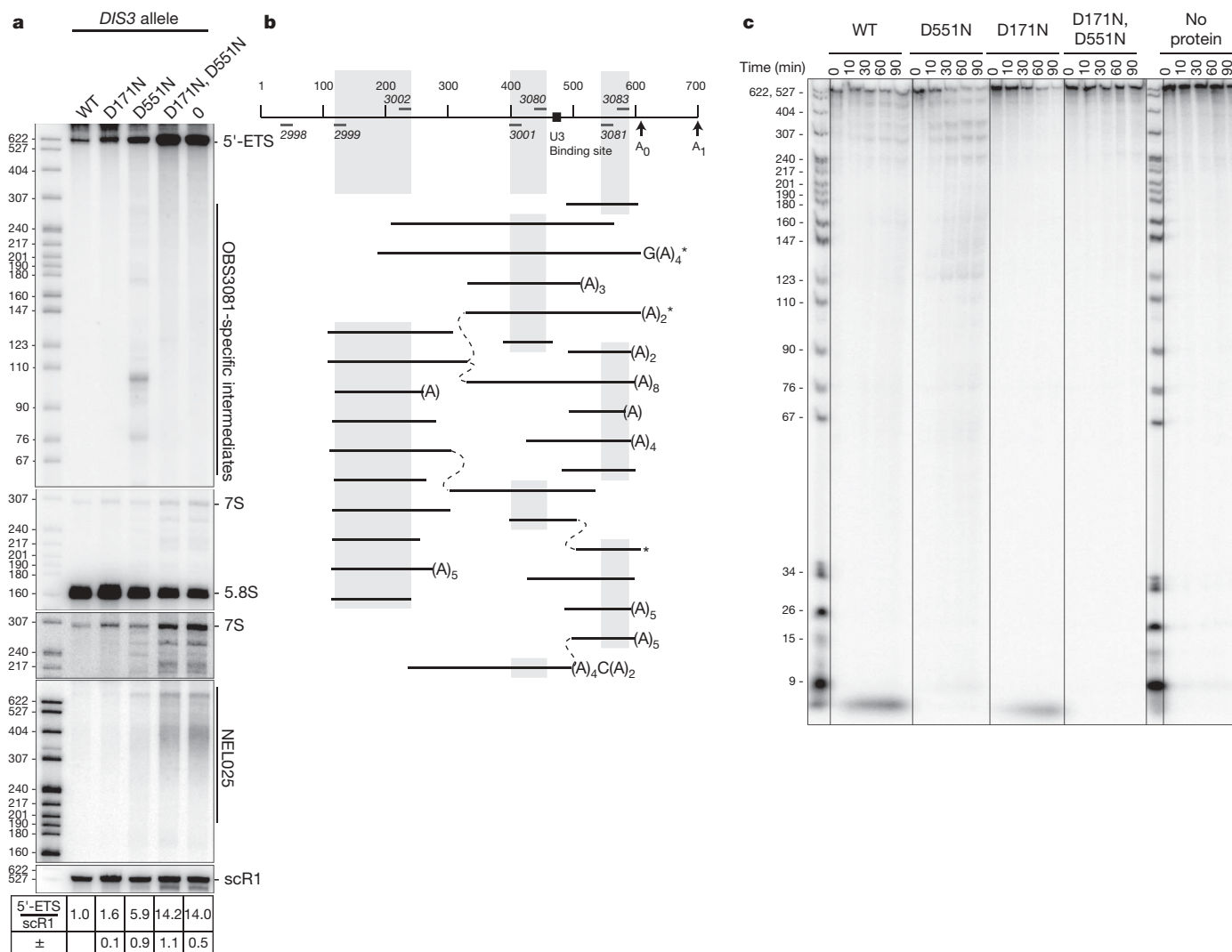


**Figure 3 | Dis3 PIN domain mediates cleavage of natural exosome substrates *in vivo*.** **a**, Detection by northern blot of 5'-ETS, 5.8S rRNA and the NEL025 CUT in total RNA isolated from wild-type and mutant Dis3 strains. The top blot was probed with OBS3081 recognizing the 3' of 5'-ETS, the middle blots with a probe complementary to the 5.8S rRNA (two exposures), and the bottom blot with a random-primed probe overlapping the NEL025 CUT. Numbers at the left indicate sizes in nucleotides of the denatured DNA ladder. 0 designates the empty vector. The values in the table represent the ratio of full-length 5'-ETS to control scR1 levels (means  $\pm$  s.d.). **b**, cRT-PCR mapping of 5'-ETS intermediates accumulating in a *dis3*<sub>D551N</sub> mutant strain. A bar indicates each intermediate

Further hybridizations performed with oligonucleotide or randomly primed probes spanning the 5'-ETS region revealed that the intermediates originated from various regions of this RNA, suggesting that they do not result from a simple 5'→3' or 3'→5' exonucleolytic decay (Supplementary Fig. 8). Deletion of *RRP6* had modest effects on the degradation pattern, indicating that 5'-ETS digestion depends essentially on both endonuclease and exonuclease activity of Dis3. We used primer extension and circularization RT-PCR (cRT-PCR<sup>18,19</sup>) to identify precisely the 5' and 3' ends of 5'-ETS intermediates accumulating in the *Dis3*<sub>D551N</sub> mutant (Fig. 3b and Supplementary Fig. 9a). Intermediates, with sizes ranging from 79 to 462 nucleotides, spanned the complete 5'-ETS. Some of them contained short non-templated 3'-terminal heterogeneous oligo(A) tails, probably synthesized by the TRAMP (Trf4/Air2/Mtr4p polyadenylation) complex, a known exosome stimulator<sup>5,20–22</sup>. More importantly, the 3' end of some species precisely abutted the 5' end of other molecules, which is further evidence of their endonucleolytic origin (Fig. 3b). 5'-ETS cleavages

identified, with grey areas highlighting the region required for PCR amplification by the selected primer pairs numbered in italics. Asterisks indicate fragments ending at A<sub>0</sub>. Dashed lines link 3' ends to 5' ends of contiguous fragments. Polyadenylated 3' ends are indicated between parentheses. **c**, *In vitro* cleavage of 5'-ETS by Dis3. 5'-ETS substrate was prepared by *in vitro* transcription and incubated alone or with various Dis3 versions for the durations indicated. Products resulting from endonucleolytic cleavages were separated by gel electrophoresis from short oligoribonucleotides resulting from exoribonucleolytic degradation that migrated at the bottom of the gel.

formed *in vivo* mapped preferentially to internal and closing loops as well as to other single-stranded regions (Supplementary Fig. 9b), making an endonucleolytic rather than an exonucleolytic origin more likely. Similar 5'-ETS cleavages could be reproduced *in vitro* (Fig. 3c; compare with intermediate sizes observed with the random-primed probe shown in Supplementary Fig. 8).

Northern blot analyses targeted to other natural exosome substrates showed that the PIN domain endonuclease activity was not specific for the 5'-ETS (Fig. 3a, lower panels). D171N and D551N mutations in Dis3 had synergistic effects on the degradation of the CUT NEL025 and on the processing of the 7S precursor into 5.8S rRNA. These effects were further enhanced in an *rrp6Δ* strain (data not shown). The endonucleolytic activity of the exosome core therefore targets a wide range of physiological RNA species, indicating that its role is general.

Our results show that the yeast exosome, and probably exosomes from other eukaryotes, have endonuclease activity in addition to

their long-known exonucleolytic activity. The current model of exosome action should therefore be revisited, because these observations have direct implications for the mechanism of recruitment and degradation of substrates. Inactivation of the Dis3 PIN domain by point mutation has limited effects on RNA processing and cell growth. This suggests that RNAs are still degraded in the absence of endonucleolytic cleavages, but probably more slowly or inefficiently. The PIN domain therefore seems to cooperate with the exonucleolytic activity of Dis3 and/or Rps6, possibly by providing them with alternative 3'-end substrates, which is consistent with the additive phenotypes seen in multiple mutants. This feature could facilitate the degradation of structured RNA species by allowing degradation reinitiation in upstream regions when exosome progression is blocked. Dis3 is therefore a unique example of a RNase in which endonucleolytic and exoribonucleolytic catalytic sites are found encoded by different domains of a single protein. Given the structure of related bacterial and archaeal enzymes, Dis3 is likely to originate from the fusion of a PIN domain to a RNase II/R enzyme during the early steps of eukaryotic evolution. In *Escherichia coli*, the main complex involved in RNA degradation, the degradosome, also has both endonucleolytic and exonucleolytic activities, even though the functions are performed by proteins with no similarity to Dis3, namely endoribonuclease E and polynucleotide phosphorylase<sup>23</sup>. This evolutionary convergence supports the functional importance for cooperation between exonucleolytic and endonucleolytic activities. Further analysis should help us to understand the relative contributions and spatial arrangements of the two active sites of core eukaryotic exosomes.

**Note added in proof:** While this work was in progress, endonucleolytic RNA cleavage mediated by another eukaryotic Pin domain during NMD in human cells, and by the yeast exosome was observed<sup>24,25</sup>.

## METHODS SUMMARY

**RNase assays.** *In vitro* enzymatic assays were performed in 20- $\mu$ l reaction volumes containing 10 mM Tris-HCl pH 8.0, 75 mM NaCl, and 1 mM 2-mercaptoethanol, with MnCl<sub>2</sub> and/or MgCl<sub>2</sub> or ZnCl<sub>2</sub> at final concentrations ranging from 0 to 3 mM. Purified protein and substrate concentrations were 0.1 and 0.2  $\mu$ M, respectively. Reaction mixtures were incubated at 30 °C for the indicated durations before the addition of 1 volume of formamide loading dye (90% formamide, 20 mM EDTA, 0.03% bromophenol blue, 0.03% xylene cyanol in 1  $\times$  TBE). Reaction products were resolved in denaturing gels containing 20% polyacrylamide, 8 M urea and 1  $\times$  TBE, and were detected with a Fuji PhosphorImager.

**cRT-PCR.** The cRT-PCR procedure, adapted from previous studies<sup>18,19</sup>, permitted the mapping of 5' and 3' ends in non-polyadenylated, non-capped RNA intermediates. Total RNA from the D551N mutant strain BSY1668[pBS3270] was treated with DNase I. RNA (7  $\mu$ g) was ligated in the presence of 1  $\mu$ l of T4 RNA ligase for 2 h at 37 °C in a 100- $\mu$ l final reaction volume. The circularized RNAs were extracted with phenol-chloroform, precipitated with ethanol-ammonium acetate, and resuspended in 20  $\mu$ l of water. Reverse transcriptions were performed on 600 ng of circularized RNA with 10 pmol of primers OBS2999, OBS3001 or OBS3081 (Supplementary Table 1) and 1  $\mu$ l of iScript reverse transcriptase (Bio-Rad). The cDNA junctions were then amplified by PCR with the cognate primer pair: either OBS2999–OBS3002 or OBS3001–OBS3080 or OBS3081–OBS3083. Products were cloned into pCR2.1-TOPO by TOPO-TA cloning (Invitrogen), and sequenced with the M13 reverse primer.

**Full Methods** and any associated references are available in the online version of the paper at [www.nature.com/nature](http://www.nature.com/nature).

Received 14 May; accepted 25 September 2008.

Published online 7 December 2008.

1. Mitchell, P. *et al.* The exosome: a conserved eukaryotic RNA processing complex containing multiple 3'→5' exoribonucleases. *Cell* **91**, 457–466 (1997).
2. Allmang, C. *et al.* Functions of the exosome in rRNA, snoRNA and snRNA synthesis. *EMBO J.* **18**, 5399–5410 (1999).

3. Anderson, J. S. & Parker, R. P. The 3' to 5' degradation of yeast mRNAs is a general mechanism for mRNA turnover that requires the SKI2 DEVH box protein and 3' to 5' exonucleases of the exosome complex. *EMBO J.* **17**, 1497–1506 (1998).
4. Isken, O. & Maquat, L. E. Quality control of eukaryotic mRNA: safeguarding cells from abnormal mRNA function. *Genes Dev.* **21**, 1833–1856 (2007).
5. Wyers, F. *et al.* Cryptic pol II transcripts are degraded by a nuclear quality control pathway involving a new poly(A) polymerase. *Cell* **121**, 725–737 (2005).
6. Lebreton, A. & Séraphin, B. Exosome-mediated quality control: Substrate recruitment and molecular activity. *Biochim. Biophys. Acta* **1779**, 558–565 (2008).
7. Dziembowski, A., Lorentzen, E., Conti, E. & Séraphin, B. A single subunit, Dis3, is essentially responsible for yeast exosome core activity. *Nature Struct. Mol. Biol.* **14**, 15–22 (2007).
8. Liu, Q., Greimann, J. C. & Lima, C. D. Reconstitution, activities, and structure of the eukaryotic RNA exosome. *Erratum. Cell* **131**, 188–189 (2007).
9. Liu, Q., Greimann, J. C. & Lima, C. D. Reconstitution, activities, and structure of the eukaryotic RNA exosome. *Cell* **127**, 1223–1237 (2006).
10. Hernandez, H. *et al.* Subunit architecture of multicentric complexes isolated directly from cells. *EMBO Rep.* **7**, 605–610 (2006).
11. Frazao, C. *et al.* Unravelling the dynamics of RNA degradation by ribonuclease II and its RNA-bound complex. *Nature* **443**, 110–114 (2006).
12. Lorentzen, E. *et al.* Structure of the active subunit of the yeast exosome core, Rps44: diverse modes of substrate recruitment in the RNase II nuclease family. *Mol. Cell* **29**, 717–728 (2008).
13. Zuo, Y. *et al.* Structural basis for processivity and single-strand specificity of RNase II. *Mol. Cell* **24**, 149–156 (2006).
14. Allmang, C. *et al.* The yeast exosome and human PM-Scl are related complexes of 3'→5' exonucleases. *Genes Dev.* **13**, 2148–2158 (1999).
15. Arcus, V. L. *et al.* Distant structural homology leads to the functional characterization of an archaeal PIN domain as an exonuclease. *J. Biol. Chem.* **279**, 16471–16478 (2004).
16. Glavan, F., Behm-Ansmant, I., Izaurralde, E. & Conti, E. Structures of the PIN domains of SMG6 and SMG5 reveal a nuclease within the mRNA surveillance complex. *EMBO J.* **25**, 5117–5125 (2006).
17. Belli, G. *et al.* An activator/repressor dual system allows tight tetracycline-regulated gene expression in budding yeast. *Nucleic Acids Res.* **26**, 942–947 (1998).
18. Couttet, P. *et al.* Messenger RNA deadenylation precedes decapping in mammalian cells. *Proc. Natl Acad. Sci. USA* **94**, 5628–5633 (1997).
19. Mandl, C. W., Heinz, F. X., Puchhammer-Stockl, E. & Kunz, C. Sequencing the termini of capped viral RNA by 5'-3' ligation and PCR. *Biotechniques* **10**, 484–486 (1991).
20. Kadaba, S. *et al.* Nuclear surveillance and degradation of hypomodified initiator tRNAMet in *S. cerevisiae*. *Genes Dev.* **18**, 1227–1240 (2004).
21. LaCava, J. *et al.* RNA degradation by the exosome is promoted by a nuclear polyadenylation complex. *Cell* **121**, 713–724 (2005).
22. Vanacova, S. *et al.* A new yeast poly(A) polymerase complex involved in RNA quality control. *PLoS Biol.* **3**, e189 (2005).
23. Carpousis, A. J. The RNA degradosome of *Escherichia coli*: an mRNA-degrading machine assembled on RNase E. *Annu. Rev. Microbiol.* **61**, 71–87 (2007).
24. Eberle, A. B., Lykke-Andersen, S., Mühlemann, O. & Jensen, T. H. SMG6 promotes endonucleolytic cleavage of nonsense mRNA in human cells. *Nature Struct. Mol. Biol.* (in the press).
25. Schaeffer, D. *et al.* The exosome contains domains with specific endoribonuclease, exoribonuclease and cytoplasmic mRNA decay activities. *Nature Struct. Mol. Biol.* (in the press).

**Supplementary Information** is linked to the online version of the paper at [www.nature.com/nature](http://www.nature.com/nature).

**Acknowledgements** We thank E. Conti and J. Basquin for providing the Dis3 PIN domain expression construct and 6 $\times$ His-SUMO protease, and E. Conti, E. Lorentzen, J. Kufel and members of our groups for insightful discussions. This work was supported by La Ligue contre le Cancer (Équipe Labellisée 2008), Agence Nationale de la Recherche project CUTs, CNRS, ESF RNA Quality program (project EUxosome) and the FP6 EU grant 3D repertoire, and an EMBO installation grant. R.T. is the recipient of the Stipend for Young Researchers from the Foundation for Polish Science and was supported through a Faculty of Biology, University of Warsaw intramural grant.

**Author Contributions** R.T. expressed and purified the recombinant proteins and performed all the *in vitro* experiments under the supervision of A.D. A.L. performed all *in vivo* experiments under the supervision of B.S. All authors discussed the results and wrote the paper.

**Author Information** Reprints and permissions information is available at [www.nature.com/reprints](http://www.nature.com/reprints). Correspondence and requests for materials should be addressed to A.D. ([andzej@ibb.waw.pl](mailto:andzej@ibb.waw.pl)) or B.S. ([seraphin@cgm.cnrs-gif.fr](mailto:seraphin@cgm.cnrs-gif.fr)).

## METHODS

**Oligonucleotides, plasmids, bacterial strains and yeast strains.** Oligonucleotides used in this work are described in Supplementary Table 1, plasmids in Supplementary Table 2 and yeast strains in Supplementary Table 3.

Plasmids pAD260 and pAD262 were generated by site-directed mutagenesis with oligonucleotides RTADZ-32 to RTADZ-33, using pAD258 or pAD259 as templates, respectively. pAD261 and pAD263 were obtained by site-directed mutagenesis with oligonucleotides RTADZ-34 to RTADZ-35, employing pAD258 or pAD259 as templates. D171N and D198N mutations were confirmed by PCR with primers T7-long to RTADZ-10, followed by digestion with TaqI or BshTI, respectively. pAD264 expression vector, encoding the N-terminal fusion of wild-type PIN domain with 6×His-SUMOTag was constructed by cloning the sequence corresponding to residues 1–241 of Dis3 into BamHI and XhoI sites of pET-28M-SUMO Kan vector. pAD265, pAD266 and pAD267 were obtained by site-directed mutagenesis with oligonucleotides RTADZ-30 to RTADZ-31, RTADZ-32 to RTADZ-33 and RTADZ-34 to RTADZ-35, respectively, and pAD264 as a template. D171N and D198N mutations were confirmed as above, and D91N mutation in pAD265 was verified by PCR with primers T7-long to RTADZ-10, followed by digestion with DraI. pAD268 was generated by cloning of a PCR product corresponding to the 5'-ETS, made with RTADZ-70 to RTADZ-71 primers using genomic DNA from BMA64 strain as template, into pCR-Blunt II-TOPO.

pBS3211 and pBS3210 were obtained by TOPO-blunt cloning (Invitrogen) of PCR products made with oligonucleotides OBS2638 and OBS2639 on DNA from yeast strains BSY1704 and BSY1708, respectively. The insert contained part of the *LYS2* sequence, the complete *DIS3* or *dis3<sup>D551N</sup>* open reading frame in fusion with a tobacco etch virus (TEV) protease cleavage site–Protein A (PA) tag, and the *TRP1* marker. The *D171N* mutation was introduced in these plasmids by site-directed mutagenesis with OBS2648 and OBS2649, giving pBS3241 and pBS3245, respectively. The four *DIS3* alleles, together with their promoter sequences and the TEV–PA tag, were excised from the TOPO vectors by digestion with *SpeI*, and cloned into the yeast *LEU2* centromeric plasmid pFL36 (ref. 26), giving pBS3269 to pBS3278. pBS3318 was obtained by TOPO-TA cloning of a PCR product corresponding to the 5'-ETS amplified with oligonucleotides OBS2616 and CS18 from genomic DNA.

For expression of the various *DIS3* alleles, BSY1668, BSY1865 and BSY1883 were transformed with plasmids pBS3269 to pBS3278. Cultures in synthetic complete medium without leucine were grown at 28 °C. The chromosomal, wild-type *DIS3* allele was repressed by the addition of doxycycline (20 µg ml<sup>-1</sup>).

**Heterologous expression and purification of recombinant proteins.** For purification of full-length Dis3 versions, *E. coli* BL21-CodonPlus-RIL strain (Stratagene) was transformed with the appropriate plasmid (pAD258 to pAD263). Selected transformants were grown in 1 l of selective medium after inoculation from a pre-culture at  $D_{600} \approx 0.1$ . Growth was performed at 37 °C until  $D_{600}$  reached 0.45–0.5. Cultures were cooled to 16 °C for 30 min. Protein expression was induced by the addition of isopropyl β-D-thiogalactoside to 0.5 mM and incubation was continued overnight at 16 °C. After centrifugation, bacterial pellets were resuspended in buffer A (20 mM Tris-HCl pH 8.0, 200 mM NaCl, 10 mM imidazole, 10 mM 2-mercaptoethanol) and lysed by sonication, followed by ultracentrifugation. Soluble fractions were loaded on a His-Trap FF Crude column on an Äkta FPLC purification system (GE Healthcare). The column was washed with buffer A and subsequently with buffer B (20 mM Tris-HCl pH 8.0; 1 M NaCl, 10 mM imidazole, 10 mM 2-mercaptoethanol). After re-equilibration with buffer A, bound proteins were eluted with buffer C (20 mM Tris-HCl pH 8.0, 200 mM NaCl, 600 mM imidazole, 10 mM 2-mercaptoethanol). Proteins were further purified by ion-exchange chromatography with a MiniQ 4.6/50 PE column followed by size-exclusion chromatography on a Superdex 200 10/300 GL column (both from GE Healthcare). Final elution was performed in buffer containing 10 mM Tris-HCl pH 8.0, 150 mM NaCl. Finally, glycerol was added to the protein preparations (30% final concentration), which were stored at –80 °C. The purity and quantity of the proteins were estimated by analysis in NuPAGE gels (Invitrogen).

Various PIN versions were purified as follows. Transformation of *E. coli* BL21-CodonPlus-RIL with expression vectors (pAD264 to pAD267; see Supplementary Table 2), culture conditions, the induction of protein expression and extract preparation procedures were the same as for the full-length Dis3 proteins (see

above). Initial purification of 6×His-SUMOTag–PIN fusion proteins was performed as described above. Fractions eluted with buffer C (containing imidazole at high concentration) were combined and dialysed overnight at 4 °C against 2 l of buffer A in the presence of 6×His-SUMO protease. After dialysis, the protein mixture was subjected to the second round of purification on a His-Trap FF Crude column, encompassing the collection of purified PIN (lacking 6×His-SUMOTag) in the flowthrough (in buffer A) and elution of 6×His-SUMOTag together with 6×His-SUMO protease in buffer D (20 mM Tris-HCl pH 8.0, 1 M NaCl, 600 mM imidazole, 10 mM 2-mercaptoethanol). PIN versions thus obtained were further purified by size-exclusion chromatography on a Superdex 75 10/300 GL column (GE Healthcare) and stored at –80 °C in the presence of 30% glycerol.

**Substrate preparation for biochemical assays.** The 17–A<sub>14</sub> oligoribonucleotide (Invitrogen) was purified on a 10% denaturing polyacrylamide gel. Gel bands containing the oligoribonucleotide were detected by ultraviolet shadowing; they were then excised and the RNAs were eluted overnight at 25 °C in an equal volume of 100 mM Tris-HCl pH 8.0, 12.5 mM EDTA, 150 mM NaCl, 1% SDS and phenol.

5'-end labelling was performed with T4 polynucleotide kinase (NEB) and [ $\gamma$ -<sup>32</sup>P]ATP (GE Healthcare) in accordance with the manufacturer's instructions.

3'-end labelling was performed with home-made [<sup>32</sup>P]pCp (prepared by incubating cytidine 3'-monophosphate with [ $\gamma$ -<sup>32</sup>P]ATP in the presence of T4 polynucleotide kinase) and T4 RNA ligase (NEB).

Circular 17–A<sub>14</sub> substrate was prepared by incubating 150 pmol of the oligoribonucleotide with 250 pmol of unlabelled ATP and 4 pmol of [ $\gamma$ -<sup>32</sup>P]ATP in 50 mM Tris-HCl pH 8.0, 10 mM MgCl<sub>2</sub>, 10 mM dithiothreitol, using T4 polynucleotide kinase and T4 RNA ligase.

5'-ETS substrate was prepared with pAD268 plasmid (see Supplementary Table 1), digested with a combination of *SapI* and *XhoI*, as template for *in vitro* transcription, which was performed with T7 RNA polymerase (NEB) in the presence of [ $\alpha$ -<sup>32</sup>P]UTP (Amersham Biosciences), in accordance with the manufacturer's instructions.

All RNA substrates were purified from 6–20% denaturing polyacrylamide gels.

**Exosome co-precipitation.** Dis3-TEV–PA-associated complexes from 400 ml of BSY1865[pBS3269-78] culture at  $D_{600} = 1$  were affinity-purified on IgG-Sepharose resin, followed by TEV cleavage as described previously<sup>27</sup>. Input fraction (0.3 µl), or 7.5 µl of the eluates, was separated by gradient SDS-PAGE, and transferred to a nitrocellulose membrane for western blot analyses. A rabbit antibody recognizing the calmodulin-binding peptide tag and cross-reacting with the Protein A tag (anti-TAP antibody; Open Biosystems) was used at a dilution of 1:2,000, followed by incubation with a goat anti-rabbit-horseradish peroxidase IgG secondary antibody (Pierce) at a dilution of 1:5,000. Signals generated by enhanced chemiluminescence (ECL; GE Healthcare) were detected with a Las3000 device (Fuji).

**Northern blots and sequencing.** Total RNA was extracted with a standard phenol procedure<sup>28</sup>. RNA (3–10 µg) was fractionated by electrophoresis on a 6% polyacrylamide–urea gel before transfer to a Hybond N<sup>+</sup> membrane (GE Healthcare). The membrane was saturated and hybridizations were performed in Church buffer, as described previously<sup>28</sup>, at 42 °C for <sup>32</sup>P-labelled oligonucleotide probes or at 55 °C for random-primed PCR probes. OBS2998, OBS2999 and OBS3081 oligonucleotides hybridized in 5'-ETS. CS5 hybridized in the 5.8S rRNA<sup>29</sup>. The PCR probes against scR1, 5'-ETS and NEL025 CUT were amplified from yeast genomic DNA with oligonucleotides FWSCR1D-R, OBS2616-CS18 and PP2-4, respectively. The three probes were labelled with [ $\alpha$ -<sup>32</sup>P]dCTP by using the MegaPrime DNA labelling system (GE Healthcare). Signals were detected by phosphorimaging on a Storm device (GE Healthcare).

26. Bonneaud, N. *et al.* A family of low and high copy replicative, integrative and single-stranded *S. cerevisiae*/*E. coli* shuttle vectors. *Yeast* 7, 609–615 (1991).

27. Rigaut, G. *et al.* A generic protein purification method for protein complex characterization and proteome exploration. *Nature Biotechnol.* 17, 1030–1032 (1999).

28. Dauger, M. C., Mauxion, F. & Séraphin, B. The yeast POP2 gene encodes a nuclease involved in mRNA deadenylation. *Nucleic Acids Res.* 29, 2448–2455 (2001).

29. Saveanu, C. *et al.* Nog2p, a putative GTPase associated with pre-60S subunits and required for late 60S maturation steps. *EMBO J.* 20, 6475–6484 (2001).



# Nuclear receptor corepressor and histone deacetylase 3 govern circadian metabolic physiology

Theresa Alenghat<sup>1,2</sup>, Katherine Meyers<sup>1,2</sup>, Shannon E. Mullican<sup>1,2</sup>, Kirstin Leitner<sup>1,2</sup>, Adetoun Adeniji-Adele<sup>3</sup>, Jacqueline Avila<sup>1,2</sup>, Maja Bučan<sup>3</sup>, Rexford S. Ahima<sup>1,2</sup>, Klaus H. Kaestner<sup>2,3</sup> & Mitchell A. Lazar<sup>1,2</sup>

Rhythmic changes in histone acetylation at circadian clock genes suggest that temporal modulation of gene expression is regulated by chromatin modifications<sup>1–3</sup>. Furthermore, recent studies demonstrate a critical relationship between circadian and metabolic physiology<sup>4–7</sup>. The nuclear receptor corepressor 1 (Ncor1) functions as an activating subunit for the chromatin modifying enzyme histone deacetylase 3 (Hdac3)<sup>8</sup>. Lack of Ncor1 is incompatible with life, and hence it is unknown whether Ncor1, and particularly its regulation of Hdac3, is critical for adult mammalian physiology<sup>9</sup>. Here we show that specific, genetic disruption of the Ncor1–Hdac3 interaction in mice causes aberrant regulation of clock genes and results in abnormal circadian behaviour. These mice are also leaner and more insulin-sensitive owing to increased energy expenditure. Unexpectedly, loss of a functional Ncor1–Hdac3 complex *in vivo* does not lead to sustained increases in known catabolic genes, but instead significantly alters the oscillatory patterns of several metabolic genes, demonstrating that circadian regulation of metabolism is critical for normal energy balance. These findings indicate that activation of Hdac3 by Ncor1 is a nodal point in the epigenetic regulation of circadian and metabolic physiology.

Mammals display circadian rhythms in behavioural and physiological processes, such as sleep, feeding, blood pressure and metabolism<sup>10–12</sup>, guided by external light–dark signals that are integrated through intrinsic central and peripheral molecular clocks<sup>13,14</sup>. Several critical clock and clock output genes have daily cycling of histone acetylation, suggesting that epigenetic regulation of chromatin has a central role in circadian regulation<sup>1–3</sup>. Nuclear receptors regulate circadian rhythm and metabolism by interacting with cofactor complexes that act at the level of chromatin<sup>15–17</sup>.

Ncor1 is a large, multidomain protein that is recruited by nuclear receptors to mediate transcriptional repression. Ncor1 stably associates with Hdac3 through its deacetylase activation domain (DAD), which is conserved in the highly related Ncor2 (also known as SMRT)<sup>8</sup>. Hdac3 deacetylase activity requires association with the Ncor1 or SMRT DAD<sup>8</sup>, and DAD mutations significantly inhibit nuclear receptor-mediated repression<sup>18</sup>. Both *Hdac3* and *Ncor1* knockout mice die early in embryogenesis<sup>9,19</sup>, indicating that these proteins are essential for normal development and postnatal survival.

The function of Ncor1 in the adult is unknown, as is the physiological significance of the Ncor1–Hdac3 association. We used a homologous recombination strategy to generate C57BL/6 mutant mice (referred to as DADm) with a single amino acid substitution (Y478A) in the Ncor1 DAD, creating a mutant protein that is stable but unable to associate with or activate Hdac3 (ref. 18; Supplementary Figs 1 and 2a, b). Levels of Ncor1 and SMRT were similar in DADm and wild-type littermates (Supplementary Fig. 2c, d), and the Hdac3 interaction with Ncor1 (but not SMRT) was lost in the DADm mice

(Supplementary Fig. 2e, f)<sup>18</sup>. DADm mice were viable, born at normal Mendelian frequencies (Supplementary Table 1) and morphologically indistinguishable from wild-type littermates at birth. Thus, Ncor1 binding to Hdac3 is not required for normal development, and the embryonic defects of mice lacking Ncor1 are due to factors other than, or in addition to, Hdac3 recruitment by Ncor1.

Ncor1 serves as corepressor for Rev-erb $\alpha$  (also known as Nr1d1), a nuclear receptor that represses the clock gene, *Bmal1* (also known as *Arntl*; refs 20 and 21). *Bmal1* is normally expressed at its lowest levels from zeitgeber time (ZT) 7–9. Consistent with an *in vivo* role for repression by Ncor1–Hdac3, *Bmal1* messenger RNA was increased from ZT7–9 in DADm mice (Fig. 1a), although its levels continued to cycle (data not shown). Histone H4 acetylation was increased at the Rev-erb response element (RORE) of the gene during this period (Fig. 1b)<sup>20</sup>. DADm mouse embryonic fibroblasts (MEFs) also displayed higher levels of *Bmal1* (Fig. 1c). HDAC inhibition increased *Bmal1* expression in wild-type but not DADm MEFs (Fig. 1d), suggesting that derepression of *Bmal1* in the DADm MEFs is epistatic with loss of Hdac3 activity. Moreover, depletion of *Rev-erba* or its haem ligand, derepressed *Bmal1* in wild-type but not DADm MEFs (Fig. 1e and Supplementary Fig. 3a), indicating that Rev-erb $\alpha$  is an important endogenous target of Ncor1–Hdac3. Although cyclic expression of a *Bmal1*–luciferase reporter requires Rev-erb $\alpha$  and Rev-erb $\beta$  (ref. 22), *Bmal1* expression remained rhythmic in DADm MEFs (Fig. 1f), potentially due to compensation by SMRT–Hdac3 or by regions of the endogenous gene not contained in the reporter construct. Nevertheless, the rhythmic expression of *Bmal1* and *Rev-erba* was abnormal in the DADm MEFs, demonstrating a cell-autonomous role for the Ncor1–Hdac3 complex in maintaining normal circadian rhythm (Fig. 1f and Supplementary Fig. 3b). Cyclic histone acetylation was similarly altered in the DADm cells (Fig. 1g). Ncor1 did not oscillate and was recruited to the *Bmal1* RORE in the DADm as well as the wild-type MEFs (Supplementary Fig. 3c, d) whereas, as predicted, Hdac3 recruitment was markedly reduced at this site in the DADm cells (Supplementary Fig. 3d).

To evaluate whether the molecular dysregulation of the clock corresponds with circadian behavioural abnormalities, we monitored locomotor activity in constant darkness. DADm mice demonstrated a free-running period of ~23.2 h compared with 23.6 h in wild-type mice (Fig. 1h, i). This decrease in the average period length of the DADm mice is highly significant and coincides with the period change reported in *Rev-erba* knockout mice<sup>21</sup>. These findings identify a critical role for activation of Hdac3 by Ncor1 in regulating normal circadian rhythm and demonstrate the dependence of circadian behaviour on dynamic epigenetic modifications.

Owing to the strong links between circadian and metabolic physiology, as well as the role of nuclear receptors in both systems, we also examined metabolic parameters. The Ncor1 DADm mice weighed

<sup>1</sup>Division of Endocrinology, Diabetes, and Metabolism, Department of Medicine, <sup>2</sup>The Institute for Diabetes, Obesity, and Metabolism, and <sup>3</sup>Department of Genetics, University of Pennsylvania School of Medicine, Philadelphia, Pennsylvania 19104, USA.

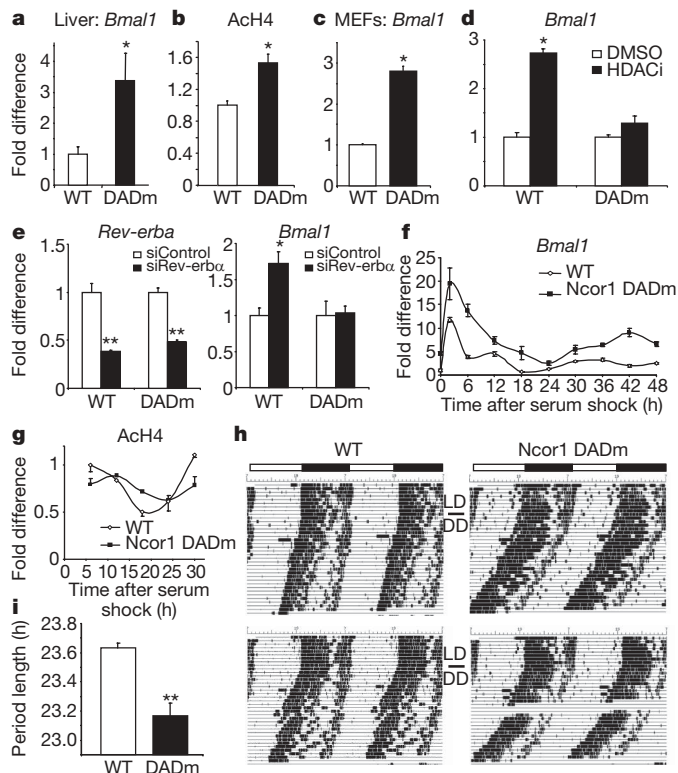


**Figure 1 | *Ncor1-Hdac3* regulates peripheral clock and circadian physiology.** **a**, *Bmal1* expression in wild type (WT) and DADm livers during ZT7–9 (WT:  $n = 6$ , DADm:  $n = 4$ ). **b**, Chromatin immunoprecipitation (ChIP) for AcH4 from wild-type and DADm livers at the *Bmal1* RORE ( $n = 3$ ). **c**, *Bmal1* expression in immortalized MEFs ( $n = 3$ ). **d**, *Bmal1* expression in MEFs after treatment with the HDAC inhibitor MS-275 (HDACi, black bars) or dimethylsulphoxide control (white bars) ( $n = 3$ ). **e**, Effect of *Rev-erba* knockdown on MEF *Rev-erba* and *Bmal1* expression, using small interfering RNA against green fluorescent protein (siControl) or against *Rev-erba* (siRev-erba) ( $n = 3$ ). **f**, *Bmal1* expression in MEFs after cell synchronization (fold difference relative to wild type, time 0;  $n = 3$  per time point). **g**, ChIP of AcH4 at the *Bmal1* RORE following 50% serum shock. Mean  $\pm$  s.e.m. of duplicate samples. Independent experiments gave similar results. **h**, Voluntary locomotor wheel running activity, double plotted in each panel. LD, 12 h light/12 h dark; DD, complete darkness. **i**, Average free running period ( $n = 3$ ). Three independent experiments gave similar results. Data are presented as mean and s.e.m. \* $P < 0.05$ , \*\* $P < 0.01$ .

the same as wild-type littermates at birth, but began to weigh significantly less between 4–6 weeks of age and maintained this difference throughout adulthood (Fig. 2a). Perigonadal fat pad weight (Fig. 2b, c) and whole body fat measured by NMR (Fig. 2d) were decreased in DADm mice. Histological evaluation of *Ncor1* DADm adipose tissue showed normal architecture, with a trend towards smaller adipocytes (Supplementary Fig. 4a). Consistent with previous reports that *Ncor1* inhibits adipogenesis, adipocyte differentiation was modestly increased in DADm MEFs, indicating that the decrease in fat tissue is not due to impaired adipogenesis (Supplementary Fig. 4b, c)<sup>23</sup>.

We next used metabolic cages to determine why the *Ncor1* DADm mice are leaner. DADm mice demonstrated similar levels of locomotor activity to the wild-type mice and food intake was increased, indicating that their decreased weight did not result from increased activity or decreased feeding (Fig. 2e, f). Instead, DADm mice showed increased oxygen consumption and heat measured by indirect calorimetry, particularly during the wakeful dark cycle (Fig. 2g–i). Therefore, these mice probably ate more food to compensate for increased catabolism. The increase in heat production is unlikely to be a primary consequence of brown adipose UCP expression which was unaltered in DADm mice (Supplementary Fig. 4d).

Hyperinsulinemic-euglycemic clamp studies revealed increased insulin sensitivity of the DADm mice on a normal chow diet (Fig. 3a).

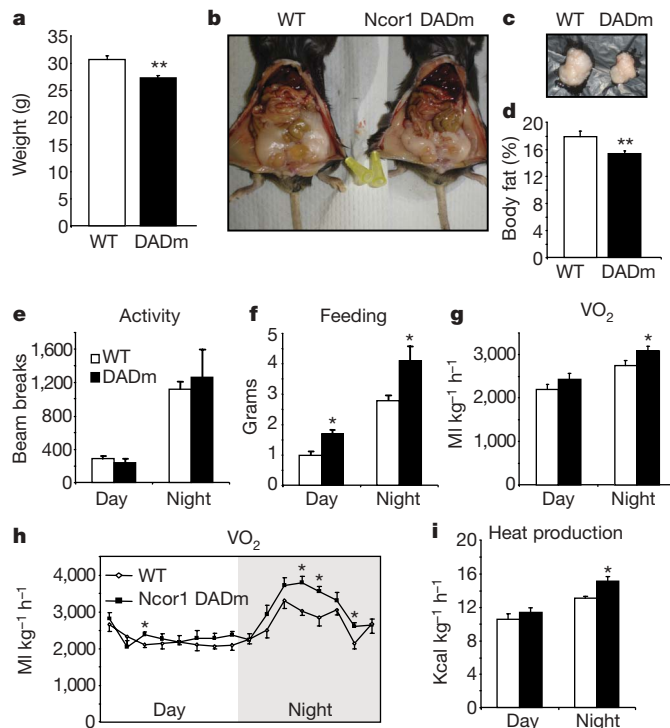


**Figure 2 | DADm mice exhibit increased energy expenditure.** **a**, Body weight of 24-week-old male wild type (WT) and DADm mice ( $n = 10$ ). **b**, Representative abdominal images of wild type and DADm mice. **c**, Perigonadal fat pads obtained from mice in **b**. **d**, Percentage body fat composition measured by NMR for cohort presented in **a**. **e–i**, Effect of DADm on locomotor activity measured by photobeam breaks (**e**), on food intake (**f**), on oxygen consumption ( $VO_2$ ) (**g, h**), and on heat production (**i**). Average  $VO_2$  for three consecutive measurements taken every 27 min is shown in **h** ( $n = 4$ ). Data are presented as mean and s.e.m. \* $P < 0.05$ , \*\* $P < 0.01$ .

On a high-fat diet (HFD), DADm mice were resistant to diet-induced obesity and were protected from developing insulin resistance (Fig. 3b, c and Supplementary Fig. 5a), with reduced hepatic glucose production in the setting of the hyperinsulinemic clamp (Supplementary Fig. 5b). This was surprising because *Rev-erba* recruits *Ncor1-Hdac3* to gluconeogenic genes to repress hepatic glucose production<sup>17</sup>. However, on normal chow before the development of large differences in insulin sensitivity, hepatic glucose output was indeed upregulated in the DADm mice (Supplementary Fig. 5c). Also, expression of the gluconeogenic *Pepck* gene was increased in the DADm livers (Supplementary Fig. 5d), and the ability of the *Rev-erba* ligand haem to repress *Pepck* gene expression was abrogated in DADm primary hepatocytes (Supplementary Fig. 5e). Apparently, in the HFD model, the gluconeogenic effects of reduced *Rev-erba* function were more than counterbalanced by the markedly reduced insulin resistance of the DADm mice. Although this insulin sensitivity was consistent with the leaner phenotype of the mice, weight-matched DADm mice fed a HFD were also more insulin sensitive (Supplementary Fig. 6), suggesting that their improved insulin tolerance may not be entirely secondary to leanness.

To understand further the altered circadian and metabolic phenotypes of the DADm mice, ketone and free fatty acid levels were measured regularly during a 24-h cycle. Serum ketones and fatty acids were significantly increased in the DADm mice at specific times during the cycle (Supplementary Fig. 7a, b), suggesting temporal dysregulation of fat metabolism such that cumulative increases in hepatic beta oxidation drive increased lipolysis. Importantly, in contrast to mice lacking *Hdac3* in liver<sup>24</sup>, there was no evidence of hepatic steatosis in the DADm mice (Supplementary Fig. 7c), suggesting a potential protective effect of residual SMRT-dependent *Hdac3* activity.

Microarray analysis at a single time point demonstrated modest changes in hepatic gene expression between the DADm and wild-type mice, although both circadian and metabolic pathways were enriched

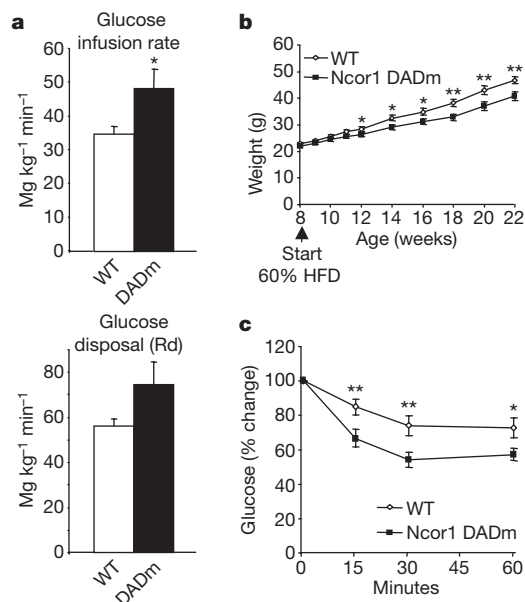


**Figure 3 | DADm mice are resistant to diet-induced obesity.**

**a**, Hyperinsulinemic-euglycemic clamp measurements for 16-week-old male wild type (WT) and DADm mice fed a normal chow diet ( $n = 4$ ). Top panel shows the glucose infusion rate, and the bottom panel shows the glucose disposal rate (Rd). **b**, Weight curve for age-matched wild type and DADm mice started on 60% HFD at 8 weeks. **c**, Insulin tolerance test for mice in **b** at ZT8 after 15 weeks on HFD (WT:  $n = 13$ , DADm:  $n = 12$ ). Data are presented as mean  $\pm$  s.e.m. \* $P < 0.05$ , \*\* $P < 0.01$ .

(data not shown). However, 24-h studies showed marked alterations in cyclic expression of several critical genes involved in lipid metabolism in the liver (Fig. 4a). DADm mice showed phase shifts in the expression of genes involved in fat breakdown, such as carnitine palmitotransferase 1a (*Cpt1a*), medium chain acyl-CoA dehydrogenase (*MCAD*, also known as *Acadm*), and their transcriptional regulator peroxisome proliferator activated receptor  $\alpha$  (*Ppara*). There was a trend toward increased expression of *Cpt1a* and *MCAD* after treatment of DADm hepatocytes with a PPAR- $\alpha$  agonist (Supplementary Fig. 8). ATP citrate lyase (*Acy*), which produces acetyl coA, and acetyl coA carboxylase 2 (*Acc2*, also known as *Acacb*), the malonyl CoA product of which allosterically inhibits *Cpt1a*, were also dysregulated but antiphase with *Cpt1a* (Fig. 4a). Elongation of long-chain fatty acids family member 6 (*Elovl6*), the deficiency of which favours leanness and insulin sensitivity<sup>25</sup>, showed fourfold lower expression at ZT10 in DADm liver. In white adipose tissue, modest circadian changes in *Cpt1a* were noted but, unlike in the liver, *Acc2* and *Ppar- $\gamma$*  expression were not altered (Fig. 4a). Taken together, these results indicate that Ncor1-Hdac3 is required for normal circadian regulation of genes involved in the breakdown, biogenesis and modification of lipids in the liver.

To determine the mechanism of altered beta oxidation cycling in DADm mice, we examined cofactor and histone acetylation at well-characterized nuclear receptor response elements in the *Cpt1a* and *MCAD* genes. As expected, Ncor1 was similarly recruited to the nuclear receptor responsive elements in the *Cpt1a* and *MCAD* genes in wild-type and DADm cells (Supplementary Fig. 9a)<sup>26,27</sup>. However, Hdac3 recruitment was markedly reduced at these same genomic sites (Fig. 4b). Moreover, circadian oscillation at these response elements was disturbed in the DADm livers in a pattern that paralleled the alterations in gene expression (Fig. 4c, d), whereas Ncor1 recruitment remained unchanged

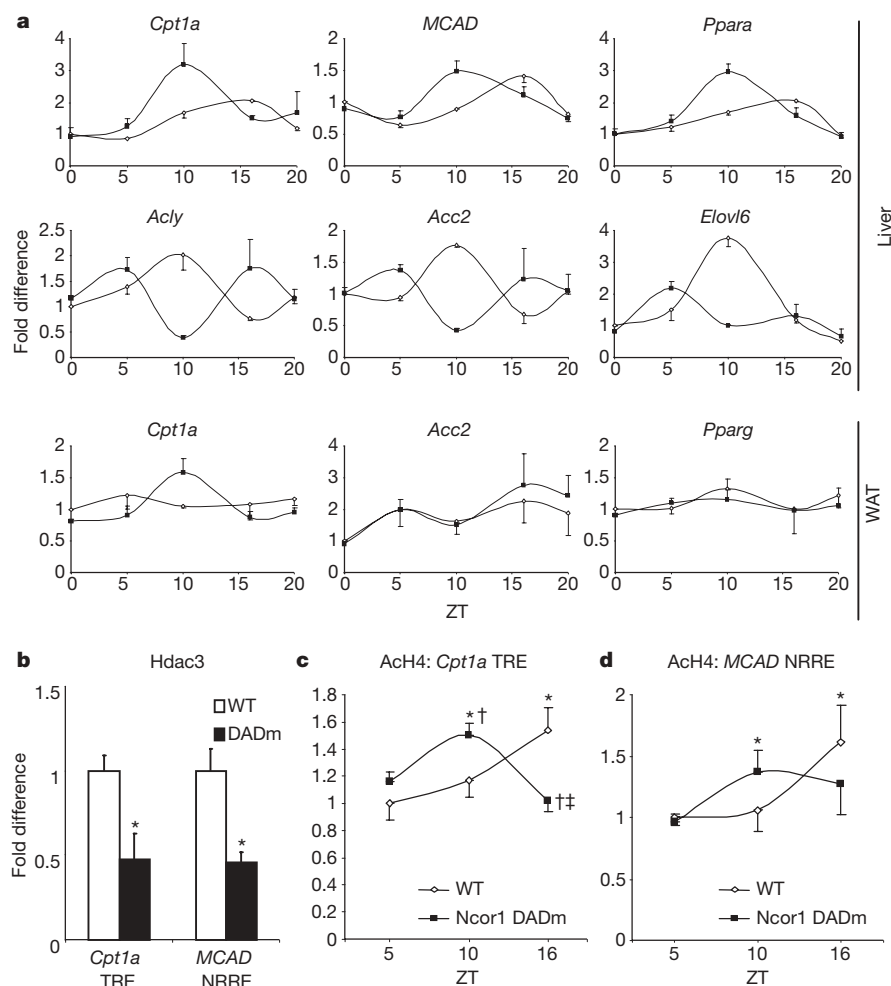


**Figure 4 | Activation of Hdac3 by Ncor1 regulates circadian metabolic gene expression in the liver.**

**a**, Diurnal expression of lipid metabolic genes (wild type, open diamonds; DADm, black squares relative to wild type, ZT0). Lights on and off at ZT0 and ZT12, respectively ( $n = 2-3$  per genotype per ZT). WAT, white adipose tissue. **b**, ChIP for Hdac3 from wild type (WT) and DADm MEFs ( $n = 3$ ). **c**, **d**, ChIP for AcH4 from livers at *Cpt1a* TRE (**c**) and *MCAD* NRRE (**d**) ( $n = 3$  per genotype per ZT). Quantitative PCR results are relative to wild type, ZT5. Data are presented as mean  $\pm$  s.e.m. \* $P < 0.05$  relative to ZT5, † $P < 0.05$  relative to wild type, ‡ $P < 0.05$  relative to ZT10.



(Supplementary Fig. 9b). An intronic region of the *Cpt1a* gene did not exhibit oscillation of histone acetylation, demonstrating site specificity of circadian histone acetylation (Supplementary Fig. 9c).

We have demonstrated that the association between Hdac3 and the transcriptional corepressor Ncor1 regulates circadian behaviour and metabolism. A transcriptional coactivator recently identified as a regulator of circadian and metabolic pathways, PGC-1 $\alpha$  (also known as PPARGC1 $\alpha$ ), does not possess intrinsic histone acetylase (HAT) activity, but interacts with HAT-containing coactivators<sup>7</sup>, and the Clock protein was recently shown to possess HAT activity<sup>2</sup>. These findings emphasize that circadian metabolic transcriptional regulation is regulated at the level of histone acetylation and that the cycling of epigenetic modifications is critical to maintaining normal energy homeostasis. Loss of Ncor1-dependent Hdac3 activity did not lead to constant increases in gene expression, as might have been predicted, probably owing to complex interaction with other histone-modifying circadian factors. Indeed, dysregulation of the molecular clock and metabolic gene expression in the DADm mice undoubtedly reflects alterations in several interconnected pathways including the molecular clock as well as signalling by several nuclear receptors.

Recent studies have demonstrated critical links between circadian regulation and normal health, longevity and diet<sup>4,28,29</sup>. The DADm mice showed markedly altered metabolic oscillatory expression, with a net effect of increased lipid consumption and a lean, insulin sensitive, obesity-resistant metabolic phenotype. Thus, although shift work and other disruptions of normal rhythms can be metabolically deleterious<sup>30</sup>, alteration of normal circadian physiology can also be associated with a favourable metabolic profile. Targeting the Ncor1–Hdac3 deacetylase enzyme would be a highly specific means of combating diseases of nutritional excess including obesity, diabetes and the metabolic syndrome.

## METHODS SUMMARY

**Generation of DADm mice.** The Y478A mutation was introduced into exon 13 of the *Ncor1* gene using a targeting vector containing a loxP-flanked neomycin resistance (*neo<sup>R</sup>*) gene downstream from exon 13. The targeting vector was electroporated into C57BL/6 embryonic stem cells and a clone confirmed to contain the homologous targeted mutation was injected into C57BL/6 blastocysts. Blastocysts were implanted in pseudopregnant female mice and germline transmission led to the generation of C57BL/6 F<sub>1</sub> Ncor1<sup>Y478A/Neo<sup>+</sup></sup> mice. These mice were mated to C57BL/6 Tg<sup>EIIa-Cre</sup> mice to remove the floxed *neo<sup>R</sup>* cassette, generating C57BL/6 Ncor1<sup>Y478A/+</sup> mice, which were bred to wild-type mice to obtain (Cre-)Ncor1<sup>Y478A/+</sup> mice. Experimental cohorts were generated from (Cre-)Ncor1<sup>Y478A/+</sup> × (Cre-)Ncor1<sup>Y478A/+</sup> breedings.

**Mice.** Age-matched male mice were used for all experiments. Animals were housed at up to five per cage in a ventilated isolator cage system in a 12 h light/dark cycle, with free access to water and chow or a HFD (60 kcal% fat). Mice used for circadian gene expression experiments were housed under strict light/dark regulation and minimal disturbance for 3 weeks. For metabolic experiments, mice were placed on a HFD at 8 weeks and insulin tolerance tests were performed after 16 weeks on the diet using 0.75 U kg<sup>-1</sup> insulin. Mice underwent body composition analysis by NMR and monitoring of feeding, locomotor activity and indirect calorimetry. For hyperinsulinemic-euglycemic clamp studies, 2.5 or 5 mU kg<sup>-1</sup> min<sup>-1</sup> insulin was administered in chow-fed mice and HFD mice, respectively.

**Full Methods** and any associated references are available in the online version of the paper at [www.nature.com/nature](http://www.nature.com/nature).

Received 15 April; accepted 14 October 2008.

Published online 26 November 2008.

- Ripperger, J. A. & Schibler, U. Rhythmic CLOCK-BMAL1 binding to multiple E-box motifs drives circadian Dbp transcription and chromatin transitions. *Nature Genet.* **38**, 369–374 (2006).
- Doi, M., Hirayama, J. & Sassone-Corsi, P. Circadian regulator CLOCK is a histone acetyltransferase. *Cell* **125**, 497–508 (2006).
- Etchegaray, J. P., Lee, C., Wade, P. A. & Reppert, S. M. Rhythmic histone acetylation underlies transcription in the mammalian circadian clock. *Nature* **421**, 177–182 (2003).
- Kohsaka, A. *et al.* High-fat diet disrupts behavioral and molecular circadian rhythms in mice. *Cell Metab.* **6**, 414–421 (2007).
- Rudic, R. D. *et al.* BMAL1 and CLOCK, two essential components of the circadian clock, are involved in glucose homeostasis. *PLoS Biol.* **2**, e377 (2004).

- Turek, F. W. *et al.* Obesity and metabolic syndrome in circadian Clock mutant mice. *Science* **308**, 1043–1045 (2005).
- Liu, C., Li, S., Liu, T., Borjigin, J. & Lin, J. D. Transcriptional coactivator PGC-1 $\alpha$  integrates the mammalian clock and energy metabolism. *Nature* **447**, 477–481 (2007).
- Guenther, M. G., Barak, O. & Lazar, M. A. The SMRT and N-CoR corepressors are activating cofactors for histone deacetylase 3. *Mol. Cell Biol.* **21**, 6091–6101 (2001).
- Jepsen, K. *et al.* Combinatorial roles of the nuclear receptor corepressor in transcription and development. *Cell* **102**, 753–763 (2000).
- Gachon, F., Nagoshi, E., Brown, S. A., Ripperger, J. & Schibler, U. The mammalian circadian timing system: from gene expression to physiology. *Chromosoma* **113**, 103–112 (2004).
- Lowrey, P. L. & Takahashi, J. S. Mammalian circadian biology: elucidating genome-wide levels of temporal organization. *Annu. Rev. Genomics Hum. Genet.* **5**, 407–441 (2004).
- Schultz, T. F. & Kay, S. A. Circadian clocks in daily and seasonal control of development. *Science* **301**, 326–328 (2003).
- Shearman, L. P. *et al.* Interacting molecular loops in the mammalian circadian clock. *Science* **288**, 1013–1019 (2000).
- Reppert, S. M. & Weaver, D. R. Molecular analysis of mammalian circadian rhythms. *Annu. Rev. Physiol.* **63**, 647–676 (2001).
- Desvergne, B., Michalik, L. & Wahli, W. Transcriptional regulation of metabolism. *Physiol. Rev.* **86**, 465–514 (2006).
- Yang, X. *et al.* Nuclear receptor expression links the circadian clock to metabolism. *Cell* **126**, 801–810 (2006).
- Yin, L. *et al.* Rev-erb $\alpha$ , a heme sensor that coordinates metabolic and circadian pathways. *Science* **318**, 1786–1789 (2007).
- Ishizuka, T. & Lazar, M. A. The nuclear receptor corepressor deacetylase activating domain is essential for repression by thyroid hormone receptor. *Mol. Endocrinol.* **19**, 1443–1451 (2005).
- Bhaskara, S. *et al.* Deletion of histone deacetylase 3 reveals critical roles in S phase progression and DNA damage control. *Mol. Cell* **30**, 61–72 (2008).
- Yin, L. & Lazar, M. A. The orphan nuclear receptor Rev-erb $\alpha$  recruits the N-CoR/histone deacetylase 3 corepressor to regulate the circadian *Bmal1* gene. *Mol. Endocrinol.* **19**, 1452–1459 (2005).
- Preitner, N. *et al.* The orphan nuclear receptor REV-ERB $\alpha$  controls circadian transcription within the positive limb of the mammalian circadian oscillator. *Cell* **110**, 251–260 (2002).
- Liu, A. C. *et al.* Redundant function of REV-ERB $\alpha$  and  $\beta$  and non-essential role for Bmal1 cycling in transcriptional regulation of intracellular circadian rhythms. *PLoS Genet.* **4**, e1000023 (2008).
- Yu, C. *et al.* The nuclear receptor corepressors NCoR and SMRT decrease peroxisome proliferator-activated receptor  $\gamma$  transcriptional activity and repress 3T3–L1 adipogenesis. *J. Biol. Chem.* **280**, 13600–13605 (2005).
- Knutson, S. K. *et al.* Liver-specific deletion of histone deacetylase 3 disrupts metabolic transcriptional networks. *EMBO J.* **27**, 1017–1028 (2008).
- Matsuzaka, T. *et al.* Crucial role of a long-chain fatty acid elongase, Elovl6, in obesity-induced insulin resistance. *Nature Med.* **13**, 1193–1202 (2007).
- Jansen, M. S., Cook, G. A., Song, S. & Park, E. A. Thyroid hormone regulates carnitine palmitoyltransferase  $\alpha$  gene expression through elements in the promoter and first intron. *J. Biol. Chem.* **275**, 34989–34997 (2000).
- Leone, T. C. *et al.* The human medium chain Acyl-CoA dehydrogenase gene promoter consists of a complex arrangement of nuclear receptor response elements and Sp1 binding sites. *J. Biol. Chem.* **270**, 16308–16314 (1995).
- Martino, T. A. *et al.* Circadian rhythm disorganization produces profound cardiovascular and renal disease in hamsters. *Am. J. Physiol. Regul. Integr. Comp. Physiol.* **294**, R1675–R1683 (2008).
- Fuller, P. M., Lu, J. & Saper, C. B. Differential rescue of light- and food-entrainable circadian rhythms. *Science* **320**, 1074–1077 (2008).
- Ramsey, K. M., Marcheva, B., Kohsaka, A. & Bass, J. The clockwork of metabolism. *Annu. Rev. Nutr.* **27**, 219–240 (2007).

**Supplementary Information** is linked to the online version of the paper at [www.nature.com/nature](http://www.nature.com/nature).

**Acknowledgements** We thank W. Pear for providing Ella-Cre C57BL/6 mice, G. Barnes and J. Rusche for providing MS-275, P. White and J. Tobias for bioinformatics assistance, and L. Yin, S.-H. You, M. Qatanani and other members of the Lazar laboratory for helpful discussions. We also thank J. Richa and The Transgenic Mouse Core, H. Collins and the Radioimmunoassay/Biomarkers Core, R. Dhier and the Metabolic Phenotyping Core of the Penn Diabetes and Endocrinology Research Center (DK19525), H. Fu and the Mouse Embryonic Stem Cell Core (DK49210) and the Morphology Core of the Center for Molecular Studies in Digestive and Liver Disease (DK50306 and DK49210) for consultation and services. This work was supported by National Institutes of Health grant DK43806 (to M.A.L.), and T.A. was supported by a National Research Training Grant in Developmental Biology.

**Author Contributions** T.A., M.B., K.H.K., R.S.A. and M.A.L. designed the research, T.A., K.M., K.L., A.A.-A., S.E.M. and J.A. acquired the data, T.A., A.A.-A., S.E.M., M.B., R.S.A. and M.A.L. analysed and interpreted the data, and T.A. and M.A.L. drafted the manuscript.

**Author Information** Reprints and permissions information is available at [www.nature.com/reprints](http://www.nature.com/reprints). Correspondence and requests for materials should be addressed to M.A.L. ([lazar@mail.med.upenn.edu](mailto:lazar@mail.med.upenn.edu)).

## METHODS

**Generation of DADm mice.** The targeting vector containing 3.5-kb arms was generated using RP23 NcoI-containing BAC clone templates (Invitrogen) followed by subcloning of PCR products into a pBluescript KS backbone (Stratagene). The Y478A mutation was introduced into exon 13 of the *Ncor1* gene using site directed mutagenesis (Stratagene). A cassette containing a loxP-flanked neomycin resistance (*neo<sup>R</sup>*) gene expressed from the phosphoglycerate kinase promoter was cloned within an intron approximately 500 base pairs (bp) downstream from exon 13. The negative selection diphtheria toxin gene was cloned downstream of the 3' arm. The targeting vector was linearized with XhoI and SacII (New England Biolabs) and electroporated into C57BL/6 embryonic stem cells (Chemicon). A clone confirmed to contain the homologous targeted mutation was injected into C57BL/6 blastocysts and these blastocysts were implanted in pseudopregnant female mice. Germline transmission led to the generation of C57BL/6 F<sub>1</sub> Ncor1<sup>Y478A NcoI/+</sup> mice. These mice were mated to C57BL/6 Tg<sup>Elia-Cre</sup> mice (Jackson Laboratory) to remove the floxed *neo<sup>R</sup>* cassette, generating C57BL/6 Ncor1<sup>Y478A/+</sup> mice which were bred to wild-type mice to obtain (Cre-)Ncor1<sup>Y478A/+</sup> mice. Experimental cohorts were generated from (Cre-)Ncor1<sup>Y478A/+</sup> × (Cre-)Ncor1<sup>Y478A/+</sup> breedings.

**Mice.** Age-matched male mice were used for all experiments. Genotyping was performed at weaning on genomic tail DNA. Animals were housed at up to five per cage in a ventilated isolator cage system in a 12 h light/dark cycle, with free access to water and chow or a high-fat diet (60 kcal% fat; Research Diets). Wheel running studies were conducted as described previously<sup>31</sup>. Mice used for circadian gene expression experiments were housed under strict light/dark regulation and minimal disturbance for 3 weeks. Mice were placed on a HFD at 8 weeks and insulin tolerance tests were performed after 16 weeks on the diet using 0.75 U kg<sup>-1</sup> insulin. Mice that had been on normal chow or high-fat diet for 16 weeks underwent body composition analysis by NMR and dual emission X-ray absorptiometry, and monitoring of feeding, locomotor activity and indirect calorimetry<sup>32</sup>. Hyperinsulinemic-euglycemic clamp was performed as previously described, except 2.5 mU kg<sup>-1</sup> min<sup>-1</sup> insulin was administered in chow fed mice and 5 mU kg<sup>-1</sup> min<sup>-1</sup> in mice on a high-fat diet<sup>32</sup>. Serum concentrations of  $\beta$ -hydroxybutyric acid (Stanbio) and non-esterified fatty acids (Wako) were measured using enzymatic colourimetric assays. Statistical analysis was performed using a Student's *t*-test. All studies were approved by the University of Pennsylvania School of Medicine Institutional Animal Care and Use Committee.

**Tissue and cell collection.** Tissue samples were collected after euthanasia and immediately frozen in liquid nitrogen. MEFs were collected from day 12.5 embryos and immortalized by repeated passages. Primary hepatocytes were obtained as described previously<sup>20</sup>. Cells were grown at 37 °C in 5% CO<sub>2</sub>. Primary MEFs were treated with 0.6  $\mu$ M dexamethasone, 10  $\mu$ g ml<sup>-1</sup> insulin, and 500  $\mu$ M 3-isobutyl-1-methylxanthine (no thiazolidinedione) to induce adipocyte differentiation. Cells were collected and stained with oil red O on day 5 after the addition of the differentiation cocktail. Immortalized MEF lines were treated with MS-275 for 24 h at 1  $\mu$ M before collection. For cell synchronization studies, MEFs were grown in serum free media for 24 h before synchronization

with 50% horse serum for 2 h, after which cells were switched back to serum-free media<sup>33</sup>. Cells were treated with 5  $\mu$ M succinylacetone for 12 h, 6  $\mu$ M haem for 6 h, or 50  $\mu$ M Wy-14,643 for 48 h. One micromolar of the siControl or siRev-erb $\alpha$  (Dharmacon) double-stranded oligonucleotides were prepared with Nucleofector Solution V (Amaxa biosystems) and 1 × 10<sup>6</sup> cells were electroporated according to the manufacturer's protocol. After 48 h, media was changed and cells were collected 24 h later.

**Immunoprecipitation and immunoblotting.** Samples for immunoprecipitation experiments were homogenized in a modified RIPA buffer containing protease inhibitor cocktail (Roche). Lysates were precleared with Protein G agarose beads and then incubated with mouse Hdac3 (Upstate) or mouse IgG (Santa Cruz) antibodies at 4 °C overnight followed by 1 h incubation with protein G agarose beads. Immunoprecipitates were washed five times with modified RIPA, eluted and subjected to immunoblot analysis. Blots were probed with the following primary antibodies: rabbit Ncor1<sup>34</sup>, rabbit SMRT (Bethyl), rabbit Hdac3 (Abcam). For liver chromatin immunoprecipitations, 50 mg of tissue from each mouse was minced and crosslinked in 1% formaldehyde for 15 min. After two washes, cells were manually lysed using a dounce and then subjected to nuclear lysis and sonication. ChIP assays were performed according to the protocol of Upstate Biotechnology with minor modifications and the following antibodies: rabbit Hdac3 (Santa Cruz/Abcam), rabbit acetylated histone H4 (Upstate) and rabbit Ncor1 (Abcam). The following primer pairs were used for ChIP experiments: *Bmal1*, 5'-AGCCTAACGACAGAGCAGAAC-3', 5'-GCCAATCAGAGAGAGCGAAC-3'; *MCAD*, 5'-CACTGGGCACACAGTCTTCTTC-3', 5'-CCTTGCCCGAGCCTAAACT-3'; *Cpt1a* TRE, 5'-GGTGACGTTGGCTGAGCAA-3', 5'-TGAGCCCTGTACACGTTTTG-3'; *Cpt1a* intron, 5'-CAGCGCCTTGAACTTGCA-3', 5'-CAAACGGTCAAAGTACAGGAAAGTC-3'.

**RNA isolation and real-time PCR analysis.** Tissue samples were homogenized using a TissueLyser (Qiagen). RNA was isolated using a RNeasy lipid tissue kit (Qiagen) then subjected to reverse transcription (Applied Biosystems). mRNA transcripts were quantified by real-time PCR analysis using TaqMan (Applied Biosystems) or Sybr (Applied Biosystems). Samples were analysed using a Prism 7900 thermal cycler and sequence detector (Perkin Elmer/ABI). Sybr dissociation curves always indicated the formation of a single PCR product. Data was analysed with a threshold set in the linear range of amplification and processed on the basis of a standard curve of serial tenfold dilutions for each primer set. The gene of interest was normalized to an unaffected endogenous control gene (*GAPDH* or *36B4*) and plotted as mean fold change ( $\pm$  s.e.m.). Statistical analysis was performed using a Student's *t*-test.

31. Kapfhammer, D. *et al.* Mutations in *Rab3a* alter circadian period and homeostatic response to sleep loss in the mouse. *Nature Genet.* **32**, 290–295 (2002).
32. Qi, Y. *et al.* Loss of resistin improves glucose homeostasis in leptin deficiency. *Diabetes* **55**, 3083–3090 (2006).
33. Balsalobre, A., Damiola, F. & Schibler, U. A serum shock induces circadian gene expression in mammalian tissue culture cells. *Cell* **93**, 929–937 (1998).
34. Ishizuka, T. & Lazar, M. A. The N-CoR/histone deacetylase 3 complex is required for repression by thyroid hormone receptor. *Mol. Cell. Biol.* **23**, 5122–5131 (2003).

# Conformational changes in an ultrafast light-driven enzyme determine catalytic activity

Olga A. Sytina<sup>1</sup>, Derren J. Heyes<sup>2</sup>, C. Neil Hunter<sup>3</sup>, Maxime T. Alexandre<sup>1</sup>, Ivo H. M. van Stokkum<sup>1</sup>, Rienk van Grondelle<sup>1</sup> & Marie Louise Groot<sup>1</sup>

The role of conformational changes in explaining the huge catalytic power of enzymes is currently one of the most challenging questions in biology<sup>1–7</sup>. Although it is now widely regarded that enzymes modulate reaction rates by means of short- and long-range protein motions<sup>3–7</sup>, it is almost impossible to distinguish between conformational changes and catalysis. We have solved this problem using the chlorophyll biosynthetic enzyme NADPH:protochlorophyllide (Pchl<sub>id</sub>) oxidoreductase, which catalyses a unique light-driven reaction involving hydride and proton transfers<sup>8</sup>. Here we report that prior excitation of the enzyme-substrate complex with a laser pulse induces a more favourable conformation of the active site, enabling the coupled hydride and proton transfer reactions to occur. This effect, which is triggered during the Pchl<sub>id</sub> excited-state lifetime and persists on a long timescale, switches the enzyme into an active state characterized by a high rate and quantum yield of formation of a catalytic intermediate. The corresponding spectral changes in the mid-infrared following the absorption of one photon reveal significant conformational changes in the enzyme, illustrating the importance of flexibility and dynamics in the structure of enzymes for their function.

Dehydrogenase enzymes catalyse proton and hydride transfer reactions with rate enhancements of up to  $10^{17}$  in comparison with the equivalent reaction in solution<sup>1</sup>. However, understanding the role of conformational changes in this catalytic power is challenging, as the hydrogen transfer processes are much faster than the structural changes associated with switching of an enzyme from an 'inactive' to an 'active' conformation<sup>9–11</sup>.

Here we study an enzyme from the family of alcohol dehydrogenases, NADPH:protochlorophyllide oxidoreductase (POR), which has provided a unique opportunity to observe the light-driven formation of an activated enzyme conformation before catalysis. The requirement of light for initiation of catalysis by POR makes it an excellent model system for studying the mechanism and time-scales of enzymatic proton and hydride transfers, as the enzyme-substrate complex can be pre-formed in the dark and catalysis initiated by a short pulse of light<sup>8</sup>. POR catalyses the *trans* addition of hydrogen from NADPH across the C17–C18 double bond of the D ring of Pchl<sub>id</sub> to produce chlorophyllide (Chl<sub>id</sub>)<sup>12</sup>, which is an important regulatory step for chlorophyll biosynthesis and the subsequent assembly of the photosynthetic apparatus<sup>8,12,13</sup>. It is proposed that a conserved Tyr residue donates a proton to the C18 position<sup>14</sup> and a hydride is transferred from the *proS* face of the NADPH nicotinamide ring to the C17 position of the Pchl<sub>id</sub> molecule<sup>15,16</sup> (Fig. 1). The involvement of the Pchl<sub>id</sub> excited state in the reduction suggests that significant parts of the reaction may occur on the picosecond timescale. Indeed, we have previously shown that catalysis can be

triggered with a 50-fs laser pulse, and, using ultrafast pump–probe absorption spectroscopy, observed that the formation of a reaction intermediate in the excited state proceeds with time constants of 3 ps and 400 ps (ref. 17). In addition, following the formation of the POR–Chl<sub>id</sub>–NADP<sup>+</sup> state there is a series of ordered product release and cofactor binding events in which domain movements and/or reorganization of the protein have an important role<sup>18–21</sup>.

Here we use ultrafast pump–probe absorption difference spectroscopy to study the initial catalytic steps in more detail, which reveals that a critical light-driven activation of the enzyme is required before catalysis. The use of a Lissajous sample scanner in combination with very high detection sensitivity facilitates quantitative measurements under single-pulse conditions, allowing us to measure reaction rates and quantum yields as functions of the total number of laser shots previously seen by the sample. Our spectrometer ensures that in each scan the sample is illuminated by only one shot of the laser, with an excitation density of  $\sim 0.03$  absorbed photons per enzyme-substrate complex. The time-dependent absorption difference spectra obtained after a laser pulse are shown in Fig. 2 for a number of subsequent scans in the form of evolution-associated-difference spectra (EADS). The EADS result from a global analysis of the data in which the time-dependent behaviour of the absorption difference spectra is fitted to three exponentials that evolve in a sequential manner,  $A \rightarrow B \rightarrow C \rightarrow$ , with increasing lifetimes  $\tau_1$ ,  $\tau_2$  and  $\tau_3$ . The

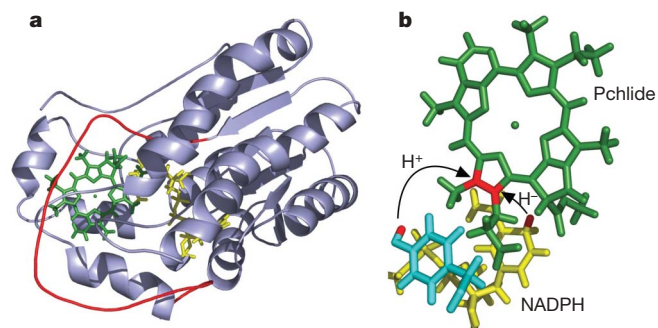


**Figure 1 | Homology model of POR from *Synechocystis*<sup>24</sup>.** **a**, The structure consists of a central parallel  $\beta$ -sheet comprising seven  $\beta$ -strands, surrounded by nine  $\alpha$ -helices. The 33-residue insertion (red) is unique to POR, and is proposed to be involved in Pchl<sub>id</sub> (green) binding. **b**, Three-dimensional model of the POR-catalysed reaction based on the structural homology model of POR<sup>24</sup> and the proposed mechanism of hydride and proton transfers<sup>14</sup>. The proton at the C18 position of Pchl<sub>id</sub> is derived from Tyr 189 (numbering in *Synechocystis* POR, cyan) and the hydride transferred to the C17 position is derived from the *proS* face of NADPH (yellow).

<sup>1</sup>Department of Physics and Astronomy, Faculty of Sciences, Vrije Universiteit, De Boelelaan 1081, 1081 HV Amsterdam, The Netherlands. <sup>2</sup>Manchester Interdisciplinary Biocentre, University of Manchester, 131 Princess Street, Manchester M1 7DN, UK. <sup>3</sup>Department of Molecular Biology and Biotechnology, University of Sheffield, Firth Court, Western Bank, Sheffield S10 2TN, UK.



EADS represent the spectra of the states A, B and C. Inspection of the absorption difference spectra shows that, although the enzyme shows spectral evolution on an ultrafast timescale, it is clear that prior exposure to light has a marked influence on the dynamics and, more profoundly, the yield of the reaction.

All scans show a negative band that peaks at 640 nm and originates in the laser-excited, enzyme-bound Pchlide substrate. However, in the later scans a significant negative band also appears at  $\sim 675$  nm, owing to a Chlide-precursor species formed in its excited state (Fig. 2b, c)<sup>17</sup>. Recent theoretical studies<sup>22</sup> together with preliminary experimental data (Supplementary Fig. 1) suggest that this precursor species ( $I_{675}^*$ ) is likely to represent a state in which Pchlide forms a strongly hydrogen-bonded complex with residues in its direct environment and/or NADPH, which is essential for the subsequent hydride and proton transfer steps to proceed on a microsecond time-scale. In the initial scans there is a progressive blue shift of the signal at 640 nm, in combination with a loss of stimulated emission at the red end of this band (Fig. 2a), and only a very small amount of negative signal at  $\sim 675$  nm is formed in 700 ps. The formation time and yield of the negative 675-nm signal, indicative of the  $I_{675}^*$  precursor, is completely dependent upon the scan number; in later scans  $I_{675}^*$  formation occurs with 4-ps and 500-ps time constants and with a much higher yield (Fig. 2c). In addition, direct excitation of the Chlide product, formed during previous scans, is observed in the later scans, as the signal at  $\sim 670$  nm is negative in the time-zero spectra (black spectra in Fig. 2b, c).

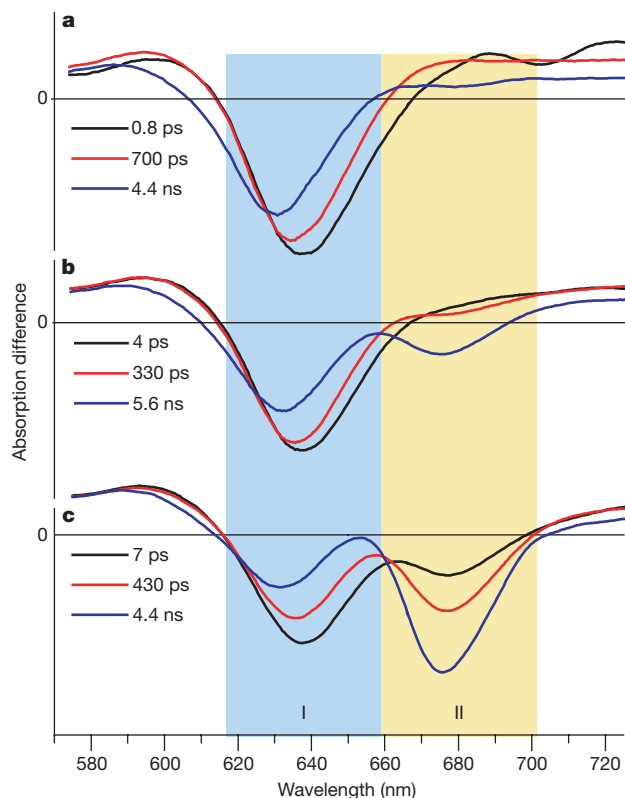


**Figure 2 | Evolution-associated difference spectra resulting from a global analysis, as a function of illumination time.** A sequential model with increasing lifetimes was used. Excitation of the POR–Pchlide–NADPH enzyme-substrate complex was at 475 nm (using a 50-fs laser pulse<sup>25</sup>), the induced absorption changes were recorded at 48 different time points between 10 ps and 5 ns, and one spectrum consists of 256 spectral points. Region I is composed of bleached absorption and stimulated emission from the Pchlide substrate, and in region II the stimulated emission signal is observed from the  $I_{675}^*$  product formed in the excited state. **a**, Scans 1 and 2; **b**, scans 6–12; **c**, scans 26–55. The vertical scale corresponds to an absorption change of  $-30 \times 10^{-3}$ .

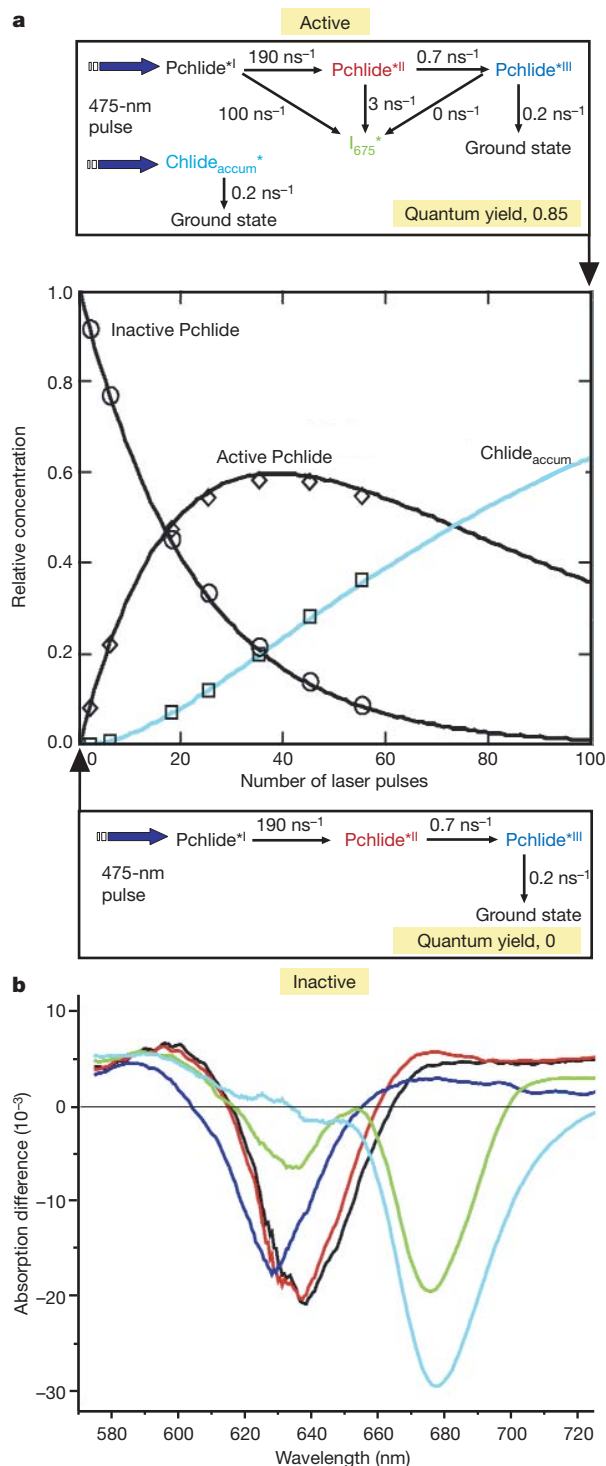


**Figure 3 | Target analysis<sup>26</sup> of the illumination-dependent POR pump-probe data sets.** **a**, Model for the ultrafast catalytic reactions in POR: kinetic scheme for active enzymes that can form the photoproduct  $I_{675}^*$  (top); concentration of active (diamonds) and inactive (circles) enzymes and accumulated Chlide (squares) as a function of applied laser pulse (middle); kinetic scheme for inactive enzymes, showing only Pchlide<sup>\*</sup> photochemistry (from Pchlide<sup>\*I</sup> to Pchlide<sup>\*II</sup> to Pchlide<sup>\*III</sup>) (bottom). The concentrations at  $t = 0$  of inactive and active enzymes and Chlide accumulated in previous scans (Chlide<sub>accum</sub><sup>\*</sup>) are assumed to follow the populations of unexcited, singly excited and twice-excited enzymes, respectively (solid lines drawn for an excitation density of 0.045/pulse). **b**, Species-associated difference spectra of POR of the Pchlide<sup>\*I</sup>, Pchlide<sup>\*II</sup>, Pchlide<sup>\*III</sup>,  $I_{675}^*$  and Chlide<sub>accum</sub><sup>\*</sup> states obtained from the target analysis; the spectra are colour coded to match the states in **a**.

To analyse the data in more detail, we fit the full set of spectra to a minimal model (Fig. 3a). In this model we divide the POR enzyme population into an 'inactive' fraction, which describes the Pchl $de^*$  dynamics (between the states denoted Pchl $de^*I$ , Pchl $de^*II$  and Pchl $de^*III$ , in that order), and an 'active' fraction, in which there is an additional reaction path from each of the Pchl $de^*I$ , Pchl $de^*II$  and Pchl $de^*III$  states to  $I_{675}^*$ . Also, the directly excited Chlide formed in previous scans is included. The results of this target analysis are shown in Fig. 3, and representative traces and fits can be found in the Supplementary Information.

The size of the fraction of active enzyme is dependent on the number of laser pulses and increases in a similar manner to the proportion of enzymes that have been excited at least once. In fully light-activated enzymes, the quantum yield of transformation of Pchl $de$  to the Chlide precursor  $I_{675}^*$  is 0.85, of which 0.35 occurs by means of the single-step mechanism, with an effective rate of  $\sim 300\text{ ns}^{-1}$  (Fig. 3a), and 0.5 by means of the two-step mechanism, with an effective rate of  $3.7\text{ ns}^{-1}$ . Also, the accumulating concentration of Chlide (Fig. 3a, cyan curve) can be described with a yield of 0.3 for the  $I_{675}^*$ -to-Chlide reaction, consistent with previous quantum yield measurements of 0.21 (ref. 18). Because we exclude any possible effects of temperature or changing sample conditions during each scan (Supplementary Fig. 2), there must be a direct relationship between the rate of the reaction and the level of illumination, in terms of the number of laser pulses used for prior activation of the enzyme-substrate complexes. Therefore, it appears that catalysis cannot proceed until the enzyme-substrate complex has been excited at least once, suggesting that the first photon turns the enzyme 'on', whereas the second photon induces catalysis. Additional experiments, in which we place an activated enzyme sample in the dark for several periods of time, reveal that the active conformation persists for at least 19 hours (Supplementary Fig. 4), suggesting that the enzyme-substrate complex has a 'memory' which lasts for a long time relative to the timescale of the catalytic events. In addition, we also show that, upon completion of a single turnover and mixing with fresh Pchl $de$ , POR retains between 80 and 100% of its catalytic activity (Supplementary Fig. 5).

These results demonstrate that the rate and quantum yield of formation of the intermediate state  $I_{675}^*$  is significantly enhanced after the Pchl $de$  substrate has cycled through the excited state at least once. This effect may arise from a more favourable catalytic configuration of the enzyme-substrate complex, caused by the changed electron distribution in the Pchl $de$  excited state. To investigate

whether conformational changes in the enzyme are induced upon the absorption of a photon, we recorded absorption difference spectra in the mid-infrared region under illumination conditions similar to those used in Fig. 3. The difference spectra (light-induced minus dark) are recorded every second using a Fourier transform infrared (FTIR) spectrometer in rapid-scan mode, while flashing with 5-ns laser pulses at a 20-Hz repetition rate to excite the enzyme-substrate complex. The traces recorded between 1,800 and 1,250  $\text{cm}^{-1}$  (Fig. 4a) clearly show different saturation behaviours at different frequencies, suggesting the occurrence of two or more different light-induced processes. The time- or photon-flux-dependent behaviour of the data can be described with a sequential model,  $A \rightarrow B \rightarrow C$ , with increasing lifetimes/photon fluxes  $\tau_1$ ,  $\tau_2$  and  $\tau_3$ , resulting in the spectra depicted in Fig. 4b. The presence of relatively large signals in the amide I and II regions shows that brief illumination of the enzyme-substrate complex (corresponding to 20 flashes of 5-ns laser pulses) yields conformational changes in the secondary structure of the enzyme. The amplitude of these signals is increased by further illumination of the sample (Fig. 4b, red spectrum), and the conformational change in POR has an extremely long lifetime of many minutes (Supplementary Fig. 6). However, in neither case are these signals accompanied by catalytic activity; only continued illumination produces the mid-infrared signatures for the disappearance of Pchl $de$  and NADPH and the formation of Chlide and  $\text{NADP}^+$  (Fig. 4b, blue spectrum).

The two distinct phases in the mid-infrared spectral evolution clearly indicate that the enzyme undergoes two separate processes upon illumination: there is an initial structural optimization, and then—only after continued illumination—is Pchl $de$  converted into Chlide. Combining the results from the femtosecond visible pump-probe and those in the mid-infrared, we conclude that absorption of the first photon activates the enzyme, which results in a high quantum yield formation of  $I_{675}^*$  on the picosecond timescale when a second photon is absorbed. The structural changes are currently difficult to quantify using the spectroscopic changes in the infrared, and may involve minor structural rearrangements, optimizing the alignment of the NADPH-nicotinamide ring and the Tyr residue with the D ring of Pchl $de$  to increase the rate of the hydride and proton transfers. On the other hand, the long lifetime and the fact that activation is not reversed upon turnover of the enzyme may suggest an irreversible process in the POR protein. It would appear that the conformational change is both highly efficient (that is, it needs only one photon) and very specific, resulting in a high catalytic

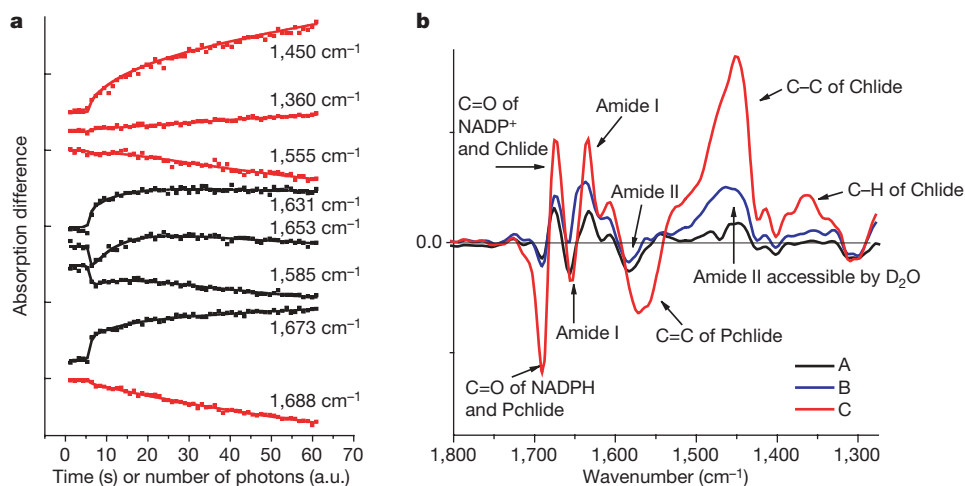


**Figure 4 | Mid-infrared absorption difference data.** **a**, Selected time/photon flux traces; **b**, corresponding evolution-associated difference spectra. The EADS result from a global analysis of the light-induced minus dark difference spectra using a sequential model with increasing lifetimes,  $A \rightarrow B \rightarrow C$ . Negative bands arise from the disappearance of infrared

absorption associated with Pchl $de$  and NADPH substrates and the POR protein in the dark state, and positive bands are due to the appearance of new species in the reaction upon illumination, such as Chlide,  $\text{NADP}^+$  and POR in its active conformation. a.u., arbitrary units.

quantum yield. It is likely that such a directional conformational change underlies efficient hydrogen and proton transfers in many other enzymes.

Several other enzymes have been found to have a 'rest' conformation and a second conformation in which the enzyme is 'active'<sup>9,10,23</sup>. In POR, however, we find that the active conformation is retained during and after turnover. This light-adaptation of POR may have an important role in green plants and other photosynthetic organisms, as it allows the enzyme to capitalize on very low or erratic photon fluxes by remaining in an activated, catalytically efficient state for long periods.

## METHODS SUMMARY

**Composition of the samples.** POR from the cyanobacterium *Thermosynechococcus elongatus* BP-1 was produced as previously described<sup>18</sup>. The samples contained 0.5 mM Pchl<sub>a</sub>, 0.5 mM POR and 2.5 mM NADPH in activity buffer (50 mM Tris (pH 7.5), 100 mM NaCl, 1% Genapol, 0.1%  $\beta$ -mercaptoethanol) and were kept in the dark at all times. For FTIR spectroscopy experiments the H<sub>2</sub>O in the buffer was replaced by D<sub>2</sub>O.

**Visible pump-probe experiments.** Absorption difference spectra at 48 different time points between -10 ps and 5 ns were collected with a set-up based on a 1-kHz amplified laser system, described in more detail in the Methods. The collection of each data set took 40 s, during which each part of the sample was illuminated by a single shot of the laser. Hence, in subsequent scans the sample was illuminated by more laser pulses.

**Target analysis.** A full description of the target analysis is given in the Methods. **FTIR spectroscopy experiments.** Light-induced minus dark difference spectra were measured by means of an FTIR Bruker IFS 66/S spectrometer in rapid-scan mode. First we collected infrared steady-state absorption spectra of the POR-NADPH-Pchl<sub>a</sub> complex in the dark, as the background, and then we recorded the induced absorption changes every second while the whole area of the sample cell was excited at 444 nm by the 20-Hz output of a Continuum Panther optical parametric oscillator pumped by a Continuum Surelite I-20 Nd:YAG laser.

**Full Methods** and any associated references are available in the online version of the paper at [www.nature.com/nature](http://www.nature.com/nature).

Received 19 February; accepted 15 August 2008.

- Benkovic, S. J. & Hammes-Schiffer, S. A perspective on enzyme catalysis. *Science* **301**, 1196–1202 (2003).
- Villà, J. & Warshel, A. Energetics and dynamics of enzymatic reactions. *J. Phys. Chem. B* **105**, 7887–7907 (2001).
- Masgrau, L. *et al.* Atomic description of an enzyme reaction dominated by proton tunneling. *Science* **312**, 237–241 (2006).
- Kohen, A., Cannio, R., Bartolucci, S. & Klinman, J. P. Enzyme dynamics and hydrogen tunnelling in a thermophilic alcohol dehydrogenase. *Nature* **399**, 496–499 (1999).
- Eisenmesser, E. Z. *et al.* Intrinsic dynamics of an enzyme underlies catalysis. *Nature* **438**, 117–121 (2005).
- Agarwal, P. K. Role of protein dynamics in reaction rate enhancement by enzymes. *J. Am. Chem. Soc.* **127**, 15248–15256 (2005).
- Wang, L., Goodey, N. M., Benkovic, S. J. & Kohen, A. Coordinated effects of distal mutations on environmentally coupled tunneling in dihydrofolate reductase. *Proc. Natl Acad. Sci. USA* **103**, 15753–15758 (2006).
- Heyes, D. J. & Hunter, C. N. Making light work of enzyme catalysis: protochlorophyllide oxidoreductase. *Trends Biochem. Sci.* **30**, 642–649 (2005).
- Eisenmesser, E. Z., Bosco, D. A., Akke, M. & Kern, D. Enzyme dynamics during catalysis. *Science* **295**, 1520–1523 (2002).
- Flomenbom, O. *et al.* Stretched exponential decay and correlations in the catalytic activity of fluctuating single lipase molecules. *Proc. Natl Acad. Sci. USA* **102**, 2368–2372 (2005).

- Boehr, D. D., McElheny, D., Dyson, H. J. & Wright, P. E. The dynamic energy landscape of dihydrofolate reductase catalysis. *Science* **313**, 1638–1642 (2006).
- Lebedev, N. & Timko, M. P. Protochlorophyllide photoreduction. *Photosyn. Res.* **58**, 5–23 (1998).
- Griffiths, W. T. Reconstruction of chlorophyllide formation by isolated etioplast membranes. *Biochem. J.* **174**, 681–692 (1978).
- Wilks, H. M. & Timko, M. P. A light-dependent complementation system for analysis of NADPH:protochlorophyllide oxidoreductase. Identification and mutagenesis of two conserved residues that are essential for enzyme activity. *Proc. Natl Acad. Sci. USA* **92**, 724–728 (1995).
- Valera, V., Fung, M., Wessler, A. N. & Richards, W. R. Synthesis of 4R- and 4S-tritium labeled NADPH for the determination of the coenzyme stereospecificity of NADPH:protochlorophyllide oxidoreductase. *Biochem. Biophys. Res. Commun.* **148**, 515–520 (1987).
- Begley, T. P. & Young, H. Protochlorophyllide reductase. 1. Determination of the regiochemistry and the stereochemistry of the reduction of protochlorophyllide to chlorophyllide. *J. Am. Chem. Soc.* **111**, 3095–3096 (1989).
- Heyes, D. J., Hunter, C. N., van Stokkum, I. H. M., van Grondelle, R. & Groot, M. L. Ultrafast enzymatic reaction dynamics in protochlorophyllide oxidoreductase. *Nature Struct. Biol.* **10**, 491–492 (2003).
- Heyes, D. J., Ruban, A. V., Wilks, H. M. & Hunter, C. N. Enzymology below 200K: the kinetics and thermodynamics of the photochemistry catalysed by protochlorophyllide oxidoreductase. *Proc. Natl Acad. Sci. USA* **99**, 11145–11150 (2002).
- Heyes, D. J. & Hunter, C. N. Identification and characterization of the product release steps within the catalytic cycle of protochlorophyllide oxidoreductase. *Biochemistry* **43**, 8265–8271 (2004).
- Heyes, D. J. *et al.* The first catalytic step of the light-driven enzyme protochlorophyllide oxidoreductase proceeds via a charge transfer complex. *J. Biol. Chem.* **281**, 26847–26853 (2006).
- Heyes, D. J., Ruban, A. V. & Hunter, C. N. protochlorophyllide oxidoreductase: 'Dark' reactions of a light-driven enzyme. *Biochemistry* **42**, 523–528 (2003).
- Zhao, G.-J. & Han, K.-L. Site-specific solvation of the photoexcited protochlorophyllide *a* in methanol: formation of the hydrogen-bonded intermediate state induced by hydrogen-bond strengthening. *Biophys. J.* **94**, 38–46 (2008).
- Lu, H. P., Xun, L. & Xie, X. S. Single-molecule enzymatic dynamics. *Science* **282**, 1877–1882 (1998).
- Townley, H. E., Sessions, R. B., Clarke, A. R., Dafforn, T. R. & Griffiths, W. T. Protochlorophyllide oxidoreductase: A homology model examined by site-directed mutagenesis. *Proteins* **44**, 329–335 (2001).
- Groot, M. L., Breton, J., van Wilderen, L. J. G. W., Dekker, J. P. & van Grondelle, R. Femtosecond visible/visible and visible/mid-IR pump-probe study of the photosystem II core antenna complex CP47. *J. Phys. Chem. B* **108**, 8001–8006 (2004).
- van Stokkum, I. H. M., Larsen, D. S. & van Grondelle, R. Global and target analysis of time-resolved spectra. *Biochim. Biophys. Acta* **1657**, 82–104 (2004).

**Supplementary Information** is linked to the online version of the paper at [www.nature.com/nature](http://www.nature.com/nature).

**Acknowledgements** This research was supported by The Netherlands Organization for Scientific Research through the Dutch Foundation for Earth and Life Sciences (Investment Grant no. 834.01.002). M.L.G. is grateful to NWO-ALW for providing financial support with a long-term fellowship (Grant no. 831.00.004) and O.S. received support from NWO-CW (Grant no. 700.53.307). D.J.H. and C.N.H. gratefully acknowledge support from the Biotechnology and Biological Sciences Research Council, UK. We thank H. Fidler and F. van Mourik for reading the manuscript.

**Author Contributions** O.A.S., D.J.H., M.T.A. and M.L.G. produced the samples and performed all of the experiments. O.A.S., I.H.M.v.S. and M.L.G. analysed the data. D.J.H., C.N.H., R.v.G. and M.L.G. coordinated the study, designed the experiments and wrote the paper. All authors discussed the results and commented on the manuscript.

**Author Information** Reprints and permissions information is available at [www.nature.com/reprints](http://www.nature.com/reprints). Correspondence and requests for materials should be addressed to C.N.H. ([c.n.hunter@sheffield.ac.uk](mailto:c.n.hunter@sheffield.ac.uk)).



## METHODS

**Ultrafast pump–probe spectroscopy.** The laser set-up has been described previously<sup>25</sup>. Briefly, the output of a regenerative Ti:sapphire amplifier operating at 1 kHz (Hurricane, Spectra Physics), producing 85-fs pulses of ~0.8 mJ, was used to pump a non-collinear optical amplifier. This amplifier was tuned to 475 nm to excite the complexes at the red edge of the Soret band (S0 → S2 transition) of Pchl<sub>ide</sub>, where the absorption of the product Chl<sub>ide</sub> is minimal. The excitation energy per laser flash was 100 nJ, focused to a spot of about 150-μm diameter. A small part of the 800-nm output was used to generate a white light continuum in a sapphire plate and, after interrogating the sample, was dispersed in a spectrograph and detected on a 256-element diode array read out at 1 kHz. Detection was in the wavelength region 600–700 nm, probing the S0 ↔ S1 transition of Pchl<sub>ide</sub> and products. The polarization of the probe light was at the ‘magic angle’ (54.7°) with respect to the excitation light. The instrument response function was about 130 fs. The sample was put in a CaF<sub>2</sub> cell of 200-μm path length, contained in a Lissajous sample scanner. The scanner was moved at such speed that a new part of the sample was illuminated at every shot (the shots taken at the corners of the scanned area, where the scanner velocity is lower, were discarded). The same volume was illuminated again after 1–2 min. One scan of the pump–delay line, recording data from –15 ps to 6 ns, took ~40 s, so each scan corresponds to one laser pulse with an energy density of ~0.03 photons per enzyme. Previous ultrafast transient absorption measurements on POR have used a flow cell for the sample (~4 ml) and the acquisition time of one scan was approximately 10 min (ref. 11). All experiments were performed at room temperature (22 °C). The data was analysed using a global fit algorithm<sup>25</sup>. The spectra shown in Fig. 2 are the averages of spectra recorded on three freshly prepared samples.

**Temperature effects.** A simple calculation shows that negligible water heating occurs in our experiment. If we suppose that half of the laser energy ( $E = 100$  nJ) is absorbed by the sample, it can be calculated that with a volume of 0.1 ml (the water thermal capacity being  $4 \text{ J ml}^{-1} \text{ K}^{-1}$ ), we would need  $8 \times 10^6$  laser shots to heat the water by 1 K, which at 500 Hz takes 4 h. This is neglecting thermalization with the environment. In a similar way, we can calculate with convection equations that if the sample is at 5 °C when it is put into the cell, it takes only about 77 s to reach room temperature. Thus, we may consider the enzymes to be at room temperature during the experiments.

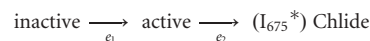
**FTIR spectroscopy experiments.** The infrared absorption difference signals in the frequency range  $1,660\text{--}1,630 \text{ cm}^{-1}$  can be assigned to the amide I protein band<sup>27</sup> and the bleaches of absorption at both  $1,580 \text{ cm}^{-1}$  and at  $1,470 \text{ cm}^{-1}$  to amide II<sup>28</sup>, the former representing amide groups not accessible by D<sub>2</sub>O and the latter representing amide groups that are accessible by the solvent. Differential bands between  $1,690$  and  $1,670 \text{ cm}^{-1}$  were assigned to carbonyl vibrations of NADPH/NADP<sup>+</sup> (ref. 28) and Pchl<sub>ide</sub>/Chl<sub>ide</sub><sup>29–31</sup>. The  $1,570\text{--}1,450 \text{ cm}^{-1}$  differential signal is assigned to the Pchl<sub>ide</sub>-to-Chl<sub>ide</sub> conversion process representing disappearance of a C=C mode and appearance of a C–C mode<sup>29–31</sup>. The signal around  $1,360 \text{ cm}^{-1}$  was assigned to the appearance of a chlorin C–H mode<sup>29–31</sup>, and therefore signals formation of Chl<sub>ide</sub>.

**Global analysis.** For each illumination condition, all 48 time-gated spectra (measured at 256 wavelengths) were collated in a matrix, which was globally fitted using a sequential kinetic scheme with increasing lifetimes<sup>26</sup>. From this the lifetimes and the EADS were estimated. The quality of the fit was judged by inspection of the singular vectors of the matrix of residuals, which had to be structureless. The instrument response function was described by a Gaussian shape, and the white-light dispersion over the spectral range was modelled as a second-order polynomial. With increasing lifetimes, and thus decreasing rates, the first of the EADS decays with the first lifetime and corresponds to the difference spectrum at time zero with an ideal, infinitely small instrument response function. The second of the EADS is formed with the first lifetime and decays with the second lifetime. The third of the EADS (and in our case the final one) represents the difference spectrum of the longest-living species. It is formed with the second lifetime and decays with the third lifetime. The error in the lifetimes obtained from the fitting procedure does not exceed 10%. EADS may not represent pure species, and they are interpreted as a weighted sum (with only positive contributions) of species-associated difference spectra (SADS). Referring to Fig. 2, we note that in the blue spectral region (612–656 nm) an evolution of the Pchl<sub>ide</sub>\* bleaching and stimulated emission is observed, whereas in the red spectral region (656–700 nm) Pchl<sub>ide</sub>\* excited-state absorption, as well as Chl<sub>ide</sub>\* bleaching and stimulated emission, contributes.

**Target analysis.** To resolve the SADS from the EADS, a target analysis was performed simultaneously on data from all seven illumination conditions (~98,000 data points in total). In this target analysis, the kinetic scheme from Fig. 3a was used to estimate the microscopic rate constants and SADS of the three

successive Pchl<sub>ide</sub>\* species (black, red and blue), the accumulated Chl<sub>ide</sub>\* (Chl<sub>ide</sub><sub>accum</sub>\*, cyan) bleaching and stimulated emission, and the stimulated emission of the I<sub>675</sub>\* product (green). We assume that the Pchl<sub>ide</sub>\* photochemistry is intrinsic for Pchl<sub>ide</sub>\* and therefore independent of the activation state of the protein.

The concentrations of inactive and active enzymes and of Chl<sub>ide</sub><sub>accum</sub>\* at  $t = 0$  for each successive scan are assumed to depend on the number of applied laser pulses according to the analytical expression for the concentration of unexcited, singly excited and twice-excited enzymes obtained by solving the coupled differential equations belonging to the following rate equation:



Here  $e_1$  is the excitation rate per pulse and  $e_2$  is the excitation rate per pulse multiplied by the quantum yield of Chl<sub>ide</sub> formation. I<sub>675</sub>\* is set within parentheses because it is a short-lived intermediate and, therefore, its concentration at the moment of excitation will be zero. Fitting this model to the data, we obtain the estimated rate constant for each reaction, as indicated in the schemes, 0.045 per pulse for the excitation rate and  $0.3 \pm 0.1$  for the quantum yield (QY) of Chl<sub>ide</sub> formation. The quantum yield of I<sub>675</sub>\* product formation in activated enzymes is 0.85, which is obtained from the following expression:  $\text{QY} = k_{\text{product}} / (k_{\text{product}} + k_{\text{loss}})$ . Here  $k_{\text{product}}$  and  $k_{\text{loss}}$  refer to the rates towards the I<sub>675</sub>\* state and to the Pchl<sub>ide</sub>\*<sup>II</sup> (or Pchl<sub>ide</sub>\*<sup>III</sup>) state, respectively. The quantum yield for product formation in inactive enzymes is zero. Therefore, in this experiment, by measuring the dynamics on a picosecond timescale and the concentrations of the different populations at time zero, we independently determine the quantum yield of formation of both I<sub>675</sub>\* and Chl<sub>ide</sub> formation and find them to be 0.85 and 0.3, respectively.

The estimated difference spectra of the Pchl<sub>ide</sub>\*<sup>I</sup>, Pchl<sub>ide</sub>\*<sup>II</sup> and Pchl<sub>ide</sub>\*<sup>III</sup> states (respectively black, red and blue) are flat in the 670–720-nm region and represent pure Pchl<sub>ide</sub> spectra. The Pchl<sub>ide</sub>\*<sup>III</sup> spectrum most likely represents a fraction of Pchl<sub>ide</sub> not bound to the POR enzyme, whereas the Pchl<sub>ide</sub>\*<sup>I</sup>-to-Pchl<sub>ide</sub>\*<sup>II</sup> dynamic process is probably due to vibrational relaxation. In previous work, we showed that formation of the state emitting at 675 nm depends on the presence of NADPH and the Tyr 189 proton donor<sup>17</sup>. H<sup>+</sup> transfer most likely occurs with a rate of  $2 \times 10^6 \text{ s}^{-1}$  (Supplementary Fig. 1); therefore, we believe that the state emitting at 675 nm is an intermediate in the catalytic reaction and represents the formation of a hydrogen-bonded complex. The spectrum resolved for the I<sub>675</sub>\* state (green) shows negative bands at 675 nm and 640 nm, consistent with stimulated emission from I<sub>675</sub>\* and bleached absorption of Pchl<sub>ide</sub>. Finally, the spectrum of the state Chl<sub>ide</sub><sub>accum</sub>\* (cyan) is consistent with that of directly excited Chl<sub>ide</sub>, which is formed in previous scans on a timescale longer than nanoseconds, outside the measuring window of the current experiment.

The root-mean-square error of the fit was  $0.9 \times 10^{-3}$ , which means that, with a maximum signal of  $26 \times 10^{-3}$ , the signal-to-noise ratio is almost 30. The matrices of residuals resulting from the target analysis were further analysed using a singular value decomposition<sup>25</sup>. The first left-singular vectors from all seven experiments (Supplementary Fig. 3) show no structure, indicating that all kinetics are described satisfactorily. The structure in the first right-singular vector (Supplementary Fig. 3) resembles the Chl<sub>ide</sub> spectrum, which probably indicates that the noise in the measurement arises from small fluctuations in the transmission of the sample (due to varying relative amounts of Pchl<sub>ide</sub> and Chl<sub>ide</sub> caused by the fact that the movement of the Lissajous scanner is not locked to the acquisition), rather than from noise in the laser pulses.

27. Barth, A. & Zscherp, C. What vibrations tell us about proteins. *Q. Rev. Biophys.* **35**, 369–430 (2002).
28. Iwaki, M., Cotton, N. P., Quirk, P. G., Rich, P. R. & Jackson, J. B. Molecular recognition between protein and nicotinamide dinucleotide in intact, proton-translocating transhydrogenase studied by ATR-FTIR Spectroscopy. *J. Am. Chem. Soc.* **128**, 2621–2629 (2006).
29. Nabedryk, E., Leonhard, M., Mäntele, W. & Breton, J. Fourier transform infrared difference spectroscopy shows no evidence for an enolization of chlorophyll a upon cation formation either in vitro or during P700 photooxidation. *Biochemistry* **29**, 3242–3247 (1990).
30. Hartwich, G., Geskes, C., Scheer, H., Heinze, J. & Maentele, W. Fourier transform infrared spectroscopy of electrogenerated anions and cations of metal-substituted bacteriochlorophyll a. *J. Am. Chem. Soc.* **117**, 7784–7790 (1995).
31. Mäntele, W. G., Wollenweber, A. M., Nabedryk, E. & Breton, J. Infrared spectroelectrochemistry of bacteriochlorophylls and bacteriopheophytins: Implications for the binding of the pigments in the reaction center from photosynthetic bacteria. *Proc. Natl Acad. Sci. USA* **85**, 8468–8472 (1988).

# naturejobs

**THE CAREERS  
MAGAZINE FOR  
SCIENTISTS**

**T**he battle for the US presidency has ended, but a visa storm may be brewing — and scientists could, in principle, be among the beneficiaries. Early this month, US president-elect Barack Obama nominated Arizona governor Janet Napolitano to head the Department of Homeland Security, which oversees citizenship and visas. Napolitano has been a staunch supporter of increasing the number of H1-B visas, which are used to hire foreign information-technology specialists, researchers and other highly skilled workers.

Critics say that H1-B visas take jobs from US workers. Proponents say they help to bring in qualified workers unavailable in the United States. Napolitano will probably face questions from both sides before she is confirmed in her new post. Already she is on record saying she supports granting foreign graduates of US universities green cards after they pass a security check, which would eliminate their need to apply for an H1-B visa. If she is appointed, Congress, not Napolitano, would set the cap number for H1-B visas, which is now at 65,000 (plus 20,000 more for people with US advanced degrees). But she could push for a higher cap and systemic changes.

Meanwhile, the European Union (EU) is moving closer to its own version of an H1-B scheme: the 'blue card', which would allow highly skilled workers and their families to live in the EU for three to five years, with the chance of permanent residence after that. The European Parliament approved the plan last month and member states will consider it early next year. It aims to increase the EU's skilled foreign workforce, which is 1.7% of the employed population, compared with 3.2% in the United States, 7.3% in Canada and 9.9% in Australia, according to Ewa Klamt, a member of the European Parliament.

But entry is, of course, only half the battle these days, as jobs continue to be shed. US unemployment has risen to a 15-year high of 6.7%, according to a labour department report earlier this month. Unfortunately, any action on visas may be accompanied by a sad irony: Western nations could open their doors to more foreign researchers just when there is a dearth of jobs for them to do.

**Paul Smaglik is moderator of the Nature Network career site.**

## CONTACTS

**Editor:** Gene Russo

**Assistant editor:** Karen Kaplan  
e-mail: [naturejobseditor@naturedc.com](mailto:naturejobseditor@naturedc.com)

**European Head Office, London**  
The Macmillan Building,  
4 Crinan Street, London N1 9XW, UK  
Tel: +44 (0) 20 7843 4961  
Fax: +44 (0) 20 7843 4996  
e-mail: [naturejobs@nature.com](mailto:naturejobs@nature.com)

**European Sales Manager:**  
Andy Douglas (4975)  
e-mail: [a.douglas@nature.com](mailto:a.douglas@nature.com)  
**Assistant European Manager:**  
Nils Moeller (4953)

**Natureevents:**  
Ghizlaine Ababou (+44 (0) 20 7014 4015)  
e-mail: [g.ababou@nature.com](mailto:g.ababou@nature.com)

**Southwest UK/RoW:**  
Alexander Ranken (4944)

## Northeast UK/Ireland:

Matthew Ward (+44 (0) 20 7014 4059)

**France/Switzerland/Belgium:**  
Muriel Lestringuez (4994)

**Scandinavia/Spain/Portugal/Italy:**  
Evelina Rubio-Hakansson (4973)

**North Germany/The Netherlands/Eastern**

**Europe:** Kerstin Vincze (4970)

**South Germany/Austria:**

Hildi Rowland (+44 (0) 20 7014 4084)

**Advertising Production Manager:**

Stephen Russell

To send materials use London address above.

Tel: +44 (0) 20 7843 4816

Fax: +44 (0) 20 7843 4996

e-mail: [naturejobs@nature.com](mailto:naturejobs@nature.com)

**Naturejobs web development:** Tom Hancock

**Naturejobs online production:** Dennis Chu

**US Head Office, New York**

75 Varick Street, 9th Floor,  
New York, NY 10013-1917

Tel: +1 800 989 7718

Fax: +1 800 989 7103

e-mail: [naturejobs@natureny.com](mailto:naturejobs@natureny.com)

**US Sales Manager:** Ken Finnegan

**India**

Vikas Chawla (+91 1242881057)

e-mail: [v.chawla@nature.com](mailto:v.chawla@nature.com)

**Japan Head Office, Tokyo**

Chiyoda Building, 2-37 Ichigayatamachi,  
Shinjuku-ku, Tokyo 162-0843

Tel: +81 3 3267 8751

Fax: +81 3 3267 8746

**Asia-Pacific Sales Manager:**

Ayako Watanabe (+81 3 3267 8765)

e-mail: [a.watanabe@natureasia.com](mailto:a.watanabe@natureasia.com)

**Business Development Manager, Greater**

**China/Singapore:**

Gloria To (+852 2811 7191)

e-mail: [g.to@natureasia.com](mailto:g.to@natureasia.com)



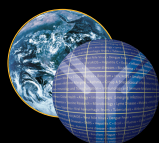
**Department of Health and Human Services  
National Institutes of Health  
National Institute of Mental Health  
Division of Intramural Research Programs**

The National Institute of Mental Health (NIMH), a major research component of the National Institutes of Health (NIH) and the Department of Health and Human Services (DHHS), is seeking exceptional candidates for the position of Deputy Scientific Director, Division of Intramural Research Programs (DIRP). The Deputy Scientific Director will work with the Scientific Director to lead and manage a vibrant intramural research program with more than 50 independent principal investigators, an extensive network of core service facilities (<http://intramural.nimh.nih.gov>), and a budget above \$160M.

The Deputy Scientific Director will assist in the recruitment of new faculty, oversee the expansion of the Division and its programs into several state-of-the-art research facilities on the NIH's Bethesda, Maryland campus and help manage the scientific resources at the NIMH DIRP.

Applicants must have a Ph.D., M.D., or equivalent degree in the biomedical sciences, with broad research experience and experience in direct administration of a multidisciplinary research program. Applicants may have the opportunity to perform independent and/or collaborative scientific studies. Applicants should be known and respected within their profession as distinguished individuals of outstanding scientific competence. Salary is commensurate with experience and accomplishments. Experience with NIH administrative policies, procedures, and operations is highly desirable but not essential.

Interested candidates should send a letter of interest, to include a complete description of research and administrative experience and rationale for applying for this particular position (2-3 pages maximum), contact information for at least six references, and a curriculum vitae and bibliography to: **Dr. Susan Swedo, Chair, Search Committee for Deputy Scientific Director, DIRP, NIMH, c/o steyer@mail.nih.gov or to Bldg. 10, Rm. 4N-222, 9000 Rockville Pike, Bethesda, MD 20892-1381.** Review of applications will begin on **March 2, 2009**, but applications will continue to be accepted and considered until the position is filled.



**NIAID**  
NATIONAL INSTITUTE OF ALLERGY  
AND INFECTIOUS DISEASES

## RESEARCH FELLOW

The National Institute of Allergy and Infectious Diseases (NIAID), a major research component of the National Institutes of Health (NIH) and the Department of Health and Human Services, is recruiting for a Research Fellow. The position will be available in the Molecular Pathology Section of the Laboratory of Immunopathology, and scientists with a M.D., Ph.D., or D.V.M. are eligible. The research activity involves (1) studies of the roles played by CTCF in imprinting, X chromosome inactivation, and the organization of transcriptional domains; and (2) analyses of BORIS expression and function in gametogenesis and stem/progenitor cells, in response to infectious agents, as well as the consequences of aberrant expression in cancers. This full-time research position offers a unique opportunity to work on investigations that range from basic molecular biology to studies of gene-manipulated mice in a collaborative environment, and provides excellent training for scientists who plan a career in molecular biology, infectious disease and cancer research.

Research Fellow applicants should have three or more years of relevant post-doctoral experience; the salary range is \$44,180 - \$108,319. A full package of benefits (including retirement, health, life and long term care insurance, Thrift Savings Plan participation, etc.) is available. Applicants with an M.D. degree are eligible for the NIH Loan Repayment Program. Applicants should send their curriculum vitae, a letter of interest, and names and addresses of three (3) references to Victor Lobanenko, Twinbrook I, Room 1417, 5640 Fishers Lane, Rockville, MD 20892, FAX: (301)-402-0077, email: [vlobanenko@niaid.nih.gov](mailto:vlobanenko@niaid.nih.gov)

For further information about NIAID and available job opportunities, please visit:

<http://healthresearch.niaid.nih.gov/dl>



THE NATIONAL INSTITUTES OF HEALTH

OPPORTUNITIES @ NIH





# Harnessing the brane-deer

It's a constant worry.

**Robert Billing**

"Fortunately," said the young squadron leader as the Land Rover bumped across the moonlit airfield, tyres hissing through the sprinkling of snow, "all eight reindeer managed to eject before it hit the ground, or we'd be scraping diced venison off the runway."

"Reindeer?" I asked. "I'm a physics teacher, not a zoo keeper."

"You'll see." He slalomed the vehicle between the blue edge lights and onto the runway. "The snow makes it easier to work out what happened. The tracks start here." He pointed to two narrow grooves in the snow. "The old chap made a good show of getting it down. It must have been handling like a brick but he managed to hit the runway and stop it more or less on the centre line."

The headlights picked out something scarlet in the distance. Something with runners. Something piled with sacks full of parcels. Beside it stood a rotund man in red, his fur-trimmed hood thrown back to reveal one of those big, greenish headsets that airline pilots wear, the microphone boom just in front of his snowy beard.

"You're having me on!" I complained, but my companion carried on driving.

"I wish I was." He parked the Land Rover alongside the sleigh. "It would be a lot easier than admitting that Father Christmas has just made a forced landing on an RAF station."

"So what do you want me to do?"

"Well, we've got this problem. We'd like to fix the sleigh and let him take off again but..." He trailed off into an embarrassed silence.

"But what?" I was cold, tired and in no mood to play games.

"We have absolutely no idea how it manages to stay up at all. Aerodynamically it's nonsense, there is no way that a reindeer can develop enough power to lift its own weight, let alone pull a sleigh off the ground."

I agreed. One particularly tubby specimen wandered up out of the darkness. I opened my window and gave it a peppermint from the packet in my coat pocket. For a moment my fingers were illuminated by a diffuse red glow.

"Did I just see its nose light up? No, don't tell me. Rudolf?"

The reindeer seemed to nod.

"The other problem," my companion said, "is the flight plan."

"What about it?"

"It's on a hard drive built into the sleigh's dashboard. There are several billion sets of coordinates, and a list of presents against each one."

"So?"

"To start and stop that many times in one night would mean accelerations of thousands of gees. And that would mean..."

"Diced venison?"

"Exactly. We think the two things are related. Whatever lets reindeer fly lets him

survive forces that would kill a human pilot in less than a second. Just think what that would mean..."

"Oh no! I am not doing this. I am not helping you convert Santa's sleigh into the ultimate fighter aircraft."

"For Queen and country?"

"No."

"A lot of money?"

"No." He paused, assessing my weak spot.

"You must realize that whoever finds out how this is done will revolutionize the world's transport systems, maybe even fix global warming, make cheap space flight possible..."

"Still no."

"And quite possibly," he paused, spinning out the sentence, "come to the attention of a certain prize committee..."

I swallowed hard. When I gave up university life for teaching I'd abandoned all hope of academic recognition. Except that if this worked I might just...

It couldn't happen.

It might.

I'd look good in a dinner jacket in Stockholm.

I opened the door and slid out of the Land Rover, my feet crunching on the thin snow. Santa was peering into an open inspection cover at the front of the sleigh, prodding at the circuit boards inside with what looked like a long, thin, tree decoration connected to a portable logic analyser.

"Channel 17 is good," he said into the

headset. "It's showing a live cat." He paused. "Can you get one of the elves from the maths department? I want to know what will happen if I open it." Then he took off his headset and beamed at me. "Merry Christmas! Have you come to help?"

"I hope so. Can you tell me what happened?"

He paused for a moment, a worried smile on his face. "We'd taken off from Lapland as normal. About ten seconds into the climb-out I started getting high temperatures on three and four." He tapped the row of gauges built in to the sleigh's dashboard. The third and fourth were labelled 'Prancer' and 'Vixen'. "I aborted the equivalence at once. About three seconds later I lost power completely and made a forced landing."

I was calculating in my head.

"Lapland to Kent in 13 seconds is around 100 miles per second, way beyond escape velocity. You don't need aerodynamics, do you? It's just raw speed that makes it fly." Santa nodded. "Although how you manage to push through the atmosphere at Mach 500 without burning up defeats me."

The old man just smiled. "It is a mystery if you don't understand."

I got up onto the sleigh, sat on the bench seat and studied the instruments. There was a little rectangular screen showing a globe of the Earth, divided by lines of latitude and longitude, the spaces between them a chequer-board of light and dark patches. Two digital readouts were labelled  $\Delta_{EW}$  and  $\Delta_{NS}$ . Both showed zero. A little farther along was another display simply labelled 'h', and next to it was an impressive red handle. Almost automatically I wound my fingers around it, ready to pull. Santa jumped. For a moment there was a flash of real terror in his eyes, then he was jolly again. Whatever it was, I'd hit it. Lambda,  $h$  and a pattern tessellating the planet, this was the key to the whole thing. Pulling the big red lever could have disastrous consequences, only it wasn't working.

Which was why the sleigh was on the ground.

I sat back. When the sleigh was in what Santa called 'the equivalence', it whistled along, slipping through the atmosphere at speeds that would fill NASA with envy. The only thing that could overtake it was light.

The secret had to be in the reindeer, or rather in the composite of engineering and biology that sleigh and reindeer made together. Perhaps some weird twist

of evolution had produced a beast that existed partly on another brane, one with a much bigger value of Planck's constant. What if Santa had found some way to harness the multiversal nature of the reindeer, to mould a subtle and unstable biological process into useful technology?

There were about 15 digits on the 'h' display, although only a single zero glowed cheerily at the right-hand end.



No, it couldn't be ...

It was. The big red lever changed the value of Planck's constant for the sleigh. Changed it so that the sleigh could convert into a single photon. A photon with a wavelength of a few metres. I tried to visualize the effect of quantum mechanics happening on a macroscopic scale, of the sleigh having a definite wavelength.

So that was what the lambda gauges measured, although I couldn't see why the north-south and east-west wavelengths were different. The sleigh would become a standing wave, rather like an electron orbit, all around Earth. No, all over Earth.

The last section of the puzzle clicked into place. The pattern on the picture of Earth was a set of spherical harmonics, the standing wave that the sleigh became when the red handle was pulled. So that was how the old chap did it. He didn't have to rush around the planet, just convert into a standing wave that was everywhere on Earth simultaneously, and wait for the midnight line to pass right around the

world under him. At any time there was a very small probability of his being in any particular chimney, but averaged over the whole night he was everywhere, once.

So why had it stopped working? What had disrupted the delicate processes inside two of the reindeer and brought the sleigh crashing back into our world?

Rudolf wandered towards the sleigh, nose flickering like a disco in an LED factory, a silly grin on his face. Suddenly I had an idea.

"Santa! The two reindeer that had high temperatures, are they boys or girls?"

Santa laughed. "Everyone knows that Vixen is female, but the books are wrong about Prancer. She's a girl as well."

There's one thing that can happen to a female mammal that plays Old Harry with delicate internal processes. I turned to the squadron leader. "We need a veterinary surgeon, now."

Twenty minutes later it was all over. Prancer and Vixen had provided positive pregnancy tests; Blitzen was being awkward about letting us have a sample.

"Rudolf!" snapped Santa, "I've told you before!"

Rudolf's nose flared an embarrassed scarlet. Santa unwrapped a parcel and pulled out a slide rule. "I'll take off on reduced power and follow the great circle back to Lapland. I should get home before they overheat again. Then I'll swap Vixen and Prancer for Robbie and Rusty. The presents may be a few hours late but they'll still get there. Thanks, and Merry Christmas."

He whistled, and the reindeer lined up ready for the harness. Then he was on the seat with the reins in his hands, Rudolf's nose started to flash like an anti-collision beacon and the sleigh accelerated down the runway. I saw one fur-gloved hand reach out to pull the big red lever, then there was a flash, a rush of wind and the sleigh was a vanishing dot on the horizon.

That's why, every Christmas, I leave a packet of peppermints, a glass of sherry and a letter by the fireplace.

"Dear Santa, for Christmas I'd really like one present. How do reindeer change the value of Planck's constant?"

And every year I receive a photograph of Rudolf's growing family.

**Robert Billing records his gratitude to the late Kenneth Pascoe, of St John's College, Cambridge, who set a supervision question that, years later, triggered the idea for this story.**

JACEY

FUTURES